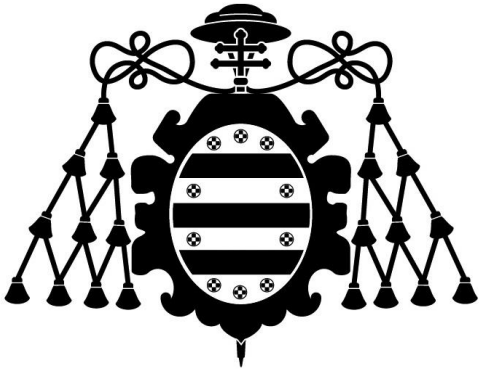

# UNIVERSIDAD DE OVIEDO

DEPARTAMENTO DE INGENIERÍA QUÍMICA Y TECNOLOGÍA DEL MEDIO AMBIENTE

Programa de Doctorado en Ingeniería Química, Ambiental y Bioalimentaria

# RECUPERACIÓN DE METANO A PARTIR DE CORRIENTES DE VENTEO EN MINAS DE CARBÓN UTILIZANDO MOFs COMO ADSORBENTES

TESIS DOCTORAL POR

**David Ursueguía Borja**

**2023**

Universidad de Oviedo

# RESUMEN DEL CONTENIDO DE TESIS DOCTORAL

| 1.- Título de la Tesis | |
|---|---|
| Español: Recuperación de metano a partir de corrientes de venteo en minas de carbón utilizando MOFs como adsorbentes | Inglés: Methane recovery from coal mining ventilation streams using MOFs as adsorbents |

| 2.- Autor | |
|---|---|
| Nombre: David Ursueguía Borja | |
| Programa de Doctorado: Ingeniería Química, Ambiental y Bioalimentaria | |
| Órgano responsable: Centro Internacional de Postgrado | |



## RESUMEN (en español)

La necesidad de fuentes de energía alternativa y la protección del medio ambiente son dos de las mayores preocupaciones mundiales. En la búsqueda de soluciones, además del desarrollo de nuevas fuentes energéticas renovables, es deseable el aprovechamiento y la mejora de procesos energéticos ya existentes, así como una mitigación eficaz de las emisiones más importantes. En este sentido, las emisiones de metano de baja concentración (0.1-1%) procedentes de la ventilación de la minería subterránea de carbón constituyen una fuente energética desaprovechada. Generalmente, estas corrientes son emitidas directamente a la atmósfera, o bien sometidas a un proceso de combustión con muy bajo rendimiento, malgastando la capacidad energética del metano, y emitiendo un gas con un importante potencial de efecto invernadero. Por tanto, la presente Tesis Doctoral plantea la posibilidad de capturar selectivamente dicho metano, evitando así su emisión, y concentrarlo posteriormente hasta valores adecuados para su aprovechamiento energético bajo rendimientos aceptables.

En la adsorción, técnica seleccionada para el proceso, la selección del material adsorbente es un parámetro fundamental. A partir de una revisión bibliográfica, se decide trabajar con metal-organic frameworks (MOFs), ya que muestran resultados muy prometedores en procesos de separación y almacenamiento de gases. Inicialmente, se seleccionan tres materiales comerciales (Basolite C300, Basolite F300 y Basolite A100), que se caracterizan morfológicamente y se estudia su rendimiento en la adsorción de metano y nitrógeno, cuya separación selectiva es clave para la concentración de metano. Dicha separación muestra ser muy dependiente de la presencia de open metal sites (OMS) estructurales, con mayor presencia en Basolite C300. Posteriormente, se realizan ensayos bajo condiciones similares a las reales en una explotación minera, entre las que destacan la presencia de humedad relativa (100%) y dióxido de carbono (0.1%). Los resultados revelan gran sensibilidad estructural y una disminución del rendimiento en presencia de humedad, especialmente en el caso de materiales con OMS. Por otro lado, los ensayos en lecho fijo muestran elevadas pérdidas de carga, debido al pequeño tamaño de partícula característico de los MOFs. Además, éstos muestran una gran sensibilidad al pelletizado mecánico, que provoca una destrucción de la cristalinidad, en un intento de incrementar el tamaño de partícula de manera sencilla. Finalmente, la multiplicidad de condiciones probadas, especialmente en lecho fijo, permite la elaboración de un modelo matemático diferencial que describa el proceso de adsorción. Tras la validación experimental, el modelo se emplea en la simulación de escenarios a mayor escala, aplicando distintas tecnologías de adsorción (temperature-swing adsorption y pressure-swing adsorption), optimizando condiciones, e incluso integrando el proceso de recuperación y concentración de metano con una turbina de gas pobre. Como resultado se obtiene un análisis económico desfavorable, principalmente debido al elevado coste actual de los MOFs comerciales, con una baja implantación industrial.

En consecuencia, se propone la síntesis de materiales compuestos, consistentes en el soporte de un MOF sobre partículas de un material mesoporoso, con propiedades favorables a la adsorción y separación de metano, con un tamaño de partícula adecuado y elevada resistencia a la humedad. De este modo, se han sintetizado combinaciones de HKUST-1 (homólogo al

Basolite C300) soportado sobre partículas de alúmina mediante distintos métodos de impregnación (solvotermal y dip-coating). Por un lado, el método de síntesis a gran escala del MOF y el bajo coste de la alúmina abaratan el proceso, mientras que el elevado tamaño de partícula disminuye la caída de presión. Además, el buen rendimiento del MOF y la gran hidrofilicidad de la alúmina actúan en sinergia y disminuyen el efecto del agua sobre la capacidad de adsorción del MOF, especialmente a bajas cargas. Los resultados son prometedores en relación a la aplicación de estos materiales en procesos bajo condiciones reales.

**RESUMEN (en inglés)**

Alternative energy sources and the environmental protection are two of the major global concerns. In the search for solutions, in addition to the development of renewable energetic sources, it is desirable the exploitation and the improvement of the already existing energy-related processes, as well as the effective mitigation of the most important emissions. In this way, low-grade (0.1-1%) methane emissions from underground coal mining exploitations constitute an unprofitable energy source. Generally, these streams are emitted directly to the atmosphere or introduced in a combustion process with very low yields, wasting the large energetic capacity of methane, and emitting a stream with an important global warming potential (GWP). Therefore, this PhD Thesis raises the possibility of selectively capturing this methane, avoiding its emission, and then concentrate it to appropriate values to its thermal upgrading with acceptable yields.

In adsorption, selected technique for the process, the fundamental parameter is the adsorbent material selection. From a literature review, metal-organic frameworks (MOFs) are the most promising materials both in gas separation and storage. Firstly, three commercial materials are selected (Basolite C300, Basolite F300 and Basolite A100), which are characterized morphologically and studied in methane and nitrogen adsorption, whose selective separation is key to the methane concentration. This separation shows to be very dependent on the presence of structural open metal sites (OMS), with major presence in Basolite C300. In a second part, essays in conditions similar to those of a coal mine are carried out, highlighting the presence of relative humidity (100%) and carbon dioxide (0.1%). Results reveal large structural sensitivity and a performance decrease in presence of humidity, especially in the case of materials with OMS. On the other hand, fixed-bed tests show elevated pressure drops, due to the small particle size characteristic of MOFs. Further, MOFs show large sensitivity to mechanical pelletizing, which destroys the crystallinity, after an attempt to increase the particle size in an easy way. Finally, the variety of tested conditions, especially in fixed-bed, allows to build a differential mathematical model whose solution describes the adsorption process. After the experimental validation, the model is used in the simulation of large-scale scenarios applying different technologies (temperature-swing adsorption and pressure-swing adsorption), optimizing conditions and even in the integration of the recovery and concentration process with a lean-gas turbine. Results show an adverse economic balance, mainly due to the elevated cost of commercial MOFs, with a low industrial implantation.

Consequently, it is proposed the synthesis of composites, consisting of the MOF support on particles of a mesoporous material, with favourable conditions to methane adsorption and separation, with an adequate particle size and elevated resistance to humidity. In this way, combinations of HKUST-1 (homologous to Basolite C300) supported on alumina particles are synthesized by different methodologies (solvothermal and dip-coating). On the one hand, the large-scale synthesis method of the MOF and the alumina low cost make cheaper the process, whereas the large particle size decreases the pressure drop. On the other hand, the good performance of the MOF and the large hydrophilicity of the alumina act in synergy and decrease the water effect on the adsorption capacity of the MOF, especially at low loads. Results are promising in relation to the application of these materials to actual conditions.

**SR. PRESIDENTE DE LA COMISIÓN ACADÉMICA DEL PROGRAMA DE DOCTORADO EN INGENIERÍA QUÍMICA, AMBIENTAL Y BIOALIMENTARIA**

# ÍNDICE GENERAL

# RESUMEN

La necesidad de fuentes de energía alternativa y la protección del medio ambiente son dos de las mayores preocupaciones mundiales. En la búsqueda de soluciones, además del desarrollo de nuevas fuentes energéticas renovables, es deseable el aprovechamiento y la mejora de procesos energéticos ya existentes, así como una mitigación eficaz de las emisiones más importantes. En este sentido, las emisiones de metano de baja concentración (0.1-1%) procedentes de la ventilación de la minería subterránea de carbón constituyen una fuente energética desaprovechada. Generalmente, estas corrientes son emitidas directamente a la atmósfera, o bien sometidas a un proceso de combustión con muy bajo rendimiento, malgastando la capacidad energética del metano, y emitiendo un gas con un importante potencial de efecto invernadero. Por tanto, la presente Tesis Doctoral plantea la posibilidad de capturar selectivamente dicho metano, evitando así su emisión, y concentrarlo posteriormente hasta valores adecuados para su aprovechamiento energético bajo rendimientos aceptables.

En la adsorción, técnica seleccionada para el proceso, la selección del material adsorbente es un parámetro fundamental. A partir de una revisión bibliográfica, se decide trabajar con *metal-organic frameworks* (MOFs), ya que muestran resultados muy prometedores en procesos de separación y almacenamiento de gases. Inicialmente, se seleccionan tres materiales comerciales (Basolite C300, Basolite F300 y Basolite A100), que se caracterizan morfológicamente y se estudia su rendimiento en la adsorción de metano y nitrógeno, cuya separación selectiva es clave para la concentración de metano. Dicha separación muestra ser muy dependiente de la presencia de *open metal sites* (OMS) estructurales, con mayor presencia en Basolite C300. Posteriormente, se realizan ensayos bajo condiciones similares a las reales en una explotación minera, entre las que destacan la presencia de humedad relativa (100%) y dióxido de carbono (0.1%). Los resultados revelan gran sensibilidad estructural y una disminución del rendimiento en presencia de humedad, especialmente en el caso de materiales con OMS. Por otro lado, los ensayos en lecho fijo muestran

elevadas pérdidas de carga, debido al pequeño tamaño de partícula característico de los MOFs. Además, éstos muestran una gran sensibilidad al pelletizado mecánico, que provoca una destrucción de la cristalinidad, en un intento de incrementar el tamaño de partícula de manera sencilla. Finalmente, la multiplicidad de condiciones probadas, especialmente en lecho fijo, permite la elaboración de un modelo matemático diferencial que describa el proceso de adsorción. Tras la validación experimental, el modelo se emplea en la simulación de escenarios a mayor escala, aplicando distintas tecnologías de adsorción (*temperature-swing adsorption* y *pressure-swing adsorption*), optimizando condiciones, e incluso integrando el proceso de recuperación y concentración de metano con una turbina de gas pobre. Como resultado se obtiene un análisis económico desfavorable, principalmente debido al elevado coste actual de los MOFs comerciales, con una baja implantación industrial.

En consecuencia, se propone la síntesis de materiales compuestos, consistentes en el soporte de un MOF sobre partículas de un material mesoporoso, con propiedades favorables a la adsorción y separación de metano, con un tamaño de partícula adecuado y elevada resistencia a la humedad. De este modo, se han sintetizado combinaciones de HKUST-1 (homólogo a Basolite C300) soportado sobre partículas de alúmina mediante distintos métodos de impregnación (solvotermal y *dip-coating*). Por un lado, el método de síntesis a gran escala del MOF y el bajo coste de la alúmina abaratan el proceso, mientras que el elevado tamaño de partícula disminuye la caída de presión. Además, el buen rendimiento del MOF y el carácter hidrofílico de la alúmina actúan en sinergia y disminuyen el efecto del agua sobre la capacidad de adsorción del MOF, especialmente a bajas cargas. Los resultados son prometedores en relación a la aplicación de estos materiales en procesos bajo condiciones reales.

# ABSTRACT

Alternative energy sources and the environmental protection are two of the major global concerns. In the search for solutions, in addition to the development of renewable energetic sources, it is desirable the exploitation and the improvement of the already existing energy-related processes, as well as the effective mitigation of the most important emissions. In this way, low-grade (0.1-1%) methane emissions from underground coal mining exploitations constitute an unprofitable energy source. Generally, these streams are emitted directly to the atmosphere or introduced in a combustion process with very low yields, wasting the large energetic capacity of methane, and emitting a stream with an important global warming potential (GWP). Therefore, this PhD Thesis raises the possibility of selectively capturing this methane, avoiding its emission, and then concentrate it to appropriate values to its thermal upgrading with acceptable yields.

In adsorption, selected technique for the process, the fundamental parameter is the adsorbent material selection. From a literature review, metal-organic frameworks (MOFs) are the most promising materials both in gas separation and storage. Firstly, three commercial materials are selected (Basolite C300, Basolite F300 and Basolite A100), which are characterized morphologically and studied in methane and nitrogen adsorption, whose selective separation is key to the methane concentration. This separation shows to be very dependent on the presence of structural open metal sites (OMS), mainly in Basolite C300. In a second part, essays in conditions similar to those of a coal mine are carried out, highlighting the presence of relative humidity (100%) and carbon dioxide (0.1%). Results reveal large structural sensitivity and a performance decrease in presence of humidity, especially in the case of materials with OMS. On the other hand, fixed-bed tests show elevated pressure drops, due to the small particle size characteristic of MOFs. Further, MOFs show large sensitivity to mechanical pelletizing, which destroys the crystallinity, after an attempt to increase the particle size in an easy way. Finally, the variety of tested conditions, especially in fixed-bed, allows to build a differential mathematical model whose solution describes the adsorption process. After the experimental validation, the model is used in the simulation

of large-scale scenarios applying different technologies (temperature-swing adsorption and pressure-swing adsorption), optimizing conditions and even in the integration of the recovery and concentration process with a lean-gas turbine. Results show an adverse economic balance, mainly due to the elevated cost of commercial MOFs, with a low industrial implantation.

Consequently, it is proposed the synthesis of composites, consisting of the MOF support on particles of a mesoporous material, with favourable conditions to methane adsorption and separation, with an adequate particle size and elevated resistance to humidity. In this way, combinations of HKUST-1 (homologous to Basolite C300) supported on alumina particles are synthesized by different methodologies (solvothermal and dip-coating). On the one hand, the large-scale synthesis method of the MOF and the alumina low cost make cheaper the process, whereas the large particle size decreases the pressure drop. On the other hand, the good performance of the MOF and the large hydrophilicity of the alumina act in synergy and decrease the water effect on the adsorption capacity of the MOF, especially at low loads. Results are promising in relation to the application of these materials to actual conditions.

# LISTA DE FIGURAS

# LISTA DE TABLAS

# DIFUSIÓN DE LA TESIS DOCTORAL

## ARTÍCULOS CIENTÍFICOS

A continuación, se indican los artículos que forman parte de la presente Tesis Doctoral. Se añaden por orden cronológico de publicación:

-1- D. Ursueguía, E. Díaz, S. Ordóñez. Adsorption of methane and nitrogen on Basolite MOFs: Equilibrium and kinetic studies. *Microporous and Mesoporous Materials* **298** (2020) 110048.

-2- D. Ursueguía, E. Díaz, A. Vega, S. Ordóñez. Methane separation from diluted mixtures by fixed bed adsorption using MOFs: Model validation and parametric studies. *Separation and Purification Technology* **251** (2020) 117374.

-3- D. Ursueguía, E. Díaz, S. Ordóñez. Densification-induced structure changes in Basolite MOFs: Effect on low-pressure $CH_4$ adsorption. *Nanomaterials* **10** (2020) 1089.

-4- D. Ursueguía, P. Marín, E. Díaz, S. Ordóñez. A new strategy for upgrading ventilation air methane emissions combining adsorption and combustion in a lean-gas turbine. *Journal of Natural Gas Science and Engineering* **88** (2021) 103808.

-5- D. Ursueguía, E. Díaz, S. Ordóñez. Metal-organic frameworks (MOFs) as methane adsorbents: From storage to diluted coal mining streams concentration. *Science of the Total Environment* **790** (2021) 148211.

-6- D. Ursueguía, E. Díaz, S. Ordóñez. Adsorbents selection for the enrichment of low-grade methane coal mine emissions by temperature and Pressure swing adsorption technologies. *Journal of Natural Gas Science and Engineering* **105** (2022) 104721.

-7- D. Ursueguía, C. Daniel, C. Collomb, C. Cardenas, D. Farrusseng, E. Díaz, S. Ordóñez. Evaluation of HKUST-1 as volatile organic compound adsorbents for respiratory filters. *Langmuir* **38** (2022) 14465-14474.

-8- D. Ursueguía, E. Díaz, S. Ordóñez. Effect of water and carbon dioxide on the performance of Basolite MOFs for methane adsorption. Enviada a revista: *Journal of Industrial and Engineering Chemistry.*

-9- D. Ursueguía, E. Díaz, S. Ordóñez, Improved stability and adsorption performance of HKUST-1@$Al_2O_3$ composites for methane recovery. Enviada a revista: *Separation and Purification Technology.*

## COMUNICACIONES A CONGRESO

Durante el desarrollo de la Tesis Doctoral, se han enviado las siguientes comunicaciones a congreso. Se añaden por orden cronológico de defensa:

-1- D. Ursueguía, E. Díaz, S. Ordóñez. Preconcentración de metano procedente de una corriente de venteo de la minería del carbón para su valorización química. *SECAT'19 Catálisis para el futuro: Avances en estructuras, procesos y aplicaciones*. Córdoba, 24, 25 y 26 de junio de 2019. Comunicación **Póster**.

-2- D. Ursueguía. Caracterización de Metal-Organic Frameworks comerciales para uso en adsorción y catálisis heterogénea. *IV Encuentro de Jóvenes Investigadores de la SECAT*. Bilbao, 21-23 de septiembre de 2020. Comunicación **Oral**.

-3- E. Díaz, D. Ursueguía, S. Ordóñez. Effect of water on the methane adsorption performance of commercial Basolite metal-organic frameworks (MOFs). *RSEQ Symposium 2021*. Online, 27-30 septiembre 2021. Comunicación **Póster**.

-4- D. Ursueguía, E. Díaz, S. Ordóñez. Selection of materials and adsorption technologies for methane upgrading from coal mine emissions. *CIS-2021 Young Researchers*. Online, 6-8 septiembre 2021. Comunicación **Oral**.

-5- D. Ursueguía, E. Díaz, S. Ordóñez. Water effect on the performance of Basolite MOFs for methane adsorption and recovery. *20$^{th}$ International Zeolite Conference (IZC)*. Valencia, 3-8 julio 2022. Comunicación **Póster**.

-6- D. Ursueguía, E. Díaz, S. Ordóñez. Enhanced structural water resistance of polar metal-organic frameworks by supporting on hydrophilic supports. *International Congress on Separation and Purification Technology*. Online, 10-14 diciembre. Comunicación **Oral**.

-7- D. Ursueguía, E. Díaz, S. Ordóñez, C. Collomb, C. Cardenas, C. Daniel, D. Farrusseng. Evaluation of HKUST-1 as volatile organic compounds adsorbent for respiratory filters. *12èmes Journées Annuelles de l'AFA*. Nancy, 26-27 enero 2023. Comunicación **Póster**.

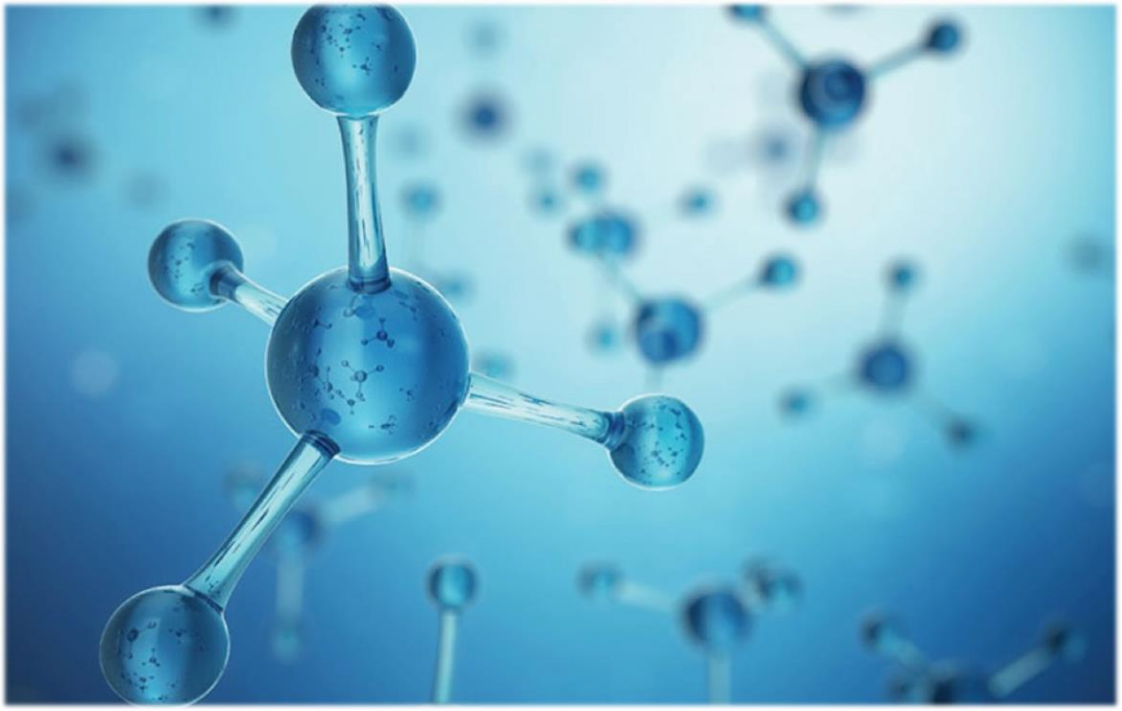

# 1. INTRODUCCIÓN

1.1. Antecedentes: Problemática energética y ambiental

1.2. Gases de efecto invernadero: El metano

1.3. Carbón como combustible: Minería y emisiones

1.4. Recuperación y aprovechamiento de VAM: Adsorción

1.5. Referencias

## 1.1. ANTECEDENTES: PROBLEMÁTICA ENERGÉTICA Y AMBIENTAL

Actualmente, los esfuerzos tecnológicos relativos al sector energético se centran en la búsqueda de fuentes de energía y combustibles alternativos a los fósiles y nucleares. En el caso de los combustibles, el desarrollo tecnológico es lento, ya que el primer motor en funcionamiento con aceite vegetal como combustible data de 1897 [1]. En cambio, no es hasta la Directiva de la Unión Europea del 22 de octubre de 2014 cuando se sientan las bases que implementan de forma definitiva estos combustibles en el mercado, aún con cuotas muy reducidas, en torno al 10% [2]. Por el contrario, las fuentes de energía alternativa —hidráulica, geotérmica, solar, eólica, mareomotriz y biomasa— están más implantadas en la sociedad actual. En especial, el inicio del siglo XXI ha supuesto un punto de inflexión en el uso de estas tecnologías en varios países, como España, con el Plan de Fomento de las Energías Renovables [3], o Estados Unidos, con una clara tendencia al alza en energía renovable total generada desde el año 2003 (Figura 1.1). Sin embargo, la energía renovable supuso únicamente un 20% del consumo total de energía entre los años 2003 y 2015, según un informe del REN21 [4]. Ambas estadísticas muestran una gran dependencia energética hacia los combustibles fósiles.

Por otra parte, en la situación actual, un mundo totalmente globalizado con una gran dependencia energética entre naciones, se incrementa la

inseguridad con respecto a un desabastecimiento energético [5]. Esta incertidumbre ha alcanzado un máximo en febrero de 2022, al desencadenarse el episodio bélico conocido popularmente como Guerra de Ucrania. El conflicto ha tensado las relaciones de Rusia con el resto de Europa, siendo el país ruso el principal suministrador de gas natural y petróleo de ciertos países europeos, como Alemania [6]. En consecuencia, en Europa, con alrededor de un 58% de la energía consumida importada [7], la situación de inestabilidad ha llevado a algunos países a plantearse la reapertura de centrales térmicas, nucleares y plantas regasificadoras, previamente en desuso [8]. En este contexto, los gobiernos miran hacia una transición ecológica como una vía de escape de la gran dependencia energética de otros países. En cambio, frente a estos modelos de transición, de momento se impone el modelo energético implantado en Europa desde la Primera (s. XVIII) y la Segunda (s. XIX) Revolución Industrial, con los combustibles fósiles —carbón, petróleo y gas natural— como eje central de una producción a gran escala y una expansión total de los medios de transporte y comunicación [9, 10].

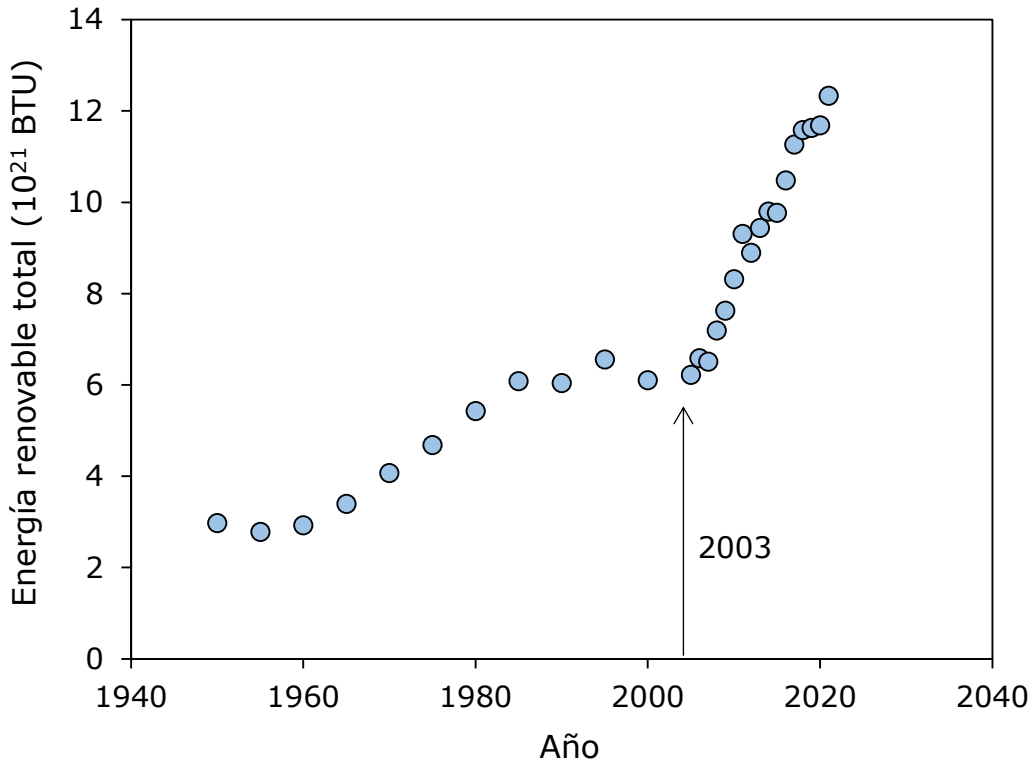


Figura 1.1. Energía total generada a partir de fuentes alternativas (hidroeléctrica, geotérmica, solar, eólica y biomasa) en los Estados Unidos entre los años 1950 y 2021. Fuente: U.S. Energy Information Administration [11].

En la misma línea, en las últimas décadas, un crecimiento poblacional exponencial, así como una intensa globalización, que conlleva la deslocalización de grandes industrias hacia países subdesarrollados con una legislación ambiental más permisiva, han provocado un agravamiento de la problemática ambiental asociada al uso de combustibles fósiles [12]. El ritmo de consumo actual, con la India emergiendo como un gran consumidor de carbón, la utilización del petróleo fuera del ámbito energético y el incremento del uso del gas natural en los países más desarrollados, pone de manifiesto la gran dependencia existente hacia los combustibles fósiles [13]. Las emisiones asociadas a su uso han provocado una tendencia creciente de la temperatura media global, que se ha visto notablemente incrementada en las últimas décadas, especialmente a partir de 1970, coincidiendo con el auge de la utilización y necesidad de combustibles y energía (Figura 1.2).

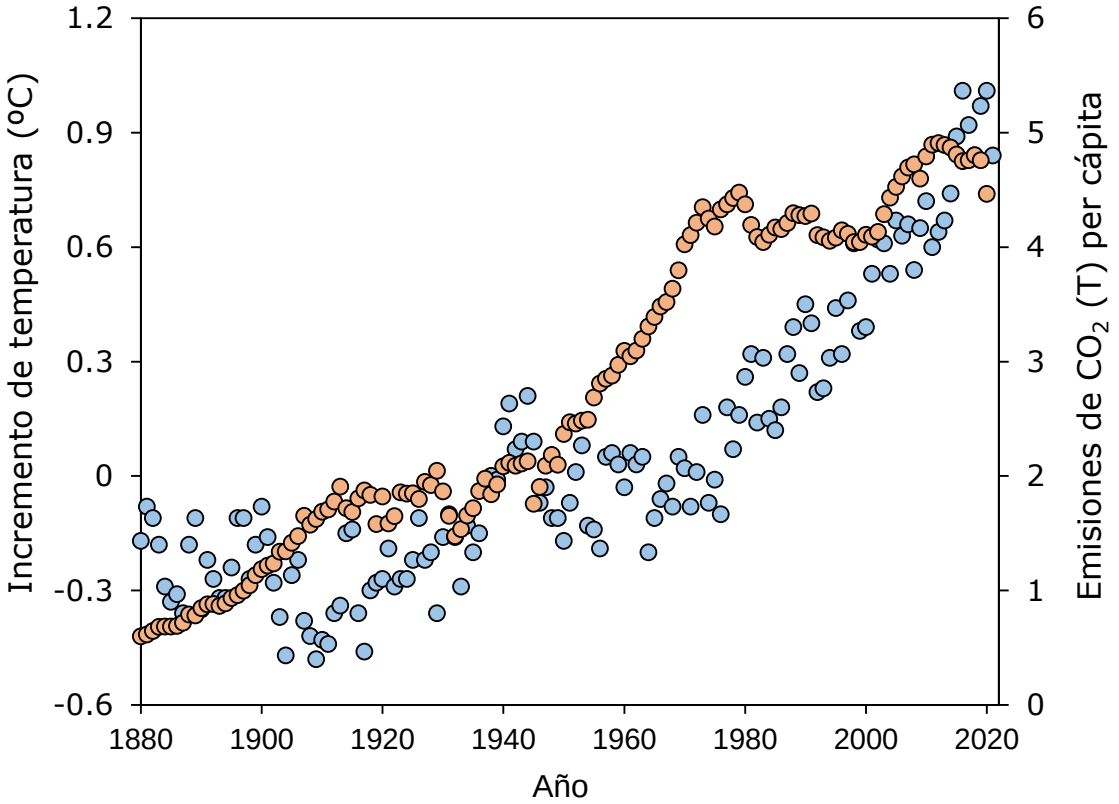


Figura 1.2. Incremento de la temperatura media terrestre (azul) en función del año, y su relación con las emisiones mundiales totales de $CO_2$ per cápita (naranja). Adaptado de [12, 14].

Multitud de expertos y organizaciones, entre ellas la Organización Mundial de la Salud (OMS) y el Panel Intergubernamental del Cambio

Climático (IPCC), consideran el calentamiento global como uno de los mayores desafíos del mundo moderno [15, 16]. Este aumento a largo plazo de la temperatura media del planeta depende directamente de la concentración de gases de efecto invernadero —dióxido de carbono, metano, óxido nitroso, ozono y clorofluorocarbonos— en la atmósfera, y está continuamente agravado por la acción humana [17]. En efecto, las restricciones de movilidad a causa de la COVID-19 redujeron notablemente las emisiones de gases de efecto invernadero en las grandes ciudades [18], poniendo de manifiesto la relevante influencia antropogénica en dicho efecto. El calentamiento global influye gravemente en la climatología (Figura 1.3), daña ecosistemas [19], y ya supone elevados costes con relación a bajas por enfermedad y facturas médicas en todo el mundo [20].

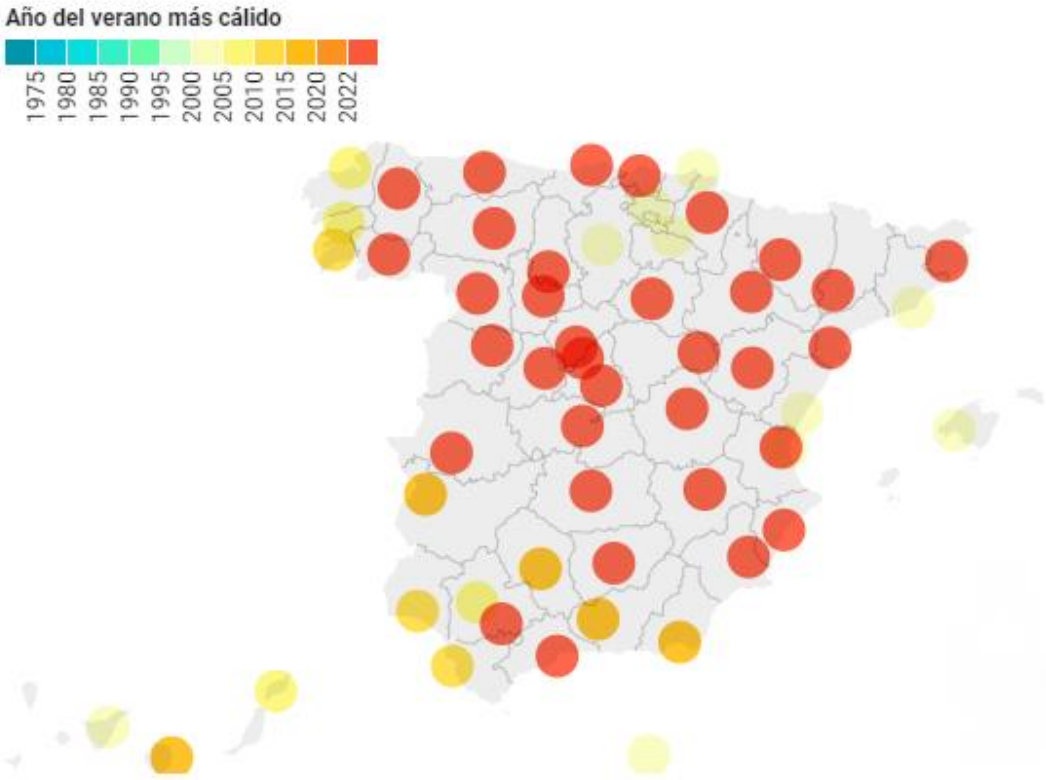


Figura 1.3. Mapa de España en el que se indica el verano más cálido desde que existen registros provinciales. Fuente: Agencia Estatal de Meteorología (AEMET) [21].

Estos hechos, junto a la fuerte presión ejercida por parte de algunos sectores activistas ambientales, han situado a la problemática ambiental en el punto de mira de los gobiernos de los países desarrollados. Uno de los países más contribuyentes al calentamiento global es China, con una gran

población y una economía totalmente orientada hacia la exportación, lo que supone un país con una gran demanda energética, suplida principalmente por combustibles fósiles, y un consecuente grave problema de contaminación atmosférica [22, 23]. En consecuencia, el progresivo aumento en el consumo de combustibles fósiles se torna en inestabilidad política, económica y social, en una situación en la que las energías renovables únicamente cubren el 20% de la demanda total.

La gran preocupación de los expertos y gobiernos se pone de manifiesto en el número de cumbres mundiales, con el cambio climático y su relación con el uso de la energía como eje central, acaecidas desde 1992, que asciende a 15. Entre estas cumbres, Conferencias de Naciones Unidas sobre Cambio Climático (COP), una de las más notables fue la COP21, que dio lugar al Acuerdo de París. Este acuerdo establece como objetivo principal el mantener un aumento de temperatura global promedio por debajo de los 2ºC respecto a niveles preindustriales. El acuerdo entró en vigor el 4 de noviembre de 2016, tratándose de un tratado internacional legalmente vinculante [24]. Para su cumplimiento, es urgente una reducción significativa de las emisiones gaseosas de efecto invernadero [25], con el menor impacto social y económico posible.

## 1.2. GASES DE EFECTO INVERNADERO: EL METANO

### 1.2.1. Principales gases de efecto invernadero

De acuerdo con un estudio realizado en el año 2020 por parte de la Agencia de Protección Ambiental de los Estados Unidos (EPA), los gases de efecto invernadero más emitidos son: dióxido de carbono (79%), metano (11%), óxido nitroso (7%) y gases fluorados (3%). Como resultado de estas emisiones, el dióxido de carbono es el gas de efecto invernadero más concentrado en la atmósfera (410 ppm), seguido por el metano (1800 ppb), óxido nitroso (330 ppb) y el resto de gases con concentraciones en el rango de partes por trillón (ppt) [26]. El mismo estudio confirma una tendencia claramente creciente de todos ellos, especialmente desde 1920, en pleno auge de la época industrial, cuando se superó el límite histórico de concentración de dióxido de carbono en la atmósfera, correspondiente a

300 ppm. Dado que el dióxido de carbono es el gas de efecto invernadero más emitido y concentrado, éste se toma generalmente como referencia, y el efecto nocivo del resto de gases se estima en función del potencial de calentamiento global estándar —*global warming potential* (GWP)— del dióxido de carbono en un período de tiempo determinado, generalmente 100 años. A partir de dicha clasificación, es posible conocer los principales gases de efecto invernadero y su potencial efecto nocivo (Tabla 1.1).

Tabla 1.1. Principales gases de efecto invernadero con sus características. Adaptado de [27].

| Gas | GWP (100 años) | Vida media (años) |
|---|---|---|
| Dióxido de carbono ($CO_2$) | 1 | 100 |
| Metano ($CH_4$) | 25 | 12 |
| Óxido nitroso ($N_2O$) | 265 | 121 |
| CFC-12 ($CCl_2F_2$) | 10200 | 100 |
| HFC-23 ($CHF_3$) | 12400 | 222 |
| Hexafluoruro de azufre ($SF_6$) | 23500 | 3200 |
| Trifluoruro de nitrógeno ($NF_3$) | 16100 | 500 |

### 1.2.2. Principales fuentes emisoras de gases de efecto invernadero

Además de conocer los principales gases de efecto invernadero y su potencial de calentamiento global, es clave establecer los sectores productivos más contribuyentes, con el objetivo de localizar y realizar un control más eficaz de las emisiones. En el caso del total de los gases de efecto invernadero emitidos en la Unión Europea en 2019, un 77% es atribuible al sector energético, seguido de un 10 y 9% correspondientes al sector agrónomo y los procesos industriales, respectivamente. Finalmente, un 3% corresponde a la gestión de residuos. El país que registra mayores emisiones de la Unión Europea es Alemania, con 810 kT eq. $CO_2$, seguido de Reino Unido, con 453 (Figura 1.4). La gran diferencia entre ambos se debe a la fuerte apuesta alemana por el carbón como fuente energética. A mayor escala, China ($1.3 \cdot 10^7$ kT eq. $CO_2$) y Estados Unidos ($6.4 \cdot 10^6$ kT eq. $CO_2$)

superan incluso al conjunto de la Unión Europea, que asciende a $4.5 \cdot 10^6$ kT eq. $CO_2$ [28].

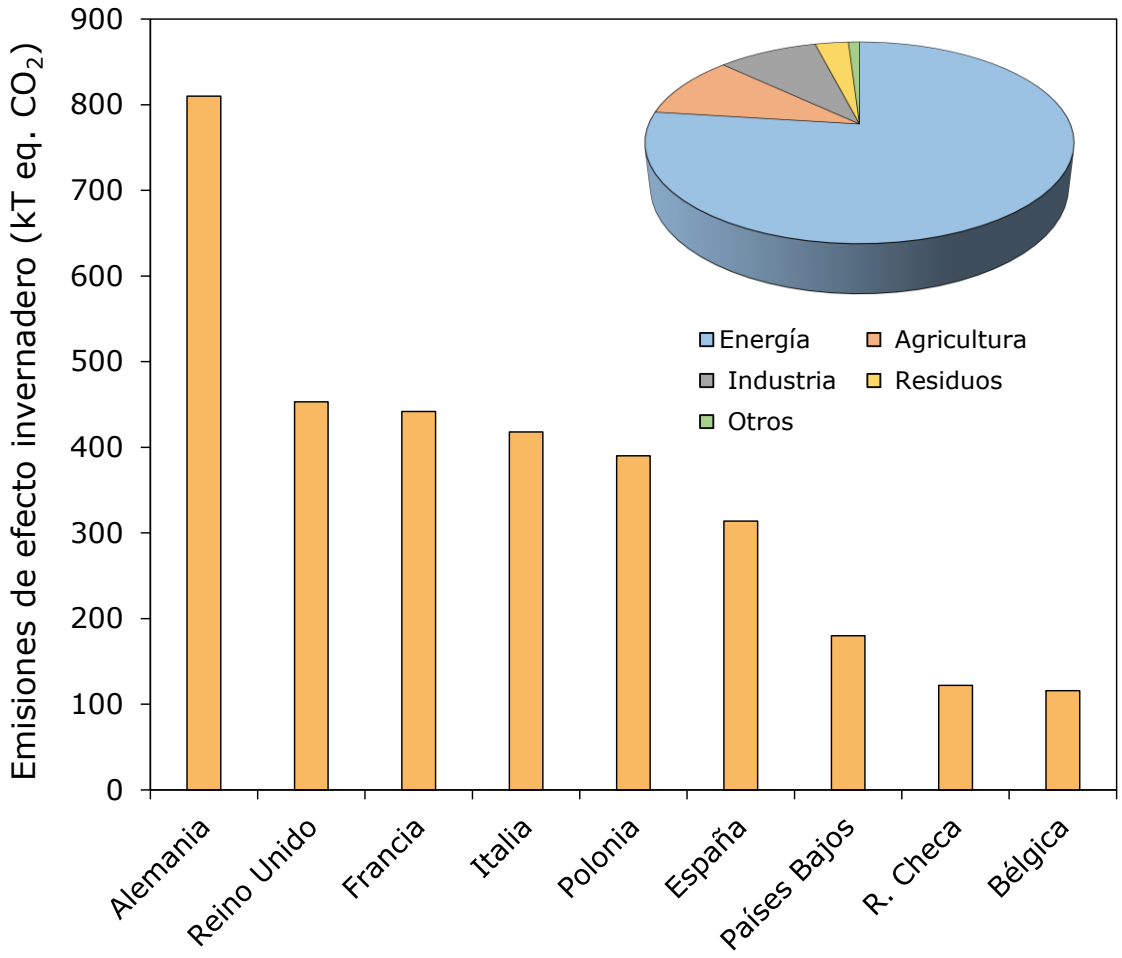


Figura 1.4. Emisiones de efecto invernadero de los principales países de la UE, junto con el porcentaje de los sectores productivos más contaminantes. Adaptado de [28].

Si se realiza un desglose por gases [29], las emisiones de dióxido de carbono proceden principalmente del sector del transporte (33%), relacionado con la utilización de combustibles fósiles, como la gasolina y el diésel (Figura 1.5). La generación de electricidad supone un 31%, mientras que un 16% corresponde a los procesos industriales que requieren energía o generan dióxido de carbono. El resto se corresponde con la agricultura y la ganadería (15%) y otros sectores (5%). En el caso del metano, el sector más importante es el del gas natural y el petróleo (32%), atribuible a emisiones fugitivas durante su producción, procesado, almacenamiento y distribución. Por otro lado, la fermentación entérica en el proceso digestivo del ganado produce emisiones de metano (27%), seguido de las emisiones fugitivas

procedentes de vertederos (17%). Por último, las emisiones de metano asociadas a la minería subterránea de carbón suponen un 6% del total, mientras que el resto (18%) se corresponde con procesos industriales, uso de la tierra y combustibles, entre otros. En el caso de los gases minoritarios, las emisiones de óxido nitroso proceden de la agricultura y el tratamiento del suelo (75%), debido al uso de fertilizantes. El resto procede de otros sectores (25%), como procesos industriales, residuos o emisiones fugitivas. Finalmente, los compuestos fluorados se emiten mayoritariamente en procesos en los que actúan como sustitutos de los compuestos clorofluorocarbonados (CFCs), en sistemas de refrigeración y como propulsores de aerosoles (93%). El resto se debe principalmente a emisiones industriales fugitivas (7%).

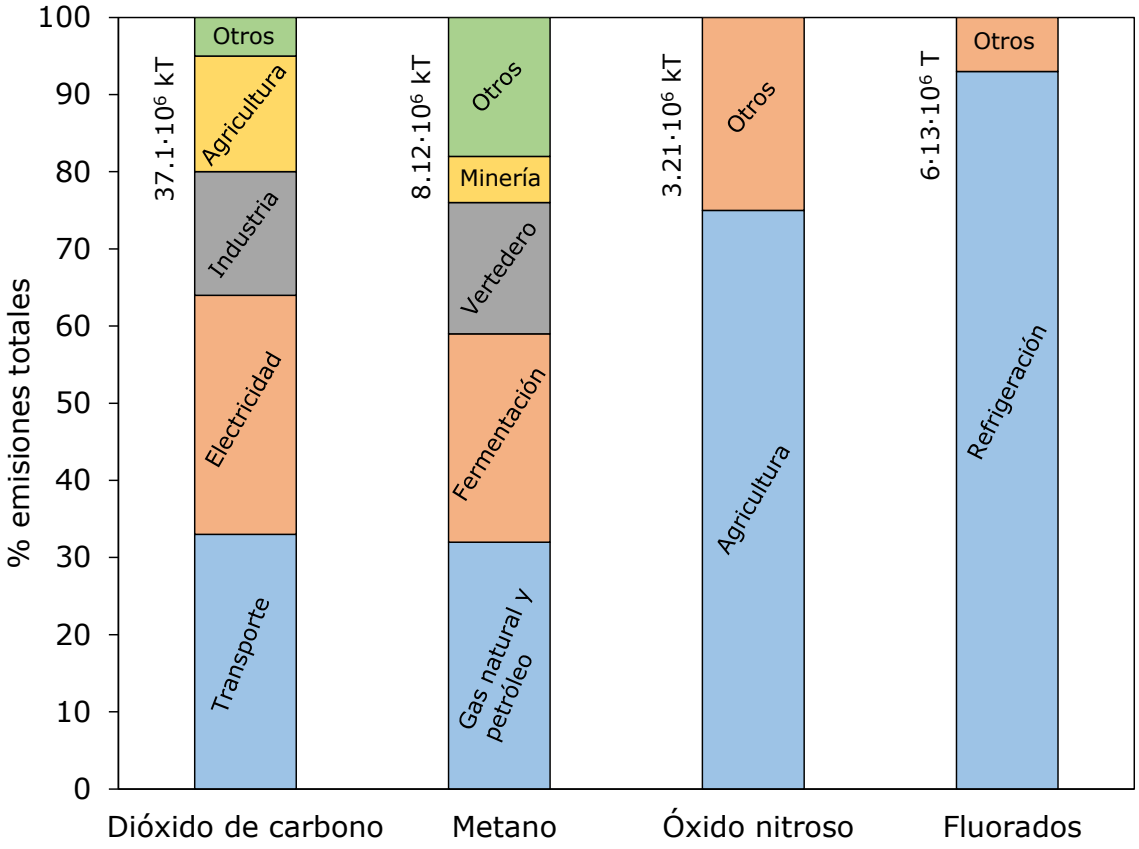


Figura 1.5. Distribución por sectores de las emisiones de los principales gases de efecto invernadero y emisiones mundiales totales. Adaptado de [28].

La clara predominancia de las emisiones de dióxido de carbono provoca que la gran mayoría de los objetivos y medidas propuestos vayan orientados hacia una descarbonización relativa a este gas. El último paquete de medidas

a nivel europeo, aprobado en diciembre de 2019, conforma el Pacto Verde Europeo, que pretende alcanzar una neutralidad climática en Europa en el año 2050. En consecuencia, se establece el denominado Objetivo 55 en julio de 2021, que traduce esta ambición en legislación vinculante. Entre las distintas rutas de acción presentadas, destacan el fomento de las energías renovables, el endurecimiento de la normativa de emisiones para turismos y furgonetas, el control de las emisiones en la aviación y el transporte marítimo, así como ajustes en el régimen comercial de los derechos de emisión [29]. Como se puede observar, las medidas están ligadas estrechamente al sector del transporte y la energía, causantes de más de un 60% de las emisiones de dióxido de carbono. En este sentido, y con el objetivo de alcanzar la neutralidad climática, es necesario tener en cuenta el resto de gases de efecto invernadero, especialmente el metano, que constituye un 11% de las emisiones totales. Además, el metano presenta un potencial de calentamiento global 25 veces mayor que el dióxido de carbono (Tabla 1.1). En consecuencia, el IPCC indica que también es necesaria una reducción significativa de los gases de efecto invernadero distintos del dióxido de carbono para mantener el calentamiento global por debajo de los 2ºC marcados como objetivo [30]. Por tanto, un control eficaz de las emisiones de metano contribuiría en gran medida a la consecución del objetivo fijado.

Si se analizan las emisiones totales de metano en los países más desarrollados, con una menor importancia del sector ganadero [31], se observa que a la cabeza se encuentran las emisiones fugitivas de metano. En el caso de los vertederos, la gran mayoría cuenta con sistemas de extracción en profundidad —pozos verticales— que evitan la formación de bolsas de metano, así como un posterior aprovechamiento energético de las emisiones [32]. La casuística es diferente en el caso de las emisiones fugitivas procedentes de la industria del gas natural y el petróleo, cuya deslocalización y discontinuidad hacen que la solución pase por la implementación de sistemas *leak detection and repair* (LDAR) eficaces, con una frecuencia de control y una sensibilidad adecuada a cada instalación [33]. Finalmente, las emisiones fugitivas de baja concentración procedentes de la minería subterránea de carbón han llegado a suponer cerca de un 2% del total mundial de las emisiones gaseosas de efecto invernadero [34]. Los elevados

caudales y la baja concentración de metano dificultan en gran medida el aprovechamiento de las emisiones, e incluso su mitigación. En efecto, hasta el momento únicamente se han aplicado, de manera general, técnicas de combustión para obtener dióxido de carbono y agua, y reducir así el potencial de calentamiento global de la emisión, a costa de un bajo rendimiento [35]. De hecho, si se aplica el cálculo de la huella de carbono a las explotaciones mineras subterráneas de carbón, se identifican las emisiones fugitivas como la mayor contribución al impacto ambiental del proceso [36]. En esta línea, es necesario buscar alternativas para la mitigación eficaz e incluso aprovechamiento de estas emisiones, pudiendo reducir el gran potencial de efecto invernadero del metano y al mismo tiempo aprovechar su gran potencial energético.

## 1.3. CARBÓN COMO COMBUSTIBLE: MINERÍA Y EMISIONES

Entre los principales combustibles fósiles existentes —carbón, petróleo y gas natural—, el carbón ha sido el más utilizado históricamente. Sin embargo, a raíz de la creciente preocupación ambiental y el consecuente Pacto de París, el carbón se ha clasificado como el más nocivo de los combustibles fósiles, reduciendo drásticamente su utilización en los países con regulaciones ambientales restrictivas. La quema de carbón genera elevadas emisiones de dióxido de carbono, así como otros compuestos contaminantes (óxidos de nitrógeno, óxidos de azufre y materia particulada), contribuyendo al calentamiento global, entre otros efectos, como la lluvia ácida. Además, la principal vía de obtención de este mineral, la minería subterránea, también ha demostrado ser un foco importante de emisiones, en forma de metano, por lo que se ha comenzado la clausura de las explotaciones mineras en toda Europa. Sin embargo, países europeos como Polonia o República Checa continúan extrayendo importantes cantidades de carbón para su propio suministro energético. Además, China e India se muestran como grandes consumidores de este mineral, con minas subterráneas en explotación, lo que supone un gran volumen anual de emisiones de metano. Además, se ha observado que, a pesar del cierre de una explotación minera, el metano continúa fluyendo a la atmósfera durante

largos períodos de tiempo, que superan incluso los 20 años, y, por tanto, supone una fuente importante de emisión de gases de efecto invernadero.

### 1.3.1. Uso del carbón como combustible: Primera Revolución Industrial

Ciertos estudios apuntan a la zona norte de China como la pionera en la utilización de carbón como fuente de energía, hace más de 4000 años [37]. En un primer momento, el carbón utilizado era de origen vegetal —obtenido a partir de madera y otros residuos vegetales a temperaturas superiores a 400ºC y en ausencia de aire—, tanto en uso doméstico como en la industria metalúrgica temprana [38]. Ya en el siglo I, se tienen registros de la utilización de carbón mineral —roca sedimentaria de origen orgánico, formada por un proceso de litificación— extraído de depósitos superficiales y pequeñas explotaciones, principalmente en la zona de Britania [39]. En consecuencia, se puede estipular que la minería de carbón es una de las técnicas más antiguas utilizadas para la obtención de combustible. Sin embargo, en un primer momento, su uso no estaba muy extendido, ya que existía una gran cantidad de madera disponible y accesible. No fue hasta el siglo XIII cuando el carbón mineral comenzó a utilizarse habitualmente para uso doméstico y se formalizaron acuerdos de explotación, como se recoge en varios pasajes de la Crónica Sajona [40]. La tendencia al alza en su uso doméstico recae en su gran capacidad energética ($3.5 \cdot 10^4$ kJ/kg), que supera a otras fuentes combustibles típicas, como la madera seca ($1.9 \cdot 10^4$ kJ/kg).

No será hasta el inicio de la Primera Revolución Industrial (s. XVIII) cuando el carbón inicial su auge como combustible. El carbón mineral comienza a utilizarse para el movimiento de maquinaria, el calentamiento de viviendas y la generación de electricidad. Además, juega un papel clave en la fabricación y ensamblaje de vías de ferrocarril, imprescindibles para el flujo de bienes y recursos en la época [41]. La tradición de uso y extracción de carbón ya existente en Gran Bretaña —antigua Britania— y la proximidad de los yacimientos a los principales núcleos urbanos, la convirtieron en el eje central del desarrollo industrial europeo [42]. La expansión industrial conllevó un pico en el consumo de carbón, provocando la búsqueda de yacimientos y la apertura de explotaciones mineras en todo el mundo, entre las que destacaron las norteamericanas. La rápida apertura de multitud de

explotaciones mineras causó una gran falta de mano de obra, generando unas condiciones laborales nefastas [43]. La necesidad y extracción de carbón continuó aumentando progresivamente hasta el primer cuarto del siglo XX (Figura 1.6). A finales del mismo siglo, el carbón comienza a ser reemplazado por petróleo y gas natural, y se buscan fuentes alternativas para la producción de electricidad, como las energías renovables. La tendencia decreciente se ha seguido de forma similar en la mayoría de países desarrollados, y de un modo más sosegado en zonas con restricciones ambientales más permisivas, como Sudamérica o África [44]. En concreto, las elevadas emisiones de dióxido de carbono generadas en la quema de carbón y la emisión de otros gases nocivos, como óxidos de nitrógeno y azufre, así como material particulado, han provocado la aplicación de medidas restrictivas al carbón por parte de la Comisión Europea [45]. De hecho, el carbón es el combustible fósil más contaminante (385 kg $CO_2$/MW·h), frente a los 200 kg $CO_2$/MW·h del gas natural [46]. El principal uso energético del carbón es la alimentación de las centrales térmicas, por lo que estas medidas también conllevarán indirectamente al cierre progresivo de la mayoría de las mismas en Europa [47].

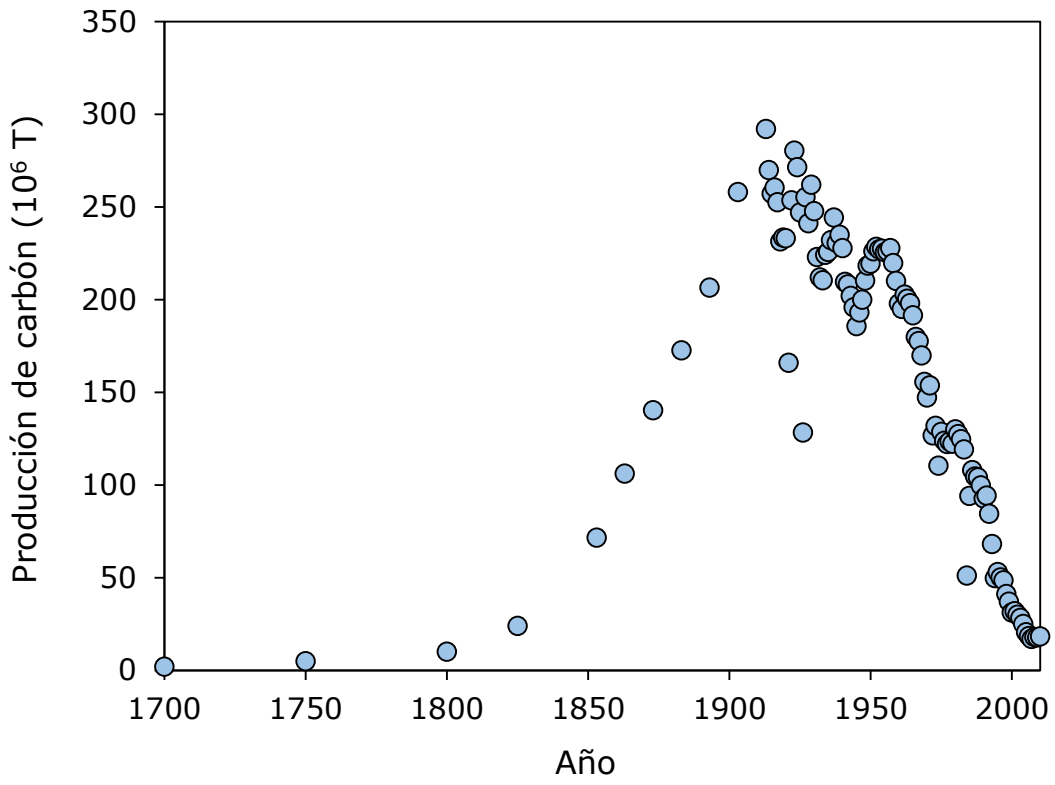


Figura 1.6. Variación de la producción anual de carbón mineral en Gran Bretaña frente al tiempo. Adaptado de [48].

Las restricciones surten efecto y han supuesto un notable descenso en la utilización del carbón como fuente de energía, en favor de vías alternativas y energías renovables. En consecuencia, un estudio realizado por Apergis y Payne [49] indica que los países que forman parte de la Organización para la Cooperación y el Desarrollo Económicos (OCDE) consumen únicamente el 35% del carbón mundial extraído. En contraposición, el carbón disponible es abundante y considerado el combustible fósil más barato, por lo que países como China o India son sus principales consumidores. De acuerdo con un estudio realizado por la compañía energética BP [44], el consumo de carbón creció un 6% en el año 2021, siendo el 70% del crecimiento atribuible únicamente a China e India. El mismo estudio indica que el 27% de la energía mundial proviene del carbón, con tasas muy elevadas en China (55%) e India (57%), y mucho más reducidas en España (2.9%) o Europa (11%).

### 1.3.2. Minería subterránea de carbón: Emisiones de metano

El carbón mineral es una roca sedimentaria de origen orgánico y tonalidad oscura, formado a partir de una litificación de restos vegetales en un ambiente pantanoso [50, 51]. La gran mayoría del carbón mineral se formó hace 300 millones de años, en el período carbonífero, por lo que es considerado un recurso no renovable [52]. De forma general, su contenido en carbono es muy elevado, llegando a superar el 85% en el caso de la antracita, considerado el carbón mineral de mayor calidad por su elevada capacidad calorífica. Actualmente, las mayores reservas mundiales de carbón mineral se encuentran en Estados Unidos, Rusia y Australia (Figura 1.7). De acuerdo al proceso de formación del mineral, las reservas se encuentran en el subsuelo en forma de vetas, que pueden llegar a extenderse varios kilómetros.

Las primeras técnicas de minería consistían en la explotación a pequeña escala de depósitos superficiales, con registros que datan del siglo I d. C. [38]. Más adelante, la gran demanda de carbón mineral provocó un intenso desarrollo de las técnicas de extracción, surgiendo la minería de carbón a gran escala, principalmente en Gran Bretaña. El intenso consumo agotó buena parte de las reservas superficiales, por lo que fue necesaria la búsqueda de vetas más profundas, desarrollando la minería subterránea de

carbón, indispensable a profundidades de más de 100 m [53]. Hasta el siglo XIX, la minería subterránea se basaba en la excavación de túneles y pozos de manera manual, por los que los mineros extraían las rocas mediante picos [54]. Con el paso del tiempo, la minería subterránea se va sofisticando, especialmente con el objetivo de mejorar el rendimiento productivo [55, 56]. Se desarrollan distintas técnicas de extracción, como la minería de sala y pilar, o la minería de frente largo [57], y se tiende hacia una automatización de los sistemas y utensilios de trabajo [58].

No obstante, una asignatura pendiente en la minería subterránea de carbón es la mejora de las medidas de seguridad y la reducción del riesgo de accidentes [59]. En esta línea, son muchos los desastres ocurridos en explotaciones mineras de todo el mundo, que han supuesto costes muy elevados en vidas humanas. El motivo más recurrente en las causas de estos accidentes es la elevada concentración de gas metano, altamente inflamable en concentraciones en aire entre 5 y 15% [60]. Algunos de los accidentes más destacados son los ocurridos en Pasta de Conchos (México) en 2006, Kémerovo (Rusia) en 2007, Heilongjiang (China) en 2009 o Amagá (Colombia) en 2010. Se trata de accidentes recientes que indican la necesidad de una mejora de los sistemas de seguridad y protección de las explotaciones mineras [61].

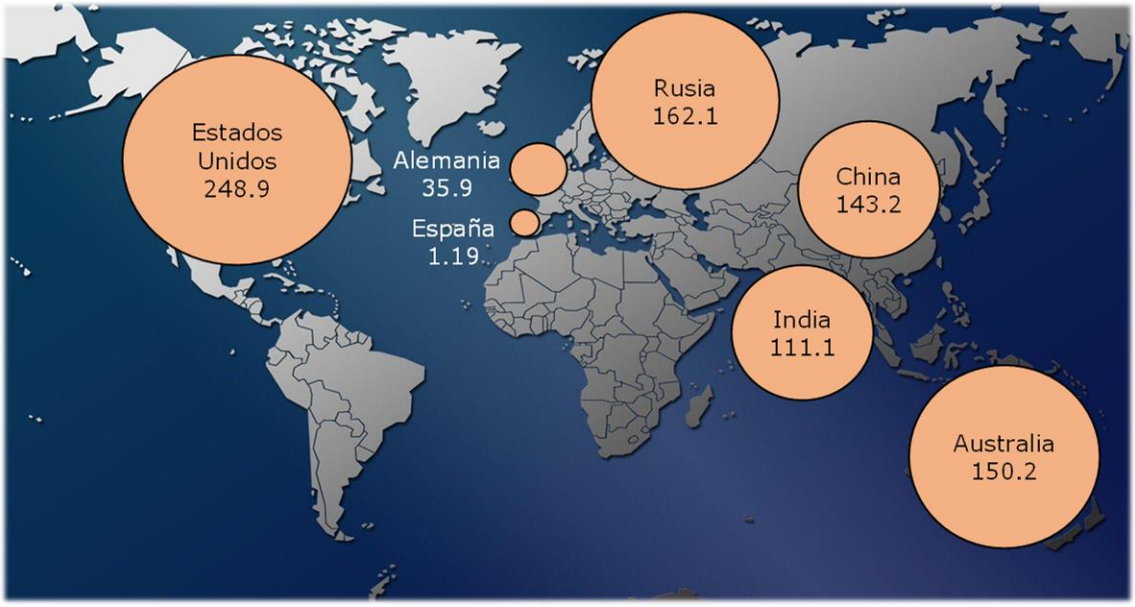


Figura 1.7. Reservas mundiales de carbón por países. Los datos numéricos se corresponden con miles de millones de toneladas. Adaptado de [44].

El metano se genera en el propio proceso de formación del carbón mineral mediante dos rutas: biogénica y termogénica. En la primera actúan bacterias y microorganismos que fragmentan macromoléculas de carbón y llevan a cabo el proceso de metanogénesis [62]. En el segundo caso, el metano se genera por la fractura de grandes moléculas carbonosas debido a procesos térmicos a elevada temperatura [63]. Más del 95% del metano generado se almacena adsorbido en la matriz del carbón, y es liberado durante la extracción del mineral, al reducirse la presión hidrostática [64]. El metano adsorbido en el carbón se incrementa con la profundidad de la veta, alcanzando más de 7000 $m^3$ por tonelada de carbón a 2000 m de profundidad [65]. La desorción de metano provoca un incremento de la concentración en las galerías de la explotación minera. Con el objetivo de evitar una alta concentración, que pueda provocar una explosión o incluso la asfixia de los trabajadores, es muy importante disponer de un adecuado sistema de ventilación, con todas las galerías interconectadas, asegurando un flujo continuo de aire [66] (Figura 1.8).

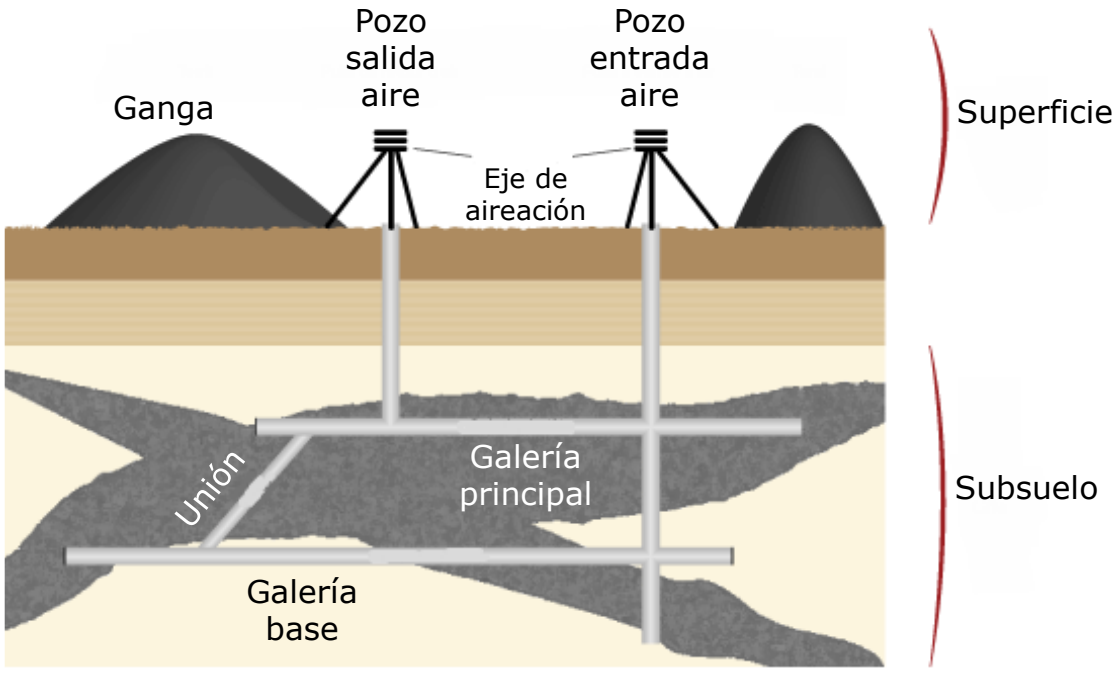


Figura 1.8. Esquema de una mina subterránea de carbón con un sistema de ventilación instalado. Adaptación de [67].

El metano desorbido del carbón se diluye mediante el flujo de ventilación, y la mezcla se descarga al exterior mediante pozos de salida de

aire. El flujo de ventilación debe estimarse de tal manera que la concentración de metano esté siempre por debajo de un 5%, correspondiente al límite inferior de explosividad, por lo que el metano emitido está muy diluido, pero los caudales totales son muy elevados (150-300 $m^3/s$) [68]. La mezcla gaseosa emitida al exterior a causa de la ventilación continua se denomina *ventilation air methane* (VAM), y posee habitualmente concentraciones de metano entre 0.1 y 1% [69]. Además de dicha emisión continua durante la operación, periódicamente es necesario realizar un drenaje total o parcial de la explotación minera, extrayendo grandes volúmenes de gas con una mayor concentración de metano (> 30%), ya que no es sometido a una dilución previa. Estas corrientes se denominan *coal mine methane* (CMM) [70]. En la misma línea, incluso tras el cierre de la explotación minera, continúa existiendo un flujo de metano hacia el exterior con elevada concentración (> 60%), que puede sostenerse hasta 20 años después de la clausura. Esta emisión se denomina *abandoned mine methane* (AMM) y procede de dos principales vías: la continuada desorción del metano adsorbido en la matriz del carbón por gradientes de presión, y el flujo al exterior del gas contenido en la explotación minera debido a la inundación de la misma, en ausencia de un drenaje periódico previo [71]. De entre los tres tipos de corrientes de metano consideradas, el VAM es la más importante, ya que supone aproximadamente un 75% del total de las emisiones de metano procedentes de la minería subterránea de carbón [72]. En este sentido, el gran número de explotaciones mineras abiertas en todo el mundo desde la Primera Revolución Industrial provoca que, a pesar de su progresivo cierre, las emisiones de metano asociadas a la minería de carbón continúen en unos niveles muy elevados. De hecho, según datos del *Global Energy Monitor* [73], las emisiones mundiales de metano anuales procedentes de la minería subterránea de carbón alcanzan los $8.3 \cdot 10^{10}$ $m^3$, con China a la cabeza, con $6.3 \cdot 10^{10}$ $m^3$, ya que domina más del 50% de las minas de carbón mundiales en operación.

## 1.4. RECUPERACIÓN Y APROVECHAMIENTO DE VAM: ADSORCIÓN

Las explotaciones mineras subterráneas de carbón emplean potentes ventiladores para la extracción del metano presente en las galerías, y así

mantener su concentración por debajo de un 5%. En consecuencia, se emiten al exterior elevados caudales de gas con muy bajas concentraciones de metano. Estas características convierten a las corrientes VAM en la principal fuente emisora de gases de efecto invernadero en el sector de la minería subterránea. En esta línea, conocido el elevado potencial de efecto invernadero del metano, así como la práctica ausencia de legislación y rutas de acción orientadas hacia la reducción de las emisiones correspondientes a este gas, la presente Tesis Doctoral abarca la posibilidad de capturar y aprovechar las emisiones de ventilación procedentes de la minería subterránea de carbón. Dicho objetivo nace de un proyecto europeo de investigación (METHENERGY+), centrado en la mitigación y aprovechamiento de las corrientes VAM procedentes de distintas explotaciones mineras europeas. Por tanto, el proyecto se centra en ambas vertientes: la mitigación, reducción de la emisión de un gas de efecto invernadero, y el aprovechamiento, obtención del máximo rendimiento del recurso disponible.

### 1.4.1. Tratamiento de VAM: Mitigación y aprovechamiento energético

En la actualidad, alrededor de un 70% del metano total emitido por la minería subterránea de carbón está desaprovechado en los principales países emisores [74]: China, Australia y Estados Unidos [75]. Los motivos principales son la dificultad de tratamiento de las emisiones por su elevado caudal y baja concentración, así como la falta de legislación y normativa relativa a la emisión de metano, que no está convenientemente incluido en el mercado mundial de emisiones [76]. Por otro lado, las principales características de estas emisiones son muy variables con el tiempo, y dependen de la explotación minera, el tipo de carbón extraído, la profundidad y la eficacia de la ventilación, lo que dificulta aún más el diseño de sistemas de tratamiento que sean aplicables en diversas explotaciones. En general, el metano se emite directamente a la atmósfera [77], o se somete a un proceso de combustión con muy bajo rendimiento [78]. Esto supone la pérdida de potencial energético, además de la emisión de un gas de efecto invernadero a la atmósfera. Sin embargo, la previsible implantación del metano en el mercado de emisiones y una potencial actualización legislativa relativa a su emisión, a propuesta del Parlamento Europeo en 2021 [79], han provocado

que los países considerados como grandes emisores comiencen a desarrollar tecnología orientada hacia una reducción de las emisiones (Figura 1.9).

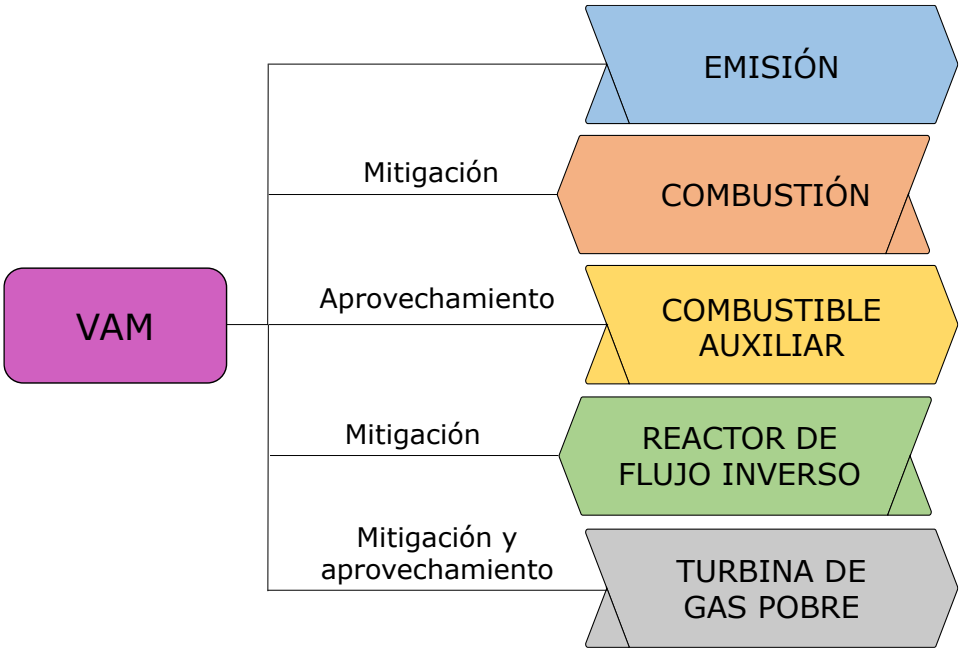


Figura 1.9. Esquema de las distintas tecnologías utilizadas en la mitigación y el aprovechamiento de VAM.

Hasta ahora, la opción más viable tecnológicamente pasaba por transformar el metano en dióxido de carbono y agua mediante una combustión directa, reduciendo el potencial de calentamiento global de la emisión. En general, la baja concentración de metano obliga a la utilización de un combustible adicional, lo que encarece el proceso y disminuye notablemente el rendimiento. Más adelante, se propuso la utilización de las corrientes VAM como combustible auxiliar en turbinas de gas [65], con la imposibilidad de tratar de manera íntegra los grandes caudales emitidos, además de requerir una planta de generación de energía próxima a la explotación minera [80]. Esta metodología se llegó a aplicar en la explotación minera de Appin (Australia), con el VAM como combustible auxiliar —entre un 4 y 10%— de una turbina de gas. Con el tiempo, la instalación cayó en desuso debido al coste asociado a la limpieza previa de las partículas de polvo de la corriente VAM, que provocaban un gran número de paradas aleatorias por obstrucciones en el sistema [81].

Con el objetivo de aminorar las pérdidas económicas, se trabaja en el diseño y la optimización de procesos que utilicen las corrientes VAM como el

combustible principal [68]. En el caso de las turbinas de gas pobre (Figura 1.10), *lean-burn gas turbines*, se aprovecha el propio calor de la combustión para precalentar la corriente de entrada hasta la temperatura de autoignición (450-1300ºC), mientras que el gas de combustión se utiliza a su vez para el movimiento de una turbina [81].

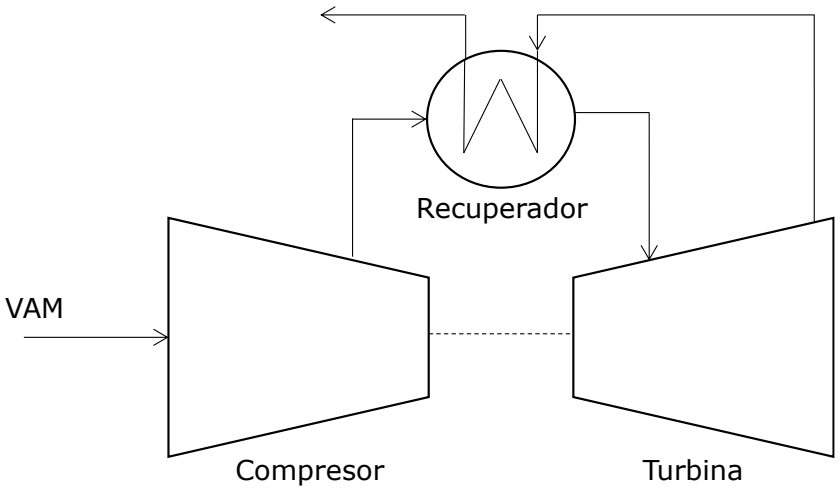


Figura 1.10. Diagrama de flujo de una turbina de gas pobre.

Estos diseños buscan la mitigación de las corrientes VAM, al mismo tiempo que un aprovechamiento energético de la emisión. El objetivo del diseño de estas turbinas es la reducción de la concentración mínima de metano necesaria para el funcionamiento de una turbina de gas convencional, que se encuentra en torno a un 25%, al no precalentar el gas de entrada [82]. Principalmente, existen dos tipos: turbinas de oxidación térmica (850-1300ºC) y turbinas de oxidación catalítica (450-800ºC), que difieren en la presencia o no de un catalizador en la zona de combustión. Esta tecnología se ha llegado a desarrollar como prototipo experimental, como la turbina diseñada por *The Energy Development Limited* (EDL), que puede operar de manera continuada con concentraciones de metano que superen el 1.6%, y con el aire precalentado inicialmente a 700ºC, por lo que requiere de la adición de metano a las corrientes de ventilación típicas (< 1%) hasta alcanzar dicha concentración. En el caso de la turbina catalítica desarrollada por CSIRO, se puede operar con concentraciones de metano en torno al 1%, permitiendo una mayor proporción de VAM en la mezcla. Varios estudios termodinámicos aseguran que se podría trabajar con concentraciones incluso

menores de metano, en torno a 0.8%. Sin embargo, la capacidad de generación de energía dependería en gran medida de la eficacia en la recuperación de la energía de combustión [83].

Otra de las técnicas desarrolladas para una mitigación eficaz de las corrientes VAM es la combustión mediante reactores de flujo inverso (Figura 1.11). Estos dispositivos consisten en reactores tubulares de lecho fijo rellenos de material sólido, en los que la dirección de flujo se modifica periódicamente. El calor de la reacción de combustión se transmite hacia el medio sólido del lecho, que incrementa posteriormente la temperatura de la corriente de entrada hasta la temperatura de autoignición del metano [84].

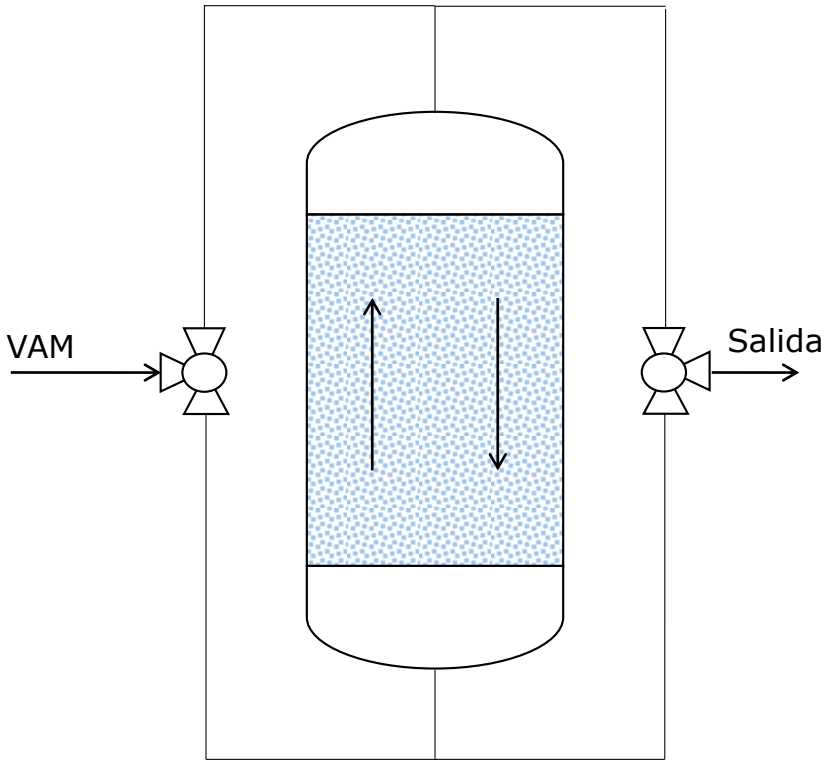


Figura 1.11. Esquema de un reactor de flujo inverso.

El cambio periódico en la dirección de flujo permite llevar a cabo una operación autotérmica sin aporte externo de energía. Existen dos tipos principales: reactor de flujo inverso térmico y reactor de flujo inverso catalítico. Ambos sistemas se rigen por el mismo principio de operación, y difieren únicamente en la utilización de un catalizador —platino, paladio, rodio, perovskita o hexaluminatos— que disminuye sustancialmente la temperatura necesaria para la combustión del metano. En el caso de la

combustión catalítica, también es posible la utilización de un reactor con disposición monolítica, que aporta mayor resistencia mecánica y menor pérdida de carga. Esta configuración favorece el tratamiento de elevados caudales, ajustándose más a una operación en condiciones reales [84]. Respecto al reactor de flujo inverso térmico, se ha desarrollado un prototipo a escala piloto, MEGTEC, en la explotación minera de West Cliff, en Australia. Su objetivo es la reducción de más de 250 kT eq. $CO_2$ por año [85]. Por otro lado, el desarrollo más avanzado en el caso de los reactores de flujo inverso catalíticos es el reactor CANMET, en Canadá [30]. Los principales problemas operativos con estos reactores son obstrucciones de polvo y elevadas caídas de presión. Además, requieren de una concentración de metano aproximadamente constante en la alimentación para una generación eficaz de energía.

A pesar de los esfuerzos descritos en el desarrollo de tecnologías capaces de mitigar y aprovechar de forma directa el VAM, multitud de estudios avalan la necesidad de una preconcentración del metano presente en las corrientes de ventilación [86, 87]. Si la concentración inicial de metano es demasiado baja, en algunos casos no será posible alcanzar temperaturas necesarias para la combustión, y en otros será necesario un reactor de gran tamaño para alcanzar una conversión adecuada, debido a la gran cantidad de inerte presente en las corrientes. Por otro lado, la inyección de metano, u otro combustible, adicional a la corriente VAM supone un notable descenso del rendimiento final de la operación. Como se ha indicado, la concentración de metano en las corrientes de ventilación depende en gran medida de la explotación minera, pero también de la legislación de cada país, lo que restringe valores muy elevados. Por ejemplo, en las minas de la India, el porcentaje de metano es generalmente muy bajo en la ventilación (0.02%) [88], mientras que en Polonia la concentración de metano puede llegar hasta un 0.7% [89]. Sin embargo, es muy complicado encontrar explotaciones mineras con concentraciones de metano superiores a un 1%, excepto en momentos puntuales. La baja concentración de partida y la amplitud del posible rango de concentración dificulta el diseño de procesos de tratamiento de VAM aplicables de manera general, por lo que se requiere una operación de concentración previa que facilite el tratamiento posterior.

### 1.4.2. Adecuación de VAM: preconcentración de metano

De acuerdo con la sección anterior, es necesaria una preconcentración del metano existente en las corrientes de ventilación para incrementar las posibilidades de mitigación y aprovechamiento energético de un modo eficaz. Si se analiza la composición química de las corrientes VAM, los principales componentes son: nitrógeno (78.1%), oxígeno (20.9%), metano (< 1%), dióxido de carbono (0.1%) y agua (100% humedad relativa). Por tanto, la purificación del metano pasa por una separación eficaz del resto de componentes de la corriente. En el caso del nitrógeno, además de tratarse del componente principal, es el más similar al metano, tanto en tamaño molecular (3.64 y 3.80 Å, respectivamente), como en la nulidad de sus momentos dipolares [90], con un mayor volumen de polarizabilidad en el caso del metano (2.44 y 1.71 $Å^3$). Estas características hacen de la separación $CH_4/N_2$ la más complicada de llevar a cabo. Con relación al resto de componentes, el oxígeno posee un tamaño molecular menor (3.46 Å), se encuentra en menor concentración que el nitrógeno, e incluso su presencia podría favorecer una posterior combustión en el tratamiento de la corriente. El dióxido de carbono posee un tamaño molecular de 3.33 Å, junto con el volumen de polarizabilidad más elevado (2.50 $Å^3$), mientras que la molécula de agua muestra un elevado momento dipolar (1.85 D) y un tamaño molecular muy reducido (2.80 Å), lo que facilitará la separación de ambas moléculas del metano mediante efectos relacionados con la polaridad, o incluso por efectos estéricos.

Cabe destacar que los procesos de separación y concentración de metano están muy presentes en la industria del gas natural, ya que se utilizan en procesos de purificación de biogás, en los que el metano es el componente principal y se retiran impurezas, principalmente de dióxido de carbono o sulfuro de hidrógeno. Existe un gran número de estudios acerca de estas separaciones de gases, siendo las técnicas más utilizadas: absorción, separación mediante membranas y adsorción. La absorción es una operación de carácter difusional en la que uno o varios componentes de una corriente gaseosa son absorbidos selectivamente en un líquido, tras un contacto líquido/gas en co o contracorriente (Figura 1.12). El principio de la separación se basa en la solubilidad del componente gaseoso a separar en el líquido

absorbente. Existen dos tipos: absorción física y absorción química. En el primer caso, no hay reacción química y la separación depende únicamente de la solubilidad. En el segundo caso, el componente reacciona selectivamente con el disolvente líquido. En general, esta metodología es muy eficaz para la concentración de un componente mediante la separación de impurezas muy reactivas en ciertos disolventes, como el caso del dióxido de carbono presente en el biogás. Para esta separación, es común la utilización de disolventes con presencia de aminas (monoetanolamina, dimetiletanolamina, dietanolamina, etc.), muy reactivos con el dióxido de carbono, efectivos a bajas presiones y con buena estabilidad química. Sin embargo, esta técnica no es adecuada para la purificación de metano en tan baja concentración y muy contaminado por aire, ya que tanto el metano como el nitrógeno no son fácilmente solubles en ningún disolvente típico y su separación no sería eficaz [91].

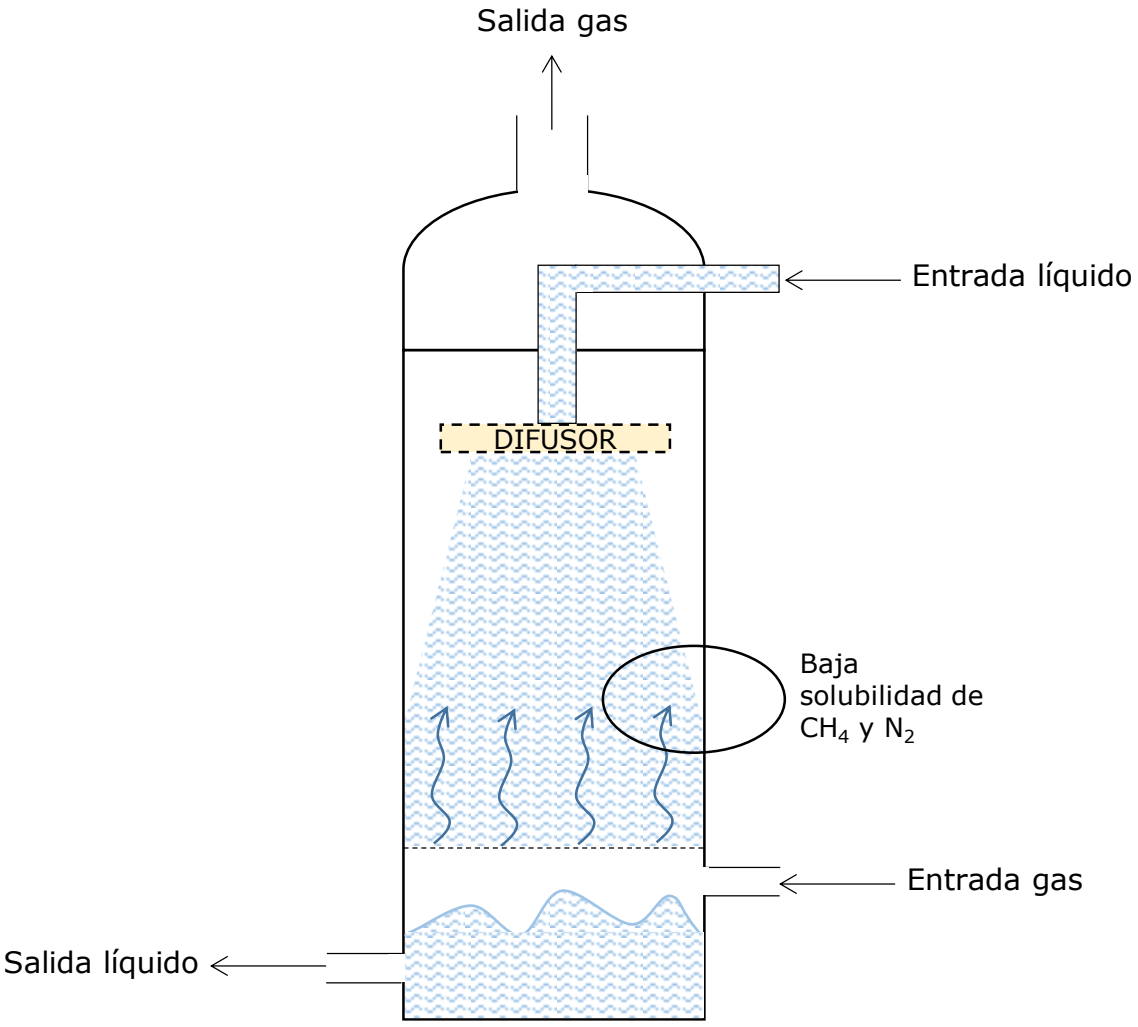


Figura 1.12. Esquema de un dispositivo de absorción de gas en líquido.

En el caso de la separación mediante membranas, éstas son materiales semipermeables capaces de separar selectivamente uno o varios componentes de una mezcla de gases (Figura 1.13). Las especies que se mueven a través de la membrana se denominan permeado, mientras que las que no la atraviesan, retenido. El transporte de los gases a través de la membrana se produce al aplicar una fuerza motriz, que generalmente se corresponde con un gradiente de presión o de concentración a ambos lados de la membrana. Existen dos tipos: densas y porosas. En el primer caso, se asume el modelo de solución-difusión, que considera una disolución del gas permeado en la membrana y una posterior difusión a través de la misma. En el caso de membranas porosas, el transporte está dominado por tres mecanismos: difusión molecular, difusión de Knudsen y flujo viscoso, cuya importancia depende del tamaño de poro de la membrana y del tamaño molecular del permeado [92]. Se han obtenido buenos resultados para membranas porosas en la separación de metano y nitrógeno [93], con selectividades $CH_4/N_2$ en torno a 3.2. Sin embargo, la baja durabilidad de las membranas y la dificultad en el escalado, con elevadas pérdidas de carga asociadas a grandes membranas, imposibilitan la utilización de este proceso en el caso de flujos tan elevados [70].

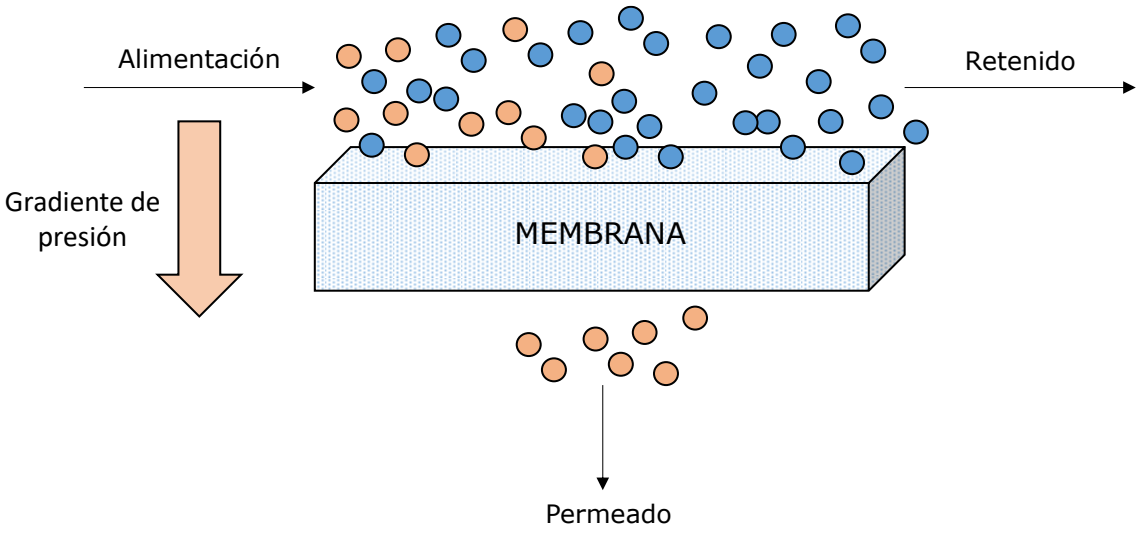


Figura 1.13. Esquema de un dispositivo de separación mediante membranas.

Por último, la adsorción es un proceso superficial que conlleva el transporte de moléculas gaseosas (adsorbato) desde un gas atraídas hasta la

superficie de un sólido, denominado adsorbente (Figura 1.14). Las moléculas o átomos de la superficie del material adsorbente poseen una energía superficial residual generada por un desequilibrio de fuerzas, lo que genera una zona de bajo potencial hacia el que las moléculas de adsorbato se ven atraídas. La atracción puede ocurrir tanto por fenómenos físicos como químicos, y generalmente es reversible, dando lugar al proceso inverso que se denomina desorción. En el caso de la adsorción física, ésta se produce por el efecto de fuerzas intermoleculares, como las fuerzas de Van der Waals, que actúan a baja temperatura y presentan baja energía de enlace. Por otro lado, la adsorción química conlleva la formación y ruptura de enlaces químicos, por lo que existe una mayor energía de enlace y muestra mayores energías de activación. En el caso de una mezcla gaseosa multicomponente, la composición en la zona más próxima a la superficie del adsorbente diferirá de la composición original del adsorbato, ya que los componentes se adsorben en función de la afinidad al adsorbente, parámetro conocido como selectividad. El componente más afín estará en mayor concentración en las zonas cercanas a la interfase gas/adsorbente. En base a esto, las propiedades que definen a un adsorbente son su selectividad, la capacidad de adsorción, su vida útil y su coste. A su vez, la selectividad y la capacidad de adsorción dependen de múltiples parámetros, como la superficie específica, el diámetro de poro, la distribución de poro y la presencia de grupos funcionales superficiales, entre otros.

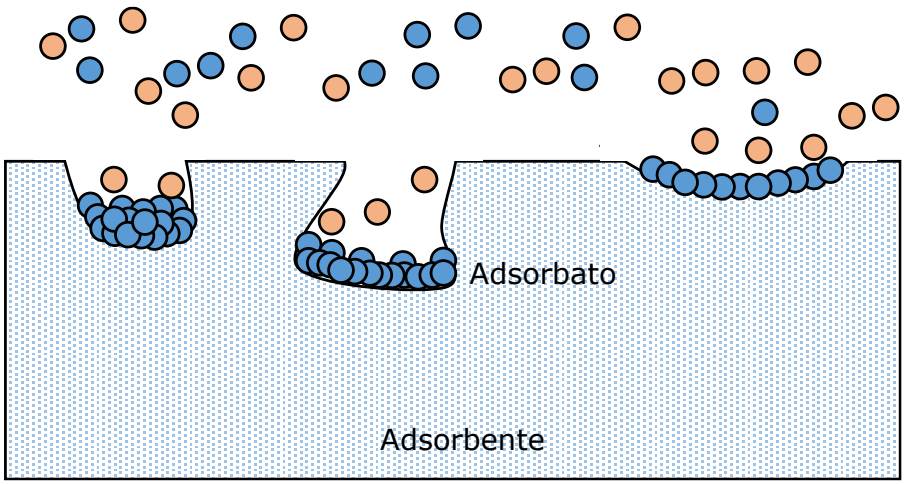


Figura 1.14. Esquema de adsorción selectiva de un adsorbato sobre un adsorbente poroso.

Con el objetivo de concentrar un componente presente en una mezcla gaseosa, se buscará una adsorción selectiva del componente de interés, para realizar posteriormente una etapa de desorción que dé lugar a una corriente más concentrada en dicho componente que la original. En este sentido, existen dos técnicas principales relativas a procesos de concentración mediante adsorción a gran escala: *temperature-swing adsorption* (TSA) y *pressure-swing adsorption* (PSA). Ambas difieren en el parámetro que se varía en el proceso para llevar a cabo la etapa de desorción, temperatura o presión, respectivamente. Por tanto, consisten en una variación cíclica de la temperatura o la presión del lecho fijo, en el que está contenido el adsorbente, alternando entre dos o más lechos disponibles. Multitud de autores han publicado buenos resultados utilizando estas técnicas para la purificación de componentes presentes en corrientes gaseosas [94-97]. En concreto, TSA ha demostrado ser más adecuada para la purificación de corrientes en las que el compuesto de interés esté en concentraciones menores de un 2% [98], además que la presurización de tan elevados caudales sería muy desfavorable económicamente. Finalmente, se puede concretar que la adsorción es una tecnología de bajo coste y con bajos requerimientos energéticos, por lo que es ampliamente utilizada en separaciones de gases de concentraciones variables [86], y por tanto adecuada para la separación de metano de mezclas de baja concentración.

## 1.5. REFERENCIAS

[1] C. Ene, A. Stancu, Impact of biofuels production on food security on selected African countries, Energy Transition (2022) 215-248.

[2] Directive 2014/94/EU of the European Parliament and of the Council of 22 October 2014 on the deployment of alternative fuels infrastructure. Text with EEA relevance. ELI: http://data.europa.eu/eli/dir/2014/94/oj.

[3] Instituto para la Diversificación y Ahorro de la Energía (página web: https://www.idae.es/). Acceso: Octubre 2022.

[4] REN21: Renewables now (página web: https://www.ren21.net/). Acceso: Octubre 2022.

[5] E. Meza-García, A. Rautenstrauch, M. Bräunig, V. Kräusel, D. Landgrebe, Energetic evaluation of press hardening processes, Procedia Manufacturing 33 (2019) 367-374.

[6] L. Lambert, J. Tayah, C. Lee-Schmid, M. Abdalla, I. Abdallah, A. Ali, S. Esmail, W. Ahmed, The EU's natural gas Cold War and diversification challenges, energy Strategy Reviews 43 (2022) 100934.

[7] Eurostat: Statistic Explained (página web: https://ec.europa.eu/eurostat/statistics-explained/). Acceso: Octubre 2022.

[8] A. Prohorovs, Russia's war in Ukraine: Consequences for European countries' businesses and economies, Journal of Risk and Financial Management 15 (2022) 295.

[9] N. Crafts, Explaining the first Industrial Revolution: Two views, European Review of Economic History 15 (2011) 153-168.

[10] H. Agarwal, R. Agarwal, First industrial revolution and second industrial revolution: technological differences and the differences in banking and financing of the firms, Saudi Journal of Humanities and Social Sciences 11 (2017) 1062-1066.

[11] U.S. Energy Information Administration (página web: https://www.eia.gov/). Acceso: Octubre 2022.

[12] Global Carbon Project (2021). Supplemental data of Global Carbon Budget 2021 (version 1.0).

[13] F. Martins, C. Felgueiras, M. Smitková, Fossil fuel energy consumption in European countries, Energy Procedia 153 (2018) 107-111.

[14] Global climate change: Vital signs of the Planet (NASA) (página web: https://climate.nasa.gov/vital-signs/global-temperature/). Acceso: Octubre 2022.

[15] The Intergovernmental Panel on Climate Change (página web: https://www.ipcc.ch/). Acceso: Octubre 2022.

[16] Organización Mundial de la Salud (página web: https://www.who.int/). Acceso: Octubre 2022.

[17] A. Magnan, H. Pörtner, V. Duvat, M. Garschagen, V. Guinder, Z. Zommers, O. Guldberg, J. Gattuso, Estimating the global risk of anthropogenic climate change, Nature Climate Change 11 (2021) 879-885.

[18] A. Kumar, P. Singh, P. Raizada, C. Mustansar, Impact of COVID-19 on greenhouse gases emissions: A critical review, Science of The Total Environment 806 (2022) 150349.

[19] S. Mahmoud, T. Gan, Impact of anthropogenic climate change and human activities on environment and ecosystem services in arid regions, Science of The Total Environment 633 (2018) 1329-1344.

[20] C. Butler, Climate change, health and existential risks to civilization: A comprehensive review (1989-2013), International Journal of Environmental Research and Public Health 15 (2018) 2266.

[21] Agencia Estatal de Meteorología (página web: https://www.aemet.es/). Acceso: Octubre 2022.

[22] Z. Mi, J. Zheng, J. Meng, Y. Shan, H. Zheng, J. Ou, D. Guan, Y. Wei, China's energy consumption in the new normal, Earth's Future 6 (2018) 1007-1016.

[23] Y. Zhao, X. Zhang, M. Chen, S. Gao, R. Li, Regional variation of urban air quality in China and its dominant factors, Journal of Geographical Sciences 32 (2022) 853-872.

[24] Naciones Unidas: Acción por el Clima (página web: https://www.un.org/es/climatechange/paris-agreement). Acceso: Octubre 2022.

[25] S. Peter, Reduction of $CO_2$ to chemicals and fuels: A so warming and energy crisis, ACS Energy Letters 3 (2018) 1557-1561.

[26] United States Environmental Protection Agency, Overview of greenhouse gases (página web: https://www.epa.gov/ghgemissions/overview-greenhouse-gases).

[27] Center for Climate and Energy Solutions (C2ES) (página web: https://www.c2es.org/). Acceso: Octubre 2022.

[28] Parlamento Europeo: Emisiones de gases de efecto invernadero por país y sector (página web: https://www.europarl.europa.eu/news/es/headlines/society/20180301STO98928/emisiones-de-gases-de-efecto-invernadero-por-pais-y-sector-infografia). Acceso: Octubre 2022.

[29] Consejo Europeo: Infografía — Objetivo 55: cómo transformará la UE los objetivos climáticos en legislación (página web: https://www.consilium.europa.eu/es/infographics/fit-for-55-how-the-eu-will-turn-climate-goals-into-law/). Acceso: Noviembre 2022.

[30] X. Feng, L. Jiang, D. Li, S. Tian, X. Zhu, H. Wang, C. He, K. Li, Progress and key challenges in catalytic combustion of lean methane, Journal of Energy Chemistry 75 (2022) 173-215.

[31] C. Lascano, E. Cárdenas, Alternatives for methane emission mitigation in livestock systems, Revista Brasileira de Zootecnia 39 (2010).

[32] M. Humer, J. Gebert, H. Hilger, Biotec systems to mitigate landfill methane emissions, International Solid Waste Association 26 (2008).

[33] T. Fox, T. Barchyn, D. Risk, A. Ravikumar, C. Hugenholtz, A review of close-range and screening technologies for mitigating fugitive methane emissions in upstream oil and gas, Environmental Research Letters 14 (2019) 053002.

[34] World Resources Institute: Climate Watch (página web: https://www.wri.org/initiatives/climate-watch). Acceso: Octubre 2022.

[35] J. Yin, S. Su, X. Yu, J. Bae, Y. Jin, A. Villella, M. Jara, M. Ashby, M. Cunnington, M. Loney, Site trials and demonstration of a novel pilot ventilation air methane mitigator, Energy Fuels 34 (2020) 9885-9893.

[36] E. Díaz, J. Fernández, S. Ordóñez, N. Canto, A. González, Carbon and ecological footprints as tools for evaluating the environmental impact of coal mine ventilation air, Ecological Indicators 18 (2012) 126-130.

[37] J. Dodson, X. Li, N. Sun, P. Atahan, X. Zhou, H. Liu, K. Zhao, S. Hu, Z. Yang, Use of coal in the Bronze Age in China, The Holocene 24 (2014) 525-530.

[38] S. Liu, T. Rehren, D. Qin, J. Chen, W. Zhou, M. Martinón-Torres, X. Huang, W. Qian, Coal-fuelled crucible lead-silver smelting in $12^{th}$-$13^{th}$ century China: A

technological innovation in the age of deforestation, Journal of Archaeological Science 104 (2019) 75-84.

[39] B. Miller, Coal energy systems, 1st edition (2001). ISBN: 9780080476605.

[40] L. Stamp, Britain's coal crisis: Geographical background and some recent literature, Geographical Review 38 (1948) 179-193.

[41] R. Allen, Why the industrial revolution was British: commerce, induced invention, and the scientific revolution, The Economic History Review 64 (2011) 357-384.

[42] A. Frenihough, K. O'Rourke, Coal and the European Industrial Revolution, The Economic Journal 131 (2021) 1135-1149.

[43] C. Tuttle, Hard at work in factories and mines: The economics of child labor during The British Industrial Revolution (1999).

[44] BP: Statistical Review of World Energy (página web: https://www.bp.com/en/global/corporate/energy-economics/statistical-review-of-world-energy.html). Acceso: Octubre 2022.

[45] European Commission: Clean energy for all Europeans package (página web: https://energy.ec.europa.eu/topics/energy-strategy/clean-energy-all-europeans-package_en). Acceso: Octubre 2022.

[46] D. Gómez, J. Watterson, Chapter 2: Stationary Combustion. IPCC Guidelines for National Greenhouse Gas Inventories (2006) (página web: https://www.ipcc-nggip.iges.or.jp/public/2006gl/vol2.html). Acceso: Noviembre 2022.

[47] Iberdrola: Closure of coal plants (página web: https://www.iberdrola.com/sustainability/thermal-power-plants-closing-against-climate-change). Acceso: Octubre 2022.

[48] Historical coal data: coal production, availability and consumption 1853 to 2021, Department for Business, Energy and Industrial Strategy (2013) (página web: https://www.gov.uk/government/statistical-data-sets/historical-coal-data-coal-production-availability-and-consumption). Acceso: Octubre 2022.

[49] N. Apergis, J. Payne, Coal consumption and economic growth: Evidence from a panel of OECD countries, Energy Policy 38 (2010) 1353-1359.

[50] A. Dmitrienko, E. Isayeva, Structural aspects of the coalification of organic materials, Coke and Chemistry 62 (2019) 552-555.

[51] E. Francis, A. Woodland, The Carboniferous period, Geological Society Publications 1 (1964) 221-232.

[52] W. Orem, R. Finkelman, 7.08 – Coal formation and geochemistry, Treatise on Geochemistry 7 (2003) 191-222.

[53] Junta de Castilla y León: Energía y minería en Castilla y León (página web: https://energia.jcyl.es/web/es/biblioteca/mineria-subterranea.html). Acceso: Octubre 2022.

[54] S. Ray, K. Dey, Coal mine water drainage: The current status and challenges, Journal of The Institution of Engineers (India): Series D 101 (2020) 165-172.

[55] Mining Technology: Environmental Sustainability (página web: https://www.mining-technology.com/environment-sustainability-in-mining/). Acceso: Octubre 2022.

[56] B. Jakkula, G. Mandela, M. Chivukula, Improvement of overall equipment performance of underground mining machines — A case study, International Information and Engineering Technology Association (2018) 6-11.

[57] World Coal Association (página web: https://www.worldcoal.org/). Acceso: Octubre 2022.

[58] Minería chilena: Equipos para minería subterránea: Más automatización, para mayor seguridad (página web: https://www.mch.cl/informes-tecnicos/equipos-mineria-subterranea-mas-automatizacion-mayor-seguridad/). Acceso: Octubre 2022.

[59] X. Li, Z. Cao, Y. Xu, Characteristics and trends of coal mine safety development, Energy Sources, Part A: Recovery, Utilization, and Environmental Effects (2020).

[60] X. Shen, B. Zhang, X. Zhang, S. Wu, Explosion behaviors of mixtures of methane and air with saturated water vapor, Fuel 177 (2016) 15-18.

[61] N. Szlazak, D. Obracaj, J. Swolkien, Enhancing safety in the Polish high-methane coal mines: an overview, Mining, Metallurgy and Exploration 37 (2020) 567-579.

[62] F. Colosimo, R. Thomas, J. Lloyd, K. Taylor, C. Boothman, A. Smith, R. Lord, R. Kalin, Biogenic methane in shale gas and coal bed methane: A review of current knowledge and gaps, International Journal of Coal Geology 165 (2016) 106-120.

[63] D. Stolper, M. Lawson, C. Davis, A. Ferreira, E. Santos, G. Ellis, M. Lewan, A. Martini, M. Schoell, A. Sessions, J. Eiler, Formation temperatures of thermogenic and biogenic methane, Science 344 (2014) 1500-1503.

[64] C. Zheng, B. Jiang, S. Xue, Z. Chen, H. Li, Coalbed methane emissions and drainage methods in underground mining for mining safety and environmental benefits: A review, Process Safety and Environmental Protection 127 (2019) 103-124.

[65] I. Karakurt, G. Aydin, K. Aydiner, Mine ventilation air methane as a sustainable energy source, Renewable and Sustainable Energy Reviews 15 (2011) 1042-1049.

[66] V. Babu, T. Maity, H. Prasad, Energy saving techniques for ventilation fans in underground coal mines — A survey, Journal of Mineral Science 51 (2015) 1001-1008.

[67] Connaissance des energies: Techniques d'exploitation des mines de charbon (página web: https://www.connaissancedesenergies.org/fiche-pedagogique/techniques-dexploitation-des-mines-de-charbon). Acceso: Octubre 2022.

[68] A. Setiawan, E. Kennedy, M. Stockenhuber, Development of combustion technology for methane emitted from coal-mine ventilation air systems, Energy Technology 5 (2017) 521-538.

[69] Z. Yang, M. Hussain, P. Marín, Q. Jia, N. Wang, S. Ordóñez, Y. Zhu, Y. Xia, Enrichment of low concentration methane: An overview of ventilation air methane, Journal of Materials Chemistry A 10 (2022) 6397-6413.

[70] X. Wang, F. Zhou, Y. Ling, Y. Xiao, B. Ma, X. Ma, S. Yu, H. Liu, K. Wei, J. Kang, Overview and outlook on utilization technologies of low-concentration coal mine methane, Energy Fuels 35 (2021) 15398-15423.

[71] S. Hu, A. Zhang, G. Feng, X. Guo, X. Miu, D. Han, J. Wang, L. Kang, Methane extraction from abandoned mines by surface vertical wells: A case study in China, Geofluids 2018 (2018) 8043157.

[72] Economic Comission for Europe methane to markets partnership, Best practice guidance for effective methane drainage and use in coal mines (2010). ISBN: 9789211170184.

[73] Global Energy Monitor (página web: https://globalenergymonitor.org/es/projects/global-coal-mine-tracker/summary-tables/). Acceso: Octubre 2022.

[74] A. Pawlaczyk, M. Suwak, Will it be possible to put into practice the mitigation of ventilation air methane emissions? Review on the state-of-the-art and emerging materials and technologies, Catalysts 11 (2021) 1141.

[75] Climate Watch: Data Explorer (página web: https://www.climatewatchdata.org/data-explorer/). Acceso: Octubre 2022.

[76] Z. Lukaszczyk, Methane — Fuel gas. Opportunities and threats, New Trends in Production Engineering 3 (2020) 430-438.

[77] A. Singh, J. Kumar, Fugitive methane emissions from Indian coal mining and handling activities: Estimates, mitigation and opportunities for its utilization to generate clean energy, Energy Procedia 90 (2016) 336-348.

[78] A. Setiawan, E. Kennedy, M. Stockenhuber, Development of combustion technology for methane emitted from coal-mine ventilation air systems, Energy Technology 5 (2017) 521-538.

[79] European Comission: Proposal for a REGULATION OF THE EUROPEAN PARLIAMENT AND OF THE COUNCIL on methane emissions reduction in the energy sector and amending Regulation (EU) 2019/942. https://eur-lex.europa.eu/legal-content/EN/TXT/?uri=COM:2021:805:FIN.

[80] F. Zhou, T. Xia, X. Wang, Y. Zhang, Y. Sun, J. Liu, Recent developments in coal mine methane extraction and utilization in China: A review, Journal of Natural Gas Science and Engineering 31 (2016) 437-458.

[81] S. Su, X. Yu, A 25 kWe low concentration methane catalytic combustion gas turbine prototype unit, Energy 79 (2015) 428-438.

[82] J. Yin, S. Su, X. Xiang, Y. Weng, Thermodynamic characteristics of a low concentration methane catalytic combustion gas turbine, Applied Energy 87 (2010) 2102-2108.

[83] S. Su, X. Yu, Progress in developing an innovative lean burn catalytic turbine technology for fugitive methane mitigation and utilization, Frontiers in Energy 5 (2011) 229-235.

[84] B. Chaedir, J. Kurnia, L. Chen, L. Jiang, A. Sasmito, Numerical investigation of ventilation air methane catalytic combustion in circular straight and helical coil channels with twisted tape insert in catalytic-monolith reactors, Catalysts 10 (2020) 797.

[85] Climate Policy Watcher: Successful demonstration of VAM processing (página web: https://www.climate-policy-watcher.org/methane-emissions/successful-demonstration-of-vam-processing.html). Acceso: Noviembre 2022.

[86] U. Chaemwinyoo, P. Marín, C. Fernández, F. Díez, S. Ordóñez, Assessment of an integrated adsorption-regenerative catalytic oxidation process for the harnessing of lean methane emissions, Journal of Environmental Chemical Engineering 10 (2022) 107013.

[87] X. He, L. Lei, Optimizing methane recovery: Techno-economic feasibility analysis of $N_2$-selective membranes for the enrichment of ventilation air methane, Separation and Purification Technology 259 (2021) 118180.

[88] H. Singh, J. Mallick, Utilization of ventilation air methane in Indian coal mines: Prospects and challenges, Procedia Earth and Planetary Science 11 (2015) 56-62.

[89] P. Ostrowski, M. Pronobis, L. Remiorz, Mine emissions reduction installations, Applied Thermal Engineering 84 (2015) 390-398.

[90] Z. Huang, P. Hu, J. Liu, F. Shen, Y. Zhang, K. Chai, Y. Ying, C. Kang, Z. Zhang, H. Ji, Enhancing $CH_4/N_2$ separation performance within aluminium-based metal-organic frameworks: Influence of the pore structure and linker polarity, Separation and Purification Technology 286 (2022) 120446.

[91] S. Su, A. Beath, H. Guo, C. Mallett, An assessment of mine methane mitigation and utilisation technologies, Progress in Energy and Combustion Science 31 (2005) 123-170.

[92] E. Nagy, Chapter 11 — Membrane contactors, Basic Equations of Mass Transport Through a Membrane Layer (Second Edition) (2019) 337-345.

[93] K. Warmuzinski, Harnessing methane emissions from coal mining, Process Safety and Environmental Protection 86 (2008) 315-320.

[94] A. Abd, M. Othman, S. Naji, A. Hashim, Methane enrichment in biogas mixture using pressure swing adsorption: process fundamental and design parameters, Materials Today Sustainability 11-12 (2021) 100063.

[95] M. Luberti, H. Ahn, Review of Polybed pressure swing adsorption for hydrogen purification, International Journal of Hydrogen Energy 47 (2022) 10911-10933.

[96] F. Zerobin, T. Pröll, Concentrated carbon dioxide ($CO_2$) from diluted sources through continuous temperature swing adsorption (TSA), Industrial and Engineering Chemistry Research 59 (2020) 9207-9214.

[97] K. Wu, S. Deng, S. Li, R. Zhao, X. Yuan, L. Zhao, Preliminary experimental study on the performance of $CO_2$ capture prototype based on temperature swing adsorption (TSA), Carbon Capture Science and Technology 2 (2022) 100035.

[98] R. Yang, Adsorbents: Fundamentals and applications, Wiley Online Library (2003).

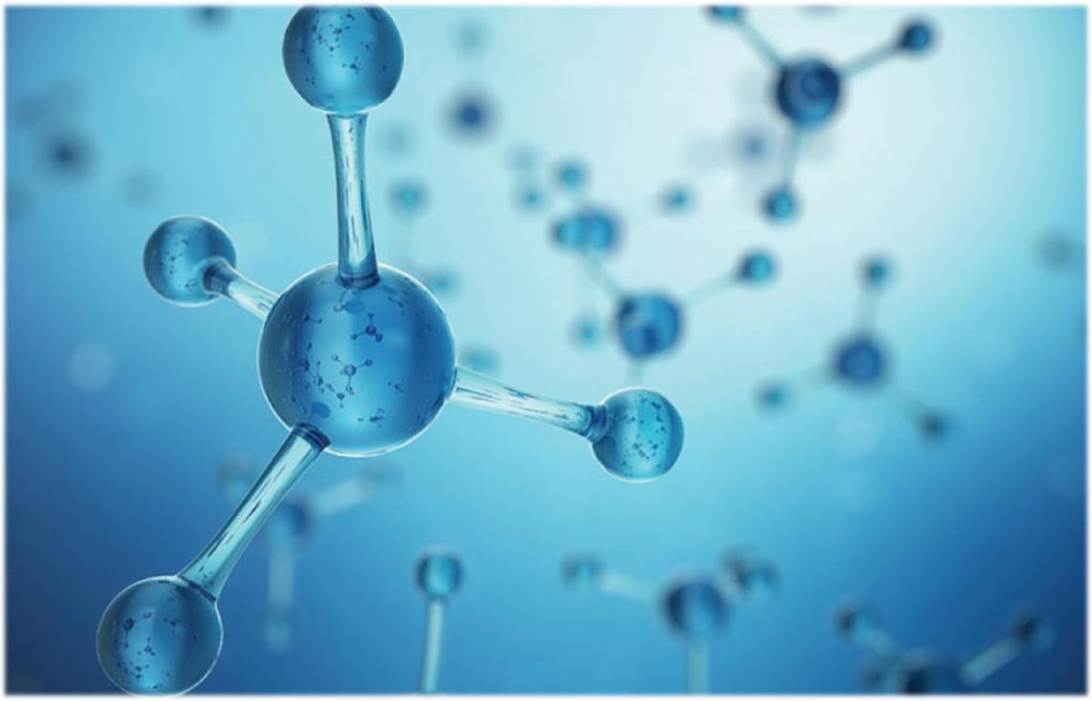

# 2. OBJETIVOS

Como se ha introducido, existe tanto un interés en la búsqueda de fuentes de energía alternativas, como una creciente preocupación por el continuo deterioro del Medio Ambiente, asociado al calentamiento global. Ambos asuntos muestran una relación directa con el uso de los combustibles fósiles —carbón, gas natural y petróleo—, ya que la gran dependencia mundial hacia los mismos provoca que las emisiones de gases de efecto invernadero se incrementen continuamente, calentando el planeta. El objetivo principal de la presente Tesis Doctoral puede enmarcarse en ambas vertientes, ya que comprende el estudio de un proceso de recuperación y concentración de metano diluido en corrientes gaseosas residuales provenientes de la ventilación de la minería subterránea de carbón (VAM). La recuperación de este metano evitaría una emisión directa a la atmósfera o una combustión de muy bajo rendimiento, así como su posterior concentración permitiría utilizarlo como combustible de manera más eficaz. El objetivo principal nace a partir de un Proyecto Europeo de investigación (RFCS216-METHENERGY PLUS, financiado por la *Research Fund of Coal and Steel*, y coordinado por la Universidad de Oviedo), que señala estas emisiones como claras contribuyentes al incremento de la concentración de gases de efecto invernadero en la atmósfera, pero también como una potencial fuente energética. Establecido el objetivo principal, tras una revisión bibliográfica de las posibilidades técnicas, se decide estudiar la adsorción en lecho fijo para la captura y concentración de dicho metano. A partir de dicha selección, los objetivos específicos son los siguientes:

➢ Selección y caracterización de adsorbentes. Se seleccionarán los mejores materiales adsorbentes disponibles para el proceso a partir de una extensa revisión bibliográfica de procesos de almacenamiento y separación de metano (Capítulo 4.1). Los materiales seleccionados, preferiblemente comerciales, se caracterizarán cinética y termodinámicamente en base a su capacidad de separación de metano y nitrógeno, considerada la separación más importante del proceso (Capítulo 4.2).

➢ Estudios de adsorción y selectividad. Los materiales comerciales seleccionados se someterán a ensayos de adsorción y desorción en lecho fijo. Se estudiará su comportamiento en distintos escenarios, tanto en condiciones moderadas, como en condiciones similares a un proceso real, en presencia de humedad y dióxido de carbono. Además, será necesario estudiar el efecto de las variaciones morfológicas necesarias para el trabajo con estos materiales a escala industrial en un lecho fijo, como el incremento de tamaño de partícula. Los resultados obtenidos se detallan en el Capítulo 4.2.

➢ Modelización matemática y simulación. La posibilidad de realizar ensayos de adsorción y desorción bajo condiciones variables será clave para disponer de datos experimentales suficientes que permitan modelizar matemática-mente el proceso. La resolución del modelo matemático se realizará a partir de los paquetes de software Aspen Adsorption y COMSOL Multiphysics, lo que permitirá simular el comportamiento de distintos materiales adsorbentes para un mismo proceso, así como realizar una optimización de la etapa de concentración de metano. Posteriormente, el modelo validado y optimizado se utilizará para simular una operación a escala real de mitigación y aprovechamiento de una corriente VAM. Los resultados se muestran y discuten en el Capítulo 4.3.

➢ Diseño de materiales adsorbentes. Una vez conocidas las propiedades necesarias más adecuadas de los materiales adsorbentes, así como la problemática asociada al trabajo en condiciones reales, se pretende la síntesis de materiales adsorbentes que reúnan las características deseadas para el proceso. Una vez sintetizados, se someterán a las etapas de caracterización y adsorción/desorción anteriores, pudiendo compararlos con los materiales utilizados previamente. Los resultados se presentan en el Capítulo 4.4.

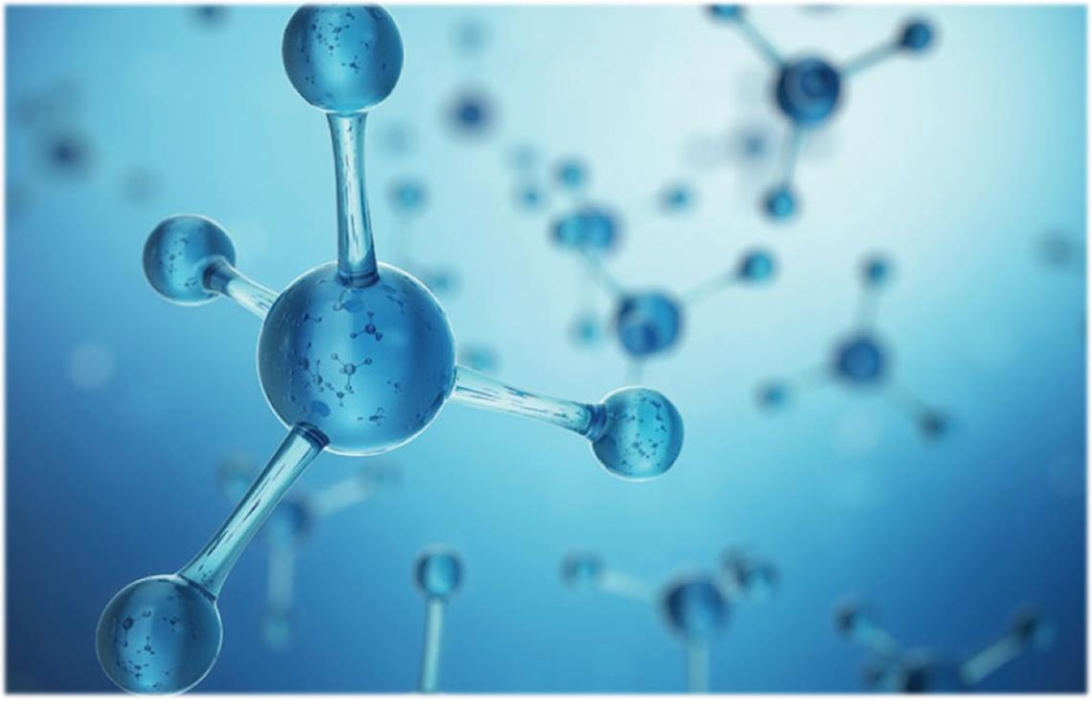

# 3. METODOLOGÍA EXPERIMENTAL

3.1. Materiales adsorbentes

3.2. Técnicas de caracterización de materiales

3.3. Equipos de adsorción y análisis

3.4. Simulación de procesos

3.5. Referencias

## 3.1. MATERIALES ADSORBENTES

El material utilizado como adsorbente es uno de los parámetros clave a la hora del diseño de un proceso de adsorción. Los materiales utilizados, así como sus características más importantes, se detallan a continuación.

### 3.1.1. Materiales comerciales

Gran parte del trabajo se ha desarrollado utilizando como adsorbentes tres materiales de tipo MOF: Basolite C300, Basolite F300 y Basolite A100. Se trata de materiales comerciales, sintetizados por la compañía BASF. En el caso de Basolite C300, está formado por 1,3,5-tribencenocarboxilato (1,3,5-BTC) como ligando orgánico, que une los iones metálicos de cobre ($Cu^{2+}$) de la estructura, que le aportan su característico color azul (Figura 3.1). Se trata de un material con elevada superficie específica BET (1500 $m^2/g$) y volumen de poro (1.25 $cm^3/g$), con cierta variedad de tamaños de poro (4, 10 y 11 Å). Por otro lado, el Basolite F300 está formado por el mismo ligando orgánico, que establece uniones entre iones metálicos de hierro ($Fe^{2+}$), con un característico color rojizo (Figura 3.1). Este material posee una superficie específica BET en torno a 960 $m^2/g$ y 0.42 $cm^3/g$ de volumen total de poro, con grandes poros de 25 y 29 Å. Por último, el Basolite A100 está formado por ácido 1,4-benzodicarboxílico como ligando orgánico, uniendo iones de aluminio ($Al^{3+}$), que le aportan un tono grisáceo (Figura

3.1). Su superficie específica BET es la menor de las tres (660 $m^2/g$), con un volumen total de poros de 1.05 $cm^3/g$, y un tamaño medio de poro de 8.5 Å, aunque ha demostrado gran flexibilidad estructural bajo ciertas condiciones.


Figura 3.1. Fotografías de los tres materiales comerciales utilizados. Basolite C300 (A), Basolite F300 (B) y Basolite A100 (C).

## 3.1.2. Materiales sintetizados

Además, en base a la información obtenida a partir de los ensayos con MOFs comerciales, se han diseñado y sintetizado otros materiales, tal y como se detalla a continuación.

### *3.1.2.1. Síntesis de HKUST-1*

El material HKUST-1 es un MOF homólogo al comercial Basolite C300, ya que posee la misma composición química y estructura atómica. Se trata de uno de los materiales de tipo MOF más estudiados, ya que sus propiedades son adecuadas para obtener resultados satisfactorios en múltiples aplicaciones. La síntesis de HKUST-1 se realiza siguiendo el procedimiento sugerido por Gascon et al. [1]: 0.875 g de nitrato de cobre tri-hidratado, $Cu(NO_3)_2 \cdot H_2O$, se disuelven en 12 ml de agua, y se mezclan con 0.42 g de ácido trimésico, $C_9H_6O_6$, previamente disueltos en 12 ml de etanol, $C_2H_6O$. La mezcla se mantiene bajo agitación vigorosa durante 30 minutos a temperatura ambiente y el resultante se introduce en un reactor de tipo autoclave de teflón (PTFE) y 100 ml de capacidad (Amar). El autoclave, sellado herméticamente, se introduce en una estufa de convección a 383 K durante 18 horas. El producto obtenido se filtra en kitasato y se lava 3 veces con agua destilada, para un posterior secado en estufa a 383 K durante

12 horas. Se obtiene un material pulverulento con tonalidad azul, muy similar en aspecto al comercial Basolite C300.

### *3.1.2.2. Síntesis de composites HKUST-1@γ-$Al_2O_3$*

Para la síntesis de HKUST-1 impregnado sobre partículas de alúmina ($Al_2O_3$), se han utilizado dos metodologías. La primera, el método solvotermal [2]: 2.02 g de partículas (355-710 μm) de alúmina se mezclan con los precursores de HKUST-1, en las mismas proporciones que las indicadas en la *Sección 3.1.2.1*. La mezcla se lleva a un autoclave de teflón, a una temperatura de 383 K durante 18 horas. El resultante se filtra y se lava, para posterior secado en estufa (383 K). Por otro lado, el método *dip-coating* [1]: 2.02 g de partículas (355-710 μm) de alúmina se impregnan gota a gota con la disolución madre de HKUST-1, llevándose posteriormente a 393 K en estufa de convección hasta la completa evaporación del disolvente. Posteriormente, las partículas se lavan con etanol y se filtran. El producto se introduce en un autoclave de teflón junto con los precursores de HKUST-1 a una temperatura de 383 K durante 18 horas y se somete a un filtrado y lavado posterior.

Además de los procedimientos estándar presentados, se ha sometido a los materiales a varias modificaciones en su proceso de síntesis. En algunos casos, se ha variado la concentración de MOF sobre la alúmina, para lo que se ha realizado, o bien una modificación en el volumen total de contacto en el autoclave, 24, 2.4 o 1 ml, una reducción de la concentración inicial de precursores en la mezcla, 100-10% de la concentración original, o se ha modificado la cantidad total de alúmina que se pone en contacto con los precursores, 2-1 g.

## 3.2. TÉCNICAS DE CARACTERIZACIÓN DE MATERIALES

Las técnicas de caracterización utilizadas son comunes para todos los materiales estudiados, tanto comerciales como sintetizados. La caracterización permite conocer las propiedades superficiales, morfológicas y físico-químicas de los materiales, para lo que se utilizan las técnicas descritas a continuación.

### 3.2.1. Fisisorción de nitrógeno

La fisisorción de nitrógeno es una técnica ampliamente utilizada en la caracterización de la estructura porosa de múltiples materiales en diversos ámbitos. Los resultados obtenidos aportan información acerca del área superficial, así como del volumen y la distribución de tamaños de poro. El principio teórico de la técnica se basa en una interacción física, generalmente débil, de una molécula sonda —adsorbato— con la superficie del material a analizar, denominado adsorbente. En este caso, se ha utilizado nitrógeno como adsorbato, pero existe la posibilidad de utilizar otras moléculas, como dióxido de carbono o argón. El contacto de la molécula sonda con el material conlleva un equilibrio de adsorción, función de la presión y la temperatura. Por tanto, a una temperatura constante (77.3 K), y conocida la presión aplicada del adsorbato, es posible conocer la cantidad de nitrógeno adsorbida sobre el material ($q_{ads}$). Para ello, se relaciona la diferencia de presiones de nitrógeno, entre la inicial y la de equilibrio, con la cantidad de nitrógeno adsorbido en la superficie y la estructura porosa del material.

Por tanto, la técnica se basa en la aplicación de una presión parcial de nitrógeno determinada sobre la muestra, seguido de un tiempo de espera hasta alcanzar el equilibrio termodinámico entre adsorbente y adsorbato. Una vez alcanzado, se estima la cantidad de nitrógeno adsorbida sobre la muestra y se varía de nuevo la presión parcial, repitiendo el proceso hasta elevadas presiones parciales. La obtención de varios puntos permitirá representar la cantidad de nitrógeno adsorbido en función de la presión parcial aplicada. La presión parcial se representa como $P/P_0$, donde $P_0$ es la presión de saturación en las condiciones experimentales, siendo P la presión real. Esta representación recibe el nombre de isoterma de adsorción, pudiendo presentar distintas formas (Figura 3.2). Como se observa, existen seis tipos de isotermas de adsorción, clasificadas en función de la forma de las curvas de adsorción y desorción del adsorbato:

- Isoterma de tipo I. Característica de sólidos microporosos, también conocida como isoterma de Langmuir. La zona de mayor pendiente, correspondiente a bajas presiones parciales, se corresponde con el llenado

de los poros en monocapa, mientras que la zona final, más plana, se corresponde con la adsorción en multicapa sobre la superficie del sólido.

- Isoterma de tipo II. Se corresponde con una interacción fuerte entre la molécula sonda y el adsorbente, en el caso de materiales no porosos. Comienza con una adsorción en monocapa seguida de una adsorción en multicapa, que comienza a partir del primer codo de la curva.

- Isoterma de tipo III. Se corresponde con una interacción débil entre la molécula sonda y el adsorbente, en el caso de materiales no porosos. La debilidad de la interacción imposibilita la adsorción a bajas presiones parciales. A medida que aumenta la presión ejercida, la presencia de moléculas de adsorbato en la superficie estimula la adsorción debido a las propias interacciones adsorbato-adsorbato.

- Isoterma de tipo IV. Característica de sólidos mesoporosos. La primera parte se corresponde con una isoterma de tipo II. A mayores presiones parciales, se observa la aparición de un ciclo de histéresis, que indica la condensación capilar del adsorbato en los mesoporos.

- Isoterma de tipo V. Característica de materiales mesoporosos. Se corresponde con una combinación de la isoterma de tipo III, a bajas presiones parciales, con una aparición de histéresis a mayores presiones ejercidas.

- Isoterma de tipo VI. Se corresponde con una adsorción en multicapa paso a paso. Cada uno de los escalones presentes en la isoterma se trata del llenado de una capa de adsorción sobre el material. Es poco común.

Con el objetivo de obtener dicha información de forma adecuada, es imprescindible realizar una desgasificación previa a la muestra. La desgasificación se realiza en condiciones de alto vacío, 2 μm Hg, y temperatura elevada, 393 K. Este proceso permite retirar del material la humedad y otros gases presentes en los poros del material, permitiendo la posterior entrada de las moléculas sonda. Posterior a la limpieza, el equipo aplicará automáticamente las distintas presiones parciales de nitrógeno hasta alcanzar el equilibrio, que se corresponde con el momento en el que la presión en el interior del tubo portamuestras no varíe. Es decir, el momento en el

que, para dicha presión parcial, el adsorbente no admite más adsorbato en su superficie.

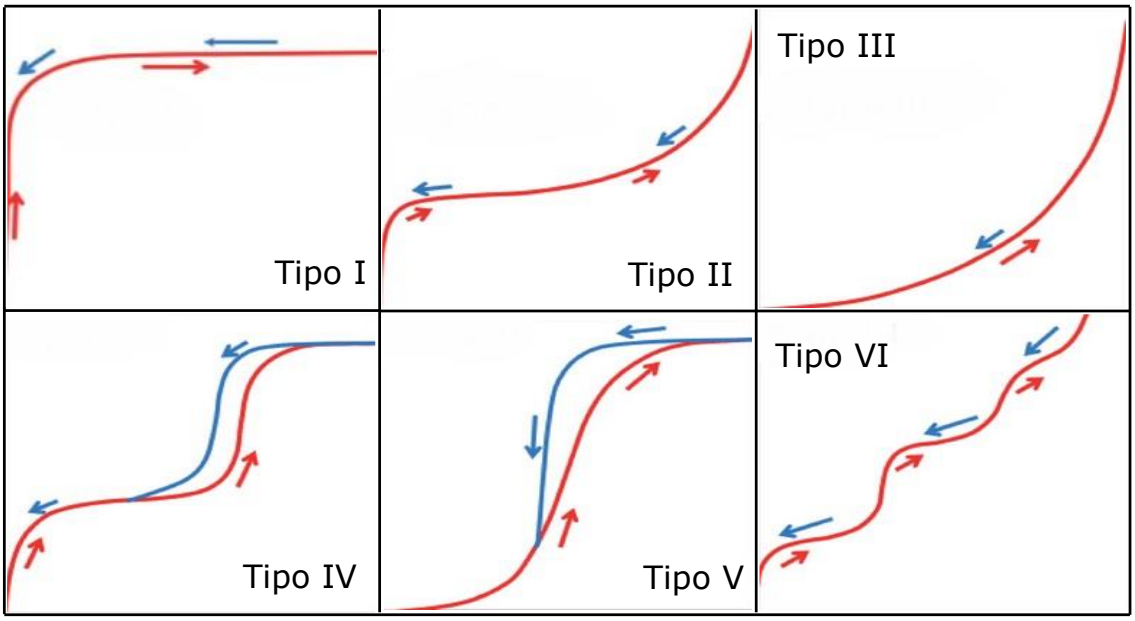


Figura 3.2. Clasificación de las isotermas de adsorción según la IUPAC. En rojo, adsorción, en azul, desorción. Adaptada de Kumar et al. [4].

A partir de la isoterma obtenida, es posible aplicar distintos modelos estimativos de los parámetros de interés en cada muestra. En el caso de la superficie específica, el método más común es el de Brunauer-Emmett-Teller (BET). Este método se utiliza en el caso de materiales con adsorción en multicapa, y es aplicable en el rango $0.05 < P/P_0 < 0.35$, tratándose de una evolución del método de Langmuir, aplicable únicamente a la adsorción en monocapa. En el caso del volumen de mesoporos ($d_p > 2$ nm), se utiliza el método de Barret-Joyner-Halenda (BJH), que asume un modelo cilíndrico de poro, mientras que para el volumen de microporos ($d_p < 2$ nm) se utilizan los métodos de Dubinin-Radushkevich (DR) o *t-plot*, ampliamente utilizados en el caso de materiales predominantemente microporosos.

Se han utilizado dos equipos muy similares que permiten aplicar la técnica de fisisorción de nitrógeno: Micromeritics ASAP 2020, en la Universidad de Oviedo, y Belsorp MAX II, en el IRCELYON, ambos representados en la Figura 3.3. El procedimiento de operación y la obtención de resultados es muy similar en ambos casos.


Figura 3.3. Equipos utilizados para la fisisorción de nitrógeno sobre los materiales estudiados. A la izquierda, Micromeritics ASAP 2020, a la derecha, BELSORP MAX II.

### 3.2.2. Técnicas de microscopía electrónica (EM)

La microscopía electrónica permite obtener información acerca de la morfología superficial (microscopía electrónica de barrido) y estructural (microscopía electrónica de transmisión) de los materiales estudiados. Se trata de una técnica muy utilizada en la caracterización de materiales, debido al gran número de aumentos de imagen que permite aplicar respecto a los microscopios ópticos tradicionales (Figura 3.4).

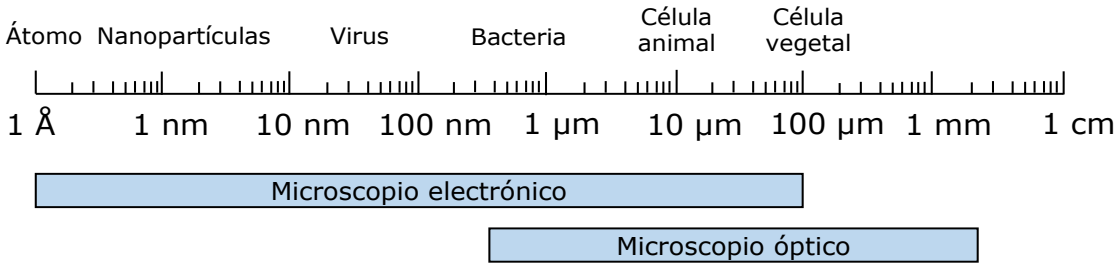


Figura 3.4. Rango eficaz de medida para los microscopios ópticos y electrónicos.

El principio teórico de la técnica consiste en la aplicación de un haz de electrones sobre la superficie de la muestra sólida a analizar. Este haz incidente provoca una respuesta, en forma de reemisión, por parte de la superficie del material, que se recoge y analiza posteriormente, dando lugar

a una imagen aumentada del material. Los aumentos de la imagen son elevados debido a la reducida longitud de onda de los electrones incidentes, mucho menor que la de los fotones utilizados en microscopios ópticos tradicionales.

A continuación, se describen las dos técnicas de microscopía electrónica más utilizadas:

- Microscopía electrónica de barrido (SEM). Técnica de caracterización superficial en la que la superficie de la muestra es bombardeada por un haz de electrones enfocado con precisión. Estos electrones, acelerados por una diferencia de potencial de 0.2-30 kV, viajan a través de una columna a vacío ($10^{-4}$ Pa). La colisión del haz de electrones con la superficie de la muestra genera la emisión de electrones superficiales, debido a las ionizaciones surgidas por el contacto con el material. Éstos son recogidos mediante diversos detectores que, a partir de la intensidad y posición de la emisión, son capaces de recrear la morfología del material estudiado. Las principales señales recogidas por los detectores son:

    - Electrones secundarios (SE). Reflejados directamente por la acción del rayo incidente. Se trata de electrones de valencia de los átomos que conforman la superficie de la muestra. Aportan información acerca de la morfología superficial.

    - Electrones retro-dispersados (BSE). Electrones de alta energía, producto de una interacción en capas más profundas del material. Aportan información acerca de la composición de la muestra de manera cualitativa, ya que están estrechamente relacionados con el número atómico de los componentes.

    - Rayos X. Emisión característica de los elementos químicos presentes en la superficie de la muestra analizada. Permite realizar un análisis semi-cuantitativo de la composición química. Esta técnica espectroscópica recibe el nombre de energía dispersiva de rayos X (EDX).

Los análisis de espectroscopía electrónica de barrido se realizan mediante un microscopio JEOL-6610LV (Figura 3.5), en los Servicios Científico-Técnicos de

la Universidad de Oviedo. Este microscopio lleva acoplada una unidad de EDX. Para un correcto uso, es necesario que la muestra a analizar sea conductora, por lo que, en el caso de no serlo, se debe recubrir con una fina capa de oro.

➢ Microscopía electrónica de transmisión de alta resolución (HR-TEM). Ofrece información acerca de la estructura cristalográfica de la muestra a una escala atómica, en un plano bidimensional. En este caso, el haz incidente de electrones penetra a través de la muestra y genera una imagen aumentada, por lo que la muestra debe ser preparada previamente como una capa muy fina. El resultado es una imagen con distintas intensidades de tono gris, que se corresponden con el grado de dispersión de los electrones incidentes, a partir de la cual es posible resolver la estructura del material a escala atómica. Para preparar la muestra a analizar, ésta se muele en un mortero, se disuelve en etanol absoluto y unas gotas de dicha disolución se dejan secar a temperatura ambiente, resultando en una fina capa del material. Para el análisis de las muestras se ha utilizado el microscopio JEOL JEM-2100 (Figura 3.5), en los Servicios Científico-Técnicos de la Universidad de Oviedo.

Figura 3.5. Equipos utilizados para la microscopía electrónica de los materiales estudiados. A la izquierda, JEOL-6610LV, a la derecha, JEOL JEM-2100.

### 3.2.3. Difracción de rayos X (DRX)

La difracción de rayos X permite determinar la geometría tridimensional y estimar el tamaño de cristalita de los materiales cristalinos analizados. Los materiales cristalinos poseen una distribución regular de

átomos en el espacio, de la cual la fracción más simple que se repite múltiples veces por traslación se conoce como celda unidad. En función de las dimensiones de la celda unidad, correspondientes con la longitud de los tres vectores espaciales, y las relaciones entre las mismas, que conforman los ángulos vectoriales, se conocen siete tipos de sistemas cristalinos distintos: cúbico, tetragonal, ortorrómbico, hexagonal, romboédrico, monoclínico y triclínico.

El principio de la técnica analítica consiste en la aplicación de un haz estrecho de rayos X sobre la superficie de una muestra pulverizada. Los rayos X son una radiación electromagnética con una longitud de onda muy corta (0.05-0.25 nm), que se producen al frenarse rápidamente partículas cargadas con suficiente energía cinética. Generalmente, los rayos X se generan mediante un cátodo con un filamento de wolframio que emite electrones, acelerados en condiciones de vacío. El haz de electrones incide sobre un blanco metálico, llamado anticátodo, emitiendo el espectro deseado de rayos X. Este anticátodo puede estar compuesto de otros metales, típicamente cobre. Los rayos X incidentes interaccionan con los átomos de la muestra a analizar, pudiendo así ser desviados en cualquiera de las sucesivas capas de átomos que conforman el material. Algunos de los rayos X del haz son desviados sin pérdida energética, con una longitud de onda del mismo orden de magnitud que las distancias interatómicas del cristal, fenómeno que se conoce como difracción o interferencia constructiva. Para que este fenómeno ocurra, debe cumplirse la Ley de Bragg (Ecuación 3.1).

$$n \cdot \lambda = 2 \cdot d \cdot sen\,(\theta) \qquad (3.1)$$

De manera esquemática, la Figura 3.6 muestra los átomos de un material en dos planos paralelos, separados por una distancia ($d$) determinada. Estos átomos son sometidos a una radiación incidente, con una longitud de onda ($\lambda$) y un ángulo de entrada conocido ($\theta$), la cual es reflejada con el mismo ángulo, sin pérdida energética.

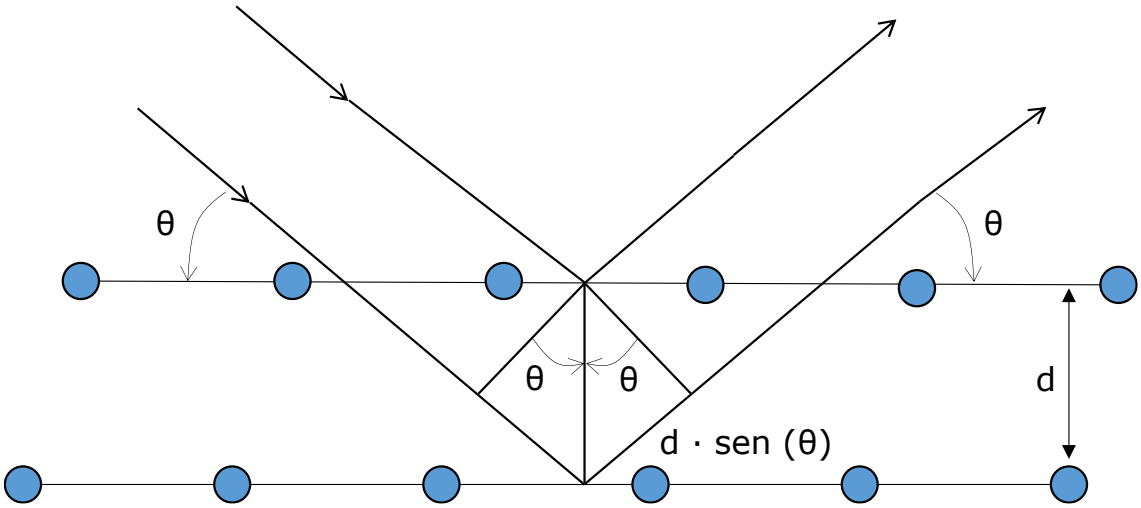


Figura 3.6. Esquema de la incidencia de rayos X en la estructura de un material cristalino. Los círculos azules representan los átomos del material.

Las intensidades de todas las interacciones constructivas, en función del ángulo de incidencia de la radiación, dan lugar a lo que se conoce como difractograma. Por tanto, variando el ángulo de incidencia y recogiendo todas las interferencias constructivas generadas, es posible obtener una gráfica de intensidad de señal reflectada frente al ángulo de incidencia. La gráfica obtenida es característica y única de cada material, y permite identificar las fases cristalinas presentes, recurriendo a bases de datos en las que los difractogramas estén recogidos. Además de la identificación de las fases cristalinas, es posible determinar el tamaño promedio de cristalita a partir del difractograma. Para ello, se utiliza la ecuación de Scherrer (Ecuación 3.2), aplicable únicamente si la red cristalina está libre de deformación y los cristales predominan de forma general en la muestra. En dicha ecuación, $\tau$ es el tamaño medio de la cristalita, $\beta$ es la anchura del pico más característico, generalmente, el de mayor intensidad, a la mitad de su altura, y $K$ es un factor adimensional cercano a la unidad.

$$\tau = \frac{K \cdot \lambda}{\beta \cdot \cos\ (\theta)} \qquad (3.2)$$

Siguiendo el principio de la técnica, existen dos vías principales para el análisis de las muestras: análisis monocristal y análisis en polvo. La primera de ellas permite determinar posiciones atómicas e incluso longitudes y

ángulos de enlace del cristal analizado. Esta técnica se utiliza para un único cristal de gran tamaño y elevada pureza. Por otro lado, DRX de polvo cristalino permite analizar materiales heterogéneos alcanzando una mayor perspectiva, a granel. El análisis proporciona información acerca de las fases cristalinas presentes en el material, así como la cristalinidad total del mismo. Por tanto, en el caso de materiales con tamaño de cristal previsiblemente no muy elevado, así como materiales sintetizados con cierta heterogeneidad, como los utilizados típicamente en adsorción y catálisis, se utilizará la técnica de DRX para polvo cristalino.

El equipo utilizado es un difractómetro Philips PW 1710, en los Servicios Científico-Técnicos de la Universidad de Oviedo (Figura 3.7). El equipo trabaja con una radiación incidente tipo $K$-$\alpha$, con un anticátodo de cobre y una longitud de onda emitida de 0.154 nm. El barrido del ángulo de incidencia es de 5-85º, con una velocidad de barrido de 2 º/min. En relación al análisis de resultados, las bases de datos generalmente contienen información disponible acerca de materiales ampliamente conocidos y estudiados. En el caso de dichos materiales, se utiliza el software *XPowderX*, que permite analizar difractogramas e identificar fases cristalinas a partir de una amplia base de datos. Además, también se utiliza el software *Match! 3*, que dispone de una amplia biblioteca de estructuras, y permite identificar fases cristalinas por similitud en la posición de los picos característicos del difractograma de la muestra a analizar. Por otro lado, en el caso de materiales menos estudiados o novedosos, el caso de la mayoría de MOFs, no se dispondrá de los difractograma modelo. Por ello, en primer lugar, será necesario definir o aproximar cuál es el sistema cristalino con mayor similitud al material analizado, tanto por semejanza a otros ya estudiados, o por la identificación de la posición de los picos más característicos. Posteriormente, será posible deducir las variaciones respecto a la estructura modelo a partir de las ecuaciones típicas de cada sistema cristalino conocido, así como los índices de Miller característicos, que definen inequívocamente sistemas de planos cristalinos.


Figura 3.7. Equipo utilizado en la difracción de rayos X para polvo cristalino. Philips PW 1710.

### 3.2.4. Espectroscopía infrarroja de reflexión difusa por transformada de Fourier (DRIFT)

La espectroscopía infrarroja de reflexión difusa consiste en la recogida y análisis de la radiación difusa reflectada, en todas las direcciones, por la muestra analizada al aplicar sobre ella un haz de radiación infrarroja. En el momento en el que el haz infrarrojo incide sobre la muestra, éste puede ser reflejado por la superficie de una partícula o puede ser transmitido a través de la misma. La energía transmitida a través de la partícula alcanzará otra partícula, pudiendo ser reflejada o de nuevo transmitida hacia otra partícula distinta. Este efecto de transmisión y reflectancia puede ocurrir en múltiples ocasiones en una misma muestra, aumentando significativamente el recorrido del haz incidente. Esta reflexión difusa se produce en todas las direcciones del espacio, y se recoge mediante instrumental óptico hacia el detector correspondiente (Figura 3.8). Los espejos concentradores, que dirigen la radiación reflectada hacia el detector, están situados en tal posición geométrica que únicamente recogen dicha radiación difusa. La intensidad de la reflexión, a través de la transformación empírica de Kubelka-Munk, puede expresarse como un espectro típico de transmisión, es decir, como absorbancia.

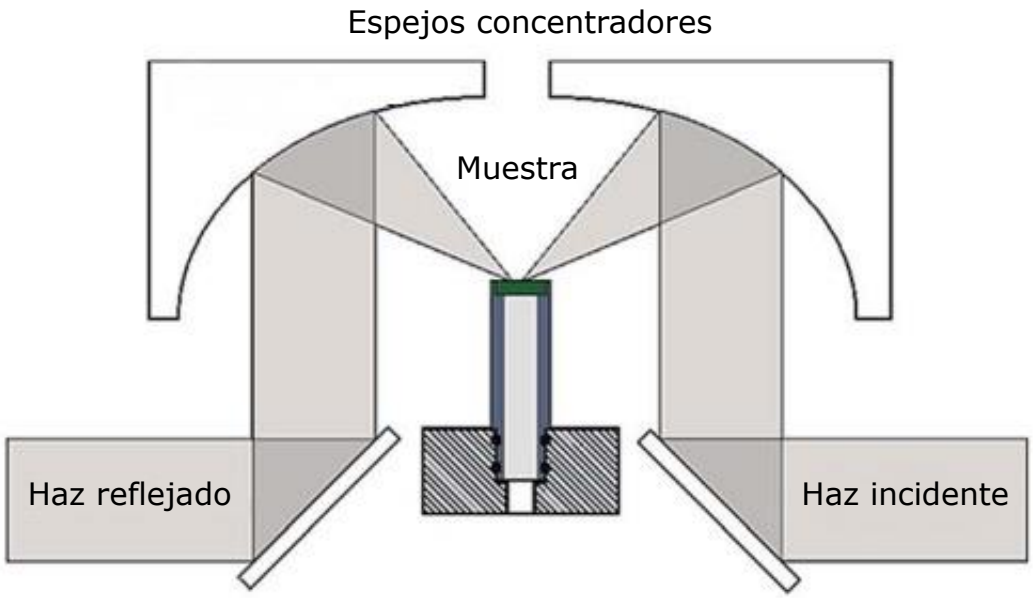


Figura 3.8. Esquema del funcionamiento de un equipo de DRIFT. Adaptado de [5].

Las bandas o picos obtenidos a cada longitud de onda pueden asociarse a la vibración, al aplicar radiación infrarroja, de ciertos enlaces químicos presentes en la muestra. La asignación de la posición de las bandas de absorbancia a cada enlace puede hacerse mediante bibliografía o analizando estándares conocidos. Por tanto, la técnica permite estudiar la variación o ruptura de enlaces ya existentes del material, así como la aparición de nuevos enlaces tras cualquier tipo de tratamiento o reacción química. Por otro lado, la adición de una celda accesorio que permita el flujo de gases sobre la muestra y un control eficaz de la temperatura, al mismo tiempo que se realiza la medida, permite estudiar los enlaces rotos o generados en una reacción química o en un proceso de adsorción bajo temperatura controlada.

El equipo utilizado es un espectrómetro Thermo Electro Nicolet FT-IR (Figura 3.9), equipado con un detector MCT/A. El espectro infrarrojo se recoge en el intervalo 700-4000 $cm^{-1}$. El equipo está calibrado con una resolución de 4 $cm^{-1}$, y realiza 128 escaneos consecutivos para la obtención de cada espectro. Es deseable trabajar con tamaños de partícula pequeños, así como una distribución de tamaño lo más estrecha posible. El equipo dispone de una celda auxiliar con ventanas de ZnSe, que permite el flujo de gases sobre la muestra, simultáneamente a la medida, así como el control de temperatura de la muestra, tanto en enfriamiento como en calentamiento.

Previo al análisis, es necesario realizar un blanco con KBr y sustraerlo en cada medida al espectro obtenido.


Figura 3.9. Equipo utilizado para la espectroscopía infrarroja de reflexión difusa por transformada de Fourier (DRIFT), Thermo Electron Nicolet FT-IR.

## 3.3. EQUIPOS DE ADSORCIÓN Y ANÁLISIS

Gran parte del trabajo se dedica al estudio de la capacidad de adsorción y separación de distintos gases sobre los materiales adsorbentes considerados. A continuación, se detallan las técnicas y equipos utilizados en el estudio de las propiedades adsortivas más importantes.

### 3.3.1. Análisis termogravimétrico

Un análisis termogravimétrico permite conocer con gran exactitud la variación de la masa de una muestra con el tiempo, en condiciones controladas de temperatura, y bajo una atmósfera determinada. El equipo utilizado se denomina balanza termogravimétrica, y consiste en una balanza de precisión solidaria con una placa o cesta, denominada crisol, en la que se sitúa la muestra, introducida a su vez en un horno eléctrico programable. Al mismo tiempo que se varía la temperatura en el horno, es posible, mediante reguladores de flujo másico, introducir caudales exactos de uno o varios gases deseados circulando sobre la muestra, pudiendo así seleccionar la atmósfera bajo la cual se realiza el análisis. La práctica más habitual consiste

en el registro de la variación de masa a medida que se incrementa gradualmente la temperatura de la muestra en condiciones inertes u oxidantes. La variación de la masa se puede deber a diversos motivos, como la pérdida de humedad, cambios moleculares, cambios de fase cristalina, destrucción de la estructura, etc. Otra práctica típica es la de mantener la temperatura constante y circular sobre la muestra un flujo de gas deseado, pudiendo así registrar el aumento de masa del material, que se corresponderá con la cantidad de componente adsorbido. La curva obtenida, capacidad de adsorción frente a tiempo, permitirá realizar posteriores estudios cinéticos de la etapa de adsorción.

Además del registro de las variaciones de masa, es posible añadir complementos al equipo que permitan realizar un análisis más completo del proceso que se lleva a cabo entre la muestra situada en el crisol y la atmósfera gaseosa, en conjunción con la temperatura aplicada. Algunos de estos complementos son la calorimetría diferencial de barrido (DSC) y el análisis de la composición de los gases efluentes (EGA). El primero de ellos permite registrar los cambios entálpicos debidos a las modificaciones en las propiedades físicas y químicas de un material en función de la temperatura y el tiempo. Por otro lado, el segundo permite un análisis cualitativo de los gases de salida de la termobalanza, pudiendo registrar la evolución de la masa junto con los gases consumidos o emitidos por la muestra analizada, dependiendo del proceso.

Se han utilizado dos balanzas termogravimétricas: Sensys Setaram y TGA 55 TA Instruments (Figura 3.10). En el caso de la balanza Sensys, ésta combina tanto la balanza de precisión como la técnica DSC. La balanza es la parte móvil del equipo, mientras que el horno se mantiene fijo. Se precisa una masa de muestra inicial de 20 mg, aproximadamente. La balanza está compuesta por dos crisoles de platino, situados en paralelo, cada uno en un ramal de la balanza. En uno de ellos se introduce la muestra, mientras que en el otro se introduce la misma masa de un material inerte de referencia, generalmente polvo de alúmina. Ambos crisoles están sometidos al mismo régimen de temperatura y atmósfera, por lo que el material inerte actúa como referencia o tara, mientras que la muestra sufrirá las variaciones de masa pertinentes. Al mismo tiempo, el equipo es capaz de registrar las variaciones

entálpicas de la muestra, a través de DSC. Para ello, se registra la cantidad de energía necesaria para mantener o incrementar la temperatura de la muestra a analizar, que se compara con el mismo procedimiento en la muestra de referencia, situada en el crisol secundario y previamente calibrada. Estos valores se pueden relacionar directamente con la entalpía, a partir de una constante de diseño del equipo utilizado.

Por otro lado, la termobalanza TGA 55 únicamente presenta la función de termogravimetría. En este caso, el horno es la parte móvil, mientras que la balanza se mantiene fija. El principio teórico de la balanza de precisión es el mismo que en el caso anterior, pero no es necesaria la utilización de un material de referencia, ya que la propia balanza realiza el tarado inicial de forma automática. Ambos equipos permiten el flujo de gas sobre la muestra con un caudal máximo de 100 ml/min y 0.1 MPa de presión total.

Figura 3.10. Equipos utilizados para los ensayos termogravimétricos. A la izquierda, Sensys Setaram, a la derecha, TGA 55 TA.

### 3.3.2. Adsorción a temperatura programada

Las técnicas de temperatura programada (TP) permiten estudiar la adsorción/desorción de un gas o la descomposición de un material al mismo tiempo que tiene lugar un control eficaz de la temperatura de la muestra. Las técnicas más utilizadas son la desorción a temperatura programada (TPD), la reducción a temperatura programada (TPR) y la oxidación a temperatura programada (TPO). Estas técnicas consisten en el flujo de un gas a través de un lecho de la muestra, bajo temperatura controlada, y un análisis en continuo de los gases de salida. El gas introducido interacciona con el material

estudiado y el efecto se verá reflejado en el análisis. Dicho análisis se puede llevar a cabo mediante diversas técnicas, como la conductividad térmica (TCD) o la espectrometría de masas (MS). Las técnicas TPD se utilizan para determinar el número y la fortaleza relativa de los centros activos de un catalizador, tanto ácidos como básicos, dependiendo del gas reactivo introducido, ya sea amoniaco ($NH_3$) o dióxido de carbono ($CO_2$), respectivamente. Por otro lado, la técnica TPR consiste en la introducción de un flujo de hidrógeno ($H_2$), a medida que se incrementa la temperatura de la muestra. Las temperaturas a las que se observe un consumo de hidrógeno significativo por parte del material coincidirán con aquellas a las que es más favorable su reducción. Por último, la técnica TPO consiste en un flujo de oxígeno ($O_2$) a través de la muestra, al mismo tiempo que se incrementa la temperatura. Se trata del proceso inverso a la técnica TPR, ya que ésta muestra la medida de oxidación de un material con la temperatura, relacionada con picos de consumo de oxígeno.

Además, el mismo equipamiento puede utilizarse para el estudio de la capacidad de adsorción del material, bajo un control adecuado de la temperatura y con el material situado conformando un lecho fijo a pequeña escala. Se introducen, aproximadamente, 50 mg del material en un tubo portamuestras cilíndrico, que se sitúa en los puertos correspondientes del equipo. El dispositivo permite el flujo de uno o varios gases deseados, con caudales preestablecidos, a través del lecho del material, controlados mediante reguladores de flujo másico previamente calibrados. Los gases a la salida del equipo se analizan mediante espectrometría de masas, que permite determinar de manera semi-cuantitativa las moléculas presentes en una mezcla gaseosa en función de su masa atómica. El espectrómetro de masas separa los núcleos atómicos en función de su relación masa/carga, previa ionización de los átomos de la corriente gaseosa mediante calentamiento en un filamento. El espectrómetro de masas utilizado es un Pfeiffer Omnistar Vacuum 300, que se conecta en línea con la salida de gases del sistema de adsorción a temperatura programada Micromeritics AutoChem II 2920 (Figura 3.11).


Figura 3.11. Equipos utilizados para la adsorción a temperatura programada. A la izquierda, Micromeritics AutoChem II 2920, a la derecha, Pfeiffer Omnistar Vacuum 300.

### 3.3.3. Adsorción en lecho fijo

Un lecho fijo consiste en un material adsorbente empacado en el interior de un recipiente tubular. Generalmente, el lecho posee forma cilíndrica, se encuentra inmovilizado y cumple las relaciones físicas $D/d_p > 10$ y $L/d_p > 50$, que aseguran un flujo de tapón a través del mismo, siendo D el diámetro del lecho, $d_p$, el diámetro de partícula y L, la longitud del lecho. El proceso de adsorción consiste en el paso de varios gases mezclados, con un caudal y una concentración deseada, a través de dicho lecho, registrando la variación de concentración con el tiempo. El análisis de los gases efluentes puede realizarse a partir de técnicas analíticas como la presentada en la Sección 3.3.2. En general, se trata de una operación de separación de los componentes de la corriente de entrada, obteniendo un efluente purificado, aunque, en ocasiones, el componente de interés también puede ser el retenido sobre el material. Se trata de una operación dinámica en la que entran varios factores en juego, como el equilibrio de adsorción, la dinámica de fluidos y la cinética de adsorción.

El registro de la concentración de salida del componente deseado permite realizar una gráfica que representa la concentración del efluente ($C/C_0$) frente al tiempo (t), denominada curva de ruptura. Las curvas de ruptura son las gráficas más importantes en la caracterización de materiales

adsorbentes en unas condiciones de adsorción dadas (Figura 3.12). En la gráfica, C se corresponde con la concentración del componente estudiado en un tiempo t, mientras que $C_0$ se corresponde con la concentración de dicho componente previo al paso por el lecho fijo, es decir, a la entrada.

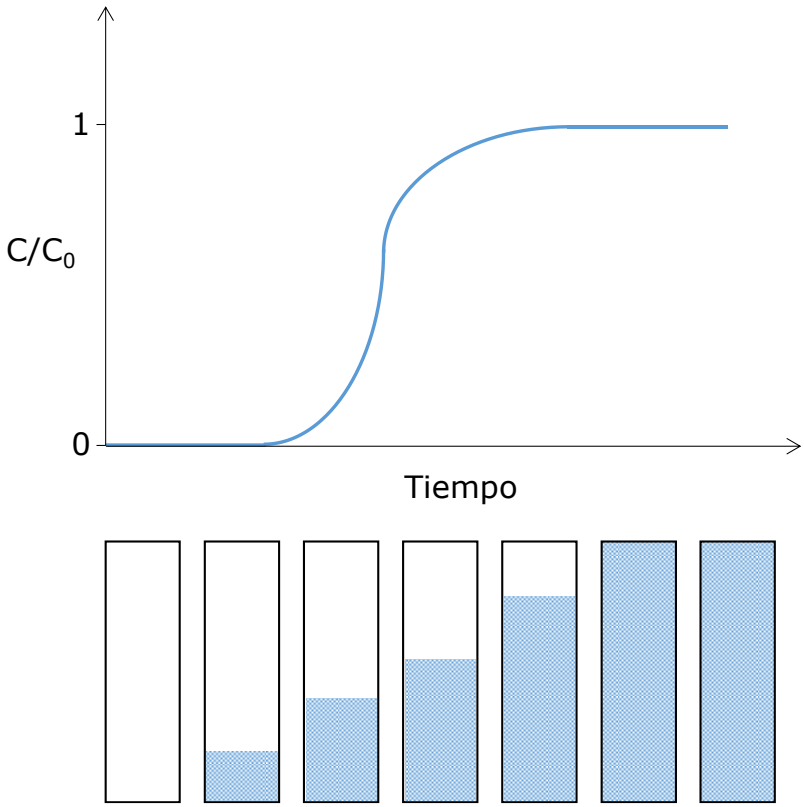


Figura 3.12. Forma típica de una curva de ruptura en la parte superior de la gráfica. En la parte inferior, avance del frente de concentración que se corresponde con la curva de ruptura. La zona sombreada indica la zona saturada del lecho.

Al comienzo de la curva de ruptura, si el material está fresco o adecuadamente regenerado, se observará a la salida del lecho una concentración prácticamente nula del componente más afín al material adsorbente. Con el paso del tiempo, el adsorbato irá saturando la superficie disponible del adsorbente, por lo que la concentración de éste en la salida irá aumentando. Cuando la concentración de salida comienza a aumentar, y se llega a $C/C_0 = 0.05$, aproximadamente, se dice que se ha alcanzado el punto de ruptura. Dependiendo de la aplicación que se le quiera dar a la corriente de salida, se podrán aceptar distintas concentraciones del componente en la corriente de salida, momento en el que se decide detener la operación y regenerar el lecho. Por otro lado, en el momento en el que se alcance una

concentración de salida del componente igual a la de entrada ($C/C_0 = 1$), el material estará totalmente saturado y no adsorberá más adsorbato. El incremento de la concentración a la salida también se denomina avance del frente de concentración. La forma y velocidad del frente dependerán de la capacidad de adsorción del material, así como de las limitaciones cinéticas al transporte de materia.

Como se ha indicado anteriormente, también cabe la posibilidad de que el componente de interés sea el más afín al material adsorbente. En dichos casos, el proceso de adsorción en lecho fijo se utiliza para obtener el componente más concentrado en una etapa posterior. Las técnicas más utilizadas son la adsorción por oscilación de temperatura (TSA) y la adsorción por oscilación de presión (PSA). En el primero de los casos, la etapa de adsorción se realiza a la menor temperatura posible, generalmente temperatura ambiente, y el componente de interés es retenido por el material adsorbente. Una vez saturado el adsorbente, se circula por el lecho un gas de arrastre inerte, por ejemplo, nitrógeno, y se incrementa la temperatura del lecho. El carácter exotérmico de los procesos de adsorción provocará la desorción del componente de interés, que se mezclará con el gas de arrastre en una concentración mayor que en la corriente original, siempre y cuando el equipo y la operación estén adecuadamente optimizados. En segundo lugar, la PSA sigue el mismo principio, pero, en este caso, la adsorción se realiza en condiciones de alta presión, para posteriormente realizar la desorción reduciendo la presión del lecho, también en presencia de un gas de arrastre.

Se han utilizado dos dispositivos experimentales para la realización de los ensayos en lecho fijo. El primero consiste en un lecho fijo metálico de 6.5 mm de diámetro y 1-4 cm de longitud, dependiendo del adsorbente utilizado, introducido en el interior de un horno eléctrico programable (Nabertherm). El dispositivo dispone de dos reguladores de flujo másico (Bronkhorst), a los que se pueden conectar las líneas de gas deseadas para cada experimento (Figura 3.13). La salida de ambos reguladores de flujo másico confluye en la entrada del lecho fijo, aunque también es posible la realización de un *bypass*. Todas las conducciones están recubiertas con manta calefactora y lana de vidrio aislante, que evita condensaciones de ciertos componentes. A la salida del lecho, se conecta en línea un

espectrómetro de masas, que permitirá obtener las curvas de ruptura pertinentes. Las conducciones, previo al lecho fijo, también presentan dos *septum* a través de los cuales se puede introducir agua mediante una bomba de jeringa (KdScientific) o de manera manual (Hamilton).

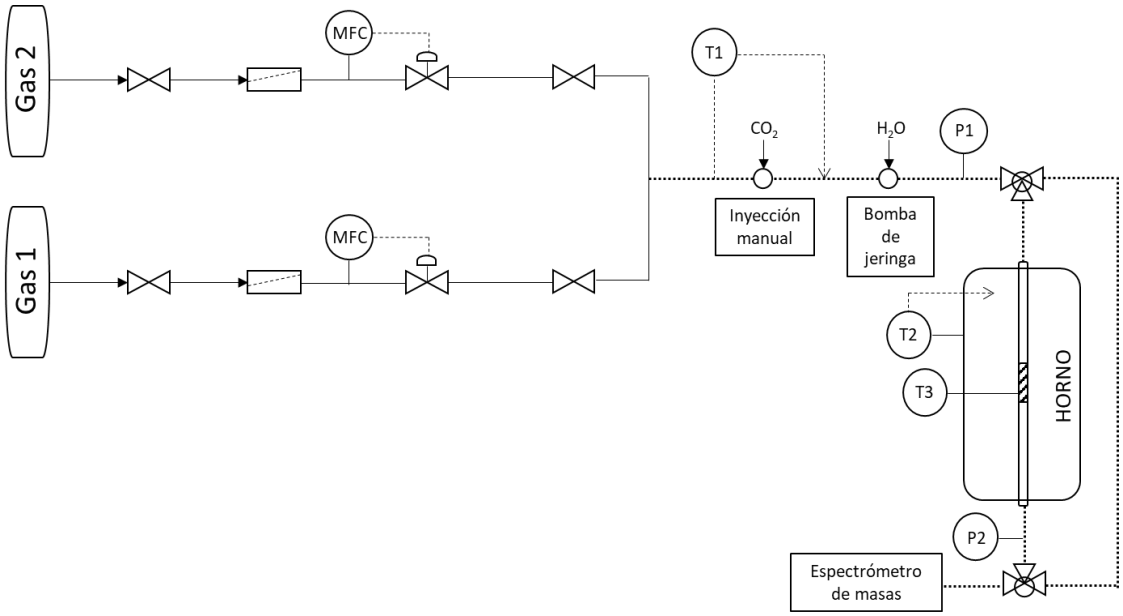


Figura 3.13. Esquema del dispositivo de adsorción en lecho fijo utilizado en la Universidad de Oviedo.

Por otro lado, el segundo dispositivo experimental se ha utilizado en el IRCELYON, y consiste en una combinación de conducciones muy similar al primer dispositivo descrito (Figura 3.14). El lecho fijo utilizado es de vidrio, con 4 mm de diámetro y 1 cm de longitud. La temperatura del lecho fijo está controlada por inmersión en un tanque de agua, envuelto en una carcasa metálica con temperatura regulada eléctricamente. La concentración del componente de estudio se regula mediante un dilutor, Alytech, que permite suministrar la cantidad del componente deseado a la corriente de arrastre introducida con un caudal exacto, establecido previamente en un regulador de flujo másico. En el caso de los experimentos en presencia de agua, la concentración se controla mediante un borboteador bajo temperatura controlada por un horno eléctrico, saturando la corriente de gas que fluye a través. En este caso, la salida del sistema se analiza mediante un equipo de espectroscopía infrarroja por transformada de Fourier (FT-IR), previamente calibrado.

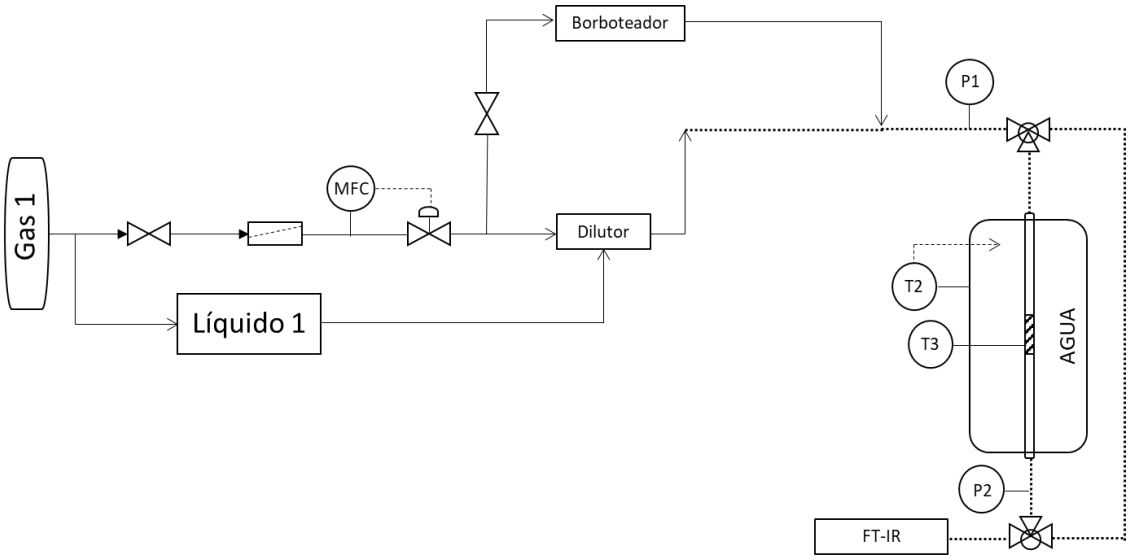


Figura 3.14. Esquema del dispositivo de adsorción en lecho fijo utilizado en IRCELYON.

## 3.4. SIMULACIÓN DE PROCESOS

La simulación de procesos permite estimar, a partir de modelos matemáticos, el comportamiento de un proceso físico-químico estudiado. La simulación de procesos se ha utilizado principalmente para la estimación de curvas de ruptura bajo unas condiciones estipuladas. Previo a la simulación del proceso, se deben definir las ecuaciones matemáticas que representen la operación de adsorción a llevar a cabo. La ecuación principal que define la variación de la concentración a la salida en el lecho con el tiempo es la correspondiente a la curva de ruptura (Ecuación 3.3). Dicha ecuación se complementa con todas las correlaciones necesarias para el cálculo de propiedades y características del material adsorbente utilizado, así como las características de la corriente de entrada al lecho fijo.

$$\frac{\partial C_i}{\partial t} = -\frac{u_0}{\varepsilon_b}\frac{\partial C_i}{\partial z} + D_e\frac{\partial^2 C_i}{\partial z^2} - \rho_b\left(\frac{1-\varepsilon_b}{\varepsilon_b}\right)\frac{\partial q_i}{\partial t} \qquad (3.3)$$

La resolución de la ecuación diferencial permitirá la obtención de la curva de ruptura para el proceso simulado. Para ello, se han utilizado dos paquetes de software distintos para la simulación de los procesos considerados, Aspen Adsorption y COMSOL Multiphysics.

### 3.4.1. Aspen Adsorption

Aspen Adsorption permite realizar la simulación y optimización de condiciones para un amplio abanico de procesos de adsorción de gases a escala industrial. El software permite la simulación directa de procesos como la adsorción reactiva o el intercambio iónico, así como procesos cíclicos como TSA y PSA. Además, dispone de una amplia base de datos con propiedades de multitud de moléculas, así como gran variedad de modelos. El programa permite, a través de una interfaz intuitiva, seleccionar y diseñar la geometría del lecho fijo, su posición en el espacio, y posee una amplia variedad de modelos cinéticos y difusionales tanto para materiales micro como macroporosos. Además, es posible simular el proceso tanto en modo dinámico, como simular directamente el resultado de las variables de interés en el punto de estado estacionario.

Para la simulación de la operación de adsorción en lecho fijo, se parte de la selección de un lecho fijo (*gas_bed*), así como de las corrientes de gas entrantes y salientes del lecho (*gas_feed*). A partir de este punto, el propio software guía al usuario a través del menú para la selección e introducción de todos los parámetros conocidos para la caracterización del lecho fijo. Algunos de los parámetros seleccionables son: método de discretización, ecuación para el cálculo de la pérdida de carga en el lecho, asunciones en el balance de materia (convección, convección y dispersión, entre otros), modelo cinético, modelo de isoterma de adsorción, balance de energía, etc. A partir de dichos valores, el software construye automáticamente la ecuación diferencial correspondiente, y la resuelve. Si la resolución es satisfactoria, será posible la realización de gráficas (*new form > plot*) que permitan observar la dependencia de unos parámetros con otros, así como la curva de ruptura del proceso. Los valores de cualquier variable con el tiempo también se pueden obtener en formato de tabla. La variación de parámetros y la observación de resultados permitirá la optimización del proceso estudiado.

### 3.4.2. COMSOL Multiphysics

El software COMSOL Multiphysics es un software de resolución de ecuaciones diferenciales por el método de elementos finitos. Además de ser

útil para la simulación de ensayos de adsorción, posee varios paquetes predefinidos para multitud de aplicaciones en física e ingeniería. La simulación comienza con la selección del plano de estudio (1D, 2D, 3D), así como la introducción de las dimensiones del elemento espacial a estudiar. El siguiente paso será la selección de la física del sistema, que facilita en gran medida la introducción de los datos posteriormente, adaptando las ecuaciones diferenciales al sistema de estudio: transferencia de calor, flujo de fluido, transporte de especies químicas, etc. En este caso, se selecciona un sistema 1D con una física de transporte de especies diluidas en medios porosos. A partir de dicha selección, al igual que en el caso de Aspen Adsorption, el software irá facilitando la introducción de los distintos parámetros necesarios para la resolución de la ecuación diferencial generada para la física introducida. De la misma forma, también es posible realizar gráficas y tablas de la variación con el tiempo de cualquiera de los parámetros presentes en el modelo.

## 3.5. REFERENCIAS

[1] J. Gascon, S. Aguado, F. Kapteijn, Manufacture of dense coatings of $Cu_3(BTC)_2$ (HKUST-1) on α-alumina, Microporous and Mesoporous Materials 113 (2008) 132-138.

[2] L. Qin, Y. Zhou, D. Li, L. Zhang, Z. Zhao, Z. Zuhra, C. Mu, Highly dispersed HKUST-1 on milimeter-sized mesoporous γ-$Al_2O_3$ beads for highly effective adsorptive desulfurization, Industrial and Engineering Chemistry Research 55 (2016) 7249-7258.

[3] K. Kumar, S. Gadipelli, B. Wood, K. Ramisetty, A. Stewart, C. Howard, D. Brett, F. Rodríguez-Reinoso, Characterization of the adsorption site energies and heterogeneous surfaces of porous materials, Journal of Materials Chemistry A 7 (2019) 10104-10137.

[4] D. Cumming, C. Tumilson, S. Taylor, S. Chansai, A. Call, J. Jacquemin, C. Hardacre, R. Elder, Development of a diffuse reflectance infrared Fourier transform spectroscopy (DRIFTS) cell for the in situ analysis of co-electrolysis in a solid oxide cell, Faraday Discussions 182 (2015) 97-111.

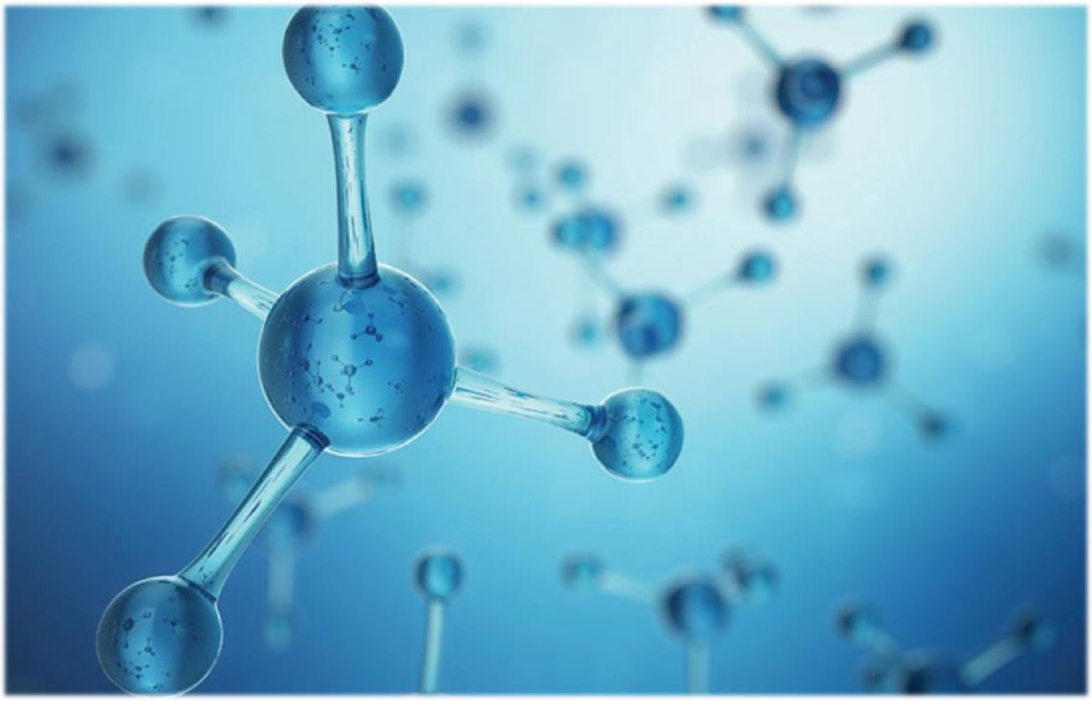

# 4. DISCUSIÓN DE RESULTADOS

4.1. Materiales adsorbentes: MOFs

4.2. Estudio de la adsorción de VAM sobre MOFs

4.3. Modelización y paso de escala del proceso de adsorción

4.4. Síntesis de materiales adsorbentes

4.5. Otros usos de MOFs

## 4.1. MATERIALES ADSORBENTES: MOFs

La selección del material adsorbente es la etapa más importante en el diseño de una operación de adsorción, ya que de su rendimiento y sus propiedades físicas dependerá el diseño de otros parámetros de la operación (tamaño de lecho, tiempo de operación, temperatura de desorción, etc.), así como la concentración máxima alcanzable de metano tras la optimización del proceso completo.

La búsqueda del material adsorbente conforma el grueso del capítulo, en el que se ha realizado una revisión bibliográfica exhaustiva de los materiales utilizados típicamente en la adsorción de metano, tanto en procesos de almacenamiento como en separaciones, a distintas presiones de operación. Los resultados muestran el bajo rendimiento de materiales carbonosos y zeolitas, que presentan dificultades a la hora de separar el metano de otros componentes muy similares molecularmente, como el nitrógeno, además de registrar moderadas capacidades de adsorción. De hecho, la mayoría de estos materiales requieren de modificaciones estructurales que incrementen su eficacia de adsorción y separación, lo que provoca un incremento del coste global de la operación. Estas limitaciones abren la posibilidad de utilizar *metal-organic frameworks* (MOFs). Se trata de materiales constituidos morfológicamente por dos partes principales: ligando orgánico e iones metálicos. El ligando orgánico une los iones metálicos en el espacio, conformando estructuras regulares, con elevada cristalinidad y muy

diversas. La gran variedad de combinaciones entre ligandos orgánicos e iones metálicos disponibles permite la funcionalización de estos materiales hacia la aplicación deseada, resultando generalmente en elevadas superficies específicas y volúmenes de poro. Consecuentemente, los MOFs surgen como una alternativa muy interesante en procesos de separación y almacenamiento de gases, con buenos resultados mostrados en el almacenamiento de hidrógeno para fines energéticos, o en la captura de dióxido de carbono en el desarrollo de sistemas de control de la contaminación atmosférica.

En la revisión bibliográfica realizada, los MOFs empleados en procesos de adsorción y separación de metano se clasifican en familias estructurales, que generalmente comparten el ligando orgánico, pudiendo así establecer las combinaciones y propiedades físico-químicas más favorables para el proceso. Los resultados muestran que la superficie específica y el volumen total de poros son más limitantes en el caso de elevadas presiones de operación, mientras que la presencia de *open metal sites* (OMS) y la densidad de átomos metálicos en la estructura es clave a bajas presiones. Bajo estas premisas, los MOFs sintetizados específicamente para el proceso, que favorecen una combinación de fuerzas de Van de Waals y de Coulomb, muestran buenos resultados de selectividad $CH_4/N_2$ (12.3) y capacidad de adsorción de metano (45 mg/g) en las condiciones deseadas.

Los resultados y su discusión se recogen en la siguiente publicación científica:

- David Ursueguía, Eva Díaz, Salvador Ordóñez, Metal-organic frameworks (MOFs) as methane adsorbents: From storage to diluted coal mining streams concentration, *Science of the Total Environment* **790** (2021) 148211. https://doi.org/10.1016/j.scitotenv.2021.148211.

Factor de Impacto (2021): 10.754
Categoría (2021): Environmental Sciences (26/279: Q1)
Número de citas: 13

## Metal-Organic Frameworks (MOFs) as methane adsorbents: From storage to diluted coal mining streams concentration

David Ursueguía, Eva Díaz, Salvador Ordóñez*

Catalysis, Reactors and Control Research Group (CRC), Department of Chemical and Environmental Engineering, University of Oviedo, Julián Clavería s/n, 33006 Oviedo, Spain

*e-mail: sordonez@uniovi.es (S. Ordóñez)

*Science of the Total Environment* **790** (2021) 148211.

https://doi.org/10.1016/j.scitotenv.2021.148211.

## ABSTRACT

Ventilation air methane (VAM) emissions from coal mines lead to environmental concern because their high global warming potential and the loss of methane resources. VAM upgrading requires preconcentration processes dealing with high flowrates of very diluted streams (< 1% $CH_4$). Therefore, methane separation and concentration is technically challenging and has important environmental and safety concerns. Among the alternatives, adsorption on metal-organic frameworks (MOFs) could be an interesting option to methane selective separation, due to its tuneable character and outstanding physical properties. Most of the works devoted to the methane adsorption on MOFs deal with methane storage. Therefore, these works were reviewed to determine the properties governing methane-MOF interactions. In addition, the metallic ions and organic linkers roles have been identified. Within these premises, decisive effects in the methane adsorption selectivity in nitrogen/methane lean mixtures have been discussed, since nitrogen is the most concentrated gas in the VAM stream, and it is very similar to methane molecule. In order to fulfill this overview, the effect of other aspects, such as the presence of polar compounds (moisture and carbon dioxide), was also considered. In addition, engineering considerations in the operation of fixed bed adsorption units and the main challenges associated to MOFs as adsorbents were also discussed.

**Keywords**: Methane; Mining; Selectivity; MOF; Adsorption; Separation

### 1. Adsorption processes for methane recovery

Methane fugitive emissions from coal mining constitute a significant contribution to greenhouse gases, even after exploitation closure [1, 2]. Typically, methane is emitted discontinuously through mining ventilation air in concentrations between 0.1 and 1% [3]. The flowrates of ventilation air methane (VAM) emissions vary from almost steady-state, through cycles that follow mineral production rates, to the hazardous phenomena of gas outburst or sudden large emissions [4]. Around 70% of the worldwide methane emissions from underground coal mines consist of VAM from coal mine shafts [5]. In these emissions, methane concentration is fixed by safety constraints. The flammability limit for methane/air mixtures is between 5 and 15% of methane. Therefore, within the limits, methane could explode, being the explosion expanded in presence of combustible coal dust [6]. In addition to the safety risks, the environmental concern is also remarkable since methane is a powerful greenhouse gas (GHG). Methane global warming potential (GWP) is about thirty times higher than that of carbon dioxide [7]. In this way, a study about the environmental impact of mining exploitations, using both carbon and ecological footprint, demonstrated that the most important contribution to the environmental impact corresponds to the ventilation of the gases generated in the shafts [8].

Despite its importance, the removal of methane from VAM is still a technological challenge. The most common practice is the combustion of exhaust mining emissions [9, 10]. However, this technique has two important drawbacks, the requirement of auxiliary fuel, and the low energy efficiency. In order to overcome those drawbacks, it is possible either to implement

catalytic combustion or regenerative catalytic oxidation (RCO). The first has low energy consumption and insignificant formation of noxious by-products such as thermal $NO_x$ [11]. In the second case, the feed flow direction is periodically reversed, achieving an autothermal operation [12]. Another possibility is to capture and utilize the stream, generating an additional energy source [13, 14], with better yields for higher methane concentration in a rotary kiln or in a gas turbine combustion, or a chemical feedstock for ethylene or methanol manufacture through catalytic reactions [15, 16]. Due to the mentioned intrinsic features of these streams, diluted gases in large flows with important variations of concentration [17-20], a previous concentration step is required [21]. The removal of nitrogen, carbon dioxide, oxygen and water from the main stream is needed to effectively concentrate the methane of these emissions [22]. The challenge is to separate methane (< 1%) from a mixture of mainly nitrogen (78.1%) and oxygen (20.9%), combined with high relative values of humidity and traces of carbon dioxide (near 0.1%), at ambient temperature and pressure with flowrates of even 45 $m^3/s$ [23, 24].

In general, the most important techniques for these separations are absorption, membrane separation and adsorption. Absorption is a mass transfer operation that uses specific solvents with different absorption capacities for different gas molecules. This operation is usually employed in the removal of impurities, instead of in the concentration of a minority compound. For example, natural gas sweetening, in which adsorbents such as di-ethylene (DE) or tri-ethylene (TE) glycol dimethyl ethers selectively remove carbon dioxide from the main stream [25]. Regarding membrane separation, the simplest purification way is to let selectively the methane pass through. Satisfactory results have been achieved by this technique for both carbon dioxide and nitrogen separations from methane [26, 27]. However, one of the most important limitations of membrane technology is the scaling up of its modules, since the pressure drop, and the module risk of damage are directly related to its size [28]. Therefore, the large-scale manufacturing of selective membranes is still not technologically mature [29]. Concerning the third proposed option, adsorption is one of the major technologies that is promising for increasing methane concentration in exhaust ventilation conducts, Figure 1. This technique can achieve the minimum methane required to operate, *e.g.*, in a gas turbine. In fact, Saleman et al. [30] reached enrichments up to 51.3% of methane from streams containing initially 2.4% of methane.

The typical adsorption equipment consists of a column packed with an adsorbent material. At the adsorption stage, it is obtained a stream enriched in the most weakly retained component. In this case, methane is supposed to be one of the most strongly adsorbed components, so subsequent desorption allows obtaining a methane enriched stream, Figure 2. Occasionally, other individual separations of vapour and gases (water, carbon dioxide, etc.) or particles (to avoid erosion, adsorbent fouling, compressor damage and explosion risk) should be previously implemented [24]. The most common possibilities for adsorption and desorption processes at large scale are the swing adsorption methods. These processes use a cyclic variation of temperature (temperature swing adsorption, TSA) or pressure (pressure swing adsorption, PSA), alternating operation conditions between two or more available beds. In TSA processes, desorption is performed by increasing the temperature of the gas stream during the regeneration. On the other hand, PSA cycles are carried out either by lowering the partial pressures of the adsorbates or by reducing the total pressure by flowing a portion of the product gas over the adsorbent [31]. Usually, for gas purification processes in which the concentration of the component of the gas stream to be removed is lower than 2%, TSA is recommended [32, 33].

To reach its scope, the adsorption process profits the different affinities of the multi-component gaseous mixture components and the adsorbent. Therefore, selected adsorbent materials are a key parameter in the adsorption process. In fact, the main features of the adsorbents can greatly influence the yield of the process both at large and small scale. Among the different available adsorbent materials, inorganic molecular sieves and carbonaceous materials are the most common, being reported several experiences of methane storage and separation from other gases on these adsorbents [34-36]. In this way, Kim et al. [37] have published a comprehensive manuscript about methane separation from diluted and medium-concentrated sources on these materials. Concerning the inorganic materials, the authors have researched experimentally 190 samples and over 87,000 simulations ordered by crystallographic structures, with the aim of looking for a material with adequate structural characteristics for the methane separation.

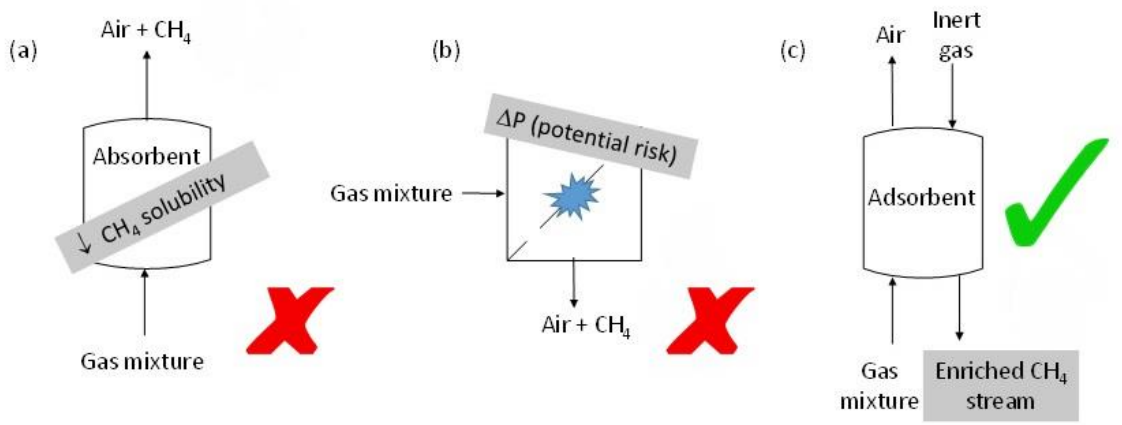


Figure 1. Simple methane enrichment technologies selection: a) absorption, b) membrane separation and c) adsorption.

For these materials, adsorption and selectivity are usually characterized by steric effects, depending on the size of the adsorbate molecule and the pore, and also by the cationic nature of the surface [38]. In general, adsorbate molecules with high quadrupole moments are preferentially adsorbed if they fit in structural pores. Hence, for methane separations from mixtures with low methane and carbon dioxide concentrations in nitrogen ($CH_4/CO_2/N_2$ = 1/1/98), scarce structures were identified with $CH_4/CO_2$ separation ratios of 1.5 onwards. Therefore, inorganic materials are not optimal for methane separation from carbon dioxide, since the strong interaction of carbon dioxide molecule on the structural cations leads to poor selectivity values. In addition, similarities between molecular size of methane and nitrogen difficult to separate them through typical steric effects [39]. Further, methane adsorption capabilities are rather low [37, 40]. On the other hand, carbonaceous materials have also shown low $CH_4/N_2$ selectivities for different kinds of coal-based activated carbons, in addition to poor total adsorption capacity results [41-43]. In general, the adsorption capacity of these materials depends on the accessibility of the adsorbate to the porous structure, due to their large specific surface area [44]. These materials have shown larger adsorption capacity for carbon dioxide than for nitrogen, methane and oxygen [45, 46]. The higher polarizability of $CO_2$ promotes its adsorption. Then, some additional difficulties in the implementation of these materials for the methane separation could appear. These are mainly related to their fixed structure, porosity and specific surface area of inorganic molecular sieves and carbonaceous materials [47].

Therefore, the usual adsorbents present serious limitations in low-concentrated methane adsorption and concentration. These materials show low methane adsorption capacity compared to carbon dioxide, and a very similar adsorption capacity compared to nitrogen. In addition, selectivity is mainly based on the molecular size differences, which in case of methane and nitrogen is very low.

In fact, many of these materials require structural modifications for improving their performance, which would greatly make the process more expensive [48, 49]. Due to these limitations, the use of the materials known as metal-organic frameworks (MOFs) has emerged as an alternative for overcoming the previous problems. The interest in these materials was initially focused on developing gas storage systems for different purposes, such as hydrogen storage for automotive applications or carbon dioxide capture due to concerns over greenhouse emissions [50]. In the case of the methane, as alternative to compressed natural gas, it consists of gas storing as an adsorbed phase in a porous solid [51]. These materials are constituted by two main building blocks: a metal ion or metal oxide and an organic linker. The structures formed by these materials are diverse, since many different combinations of metallic ions and the organic linkers can be made. In addition, the variety of linker molecules, which may be functionalized to introduce changes directly into the framework, offers the possibility of turning the host/guest interactions and tailoring the materials rationally for a determinate separation [51, 52]. A vast number of works have related the surface area, pore size, adsorption heat, open metal sites and ligand functionalization with methane storage performance [53, 54]. Consequently, finding the most effective features of MOFs for the storage and separation of methane from diluted streams can be a turning point in the methane emissions recovery process.

MOFs are then considered as an interesting alternative for methane concentration from VAM emissions. In order to explore this possibility, we will firstly discuss the mechanism of the methane adsorption on these materials (using available data in methane storage). The characteristics of the best materials will be described by families, in order to determine the most suitable features for the adsorption of methane. After this, the selectivity for methane adsorption in inert mixtures will be studied, determining those factors limiting the adsorption performance in gas mixtures. Finally, the effect of other reactive gases (such as humidity or $CO_2$) in the MOF performance and stability will be discussed. In the last part of the review, we will focus on the engineering aspects linked to the use of MOFs as methane adsorbent in practical applications. Aspects as pressure drop or adsorbent conformation, very scarcely treated in the open literature, will be considered at this point.

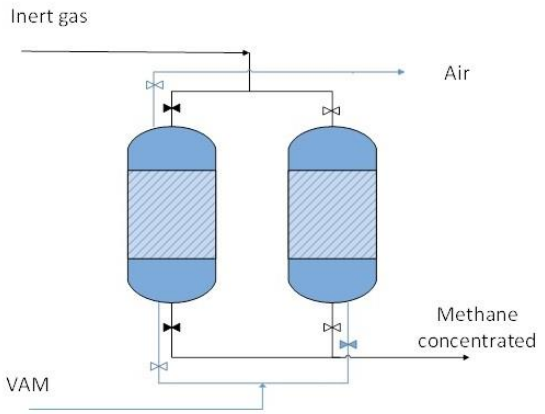


Figure 2. Schematic figure of an adsorption unit. Alternatively, one bed is in adsorption (grey line), whereas the other one is in regeneration mode (black line).

## 2. Adsorption of pure methane on MOF materials: insights from methane storage

Adsorption is an equilibrium-limited process, in which the different physical and chemical interactions between the adsorbent and the gas stream components allow the gas separation or storage [32]. Therefore, in addition to convenient mechanical properties, both methane total adsorption capacity and its selective adsorption are decisive in the adsorbent material selection. Besides, favourable adsorption kinetics and high regenerability are desirable properties. These properties are usually related to the specific surface area, pore size, material composition and the existence of preferential active sites for adsorption, in addition to the surface characteristic polarity [31].

From the point of view of methane-MOF interaction, MOFs present two main sites for methane adsorption: 1) coordinatively un-saturated metal ions (CUS), also called open metal sites (OMS), in which methane binds directly with the metallic ions of the structure through an electrostatic interaction, and 2) enhanced Van der Waals (VdW) potential pockets, in which there is a much weaker interaction, mainly related to the pore size [53]. These features lead to adsorption capacities largely higher than the corresponding to carbonaceous materials and zeolites, being this difference more marked at mild conditions [54, 55]. The adsorption isotherms of MOFs usually follow a type-I trend, reaching saturation at high pressures. Dietzel et al. [56] presented the adsorption isotherms for different MOFs and adsorbates, evidencing the existence of these two main adsorption sites. Moreover, it is observed a decrease of the adsorption isosteric heat once the open metal sites are fully saturated with methane. In this way, Wu et al. [57] have described the two adsorption sites in the structure of different MOFs for methane adsorption (Figure 3).

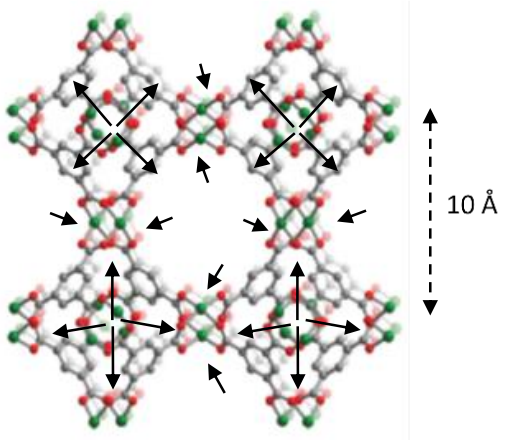


Figure 3. Distribution of methane adsorbed onto HKUST-1 structure [58]. The arrows point towards the higher mass methane load in the structure.

In recent years, many experiments and molecular simulations have dealt with methane and natural gas storage in MOFs. The main objective is to achieve a high density of methane at charge pressure, and be almost completely released at discharge pressure, thus boosting the working capacity. Computational screening has enabled the study of thousands of MOFs and suggested the existence of a physical limitation on methane storage with a maximum working capacity of 200 $cm^3$ (STP) $cm^{-3}$ [58, 59]. Most of these experiments were developed at high pressures, with the uptake measured by two methods: 1) gravimetric, with a microbalance recording the change in weight of a sample at

different methane pressures, and 2) volumetric, with a Sievert's equipment measuring the pressure change when dosing methane into a cell filled with the adsorbent. In Table 1, a compilation of MOFs is classified at intervals of pressure by total methane adsorption capacity. For each one, information about their physical features, such as specific surface area or open metal sites presence, as well as the mechanism of methane adsorption, is collected. Subsequently, it is carried out a family classification. Some of these features along with the adsorption capacity will be very useful for selecting the best materials for the gas separation process. The vast number of materials tested at pressures equal or lower than 35 bar is due to that pressure is the maximum achievable by a one-step compressor [60]. Therefore, a large number of experiments were performed to further extrapolation to higher pressures, trying to meet more easily DOE's objective: 350 $cm^3$ (STP) $cm^{-3}$ [61]. In addition, it is possible to observe great discrepancies among adsorption capacities obtained for the same materials and at similar conditions. At this point, it is important to remark that both experimental, by different techniques, and simulated values are included. Likewise, Chowdhury et al. [62] pointed out that impurities or defects on the crystalline structure of MOFs could be responsible of large differences in the adsorption behaviour, being the point especially relevant since most of the reported MOFs have been synthetized at small scale in the laboratory.

### 2.1. DUT MOFs

Four DUT (Dresden University of Technology) MOFs were presented for methane adsorption at 298 K and different pressures. DUT-49, the material with the highest methane adsorption capacity, is formed by a carbazole derived and metallic ions of copper [94]. This material is an example of a pressure-amplifying material (Figure 4), which enhances methane adsorption capacity at high pressures [95, 96]. It presents a BET specific surface area of 5480 $m^2/g$ and a total pore volume of 2.91 $cm^3/g$ [97]. DUT-6, formed by metallic ions of zinc, presents a high methane adsorption capacity at 100 bar. Its high methane adsorption capacity at high pressures is attributed to its mesoporous character, combined with a high BET specific surface area of 2874 $m^2/g$ and a total pore volume of 2.02 $cm^3/g$ [65, 98].

DUT-9 is formed by benzene-1,3,5-tribenzoate linkers and nickel clusters. It has a BET specific surface area of 3400 $m^2/g$ and two different pore sizes (13 and 25 Å) [65]. It presents a remarkable methane adsorption capacity of 203 mg/g at 35 bar, which is attributed to its high specific surface area and the presence of open metal sites in its structure. In contrast, DUT-52, formed by the link of 2,6-naphtalenedicarboxylate and metallic ions of zinc, presents a poor total methane adsorption capacity at 40 bar, which is related to its low BET specific surface area (1399 $m^2/g$) and accessibility, with a pore size of 8.6 Å [95]. Therefore, these materials confirm that, at high pressures, high specific surface area materials and pore accessibility ensure the good behaviour as methane adsorbent.

### 2.2. Metal azolate frameworks (MAFs)

In this case, the same statement is applicable as for the DUT MOFs. MAF-38 is a metal azolate framework conformed by metallic zinc ions and 4-(1H-pyrazol-4-yl)pyridine and 1,3,5-benzene-tricarboxylate as organic ligands, Figure 5. Although its methane adsorption capacity (246.4 mg/g) at 65 bar is considerable ($S_{BET}$ = 2229 $m^2/g$), it is in an intermediate position to MOF-210/UTSA-76 and Ni-MOF-74, characterized by its high density of open metal sites [70]. Thus, its reduced pore sizes (6.2 and 8.6 Å) and total pore volume (0.808 $cm^3/g$) could reduce its adsorbent potential [99].

### 2.3. $Zn_4O$ based MOFs

This group of MOFs is one of the most important, in terms of the number of materials, including the isoreticular metal-organic-frameworks (IRMOFs). The IRMOF structure is made of $Zn_4O$ tetranuclear clusters connected by rigid dicarboxylic linkers to create a cubic framework, with square channels, which are connected in the three dimensions [100, 101], Figure 6. MOF-210, with biphenyl-4,4' dicarbo-xylate as organic linker, presents a BET specific surface area of 6240 $m^2/g$ and a maximum pore size of 48.3 Å, with an aperture pore of 26.9 Å [73]. This specific surface area is one of the largest surfaces ever reported for a crystalline material. In addition, MOF-177 is formed by benzene-1,3,5-tribenzoate as organic linker, and presents a BET specific surface area of 4630 $m^2/g$, with a pore size of 12.7 Å [102, 103]. The great adsorption capacity of MOF-177 at 100 bar, 221 mg/g, remarks the role of surface area in methane storage at high pressures [102].

Following the order of Table 1, IRMOF-14, with pyrene-2,7-dicarboxylate molecule as organic linker, presents one of the highest methane uptakes, attributed to its BET specific surface area of 4923 $m^2/g$ and a pore size of 14.7 Å [105].

Table 1. Methane storage capacity at different pressures. Shaded areas facilitate the reading between pressures.

| Adsorbent | Uptake (mg/g) | Pressure (bar) | Temperature (K) | Technique | Reference |
|---|---|---|---|---|---|
| Al-BTC | 139.2 | 200 | 303 | Volumetric | [63] |
| DUT-49 | 308 | 110 | 298 | Gravimetry | [64] |
| DUT-6 | 230 | 100 | 298 | Volumetric | [65] |
| MOF-177 | 221 | 100 | 298 | Volumetric | [66] |
| DUT-9 | 188 | 100 | 298 | Gravimetry | [65] |
| MOF-5 | 172 | 100 | 298 | Volumetric | [66] |
| Mg-MOF-74 | 120 | 100 | 298 | Volumetric | [56] |
| Ni-MOF-74 | 100 | 100 | 298 | Volumetric | [56] |
| MIL-101(Cr) | 239 | 80 | 298 | Volumetric | [67] |
| Al-soc-MOF-1 | 510 | 65 | 270 | Simulation | [59] |
| Al-soc-MOF-1 | 420 | 65 | 298 | Volumetric | [68] |
| Al-soc-MOF-1 | 414 | 65 | 298 | Simulation | [59] |
| MOF-210 | 410 | 65 | 298 | Simulation | [59] |
| UTSA-76 | 263 | 65 | 298 | Simulation | [69] |
| MAF-38 | 246.4 | 65 | 298 | Simulation | [70] |
| HKUST-1 | 216 | 65 | 298 | Simulation | [59] |
| Ni-MOF-74 | 148 | 65 | 298 | Simulation | [59] |
| NU-111 | 320 | 60 | 298 | Volumetric | [71] |
| NU-125 | 250 | 60 | 298 | Volumetric | [71] |
| HKUST-1 | 200 | 60 | 298 | Volumetric | [71] |
| PCN-14 | 180 | 60 | 298 | Volumetric | [71] |
| UTSA-20 | 130 | 60 | 298 | Volumetric | [71] |
| Ni-MOF-74 | 110 | 60 | 298 | Volumetric | [71] |
| MIL-101(Cr) | 122 | 50 | 303 | Gravimetry | [72] |
| MIL-125(Ti) | 116 | 50 | 303 | Gravimetry | [72] |
| MIL-100(Fe) | 104 | 50 | 303 | Gravimetry | [72] |
| UiO-66 | 80 | 50 | 303 | Gravimetry | [72] |
| MOF-177 | 170 | 40 | 298 | Volumetric | [73] |
| UiO-67 | 83.2 | 40 | 298 | Simulation | [74] |
| UiO-66 | 80 | 40 | 298 | Simulation | [74] |
| DUT-52 | 76.8 | 40 | 298 | Simulation | [74] |
| Mg-MOF-74 | 363 | 35 | 298 | Volumetric | [75] |
| Ni-MOF-74 | 283.4 | 35 | 298 | Volumetric | [75] |
| MOF-210 | 237 | 35 | 298 | Volumetric | [58] |
| DUT-9 | 203 | 35 | 298 | Volumetric | [58] |
| ZJU-5 | 200 | 35 | 298 | Volumetric | [58] |
| NJU-Bai10 | 199 | 35 | 290 | Volumetric | [76] |
| IRMOF-14 | 194 | 35 | 298 | Simulation | [51] |

| | | | | | |
|---|---|---|---|---|---|
| PCN-16 | 190 | 35 | 298 | Volumetric | [58] |
| IRMOF-14 | 186 | 35 | 298 | Gravimetry | [77] |
| HKUST-1 | 183 | 35 | 298 | Volumetric | [58] |
| PCN-14 | 181 | 35 | 298 | Volumetric | [54] |
| Cu-tbo-MOF-5 | 175 | 35 | 298 | Volumetric | [78] |
| IRMOF-6 | 172 | 35 | 298 | Gravimetry | [77] |
| IRMOF-6 | 171 | 35 | 298 | Gravimetry | [79] |
| IRMOF-1 | 165 | 35 | 298 | Gravimetry | [78] |
| PCN-11 | 163 | 35 | 298 | Volumetric | [80] |
| IRMOF-993 | 160 | 35 | 298 | Simulation | [54] |
| Mg-MOF-74 | 158 | 35 | 298 | Volumetric | [81] |
| IRMOF-1 | 156 | 35 | 298 | Simulation | [54] |
| UTSA-20 | 155 | 35 | 298 | Volumetric | [81] |
| IRMOF-6 | 149 | 35 | 298 | Simulation | [54] |
| Cu-BTC | 144 | 35 | 298 | Gravimetry | [82] |
| Fe(bdp) | 144 | 35 | 298 | Volumetric | [83] |
| Ni-MOF-74 | 138 | 35 | 298 | Volumetric | [58] |
| Co-MOF-74 | 135 | 35 | 298 | Volumetric | [58] |
| MOF-5 | 133 | 35 | 298 | Volumetric | [54] |
| HKUST-1 | 130 | 35 | 298 | Volumetric | [53] |
| Co(bdp) | 128 | 35 | 298 | Volumetric | [83] |
| $Zn_2(BDC)_2(dabco)$ | 125 | 35 | 298 | Volumetric | [82] |
| IRMOF-991 | 121 | 35 | 298 | Simulation | [51] |
| $Mg_2(dhtp)$ | 118 | 35 | 298 | Volumetric | [54] |
| MIL-53-Cr | 114 | 35 | 304 | Volumetric | [53] |
| Ni-MOF-74 | 113 | 35 | 298 | Volumetric | [53] |
| $Ni_2(dhtp)$ | 113 | 35 | 298 | Volumetric | [53] |
| $CuSiF_6(4,4'-byp)$ | 108 | 35 | 298 | Gravimetry | [77] |
| $Co_2(dhtp)$ | 107 | 35 | 298 | Volumetric | [54] |
| $Mn_2(dhtp)$ | 105 | 35 | 298 | Volumetric | [54] |
| $Zn_2(dhtp)$ | 100 | 35 | 298 | Volumetric | [82] |
| IRMOF-0 | 96 | 35 | 298 | Simulation | [51] |
| IRMOF-992 | 92 | 35 | 298 | Simulation | [51] |
| MOF-205 | 120 | 20 | 298 | Simulation | [84] |
| MOF-177 | 100 | 20 | 298 | Simulation | [84] |
| MIL-125(Ti) | 84 | 20 | 303 | Gravimetry | [72] |
| MOF-210 | 80 | 20 | 298 | Simulation | [84] |
| MOF-200 | 80 | 20 | 298 | Simulation | [84] |
| MOF-5 | 70 | 20 | 298 | Simulation | [84] |
| Mg-MOF-74 | 93 | 10 | 298 | Simulation | [85] |
| Zn-MOF-74 | 77 | 10 | 298 | Simulation | [85] |

| | | | | | |
|---|---|---|---|---|---|
| Co-MOF-74 | 64 | 10 | 298 | Simulation | [85] |
| Ni-MOF-74 | 64 | 10 | 298 | Simulation | [85] |
| Ni-MOF-74 | 60 | 4 | 298 | Volumetric | [56] |
| Mg-MOF-74 | 50 | 4 | 298 | Volumetric | [56] |
| Basolite F300 | 110 | 1 | 130 | Gravimetry | [86] |
| HKUST-1 | 30.4 | 1 | 298 | Volumetric | [87] |
| Mg-MOF-74 | 28.8 | 1 | 278 | Volumetric | [88] |
| Ni-MOF-74 | 20.4 | 1 | 298 | Gravimetry | [89] |
| Mg-MOF-74 | 17.6 | 1 | 298 | Volumetric | [88] |
| HKUST-1 | 16 | 1 | 278 | Volumetric | [90] |
| Mg-MOF-74 | 16 | 1 | 298 | Volumetric | [88] |
| HKUST-1 | 14.4 | 1 | 288 | Volumetric | [91] |
| HKUST-1 | 12 | 1 | 278 | Volumetric | [90] |
| HKUST-1 | 11.2 | 1 | 298 | Volumetric | [91] |
| MIL-53 | 11.2 | 1 | 278 | Volumetric | [91] |
| MIL-53 | 9.6 | 1 | 288 | Volumetric | [91] |
| Mg-MOF-74 | 9.6 | 1 | 318 | Volumetric | [88] |
| MOF-177 | 9 | 1 | 298 | Volumetric | [66] |
| UTSA-16/GO | 8 | 1 | 296 | Volumetric | [92] |
| HKUST-1 | 6.4 | 1 | 323 | Volumetric | [91] |
| MIL-53 | 6.4 | 1 | 298 | Volumetric | [91] |
| ZIF-8 | 6.4 | 1 | 278 | Volumetric | [91] |
| ZIF-8 | 4.8 | 1 | 288 | Volumetric | [91] |
| Fe(bdp) | 4.8 | 1 | 273 | Volumetric | [83] |
| Fe(bdp) | 4 | 1 | 285 | Volumetric | [83] |
| ZIF-90 | 3.5 | 1 | 303 | Simulation | [93] |
| Fe(bdp) | 3.2 | 1 | 298 | Volumetric | [83] |
| Co(bdp) | 3.2 | 1 | 273 | Volumetric | [83] |
| MIL-53 | 3.2 | 1 | 323 | Volumetric | [91] |
| ZIF-8 | 3.2 | 1 | 278 | Volumetric | [91] |
| Co(bdp) | 2.4 | 1 | 285 | Volumetric | [83] |
| MOF-5 | 2 | 1 | 298 | Volumetric | [66] |
| Co(bdp) | 1.6 | 1 | 298 | Volumetric | [83] |
| ZIF-8 | 1.6 | 1 | 323 | Volumetric | [91] |

IRMOF-6 and IRMOF-1, also called MOF-5, exhibit decreasing surface areas of 3025 $m^2/g$ [48, 74] and 3100 $m^2/g$ [104], respectively, as well as decreasing pore volume, 9.1 Å [48, 74] and 10 Å. Additionally, Cu-tbo-MOF-5, a modification of IRMOF-1, was synthetized with the aim to improve methane storage [78], from 165 to 175 mg/g at 35 bar and 298 K. Also in this group, and with more reduced adsorption values, there are other materials that have in common its lower specific surface areas and reduced accessible pore diameters, conditioning in this way the methane uptake at these conditions. IRMOF-991, with ethinedicarboxylate as organic linker, presents a BET specific surface area of 3179 $m^2/g$ and a pore size of 11.7 Å. IRMOF-993, with anthracene-9,10-

dicarboxylate (ADC) as organic linker [105], presents a BET specific surface area of 1529 $m^2/g$ and a pore size of 6.3 Å. This last material keeps a relevant methane uptake due to the increment of the number of interaction sites and the reduction of the pore size near to the optimum value [51]. Contrary, IRMOF-0, with a BET specific surface area of 1994 $m^2/g$ and pore sizes of 8.5 and 9.7 Å and IRMOF-992, with 1381 $m^2/g$ and 11 Å, respectively, have the poorest results, being attributed to the reduction of carbon atoms per cavity, which decrease the number of available active centers [51].

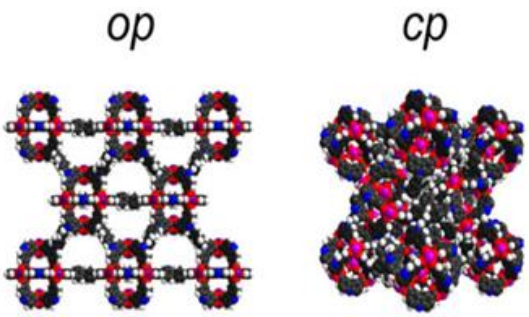


Figure 4. Structure of DUT-49 in open and closed pore states: op and cp, respectively [96]. Cu, blue; O, red; C, grey.

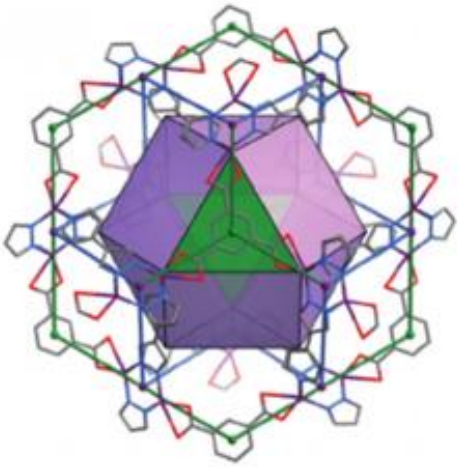

Figure 5. Large quasi-cuboctahedral cage of MAF-38 [99]. Zn, violet; C, grey; N, blue; O, red.

Figure 7 shows a direct relationship between the morphological properties of $Zn_4O$ based MOFs and their adsorption capacity at 35 bar. Consequently with previous discussions, at high pressures, methane total adsorption capacity increases with both specific surface area and pore size.

At 20 bar of pressure, most of the MOFs summarized in Table 1 belong to this group. As it is observed, methane adsorption capacity decreases significantly to values between 120 and 70 mg/g. MOF-205, with 2,6-naphtalene dicarboxylic acid as organic linker, exhibits a BET specific surface area of 4460 $m^2/g$ and a pore size of 30 Å [73], what could be causing the highest adsorption capacity at these conditions. In the same way, MOF-200, formed by 4,4′,4′′-(benzene-1,3,5-triyl-tris(ethyne-2,1-diyl)) tribenzoate as organic linker, presents a BET specific surface area of 4530 $m^2/g$ and a pore size of 28 Å, with an adsorption capacity identical to MOF-210.

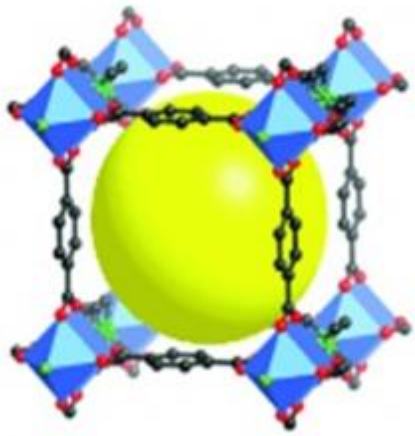

Figure 6. Structure of IRMOF-1 [104]. The structure is common for the rest of the materials of the group.

2.4. Square-octahedral (soc) based MOFs

MOFs based on the square-octahedral (soc) topology are expanded isoreticular structures [68], and present the maximum capacities at 65 bar. Among them, Al-soc-MOF is formed by carboxyphenyl derived linkers and metallic ions of aluminium (Figure 8). It has more than 2 $cm^3/g$ of total pore volume and a BET specific surface area of 5585 $m^2/g$ [68, 106]. The structure encloses cubic-shaped cages of 14.3 Å, and exhibits either enhanced volumetric or gravimetric uptake equilibrium, with a strong influence of the temperature for constant pressures.

Alezi et al. [68] aimed that this material exhibits a pore size near to the optimum for methane adsorption at high pressure. The same authors have done experiments maintaining the Al-soc-MOF platform, varying the MOF number (MOF-1,2,3). MOF-1 resulted the material with the highest BET specific surface area and the highest uptake capacity, surpassing at certain pressures DOE's objective. Therefore, the high capacity of this material at high pressures, even above other materials with a larger specific surface area, reveals that the total pore volume and the pore size are also very influential parameters in the adsorption.

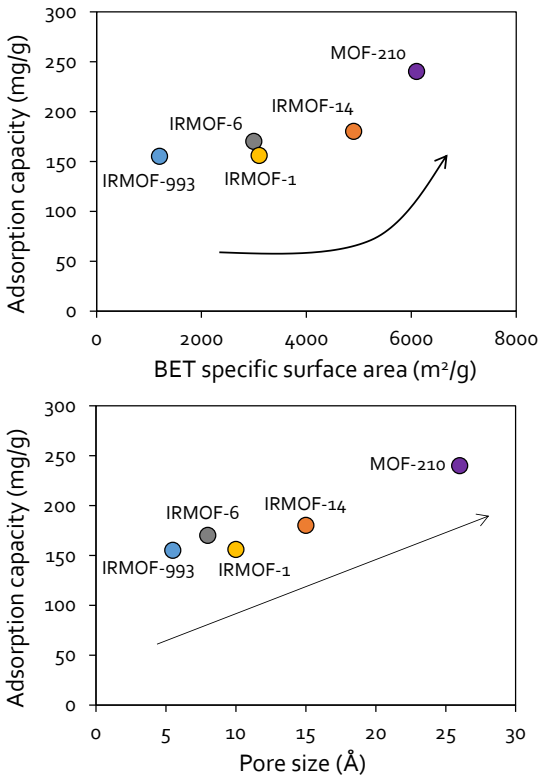


Figure 7. Relationship between morphological properties and methane adsorption capacity at 35 bar for different MOFs.

## 2.5. NU-MOFs

The NU-MOFs (Northwestern University) series belong to rht-copper hexacarboxylate frameworks. These materials arose from the search for greater adsorption capacity without compromising stability. NU-111 presents four different pore sizes (14, 17, 19 and 24 Å), which together with its large BET specific surface area (6140 $m^2/g$), make it an excellent adsorbent [107]. Another NU-MOF, NU-125 (Figure 9), formed by the link of hexacarboxylic acid and metallic ions of copper, presents a BET specific surface area of 3105 $m^2/g$ and good adsorption values at very low temperatures [108]. These materials confirm the previously exposed theory, they are the best materials at 65 bar due to their high specific surface area. In addition, NU-111 presents about 50% more specific surface area than NU-125, which corresponds to an increase in methane adsorption capacity of 22% at 65 bar [71].

## 2.6. MIL-MOFs

MIL-MOFs (Materials Institute Lavoisier) are formed by terephtalic acid and different metallic ions with many possible combinations, Figure 10. All the materials reported from this group presented similar uptake capacities despite its different structure. MIL-101(Cr) has a pore diameter of 16 Å and a BET specific surface area of 4000 $m^2/g$ [109]. This material presents terminal water molecules connected to the octahedral trinuclear $Cr(III)_3O$ building units, creating potential Lewis acid sites, which conferees remarkable stability towards water [110-112].

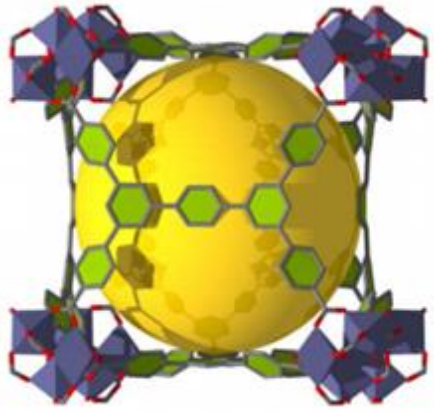

Figure 8. Structure of Al-soc-MOF-1 [68].

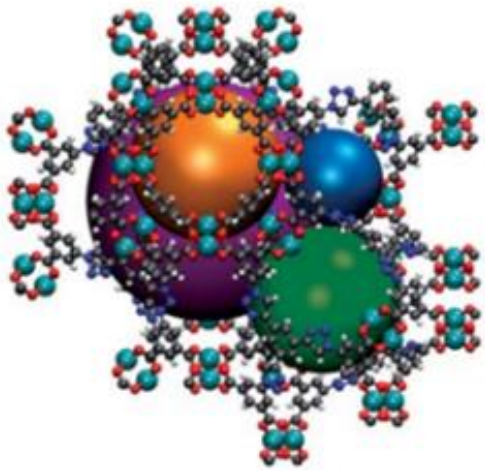

Figure 9. Structure of NU-125 [107]. C, grey; H, white; O, red; N, blue; Cu, cyan.

On the other hand, MIL-125(Ti) has titanium as metallic ions, a BET specific surface area of 1469 $m^2/g$ and a minimum pore size of about 6 Å [114, 115]. MIL-100(Fe) has iron as metallic ions, and a BET specific surface area of 1500 $m^2/g$ [116]. It presents two sets of mesoporous cages that are accessible through microporous windows of 5.5 and 8.6 Å [117]. These results evidence the dominant role of surface area and pore volume in the methane adsorption capacity, as Lee et al. [118] have demonstrated for these materials. The same authors remarked that MOFs should have high porosity for being applied as methane adsorbents.

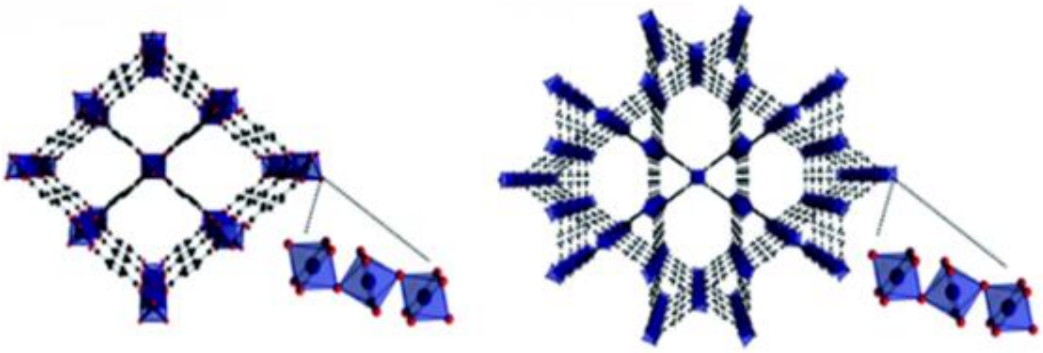

Figure 10. Structure of MIL-MOFs (left: MIL-53(Al), right: MIL-68(Al)) [113].

2.7. UiO-MOFs

UiO-MOFs (Universitetet i Oslo) are made of $Zr_6O_4(OH)_4$ clusters. UiO-66 consists of a cubic framework with a BET specific surface area of 1100 $m^2/g$ and pores of 10 and 7 Å. It is one of the adsorbents most widely used, due to its high chemical and thermal resistance [119]. UiO-67 presents biphenyl-4,4'-dicarboxylate organic linkers, a BET specific surface area of 2583 $m^2/g$ and pores of 23 and 11.5 Å [114, 120, 121].

Similarly to MIL-MOF structures, UiO-MOFs present large octahedral and small tetrahedral pores (Figure 11). Likewise, a significant amount of zirconium Lewis acid sites were observed on these materials [115]. These characteristics provide excellent thermal, chemical and mechanical stability to these structures.

Cavka et al. [123] and Al-Jadir and Siperstein [124] have studied the influence of the pore size and BET specific surface area on the performance of the UiO MOFs. It was observed that methane adsorption capacity is governed by the specific surface area, in agreement with previous observations at high pressures. In addition, it was concluded that the effect of the organic linker on macroscopic properties, such as pore size, is negligible at low pressures, becoming evident at higher ones.

2.8. M-MOF-74

These materials are formed by the link of 2,5-dihydroxyterephthalic acid as organic linker and different metallic ions. These MOFs exhibit a honeycomb-type structure in which the metal cations occupy the corners of hexagons formed by the organic linker (Figure 12). The difference in metallic ion (Mg, Ni, Zn, Mn, Co) can influence the morphology of the material, varying, *e.g.*, from around 1500 $m^2/g$ for Mg-MOF-74 to 500 $m^2/g$ for Zn-MOF-74 [125]. The pore size is about 11-12 Å, conditioning in this way their applications [126]. In addition, the strength of the Lewis acid sites of MOF-74, arising from the presence of open metal sites, decreases in the order: Mg-MOF-74 > Ni-MOF-74 > Co-MOF-74 > Cu-MOF-74 [127]. This order is not the same in case of the concentration of open metal sites, which is between 2.9 and 3.4 mmol/g: Ni-MOF-74 > Co-MOF-74 > Mg-MOF-74 > Cu-MOF-74. Therefore, it is observed that, at low pressures, the concentration of open metal sites takes more importance than its strength, since Ni-MOF-74 presents higher methane adsorption capacity values than Mg-MOF-74. In addition, the presence of open metal sites provokes that the one-dimensional channels of the structure are easily filled with water, which can be removed by a mild thermal treatment [128].

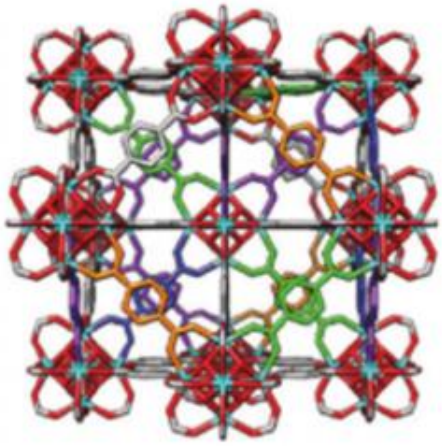

Figure 11. Structure of UiO-66 [122]. Zr, light blue.

These results point out the strong impact of the metal site since the order in the adsorption capacity is not possible to be explained just by the morphology. For example, MIL-125(Ti), with a similar specific surface area than Mg-MOF-74, presents slightly lower adsorption capacity. Although the accessibility of MIL-125(Ti) is favoured, with a medium pore aperture of 69.8 Å versus to 11 to 12 Å for Mg-MOF-74, its higher strength and concentration of open metal sites

make a difference [127]. Likewise, a decrease in the adsorption pressure from 10 to 4 bar just reduces in a 6% the methane uptake for Ni-MOF-74, whereas in case of Mg-MOF-74, this reduction value increases to 35%. Therefore, it is again demonstrated that the methane adsorption at reduced pressures is specially favoured by the concentration of open metal sites, instead of by its strength. In fact, open metal sites concentration at room temperature for Ni-MOF-74 is around 3.5 mmol/g for Ni-MOF-74, and 3 mmol/g for Mg-MOF-74 [127, 130].

### 2.9. PCN-MOFs

PCN-MOFs (Porous Coordination Network) is a sub-group formed by the link of different organic ligands and copper as metallic ions (Figure 13). PCN-16 presents a NbO-type structure designated as the α-phase, a BET specific surface area of 2273 $m^2/g$ and a pore size of 11 Å [131]. On the other hand, PCN-14, with dinuclear $Cu_2(CO_2)_4$ paddle-wheel clusters, presents open metal sites that intensify the adsorption of gas molecules [132]. Copper metallic ions are linked by 5,5′-(9,10-anthracenedyil)diisophthalate [58]. It has a BET specific surface area of 1984 $m^2/g$ and a pore size of 8.3 Å. For a long time, it was one of the best materials for methane storage, so it was studied widely in several manuscripts [71, 133]. Finally, PCN-11 contains trans-stilbene-3,3′,5,5′-tetra-carboxylate as organic linker. It has a BET specific surface area of 1931 $m^2/g$ and a pore size of 12.5 Å [58]. These materials follow the same rule at high pressures as those discussed above. In this case, at 35 bar, the order of adsorption capacity is the same as the BET specific surface area.

### 2.10. Basolite MOFs

Basolite is the commercial name of different adsorbent materials commercialized by BASF. Al-BTC, commercially available under the name Basolite A520, is formed by trimesic acid (1,3,5-benzenetricarboxylic acid) as organic linker and aluminium metallic ions. The structure presents a significant pore volume (0.59 $cm^3/g$) and a BET specific surface area of 1422 $m^2/g$, in addition to a large volume of mesopores of 50 Å [63]. HKUST-1, also called Basolite C300, is formed by trimesic acid and copper metallic ions. It presents a BET specific surface area of 2100 $m^2/g$ and a structure with small cages of 4, 10 and 11 Å [71]. After removal of the axial water molecules typically linked to the structure, the copper atoms become coordinatively unsaturated for binding other gas molecules [39]. Only the cube-octahedral cage has open copper coordination sites into the pore (Figure 14) [135]. Similarly, Fe-BTC, also called Basolite F300, is formed by iron ions and trimesic acid. It has a BET specific surface area of 1600 $m^2/g$ and a pore size of 21.7 Å [117], and presents available iron metal sites for methane adsorption. On the other hand, ZIF-8, also called Basolite Z1200, is a zinc-based material, with a BET specific surface area of 1947 $m^2/g$ and a pore size of 3.4 Å [136]. As seen in the compilation, these materials follow the same previously described rule: the open metal sites enhance the adsorption capacity at low pressures, whereas the limited specific surface areas, in comparison to other MOFs, cause poor yields at high pressures. Likewise, ZIF-8, with narrow pore size of difficult accessibility, is one of the worst materials of the list.

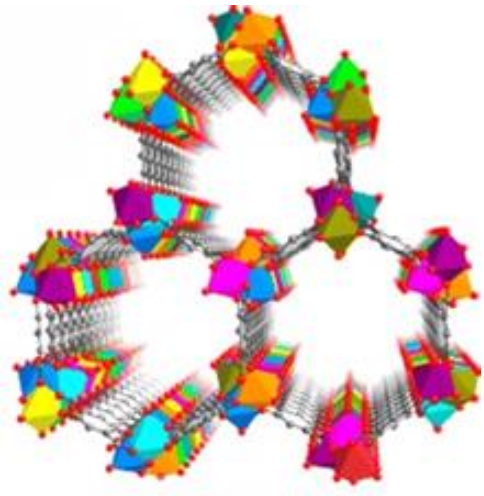

Figure 12. Structure of M-MOF-74 [129].

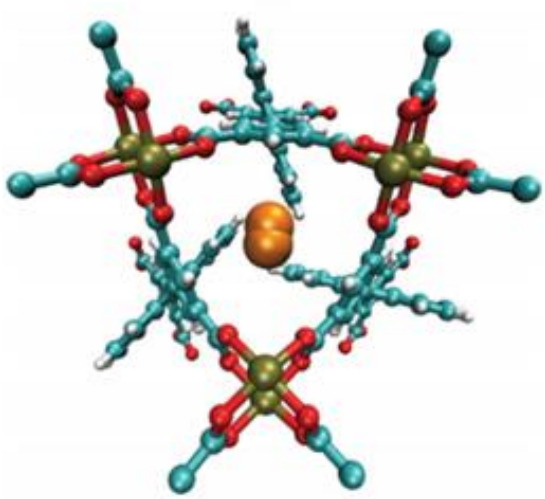

Figure 13. Structure of PCN-14 [134]. C, cyan; H, white; O, red; Cu, tan.

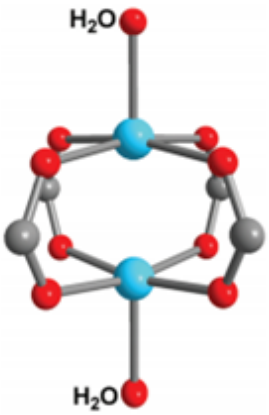


Figure 14. Paddle-wheel unit of HKUST-1 [135].

2.11. UTSA MOFs

UTSA-20 (University of Texas San Antonio) is formed by triylhexabenzoic acid and metallic ions of copper. It presents a moderate BET specific surface area of 1150 $m^2/g$. The structure is formed by two different types of one-dimensional channels: one formed by rectangular pores (3.4 x 4.8 Å) and another cylindrical of 8.5 Å, with high density of open metal sites [137]. On the other hand, UTSA-16, which is formed by the link of cobalt citrate and potassium ions, has a BET specific surface area of 687 $m^2/g$, and a pore size of 33 Å (Figure 15). Its scarce surface available reduces considerably the methane uptake. However, it presents an impressive $CO_2/CH_4$ selectivity, with a ratio of 114.4 [138].

UTSA-76 is formed by metallic ions of copper and the semi-rigid organic linker $H_4L$. It presents a BET specific surface area of 2820 $m^2/g$ and pore volume of 1.09 $cm^3/g$ [69]. In this case, despite the high density of open metal sites present in UTSA-20, at high pressures, the much larger specific surface area shown by UTSA-76 enhances the methane adsorption capacity.

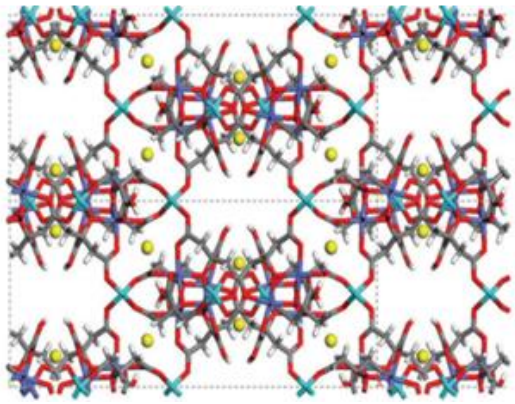

Figure 15. Structure of UTSA-16 along x-axis [138]. C, grey; H, white; O, red; Co, light blue for tetrahedral $Co^{2+}$ and violet for octahedral $Co^{2+}$; K, yellow.

2.12. Other MOFs

In addition to the families presented above, other MOFs have been included in Table 1. Two structures with copper as metallic ion present values of methane adsorption capacity, at 35 bar, around 200 mg/g, NJU-Bai10 (Nanjing University Bai's Group) and ZJU-5 (Zhejiang University), both also with pyridine-derived organic linkers. The former has a BET specific surface area of 2883 $m^2/g$, and three different pore sizes (11, 13 and 7 Å) [76]. In addition, the latter has a BET specific surface area of 2823 $m^2/g$ and it is characterized by its Lewis basic pyridyl sites and its suitable pore space (10.5 Å) [139]. As seen, at high pressures, materials with similar BET specific surface area and pore size, present similar methane uptake capacities.

On the other hand, CuSiF6(4,4'-byp) presents copper as metallic ion, and an adsorption capacity of around 100 mg/g at high pressures. Its lower adsorptive capacity can be attributed to the low BET specific surface area (1100 $m^2/g$) [70]. Finally, concerning ZIF-90, it is a zinc based MOF. It possesses a BET specific surface area of 1270 $m^2/g$ and a pore size of 3.5 Å [140]. Its low methane adsorption capacity may be due to its narrow pore size.

2.13. Other materials

Other materials were tested for methane adsorption, under similar conditions, with the aim of comparison. Following the pressure order, zeolite 5A has presented an uptake capacity of 144 mg/g at 100 bar and 298 K [66, 75], and 99.2 mg/g at 50 bar and 302 K [72]. This material presents a pore size similar to the size of the methane molecule, which eases the adsorption process [141]. Here, it is pointed out a great difference on the adsorption process between zeolites and MOFs. In the former, the adsorption could occur until filling the pore, whereas in the latter, it occurs a stronger interaction with metal centers combined with Van der Waals forces, or only Van der Waals forces in case of absence of open metal sites [85].

Kizzie et al. [142], working with a porous polymer network (PPN), PPN-4, have observed an uptake of 150 mg/g at 50 bar and 298 K. The good properties of PPN: high adsorption capacity, low cost, ease of processing and high thermal stability [143], are just limited by the specificity of the interaction, which could limit their subsequent application for selective separations. Likewise, Alonso et al. [75] raised the use of activated carbon, with an uptake of 224 mg/g at 47 bar and 298 K, whereas Wiersum et al. [72] proposed the

NaX zeolite, with an uptake of 56 mg/g at 40 bar and 303 K. Furukawa et al. [73], in a compilation about covalent organic frameworks (COFs), organic linkers held together by boron oxide clusters by means of covalent bonds, offer very different adsorption capacities [144]. In this way, COF-102, with an adsorption capacity of 187 mg/g at 35 bar and 298 K, presents the best performance. Likewise, mesoporous materials, such as MSM-41, have demonstrated poorer results at the same conditions: 41 mg/g [54].

### 2.14. Suitable features for methane adsorption

From the reviewed data, it is deduced that pure methane adsorption in MOFs upon 60 bar and 270 K is mainly proportional to the specific surface area and pore volume, whereas other features are less relevant. In the 40-60 bar range, the influence of the available surface area and pore volume is also significant, although the surface chemistry becomes more important. In the 30-40 bar interval, a change of the key factor is observed: add to the high surface area, the presence of open metal sites (main contributors to Lewis acidity), as well as metal atoms density within the cavity, contribute to enhance the methane uptake. This trend is more evident at atmospheric pressure. The positive influence of the concentration of active sites versus the strength of its interaction being also evident. In fact, the interaction strength decreases the adsorption capacity and hinders the subsequent desorption. Besides, the size of the cavities in which adsorption occurs and the size of the adsorbate molecule should be as close as possible, to increase the relevance of Van der Waals forces. Figure 16 shows the influence of the surface area of the MOFs in the methane uptake. At atmospheric pressure, a clear benefit of the presence of open metal sites is observed for methane adsorption, especially for MOF-74 and HKUST-1.

From the point of view of operation, in addition to a high adsorption capacity, it is desirable that the adsorbent is easily regenerable. In TSA configuration, where thermal regeneration occurs, it is convenient that low temperature increments promote adsorbate desorption. At this point, Figure 17 shows the appropriate behaviour of Mg-MOF-74, for which an increment of 20 K decreases in a 40% the methane storage. Its high concentration of open metal sites –instead of the strength– is determinant for the methane uptake and regeneration process. Similar reduction percentage (40%) is observed for the MIL-53 structure, but for a lower methane uptake value. In the case of HKUST-1, the material with the largest methane adsorption capacity at atmospheric pressure, the uptake reduction is around 30%. Therefore, here it is shown that the selection of adsorbent requires taking into account not only the adsorption capacity at the working conditions, but also the ease of regeneration.

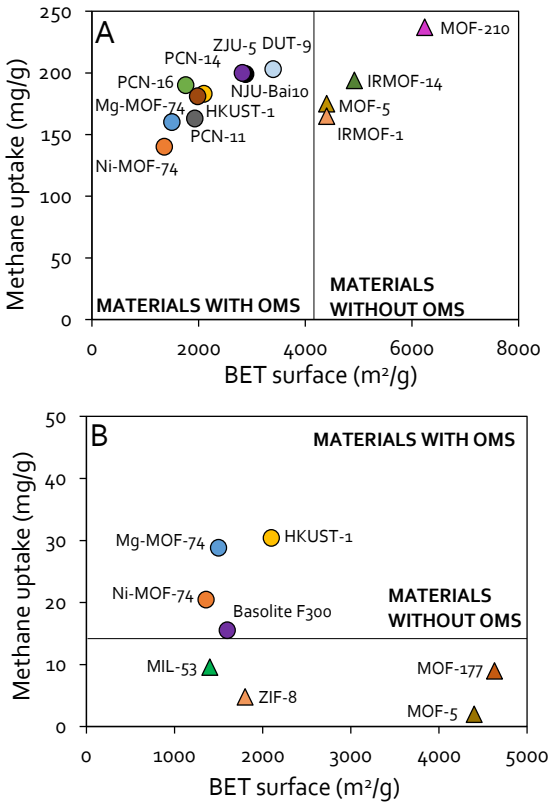


Figure 16. Relation between methane uptake and BET specific surface area depending on the presence of open metal sites in the structure. A: 35 bar, B: 1 bar.

## 3. Methane adsorption in gas mixtures

The scope of the previous section about pure methane adsorption was studying MOF properties determining methane adsorption performance: pure methane adsorption data provide information about the maximum adsorption capacity. However, diluted methane streams also require the study of selective adsorption from a multicomponent mixture [145]. In the case of VAM, methane separation from nitrogen is challenging because of the physicochemical similarities between methane and nitrogen molecules (Table 2). The dominant presence of nitrogen and the similar molecular radius with methane, require a separation based on the different affinities between both molecules to the adsorbent. Open metal sites act as the primary adsorption site for methane. However, a strong interaction of adsorbate on these sites will avoid methane desorption, therefore, the work capacity

will decrease while a higher desorption temperature will be required.

Similarly to the previous section, Table 3 summarizes the scarce works dealing with methane selective adsorption on MOFs from mixtures with nitrogen at low pressures. The first materials presented in Table 3 were either specifically synthesized for methane-nitrogen separations, or typical MOFs tailored with the same purpose. Al-CDC is formed by the link of trans-1,4-cyclohexanedicarboxylic acid and metallic ions of aluminium. It presents a BET specific surface area of 380 $m^2/g$ and a pore size of 5.4 Å [148]. The presence of a specific zone for methane adsorption in the structure increases the selectivity over nitrogen. In addition, the open metal sites promote the high adsorption capacity at low pressures even with a low specific surface area. Li et al. [149] synthesized an ultra-microporous MOF with a BET specific surface area of 75.6 $m^2/g$ and pore dimensions of 4.1 x 4.3 Å, $Co_3(C_4O_4)_2(OH)_2$. It is formed by enhanced negative oxygen binding sites, which add to high methane selectivity, it shows a low methane uptake.

Table 2. Properties of the different molecules present in VAM stream [80].

| Compound | Molecular diameter (Å) | Dipole moment (D) | Polarizability ($Å^3$) |
|---|---|---|---|
| $CH_4$ | 3.82[a] | 0 | 2.448 |
| $N_2$ | 3.65[b] | 0 | 1.710 |
| $CO_2$ | 3.33[c] | 0 | 2.507 |
| $O_2$ | 3.47[b] | 0 | 1.562 |
| $H_2O$ | 2.80[d] | 1.855 | 1.501 |

[a][81]
[b][146]
[c][26]
[d][147]

In the structure, both molecules interact with the framework through multiple Van der Waals interactions, O←→H-C in case of methane and N←→O for nitrogen. The higher selectivity to methane is due to the more suitable pore size and the higher polarizability of the molecule [149]. It is remarkable that the absence of important coulombic forces, due to the absence of open metallic sites, enhances the Van der Waals forces, which improves the separation efficiency, but decreases the total adsorption capacity.

Cu-MOF is a modification of the Basolite C300 (HKUST-1) with a distorted structure. This material presents a BET specific surface area of 110 $m^2/g$ and pore sizes of 7 and 5 Å [150]. In this case, the copper open metal sites are not exposed. This disposition leads to two new types of micropores. The link distance of methane and nitrogen with these micropores is lower for methane, indicating a higher attraction. As previously, the Van der Waals forces ensure the selectivity; however, both the low specific surface area and the absence of open metal sites, lead to low methane adsorption capacities. In addition, ATC-Cu is synthetized by 1,3,5,7-adamantane tetracarboxylic acid as organic linker and copper as metallic ions. It possesses a BET specific surface area of 600 $m^2/g$ and 0.23 $cm^3/g$ of total pore volume. The arrangement of the atoms forms two cavities in which methane is adsorbed: 4.4 x 5.4 Å and 3.5 Å [151].

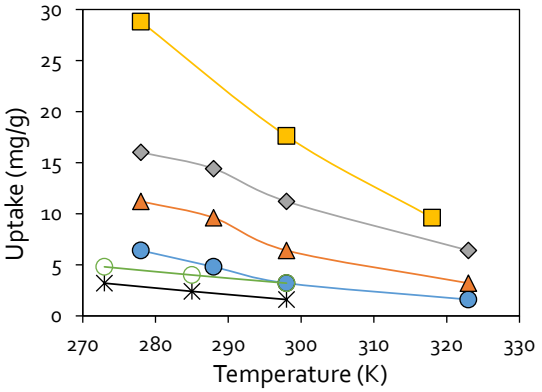


Figure 17. Methane uptake profile with temperature for adsorption at 1 bar for different MOF structures. ZIF-8 (filled blue circles), MIL-53 (filled orange triangles), HKUST-1 (filled grey rhombus), Mg-MOF-74 (filled yellow squares), Co(bdp) (black flakes), Fe(bdp) (empty green circles).

In this material, both attractive forces have an important role, since it has two zones for the adsorption of methane with very high adsorption enthalpies. In fact, selectivity and adsorption capacity are two of the highest of all the materials compiled. Other material is $Cu(INA)_2$, which consists of isonicotinic acid and metallic ions of copper. It presents a BET specific surface area of 251.8 $m^2/g$ and a total pore volume of 0.12 $cm^3/g$. Its pores are rectangular channels of 4.7 Å [152]. In this case, equal than for $Co_3(C_4O_4)_2(OH)_2$, Van der Waals forces have more importance, increasing the selectivity ratio. Finally, Kim et al. [153] demonstrated that the incorporation of functional groups with high polarizability can enhance the methane uptake and the selectivity. It is the case of UiO-66, with the addition of $Br_2$. It presents a BET specific surface area of 622 $m^2/g$ and a pore size between 7 and 8 Å. It presents a high desorption improvement in comparison with pristine

UiO-66. This knowledge about the main characterristics in order to tailor the MOFs to improve methane separation was used by several authors to selectively separate methane from very diluted streams. For example, Chanajaree et al. [157] and Li et al. [158] have done Monte Carlo simulations for methane separation on ZIF MOFs. In case of a stream with 10% of methane in nitrogen at 298 K and atmospheric pressure, it was achieved a selectivity of 4.1 for the ZIF-78 MOF.

Concerning materials already described in methane storage section (Ni-MOF-74, Mg-MOF-74, MIL-100(Cr), HKUST-1 and MIL-100V), the adsorption mechanisms are really similar, that is, the interaction between the adsorbate molecules and the open metal sites of the adsorbent [89]. MOF-5 and MOF-177 adsorption is based mainly on its high BET specific surface area values in absence of open metal sites. Figure 18 shows as the highest uptake capacities are for materials with open metal sites, whereas the highest selectivities are more related with pore size and the existence of specific zones for methane adsorption. Therefore, at low pressures, the pore size and the presence of both adsorptive forces (coulombic and Van der Waals) are more important than the BET specific surface area or total pore volume. Therefore, to achieve an efficient methane/nitrogen separation, materials must be designed with a pore size adjusted to the adsorbate, with the presence of not very strong open metal sites and with cavities in which Van der Waals forces are generated between the oxygen of the structure and the four hydrogens of the methane molecule.

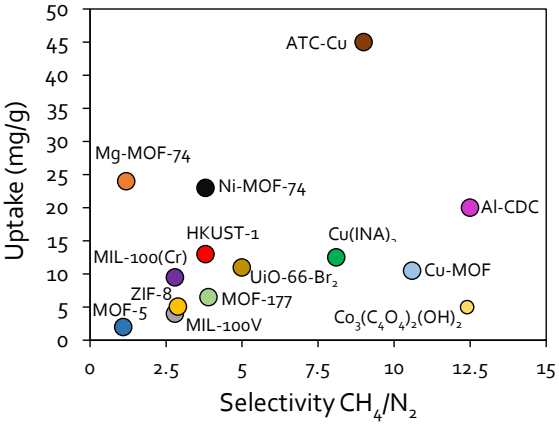


Figure 18. Relation between methane uptake and $CH_4/N_2$ selectivity for different MOF materials.

### 4. Effect of other components of the emissions on MOF adsorption properties

The comparison of the properties of the main VAM components, shows that all the molecules are non-polar, except water, and that carbon dioxide has the highest polarizability (Table 2). Concerning water, the presence of open metal sites hinders the performance of these materials in presence of moisture [159]. Different works have obtained results that indicate that materials with high metallic valences (tri- or tetravalent metallic ions) are active water adsorbents [160].

The polarity of the water molecule causes this attraction, enhancing the coverage of all the adsorption active sites, which hinders methane adsorption. In fact, Gonçalves et al. [161] have studied the effect of the presence of water on the methane adsorption capacity of some of the most common MOFs (Cu-BTC, IRMOF-1, Mg-MOF-74, etc.), observing that the MOFs with open metal sites are the most affected by water. Cu-BTC presented a decrease of 2.2% in the total amount of methane adsorbed between pure methane and methane with 140 ppm of water, whereas Mg-MOF-74 presented a decrease of 20% at the same conditions. On the other hand, materials without open metal sites do not present remarkable performance decreases. Likewise, the relative humidity influence was studied by demonstrated by Chidambaram et al. [162]. Accordingly, Rogacka et al. [163] have made a screening of the best MOF materials for the separation of methane and carbon dioxide in presence of water.

Some of the proposed MOFs are really hydrophilic, since the carbon dioxide adsorbed is displaced from open metal sites due to the presence of water. Most of the MOFs have been really affected by relative humidity over 30%. Likewise, García and Navalón [164] have done a comprehensive compilation about the differences in adsorption depending on the moisture in the MOF structure. In order to avoid effectiveness losses, several authors have studied the different pathways to increase the hydrophobicity of the materials [165]. Some of them have achieved good results, even largely retaining the original adsorptive properties of the materials. In spite of this, the techniques are not fully developed yet, so it would be recommended to perform a prior separation of moisture from the streams.

Concerning the other gases, the interaction strength on a polar adsorbent is $CO_2 > CH_4 > N_2 > O_2$ [166]. The higher polarizability of carbon dioxide than methane makes stronger the link with the open metal sites of the adsorbent [167]. In fact, carbon dioxide adsorption enthalpy is above 30 kJ/mol in some cases, which indicates an elevated bond strength [168].

Table 3. MOFs performance for selective adsorption.

| Adsorbent | $CH_4/N_2$ selectivity | Uptake (mg $CH_4$/g) | Pressure (bar) | Temperature (K) | Reference |
|---|---|---|---|---|---|
| Al-CDC | 13 | 20.96 | 1 | 298 | [148] |
| $CO_3(C_4O_4)_2(OH)_2$ | 12.5 | 5.92 | 1 | 298 | [149] |
| Cu-MOF | 11 | 9.82 | 1 | 298 | [150] |
| ATC-Cu | 9 | 44.8 | 1 | 298 | [151] |
| $Cu(INA)_2$ | 8.3 | 13.23 | 1 | 298 | [152] |
| UiO-66-$Br_2$ | 5.1 | 11.52 | 1 | 298 | [153] |
| MOF-177 | 4 | 8.18 | 1 | 298 | [66] |
| Ni-MOF-74 | 3.8 | 22.75 | 1 | 298 | [89] |
| HKUST-1 | 3.7 | 13.15 | 1 | 298 | [154] |
| ZIF-8 | 3.1 | 5.2 | 1 | 196 | [155] |
| MIL-100(Cr) | 3 | 8.83 | 1 | 298 | [89] |
| MIL-100V | 3 | 3.57 | 1 | 298 | [156] |
| Ni-MOF-74 | 3 | 20.48 | 4 | 298 | [89] |
| Mg-MOF-74 | 1.5 | 24.27 | 1 | 298 | [89] |
| MOF-5 | 1.1 | 1.23 | 1 | 298 | [66] |

The same than in separation from nitrogen, some authors like Duan et al. [169] have treated to enhance gas molecule-framework interaction by adjusting the cage size through changing the metal cluster, organic linker or synthesis conditions. In recent times, there are several manuscripts that deal with the $CO_2/CH_4$ separation [170-173]. All the materials studied, including MOFs, presented higher affinity for carbon dioxide than for methane. The nonpolar covalent bonds in methane promote lower uptakes, due to the hydrophilic walls of these frameworks [174]. Hence, the importance carbon dioxide of pre-separation from the stream, avoiding the poisoning of the adsorbent. It should also be noted that, in ventilation streams, the concentration of carbon dioxide is low, sometimes even at trace level.

## 5. Engineering aspects of the adsorption processes using MOFs

Concerning the packing of the solid adsorbent, conventional concentrators usually perform using fixed beds of granular adsorbents. In this way, the associated pressure drop leads to larger gas pumping costs. The pressure drop in a packed bed is usually described by the Ergun equation (Equation 1). Where $u_0$ is the surface velocity, $\rho$ and $\mu$ are the density and viscosity of the gas, respectively, $D_p$ the particle diameter, L the length of the bed, and $\varepsilon$, the bed porosity. In a typical operation, for a surface velocity of 0.125 m/s and particle diameters of 162.5 and 520 μm, the pressure drop is of 172.5 and 53.7 Pa/m, respectively. This example illustrates the importance of the particle diameter both in the adsorption process and, hence, in energy consumption. Rezaei and Webley [175] remarked that, in the case of structured adsorbents, monoliths or laminate structures ease suitable values of bed porosity ($\varepsilon$). In this way, Hong et al. [176] proposed a MIL-101(Cr) monolith for carbon dioxide adsorption working at high pressure and low temperatures. Likewise, Rezaei et al. [177] immobilized two MOFs, Ni-MOF-74 and UTSA-16 on commercial cordierite monolith for carbon dioxide capture, obtaining moderate adsorption capacities and fast kinetics. Several MOFs present high adsorption capacity losses after the shaping process, especially if these are modifications made by mechanical pressurization [178]. Therefore, the MOF shaping is a challenge for decreasing the pressure drop in concentrator units. These shaping processes should consider the relatively low thermal, chemical and mechanical stability of the materials, ensuring that adsorption properties of the material remain unaltered.

Concerning MOFs shaping, different approaches have been considered. Stable slurries formation, using organic binders such as polyvinyl alcohol aqueous solution, allows further material shaping by granulation or extrusion [179].

$$\Delta P = \frac{150 \cdot \mu \cdot L}{{D_p}^2} \frac{(1-\varepsilon)^2}{\varepsilon^3} u_0 + \frac{1.75 \cdot L \cdot \rho}{D_p} \frac{(1-\varepsilon)}{\varepsilon^3} {u_0}^2 \quad (1)$$

Other approaches deal with the milling of the MOF with a solid binder, such as graphite, followed by a pressure-driven pelletization of the mixture. In this case, the effect of the pelletizing pressure on the morphological properties of the MOFs must be considered. Finally, another possibility is the 3D printing technique. In fact, 3D-printed Ni-MOF-74 and UTSA-16 monoliths were tested for CO adsorption [180], with adsorption capacities of 1.35 and 1.31 mmol/g at 298 K, respectively, which represent the 79 and 87% of the capacities of their analogues MOF under the same conditions. Another important issue, in order to achieve that MOFs will be used at large-scale applications, consists of its production. Since the first patent in 1995, MOFs production has progressed gradually, but a key point is the possibility of synthesizing these materials in large quantities with high efficiency. In this way, several efforts were made based on the solvent-free approach and water-based synthesis [179]. However, add to the synthesis route, the downstream processing should be also improved, so large-scale application of MOFs will be limited by their commercial availability. Efforts in MOF commercialization have led to the creation of several spin off companies, such as MOF Apps, MOF Technologies and ProMOF. Likewise, among the MOF distributors, it is possible to find STREM Chemicals and Sigma Aldrich, the latter from BASF.

In summary, chemically suitable materials (adequate organic ligand and metal sites) are required, but without neglecting the engineering aspects. In this way, the ideal material would involve a low pressure drop design, resistant to humidity and high temperatures, and that could be manufactured on a large scale.

## 6. Conclusions and future recommendations

Methane separation from VAM streams by adsorption was discussed in this work. The features of these streams are: low methane concentration (< 1%) in air, combined with high relative values of humidity and traces of carbon dioxide, at ambient temperature and pressure with high flowrates. With these conditions, MOFs are considered as an interesting choice for overcoming the limitations of the common adsorbents. In this review, a vast revision on the behaviour for methane storage at different pressures, and on different MOF structures was carried out. Pure methane adsorption in MOFs is mainly proportional to the specific surface area and pore volume at high pressures, whereas the presence of open metal sites (main contributors to Lewis acidity), as well as metal atoms density within the cavity, contribute to enhance the methane uptake at low pressures. Thus, structures like HKUST-1 and MOF-74 stand out for their methane storage capacity at atmospheric pressure, and also with ease of thermal regeneration.

The main challenge is the methane/nitrogen separation, for which combination of Van der Waals and coulombic forces are required. The first depends on the attraction between oxygen atoms of the adsorbent structure and the adsorbate molecules, being increased with a more tailored pore topology. The second effect depends on the presence of open metal sites in the structure. Likewise, an equilibrium between the number of open metal sites and their strength, which could lead to irreversible adsorption, is advisable. Materials presenting the best results are the ones specifically synthesized for this separation: (Al-CDC, $CO_3(C_4O_4)_2(OH)_2$, Cu-MOF and ATC-Cu).

The ideal material for the process must gather the features discussed above: high adsorption capacity (presence of a high concentration of open metal sites), hydrophobicity (low metallic oxidation states and as low as possible relative humidity conditions), easy regenerability by temperature increment and good methane selectivity values (high importance of Van der Waals forces). Based on discussion here presented, future research studies should rely on these characteristics for the design of new materials applied to actual gas separation cases. In addition to the effectiveness of separation under ideal conditions, material stability at operation conditions should be also considered, thus shaping is a key point.

## CRediT authorship contribution statement

**David Ursueguía**: Writing — original draft, Data curation, Writing — review & editing, Formal analysis. **Eva Díaz**: Writing — review & editing, Visualization, Conceptualization, Project administration. **Salvador Ordóñez**: Visualization, Conceptualization, Project administration, Supervision.

## Declaration of competing interest

The authors declare that they have no known competing financial interests or personal

relationships that could have appeared to influence the work reported in this paper.

**Acknowledgments**

This work was supported by the Research Fund for Coal and Steel of the European Union (contract 754077 — METHENERGY PLUS).

David Ursueguía acknowledges the Spanish Ministry of Education for the PhD grant that supports his research (FPU program).

**References**

[1] F. Pavloudakis, C. Roumpos, E. Karlopoulos, N. Koukouzas, Energies 13 (2020) 3995.

[2] J. Gao, C. Guan, B. Zhang, Sci. Total Environ. 725 (2020) 138295.

[3] S. Su, A. Beath, H. Guo, C. Mallett, Prog. Energy Combust. Sci. 31 (2005) 123-170.

[4] N. Szlazak, D. Obracaj, J. Swolkien, Mining Metall. Explor. 37 (2020) 567-579.

[5] M. Borowski, P. Zyczkowski, R. Luczak, M. Karch, J. Cheng, Energies 13 (2020) 44.

[6] S. Erdogan, O. Karacan, E. Okandan, Int. J. Rock Mech. Min. Sci. 63 (2014) 148-158.

[7] R. Derwent, Atmopshere 11 (2020) 486.

[8] E. Díaz, J. Fernández, S. Ordóñez, N. Canto, A. González, Ecol. Indic. 18 (2012) 126-130.

[9] K. Shah, B. Moghtaderi, E. Doroodchi, J. Sandford, Fuel Process. Technol. 140 (2015) 285-296.

[10] B. Qin, L. Li, D. Ma, Y. Lu, X. Zhong, Y. Jia, PSEP 103 (2016) 203-211.

[11] R. Niu, P. Liu, W. Li, S. Wang, J. Li, Micropor. Mesopor. Mat. 284 (2019) 235-240.

[12] Z. Li, Z. Wu, Z. Qin, H. Zhu, J. Wu, R. Wang, L. Lei, J. Chen, M. Dong, W. Fan, J. Wang, Fuel Process. Technol. 160 (2017) 102-108.

[13] B. Oboirien, B. North, S. Obayopo, J. Odusote, E. Sadiku, Energy Stra. Rev. 20 (2018) 64-70.

[14] A. Singh, J. Kumar, Energy Procedia 90 (2016) 336-348.

[15] S. Xie, S. Lin, Q. Zhang, Z. Tian, Y. Wang, J. Energy Chem. 27 (2018) 1629-1636.

[16] M. Álvarez, P. Marín, S. Ordóñez, Mol. Catal. 487 (2020) 110886.

[17] J. Yin, S. Su, X. Yu, J. Bae, Y. Jin, A. Villella, M. Jara, M. Ashby, M. Cunnington, M. Loney, Energ. Fuel. 34 (2020) 9885-9893.

[18] D. Cluff, G. Kennedy, J. Bennett, P. Foster, Appl. Therm. Eng. 90 (2015) 1151-1163.

[19] B. Zheng, Y. Liu, R. Liu, J. Meng, Int. J. Hydrogen Energy 40 (2015) 3381-3387.

[20] K. Baris, Energy Sustain. Dev. 17 (2013) 13-23.

[21] I. Karakurt, G. Aydin, K. Aydiner, Renew. Sust. Energ. Rev. 15 (2011) 1042-1049.

[22] N. Goraya, N. Rajpoot, B. Sivagnanam, ChemistrySelect 4 (2019) 3585-3601.

[23] J. Fernández, P. Marín, F. Díez, S. Ordóñez, App. Thermal Eng. 102 (2016) 167-175.

[24] S. Su, H. Chen, P. Teakle, S. Xue, J. Environ. Manag. 86 (2008) 44-62.

[25] A. Henni, P. Tontiwachwuthikul, A. Chakma, J. Chem. Eng. Data 51 (2006) 64-67.

[26] M. Anderson, H. Wang, YS. Lin, Rev. Chem. Eng. 28 (2012) 101-121.

[27] K. Lokhandwala, I. Pinnau, Z. He, K. Amo, A. DaCosta, J. Wijmans, R. Baker, J. Memb. Sci. 346 (2010) 270-279.

[28] R. Koc, N. Kazantzis, W. Nuttall, Y. Ma, J. Loss Prev. Process Ind. 26 (2013) 468-477.

[29] B. Mi, Science 364 (2019) 1033-1034.

[30] T. Saleman, G. Li, T. Rufford, P. Stanwix, K. Chan, S. Huang, E. May, Chem. Eng. J. 281 (2015) 739-748.

[31] J. Li, R. Kuppler, H. Zhou, Chem. Soc. Rev. 38 (2009) 1477-1504.

[32] R. Yang, Adsorbents: fundamentals and applications, first ed., John Wiley & Sons, 2003.

[33] A. Ghoshal, S. Manjare, J. Loss. Prev. Process Ind. 15 (2002) 413-421.

[34] M. Kacem, M. Pellerano, A. Delebarre, Fuel Process. Technol. 138 (2015) 271-283.

[35] J. Delgado, M. Uguina, J. Sotelo, B. Ruíz, M. Rosário, J. Nat. Gas Chem. 16 (2007) 235-243.

[36] S. Cavenati, CA. Grande, AE. Rodrigues, J. Chem. Eng. Data 49 (2004) 1095-1101.

[37] J. Kim, A. Maiti, L. Lin, J. Stolaroff, B. Smit, R. Aines, Nat. Commun. 4 (2013) 1-7.

[38] F. Gholipour, M. Mofarahi, J. Supercritical Fluids 111 (2016) 47-54.

[39] M. Ghazvini, M. Vahedi, S. Nobar, F. Sabouri, J. Environ. Chem. Eng. 9 (2021) 104790.

[40] R. Javani, H. Maghsoudi, S. Gilan, M. Majidpour, Sep. Sci. Tech. (2020) 1-16.

[41] H. Yi, F. Li, P. Ning, X. Tang, J. Peng, Y. Li Y, Chem. Eng. J. 215-216 (2013) 635-642.

[42] D. Yuan, Y. Zheng, Q. Li, B. Lin, G. Zhang, J. Liu, Powder Technol. 333 (2018) 377-384.

[43] Y. Zheng, Q. Li, C. Yuan, Q. Tao, Y. Zhao, G. Zhang, J. Liu, Powder Technol. 347 (2019) 42-49.

[44] X. Hou, S. Liu, Y. Zhu, Y. Yang, Fuel 268 (2020) 117349.

[45] I. Esteves, M. Lopes, P. Nunes, J. Mota, Sep. Purif. Technol. 62 (2008) 281-296.

[46] P. Carrott, I. Cansado, M. Carrott, Appl. Surf. Sci. 252 (2006) 5948-5952.

[47] Y. Lin, C. Kong, Q. Zhang, L. Chen, Adv. Energy Mater. 7 (2017) 1601296.

[48] X. Zhang, P. Xiao, G. Chen, C. Sun, L. Yang, Chem. Eng. Tech. 41 (2018) 1818-1825.

[49] Y. Wang, R. Yang, ACS Sustainable Chem. Eng. 7 (2019) 3301-3308.

[50] P. Sridhar, N. Kaisare, J. Ind. Eng. Chem. 85 (2020) 170-180.

[51] T. Düren, L. Sarkisov, O. Yaghi, R. Snurr, Langmuir 20 (2004) 2683-2689.

[52] T. Ghanbari, F. Abnisa, W. Daud, Sci. Total. Environ. 707 (2020) 135090.

[53] W. Zhou, Chem. Rec. 10 (2010) 200-204.

[54] H. Wu, W. Zhou, T. Yildirim, J. Am. Chem. Soc. 131 (2009) 4995-5000.

[55] J. Rother, T. Fieback, Adsorption 19 (2013) 1065-1074.

[56] P. Dietzel, V. Besikiotis, R. Blom, J. Mat. Chem. 19 (2009) 7362-7370.

[57] H. Wu, J. Simmons, Y. Liu, C. Brown, X. Wang, S. Ma, V. Peterson, P. Southon, C. Kepert, H. Zhou, T. Yildirim, W. Zhou, Chem. Eur. J. 16 (2010) 5205-5214.

[58] J. Mason, M. Veenstra, J. Long, Chem. Sci. 5 (2014) 32-51.

[59] B. Li, H. Wen, W. Zhou, Q. Xu Jeff, B. Chen, Chem. 1 (2016) 557-580.

[60] E. Ramos-Fernández, Boletín del Grupo Español del Carbón 32 (2014) 19-25.

[61] B. Li, H. Wen, W. Zhou, J. Xu, B. Chen, Chem 1 (2016) 557-580.

[62] P. Chowdhury, C. Bikkina, D. Meister, F. Dreisbach, S. Gumma, Micropor. Mesopor. Mat. 117 (2009) 406-413.

[63] M. Knyazena, A. Tsivadze, O. Solovtsova, A. Fomkin, A. Pribylov, A. Shkolin, A. Pulin, I. Menshchikov, Physicochem. Process. Interfaces 55 (2019) 9-14.

[64] V. Bon, Green Sus. Chem. 4 (2017) 44-49.

[65] K. Gedrich, I. Senkovska, N. Klein, U. Stoeck, A. Henschel, R. Lohe Martin, Angew. Chem. 49 (2010) 8489-8492.

[66] D. Saha, Z. Bao, F. Jia, S. Deng, Environ. Sci. Technol. 44 (2010) 1820-1826.

[67] P. Llewellyn, S. Bourrelly, C. Serre, A. Vimont, M. Daturi, L. Hamon, Langmuir 24 (2008) 7245-7250.

[68] D. Alezi, Y. Belmabkhout, M. Suyetin, PM. Bhatt, LJ. Weseliński, V. Solovyeva, J. Am. Chem. Soc. 137 (2015) 13308-13318.

[69] B. Li, H. Wen, H. Wang, H. Wu, M. Tyagi, T. Yildirim, W. Zhou, B. Chen, J. Am. Chem. Soc. 136 (2014) 6207-6210.

[70] H. Li, K. Wang, Y. Sun, C. Lollar, J. Li, H. Zhou, Mater. Today 21 (2018) 108-121.

[71] Y. Peng, V. Krungleviciute, I. Eryazici, JT. Hupp, OK. Farha, T. Yildirim, J. Am. Chem. Soc. 135 (2013) 11887-11894.

[72] A. Wiersum, J. Chang, C. Serre, P. Llewellyn, Langmuir 29 (2013) 3301-3309.

[73] H. Furukawa, N. Ko, Y. Go, N. Aratani, S. Choi, E. Choi, A. Özgür, R. Snurr, M. O'Keeffe, J. Kim, O. Yaghi, Science 23 (2010) 424-428.

[74] S. Vandenbrande, T. Verstraelen, JJ. Gutiérrez-Sevillano, M. Waroquier, V. Van Speybroeck, J. Phy. Chem. C 121 (2017) 25309-25322.

[75] A. Alonso, J. Moral-Vico, A. Abo Markeb, M. Busquets-Fité, D. Komilis, V. Puntes V, Sci. Total Environ. 595 (2017) 51-62.

[76] Z. Lu, L. Du, K. Tang, J. Bai, Cryst. Growth Des. 13 (2013) 2252-2255.

[77] I. Senkovska, S. Kaskel, Micropor. Mesopor. Mat. 112 (2008) 108-115.

[78] I. Spanopoulos, C. Tsangarakis, E. Klontzas, E. Tylianakis, G. Froudakis, K. Adil, J. Am. Chem. Soc. 138 (2016) 1568-1574.

[79] S. Ma, H-C. Zhou, Chem. Commun. 46 (2010) 44-53.

[80] F. Lovas, R. Suenram, J. Coursey, S. Kotochigova, J. Chang, K. Olsen, R. Dragoset, NIST standard reference database 115 (2004).

[81] Z. Bao, S. Alnemrat, L. Yu, I. Vasiliev, Q. Ren, X. Lu, S. Deng, J. Colloid Inter. Sci. 357 (2011) 504-509.

[82] L. Hamon, E. Jolimaître, GD. Pirngruber, Ind. Eng. Chem. Res. 49 (2010) 7497-7503.

[83] JA. Mason, J. Oktawiec, MK. Taylor, MR. Hudson, J. Rodriguez, JE. Bachman, Nature 527 (2015) 357-361.

[84] M. Tahmooresi, F. Sabzi, Fluid Ph. Equilibria. 381 (2014) 83-89.

[85] T. Becker, J. Heinen, D. Dubbeldam, L. Lin, T. Vlugt, J. Phy. Chem. C 121 (2017) 4659-4673.

[86] B. Sun, S. Kayal, A. Chakraborty, Energy 76 (2014) 419-427.

[87] D. Wu, X. Guo, H. Sun, A. Navrotsky, J. Phy. Chem. Lett. 6 (2015) 2439-2443.

[88] Z. Bao, L. Yu, Q. Ren, X. Lu, S. Deng, J. Colloid Interface. Sci. 353 (2011) 549-556.

[89] L. Li, J. Yang, J. Li, Y. Chen, J. Li, Micropor. Mesopor. Mat. 198 (2014) 236-246.

[90] X. Wu, B. Yuan, Z. Bao, S. Deng, J. Colloid Interface. Sci. 430 (2014) 78-84.

[91] A. García, A. Vallone, S. Korili, A. Gil, K. Sapag, Micropor. Mesopor. Mat. 224 (2016) 323-331.

[92] B. Szczęśniak, J. Choma, M. Jaroniec, J. Colloid Interface. Sci. 514 (2018) 801-813.

[93] V. Phuong, T. Chokbunpiam, S. Fritzsche, T. Remsungnen, T. Rungrotmongkol, C. Chmelik, Micropor. Mesopor. Mat. 235 (2016) 69-77.

[94] U. Stoeck, S. Krause, V. Bon, I. Senkovska, S. Kaskel, Chem. Commun. 48 (2012) 10841-10843.

[95] S. Krause, V. Bon, I. Senkovska, DM. Többens, D. Wallacher, RS. Pillai, Nat. Commun. 9 (2018) 1573.

[96] D. Polyukhov, S. Krause, V. Bon, A. Poryvaev, S. Kaskel, M. Fedin, J. Phys. Chem. Lett. 11 (2020) 5856-5862.

[97] X. Zhang, Z. Chen, X. Liu, S. Hanna, X. Wang, R. Taheri-Ledari, A. Maleki, P. Li, O. Farha, Chem. Soc. Rev. 49 (2020) 7406-7427.

[98] B. Sahoo, Synthesis and characterizations of novel metal-organic frameworks (MOFs), Visible light photocatalyzed redox-neutral organic reactions and

synthesis of novel metal-organic frameworks, Springer (2016).

[99] J. Lin, C. He, Y. Liu, P. Liao, D. Zhou, J. Zhang, X. Chen, Angew. Chem. Int. 55 (2016) 4674-4678.

[100] R. Xiong, K. Odbadrakh, A. Michalkova, JP. Luna, T. Petrova, DJ. Keffer, Sens. Actuators B Chem. 148 (2010) 459-468.

[101] A. Wong-Foy, A. Matzger, O. Yaghi, J. Am. Chem. Soc. 128 (2006) 3494-3495.

[102] D. Saha, S. Deng, J. Phy. Chem. Lett. 1 (2010) 73-78.

[103] D. Saha, S. Deng, Tsinghua SciTechnol. 15 (2010) 363-376.

[104] S. Kaye, A. Dailly, O. Yaghi, J. Long, J. Am. Chem. Soc. 129 (2007) 14176-14177.

[105] L. Yang, P. Ravindran, P. Vajeeston, M. Tilset, Phys. Chem. Chem. Phys. 14 (2012) 4713-4723.

[106] B. Wang, J. Liu, J. Yu, J. Lv, C. Dong, J. Li, J. Hazard. Mater. 382 (2020) 121018.

[107] O. Farha, C. Wilmer, I. Eryazici, B. Hauser, P. Parilla, K. O'Neill, J. Am. Chem. Soc. 134 (2012) 9860-9863.

[108] C. Wilmer, O. Farha, T. Yildirim, I. Eryazici, V. Krungleviciute, A. Sarjeant, R. Snurr, J. Hupp, Energ. Environ. Sci. 6 (2013) 1158-1163.

[109] T. Zhao, F. Jeremias, I. Boldog, B. Nguyen, SK. Henninger, C. Janiak, Dalton Trans. 44 (2015) 16791-16801.

[110] Y. Hwang, D. Hong, J. Chang, S. Jhung, Y. Seo, J. Kim, Angew. Chem. 120 (2008) 4212-4216.

[111] D. Hong, Y. Hwang, C. Serre, G. Ferey, J. Chang, Adv. Funct. Mater. 19 (2009) 1537-1552.

[112] Q. Liu, L. Ning, S. Zheng, M. Tao, Y. Shi, Y. He, Sci. rep. 3 (2013) 2916.

[113] H. Embrechts, M. Kriesten, M. Ermer, W. Peukert, M. Hartmann, M. Distaso, RSC Adv. 10 (2020) 7336-7348.

[114] A. Rahmani, H. Emrooz, S. Abedi, A. Morsali, Mater. Sci. Semicond. Process. 80 (2018) 44-51.

[115] N. Ramsahye, P. Trens, C. Shepherd, P. Gonzalez, T. Trung, F. Ragon, Micropor. Mesopor. Mat. 189 (2014) 222-231.

[116] F. Tan, M. Liu, K. Li, Y. Wang, J. Wang, X. Guo, Chem. Eng. J. 281 (2015) 360-367.

[117] A. Dhakshinamoorthy, M. Alvaro, P. Horcajada, E. Gibson, M. Vishnuvarthan, A. Vimont, ACS Catal. 2 (2012) 2060-2065.

[118] J. Lee, S. Jhung, J. Yoon, Y. Hwang, J. Chang, J. Ind. Eng. Chem. 15 (2009) 674-676.

[119] F. Ahmadijokani, S. Ahmadipouya, H. Molavi, M. Rezakazemi, T. Aminabhavi, M. Arjmand, J. Environ. Manage. 274 (2020) 111155.

[120] M. Katz, Z. Brown, Y. Colón, P. Siu, K. Scheidt, R. Snurr, Chem. Commun. 49 (2013) 9449-9451.

[121] S. Øien-Ødegaard, B. Bouchevreau, K. Hylland, L. Wu, R. Blom, C. Grande, Inorg. Chem. 55 (2016) 1986-1991.

[122] I. Lázaro, C. Wells, R. Forgan, Angew. Chem. Int. Edit. 59 (2020) 5211-5217.

[123] J. Cavka, S. Jakobsen, U. Olsbye, N. Guillou, C. Lamberti, S. Bordiga, J. Am. Chem. Soc. 130 (2008) 13850-13851.

[124] T. Al-Jadir, F. Siperstein, Micropor. Mesopor. Mat. 271 (2018) 160-168.

[125] T. Glover, G. Peterson, B. Schindler, D. Britt, O. Yaghi, Chem. Eng. Sci. 66 (2011) 163-170.

[126] P. Valvekens, M. Vandichel, M. Waroquier, V. Van Speybroeck, D. De Vos, J. Catal. 317 (2014) 1-10.

[127] C. Cabello, G. Pozuelo, M. Opanasenko, P. Nachtigall, J. Čejka, ChemPlusChem 81 (2016) 828-835.

[128] F. Bonino, S. Chavan, JG. Vitillo, E. Groppo, G. Agostini, C. Lamberti, Chem. Mat. 20 (2008) 4957-4968.

[129] L. Wang, H. Deng, H. Furukawa, F. Gándara, K. Cordova, D. Peri, Inorg. Chem. 53 (2014) 5881-5883.

[130] Y. He, B. Li, M. O'keeffe, B. Chen, Chem. Soc. Rev. 43 (2014) 5618-5656.

[131] D. Sun, S. Ma, J. Simmons, J. Li, D. Yuan, H. Zhou, Chem. Commun. 46 (2010) 1329-1331.

[132] S. Lucena, P. Mileo, P. Silvino, C. Cavalcante, J. Am. Chem. Soc. 133 (2011) 19282-19285.

[133] S. Ma, D. Sun, J. Simmons, C. Collier, D. Yuan, H. Zhou, J. Am. Chem. Soc. 130 (2008) 1012-1016.

[134] T. Pham, K. Forrest, B. Space, Phys. Chem. Chem. Phys. 18 (2016) 21421-21430.

[135] U. Kokçam, A. Goldman, L. Esrafili, M. Gharib, A. Morsali, O. Weingart, C. Janiak, Chem. Soc. Rev. 49 (2020) 2751-2798.

[136] K. Park, Z. Ni, A. Côté, J. Choi, R. Huang, F. Uribe-Romo, H. Chae, M. O'Keeffe, O. Yaghi, PNAS 103 (2006) 10186-10191.

[137] Z. Guo, H. Wu, G. Srinivas, Y. Zhou, S. Xiang, Z. Chen, Angew. Chem. 50 (2011) 3178-3181.

[138] A. Masala, JG. Vitillo, F. Bonino, M. Manzoli, CA. Grande, S. Bordiga, Phys. Chem. Chem. Phy. 18 (2016) 220-227.

[139] X. Rao, J. Cai, J. Yu, Y. He, C. Wu, W. Zhou, Chem. Commun. 49 (2013) 6719-6721.

[140] E. Nosike, Z. Jiang, L. Miao, O. Akakuru, B. Yuan, S. Wu, Y. Zhang, Y. Zhang, A. Wu, J. Hazard. Mater. 392 (2020) 122288.

[141] R. Triebe, F. Tezel, K. Khulbe, Gas Sep. Pur. 10 (1996) 81-84.

[142] A. Kizzie, A. Dailly, L. Perry, M. Lail, W. Lu, T. Nelson, Mater. Sci. Appl. 5 (2014) 387.

[143] W. Lu, D. Yuan, D. Zhao, C. Schilling, O. Plietzsch, T. Muller, Chem. Mat. 22 (2010) 5964-5972.

[144] Y. Liu, D. Liu, Q. Yang, C. Zhong, J. Mi, Ind. Eng. Chem. Res. 49 (2010) 2902-2906.

[145] M. Tagliabue, D. Farrusseng, S. Valencia, S. Aguado, U. Ravon, C. Rizzo, Chem. Eng. J. 155 (2009) 553-566.

[146] M. Niwa, K. Yamazaki, Y. Murakami, Ind. Eng. Chem. Res. 30 (1991) 38-42.

[147] B. Bunker, J. Non-Crystalline Solids 179 (1994) 300-308.

[148] M. Chang, Y. Zhao, D. Liu, J. Yang, J. Li, C. Zhong, Sustainable Energy & Fuels 4 (2020) 138-142.

[149] L. Li, L. Yang, J. Wang, Z. Zhang, Q. Yang, Y. Yang, Q. Ren, Z. Bao, AICHE J. 64 (2018) 3681-3689.

[150] M. Chang, Y. Zhao, Q. Yang, D. Liu, ACS Omega 4 (2019) 14511-14516.

[151] Z. Niu, X. Cui, T. Pham, P. Lan, H. Xing, K. Forrest, L. Wojtas, B. Space, S. Ma, Angew. Chem. Int. Edit. 58 (2019) 10138-10141.

[152] J. Hu, T. Sun, X. Liu, Y. Guo, S. Wang, RSC Adv. 6 (2016) 64039-64046.

[153] T. Kim, S. Kim, T. Yoon, M. Kim, W. Park, H. Han, C. Kong, C. Park, J. Kim, Y. Bae, Chem. Eng. J. 399 (2020) 125717.

[154] Q. Wang, D. Shen, M. Büllow, M. Lau, S. Deng, F. Fitch, N. Lemcoff, J. Semanscin, Micropor. Mesopor. Mat. 55 (2002) 217-230.

[155] S. Eyer, N. Stadie, A. Borgschulte, L. Emmenegger, J. Mohn, Adsorption 20 (2014) 5-6.

[156] J. Yang, Y. Wang, L. Li, Z. Zhang, J. Li, J. Colloid Interface. Sci. 456 (2015) 197-205.

[157] R. Chanajaree, T. Chokbunpiam, J. Kärger, S. Hannongbua, S. Fritzsche, Micropor. Mesopor. Mat. 274 (2019) 266-276.

[158] Z. Li, G. Xiao, Q. Yang, Y. Xiao, C. Zhong, Chem. Eng. Sci. 120 (2014) 59-66.

[159] C. Wang, Y. Luo, X. He, D. Hong, J. Wang, F. Chen, C. Chen, B. Sun, Inorg. Chem. 58 (2019) 3058-3064.

[160] A. Inamdar, A. Pathak, M. Usman, K. Chiou, P. Tsai, S. Mendiratta, S. Kamal, Y. Liu, J. Chen, M. Chiang, K. Lu, J. Mater. Chem. A 8 (2020) 11958-11965.

[161] D. Gonçalves, R. Snurr, S. Lucena, Adsorption 25 (2019) 1633-1642.

[162] A. Chidambaram, D. Le, J. Navarro, K. Stylianou, Applied Mat. Today 22 (2021) 100933.

[163] J. Rogacka, A. Seremak, A. Luna-Triguero, F. Formalik, I. Matito-Martos, L. Firlej, S. Calero, B. Kuchta, Chem. Eng. J. 403 (2021) 126392.

[164] H. García, S. Navalón, Metal-Organic Frameworks: Applications in Separations and Catalysis, first ed. John Wiley & Sons, 2018.

[165] L. Xie, M. Xu, X. Liu, M. Zhao, J. Li, Adv. Sci. 7 (2020) 1901758.

[166] Z. Sui, B. Han, Carbon 82 (2015) 590-598.

[167] Z. Li, P. Liu, C. Ou, X. Dong, ACS Sustainable Chem. Eng. 8 (2020) 15378-15404.

[168] R. Lin, L. Li, A. Alsalme, B. Chen, Small Structures 1 (2020) 2000022.

[169] X. Duan, B. Yu, R. Lv, Z. Ji, B. Li, Y. Cui, Polyhedron 155 (2018) 332-336.

[170] A. Awadallah, S. Al-Muhtaseb, Appl. Sci. 11 (2021) 265.

[171] H. Chen, L. Fan, X. Zhang, L. Ma, ACS Appl. Nano Mater. 3 (2020) 2680-2686.

[172] L. Sheng, Y. Guo, D. Zhao, J. Ren, S. Wang, M. Deng, J. Nat. Gas Sci. Eng. 75 (2020) 103123.

[173] M. Mozafari, A. Rahimpour, R. Abedini, J. Ind. Eng. Chem. 85 (2020) 102-110.

[174] M. Mohan, M. Essalhi, D. Durette, L. Rana, F. Ayevide, T. Maris, A. Duong, ACS Appl. Mater. Interfaces 12 (2020) 50619-50627.

[175] F. Rezaei, P. Webley, Sep. Purif. Technol. 70 (2010) 243-256.

[176] W. Hong, S. Perera, A. Burrows, Micropor. Mesopor. Mat. 214 (2015) 149-155.

[177] F. Rezaei, S. Lawson, H. Hosseini, H. Thakkar, A. Hajari, S. Monjezi, A. Rownaghi, Chem. Eng. J. 313 (2017) 1346-1353.

[178] D. Ursueguía, E. Díaz, S. Ordóñez, Nanomaterials 10 (2020) 1089.

[179] M. Rubio-Martínez, C. Avci-Camur, A. Thornton, I. Imaz, D. Maspoch, M. Hill, Chem. Soc. Rew. 46 (2017) 3453-3480.

[180] H. Thakkar, S. Eastman, Q. Al-Naddaf, A. Rownaghi, F. Rezaei, Appl. Mater. Interfaces 9 (2017) 35908-35916.

## 4.2. ESTUDIO DE LA ADSORCIÓN DE VAM SOBRE MOFs

Se han seleccionado tres MOFs con elevada superficie específica, volumen total de poros y disponibilidad de OMS estructurales. Además, los tres materiales están disponibles comercialmente: Basolite C300, Basolite F300 y Basolite A100, lo que asegura reproducibilidad en los ensayos, así como la existencia de un proceso de síntesis de los adsorbentes a escala industrial, facilitando un posible paso de escala de la operación de separación.

Inicialmente, se parte de una caracterización de los materiales en función de su capacidad de separación de metano y nitrógeno, considerada la separación más complicada en corrientes VAM. Los resultados muestran una selectividad $CH_4/N_2$ adecuada, mayor en el caso de los materiales que presentan *open metal sites* (OMS) más accesibles en la estructura: Basolite C300 (2.2) y Basolite A100 (2.1). Estos centros metálicos activos atraen preferencialmente al metano, con mayor volumen de polarizabilidad, $26 \cdot 10^{-25}$ $cm^3$, que el nitrógeno, $17.6 \cdot 10^{-25}$ $cm^3$. A partir de ensayos termogravimétricos de adsorción, se obtienen las capacidades de adsorción de metano para cada material: 52, 30 y 16 mg/g, para Basolite C300, Basolite F300 y Basolite A100, respectivamente. Estas capacidades de adsorción muestran ser superiores que las obtenidas para otros adsorbentes típicos, pertenecientes a las familias de los materiales carbonosos y las zeolitas. Además, los resultados permiten realizar un análisis cinético y termodinámico del proceso, ajustando las isotermas de adsorción a modelos conocidos como Freundlich o Sips. La bondad del ajuste, $R^2 > 0.9$ en todos los casos, muestra la importancia de la heterogeneidad superficial de los materiales estudiados en procesos de adsorción, lo que confirma la importancia de la presencia de OMS estructurales.

Una vez establecidos los MOFs seleccionados como adecuados para la separación de metano y nitrógeno, es necesario estudiar su comportamiento bajo condiciones similares a una operación a escala real. En primer lugar, considerando un paso de escala, se requiere partir de un tamaño de partícula adsorbente adecuado para trabajar en un lecho fijo en condiciones de caída de presión asumibles, especialmente trabajando con flujos de adsorbato tan elevados como los característicos de las corrientes VAM. En el caso de los

MOFs, su procedimiento típico de síntesis genera polvos muy finos, lo que imposibilita su uso directo a gran escala. En consecuencia, se realiza un estudio acerca de la posibilidad de incrementar el tamaño de partícula de los materiales considerados a partir de una compresión mecánica, la técnica más viable y económicamente favorable para este tipo de materiales, que demuestran gran inestabilidad en presencia de los disolventes típicos utilizados en la fabricación de *binders*. Los estudios de caracterización (SEM, DRX y fisisorción de nitrógeno), así como la adsorción de metano pre- y post-compresión mecánica en prensa hidráulica a distintas presiones, muestran un gran efecto nocivo sobre estos materiales nanoestructurados. Se observan reducciones en la capacidad de adsorción (40%), en la cristalinidad (70%) y en la superficie específica disponible (90%). Este efecto es muy crítico en el Basolite C300, y se demuestra menos determinante en el Basolite F300, originalmente más amorfo y mesoporoso, o en el Basolite A100, con una flexibilidad estructural característica que soporta mejor la compresión.

Finalmente, los materiales seleccionados también deberán lidiar con la presencia de componentes potencialmente nocivos en las corrientes VAM, como el dióxido de carbono y el agua. Ambos componentes muestran importantes propiedades polares, que pueden interferir en la adsorción y separación de metano, especialmente sobre los OMS superficiales. En este sentido, se estudia cómo la presencia de estas moléculas en las corrientes de adsorbato afecta a la capacidad de adsorción y separación de los materiales considerados. Se realizan ensayos en termobalanza y lecho fijo en presencia simultánea de todos los componentes. El dióxido de carbono, presente a nivel de trazas (~ 0.1%), muestra una leve influencia en la capacidad de separación y adsorción inicial de los materiales, mientras que el agua, presente en valores de elevada humedad relativa (~ 100% HR), muestra un gran efecto nocivo. El agua no afecta únicamente a la capacidad de adsorción y separación de los materiales, bloqueando la superficie activa disponible, sino también a la estructura del material, ya que es capaz de hidrolizar los enlaces entre ligando orgánico e ión metálico. El material adsorbente más afectado por la presencia de agua es el Basolite C300, con una disminución de la capacidad de adsorción de hasta un 33.3% tras 24 horas de operación en condiciones húmedas.

Los resultados y su discusión detallada se incluyen en las siguientes publicaciones científicas:

- David Ursueguía, Eva Díaz, Salvador Ordóñez, Adsorption of methane and nitrogen on Basolite MOFs: Equilibrium and kinetic studies, Microporous and Mesoporous Materials 298 (2020) 110048.
https://doi.org/10.1016/j.micromeso.2020.110048.
Factor de Impacto (2020): 5.455
Categoría (2020): Applied Chemistry (12/74: Q1)
Número de citas: 15

- David Ursueguía, Eva Díaz, Salvador Ordóñez, Densification-induced structure changes in Basolite MOFs: Effect on low-pressure $CH_4$ adsorption, Nanomaterials 10 (2020) 1089.
https://doi.org/10.3390/nano10061089.
Factor de Impacto (2020): 5.076
Categoría (2020): Multidisciplinary Chemistry (55/178: Q2)
Número de citas: 13

- David Ursueguía, Eva Díaz, Salvador Ordóñez, Effect of water and carbon dioxide on the performance of Basolite MOFs for methane adsorption. Enviada a revista: Journal of Industrial and Engineering Chemistry.

## Adsorption of methane and nitrogen on Basolite MOFs: Equilibrium and kinetic studies

David Ursueguía, Eva Díaz, Salvador Ordóñez*

Catalysis, Reactors and Control Research Group (CRC), Department of Chemical and Environmental Engineering, University of Oviedo, Julián Clavería s/n, 33006 Oviedo, Spain

*e-mail: sordonez@uniovi.es (S. Ordóñez)

*Microporous and Mesoporous Materials* **298** (2020) 110048.

https://doi.org/10.1016/j.micromeso.2020.110048

## ABSTRACT

The adsorption/desorption behaviour of methane and nitrogen on three different metal-organic frameworks (MOFs) was studied in this work. The objective was to obtain new insights into the adsorption process of both molecules, since the similarity in the sizes of methane and nitrogen hinders the methane recovery from lean methane-containing emissions using adsorption technologies. In that way, the capacity of adsorption of methane and nitrogen was measured on Basolite C300, Basolite F300 and Basolite A100, being remarkable the Cu interaction of the Basolite C300 with the methane, as it was deduced from both the capacity and the heat of adsorption. Evaluation of the kinetic models of adsorption leads to observe the best fitting of the Langmuir and the fractional order models. For both adsorbates, the adsorption is easier than desorption on the surface of the three materials. The main differences observed among the adsorbents were the faster adsorption of both gases on Basolite A100, as well as the larger dependence on the occupied adsorption sites. Likewise, different adsorption isotherms were used for modelling the equilibrium results obtained, Freundlich and Sips isotherms providing the best results. These facts highlight the key role of certain surface heterogeneities on the adsorption capacity. Furthermore, parameters of both the adsorption isotherms and the kinetic models could explain the differences among the adsorbents in the adsorption and desorption performance, highlighting the utility of the proposed models.

**Keywords**: Equilibrium; Adsorption capacity; Adsorption kinetics; Greenhouse gases abatement; Adsorption regeneration

### 1. Introduction

Ventilation air methane (VAM) from underground coal mines are fugitive gas emissions that constitute a significant contribution to greenhouse gases, due mainly to the methane emissions in concentrations between 0.1 and 1 %, diluted in other gases such as air or carbon dioxide [1]. Concentration of these emissions is fixed by safety constraints, since the explosive range of methane in air is between 5 and 15 %. Although this hazard has generally been minimized by combustion, this stream is, in fact, an energy source or even a chemical feedstock that could be exploited [2-5]. Therefore, the upgrade of these emissions would be of great interest. However, two intrinsic features of these streams: the dilution in large flows and the great variation of concentration [6-9], make compulsory a concentration step [10].

Adsorption is one of the main technologies that is promising for increasing methane concentration in exhaust ventilation conducts, in fact, this technique achieved enrichments up to 51.3% mol of methane from streams containing initially 2.4% mol of methane [11]. Considering that VAM stream consists mainly of $N_2$, $O_2$ and $CH_4$, add to impurities, with molecular dynamic radius of 3.64, 3.46 and 3.82 Å, respectively, it is observed that the molecular diameter of methane is slightly larger. Special attention should be paid to nitrogen, as it is the major component in the mixture and its molecular size is the most similar to methane. Both $N_2$ and $CH_4$ present null dipole moment, but polarizability is greater for methane; therefore the theoretical strength of interaction of

the methane molecule on a polar adsorbent surface should be higher than for nitrogen [12]. Among the possible adsorbents to be used, both activated carbons and zeolites [13, 14] are suitable adsorbent media. However, in both cases, the $CH_4/N_2$ separation factor, as well as with other gases essayed as $O_2$, are quite poor [15-18].

Metal-organic frameworks (MOFs), highly porous materials with outstanding properties in the methane storage, are in an advantageous position as adsorbents in order to achieve methane concentration from aforementioned diluted streams. MOFs constitute a family of porous materials formed by two major components, a metal ion or metal oxide and an organic linker. These structures present high surface area and pore volume, and offer the possibility of obtaining many different combinations of its components. Likewise, the great variety of possible organic molecules —which can be functionalized— linking the metallic ions, allow tailoring the material to a specific separation [19]. In fact, this family of porous materials has been used in recent years for different applications related to gas storage, mainly in order to solve various challenges in relation with energy, environment and healthcare sectors [20]. It is for this application, which research in MOFs materials has advanced greatly in order to develop materials for high-capacity methane storage [21], with the objective fixed by the US Department of Energy (DOE) of 350 $cm^3$ (STP) $cm^{-3}$ of methane storage capacity, based on the crystallographic density of MOF materials [22]. Although this approach has overestimated the actual storage capacity of MOFs, these materials could be competitive adsorbents for methane concentration from dilute mixtures. To achieve that, it is critical to obtain detailed information about the required adsorption process. Most of the available manuscripts deal with the capacity storage determination and, in the great majority of the cases, at elevated pressures. Furthermore, the most commonly employed method is the determination of adsorption isotherms and the isosteric heat of $CH_4$ adsorption. However, it does not focus on other parameters that can provide very valuable information to understand the process, such as adsorption isotherms, kinetic models, studying the material regenerability or even making a comparative among different reproducible (commercial) MOFs.

In this context, the present research is focused on the role of the surface morphology and chemistry of three commercial MOFs on the methane and nitrogen adsorption capacity of these materials. Special attention was paid to the strength and the specificity of the interaction, recording adsorption data at total pressures close to the atmospheric, which is more usual in the methane adsorption from lean mixtures. These interactions were studied from the point of view of the adsorption isotherms fitting and kinetic models, as well as the regenerability in order to evaluate their potential for practical use. The three MOFs are commercialized by BASF: Basolite C300, F300 and A100. Basolite structures C300 and F300 are constituted by 1,3,5-benzene tricarboxylic acid (1,3,5-BTC) as ligand coordinated to $Cu^{2+}$ and $Fe^{3+}$, respectively. The former shows the HKUST-1 structure, whereas the second MOF, Fe-BTC, contains 21.2 % of iron, Fe(III) as nodal metal, and tripodal BTC as ligand. In the case of Basolite F300, its composition is similar to MIL-100(Fe) MOF, although the commercial product corresponds to a distorted structure of the crystalline MIL-100(Fe) [23]. Concerning Basolite A100, it presents a MIL-53 structure, with the benzene-1,4-dicarboxylate (bdc) as ligand coordinated to $Al^{+}$ [24]. The studied behaviour of both methane and nitrogen interaction on the MOFs surface has a direct practical implication for the development of MOFs for enhanced methane separation from diluted mixtures.

## 2. Experimental section

### 2.1. Materials

Basolite C300 [$Cu_3(C_9H_3O_6)_2$], Basolite F300 [$C_9H_3FeO_6$] and Basolite A100 [$C_8H_5AlO_5$] were supplied by BASF (96 %; mass basis purity). All three materials are in the form of powder (10-30 μm), and were stored in a desiccator to avoid its contact with the ambient air. Methane, nitrogen and helium, with a purity > 99.995 % mol, were supplied by Air Liquide.

### 2.2. Methods

The $CH_4$ and $N_2$ adsorption-desorption amount on the adsorbents as a function of time was measured by a thermal gravimetric analyzer (Setaram, Sensys) in order to obtain information on the equilibrium and kinetics [25, 26]. Samples (10 mg) were pretreated in situ at 498 K and 0.1 MPa in pure He flowing at 20 ml/min for 1.5 h before measurement of either $CH_4$ or $N_2$ adsorption at 0.1 MPa and temperatures from 498 to 298 K with total flowrates of 20 ml/min. It should be noted that the maximum temperature is, in all cases, under decomposition temperature of the materials, as it was checked by thermogravimetry. The gas adsorption is measured by the

weight increase during the experiment. Once the equilibrium is reached, the adsorption temperature is decreased stepwise until the ambient temperature. In order to obtain accurate values of methane and nitrogen uptake, the buoyancy effect was taken into consideration during heating/cooling. All weight changes with respect to adsorption/desorption data were corrected using a quartz blank calibration. Differential scanning calorimetry (DSC) measurements of total adsorption heats were made simultaneously in the same apparatus.

Adsorption isotherms were obtained in an AutoChem II 2920 apparatus by flowing a methane-nitrogen mixture at a total pressure of 0.1 MPa. Experiments were performed at 298 K and 50 ml/min (STP) total flowrate. The evolution of $CH_4$ and $N_2$ desorption signals were followed in a Pfeiffer Vacuum Omnistar Prisma mass spectrometer at 298 K, in order to obtain the final uptake for each gas on each material through a previous calibration of the device. The regenerability of the adsorbents was essayed by six successive experiences of adsorption and desorption for each gas. In this case, once the surface of the adsorbent was saturated by flowing the pure gas (0.1 MPa, 298 K and 50 ml/min) for 2 h, its desorption was measured at increasing temperature until 463 K with a temperature ramp of 5 K/min and pure helium flowing at 0.1 MPa and 50 ml/min.

## 3. Results and discussion

### 3.1. Pure components adsorption capacity

Thermogravimetry at several temperatures between 498 and 298 K (Figure 1) determined the adsorption capacities of pure components stepwise. After observing null retention at 498 K for both methane and nitrogen, the temperature was decreased and kept at each step until adsorption equilibrium was reached. It should be noted that the equilibrium was reached faster at the highest temperatures (about 1 h) and required a longer period at 298 K (over 30 h). Below 330 K, the uptake of both $CH_4$ and $N_2$ is higher for Basolite C300, whereas over this temperature, Basolite F300 presents a slightly higher retention. At the entire interval, the Basolite A100 presents the lowest adsorption capacity.

The highest adsorption capacity of Basolite C300 below 330 K can be easily justified by the morphological features of the materials. Its surface area is 1514 $m^2/g$, with a microporous volume of 0.56 $cm^3/g$, whereas Basolite F300 presents a BET surface of 962 $m^2/g$ with a microporous volume of 0.30 $cm^3/g$ [23]. Concerning the Basolite A100, the BET surface area is much lower, 662 $m^2/g$ [27], with a microporous volume of 0.35 $cm^3/g$ [28]. Furthermore, the plot of the $CH_4$ and $N_2$ uptake versus the surface area of the three adsorbents suggest that the adsorption capacity of both gases at 298 K is mainly related with the surface area, Figure 2. Likewise, although the uptake is most favorable for methane, it is remarkable the similar slope for both molecules, attributed to the similar diameter of both: 3.65 Å for $N_2$ and 3.82 Å for $CH_4$ [29, 30]. Capacities of adsorption here shown are higher than the 12 mg/g reported for $CH_4$ uptake on a zeolite 5A at atmospheric pressure and 298 K [31] or a MOF-MWCNT nanocomposite (12 mg/g) [32]; and similar, in the case of Basolite C300, to NaX zeolite.

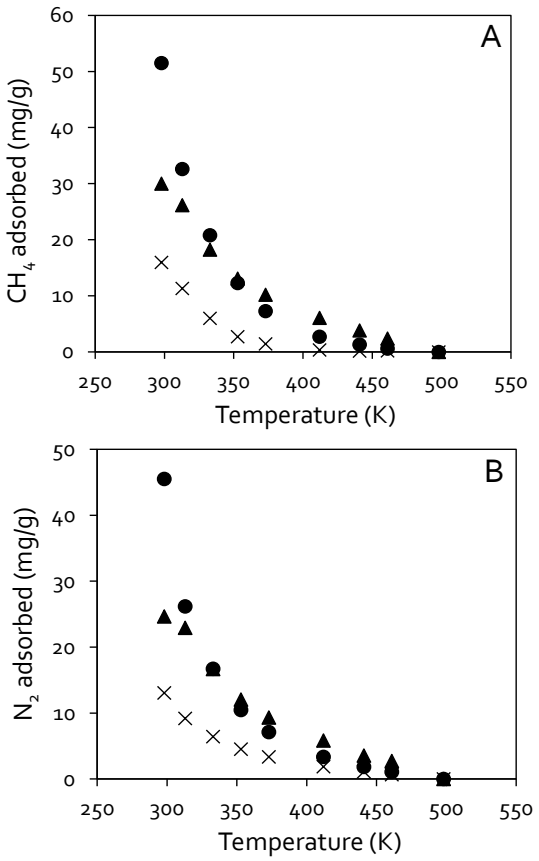


Figure 1. Evolution of $CH_4$ (A) and $N_2$ (B) adsorption with the temperature in the interval 298-498 K for the three MOFs considered: F300 (▲), C300 (●) and A100 (x). Experimental conditions: 0.1 MPa and 20 ml/min.

Above 330 K, the adsorption capacity of both gases decreases drastically, especially for Basolite C300. The lower adsorption capacity value of Basolite C300 than for the Basolite F300, could be attributed to the higher accessibility of active sites in the case of Basolite F300, because of its lower fraction of microporous surface area (645 $m^2/g$,

67%) versus 1268 m²/g for the Basolite C300 (83%) [23]. This explanation is confirmed by the Basolite A100, with a 66% of microporous surface area (437 m²/g) [28]. Therefore, above 330 K, the adsorption capacity follows the same order as the mesoporous surface area: F300 (317 m²/g) > C300 (246 m²/g) > A100 (225 m²/g).

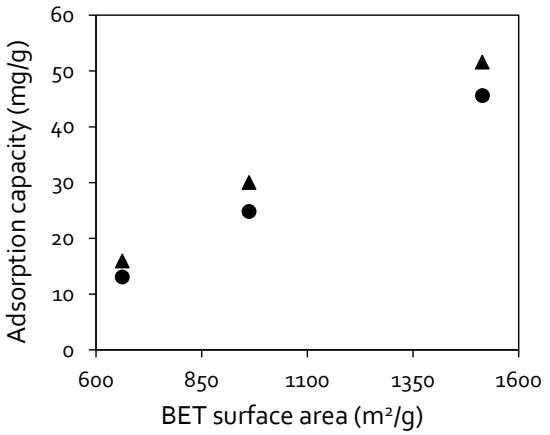


Figure 2. Relation between surface area of the three adsorbents essayed and $CH_4$ (▲) and $N_2$ (●) pure gas adsorption capacity at 298 K, 0.1 MPa and 20 ml/min of total flow.

Basolite C300 presents a HKUST-1 structure formed by the link of benzene 1,3,5-tricarboxylate (BTC) and copper ions with a pore size of 10 Å [33, 34], but it also presents small cages of about 4, 10 and 11 Å diameter [35]; whereas Basolite F300 presents a structure similar to MIL-100(Fe), constituted by Fe atoms and BTC linker, with pore sizes of 25 and 29 Å [36]. Concerning Basolite A100, it has a MIL-53(Al) metal organic framework made up of Al and oxygen nodes with 1,4-benzodicarboxylic acid struts between the nodes, with an average pore size of 8.5 Å [37]. Furthermore, although MIL-53 structure is characterized by its enormous flexibility and the occurrence of an oscillation (or breathing) during adsorption between two distinct conformations, called the large-pore phase (lp) and the narrow-pore phase (np), its capacity of adsorption is in all cases reduced [38].

Observation of the $CH_4/N_2$ adsorption ratio with temperature (Figure 3) —calculated as the methane and nitrogen molar adsorption ratio, at 0.1 MPa, and for each temperature— evidences the increasing separation factor between both gases at the lowest temperature for Basolite F300 and A100, whereas in the case of Basolite C300 it is observed a maximum in the $CH_4/N_2$ ratio at 313-333 K. This behavior suggests a methane physical interaction with both Basolite F300 and A100, which in the last case is more pronounced with the absence of specific interaction with the hydroxyl groups of the structure. Contrary, for Basolite C300, the chemical specificity of the open Cu site could dominate the methane interactions. In fact, although both molecules (methane and nitrogen) present null dipole moment, the polarizability of the methane molecule is slightly higher ($26{\cdot}10^{-25}$ and $17.6{\cdot}10^{-25}$ cm³, respectively) [39].

Long Xue et al. [40] reported adsorption isotherms for both $CH_4$ and $N_2$ on zeolite X/activated carbon composites. They observed a maximum methane adsorption capacities of 16 mg/g at 273 K, and a $CH_4/N_2$ ratio of the same order of magnitude as for Basolites, but at 20 K lower, thus, $CH_4/N_2$ separation on MOFs is more favoured. On the other hand, Chanajaree et al. [41] based on Monte Carlo simulations, obtained for the ZIF-78 MOF a $CH_4/N_2$ selectivity that doubles that obtained by the Basolites.

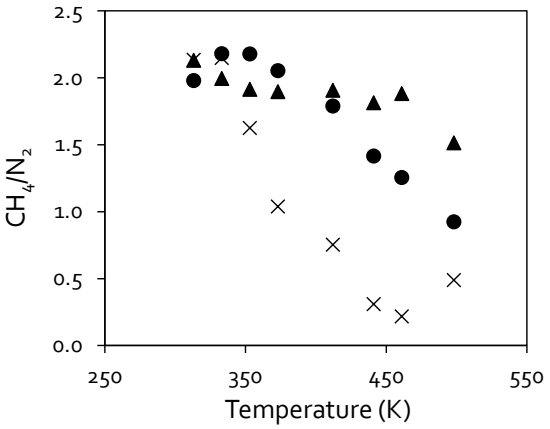


Figure 3. $CH_4/N_2$ molar adsorption capacity ratio for pure gas uptake for the three MOFs: F300 (▲), C300 (●) and A100 (x). Adsorption capacities were obtained at 0.1 MPa of total pressure.

### 3.2. Adsorption enthalpy for pure components adsorption

Enthalpy changes derived of adsorption measurements were determined directly by DSC. The variation in the peaks in the interval 298-333 K was practically negligible. The average heat of adsorption at this interval was determined for methane, decreasing in the following order: 26.56 kJ/mol (Basolite C300) > 26.02 kJ/mol (Basolite A100) > 25.28 kJ/mol (Basolite F300). In the case of nitrogen, the order is coincident: 15.68 kJ/mol (Basolite C300) > 14.86 kJ/mol (Basolite A100) > 14.72 kJ/mol (Basolite F300). Therefore, the interaction of methane with the adsorbents is stronger than in the case of nitrogen, although there are not important differences among the three different Basolites.

The value presented for methane heat of adsorption for Basolite C300 is similar to the

26.8 kJ/mol experimentally observed at zero-coverage for ATC-CU material, which is characterized by oppositely adjacent open metal sites interaction to be separated from nitrogen [42]. Thus, it could be inferred that the Cu available sites to be responsible of this type of interactions. Likewise, for the HKUST-1 structure, values of 21.1 kJ/mol were reported at zero coverage [43]; whereas in the case of MIL-53(Al) structure, 17 kJ/mol were reported at low pressures [44]. It should be taken into account that the contribution of high-energy sites will be significantly outweighed at zero coverage, thus, it could be reasonable to obtain larger enthalpies at the lowest adsorbate concentration. However, add to this, the increase in the interaction potential in micropores, and also, in the case of MIL-53(Al) structure, the oscillation of the structure could influence. Thus, the Basolite A100, with the lowest percentage of microporosity, is the adsorbent with the lowest enthalpy of adsorption at low coverage.

### 3.3. Kinetic models for methane and nitrogen adsorption onto MOFs

The development and study of a kinetic model is useful in order to explore the adsorption mechanism and for designing or optimizing the adsorption process. In this way, adsorption uptake curves of both methane and nitrogen at 298 K (which is the temperature of the largest capacity and hence, of higher interest), and 0.1 MPa flowing at 20 ml/min were fitted to several kinetic models. In general, the adsorption process is constituted by three consecutive steps: external mass transfer of the adsorbate from the bulk to the external surface of the adsorbent, internal diffusion of the adsorbate to the sorption sites and, finally, the adsorption itself. In order to analyse the adsorption kinetics of both methane and nitrogen, correlation between adsorbed amounts and time were employed. Data were fitted to adsorption models where the adsorption step is considered the slowest stage: pseudo-first order, pseudo-second order, Langmuir model and fractional-order kinetic one; as well as the intra-particle diffusion model, where its rate depends on the rate at which components diffuse towards one another. The pseudo-first order kinetic equation [45]:

$$q_t = q_e \cdot \left(1 - e^{-k_f \cdot t}\right)$$

Where $q_e$ and $q_t$ are the adsorption capacities on the adsorbents at saturation time and at a given time, $t$, respectively; $k_f$ is the kinetic constant ($s^{-1}$).

The pseudo-second order kinetic equation:

$$q_t = \left(\frac{q_e^2 \cdot k_s \cdot t}{1 + q_e \cdot k_s \cdot t}\right)$$

Where $k_s$ is the kinetic constant (g/mg·s).

The Langmuir model:

$$q_t = q_e \cdot \frac{k_{ads}}{k_{ads} + k_{des}} \left(1 - e^{-(-k_{ads} + k_{des})t}\right)$$

Where $k_{ads}$ is the reaction constant of adsorption terms, $s^{-1}$, and $k_{des}$ is the reaction constant of desorption terms, $s^{-1}$.

The fractional order kinetic equation:

$$q_t = q_e - \frac{1}{\left[\frac{(n-1) \cdot k \cdot t^m}{m} + \frac{1}{q_e^{(n-1)}}\right]^{[1-(n-1)]}}$$

Where $k$ ($s^{-1}$), $m$ and $n$ are the constants of the model.

And, finally, the intraparticle diffusion model equation [46]:

$$q_t = k_i \cdot t^{0.5} + C$$

Where $k_t$ is the rate constant, $mg \cdot (g \cdot min^{0.5})^{-1}$, and $C$ is related to the boundary layer thickness.

Table 1 summarizes the calculated constants and the accuracy of each model, whereas experimental adsorption capacities and adsorption kinetic models are shown in Figure 4. Pseudo-first and pseudo-second order models are the most commonly used adsorption rate models. The first one assumes that the adsorption rate is proportional to the number of free adsorption sites, whereas the second one assumes that the adsorption capacity is proportional to the amount of active sites on the adsorbent. As it is observed, although pseudo-first order kinetic model can be fitted with the trend for the adsorption kinetic curves, there are some differences from the actual adsorption process, consisting mainly on the faster adsorption rate than the model prediction. It is especially remarkable the bad of the fitting for Basolite A100. In case of the pseudo-second order kinetic model, it is observed for Basolite C300 and F300 that, although the fitting of the model at the lowest times is accurate, the predicted equilibrium adsorption capacities is in all cases lower than the actual one. It is different the behavior of the model in the case of Basolite A100, which is quite good for the methane adsorption, although in the case of nitrogen, it predicts a faster process and larger adsorption capacity.

According to the assumption of the chemical adsorption, from the pseudo-second order model, it can be inferred some type of preferential

adsorption between the methane and the Basolite A100, by contraposition to nitrogen adsorption. This could be somehow related to the breathing effect of MIL-53(Al) structure, since it was reported that at 1 bar and high methane concentration, it is expected a structure in the lp state [47].

Concerning the Langmuir model, it considers that the rate of adsorption is proportional to the percentage of unoccupied active sites and the concentration of the gas —which remains constant for the three adsorbents—, and the rate of desorption is proportional to the percentage of the covered surface. This model fits to the experimental data for Basolite F300 and C300, although some discrepancies are observed in the case of the Basolite A100. Considering just Basolite C300 and Basolite F300, with curves of adsorption more similar, the Basolite C300 shows higher values of the adsorption constant, which is congruent with the higher value of adsorption heat in comparison to Basolite F300. In the case of Basolite A100, the values of $k_{ads}$ and $k_{des}$ calculated are one order of magnitude larger than for Basolite C300 and Basolite F300. These larger values are congruent with the lower number of active sites available for the gas adsorption and then, a faster saturation.

Finally, the fractional order kinetic model is a semiempirical kinetic equation [48] that assumes that the adsorption rate is proportional to the $n^{th}$ power of the driving force and $m^{th}$ power of the adsorption time. That is, this model describes the adsorption rate by: $k$, an overall parameter that may couple various adsorption related factors; $m$, refers to diffusion resistance and $n$, reflects the effect of the driving force (number of unoccupied sites) which was related to the adsorption apparatus and filling mode of the adsorbent [49]. However, this constant is not actually the kinetic constant the adsorption itself, but a complex combination of different parameters such as the kinetic constant for desorption, the surface coverage at equilibrium and the change of adsorbate concentration during the process [49]. From Figure 4 it is observed that equilibrium is first reached on Basolite A100, being especially relevant the largest *n* value for both gases in comparison to the other adsorbents; although the fitting of this model on this adsorbent, especially for nitrogen, is really poor. From the *n* parameter, lower than one in all cases (except for nitrogen on Basolite A100), and really near to one for methane adsorption on Basolite A100, it is deduced than the rate of adsorption is not so dependent on the driving force for Basolite C300 and F300. On the other hand, the dependence of Basolite A100 to the percentage of the covered surface matches with the results obtained for Langmuir model. It is remarkable the good fitting to this kinetic model of experimental data with the only exception of the adsorption of nitrogen on Basolite A100. This leads to the conclusion that both the completely unspecific interaction of nitrogen molecule (null dipole moment and very low polarizability), and the dual configuration of the MIL-53(Al) structure, could avoid this fitting.

The kinetic data were further fitted to the intraparticle diffusion model, for separating different diffusion stages of the adsorption process. Generally, if the so-called Weber-Morris plot of $q_t$ vs $t^{0.5}$ gives a straight line, the sorption process is controlled by intra-particle diffusion only. In the case the data exhibit multi-linear plots, then two or more steps influence the adsorption process [46]. Figure 5 shows the plots of both methane and nitrogen uptake versus $t^{0.5}$ for the three adsorbents. The curves obtained for both molecules exhibit multi-linearity, which confirms that adsorption takes places in different regimes. Furthermore, for Basolite C300 and Basolite F300, it is possible to distinguish even four differenced zones, which could be attributed to the film diffusion, gradual adsorption in mesopores, gradual adsorption in micropores, and finally, the equilibrium stage. The rate constant is obtained from the slope of the plot, thus adsorption both in mesoporous and micropores are the faster steps. In the case of Basolite A100, three areas can be observed, and the equilibrium step is reached at times scarcely over 100 min. For this material, a clear differenced behaviour is observed, since the adsorption stage is much shorter and uniform, probably due to its flexibility during the adsorption process.

### 3.4. Methane/nitrogen adsorption isotherms

The experimental data of adsorption isotherms at 298 K for both $CH_4$ and $N_2$ and the corresponding isotherm models fitting curves are illustrated in Figure 6. This is useful in order to explore the adsorption mechanism, pointing out the possible differences among the adsorbents. In this work, a one-parameter isotherm, Henry, and two and three parameter ones were fitted to the experimental data, being summarized the parameters of each one in Table 2. Henry isotherm is the simplest one, and in this case, the amount of adsorbed adsorbate is proportional to the partial pressure of the adsorptive gas [50]:

$$q_e = K_H \cdot c_e$$

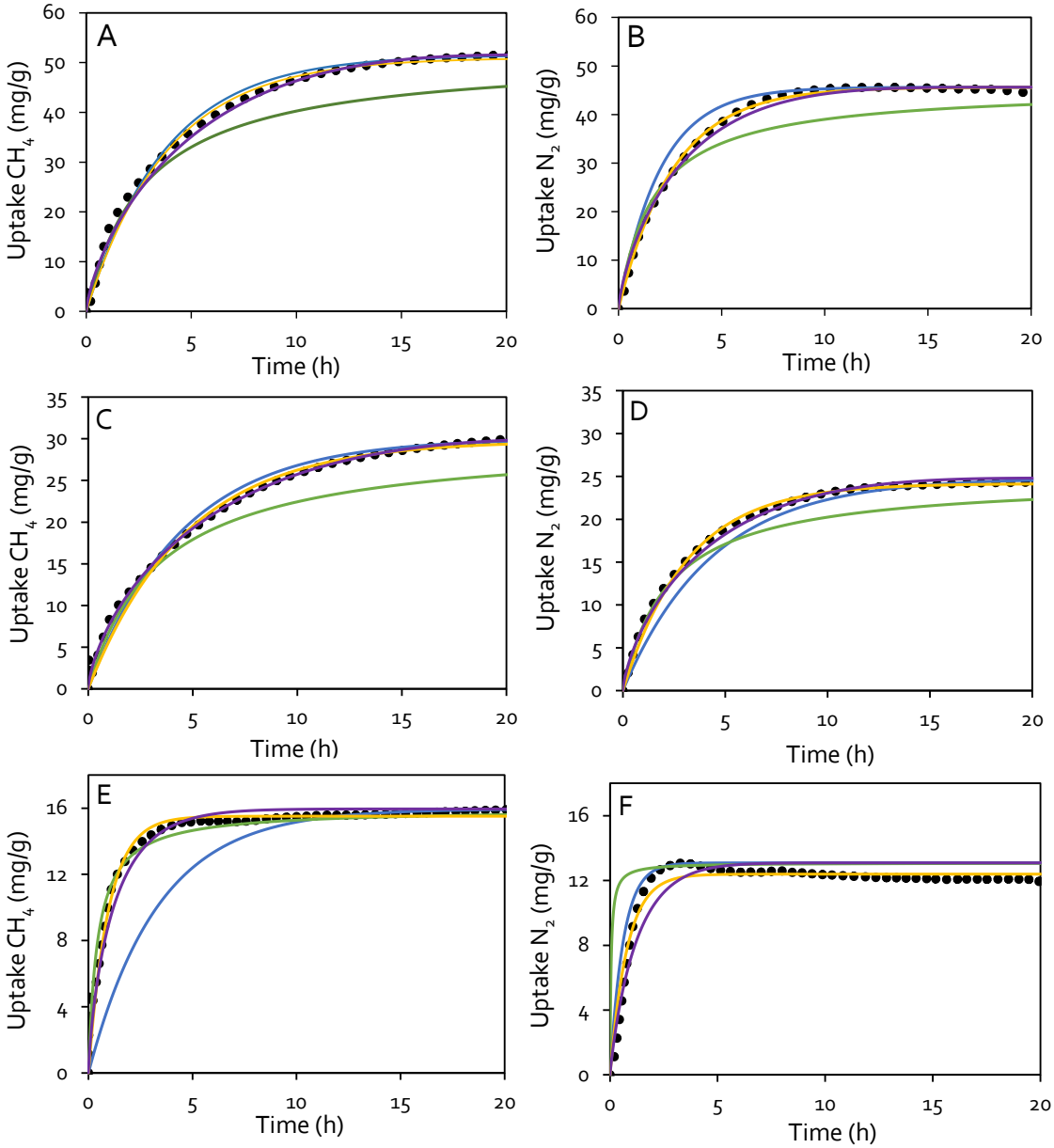


Figure 4. Experimental adsorption capacity and adsorption kinetic models for Basolite C300 (A, B), Basolite F300 (C, D) and Basolite A100 (E, F) for the adsorption of methane and nitrogen. Experimental (●) and models: pseudo-first (blue), pseudo-second (green), Langmuir (yellow) and fractional order (purple). Curves were obtained by thermogravimetry (298 K, 0.1 MPa and 20 ml/min of pure gas).

Where $q_e$ is the amount of adsorbate at the equilibrium, $c_e$, the equilibrium concentration, and $K_H$, the Henry's constant. Although the fit is quite good for the three adsorbents and the two gases, it can be observed how the fitting is more appropriate at relative pressures lower than 0.4, as expected with this simplified equilibrium model. Likewise, the main deviations were observed for nitrogen adsorption, although in the case of Basolite F300 methane $R^2$ is just of 0.97.

The other equilibrium models tested in this work are of two or three parameters. Hill-Deboer isotherm describes a situation in which there is mobile adsorption as well as lateral interaction among adsorbed molecules [51]:

$$ln\left[\frac{c_e(1-\theta)}{\theta}\right]-\frac{\theta}{1-\theta}=-ln(k_1)-\frac{k_2\cdot\theta}{RT}$$

Where $\theta$ is the fractional coverage, $k_1$ is the Hill-Deboer constant, and $k_2$ is the energy constant of the interaction between adsorbed molecules.

Table 1. Kinetics of adsorption for the removal of methane and nitrogen.

| Material | Methane | | | Nitrogen | | | |
|---|---|---|---|---|---|---|---|
| *Pseudo-first order model* | | | | | | | |
| | $k_f$ ($s^{-1}$) | | $R^2$ | $k_f$ ($s^{-1}$) | | | $R^2$ |
| C300 | $7.00 \cdot 10^{-5}$ | | 0.990 | $1.00 \cdot 10^{-4}$ | | | 0.996 |
| F300 | $6.00 \cdot 10^{-5}$ | | 0.988 | $6.00 \cdot 10^{-5}$ | | | 0.903 |
| A100 | $8.00 \cdot 10^{-5}$ | | 0.589 | $4.00 \cdot 10^{-4}$ | | | 0.782 |
| *Pseudo-second order model* | | | | | | | |
| | $k_s$ (g/mg·s) | | $R^2$ | $k_s$ (g/mg·s) | | | $R^2$ |
| C300 | $1.92 \cdot 10^{-6}$ | | 0.788 | $3.59 \cdot 10^{-6}$ | | | 0.797 |
| F300 | $2.73 \cdot 10^{-6}$ | | 0.800 | $4.97 \cdot 10^{-6}$ | | | 0.836 |
| A100 | $3.92 \cdot 10^{-5}$ | | 0.954 | $4.40 \cdot 10^{-4}$ | | | 0.112 |
| *Langmuir model* | | | | | | | |
| | $k_{ads}$ ($s^{-1}$) | $k_{des}$ ($s^{-1}$) | $R^2$ | $k_{ads}$ ($s^{-1}$) | $k_{des}$ ($s^{-1}$) | | $R^2$ |
| C300 | $7.16 \cdot 10^{-5}$ | $8.12 \cdot 10^{-7}$ | 0.991 | $1.05 \cdot 10^{-4}$ | 0 | | 0.997 |
| F300 | $5.87 \cdot 10^{-5}$ | $5.30 \cdot 10^{-7}$ | 0.990 | $8.60 \cdot 10^{-5}$ | $2.32 \cdot 10^{-6}$ | | 0.995 |
| A100 | $2.82 \cdot 10^{-4}$ | $7.94 \cdot 10^{-6}$ | 0.969 | $3.28 \cdot 10^{-4}$ | $1.85 \cdot 10^{-5}$ | | 0.936 |
| *Fractional-order kinetic model* | | | | | | | |
| | k ($s^{-1}$) | m | n | $R^2$ | k ($s^{-1}$) | m | n | $R^2$ |
| C300 | 0.002 | 0.631 | 0.730 | 0.993 | 0.001 | 0.749 | 0.768 | 0.990 |
| F300 | 0.002 | 0.620 | 0.696 | 0.999 | 0.002 | 0.691 | 0.730 | 0.992 |
| A100 | 0.001 | 0.787 | 0.998 | 0.963 | 0.001 | 0.900 | 1.120 | 0.791 |

As can be observed, both in Figure 6 as in Table 2, the fitting is really poor for this isotherm in all cases, thus, the initial hypothesis of mobile adsorption among the adsorption sites and the lateral interaction among either the adsorbed methane or nitrogen can be discarded.

Fowler-Guggenheim isotherm takes into consideration the lateral interaction of the adsorbed molecules [51]:

$$ln\left[\frac{c_e(1-\theta)}{\theta}\right] = -ln(k_{FG}) + \frac{2 \cdot w \cdot \theta}{RT}$$

Where $k_{FG}$ is the Fowler-Guggenheim equilibrium constant, and $w$ is the interaction energy between adsorbed molecules. The fitting quality is better than in the previous case, although this fit is markedly worst for $N_2$ adsorption.

As it is observed in Table 2, the values of $w$ are in all cases negative, which, according to the isotherm, is congruent with repulsive forces among adsorbed molecules. This fact is consistent with the observance based on the previous adsorption isotherm.

Langmuir isotherm assumes that the adsorption sites on the adsorbent surface have the same adsorption probability and that there is no interaction between adsorbed molecules [45]:

$$\frac{c_e}{q_e} = \frac{1}{q_m \cdot k_L} + \frac{c_e}{q_m}$$

Where $k_L$ is Langmuir constant related to adsorption capacity and is referred to the monolayer adsorption capacity. Once again, the adjustment is better in the case of methane than nitrogen, resulting remarkable in the case of Basolite F300 (which presents the best fitting) the equal value of $k_L$ for nitrogen than for methane, although in all cases it is observed that the monolayer is higher for methane.

Freundlich equation is applicable to adsorption processes that occur on heterogeneous surfaces. This isotherm in the linear form is as follows [51]:

$$\log(q_e) = \log(k_F) + \frac{1}{n}\log(c_e)$$

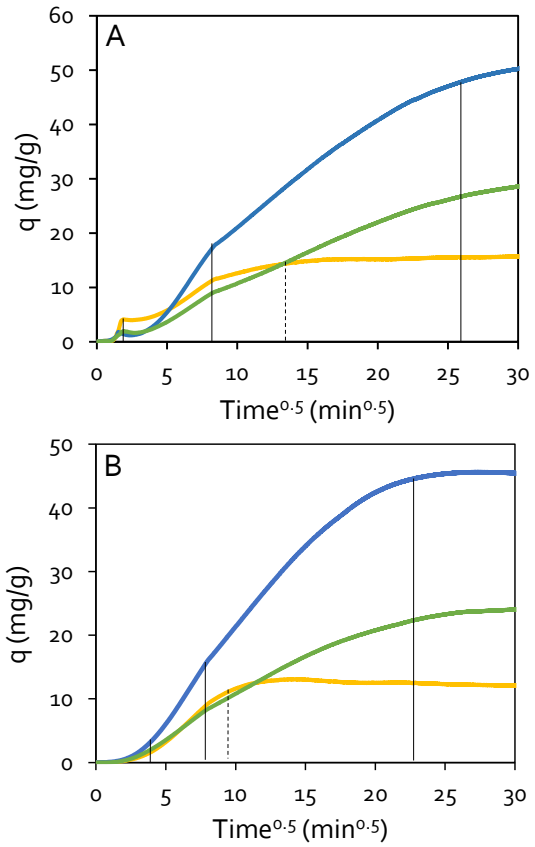


Figure 5. Intraparticle diffusion model plots for (A) methane and (B) nitrogen adsorption for the three adsorbents: Basolite C300 (blue), Basolite F300 (green) and Basolite A100 (yellow). The continuous line split the areas for Basolite C300 and Basolite F300. Discontinuous line refers to Basolite A100.

Where $k_F$ is the Freundlich constant related to adsorption capacity and $n$ refers to the adsorption intensity. According to Figure 6, it is observed how the predicted adsorption isotherms present the same trend as the experimental data in all cases, with very good correlation coefficients. Only in the case of the nitrogen adsorption on Basolite A100 it is observed a worse regression, but even in this case, the trend data is appropriate. Thus, it is especially relevant the information obtained from the Freundlich isotherm. Hence, add to the heterogeneity of the surface, something intrinsic to the MOFs nature, it is observed higher values of the $k_F$ for methane than nitrogen over all the adsorbents, in agreement with the adsorption capacities of the three adsorbents, Figure 1. Likewise, the decreasing order of $k_F$, C300 > A100 > F300, is the same as the slope of mesopores zone in the intraparticle diffusion model equation, which corresponds to the adsorption rate in this part. Concerning the $n$ parameter, presents in all cases values less than one, compatible with the increasing trend of the adsorption isotherms [52], Figure 6.

The Temkin isotherm takes into account the effects of indirect adsorbate/adsorbent interactions on the adsorption process. The isotherm is as follows:

$$q_e = \frac{RT}{b}\ln k_T + \frac{RT}{b}\ln c_e$$

Where $b$ is the Temkin constant, which is related to the heat of adsorption, and $k_T$ is the Temkin isotherm constant. This model, in all cases predict nearly absence of adsorption at very low relative pressures followed by a type-I curve trend, which does not correspond to the experimental data.

Sips, also called Langmuir-Freundlich, isotherm is a semiempirical model that follows the following equation in the linearized form [53]:

$$\ln\left(\frac{c}{c_0 - c}\right) = \frac{1}{n}\ln p + \ln\left(a^{1/n}\right)$$

Where $c_0$ is iteratively found to obtain a linear relation between $\ln p$ and $\ln(\frac{c}{c_0-c})$, next $n$ is determined by the slope and then $a$ by the intersect point. The parameter $a$ in the Sips model is the affinity constant and $n$ is the heterogeneity coefficient of the adsorbate-adsorbent system. The larger the deviation of $n$ from 1, the stronger the non-uniformity of the surface in the adsorption system [54]. At this point, remark that for $n$ equal to 1, this equation is the Langmuir one. In fact, from Table 2 is evidenced the proximate values of $n$ parameter to the unity for Basolite A100, observing the largest differences for Basolite F300. This can be attributed even to the surface morphology, since in this material the microporosity is about 67% of the whole surface, whereas for the other two adsorbents a higher uniformity was observed.

Similarly, Shang et al. [55] found values of $n$ lower than 1 in the methane and nitrogen adsorption on molecular sieves with CHA-type structure. Figure 6 evidences the goodness of the fitting, especially in the case of methane adsorption, with the only exception of the nitrogen adsorption on Basolite A100. This model is a combined form of Langmuir and Freundlich expressions used for predicting the heterogeneous adsorption system and overcoming the drawback associated with Freundlich isotherm model of continuing increase in the adsorbed amount with an increase in concentration.

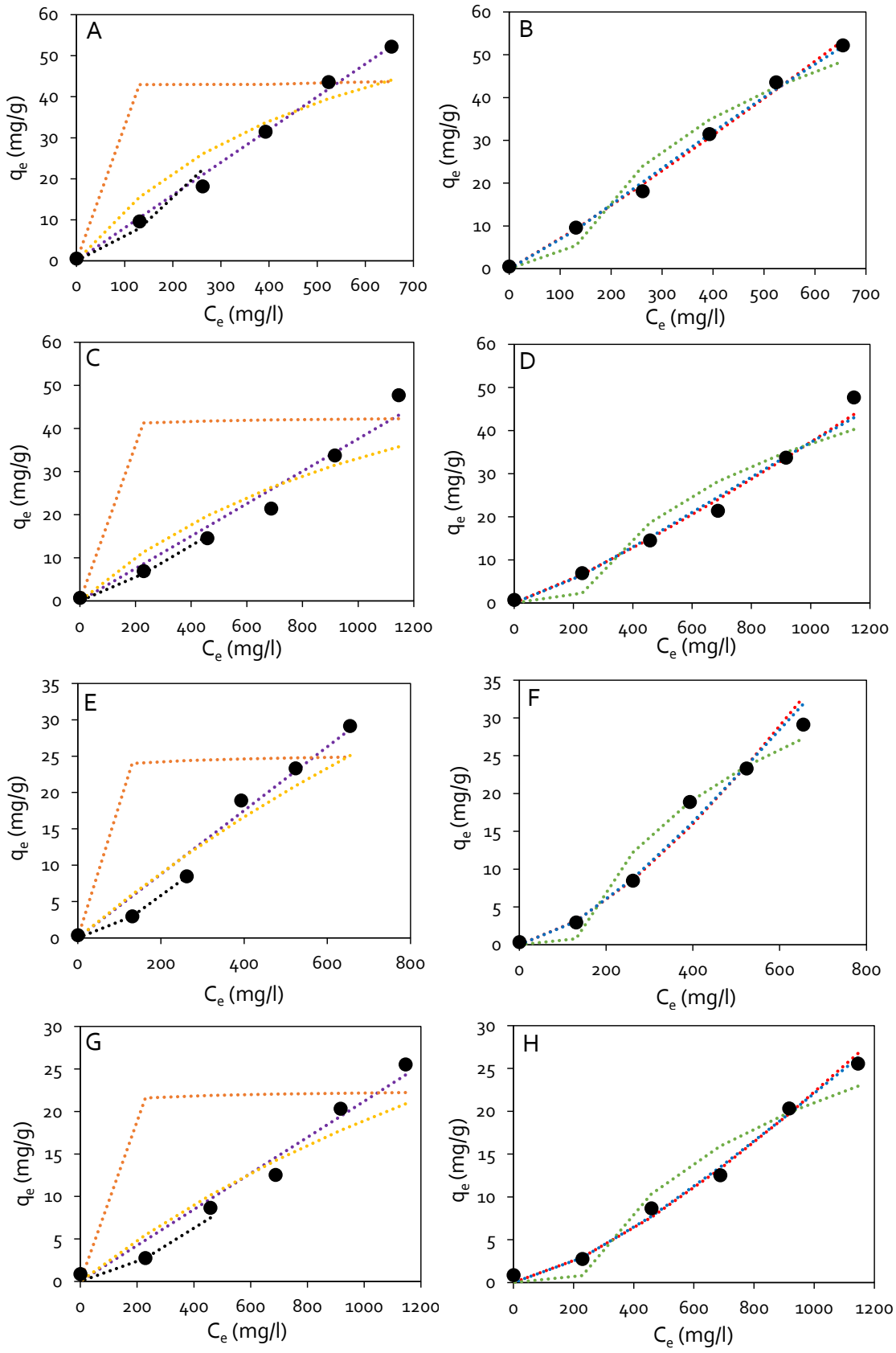
A
B
C
D
E
F
G
H
$q_e$ (mg/g)
$C_e$ (mg/l)

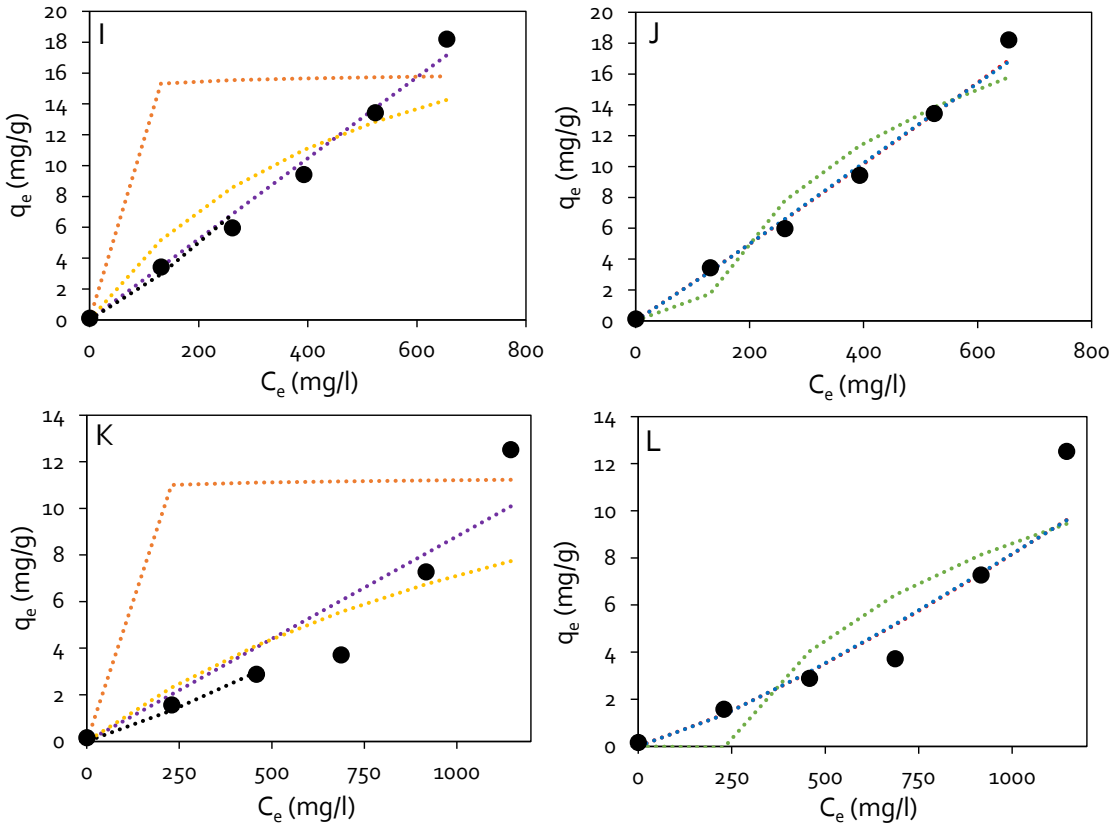


Figure 6. Comparison of different isotherm models with experimental data of Basolite C300 (A and B for methane, C and D for nitrogen), F300 (E and F for methane, G and H for nitrogen) and A100 (I and J for methane, K and L for nitrogen). Experimental (●) and models (dotted lines). Left plots: Henry (purple), Hill-Deboer (orange), Fowler-Guggenheim (black) and Langmuir (yellow). Right plots: Freundlich (red), Temkin (green) and Sips (blue). Curves were obtained from a AutoChem II 2920 (298 K, 0.1 MPa and 50 ml/min of total flow).

Sips equation is similar to the Freundlich equation, but it has a finite limit when the concentration is sufficiently high. In fact, comparing value of $R^2$ of all the isotherms, the Freundlich and Sips models have the highest values of $R^2$, and the isotherm with a better fitting for both molecules on the three adsorbents is the Sips one, pointing out the heterogeneous nature of the adsorbents. Moreover, the worst adjustment in all cases is for Basolite A100, and especially for nitrogen could be due to the adsorption-induced structural transition (breathing) characteristic of this structure. This phenomenon was already observed by the hysteresis loops in the adsorption and desorption of xenon and methane on MIL-53(Al) structure [38].

### 3.5. Regenerability of the adsorbent

The stability of the adsorbent for the methane and nitrogen adsorption was studied by adsorption/desorption cycles. Figure 7 (A) shows the maximum adsorption capacity of each gas in the first cycle and Figure 7 (B) the adsorption index (adsorption capacity divided by the maximum adsorption capacity) of the three Basolites. Both methane and nitrogen adsorption experiments were carried out at 298 K, and then, its desorption was performed in pure helium at 423 K. After six cycles, the adsorption capacity of methane is over 80% for Basolite F300 and A100, whereas decreases until 64% for Basolite C300. In the case of nitrogen, the capacity in the last cycle is always over 80%, reaching 92% for Basolite A100. Therefore, it can be seen that the regenerability of nitrogen is easier than in the case of methane, in agreement with both the molecular properties of the adsorbates, and also the lower capacity and heat of adsorption.

At a first insight, the regenerability seems not to be related to the kinetic constants deduced from the Langmuir model, from which the Basolite C300 presented higher values of the adsorption constant than Basolite F300. What is more, Basolite A100 exhibited the largest values of both adsorption and desorption constants of methane and nitrogen, not hindering this fact the good regenerability of the material, probably due to the breathing effect.

Table 2. $CH_4$ and $N_2$ adsorption parameters for the Basolite C300, F300 and A100.

| Material | Methane | | | Nitrogen | | |
|---|---|---|---|---|---|---|
| *Henry* | | | | | | |
| | $k_H$ (l·g$^{-1}$) | | $R^2$ | $k_H$ (l·g$^{-1}$) | | $R^2$ |
| C300 | 0.080 | | 0.99 | 0.037 | | 0.96 |
| F300 | 0.043 | | 0.97 | 0.021 | | 0.97 |
| A100 | 0.026 | | 0.98 | 0.008 | | 0.86 |
| *Hill-Deboer* | | | | | | |
| | $k_1$ (l·mg$^{-1}$) | $k_2$ (kJ·mol$^{-1}$) | $R^2$ | $k_1$ (l·mg$^{-1}$) | $k_2$ (kJ·mol$^{-1}$) | $R^2$ |
| C300 | -5.87 | -24.24 | 0.58 | -3.932 | -15.58 | 0.43 |
| F300 | -3.50 | -20.55 | 0.63 | -7.33 | -21.02 | 0.52 |
| A100 | -2.36 | -16.68 | 0.64 | -3.29 | -12.17 | 0.70 |
| *Fowler-Guggenheim* | | | | | | |
| | $k_{FG}$ (l·g$^{-1}$) | w (kJ·mol$^{-1}$) | $R^2$ | $k_{FG}$ (l·mg$^{-1}$) | w (kJ·mol$^{-1}$) | $R^2$ |
| C300 | 0.00090 | -3.30 | 0.94 | 0.00049 | -2.78 | 0.90 |
| F300 | 0.00063 | -3.85 | 0.97 | 0.00037 | -3.67 | 0.93 |
| A100 | 0.00105 | -2.56 | 0.91 | 0.00041 | -2.56 | 0.78 |
| *Langmuir* | | | | | | |
| | $k_L$ (mg·g$^{-1}$) | $q_m$ (mg·g$^{-1}$) | $R^2$ | $k_L$ (mg·g$^{-1}$) | $q_m$ (mg·g$^{-1}$) | $R^2$ |
| C300 | 0.0017 | 81.9 | 0.91 | 0.0007 | 77.5 | 0.85 |
| F300 | 0.0003 | 123 | 0.93 | 0.0003 | 70.9 | 0.91 |
| A100 | 0.0019 | 25.4 | 0.87 | 0.0006 | 18.8 | 0.78 |
| *Freundlich* | | | | | | |
| | $k_F$ (l·g$^{-1}$) | N | $R^2$ | $k_F$ (l·mg$^{-1}$) | n | $R^2$ |
| C300 | 0.047 | 0.92 | 0.99 | 0.011 | 0.85 | 0.98 |
| F300 | 0.002 | 0.68 | 0.96 | 0.001 | 0.72 | 0.99 |
| A100 | 0.020 | 0.96 | 0.98 | 0.001 | 0.82 | 0.89 |
| *Temkin* | | | | | | |
| | $k_T$ (l·g$^{-1}$) | b (J·mol$^{-1}$) | $R^2$ | $k_T$ (l·g$^{-1}$) | b (J·mol$^{-1}$) | $R^2$ |
| C300 | 0.0093 | 92.6 | 0.96 | 0.0048 | 104 | 0.90 |
| F300 | 0.0080 | 150 | 0.96 | 0.0046 | 180 | 0.94 |
| A100 | 0.0093 | 283 | 0.92 | 0.0043 | 419 | 0.78 |
| *Sips* | | | | | | |
| | $c_0$ (mg·g$^{-1}$) | n | a (bar$^{-1}$) | $R^2$ | $c_0$ (mg·g$^{-1}$) | n | a (bar$^{-1}$) | $R^2$ |
| C300 | 200 | 0.80 | 0.00065 | 0.99 | 200 | 0.76 | 0.00032 | 0.97 |
| F300 | 200 | 0.64 | 0.00052 | 0.99 | 200 | 0.70 | 0.00020 | 0.99 |
| A100 | 200 | 0.92 | 0.00016 | 0.98 | 200 | 0.80 | 0.00008 | 0.89 |

However, regenerability is carried out in a helium flow, fact that marks the difference since no adsorbate pressure is exerted.

## 4. Conclusions

This work presented a thermodynamic and kinetic analysis of the methane and nitrogen adsorption on three different commercial metal-

organic frameworks (MOFs): Basolite C300, Basolite F300 and Basolite A100.

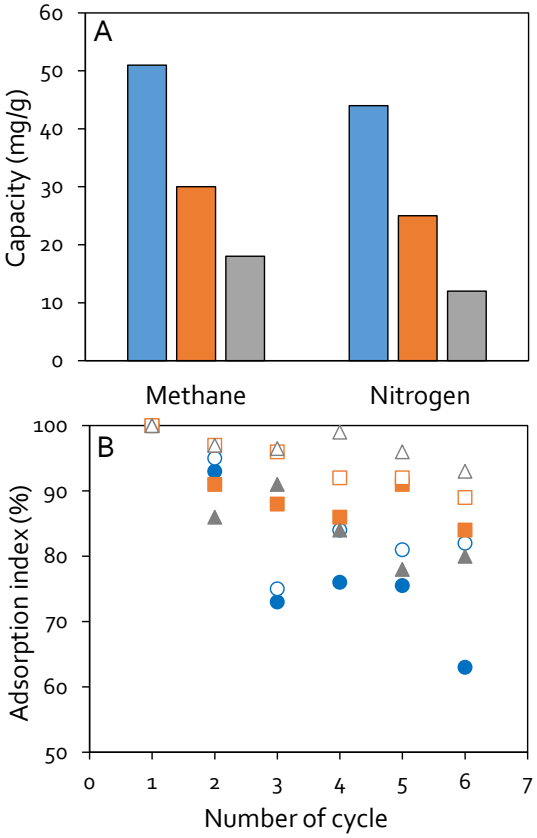


Figure 7. Adsorption capacity of the first cycle of both methane and nitrogen for different MOFs: C300 (blue), F300 (orange) and A100 (grey) (A); Adsorption index performance for the different MOFs: C300 (●), F300 (■) and A100 (▲). Filled symbols correspond to methane and empty symbols to nitrogen.

The capacity of adsorption of both pure gases were analysed under isothermal conditions in the interval 298-498 K, observing higher adsorption capacity at the lowest temperature, and being remarkable the Cu interaction of the Basolite C300 with the methane, as it was deduced both from the capacity and the heat of adsorption. The curves of adsorption of both gases versus time at 298 K were fitted to several kinetic models. Among them, the Langmuir and fractional order models are the most suitable to describe the adsorption of both gases on the three adsorbents. Likewise, from the intraparticle diffusion model, it is observed a different behaviour between Basolite A100 and the other two adsorbents, reaching faster the equilibrium stage for the former. For both adsorbates, the adsorption is easier than desorption on the surface of the three materials. The main differences observed among the adsorbents were the faster adsorption of both gases on Basolite A100, as well as the larger dependence on the occupied adsorption sites.

Equilibrium of the adsorption was fitted to several adsorption isotherms of one, two or three parameters, being the Freundlich and Sips isotherms which obtained the best adjustment due to the assumptions of certain surface heterogeneity and the increasing adsorption capacity with the increasing pressure (limited in the case of the Sips one). Concerning the regenerability of the Basolites, after six cycles, the regenerability of nitrogen is easier than in the case of methane, in agreement with both the molecular properties of the adsorbates, and also the lower capacity and heat of adsorption. As for the ease of regeneration, the Basolite A100 stands out, probably due to its breathing effect.

## Declaration of competing interest

The authors declare that they have no known competing financial interests or personal relationships that could have appeared to influence the work reported in this paper.

## CRediT authorship contribution statement

**David Ursueguía**: Investigation, Formal analysis, Writing – original draft. **Eva Díaz**: Data curation, Methodology, Writing – review & editing. **Salvador Ordóñez**: Conceptualization, Supervision, Writing – review & editing.

## Acknowledgements

This work was supported by the Research Fund for Coal and Steel of the European Union (contract UE-17-RFCS216-METHENERGY PLUS).

D. Ursueguía acknowledges the Spanish Government for the FPU fellowship (FPU18/01448).

## References

[1] S. Su, A. Beath, H. Guo, C. Mallet, Prog. Energ. Combust. 31 (2005) 123-70.

[2] B. Oboirien, B. North, S. Obayopo, J. Odusote, E. Sadiku, Energy Strateg. Rev. 20 (2018) 64-70.

[3] A. Singh, J. Kumar, Energy Procedia 90 (2016) 336-48.

[4] S. Xie, S. Lin, Q. Zhang, Z. Tian, Y. Wang, J. Energy Chem. 27 (2018) 1629-1636.

[5] Z. Zakaria, S. Kamarudin, Renew. Sust. Energy Rev. 65 (2016) 250-261.

[6] R. Thiruvenkatachari, S. Su, XX. Yu, J. Hazard Mater. 172 (2009) 1505-1511.

[7] DL. Cluff, GA. Kennedy, JG. Bennett, PJ. Foster, App. Therm. Eng. 90 (2015) 1151-1163.

[8] B. Zheng, Y. Liu, R. Liu, J. Meng, Int. J. Hydrogen Energy 40 (2015) 3381-3387.

[9] K. Baris, Energy Sustain. Dev. 17 (2013) 13-23.

[10] I. Karakurt, G. Aydin, K. Aydiner, Renew. Sust. Energ. Rev. 15 (2011) 1042-1049.

[11] T. Saleman, G. Li, T. Rufford, P. Stanwix, K. Chan, S. Huang, E. May, Chem. Eng. J. 281 (2015) 739-748.

[12] Z-Y. Sui, B-H. Han, Carbon 82 (2015) 590-598.

[13] R. Seabra, A. Ribeiro, K. Gleichmann, A. Ferreira, A. Rodrigues, Micropor. Mesopor. Mat. 277 (2019) 105-114.

[14] D. Kennedy, F. Tezel, Micropor. Mesopor. Mat. 262 (2018) 235-250.

[15] P. Li, H. Tezel, Micropor. Mesopor. Mat. 98 (2007) 94-101.

[16] X. Xu, X. Zhao, L. Sun, X. Liu, J. Nat. Gas Chem. 18 (2009) 167-172.

[17] JA. Menéndez-Díaz, I. Martín-Gullón, In: Bandosz TJ (Eds.), Interface Science and Technology, Elsevier, 2006. pp. 1-47.

[18] H. Yi, F. Li, P. Ning, X. Tang, J. Peng, Y. Li Y, Chem. Eng. J. 215 (2013) 635-642.

[19] T. Düren, L. Sarkisov, O. Yaghi and R. Snurr, Langmuir 20 (2004) 2683-2689.

[20] D. Alezi, Y. Belmabkhout, M. Suyetin, P. Bhatt, L. Weselinski, V. Solovyeva, K. Adil, I. Spanopoulos, P. Trikalitis, A. Emwas, M. Eddaoudi, J. Am. Chem. Soc. 137 (2015) 13308-13318.

[21] Y. He, W. Zhou, G. Qian, B. Chen, Chem. Soc. Rev. 16 (2014) 5657-5678.

[22] B. Li, H. Wen, W. Zhou, J. Xu, B. Chen, Chem 1 (2016) 557-580.

[23] I. Gutiérrez, E. Díaz, A. Vega, S. Ordóñez, A. Ruiz, E. Castillejos, I. Rodríguez, Thermochim. Acta 602 (2015) 36–42.

[24] J. Hsieh, K. Balkus, J. Ferraris, I. Musselman, Micropor. Mesopor. Mat. 196 (2014) 165-174.

[25] Y. Wang, T. Du, Z. Qiu, Y. Song, S. Che, X, Fang, Mat. Chem. Phys. 207 (2018) 105-113.

[26] Y. Yang, X. Yan, X. Hu, R. Feng, M. Zhou, W. Cui, Colloid. Surface. A 552 (2018) 16-23.

[27] G. Blanco, J. Campos, S. Al-Zahrani, J. Fierro, Fuel 90 (2011) 190-197.

[28] N. Heymans, S. Vaesen, G. De Weireld, Micropor. Mesopor. Mat. 154 (2012) 93-99.

[29] Z. Bao, S. Alnemrat, L. Yu, I. Vasiliev, Q. Ren, X. Lu, S. Deng, J. Colloid Inter. Sci. 357 (2011) 504-509.

[30] M. Niwa, K. Yamazaki, Y. Murakami, Ind. Eng. Chem. Res. 30 (1991) 38-42.

[31] D. Saha, Z. Bao, F. Jia, S. Deng, Environ. Sci. Technol. 44 (2010) 1820-1826.

[32] A. Alonso, J. Moral-Vico, A. Abo Markeb, M. Busquets-Fité, D. Komilis, V. Puntes V, Sci. Total Environ. 595 (2017) 51-62.

[33] K. Lin, A. Krishna, C. Ku, C. Chiang, H. Kuo, Int. J. Hydrogen Energ. 37 (2012) 13865-13871.

[34] E. Pérez-Mayoral, J. Cejka, ChemCatChem 3 (2011) 157-159.

[35] Y. Peng, V. Krungleviciute, I. Eryazici, J. Hupp, O. Farha, T. Yildirim, J. Am. Chem. Soc. 135 (2013) 11887-11894.

[36] A. Dhakshinamoorthy, M. Alvaro, P. Horcajada, E. Gibson, M. Vishnuvarthan, A. Vimont, J. Greneche, C. Serre, M. Daturi, H. Garcia, ACS Catal. 2 (2012) 2060-2065.

[37] J. Mollmer, M. Lange, A. Moller, C. Patzschke, K. Stein, D. Lassig, J. Lincke, R. Glaser, H. Krautscheid, R. Staudt, J. Mater. Chem. 20 (2012) 10274-10286.

[38] A. Boutin, F. Coudert, M. Springuel, A. Neimark, G. Ferey, A. Fuchs, J. Phys. Chem. C 114 (2010) 22237-22244.

[39] R.T. Yang, Adsorbents: fundamentals and applications, first ed., John Wiley & Sons, 2003.

[40] C. Long Xue, W. Ping Cheng, W. Ming Hao, J. Hong Ma, R. Feng Li, J. Chem. (2019) 1-9.

[41] R. Chanajaree, T. Chokbunpiam, J. Kärger, S. Hannongbua, S. Fritzsche, Micropor. Mesopor. Mat. 274 (2019) 266-276.

[42] Z. Niu, X. Cui, T. Pham, P. Lan, H. Xing, K. Forrest, L. Wojtas, B. Space, S. Ma, Angew. Chem. Int. Edit. 58 (2019) 10138-10141.

[43] D. Wu, X. Guo, H. Sun, A. Navrotsky, J. Phys. Chem. Lett. 6 (2015) 2439-2443.

[44] S. Bourrelly, P. Llewellyn, C. Serre, F. Millange, T. Loiseau, G. Ferey, J. Am. Chem. Soc. 127 (2005) 13519-13521.

[45] Y. Wang, T. Du, Z. Qiu, Y. Song, S. Che, X. Fang, Mat. Chem. Phys. 207 (2018) 105-113.

[46] V. Fierro, V. Torné-Fernández, D. Montané, A. Celzard, Micropor. Mesopor. Mat. 111 (2008) 276-284.

[47] V. Finsy, L. Ma, L. Alaerts, D. De Vos, G. Baron, J. Denayer, Micropor. Mesopor. Mat. 120 (2009) 221-227.

[48] A. Heydari-Gorji, A. Sayari, Chem. Eng. J. 1173 (2011) 72-79.

[49] Q. Liu, J. Shi, S. Zheng, M. Tao, Y. He, Y. Shi, Ind. Eng. Chem. Res. 53 (2014) 11677-11683.

[50] D. M. Ruthven, Principle of adsorption and adsorption processes, John Willey and Sons, New Jersey, NJ, USA, 1984.

[51] N. Ayawei, A. Ebelegi, D. Wankasi, Hindawi J. Chem. (2017) 1-11.

[52] Y. Patiño, E. Díaz, S. Ordóñez, Chemosphere 119S (2015) S124-S130.

[53] N. Tzabar, H.J.M. ter Brake, Adsorption 22 (2016) 901-914.

[54] R. Sips, J. Chem. Phys. 16 (1948) 490-495.

[55] H. Shang, Y. Li, J. Liu, X. Tang, J. Yang, J. Li, Chinese J. Chem. Eng. 27 (2019) 1044-1049.

## Densification-induced structure changes in Basolite MOFs: Effect on low-pressure $CH_4$ adsorption

David Ursueguía, Eva Díaz, Salvador Ordóñez*

Catalysis, Reactors and Control Research Group (CRC), Department of Chemical and Environmental Engineering, University of Oviedo, Julián Clavería s/n, 33006 Oviedo, Spain

*e-mail: sordonez@uniovi.es (S. Ordóñez)

*Nanomaterials* **10** (2020) 1089.

https://doi.org/10.3390/nano10061089

## ABSTRACT

The adsorption potential of metal-organic frameworks (MOFs) is significantly reduced by turning the original powder into pellets or granules, a mandatory step for their use at industrial scale. Pelletization is commonly performed by mechanical compression, which often induces the amorphization or pressure-induced phase transformations. The objective of this work is the rigorous study of the impact of mechanical pressure (55.9, 111.8 and 186.3 MPa) onto three commercial materials (Basolite C300, F300 and A100). Phase transformations were determined by powder X-ray diffraction analysis, whereas morphological changes were followed by nitrogen physisorption. Methane adsorption was studied in an atmospheric fixed bed. Significant crystallinity losses were observed, even at low applied pressures (up to 69.9% for Basolite C300), whereas a structural change occurred to Basolite A100 from orthorhombic to monoclinic phases, with a high cell volume reduction (13.7%). Consequently, adsorption capacities for both methane and nitrogen were largely reduced (up to 53.6% for Basolite C300), being related to morphological changes (surface area losses). Likewise, the high concentration of metallic active centres (Basolite C300), the structural breathing (Basolite A100) and the mesopore-induced formation (Basolite F300) smooth the dramatic loss of capacity of these materials.

**Keywords**: Coordination polymers; Methane storage; XRD crystallinity measurements; Mechanical shaping; Compaction; VAM; Gas separation; MOF pelletization

### 1. Introduction

Energy demand estimations for the next decades, mainly due to the global population and industrialization process increments, boost the development of techniques and processes able to make the most of available resources [1]. What is more, the recent COVID-19 pandemic, with millions of people confined to their homes, pointed out even more our domestic reliance on electricity. In most economies that have taken strong confinement measures in response to the coronavirus, electricity demand has declined by around 15%, and the share of variable renewables like wind and solar had become higher than normal [2]. Even when electricity from wind and solar would satisfy the majority of demand, systems need to maintain flexibility in order to be able to ramp up other resources of generation quickly when the pattern of supply shifts, such as when the sun sets. That is, electricity system operators have to constantly balance demand and supply in real time to prevent blackouts, which in recent times occurred mainly during periods of low demand [2]. In this context, natural gas power plants can quickly ramp generation up or down at short notice, providing in this way flexibility, underlining the critical role of gas in the longed-for clean energy transition.

In the natural gas industry, methane purification is a major process for upgrading the streams [3]. In these streams, methane concentration is originally elevated (> 90%), so satisfactory results have been reported using fixed-bed adsorption techniques [4, 5]. In these cases, the usual practice is to separate the component that is in lower concentration by adsorption (typically $CO_2$). Adsorbents usually used for this purpose are activated carbons and zeolites, which have good $CO_2$ adsorption yields and their cost is relatively low [6, 7]. On the other

hand, these techniques present difficulties when methane is the component with the lowest concentration in the stream. Activated carbons and zeolites present low selectivity towards methane with respect to other very similar compounds in molecular size and polarity, like nitrogen [8, 9]. This is the case of one of the new alternative methane sources that has begun to be studied in recent years, the recovery of methane from ventilation gases from mining exploitation (VAM). Until now, these streams, which contain typically less than 1% in methane, has been burned directly, with the need of an auxiliary fuel. VAM could be used in order to obtain energy or chemical products, as well as to prevent greenhouse gas emissions into the atmosphere [10, 11]. For these operations to be profitable, it is necessary to perform a previous concentration step, whose success depends on the separation capacity of the adsorbent used [12].

Among the materials studied for this purpose, due to its amazing properties, metal-organic frameworks (MOFs) have been shown to present large adsorption and gas separation yields [13, 14], these being among the most promising materials in this field. Their high specific surface area (even values up to 6255 $m^2/g$ [15]) combined with high total pore volume (1.303 $cm^3/g$ [16]) and great porosity (91.1% [17]) are responsible for the large adsorption capabilities, exceeding in the majority of cases other common materials [18]. The structure of these materials is made up by an organic ligand, such as imidazole or pyrazine, which links different metal ions or clusters corresponding to each MOF type (copper, aluminium, etc.). These combinations form a cage-like structure that is repeated continuously, conferring on these materials a high degree of crystallinity [19]. Two of the main characteristics of the MOFs are the flexibility in the design, which means a huge variety of organic ligands and metallic ions that allow on-demand materials to be made, and the pore functionalization, presenting high interesting adsorptive and catalytic properties. The possibility of performing a large number of combinations has led to an astonishing number of works related to the synthesis of MOFs suitable for different applications, which include gas storage and separation [20]. For example, in the case of methane separation from other gases, Arami-Niya et al. [21] have tested the zeolitic imidazolate framework (ZIF-7) for the separation of methane from nitrogen, obtaining a selectivity of more than 10 for an equimolar mixture at 303 K. In addition, other authors such as Eyer et al. [22] have studied different materials capable of selectively adsorb methane from air mixtures, obtaining promising results in the case of HKUST-1, with a selectivity methane/nitrogen of 2.8 and a large gravimetric methane adsorption capacity (171.36 mg/g) at 100 kPa and 196 K. Thus, MOFs have led to satisfactory results at the laboratory level in the case of low-concentrated methane separation from mixtures [23, 24], with no experiences being performed at greater scales.

Therefore, most of the experimentation at lab scale and the study of properties are done on the original powder form, since the most-used techniques for the MOFs synthesis are solvo-thermal methods, which generally produce powders [25]. Industrial-scale difficulties occur as a result of pressure drops associated with powder-filled beds, high diffusional problems and low density of the materials [26, 27]. In order to reduce the pressure drop through the bed, there are techniques for increasing particle size and MOF densification: mechanical, hydraulic or hot pressing, extrusion, solid or emulsion templating, and the use of a polymeric binder [28, 29]. In addition, there are also other techniques currently in development, such as the sol-gel monolithic synthesis [30]. Among them, mechanical compression is an inexpensive procedure and avoids the use of additional components like polymeric binders, with may change the physical properties of MOFs [31]. However, compression pelletization could also induce amorphization as well as phase transformations, which could influence also the adsorption capacities of the MOFs [32, 33].

In this way, several studies deal with the effect of mechanical compression on hydrogen adsorption for MOF-5 [34, 35] and MIL-101 [36] MOFs; as well as on $CO_2$ adsorption [37]. By contrast, there are fewer works related to the influence of MOFs' densification on the methane adsorption. For example, Yuan et al. [38] have studied the behaviour of PCN-250 on the methane and nitrogen adsorption at densification pressures up to 300 MPa [38]. General pressure-effects are, added to the loss of gravimetric performance, an increase in the volumetric adsorption capacity, in addition to higher stability in a humid ambient. Typically, these adsorption studies are done at elevated gas pressures since the main objective is to increase material density and volumetric adsorption capacity for meeting gas storage challenges. In this work, the aim is the separation of methane from low-concentration streams, so adsorption studies have been conducted at low pressure (0.1 MPa).

Therefore, the aim of this work is to study, firstly, the pressure-induced changes on the morphology and structure of three of the most common (and commercially available) MOFs, Basolite C300, Basolite F300 and Basolite A100; and, secondly, on the methane and nitrogen adsorption capacity at low pressure (0.1 MPa). The study of the adsorption capacity for methane (component to be recovered in VAM) and nitrogen (major component in VAM) establishes a benchmark for the use of these commercial materials at industrial scale for obtaining profiting lean emissions as a novel energy source.

## 2. Materials and Methods

Basolite C300 [$Cu_3(C_9H_3O_6)_2$], Basolite F300 ($C_9H_3FeO_6$) and Basolite A100 ($C_8H_5AlO_5$) were manufactured by BASF and supplied by Aldrich (96% mass basis purity, Steinheim, Germany). All three materials were stored in a desiccator in order to avoid its contact with the ambient air. Particles were used in powder form, being the commercial size: Basolite C300 (16 μm, D50), Basolite F300 (5 μm) and Basolite A100 (32 μm, D50). Methane ($CH_4$), nitrogen ($N_2$) and helium (He), with a purity > 99.995 % mol, were supplied by Air Liquide (Madrid, Spain).

The pelletization method was performed using a hydraulic press (Graseby SPECAC 15.011, Orpington, UK) at compression pressures of 55.9, 111.8 and 186.3 MPa, for 30 s. Starting pressure was selected after two considerations: ensuring the pelletization of the material to work at the actual conditions, and the lower operating limit of the hydraulic press used for this purpose. The resulting pellets were crushed and sieved in order to obtain powder (< 50 μm) to perform the successive analysis.

Breakthrough adsorption curves were obtained by flowing either $CH_4$ or $N_2$ (60 %) diluted in He with a total flowrate of 50 ml/min, 298 K and 0.1 MPa of total pressure in a Micromeritics AutoChem II 2920 apparatus (Norcross, GA, USA) through a fixed bed of each sample (30 mg). The evolution of $CH_4$, $N_2$ and He signals were followed in a Pfeiffer Vacuum Omnistar Prisma mass spectrometer (Pfeiffer Vacuum, Asslar, Germany). Adsorption gravimetric capacity was obtained from desorption experiments that were performed in the same apparatus flowing a He stream (20 ml/min and 0.1 MPa) with a temperature ramp of 5 K/min from 298 K to 463 K, recording also the outlet with the mass spectrometer.

The textural characteristics of specific surface area and pore volume were estimated by $N_2$ physisorption at 77 K in a Micromeritics ASAP 2020 surface area and porosity analyzer (Norcross, GA, USA). Physisorption data has been processed using Brunauer-Emmett-Teller (BET), Barrett-Joyner-Halenda (BJH) and t-plot approaches for determining surface area, total mesopore volume and total micropore volume, respectively. Variations in average pore size were calculated by assuming pore cylindrical geometry. Scanning electron microscopy (SEM) images were obtained by using a JEOL 6610LV scanning electron microscope (JEOL, Yvelines, France). The samples were coated with gold prior to observation.

The crystallographic structures of the materials were determined by powder X-ray diffraction (PXRD) using a Philips PW 1710 diffractometer (Koninklijke Philips, Amsterdam, The Netherlands), working with the Cu-$K_\alpha$ line ($\lambda$ = 0.154 nm) in the 2$\theta$ range of 5°-85° at a scanning rate of 2°/min. Variations in the cell structure of the materials were verified by the Bragg Law. Consequently, variations in lattice parameters of the structures were obtained through the standard equations for cubic, orthorhombic and monoclinic structures.

## 3. Results

### 3.1. Materials characterization

Figures 1-3 show the SEM images of powder in the commercial form, as well as the sieved powder after the three pressure treatments. As can be observed, materials in the original form show well-defined particulate shapes, polyedric form in case of Basolite C300, and rounded shape in case of Basolite F300 and Basolite A100. Size distribution seems to be wide for all of them, being the original size order: Basolite A100 > Basolite C300 > Basolite F300. Pressure increments lead to particle fragmentation, with the subsequent formation of irregular particle agglomerates. At the highest pressure (186.3 MPa) individual particles are practically indistinguishable, which become part of a large individual no-shaped bulk, especially for Basolite C300 and A100.

Figure 4 shows the adsorption-desorption isotherms determined by $N_2$ physisorption analysis at 77 K. As shown in the figure, pristine samples exhibit a combination of type I (b) and type II isotherms, according to the International Union of Pure and Applied Chemistry (IUPAC). The first zone (up to $P/P_0$ = 0.8) resembles a type I (b) isotherm, with a steep elevation of the adsorbed quantity at very low pressure, and a subsequent maintenance.

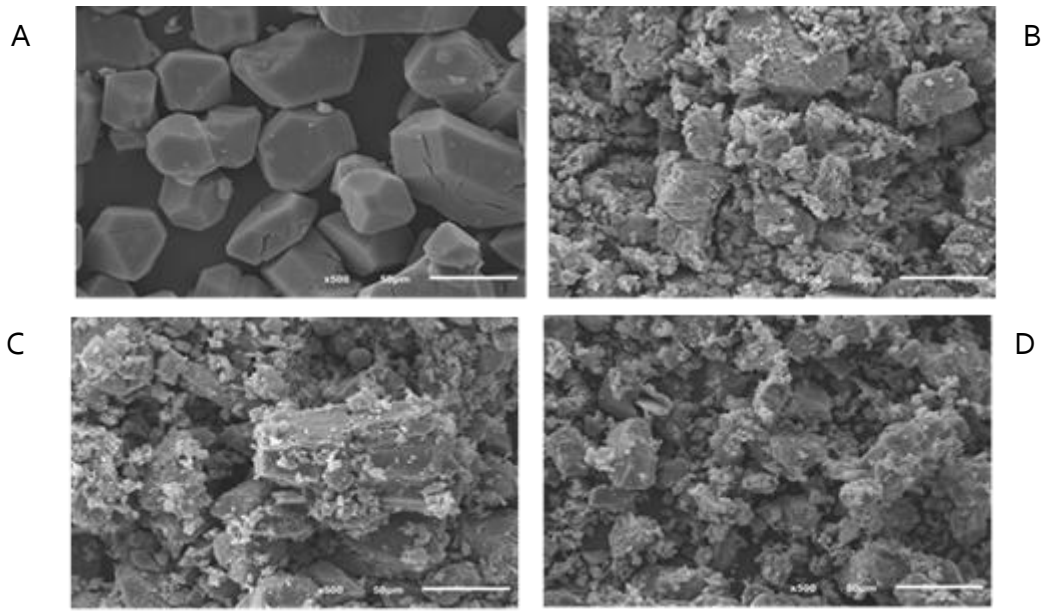


Figure 1. Scanning electron microscope (SEM) images of Basolite C300 (zoom in 50 µm) (A: original, B: 55.9 MPa, C: 111.8 MPa, D: 186.3 MPa).

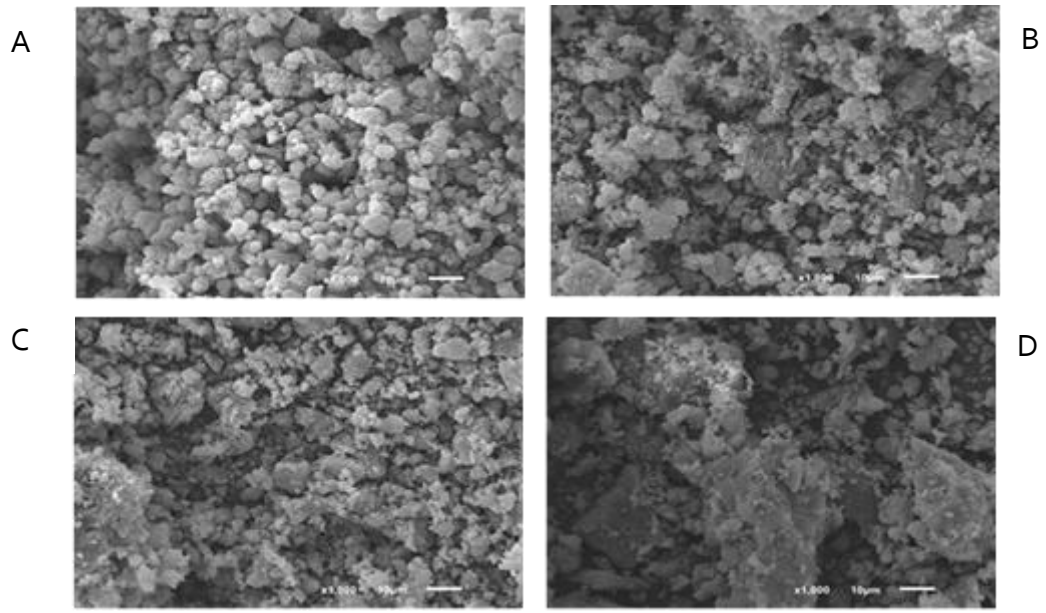


Figure 2. SEM images of Basolite F300 (zoom in 10 µm) (A: original, B: 55.9 MPa, C: 111.8 MPa, D: 186.3 MPa).

It is characteristic of microporous materials with wide micropores and possibly narrow mesopores [39]. The second area, up to a $P/P_0 = 1$, shows a more pronounced increase of adsorbate retained, which resembles the final part of a type II isotherm. This indicates the adsorption onto macroporous or non-porous materials in multi-layer disposition, which corresponds to the external phase of MOFs [40]. A combination of these two isotherms usually results in a type IV isotherm, but in this case no characteristic hysteresis is observed, and the end of the isotherms is not a plateau [41]. As the densification pressure increases, the isotherms are closer to type I (b), due to the material agglomeration and the consequent loss of external surface availability. In addition, in all the materials it is observed a marked reduction in the quantity adsorbed at low $P/P_0$ after pressure compression, indicative of a reduction in the total micropore volume, as it can be seen in the expanded graph (Figure 4). Micropores are clogged when particles are agglomerated with each other, in agreement with SEM images (Figure 1-3).

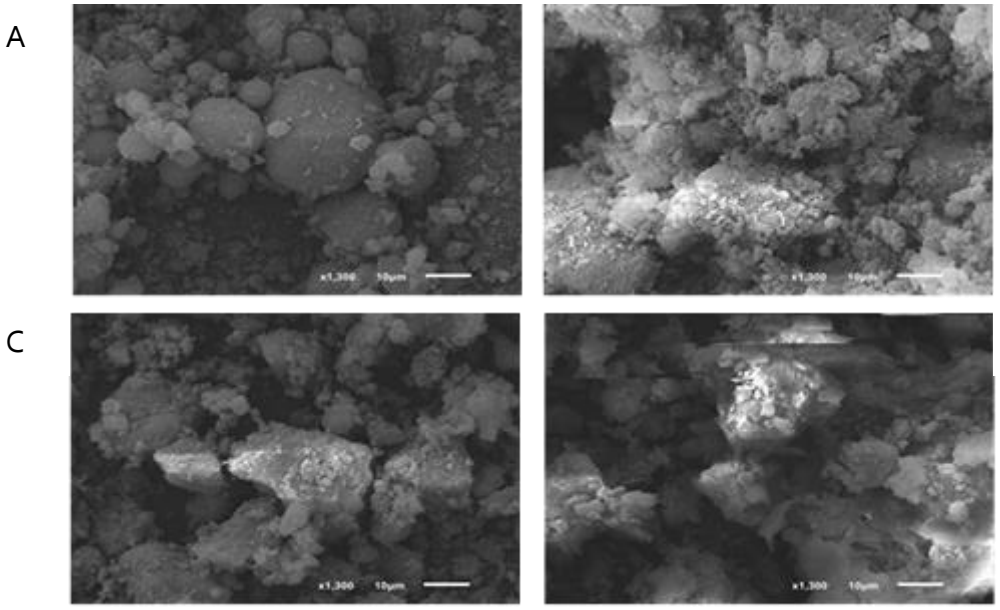


Figure 3. SEM images of Basolite A100 (zoom in 10 µm) (A: original, B: 55.9 MPa, C: 111.8 MPa, D: 186.3 MPa).

The results show a significant effect of pelletization pressure on the morphology of the three MOFs (Table 1). Basolite C300 exhibits the highest BET surface loss (95.4%) at the highest pressure, although even at 55.9 MPa, the BET surface decrease reaches a value of 54.2%, in addition to 69.4% for total pore volume, which rules out the appearance of mesopores in the structure. In agreement, Casco et al. [42] have observed a great structural collapse by applying mechanical pressure (1.5 tons) to this material.

Basolite F300 presents high decreases in specific surface area (up to 93.3%) and micropore volume (96.3%), but lower in mesopore volume (up to 56.8%). The sharp BET decrease at 55.9 MPa shows easiness for micropores collapse. However, the scarce total pore volume variation in the whole pressure range indicates the appearance of narrow mesopores in the structure (Table 1), as it is confirmed by the presence of some hysteresis (H4 type, according to IUPAC) at high $P/P_0$ values, marked in case of 55.9 and 111.8 MPa. It is also remarkable the appearance of two leaps in total mesopore volume value, one between original material and 55.9 MPa and the other between 111.8 and 186.3 MPa. This indicates that the appearance of mesopores is higher at 111.8 MPa, increasing the total pore volume even above of the previous applied pressure (55.9 MPa). Despite that, the total pore volume is reduced (0.15 to 0.13 $cm^3/g$) in that pressure increment. This could be attributed to the formation from the voids of interparticular pore volume, as a result of the compaction.

Finally, Basolite A100 presents also high specific surface and total pore volume losses, but with a different trend than the others. The first applied pressure (55.9 MPa) provokes the highest BET surface decrease (42.1 %). However, the following pressure does not affect greatly either the BET surface nor the pore volume (Table 1). In agreement, Ribeiro et al. [43], after application of 62 and 125 MPa to the material observed null relation between applied pressure and the morphological parameters, obtaining really similar results for both pressures. Finally, at the maximum pressure, a BET surface and pore volume decrease of 94.6 and 92.1 % was reached, respectively.

Figure 5 illustrates the effect of the applied pressure on the crystallinity of both pristine and pressure-modified MOFs. The relative crystallinity is obtained by comparison of the main peak among the series of each material, assuming 100% of crystallinity for the commercial material (Table 2) [44]. In addition, the displacement of peaks along the x-axis and the appearance of new ones may mean changes in the material structure (Table 3).

The pristine Basolite C300 powder X-ray diffraction (PXRD) pattern shows the typical peaks reported for this material at $2\theta$ = 6.7, 9.5, 11.65, 13.5, 19.3 and 26°, in addition to three little peaks at 35.5, 38.7 and 36.43°, which indicate some CuO and $Cu_2O$ impurities [45, 46]. After pressure is applied, the intensity of the peaks decreases progressively, indicative of crystallinity loss (Table 2).

Table 1. Variations of Brunauer-Emmett-Teller (BET) surface area, Barrett-Joyner-Halenda (BJH) total mesopore volume, t-plot total micropore volume and average pore size with applied pressure.

| Material | Applied pressure (MPa) | BET surface area ($m^2/g$) | BJH mesopore volume ($cm^3/g$) | t-plot micropore volume ($cm^3/g$) | Average pore size (Å) |
|---|---|---|---|---|---|
| C300 | 0 | 1466 | 0.53 | 0.71 | 33.7 |
| | 55.9 | 671 | 0.09 | 0.29 | 22.9 |
| | 111.8 | 364 | 0.07 | 0.14 | 23.2 |
| | 186.3 | 67 | 0.06 | 0.02 | 47.3 |
| F300 | 0 | 1015 | 0.15 | 0.27 | 16.5 |
| | 55.9 | 276 | 0.09 | 0.06 | 22.3 |
| | 111.8 | 173 | 0.11 | 0.02 | 28.8 |
| | 186.3 | 67 | 0.06 | 0.01 | 41.2 |
| A100 | 0 | 655 | 0.77 | 0.28 | 64.1 |
| | 55.9 | 380 | 0.57 | 0.06 | 65.8 |
| | 111.8 | 362 | 0.54 | 0.05 | 65.1 |
| | 186.3 | 35 | 0.06 | 0.01 | 70.1 |

As its PXRD pattern is practically coincident with HKUST 1, a face-centered cubic structure is assumed [47], consisting of 16 copper atoms, 8 at the corners, as well as 6 at the center of the cube faces. Low-angle peaks (9.5, 11.65 and 13.5°) present (220), (222) and (400) as Miller indices [48]. The net parameter (a) is obtained from the lattice plane of (222), Table 3. As shown, the cell volume remains practically unalterable (maximum variation of 1 %), due to the structure rigidity [49]. In agreement, McKellar et al. [50] reported variations of 2.6 % for densification pressures of 3.9 GPa. Likewise, the non-appearance of new crystalline peaks indicates that the cubic structure is maintained [51, 52]. Therefore, the pressure effect on Basolite C300 consists of crystallinity destruction, in agreement with the BET surface area and pore volume reduction with the pressure, but remaining unaltered the cubic structure of unaltered cells. In agreement, Peng et al. [53] have studied the effect of mechanical pressure (up to 5 tons) onto HKUST-1, indicating a great micropore volume loss ($N_2$ physisorption analysis), in addition to a total collapse of the crystalline structure (PXRD analysis).

For pristine Basolite F300, a characteristic peak at 2θ = 11° is observed, despite the low resolution of the pattern as a consequence of the semiamorphous nature of the material and the elevated background values due to the iron fluorescence [54]. In fact, Basolite F300 is a distorted form of crystalline MIL-100(Fe) [55], and possesses a zeolite MTN topology [56]. In this case, the semiamorphous nature of the material just allows observing an increase of the amorphous matter with the pressure (Table 2). As it is a semiamorphous material, crystallinity is slightly reduced in relative terms [57], not reflected in the BET surface, which does not depend on crystallinity and is severely affected with increased pressure. Particle agglomeration causes the collapse of micropores, as it was demonstrated in Figure 4.

Table 2. Relative crystallinity losses associated with applied pressure (referred to the original material).

| Material | Pressure (MPa) | Crystallinity loss (%) |
|---|---|---|
| C300 | 0 | 0 |
| | 55.9 | 19.5 |
| | 111.8 | 62.1 |
| | 186.3 | 69.9 |
| F300 | 0 | 0 |
| | 55.9 | 0 |
| | 111.8 | 4.3 |
| | 186.3 | 14.1 |
| A100 | 0 | 0 |
| | 55.9 | 69.3 |
| | 111.8 | 68.5 |
| | 186.3 | 68.4 |

Finally, in case of Basolite A100, it shows a structure practically coincident with MIL-53(Al) MOF, with characteristic peaks at 2θ = 8.8, 15.25 and 17.75° [58]. The original pattern obtained is close to that of the large-pore (lp) phase of MIL-53(Al), which is coincident with an orthorhombic structure [59]. For this result, three different net parameters make up the structure and all the angles are right. Diffracting planes that match the characteristic peaks are (101), (011) and (210) [60, 61]. As the applied pressure progresses, the appearance of new peaks around 2θ = 20° indicates a movement to the narrow-pore (np) phase [62, 63]. In this case, structural changes are high, due to the phase transition, reaching differences up to 13.7 % for total cell volume (Table 3). In fact, according to Ghoufi et al. [64], the cell shows a monoclinic structure [65] from, approximately, 53 MPa onwards. As can be observed, transition to the np structure has an associated reduction of the total cell volume, as well as a decrease of the $a$ parameter, in

conjunction with increasing trends in the rest of the parameters, including the $\beta$ angle. This increase in the $\beta$ angle denotes a flattening on one of its axes [62, 66], being these phase changes reversible [59]. Thus, this structure is characterized by its great flexibility. Regarding crystallinity, after the initial loss at the lowest pressure, it remains practically unchanged. The first applied pressure changes the material structure to np phase, which is known for its high resistance to external pressure and flexibility [63], thus maintaining crystallinity for successive applied pressures. The same occurs at 55.9 and 111.8 MPa in case of BET available surface and total pore volume, which are practically maintained after an abrupt decrease despite the increase of applied pressure.

### 3.2. Performance analysis

The gravimetric adsorption capacity of the samples was calculated from desorption analyses. Figure 6 plots adsorption capacity at different applied pressures as well as the relationship between adsorption capacity and BET specific surface area for each material. Basolite C300 shows a dramatic total decrease of its adsorption capacity with applied pressure, following a progressive trend as in the case of crystallinity and BET surface area. After the first pressure applied, some microporosity is still available, observing decreases of the adsorption capacity of 10.8% for nitrogen and 6.25% for methane. A further pressure increase will led to the total loss of adsorption capacity, BET surface and crystallinity. Additionally, the adsorption capacity/ BET surface area ratio is practically linear at low applied pressures, showing certain dependence of BET surface. At the highest pressure, it is observed a sharp increase, probably due to the increased role of active metal centres in the adsorption, once the crystalline structure was collapsed.

In case of Basolite F300, a decreasing trend of the capacity of adsorption with the applied pressure is observed, the downward trend being more pronounced at the highest pressure (loss of 41.3% for $N_2$ and 36.5% for $CH_4$), Figure 6B. Adsorption capacity follows a similar trend to BJH total mesopore volume (Table 1), which could be related to its originally semi-amorphous properties, in which the adsorption capacity is not drastically reduced until a certain pressure limit. The accessibility to metal adsorption sites is maintained due to the appearance of mesopores and, thus, the intracrystalline diffusivity increase. This increase in accessibility is closely related to the smooth downward trend in adsorption capacity, showing an almost linear relationship with the specific available surface.

For Basolite A100, a sharp decrease is observed after the first applied pressure, coincident with the asymptotic trend of BET surface area to the last applied pressures (Figure 6). This may be due to the presence of pure $CH_4$ and $N_2$, which provokes the transition to the lp phase at ambient conditions, thus increasing the adsorption capacity by increasing the accessibility to metallic adsorption centers [67]. In fact, from adsorption capacity/BET surface ratio, it is observed a constant behavior at the lowest pressures, and a sudden increase at the highest one, due to the drastic reduction of specific surface area after the transition to the lp phase which allows the metallic adsorption centers to have great relevance in the adsorption. Comparing with other techniques, Finsy et al. [68] have studied the effect of making pellets of MIL-53(Al) using polyvinyl alcohol as a binder. They indicated a reduction of 32% in micropore volume with a pore accessibility reduction of 19 % in the best of the cases, which hinders adsorption processes. In fact, it must be pointed out that the presence of a binder can affect the adsorption behavior of the material [69].

From Figure 6 it is observed that the relative adsorption capacity decreases are higher for $N_2$ than for $CH_4$, and it may be related to metal adsorption centers being available, and more selective towards $CH_4$ than $N_2$ [70]. Thus, after surface area and total pore volume reduction, the available active metallic centers play a more relevant role in the selective gas adsorption, especially in Basolite C300 and A100 cases. The influence of the applied pressure in the $CH_4/N_2$ selectivity is shown Figure 7. The increasing slope for Basolite C300 is markedly higher than for the other materials , due to the presence of a higher percentage (31.5, 21.2 and 12.9 % of copper, iron and aluminium for Basolite C300, F300 and A100, respectively). Therefore, the higher metal content in the structure, the greater the selectivity-increasing trend with applied pressure.

Breakthrough adsorption curves for $CH_4$ and $N_2$ in a fixed bed are shown in Figure 8. In general, for all the samples, breakthrough times (hence, adsorption capacity) are higher for $CH_4$ than for $N_2$, being attributed to the presence of metallic active adsorption sites and the difference in polarizability of both molecules [70].

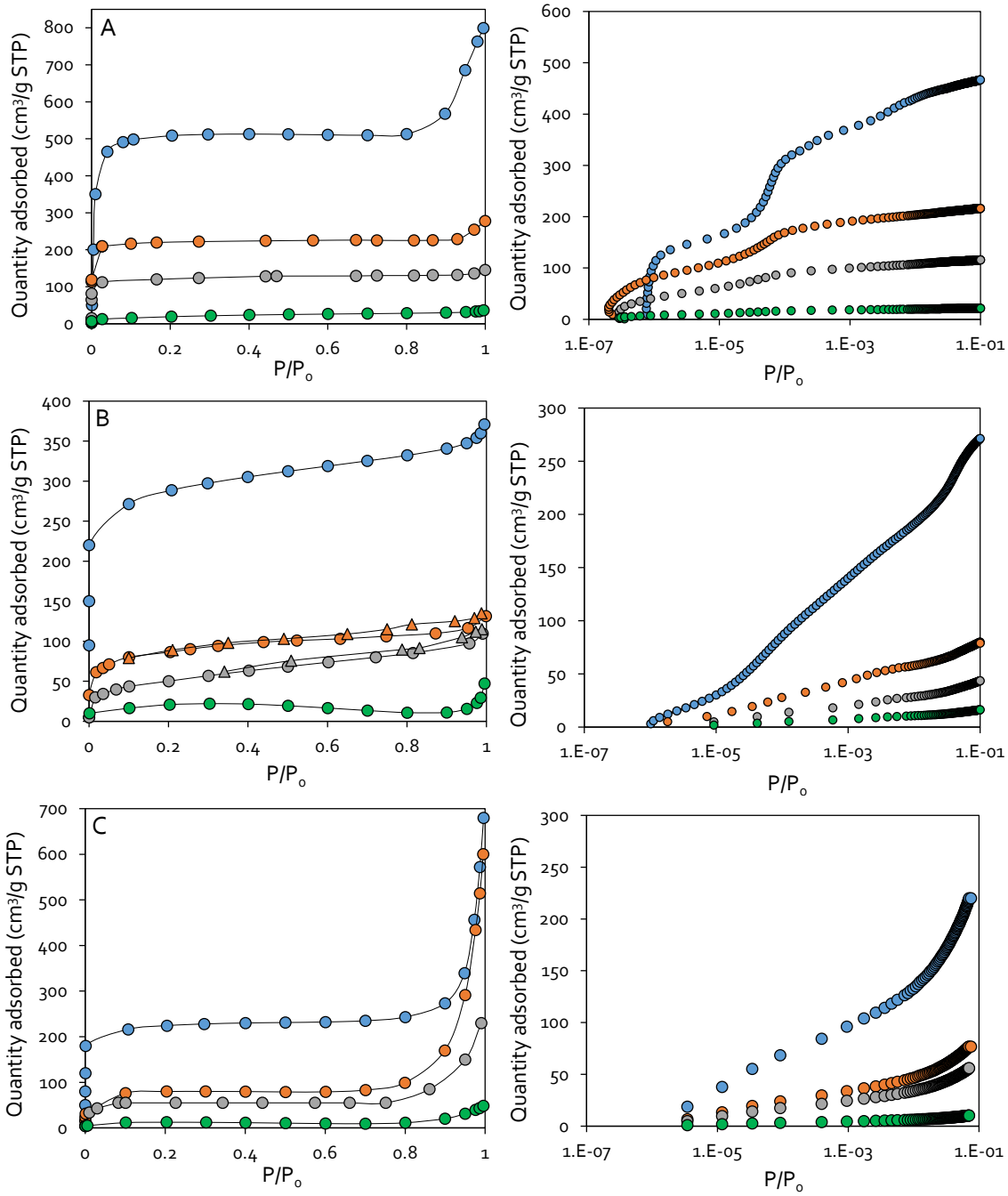


Figure 4. Adsorption (●) and desorption (▲) $N_2$ isotherms (77 K). Basolite C300 (A), Basolite F300 (B) and Basolite A100 (C). Original sample (blue), 55.9 MPa (orange), 111.8 MPa (grey) and 186.3 MPa (green). The graphs on the right are zoom of the low pressure zone (up to $P/P_0 = 0.1$) on logarithmic scale.

In case of Basolite C300, there is a slight difference in the slope between the original material and the others, most obvious in $N_2$ case. As $N_2$ molecular size is lower than $CH_4$ (3.65 and 3.82 Å, respectively), this molecule may penetrate in narrower pores than $CH_4$. Likewise, a decrease in the Knudsen diffusion coefficient led to more inclined curves [71, 72]. The Knudsen diffusion coefficient ($D_K$) depends on the pore diameter ($d_{pore}$) since the other parameters are constant for all the experiments. Variations in Knudsen diffusion coefficient affects directly the breakthrough curve, since it influences adsorbate mass transfer kinetics within the microporous adsorbent.

The reduction in total available specific surface, especially in micropores zone (low $P/P_0$), indicates that these narrower pores have been totally collapsed by compression (Figure 4). This collapse is common in MOFs when pressure is applied, due to their extraordinary initial porosity [73]. This provokes the following applied pressures to present less-inclined breakthrough curve

slopes, but also having less adsorptive capacity, as evidenced by the x-axis order of their breakthrough times (Figure 8). Breakthrough times follow, approximately, the same trend than BET surface area.

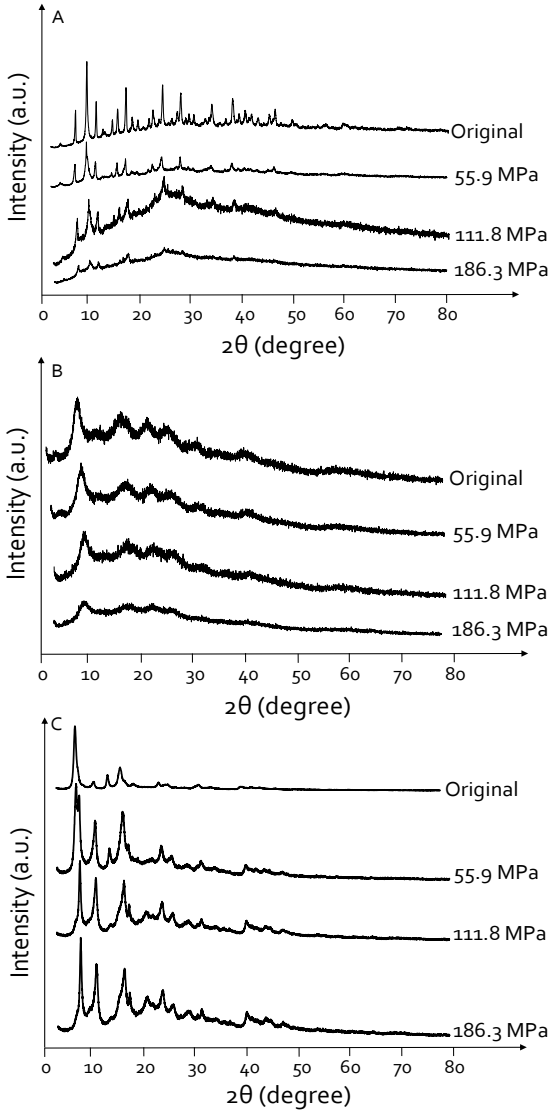


Figure 5. PXRD patterns of the three materials at different applied pressures (A: Basolite C300, B: Basolite F300 and C: Basolite A100). Applied pressures are ordered from top to bottom in increasing order (0, 55.9, 111.8 and 186.3 MPa).

In the case of Basolite F300, all the samples, except the original one, show the same slope for breakthrough curves, but in this case the difference is lower than in C300 case. The original sample presents a more inclined breakthrough curve for both adsorbates, which indicates a lower Knudsen diffusion coefficient.

Applied pressure modified the pore structure, plugging the micropores, but without reducing greatly the total pore volume by the appearance of mesopores that facilitate the penetration, so the differences in accessibility are softer (Figure 4). The high resemblance between the 55.9 and 111.8 MPa curves (Figure 8) is remarkable and can be related with the no-clear total mesopore volume dependence on pressure (Table 1). The appearance of mesopores in the structure enhance the intracrystalline diffusivity [74], which may be the dominant factor in this case, since the crystallinity is not great affected by mechanical pressure. Dhakshinamoorthy et al. [75] have studied the high relevance of the intracrystalline diffusivity in this material, applied to the case of a oxidation reaction.

Finally, in case of Basolite A100, despite the change from orthorhombic to monoclinic structure and the total cell volume reduction, the presence of pure $CH_4$ and $N_2$ causes the return to the lp phase at ambient conditions, for which the penetration is easier, obtaining a steep curve for all cases due to the structure flexibility [76]. As it is also observed, the breakthrough curves of the original material present more resistance than the others, especially for $N_2$. Despite the return to lp phase, the agglomeration provoked a certain irreversible reduction of micropore volume, which increases the Knudsen diffusion coefficient since the average available pore size is higher (Table 1). It is remarkable that differences in $CH_4$ breakthrough times follow almost the same trend than crystallinity, whereas in $N_2$ case, the trend is similar to specific surface or total pore volume.

## 4. Conclusions

Structural and morphological transformations of three MOFs (Basolite C300, Basolite F300 and Basolite A100), as well as $CH_4$ and $N_2$ uptakes variation, were studied after application of mechanical pressure to the materials. Basolite C300, a rigid crystalline material, experimented a dramatic and progressive loss of crystallinity, as well as surface area and pore volume, which implies lower adsorption capacity due to its characteristic pores collapse. In the case of Basolite F300, a semiamorphous material, it experimented also a high decrease of surface area and micropore collapse due to agglomeration, but keeping total pore volume due to the appearance of mesopores in the structure. This transformation implies an increase of intracrystalline diffusivity and, then, lower adsorption capacity losses. For Basolite A100, a flexible crystalline MOF, it is observed a transformation from orthorhombic disposition to monoclinic structure from 55.9 MPa onwards, in addition to high permanent losses of microporosity due to agglomeration. This structure change is reversible, returning to the lp

phase in presence of $CH_4$ and $N_2$ at ambient conditions. This fact increases the accessibility to metallic active centers and an asymptotic decrease of the adsorption capacity is observed.

Additionally, the key role of metal active sites in the $CH_4/N_2$ selectivity was pointed out. In fact, it was observed an increased selectivity for the three MOFs with the applied pressure, decreasing this positive effect in the order: Basolite C300 (Cu, 31.5%) > Basolite F300 (Fe, 21.2%) > Basolite A100 (Al, 12.9%). However, the total gravimetric adsorption capacity has experimented high losses for all of them. Despite that, Basolite C300 stands out above the other two. It has greater adsorption capacity and also a higher metallic content in its structure. In addition, it is able to retain 94% of its adsorption capacity when applying a pressure of 55.9 MPa, enough to increase its particle size and be able to operate in real adsorption stages.

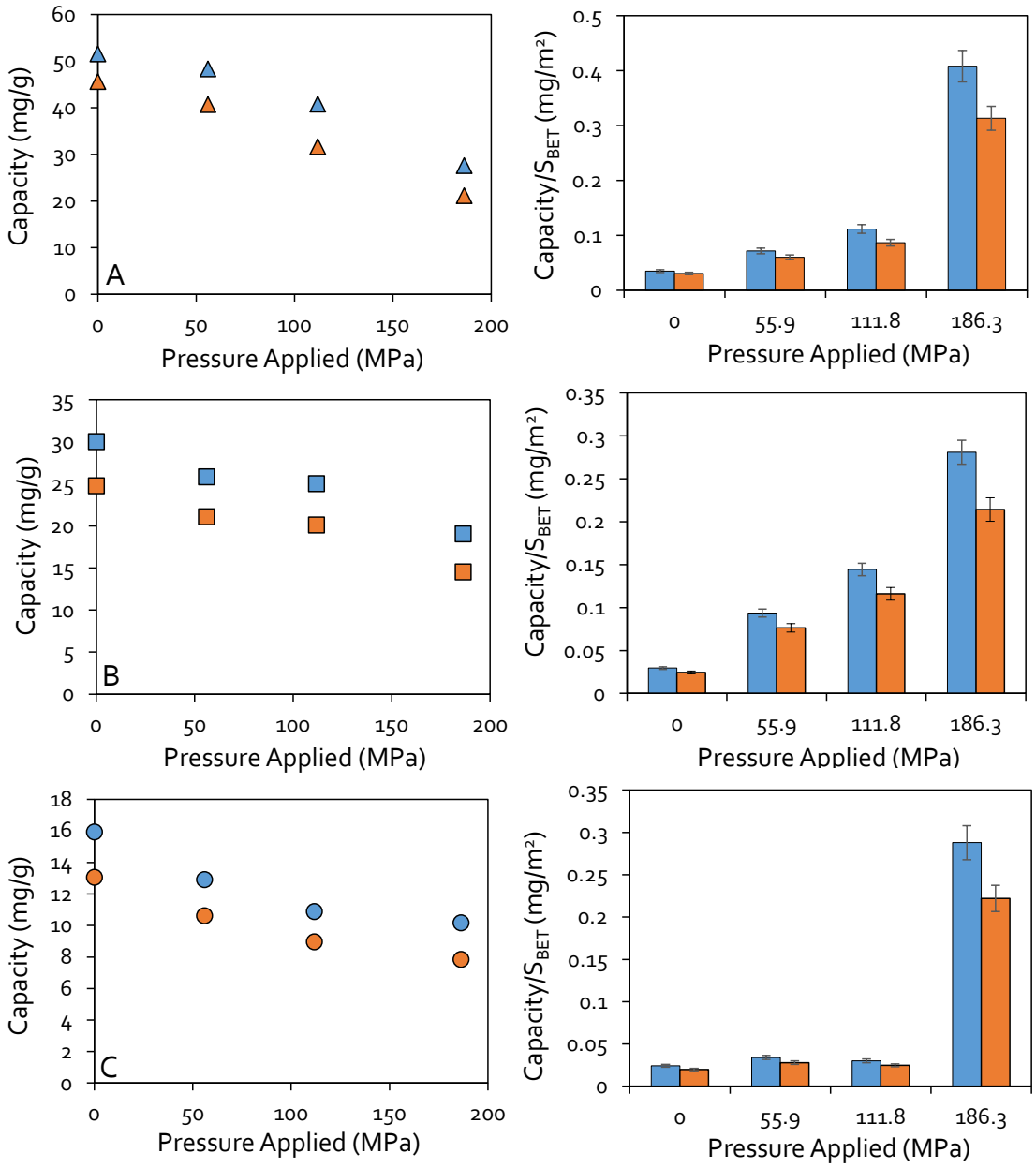


Figure 6. Adsorption capacity for pure methane (blue) and nitrogen (orange) for different applied pressures at 298 K and 0.1 MPa of total pressure (figures on the left), and its relation with BET specific surface area (figures on the right). Basolite C300 (A, ▲), Basolite F300 (B, ■) and Basolite A100 (C, ●).

Table 3. Cell total volume and lattice parameters for each structure depending on applied pressure.

| Material | Pressure (MPa) | a (Å) | b (Å) | c (Å) | α (º) | β (º) | γ (º) | Volume (Å$^3$) |
|---|---|---|---|---|---|---|---|---|
| C300 | 0 | 25.9 | 25.9 | 25.9 | 90 | 90 | 90 | 17452 |
| | 55.9 | 26.2 | 26.2 | 26.2 | 90 | 90 | 90 | 17992 |
| | 111.8 | 26.2 | 26.2 | 26.2 | 90 | 90 | 90 | 17992 |
| | 186.3 | 26.1 | 26.1 | 26.1 | 90 | 90 | 90 | 17901 |
| A100 | 0 | 16.1 | 6.56 | 13.2 | 90 | 90 | 90 | 1397 |
| | 55.9 | 6.56 | 14.3 | 14.8 | 90 | 105 | 90 | 1351 |
| | 111.8 | 6.43 | 12.9 | 16.2 | 90 | 108 | 90 | 1280 |
| | 186.3 | 5.83 | 13.7 | 16.1 | 90 | 110 | 90 | 1205 |

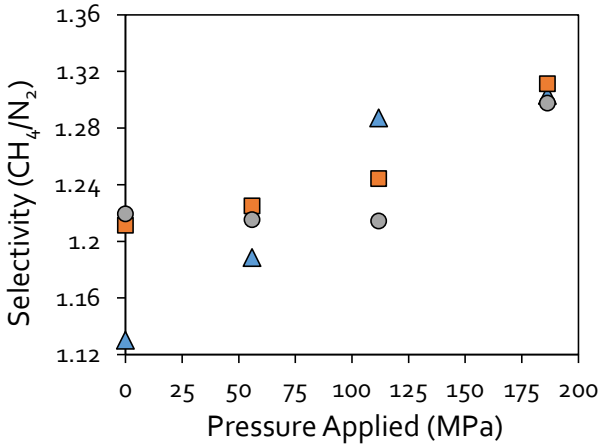


Figure 7. Adsorption $CH_4/N_2$ selectivity (mass basis) for each material at different applied pressures, at 298 K and 0.1 MPa of total pressure. Basolite C300 (▲), Basolite F300 (■) and Basolite A100 (●).

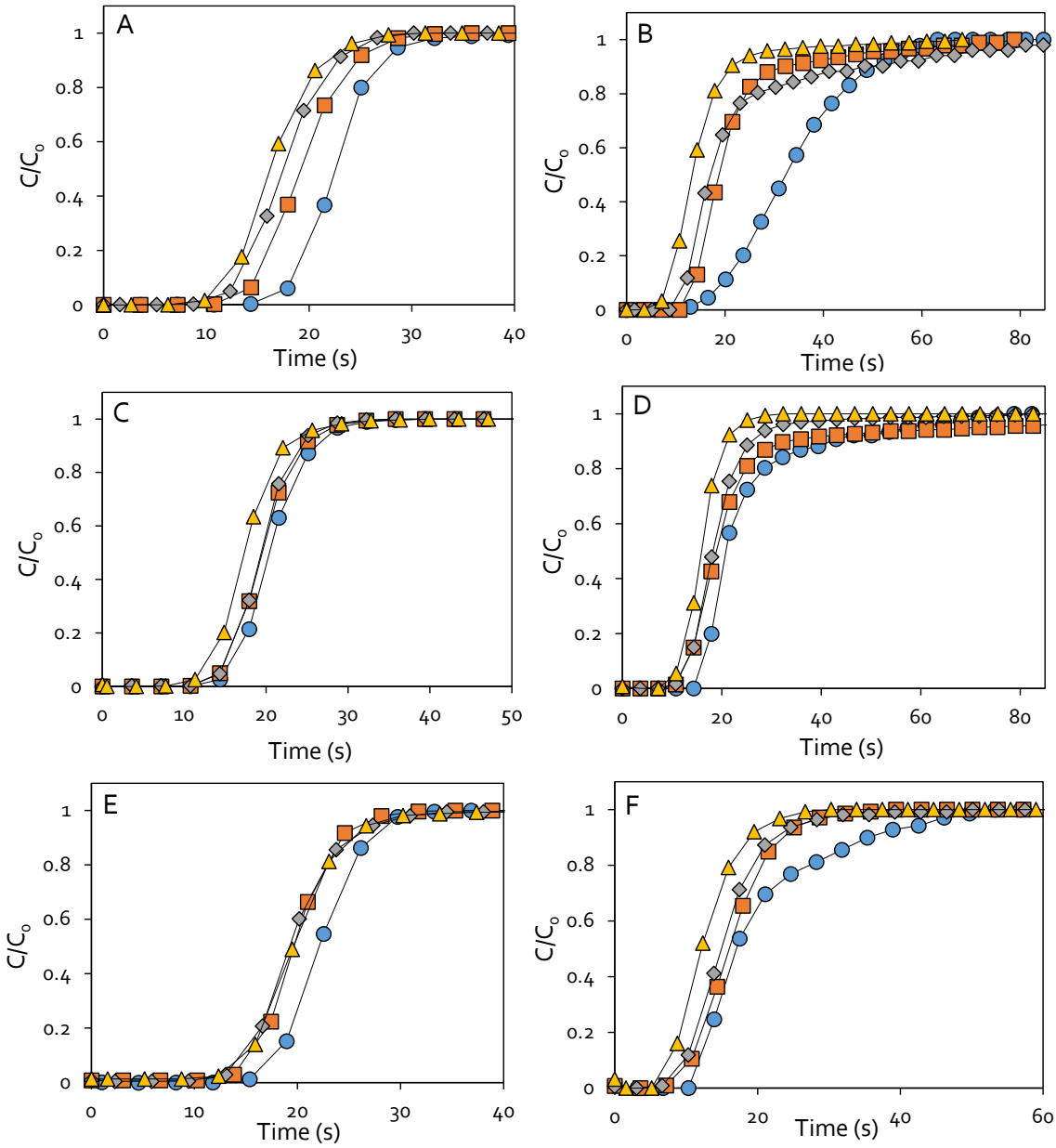


Figure 8. Adsorption breakthrough curves for $CH_4$ and $N_2$ onto the three MOFs at different applied pressures (Original: blue circles, 55.9 MPa: orange squares, 111.8 MPa: grey rhombus, 186.3 MPa: yellow triangles). Basolite C300 (A: methane, B: nitrogen), Basolite F300 (C: methane, D: nitrogen) and Basolite A100 (E: methane, F: nitrogen). Black lines are used to guide the view.

**Author Contributions**: Conceptualization, **S.O.**; methodology, **E.D.**; formal analysis, **D.U.**; investigation, **D.U.**; data curation, **E.D.**; writing—original draft preparation, **D.U.**; writing—review and editing, **E.D.** and **S.O.**; supervision, **S.O.**; All authors have read and agreed to the published version of the manuscript.

**Funding**: This research was funded by the Research Fund for Coal and Steel of the European Union, contract 754077 METHENERGY PLUS.

**Acknowledgements**: D. Ursueguía acknowledges the Spanish Government for the FPU fellowship (FPU18/01448). The authors would like to acknowledge the technical support provided by *Servicios Científico-Técnicos* de la Universidad de Oviedo.

**Conflicts of Interest**: The authors declare that they have no known competing financial interests or personal relationships that could have appeared to influence the work reported in this paper.

## References

[1] Newell, R; Raimi, D; Aldana, G. Global energy outlook 2019: The next generation of energy. Resources for the Future 2019, Report 8-19.

[2] Coronavirus has reminded us how much we depend on electricity. Available online: www.weforum.org/agenda/2020/03/coronavirus-crisis-future-of-energy (accessed on 29 March 2020).

[3] Ferreira, A; Ribeiro, A; Kulaç, S; Rodrigues, A. Methane purification by adsorptive processes on MIL-53(Al). Chem. Eng. Sci. 2015, 124, 79-95.

[4] Cavenati, S; Grande, C; Rodrigues, A. Separation of $CH_4/CO_2/N_2$ mixtures by layered pressure swing adsorption for upgrade of natural gas. Chem. Eng. Sci. 2006, 61, 3893-3906.

[5] Moreira, M; Ribeiro, A; Ferreira, A; Rodrigues, A. Cryogenic pressure temperature swing adsorption process for natural gas upgrade. Sep. Pur. Tech. 2017, 173, 339-356.

[6] Campo, M; Ribeiro, A; Ferreira, A; Santos, J; Lutz, C; Loureiro, J; Rodrigues, A. Carbon dioxide removal for methane upgrade by a VSA process using an improved 13X zeolite. Fuel Process. Tech. 2016, 143, 185-194.

[7] Alonso-Vicario, A; Ochoa-Gómez, J; Gil-Río, S; Gómez-Jiménez, O; Ramírez-López, C; Torrecilla-Soria, J; Domínguez, A. Purification and upgrading of biogas by pressure swing adsorption on synthetic and natural zeolites. Micropor. Mesopor. Mat. 2010, 134, 100-107.

[8] Li, P; Tezel, H. Adsorption separation of $N_2$, $O_2$, $CO_2$ and $CH_4$ gases by β-zeolite. Micropor. Mesopor. Mat. 2007, 98, 94-101.

[9] Yi, H; Li, F; Ning, P; Tang, X; Peng, J; Li, Y; Deng, H. Adsorption separation of $CO_2$, $CH_4$ and $N_2$ on microwave activated carbon. Chem. Eng. J. 2013, 215, 635-642.

[10] Singh, A; Kumar, J. Fugitive methane emissions from Indian coal mining and handling activities: Estimates, mitigation and opportunities for its utilization to generate clean energy. Energy Procedia 2016, 90, 336-348.

[11] Cluff, D; Kennedy, G; Bennett, J; Foster, P. Capturing energy from ventilation air methane a preliminary design for a new approach. Appl. Therm. Eng. 2015, 90, 1151-1163.

[12] Karakurt, I; Aydin, G; Aydiner, K. Mine ventilation air methane as a sustainable energy source. Renew. Sust. Energ. Rev. 2011, 15, 1042-1049.

[13] Li, Q; Ruan, M; Zheng, Y; Mei, X; Lin, B. Investigation on the selective adsorption and separation properties of coal mine methane in ZIF-68 by molecular simulations. Adsorption 2017, 23, 163-174.

[14] Norouzi, A. Modeling of adsorption in a packed bed tower, the case study of methane removal and parametric calculation. J. Environ. Treat. Tech. 2019, 7, 324-333.

[15] Grünker, R.; Bon, V; Müller, P; Stoeck, U; Krause, S; Mueller, U; Senkovska, I; Kaskel, S. A new metal-organic framework with ultra-high surface area. ChemmComm 2014, 50, 3450-3452.

[16] Senkovska, I; Kaskel, S. High pressure methane adsorption in the metal-organic frameworks $Cu_3(btc)_2$, $Zn_2(bdc)_2dabco$, and $Cr_3F(H_2O)_2O(bdc)_3$. Micropor. Mesopor. Mat. 2008, 112, 108-115.

[17] Rowsell, J; Yaghi, O. Metal-organic frameworks: a new class of porous materials. Micropor. Mesopor. Mat.2004, 73, 3-14.

[18] Liang, Z; Marshall, M; Chaffee, A. $CO_2$ adsorption-based separation by metal organic framework (Cu-BTC) versus zeolite (13X). Energy Fuels 2009, 23, 2785-2789.

[19] Blanco-Brieva, G; Campos-Martin, J.M; Al-Zahrani, S.M; Fierro, J.L.G. Effectiveness of metal-organic frameworks for removal of refractory organo-sulfur compound present in liquid fuels. Fuel 2011, 90, 190-197.

[20] Jiao, L; Seow, J; Skinner, W; Wang, Z; Jiang, H. Metal-organic frameworks: Structures and functional applications. Mat. Today 2019, 27, 43-68.

[21] Arami-Niya, A; Birkett, G; Zhu, Z; Rufford, T. Gate opening effect of zeolitic imidazolate framework ZIF-7 for adsorption of $CH_4$ and $CO_2$ from $N_2$. J. Mater. Chem. A 2017, 5, 21389-21399.

[22] Eyer, S; Stadie, N; Borgschulte, A; Emmenegger, L; Mohn, J. Methane preconcentration by adsorption: A methodology for materials and conditions selection. Adsorption 2014, 20, 657-666.

[23] Bastin, L; Bárcia, P; Hurtado, E; Silva, J; Rodrigues, A; Chen, B. A microporous metal-organic framework for separation of $CO_2/N_2$ and $CO_2/CH_4$ by fixed-bed adsorption. J. Phys. Chem. C 2008, 112, 1575-1581.

[24] Bloch, E; Queen, W; Krishna, R; Zadrozny, J; Brown, C; Long, J. Hydrocarbon separations in a metal-organic framework with open iron(II) coordination sites. Science 2012, 335, 1606-1610.

[25] Evans, J; Garai, B; Reinsch, H; Li, W; Dissegna, S; Bon, V; Senkovska, I; Fischer, R; Kaskel, S; Janiak, C; Stock, N; Volkmer, D. Metal-organic frameworks in Germany: From synthesis to function. Coordin. Chem. Rev. 2019, 380, 378-418.

[26] Koekemoer, A; Luckos, A. Effect of material type and particle size distribution on pressure drop in packed beds of large particles: Extending the Ergun equation. Fuel 2015, 158, 232-238.

[27] Malkoc, E; Nuhoglu, Y; Abali, Y. Cr(VI) adsorption by waste acorn of Quercus Ithaburensis in fixed beds: Prediction of breakthrough curves. Chem. Eng. J. 2006, 119, 61-68.

[28] Edubilli, S; Gumma, S. A systematic evaluation of UiO-66 metal organic framework for $CO_2/N_2$ separation. Sep. Pur. Tech. 2019, 224, 85-94.

[29] Hou, P; Orikasa, H; Itoi, H; Nishihara, H; Kyotani, T. Densification of ordered microporous carbons and controlling their micropore size by hot-pressing. Carbon 2007, 45, 2011-2016.

[30] Tian, T; Zeng, Z; Vulpe, D; Casco, M; Divitini, G; Midgley, P; Silvestre-Albero, J; Tan, J; Moghadam, P; Fairen-Jimenez, D. A sol-gel monolithic metal-organic framework with enhanced methane uptake. Nat. Mater. 2018, 17, 174-179.

[31] Hu, Z; Wang, Y; Shah, B; Zhao, D. $CO_2$ capture in metal-organic framework adsorbents: An engineering perspective. Adv. Sustain. Syst. 2018, 3, 1800080.

[32] Beurroies, I; Boulhout, M; Llewellyn, P; Kuchta, B; Férey, G; Serre, C; Denoyel, R. Using pressure to

provoke the structural transition of metal-organic frameworks. Angew. Chem. Int. Edit. 2010, 49, 7526-7529.

[33] Manos, G; Dunne, L. Predicting the features of methane adsorption in large pore metal-organic frameworks for energy storage. Nanomaterials 2018, 8, 818-835.

[34] Purewall, J.J; Liu, D; Yang, J; Sudik, A; Siegel, D.J; Maurer, S; Müller, U. Increased volumetric hydrogen uptake of MOF-5 by powder densification. Int. J. Hydrogen Energ. 2012, 37, 2723-2727.

[35] Nandasiri, M; Jambovane, S; McGrail, B; Schaef, H; Nune, S. Adsorption, separation, and catalytic properties of densified metal-organic frameworks. Coordin. Chem. Rev. 2016, 311, 38-52.

[36] Anderlean, O; Blanita, G; Borodi, G; Lazar, M; Misan, I; Coldea, I; Lupu, D. Volumetric hydrogen adsorption capacity of densified MIL-101 monoliths. Int. J. Hydrogen Energ. 2013, 38, 7046-7055.

[37] Majchrzak-Kuçeba, I; Sciubidlo, A. Shaping metal-organic framework (MOF) powder materials for $CO_2$ capture applications – a thermogravimetric study. J Therm. Anal. Calorim. 2019, 138, 4139-4144.

[38] Yuan, S; Sun, X; Pang, J; Sun, D; Liu, D; Zhou, H. PCN-250 under pressure: Sequential phase transformation and the implications for MOF densification. Joule 2017, 1, 806-815.

[39] Thommes, M; Kaneko, K; Neimark, A; Olivier, J; Rodríguez-Reinoso, F; Rouquerol, J; Sing, K. Physisorption of gases, with special reference to the evaluation of surface and pore size distribution (IUPAC technical report). Pure Appl. Chem. 2015, 87, 1051-1069.

[40] Sing, K; Everett, D; Haul, R; Moscou, L; Pierotti, R; Rouquérol, J; Siemieniewska, T. Reporting physisorption data for gas/solid systems with special reference to the determination of surface area and porosity. Pure Appl. Chem. 1985, 57, 603-619.

[41] Muttakin, M; Mitra, S; Thu, K; Ito, K; Saha, B. Theoretical framework to evaluate minimum desorption temperature for IUPAC classified adsorption isotherms. Int. J. Heat Mass. Trans. 2018, 122, 795-805.

[42] Casco, M; Fernández-Catalá, J; Martínez-Escandell, M; Rodríguez-Reinoso, F; Ramos-Férnandez, E; Silvestre-Albero, J. Improved mechanical stability of HKUST-1 in confined nanospace. Chem. Comm. 2015, 51, 14191-14194.

[43] Ribeiro, R; Antunes, C; Garate, A; Portela, A; Plaza, M; Mota, J; Esteves, A. Binderless shaped metal-organic framework particles: Impact on carbon dioxide adsorption. Micropor. Mesopor. Mat. 2019, 275, 111-121.

[44] Wang, J; Liu B; Nakata, K. Effects of crystallinity, {001}/{101} ratio, and Au decoration on the photocatalytic activity of anatase $TiO_2$ crystals. Chinese J. Catal. 2019, 40, 403-412.

[45] Nobar, S. Cu-BTC synthesis, characterization and preparation for adsorption studies. Mater. Chem. Phys. 2018, 213, 343-351.

[46] Schlichte, K; Kratzke, T; Kaskel, S. Improved synthesis, thermal stability and catalytic properties of the metal-organic framework compound $Cu_3(BTC)_2$. Micropor. Mesopor. Mat. 2004, 73, 81-88.

[47] Prestipino, C; Regli, L; Vitillo, J.G; Bonino, F; Damin, A; Lamberti, C; Zecchina, A; Solari, P; Kongshaug, K; Bordiga, S. Local structure of framework Cu(II) in HKUST-1 metallorganic framework: Spectroscopic characterization upon activation and interaction with adsorbates. Chem. Mater. 2006, 18, 1337-1346.

[48] Yang, A; Li, P; Zhong, J. Facile preparation of low-cost HKUST-1 with lattice vacancies and high-efficiency adsorption for uranium. RCS Adv. 2019, 9, 10320-10325.

[49] Yang, K; Zhou, G; Xu, Q. The elasticity of MOFs under mechanical pressure. RCS Adv. 2016, 44, 37506-37514.

[50] McKellar, S; Moggach, S; Structural studies of metal-organic frameworks under high pressure. Acta Cryst. 2015, B71, 587-607.

[51] Terracina, A; Todaro, M; Mazaj, M; Agnello, S; Gelardi, F; Buscarino, G. Unveiled the source of the structural instability of HKUST-1 powders upon mechanical compaction: Definition of a fully preserving tableting method. J. Phys. Chem. C 2018, 123, 1730-1741.

[52] Wu, H; Yildirim, T; Zhou, W. Exceptional mechanical stability of highly porous zirconium metal-organic framework UiO-66 and its important implications. J. Phys. Chem. Lett. 2013, 4, 925-930.

[53] Peng, Y; Krungleviciute, V; Eryazici, I; Hupp, J; Farha, O; Yildirim, T. Methane storage in metal-organic frameworks: Current records, surprise findings, and challenges. J. Am. Chem. Soc. 2013, 135, 11887-11894.

[54] Sánchez-Sánchez, M; Asua, I; Ruano, D; Díaz, K. Direct synthesis, structural features, and enhanced catalytic activity of the Basolite F300-like semiamorphous Fe-BTC framework. Cryst. Growth Des. 2015, 15, 4498-4506.

[55] Dhakshinamoorthy, A; Alvaro, M; Horcajada, P; Gibson, E; Vishnuvarthan, M; Vimont, A; Greneche, J; Serre, C; Daturi, M; Garcia, H. Comparison of porous iron trimesates Basolite F300 and MIL-100(Fe) as heterogeneous catalysts for Lewis acid and oxidation reactions: Roles of structural defects and stability. ACS Catal. 2012, 2, 2060-2065.

[56] Seo, Y; Yoon, J; Lee, J; Lee, U; Hwang, Y; Jun, C; Horcajada, P; Serre, C; Chang, J. Large scale fluorine-free synthesis of hierarchically porous iron(III) trimesate MIL-100(Fe) with a zeolite MTN topology. Micropor. Mesopor. Mat. 2012, 157, 137-145.

[57] Bennet, T; Cheetham, A. Amorphous Metal-Organic Frameworks. Acc Chem. Res. 2014, 47, 1555-1562.

[58] Chowdhury, T; Zhang, L; Zhang, J; Aggarwal, S. Removal of arsenic(III) from aqueous solution using metal organic framework-graphene oxide nanocomposite. Nanomaterials 2018, 8, 1062-1079.

[59] Mishra, P; Uppara, H; Mandal, B; Gumma, S. Adsorption and separation of carbon dioxide using MIL-53(Al) metal-organic framework. Ind. Eng. Chem. Res. 2014, 53, 19747-19753.

[60] Llewellyn, P; Horcajada, P; Maurin, G; Devic, T; Rosenbach, N; Bourrelly, S; Serre, C; Vincent, D; Loera-Serna, S; Filinchuk, Y; Férey, G. Complex adsorption of short linear alkanes in the flexible metal-organic-framework MIL-53(Fe). J. Am. Chem. Soc. 2009, 131, 13002-13008.

[61] Alaerts, L; Kirschhock, C; Maes, M; Veen, M; Finsy, V; Depla, A; Martens, J; Baron, G; Jacobs, P; Denayer, J; Vos, D. Selective adsorption and separation of xylene isomers and ethylbenzene with the microporous vanadium(IV) terephthalate MIL-47. Angew. Chem. 2007, 119, 4371-4375.

[62] Neimark, A; Coudert, F; Triguero, C; Boutin, A; Fuchs, A; Beurroies, I; Denoye, R. Structural transitions in MIL-53(Cr): View from outside and inside. Langmuir 2011, 27, 4734-4741.

[63] Serra-Crespo, P; Dikhtiarenko, A; Stavitski, E; Juan-Alcañiz, J; Kapteijn, F; Coudert, F; Gascon, J. Experimental evidence of negative linear compressibility in the MIL-53 metal-organic framework family. CrystEngComm 2015, 17, 276-280.

[64] Ghoufi, A; Subercaze, A; Ma, Q; Yot, P; Ke, Y; Puente-Orench, I; Devic, T; Guillerm, V; Zhong, C; Serre, C; Férey, G; Maurin, G. Comparative guest, thermal, and mechanical breathing of the porous metal organic framework MIL-53(Cr): A computational exploration supported by experiments. J. Phys. Chem. C 2012, 116, 13289-13295.

[65] Reinsch, H; Pillai, R; Siegel, R; Senker, J; Lieb, A; Maurin, G; Stock, N. Structure and properties of Al-MIL-53-ADP, a breathing MOF based on the aliphatic linker molecule adipic acid. Dalton Trans. 2016, 45, 4179-4186.

[66] Ghysels, A; Vanduyfhys, L; Vandichel, M; Waroquier, M; Speybroeck, V; Smit, B. On the thermodynamics of framework breathing: a free energy model for gas adsorption in MIL-53. J. Phys. Chem. C 2013, 117, 11540-11554.

[67] Boutin, A; Couck, S; Coudert, F; Serra-Crespo, P; Gascon, J; Kapteijn, F; Fuchs, A; Denayer, J. Thermodynamic analysis of the breathing of amino-functionalized MIL-53(Al) upon $CO_2$ adsorption. Micropor. Mesopor. Mat. 2011, 140, 108-113.

[68] Finsy, V; Ma, L; Alaerts, L; Vos, D; Baron, G; Denayer, J. Separation of $CO_2/CH_4$ mixtures with the MIL-53(Al) metal-organic framework. Micropor. Mesopor. Mat. 2009, 120, 221-227.

[69] Valekar, A; Cho, K; Lee, U; Yoon, J; Hwang, Y; Lee, S; Cho, S; Chang, J. Shaping of porous metal-organic framework granules using mesoporous p-alumina as a binder. RSC Adv. 2017, 7, 55767-55777.

[70] Ursueguía, D; Díaz, E; Ordóñez, S. Adsorption of methane and nitrogen on Basolite MOFs: Equilibrium and kinetic studies. Micropor. Mesopor. Mat. 2020, 298, 110048.

[71] Kosuge, K; Kubo, S; Kikukawa, N; Takemori, M. Effect of pore structure in mesoporous silicas on VOC dynamic adsorption/desorption performance. Langmuir 2007, 23, 3095-3102.

[72] Murillo, R; García, T; Aylón, E; Callén, M; Navarro, M; López, J; Mastral, A. Adsorption of phenanthrene on activated carbons: Breakthrough curve modeling. Carbon 2004, 42, 2009-2017.

[73] Howarth, A; Liu, Y; Li, P; Li, Z; Wang, T; Hupp, J; Farha, O. Chemical, thermal and mechanical stabilities of metal-organic frameworks. Nat. Rev. Mater. 2016, 1, 1-15.

[74] Mehlhorn, D; Valiullin, R; Kärger, J; Cho, K; Ryoo, R. Intracrystalline diffusion in mesoporous zeolites. ChemPhysChem 2012, 13, 1495-1499.

[75] Dhakshinamoorthy, A; Alvaro, M; Hwang, Y; Seo, Y; Corma, A; Garcia, H. Intracrystalline diffusion in metal organic framework during heterogeneous catalysis: Influence of particle size on the activity of MIL-100(Fe) for oxidation reactions. Dalton Trans. 2011, 40, 10719-10724.

[76] Lyubchyk, A; Esteves, I; Cruz, F; Mota, J. Experimental and theoretical studies of supercritical methane adsorption in the MIL-53(Al) metal organic framework. J. Phys. Chem. C 2011, 115, 20628-20638.

## Effect of water and carbon dioxide on the performance of Basolite MOFs for methane adsorption

David Ursueguía, Eva Díaz, Salvador Ordóñez*

Catalysis, Reactors and Control Research Group (CRC), Department of Chemical and Environmental Engineering, University of Oviedo, Julián Clavería s/n, 33006 Oviedo, Spain

*e-mail: sordonez@uniovi.es (S. Ordóñez)

Submitted to: Journal of Industrial and Engineering Chemistry

## ABSTRACT

MOFs are potential materials for methane adsorption, with the drawbacks of humidity and carbon dioxide. The behaviour of three MOFs, Basolite C300, F300 and A100, was studied under both demanding conditions. Basolite C300 is the most affected material. Its $Cu^{2+}$ open metal sites are very hydrophilic, decreasing the methane adsorption capacity (33.3%) and the $CH_4/N_2$ selectivity (21.6%) after 24 hours of operation at a relative humidity of 100%. In case of Basolite A100, the methane adsorption capacity decreases 26.1% due to certain hydrophobicity, related to $Al^{3+}$ open metal sites, which protects the structure. Surprisingly, Basolite F300 is the most resistant material, with a capacity loss of 9.25%. $Fe^{3+}$ open metal sites exhibit scarce influence on the adsorption, and the mesopores (29 Å) reduce the effect of water capillary condensation, avoiding remarkable structural damages. However, the moist-treatment largely reduces the pore volume (23.8%), mainly in micropores, but can also generate hydrates on the surface promoting methane adsorption. Carbon dioxide traces (0.33%) lead to an increase of methane retention by Basolite A100 (12.4%), although the combination of humidity and $CO_2$ decreases significantly (18.1%) its performance. The effect of the presence of $CO_2$ in case of Basolite C300 and F300 was negligible, as well as their synergic effect with the presence of moisture.

**Keywords**: Adsorption; fixed-bed; moisture; MOF; methane upgrading; carbon dioxide

### 1. Introduction

Methane mining fugitive emissions constitute an important greenhouse gas (GHG) source, but they can be also considered as potential resources for both energy and chemicals [1]. These fugitive streams are classified into coal bed methane (CBM), abandoned mine methane (AMM) and ventilation air methane (VAM) [2]. These streams are usually composed of methane, air, high relative humidity (100%) and traces of carbon dioxide (0.1%) [3]. Based on these features, the interest is mainly focused on obtaining energy directly through combustion in case of higher methane concentrations (CBM and AMM, > 30%), or even a direct emission to the atmosphere in case of low methane concentrations (VAM, < 5%). However, VAM methane could also be recovered and concentrated for subsequent chemical upgrading or a more efficient thermal harnessing. In previous works, swing adsorption techniques were established as the best available techniques for methane recovery from these diluted streams [4]. Concerning suitable adsorbent materials, metal-organic frameworks (MOFs) have emerged as an alternative to activated carbons and zeolites because of their improved performance, as they present high specific surface areas and total pore volumes. Their structure, based on metallic ions joined by organic ligands, is perfectly ordered and reproducible, with the existence of tuneable preferential adsorption sites. In certain MOFs, metallic ions form stronger adsorption zones than the rest of the structure, being called open metal sites (OMS), which can be very attractive for some gas molecules, such as methane, carbon dioxide or hydrogen [5]. In addition, MOFs morphology can be designed over a broad range to be adapted to the operation requirements. Besides the proved gas storage ability of these materials [6], MOFs were also widely studied in the separation of nitrogen from natural gas [7] and other gas separations. Previous works have also demonstrated the ability of some MOFs to separate methane from low-grade streams [8].

Despite the outstanding qualities of MOFs as adsorbents, the coexistence in the adsorbate streams of other spectator species, such as moisture, can damage the adsorbent by either decreasing its adsorption capacity or by inducing serious structural modifications [9]. This fact hinders the use of these materials for actual applications. Canivet et al. [10] have made a compilation of different water-sensitive MOFs, whereas Safy et al. [11] have even developed a model to predict the harmful effect of moisture on different MOFs, observing a dramatic noxious effect for most of the MOFs. Although some works aimed that the strength of the metal-ligand bond is one of the most important parameters for determining the resistance to the presence of water [10], other works observed relationships between some structural features (OMS, pore size, etc.) and the negative effect of water [10-13]. Despite the fact that the effect of moisture on the $CO_2$ adsorption is widely studied in the literature [14-16], studies about the effect of humidity on methane adsorption are very scarce, specially from diluted streams [17]. It should be noted that adsorption mechanisms can be very different from $CO_2$ and $CH_4$, leading also to a different effect of the humidity on this adsorption.

Hence, this work aims to study the behaviour of three commercial MOFs, Basolite C300, Basolite F300 and Basolite A100, at the real conditions of fugitive methane streams, such as humidity and presence of carbon dioxide. These conditions have been tested in a low-grade methane adsorption process in a fixed bed. These MOFs have been selected after previous studies that pointed out their good performance in adsorption and separation methane processes [18], in addition to the clear advantage of being commercial materials, enabling their availability at industrial scale. Results will allow to understand the behaviour of these MOFs under demanding conditions in a scenario similar to a full-scale operation. Additionally, adsorbents characterization (PXRD, SEM, DRIFT, etc.) allow getting deeper insights about the chemistry of these effects. These results provide information about the required features of the materials to be used in these recovery processes, and the potential of the already available materials for this application.

## 2. Experimental section

### 2.1. Materials

Three commercial materials supplied by BASF (Basolite C300, Basolite F300 and Basolite A100) were tested (96%, mass basis purity) in its original powder form, without any previous chemical or physical modification, and previous contacts with ambient air and moisture were avoided. Gases (methane, air, nitrogen, oxygen, helium and carbon dioxide) were supplied by Air Liquide (> 99.995% mol). Water fed in the experiments was previously distilled.

### 2.2. Adsorption apparatus and experimental procedure

Fixed-bed adsorption studies were carried out in a stainless steel tube, 45 and 0.65 cm in length and internal diameter, respectively, filled with 0.15 g of each material (selected in order to avoid excessive pressure drops and gradients in the adsorbent bed). The temperature of the fixed bed was controlled by an electric tubular furnace (Nabertherm, Germany). In adsorption stages, the gas flows of air (47.5 ml/min) and methane (2.5 ml/min) were introduced by mass flow controllers (MFC) previously calibrated (Bronkhorst, Netherlands), and the operation temperature was 298 K. In desorption stage, once the adsorbent is completely saturated, 47.5 ml/min of air were introduced in the fixed bed and the temperature was increased up to 423 K. In all cases, the outlet of the fixed bed was analysed by a mass spectrometer (Pfeiffer, Germany) previously calibrated. A detailed scheme of the fixed-bed device is attached in Figure S1.

In the case of the experiments performed in presence of humidity, water was introduced in liquid form, prior to the fixed bed, by a liquid syringe (Hamilton, USA) of 5 ml powered by a Legato 100 syringe pump (kdScientific, USA), being immediately vaporized due to the action of several isolated heaters along the conductions, at 383 K. Water flowrates were selected according to the relative humidity (RH) desired in the inlet stream: 0.1 ml/h for 75% RH and 0.14 ml/h for 100% RH, that is at 44250 and 59000 ppm, respectively. In addition, the ageing of the materials under a wet gas flow (100% RH) was carried out in the same fixed-bed device for 24 h, prior to subsequent characterization. Fixed-bed adsorption experiments were carried out for three consecutive cycles.

In addition, pure methane, nitrogen and carbon dioxide adsorption was evaluated by a thermal gravimetric analyser (Setaram Sensys, France). Samples (15-30 mg) were pretreated in situ at 423 K and 0.1 MPa in pure nitrogen flowing at 60 ml/min for 2 h before measurement of the mass changes under a flow of 60 ml/min of the desired gas, at 298 K. All weight changes respect to the adsorption data were corrected using a

blank calibration. Purge gas was nitrogen flowing continuously at 40 ml/min.

2.3. Materials characterization

The morphology of the adsorbents, specific surface area and pore volume, was estimated by nitrogen physisorption at 77 K in an ASAP 2020 surface area and porosity analyser (Micromeritics, USA). Physisorption data were processed using the Brunauer-Emmett-Teller (BET) model for determining the specific surface area of the materials. It was calculated in a range of $P/P_0$ between 0.05 and 0.3, with correlation coefficients ($R^2$) higher than 0.996 in all cases. Mesoporous volume were estimated by Barrett-Joyner-Halenda (BJH) method, which is one of the most widely used for these materials [19]. Finally, microporous volume was calculated using Dubinin-Radushkevich method, preferentially used for microporous solids like MOFs [20, 21]. Infrared spectra were acquired by DRIFT spectroscopy with a Thermo Nicolet FT-IR (Nexus, England) equipped with a MCT/A detector. The sample of adsorbent (around 20 mg) was placed inside the temperature-controlled chamber. The material was pretreated with a mixture of methane (5%) and air (95%) with different RH (75 and 100%) at 298 K, subsequent cleaning of the surface (423 K, helium) and, afterwards, a reflectance measurement of the passage of a dry-methane flowing mixture. All the streams were 40 ml/min in total. Spectra were recorded in the 650-4000 $cm^{-1}$ wavenumber range, subtracting the correspondent KBr standard background.

Crystallographic structures of the materials were determined by powder X-ray diffraction (PXRD) using a Philips PW 1710 diffractometer (Koninklijke Philips, Netherlands). It works with the Cu-Kα line (λ = 0.154 nm) in the 2θ range of 5-85º at a scanning rate of 2º/min. Finally, SEM images were taken through a JEOL 6610LV (JEOL, USA) scanning electron microscope before and after the applied water treatment on the fixed bed.

## 3. Results and discussion

3.1. Adsorption at mild conditions

A simulated underground mining emission at mild conditions, 5% $CH_4$ – 95% air, was fed to a fixed bed, for the three adsorbents, Figure 1. Fixed bed was filled with 0.15 g of each adsorbent, thus working at isomass conditions with different bed morphologies, and the adsorption temperature was 298 K. Results show that methane adsorption capacity of Basolite C300 is 18.6 and 20.4% higher than for Basolite F300 and Basolite A100, respectively, following the same trend than the BET specific surface areas of the pristine materials: 1514 (Basolite C300) > 962 (Basolite F300) > 662 (Basolite A100) $m^2/g$.

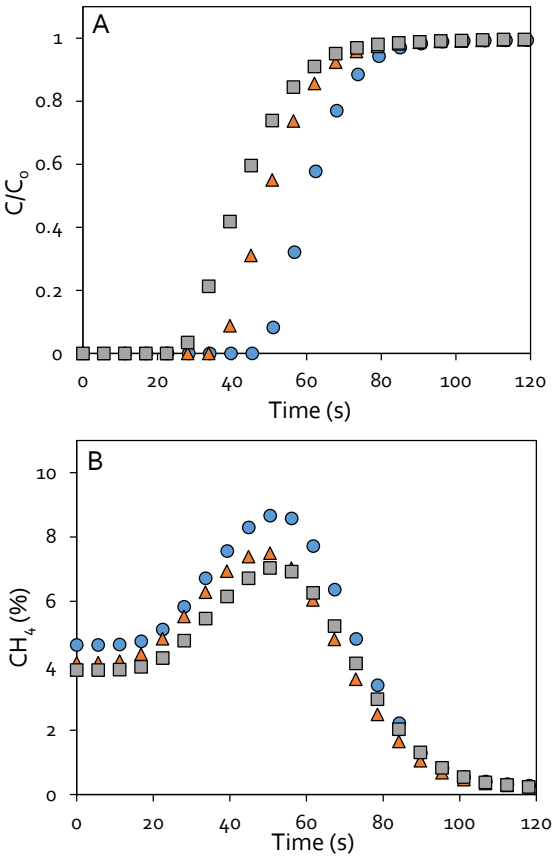


Figure 1. Adsorption (A) and desorption (B) curves for methane (Co = 5%) and air (95%) in a fixed bed device at 298 K in adsorption, and 423 K in desorption (100% air). Basolite C300 (blue circles), Basolite F300 (orange triangles) and Basolite A100 (grey squares).

All the reported experiments were duplicated with deviations lower than 1% in all the cases. The different adsorption behaviour can be also justified by the structural differences among the materials [22]. In case of Basolite C300, homologous material to HKUST-1, it is composed by copper ($Cu^{2+}$) metallic ions, linked by 1,3,5-tribenzenecarboxylate (1,3,5 BTC) organic ligands. The structure results in face-centered cubic (fcc) crystals with large square-shaped pores of 9 x 9 Å [23]. The copper ions conform OMS with high affinity to methane, which have high influence on the adsorption process [24]. On the other hand, Basolite F300 is a distorted MIL-100(Fe) structure, with low crystallinity and formed by iron ($Fe^{3+}$) metallic ions linked by 1,3,5-BTC organic ligands. This material also presents OMS, in form of iron, but in a concentration around 40% lower than Basolite C300 [25]. In addition, this material presents two types of cages with free apertures of 25 and 29 Å [26]. Basolite F300 presents lower

specific surface area and total pore volume than its crystalline homologous, MIL-100(Fe), which generates more diffusional problems through the structure, partially hindering access to OMS [27]. In fact, adsorbed molecules are homogeneously distributed on the surface and not in specific areas [28]. Finally, Basolite A100, homologous to MIL-53(Al), is formed by aluminium ($Al^{3+}$) metallic ions and terephtalic acid as organic ligand. It is disposed in an orthorhombic structure, with pores of free diameter close to 8.5 Å. It presents $Al^{3+}$ OMS available in the structure, but with lower affinity to methane than in case of copper ones [28, 29]. In the same way than Basolite C300, adsorbed molecules are preferentially distributed near to OMS [28]. Therefore, in addition to a large specific surface area, the presence of open metal sites in Basolite C300 generates even more attraction towards methane.

In addition, desorption is performed after the completely saturation of the material with the inlet stream. In the desorption step, the inlet stream is composed only by air, and the fixed bed is heated up to 423 K. The outlet stream is analysed in the same way than in adsorption case, recording the intensities of the components in the mass spectrometer, directly related to the molar concentration in the stream. In this way, Figure 1B shows a maximum methane concentration increment after desorption of around 41.7, 36.6 and 34.8% for Basolite C300, Basolite F300 and Basolite A100, respectively, in comparison to the original feed stream ($C_0$ = 5%). In the desorption step, replications of the experiments show variations around 1.2% for each material. As seen in a previous work [18], Basolite C300 presents the highest methane heat of adsorption among the three materials, which can explain the higher methane adsorption and concentration capacity.

Furthermore, thermogravimetric adsorption studies of the involved molecules are useful for explaining the results obtained at fixed bed conditions and to predict the adsorption mechanism of the different molecules. Adsorption thermograms obtained at 298 K are shown in Figure S2. Adsorption capacity increases in the order: $CH_4$ > air constituents for all the materials. In addition, the shape of the adsorption curves is similar for all the materials and components, reaching the saturation faster in case of methane, indicating the great affinity of the materials towards that molecule, as it was observed by fixed bed curves and the final concentration results. Adsorption behaviour has been demonstrated to follow a Langmuir isotherm in previous works [18]. Despite the good results, the separation of these molecules, methane, nitrogen and oxygen, is complicated by adsorption, due to its similarities in molecular size (3.82, 3.65 and 3.47 Å), polarizability (2.45, 1.71 and 1.56 $Å^3$) and null dipole moment, respectively [8]. Total adsorption capacities of the materials and selectivities are summarized in Table 1. These results show that Basolite A100 is the best material for a $CH_4/N_2$ separation, due to its great affinity to methane, but it exhibits the lowest adsorption capacities. Basolite C300 presents a remarkable $CH_4/O_2$ separation capacity, and presents the highest adsorption capacities, but it fails in the $CH_4/N_2$ separation. Basolite F300 presents a medium $CH_4/N_2$ separation capacity, and very low selectivity towards methane in presence of oxygen.

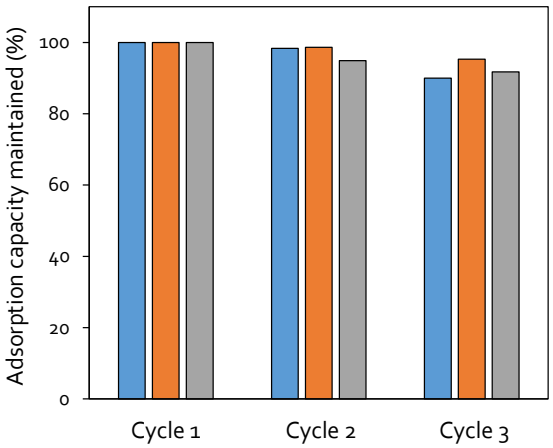


Figure 2. Methane adsorption capacity maintained after three consecutive cycles of methane (5%) and air (95%) adsorption on the fixed bed at 298 K. Desorption was carried out with pure air at 423 K between cycles. Basolite C300 (blue), Basolite F300 (orange) and Basolite A100 (grey).

Furthermore, adsorption experiments have been replicated using the same material three consecutive times, and the effect of cycles on the adsorption capacity has been verified (Figure 2). Between consecutive cycles, desorption is carried out under air at 423 K. Studied materials present a good stability when working in successive adsorption-desorption cycles, especially Basolite F300, with a maximum loss of 4.7%. The maximum loss was registered for Basolite C300 in the third cycle, 10%. Nevertheless, these results show adequate adsorption capacity resistance in fixed-bed adsorption in absence of humidity (only feeding methane and air).

Results can be compared with the performance of other sorbents proposed in the literature for this purpose. Qadir et al. [30] have used $Cu(INA)_2$ MOF for the adsorption and separation of methane from air. The adsorption capacity of this MOF, with a BET specific surface area of just 250 $m^2/g$, for

pure methane is around 12.8 mg/g. In addition, the selectivity towards methane is high and it was obtained good methane recovery (90.3%) and final concentration (50%), starting from a 15% of methane. On the other hand, Zhu et al. [31] have tested the effectiveness of activated carbon in the separation and concentration of methane ($C_0$ = 0.3%) in an air stream. A final concentration of 0.59% was obtained. Furthermore, Wang et al. [32] have made a vast compilation of the performance of different adsorbent materials (MOFs, zeolites and activated carbons) for the methane separation from nitrogen rich gases. It can be deduced that the Basolites studied in this work are very competitive in terms of methane adsorption capacity, and, at minor extent, in terms of selectivity towards methane.

### 3.2. Adsorption in presence of $CO_2$

Theoretically, the low molecular size (3.33 Å) and high polarizability (2.51 Å$^3$) of carbon dioxide molecule, which is present at low concentration in the fugitive methane streams (around 0.1%), could interfere in the methane adsorption capacity on the open metal sites [8]. Ghazvini et al. [33] have indicated that $CO_2$ commonly establishes dipole-quadrupole interactions with the OMS of the MOFs, which are usually stronger than for other gas molecules. In fact, $CO_2/CH_4$ selectivities for Basolite C300, Basolite F300 and Basolite A100 are reported in the literature as 6, 5.3 and 3.8, respectively [34-36]. Therefore, the adsorption behaviour of these materials in a 0.33% $CO_2$, 5% $CH_4$ and 95% air stream was studied in a fixed-bed device. After the described adsorption period, desorption was carried out analogous to the previous case (423 K, air), recording the intensity of methane. Desorption curve gives the information about the methane actually adsorbed during the process, and its final concentration. Figure 3 compares methane desorption curves in presence and absence of carbon dioxide, observing slight reductions in methane adsorption capacity for Basolite C300 (0.9%) and Basolite F300 (1.1%), whereas even an increase of 12.4% was observed for Basolite A100. The variation of the first two is in the order of magnitude of the experimental determinations, estimated by duplicates, so it is possible to consider it as negligible. The behaviour of Basolite A100 can be understood by the permanence of the material in its state of large pore (lp) [37]. In this state, the access to active metal centres by methane is easier, since the passage is facilitated due to wider pores [38]. In addition, the selectivity towards carbon dioxide is not too high (3.8) and the concentration is low. The combination of these factors causes an increase in methane adsorption capacity.

In addition, thermogravimetric results (Figure S3) show great affinity of the three materials towards carbon dioxide, higher in all the cases than for the other studied molecules. Saturation is reached at similar time than in case of methane, following a Langmuir-type profile. Results indicate that Basolite A100 presents a poor performance for methane separation in presence of carbon dioxide, which also affects the performance of Basolite C300 (Table 2). Finally, Basolite F300 is the material least affected by the $CO_2$ presence. Therefore, despite the high affinity of these materials towards carbon dioxide, Basolite C300 and Basolite F300 methane adsorption capacities are barely affected by the presence of carbon dioxide in the adsorbate stream at very low partial pressures (0.33%). As regards the shape of the adsorption curve, carbon dioxide follows practically the same model than methane and nitrogen on the three materials considered. Despite that, in case of Basolite C300, Teo et al. [39] have demonstrated, by Monte Carlo simulations, that a carbon dioxide low partial pressure, it does not share adsorption sites with methane, which means that there is no carbon dioxide interference in methane adsorption.

On the other hand, in case of Basolite F300, Xian et al. [35] have demonstrated, for MIL-100(Fe), a high influence of carbon dioxide concentration in the selectivity, so at such low carbon dioxide concentrations, the carbon dioxide does not affect the methane adsorption.

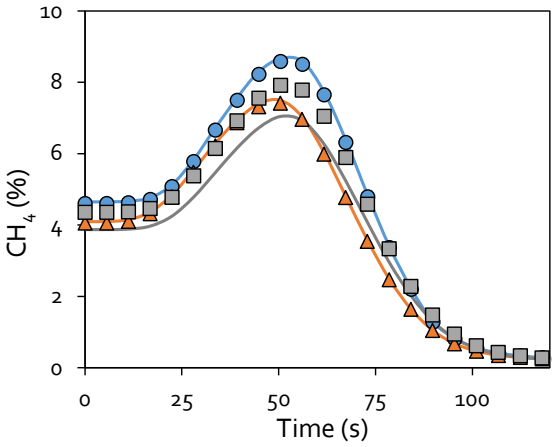


Figure 3. Comparative of desorption curves of the three materials after methane (5%) and air (95%) adsorption (continuous line) and after methane (5%), air (balance) and carbon dioxide (0.33%) adsorption (pointed lines). Basolite C300 (blue), Basolite F300 (orange) and Basolite A100 (grey).

Table 1. Total adsorption capacities determined by thermogravimetry (298 K, 0.1 MPa), for the considered materials, of the different adsorbates considered, at pure conditions, and the correspondent selectivities respect to methane.

| Material | $CH_4$ (mg/g) | $N_2$ (mg/g) | $O_2$ (mg/g) | $CH_4/N_2$ | $CH_4/O_2$ |
|---|---|---|---|---|---|
| Basolite C300 | 45.3 | 30.2 | 19.3 | 1.51 | 2.34 |
| Basolite F300 | 28.1 | 18.2 | 26.4 | 1.54 | 1.06 |
| Basolite A100 | 14.2 | 7.20 | 8.90 | 1.97 | 1.59 |

In the same way than in the previous case, three consecutive cycles of fixed-bed methane adsorption were performed in presence of carbon dioxide (Figure 4). The aim of these experiments is to observe if carbon dioxide has, even at low concentration, any noxious effect on the performance of the materials after several cycles. Results show that the presence of carbon dioxide does not affect in consecutive cycles on any of the three materials, registering almost the same capacity losses than in the case of only methane and air.

Table 2. Total adsorption capacities determined by thermogravimetry (298 K, 0.1 MPa), for the considered materials, of carbon dioxide, at pure conditions, and the correspondent selectivities respect to methane.

| Material | $CO_2$ (mg/g) | $CH_4/CO_2$ |
|---|---|---|
| Basolite C300 | 117.5 | 0.38 |
| Basolite F300 | 48.8 | 0.57 |
| Basolite A100 | 58.3 | 0.24 |

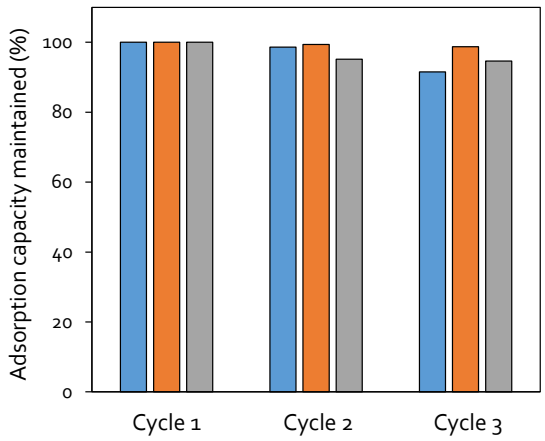


Figure 4. Methane adsorption capacity maintained after three consecutive cycles of methane (5%), carbon dioxide (0.33%) and air (95%) adsorption on the fixed bed at 298 K. Desorption was carried out with pure air at 423 K between cycles. Basolite C300 (blue), Basolite F300 (orange) and Basolite A100 (grey).

Comparing with the literature, the vast majority of the materials employed for methane and carbon dioxide separation present larger affinity to carbon dioxide, as their objective is the biogas purification. For example, Yan et al. [40] have designed porphyrin-based nanoporous organic polymers (PNOPs), which present low methane (~ 9.6 mg/g) and high carbon dioxide (~ 97.1 mg/g) capacities, thus the $CO_2/CH_4$ selectivity is very elevated, 9.5. In addition, Wee et al. [41] have synthesized COK-17, a new zeolitic-imidazolate framework (ZIF), with 110 and 19.8 mg/g of carbon dioxide and methane adsorption capacities, respectively. They have reported good $CO_2/CH_4$ selectivity values, improving at high pressure and $CO_2$ initial concentrations. In line with these findings, Ghazvini et al. [33] have compiled the carbon dioxide selectivities of different adsorbents, showing very good results in most of them, reaching even values of 130 for IRMOF-14. In addition, a previous work [8] has also pointed out that majority of adsorbent materials present more affinity to carbon dioxide than methane. However, in case of VAM, the carbon dioxide concentration is so low that it has practically no effect on performance. On the other hand, these considered materials may be suitable for the purification of biogas with representative amounts of $CO_2$, as their adsorption capacity and selectivity is high.

### 3.3. Effect of water on methane adsorption behaviour

Based on the literature, these commercial materials have not been tested under wet conditions in the presence of other potential adsorbates, except some fixed-bed experiments at low water concentrations or computer simulations [17, 42]. Therefore, methane retention in a fixed-bed adsorption device was tested at two different and high RH, 75 and 100%, which corresponds to the high relative humidities that can be found in actual streams [43] (Figure 5). In presence of water, experimental duplicates show a possible error of around 1%. In this way, the lower RH scarcely influences the methane adsorption capacity, being observed for Basolite C300 the highest reduction, 6.2%. Results can be explained

according to the studies about water-MOF interactions performed by Küsgens et al. [44], reporting a significant strength of interaction with open Cu-sites in different MOFs. This interaction is weaker in the case of iron sites [45] and hence, humidity has a positive effect (4.6%) on the methane adsorption behaviour of Fe-containing MOF when working below saturation conditions. This may be due to one of several effects that water has on surfaces [46]. In fact, Mileo et al. [47] have demonstrated by simulations that water molecules could generate a surface hydrate via hydrogen bonds, on which methane could be co-adsorbed due to its high polarizability. Finally, Basolite A100 presents a mid-level affectation (3.8%), since despite the easy access, the presence of aluminium ($Al^{3+}$) open metal sites generates more resistant structures to water [48]. At the highest considered RH, the total methane capacity decreased for all the materials. Basolite C300 presents a total reduction of 18.6%, whereas 2.7 and 5.2% were observed for Basolite F300 and Basolite A100, respectively. In case of Basolite C300 and Basolite A100, the water induces the same effect than at lower relative humidities, water molecules link with available open metal sites, occupying the available space for methane molecules. On the other hand, Rezk et al. [49] observed that water adsorption capacity of Basolite F300 is very dependent on the water partial pressure, with a steep increase once the lowest pressures have passed. Therefore, the water that previously generated hydrates on the surface begins to cover the available surface and to block these hydrophilic centres, causing the reduction in methane adsorption capacity [47].

As in the previous cases, 3 consecutive cycles of the same fixed bed experiment are performed to observe the effect on the capacity of the material (Figure 6). The results show that Basolite C300 is the material most affected by water presence, with a decrease of 46.5% of capacity after the first cycle. On the other hand, Basolite F300 follows the results discussed above, showing even an increase in capacity after contact with water. Finally, Basolite A100 suffers some capacity loss (14.5%), but lower than Basolite C300. These results demonstrate that water has a strong effect on the adsorption performance of MOFs.

Scarce works deal with methane adsorption under humid conditions, and, in this case, they use hydrophobic adsorbents. For example, Liu et al. [50] have used the TUT-100 MOF for the $CH_4/N_2$ separation under humid conditions. In that case, for a RH of 96%, the material maintains the same selectivity and adsorption capacity as in a dry environment. In addition, Shang et al. [51] have presented a compilation of different adsorbents with certain hydrophobicity, demonstrating that water has low influence on the $CH_4/N_2$ separation in case of working with hydrophobic adsorbents. For example, in case of silicalite-1, they have reported a concentration factor of 1.59, regardless of the water presence. Finally, Yang et al. [52] compiled several adsorbents suitable for this separation, highlighting the importance of the adsorbents behaving adequately under humid conditions. However, they pointed out that more experimentation is needed, as almost none have been tested under these conditions.

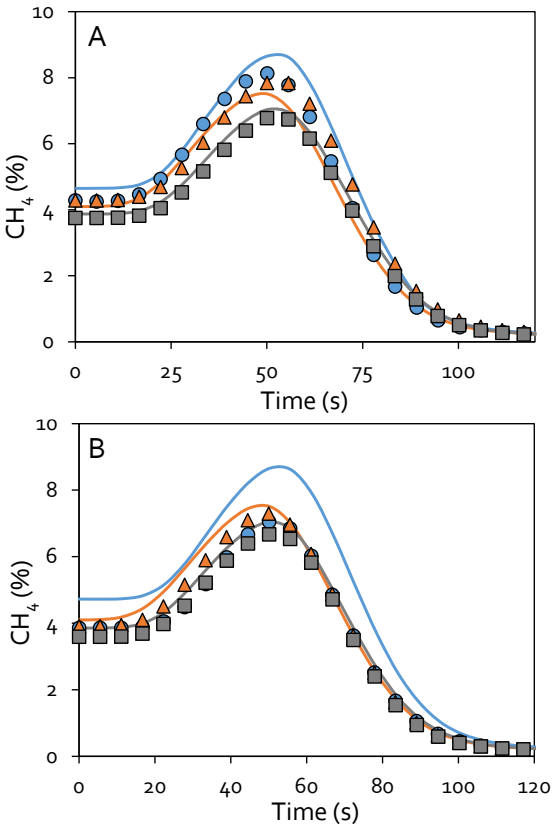


Figure 5. Comparative of desorption curves of a dry stream (continuous lines) and the same stream with different relative humidities (pointed lines). A: 75% RH and B: 100% RH. Basolite C300, blue, Basolite F300, orange and Basolite A100, grey.

In addition to the dynamic fixed-bed experimentation of the separation, characterization of the materials after being treated under 100% RH was carried out. The humid treatment consists in ageing the material situated in the fixed bed with a methane (5%), air (95%) and water (100% RH) for 24 h at 298 K, 0.1 MPa and a total flowrate of 50 ml/min. Nitrogen physisorption isotherms, Figure S4, reveal a decrease in BET specific surface area and pore volume for all the materials (Table 3), in agreement with Al-Janabi et al. [13], which have

also reported for HKUST-1 a drastic reduction of specific surface area in presence of water. As observed, pristine samples exhibit a type-II adsorption isotherm with a soft increase in the adsorbed volume in the range of 0.1 to 0.9 ($P/P_0$) followed by a steep adsorption with $P/P_0$ greater than 0.95 for Basolite A100 and, in lower extent, in Basolite C300. For Basolite F300, an isotherm with similarities to type I is observed. Water induces changes in the isotherms, especially for Basolite C300 and Basolite A100, for which isotherm transitions to the patterns of type IV are shown. The isotherm is characteristic of mesoporous materials. Basolite A100 presents a barely distinguishable hysteresis loop in the range of $P/P_0$ 0.90-0.99, which is an indication of the interparticle porosity. Basolite C300 exhibits a hysteresis loop of H3-type at $P/P_0$ 0.42-0.97, representative of slit-like pores. Hence, water enhances adsorption in the mesoporous zone, with multilayer adsorption and condensation phenomena at high pressures in detriment of adsorption in micropores. It is remarkable that Basolite F300 experiments an enhanced adsorption due to the mesopores contribution, justifying the limited water effect on methane adsorption on this material, even though the stability of the material is poor in comparison to the homologous crystalline MIL-100(Fe) [53]. Finally, although the morphological features are reduced after water treatment for Basolite A100, these morphological changes are not directly correlated to the methane adsorption capacity, remarking in this way the influence of the aluminium open metal sites.

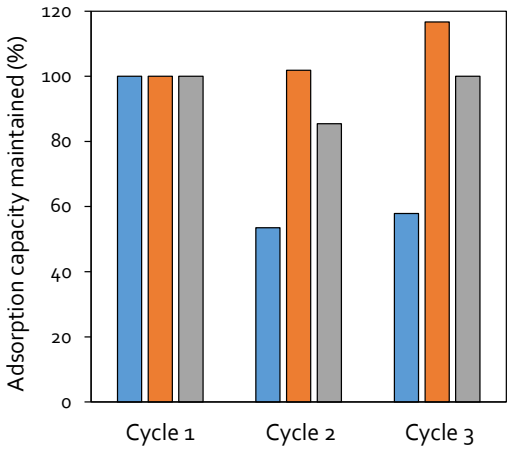


Figure 6. Methane adsorption capacity maintained after three consecutive cycles of methane (5%), air (95%) and 100% RH adsorption on the fixed bed at 298 K. Desorption was carried out with pure air at 423 K between cycles. Basolite C300 (blue), Basolite F300 (orange) and Basolite A100 (grey).

In addition, in order to better understand the influence of water on the structure of the adsorbents and the methane adsorption, the evolution of adsorbed species was analysed by DRIFT. Figure S5 includes spectra of the materials recorded at 298 K without contact to water, and after aging at RH of 75 and 100% directly on the equipment (40 ml/min). The common bands for all the materials at 1304 and 3016 $cm^{-1}$ are attributed to methane C-H bonds [54]. In case of Basolite C300 spectra, clear bands characteristic of the material are observed below 2000 $cm^{-1}$: the peaks in the range 1300-1500 $cm^{-1}$ and 1500-1700 $cm^{-1}$ are related to -O-C-O- groups, whereas peaks in 1374-1559 $cm^{-1}$ correspond to double bonds C=C, which demonstrate the incorporation of the organic ligand 1,3,5-BTC in the structure. Furthermore, the band in the region 3200-3500 $cm^{-1}$ can be related to the –OH bond of water to the structure [55]. As seen, a continuous displacement of bands at 1500-1700 $cm^{-1}$ and apparition of new peaks, corresponding to -O-C-O- groups, is observed with increasing number of cycles, suggesting water-induced changes in the structure. Basolite F300 shows a similar spectrum to Basolite C300, due to the presence of the same organic ligand. Additionally, there is no displacement or appearance of new peaks along all the wavelength range, discarding structural changes due to water presence. In case of Basolite A100, peaks at 760 $cm^{-1}$ corresponds to vibration of the hydrogen in the aromatic ring, whereas peaks at 860 and 1025 $cm^{-1}$ are related to the carboxyl bonds and, between 1460-1700 $cm^{-1}$, to the double bond C=C [56]. Similarly to Basolite F300, any structural change is observed after the water treatment, without displacement or appearance of new peaks. In addition, the three MOFs present an intense water desorption capacity at high temperature (423 K), since the band corresponding to the –OH link (3200-3550 $cm^{-1}$) is low in all the three cycles for each material, which indicates that there is no water left after the cleaning stages. These bands are a little higher in case of Basolite C300, which presents more hydrophilic metal centres and desorbs water more slowly at the same temperature than the other two materials. In fact, these active centres are the ones that cause the greatest reduction in methane adsorption capacity in the presence of water for Basolite C300, as seen above.

Figure S6 shows the diffractograms obtained by PXRD in order to identify moisture-induced crystallinity changes, noting three different scenarios. Basolite C300 exhibits changes in the intensity of peaks at 6.7º and 11.6º, suggesting changes in crystallinity, but invariability in the crystalline structure [13].

Table 3. Morphological features of each material before and after water treatment (100% RH, 24 h).

| Material | Pristine BET ($m^2/g$) | Pristine mesopore volume ($cm^3/g$) | Pristine micropore volume ($cm^3/g$) | Treated BET ($m^2/g$) | Treated mesopore volume ($cm^3/g$) | Treated micropore volume ($cm^3/g$) |
|---|---|---|---|---|---|---|
| Basolite C300 | 1515 | 0.53 | 0.70 | 695 | 0.75 | 0.18 |
| Basolite F300 | 962 | 0.15 | 0.27 | 697 | 0.24 | 0.08 |
| Basolite A100 | 656 | 0.77 | 0.28 | 307 | 0.68 | 0.14 |

Thereby, Gul-E-Noor et al. [57] observed that the stability of this material depends on both the water concentration and the time of exposure.

Basolite F300, pristine material with a low-crystalline structure, does not introduce noticeable changes caused by the humidity. However, Basolite A100 shows a large increase in the amorphous phase, especially after values of 2θ higher than 15º. In addition, it is noted the apparition of two new peaks around 25º, so water can induce a crystalline phase change on this material. Peaks apparition are similar to the obtained in a previous work after pressurization of the material [58], which suggests the presence of phase changes and certain amorphization. Therefore, Basolite A100 is less resistant to the presence of water than its homologous, MIL-53(Al), which was unaltered even after immersions at different pH values [59]. According to these results, methane adsorption does not depend to a large extent on the crystal structure of the adsorbent material, but on other morphological features such as specific surface area or total pore volume. Additionally, SEM images of the materials were taken in order to observe modifications after the water ageing treatment in the fixed bed, Figure S7. Only Basolite C300, with original rhombohedric geometrical shapes, presents some additional fissures, agglomeration and loss of shape, which can be related both to the crystallinity losses and the -O-C-O- groups displacement observed by DRIFT. All this casuistry would make this the material most affected by the presence of water in methane adsorption, in consonance to Al-Janabi et al. [13] in the $CO_2$ adsorption on HKUST-1 in presence of water. For Basolite A100, the presence of agglomerations of the pseudo-spheres is the only distinctive, since these agglomerations could leave small cavities such as those shown in $N_2$ isotherms.

Finally, the influence of moisture on both the adsorption capacity and selectivity of methane and nitrogen was studied by thermogravimetry. These two molecules were selected by their similarities, hence the most difficult separation (Figure 7).

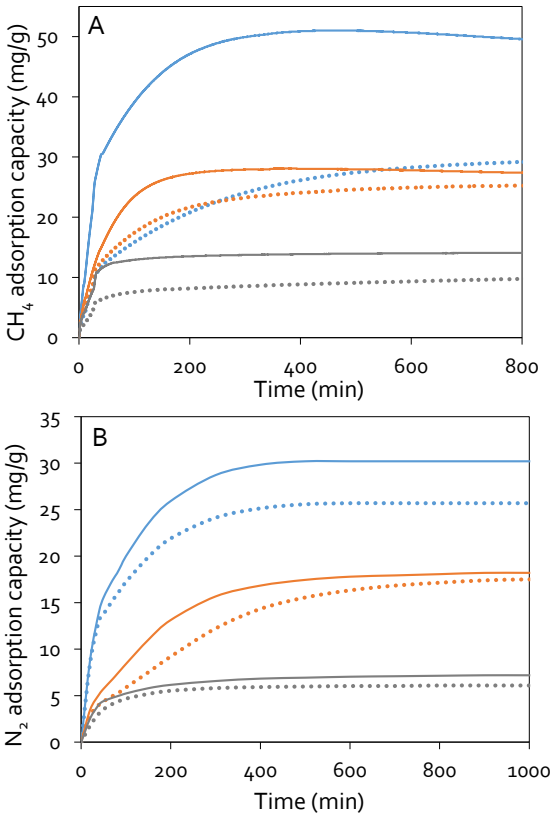


Figure 7. Comparative of adsorption curves for methane (A) and nitrogen (B) on pristine (continuous line) and water-treated (pointed line) materials. Basolite C300 (blue), Basolite F300 (orange) and Basolite A100 (grey).

Concerning the shape of thermogravimetric adsorption curves, higher differences were observed between the pristine and water-aged materials for methane than for nitrogen adsorption. The porosity loss makes difficult that methane, with higher molecular diameter and adsorption density on the OMS than nitrogen, moves through the structure of the materials.

Table 4. Adsorption capacity (298 K, 60 ml/min) results for the three materials before and after the water treatment.

| Material | Pristine $CH_4$ (mg/g) | Pristine $N_2$ (mg/g) | Treated $CH_4$ (mg/g) | Treated $N_2$ (mg/g) |
|---|---|---|---|---|
| Basolite C300 | 45.3 | 30.2 | 30.2 | 25.7 |
| Basolite F300 | 28.1 | 18.2 | 25.5 | 17.5 |
| Basolite A100 | 14.2 | 7.2 | 10.5 | 6.10 |

In addition, pore sizes of the three materials are 4,10 and 11 Å for Basolite C300, 25 and 29 Å for Basolite F300 and 8.5 Å for Basolite A100, respectively [18]. Therefore, as it is observed, the largest pores (25 and 29 Å) correspond to the material least affected by water, which could be related with capillary condensation phenomena, which preferentially affects to small pores, establishing links water-structure.

Table 4 summarizes the adsorption capacity before and after the water ageing. In agreement with previous characterization of water aged samples, Basolite C300 shows the most important loss of methane adsorption capacity due to water, pointing out the great influence of copper open metal sites in the adsorption mechanism, which now are occupied by water. In fact, Maia et al. [60] remarked the role of these preferential sites on the adsorption mechanism of this material. These sites are clearly hydrophilic and are saturated with water during the moist treatment. In fact, $CH_4/N_2$ selectivity is particularly impaired by the presence of water, decreasing from 1.51 to 1.18, due to the reduced dependence of $N_2$ molecules on the active metal sites for adsorption.

In case of Basolite F300, it is demonstrated the low influence of iron metal sites on the adsorption mechanism, since the reduction of capacity is similar for both molecules despite the differences in polarizability. In fact, the selectivity $CH_4/N_2$ is maintained for both cases around 1.5. This fact probably occurs due to the minor open metal sites exposition than other materials such as Basolite C300, due to the diffusion difficulties encountered by some molecules in the adsorption process on Basolite F300 [27, 61]. Finally, in case of Basolite A100, the influence of aluminium open metal sites is demonstrated since the reduction in case of methane is more pronounced than for nitrogen. The $CH_4/N_2$ selectivity goes from 1.9 to 1.7, since it presents specific or more likely areas for methane adsorption, close to active metal centres [28].

3.4. Adsorption at actual conditions

Figure 8 shows the effect of carbon dioxide (0.33%) in case of wet streams (100% RH), reproducing similar conditions to an actual stream to be treated. The stream preparation procedure is the same than in case of carbon dioxide under dry conditions, but introducing also water through the syringe pump. The differences observed between experiment duplicates are around 2.1%. A scarce influence of $CO_2$, in case of Basolite C300 and Basolite F300, is detected (Table 5). Even so, it is observed a slight reduction increment in methane adsorption capacity for both materials after carbon dioxide and water simultaneous feed. In agreement, Yazaydin et al. [62] indicated that the $CO_2$-$H_2O$ strong interaction leads to an increment of $CO_2$ adsorption capacity in presence of water. On the other hand, the simultaneous presence of carbon dioxide and water provokes modifications in the breathing structure Basolite A100, causing a very harmful effect when water easily penetrates the structure [63].

Table 5. Effect of $H_2O$ (100% RH, 24 h) and $CO_2$ (0.33%) presence in total $CH_4$ adsorption capacity in comparison to dry conditions experiment.

| Material | Capacity reduction with $H_2O$ (%) | Capacity reduction with $CO_2$ (%) | Capacity reduction with $H_2O$ and $CO_2$ (%) |
|---|---|---|---|
| Basolite C300 | 18.6 | 0.9 | 21.1 |
| Basolite F300 | 2.7 | 1.1 | 4.1 |
| Basolite A100 | 5.2 | 12.4* | 18.1 |

*In case of Basolite A100, the $CO_2$ presence provokes a methane adsorption capacity increase.

Three consecutive methane adsorption cycles were performed in presence of carbon dioxide and water (Figure 9). These cycles represent the closest approximation to a strength study of these materials under real conditions. Results are similar, in case of Basolite C300 and Basolite F300, to the case of methane, air and water (Figure 6). In contrast, as indicated above, the coincidence of water and carbon dioxide is very harmful in the case of Basolite A100. Therefore, the methane

adsorption capacity is greatly reduced with the cycles.

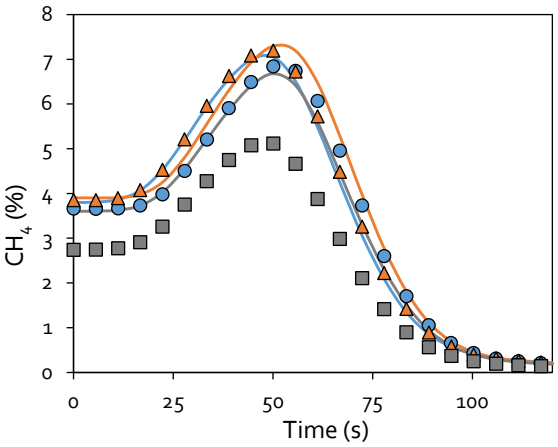


Figure 8. Comparative of desorption curves for methane, air and water (RH: 100%) (continuous line) and the same stream with carbon dioxide (pointed line). Basolite C300 (blue), Basolite F300 (orange) and Basolite A100 (grey).

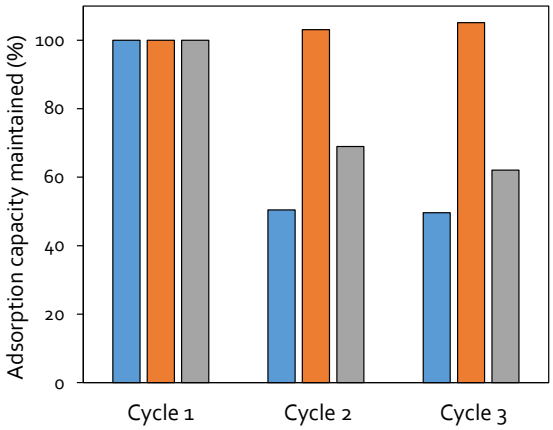


Figure 9. Methane adsorption capacity maintained after three consecutive cycles of methane (5%), air (95%), carbon dioxide (0.33%) and 100% RH adsorption on the fixed bed at 298 K. Desorption was carried out with pure air at 423 K between cycles. Basolite C300 (blue), Basolite F300 (orange) and Basolite A100 (grey).

Concerning the available literature, as far as the authors know, there is no work that has taken into account the confluence of methane, air, carbon dioxide and water in a dynamic adsorption study. In fact, most works indicate that dehumidification of the streams prior to passage through the fixed bed is necessary [64], but this would be an unbearable expense for a process of recovery of a gaseous waste at such low concentration.

## 4. Conclusions

This work analyses the methane adsorption performance of three commercial MOFs, Basolite C300, Basolite F300 and Basolite A100, under demanding conditions: wet streams and carbon dioxide presence. These conditions are yet considered as issues to be studied in relation to potential adsorbent materials in methane recovery from fugitive underground coal streams. In relation with carbon dioxide, it causes limited loss of adsorption capacity for Basolite C300 and Basolite F300, since low-pressure carbon dioxide does not share preferential adsorption sites with methane. For Basolite A100, it is observed even an increase of methane adsorption capacity, which is related to the favouring lp state of the breathing effect, making easy the methane penetration to the structure. Additionally, humid streams evidenced to be really harmful for these materials, especially for those with accessible open metal sites on its structure, such as Basolite C300 and Basolite A100. DRIFT, SEM and nitrogen physisorption analysis reveal that water molecule chemisorbs to copper ($Cu^{2+}$) open metal sites of Basolite C300, changing textural properties, and reducing both the structural crystallinity and the methane adsorption capacity. Basolite A100 also evidenced a decrease in methane adsorption capacity in presence of water, but aluminium ($Al^{3+}$) open metal sites are more resistant to water than $Cu^{2+}$ ones, showing certain hydrophobicity that protects the structure. This effect is softer in case of Basolite F300. Its distorted structure avoids easy access of water to iron ($Fe^{3+}$) metal sites, even favouring the methane adsorption, creating hydrophilic centres on the surface at low water partial pressures. This makes Basolite F300 the best material for the low-grade methane recovery process, maintaining the original $CH_4/N_2$ selectivity even after the water treatment. In addition, all the capacity losses were increased in presence of water and carbon dioxide simultaneously, especially in case of Basolite A100 and its characteristic breathing effect, being again low in case of Basolite F300, which only loses 4% of its original capacity under conditions similar to the actual ones, due to the strong $CO_2$-$H_2O$ interaction.

These results are promising, since, for example, in the case of Basolite F300, it is demonstrated the existence of a fully commercial material that is capable of obtaining good results for the separation of methane from low-concentrated streams. These good results are maintained also in presence of water and carbon dioxide, two of the most harmful components in this type of processes. These results allow to start using commercial MOFs in large-scale methane separation processes, as good results had previously been obtained for separation, but in the case of non-scalable materials at this time. The

next steps would consist of experimenting with these materials at intermediate scales (pilot plant) before moving to an industrial scale.

**Acknowledgements**

This work was supported by the Research Fund for Coal and Steel of the European Union (contract RFCS 754077-METHENERGY PLUS) and by the Asturian Government (contract GRUPIN AYUD/2021/50450).

The authors acknowledge the technical support provided by Servicios Científico-Técnicos from Universidad de Oviedo.

David Ursueguía acknowledges the Spanish Ministry of Education for the PhD grant that supports his research (FPU2018-01448).

**References**

[1] J. Gao, C. guan, B. Zhang, China's $CH_4$ emissions from coal mining: A review of current bottom-up inventories, Science of The Total Environment 725 (2020) 138295.

[2] C. Karacan, P. Warwick, Assessment of coal mine methane (CMM) and abandoned mine methane (AMM) resource potential of longwall mine panels: Example from Northern Appalachian Basin, USA, International Journal of Coal Geology 208 (2019) 37-53.

[3] C. Karacan, F. Ruiz, M. Coté, S. Phipps, Coal mine methane: A review of capture and utilisation practices with benefits to mining safety and to greenhouse gas reduction, International Journal of Coal Geology 86 (2011) 121-156.

[4] D. Ursueguía, P. Marín, E. Díaz, S. Ordóñez, A new strategy for upgrading ventilation air methane emissions combining adsorption and combustion in a lean-gas turbine, Journal of Natural Gas Science and Engineering 88 (2021) 103808.

[5] R. Wang, Y. Zou, C. Zhang, X. Wang, M. Yang, D. Xu, Combining crystal graphs and domain knowledge in machine learning to predict metal-organic frameworks performance in methane adsorption, Microporous and Mesoporous Materials 331 (2022) 111666.

[6] B. Wang, X. Zhang, H. Huang, Z. Zhang, T. Yildirim, W. Zhou, S. Xiang, B. Chen, A microporous aluminium-based metal-organic framework for high methane, hydrogen, and carbon dioxide storage, Nano Research 14 (2021) 507-511.

[7] Y. Chen, H. Wu, Y. Yuan, D. Lv, Z. Qiao, D. An, X. Wu, H. Liang, Z. Li, Q. Xia, Highly rapid mechanochemical synthesis of a pillar-layer metal-organic framework for efficient $CH_4/N_2$ separation, Chemical Engineering Journal 385 (2020) 123836.

[8] D. Ursueguía, E. Díaz, S. Ordóñez, Metal-Organic Frameworks (MOFs) as methane adsorbents: From storage to diluted coal mining streams concentration, Science of The Total Environment 790 (2021) 148211.

[9] S. Zhang, J. Wang, Y. Zhang, J. Ma, L. Huang, S. Yu, L. Chen, G. Song, M. Qiu, X. Wang, Applications of water-stable metal-organic frameworks in the removal of water pollutants: A review, Environmental Pollution 291 (2021) 118076.

[10] J. Canivet, A. Fateeva, Y. Guo, B. Coasne, D. Farrusseng, Water adsorption in MOFs: fundamentals and applications, Chemical Society Reviews 43 (2014) 5594-5617.

[11] M. Safy, M. Amin, R. Haikal, B. Elshazly, J. Wang, Y. Wang, C. Wöll, M. Alkordi, Probing the water stability limits and degradation pathways of metal-organic frameworks, Chemistry – A European Journal 26 (2020) 7109-7117.

[12] K.M.C. Santos, T.R. Menezes, M.R. Oliveira, T.S.L. Silva, K.S. Santos, V.A. Barros, D.C. Melo, A.L. Ramos, C.C. Santana, E. Franceschi, C. Dariva, S.M. Egues, G.R. Borges, J.F. De Conto, Natural gas dehydration by adsorption using MOFs and silicas: A review, Separation and Purification Technology 276 (2021) 119409.

[13] N. Al-Janabi, P. Hill, L. Torrente, A. Garforth, P. Gorgojo, F. Siperstein, X. Fan, Mapping the Cu-BTC metal-organic framework (HKUST-1) stability envelope in the presence of water vapour for $CO_2$ adsorption from flue gases, Chemical Engineering Journal 281 (2015) 669-677.

[14] N. Chanut, S. Bourrelly, B. Kuchta, C. Serre, J. Chang, P. Wright, P. Llewellyn, Screening the effect of water vapour on gas adsorption performance: Application to $CO_2$ capture from flue gas in metal-organic frameworks, ChemSusChem 10 (2017) 1543-1553.

[15] N. Jiang, Z. Deng, S. Liu, C. Tang, G. Wang, Synthesis of metal organic framework (MOF-5) with high selectivity for $CO_2/N_2$ separation in flue gas by maximum water concentration approach, Korean Journal of Chemical Engineering 33 (2016) 2747-2755.

[16] P. Boyd, A. Chidambaram, E. García-Díez, C. Ireland, T. Daff, R. Bounds, A. Gladysiak, P. Schouwink, S. Moosavi, M. Maroto-Valer, J. Reimer, J. Navarro, T. Woo, S. Garcia, K. Stylianou, B. Smit, Data-driven design of metal-organic frameworks for wet flue gas $CO_2$ capture, Nature 576 (2019) 253-256.

[17] J. Coelho, A. Ribeiro, A. Ferreira, S. Lucena, A. Rodrigues, D. Azevedo, Stability of an Al-fumarate MOF and its potential for $CO_2$ capture from wet stream, Industrial and Engineering Chemistry Research 55 (2016) 2134-2143.

[18] D. Ursueguía, E. Díaz, S. Ordóñez, Adsorption of methane and nitrogen on Basolite MOFs: Equilibrium and kinetic studies, Microporous and Mesoporous Materials 298 (2020) 110048.

[19] G. Jeong, A. Singh, M. Kim, K. Gyak, U. Ryu, K. Choi, D. Kim, Metal-organic framework patterns and membranes with heterogeneous pores for flow-assisted switchable separations, Nature Communications 9 (2018) 3968.

[20] J. Shen, J. Sulkowski, M. Beckner, A. Dailly, Effects of textural and surface characteristics of metal-organic frameworks on the methane adsorption for natural gas vehicular application, Microporous and Mesoporous Materials 212 (2015) 80-90.

[21] A. Gil, P. Grange, Application of the Dubinin-Radushkevich and Dubinin-Astakhov equations in the characterization of microporous solids, Colloids and Surfaces A: Physicochemical and Engineering Aspects 113 (1996) 39-50.

[22] Ü. Demir, A. Goldman, L. Esrafili, M. Gharib, A. Morsali, O. Weingart, C. Janiak, Coordinatively unsaturated metal sites (open metal sites) in metal-organic frameworks: design and applications, Chemical Society Reviews 49 (2020) 2751-2798.

[23] D. Sharma, S. Rasaily, S. Pradhan, K. Baruah, S. Tamang, A. Pariyar, HKUST-1 metal organic framework as an efficient dual-function catalyst: aziridination and one-pot ring-opening transformation for formation of β-aryl sulphonamides with C-C, C-S, and C-O bonds, Inorganic Chemistry 60 (2021) 7794-7802.

[24] J. Kim, H. Cho, W. Ahn, Synthesis and adsorption/catalytic properties of the metal organic framework CuBTC, Catalysis Surveys from Asia 16 (2012) 106-119.

[25] M. Ojer, M. Shamzhy, J. Cejka, E. Mayoral, Basolites: a type of metal organic frameworks highly efficient in the one-pot synthesis of quinoxalines from α-hydroxy ketones under aerobic conditions, Catalysis Today 345 (2020) 258-266.

[26] J. Hall, P. Bollini, Structure, characterization, and catalytic properties of open-metal sites in metal organic frameworks, Reaction Chemistry and Engineering 4 (2019) 207-222.

[27] M. Sanchez, I. Asua, D. Ruano, K. Diaz, Direct synthesis, structural features, and enhanced catalytic activity of the Basolite F300-like semiamorphous Fe-BTC framework, Crystal Growth and Design 15 (2015) 4498-4506.

[28] E. Deniz, F. Karadas, H. Patel, S. Aparicio, C. Yavuz, M. Atilhan, A combined computational and experimental study of high pressure and supercritical $CO_2$ adsorption on Basolite MOFs, Microporous and Mesoporous Materials 175 (2013) 34-42.

[29] A. Blanco, A. Vallone, S. Korili, A. Gil, K. Sapag, A comparative study of several microporous materials to store methane by adsorption, Microporous and Mesoporous Materials 224 (2016) 323-331.

[30] S. Qadir, D. Li, Y. Gu, Z. Yuan, Y. Zhao, S. Wang, S. Wang, Experimental and numerical investigations on the separation performance of $[Cu(INA)_2]$ adsorbent for $CH_4$ recovery by VPSA from oxygen-bearing coal mine methane, Chemical Engineering Journal 408 (2021) 127238.

[31] T. Zhu, R. Wang, X. Zhang, Y. Han, W. Bian, Y. Ma, M. Xue, Enrichment and separation of methane gas by vacuum pressure swing adsorption, Adsorption Science and Technology 2021 (2021) 5572698.

[32] Q. Wang, Y. Yu, Y. Li, X. Min, J. Zhang, T. Sun, Methane separation and capture from nitrogen rich gases by selective adsorption in microporous materials: A review, Separation and Purification Technology 283 (2022) 120206.

[33] M. Ghazvini, M. Vahedi, S. Nobar, F. Sabouri, Investigation of the MOF adsorbents and the gas adsorptive separation mechanisms, Journal of Environmental Chemical Engineering 9 (2021) 104790.

[34] S. Salehi, M. Anbia, F. Razavi, Improving $CO_2/CH_4$ and $CO_2/N_2$ adsorptive selectivity of Cu-BTC and MOF-derived nanoporous carbon by modification with nitrogen-containing groups, Environmental Progress and Sustainable Energy 39 (2019) 13302.

[35] S. Xian, J. Peng, Z. Zhang, Q. Xia, H. Wang, Z. Li, Highly enhanced and weakened adsorption properties of two MOFs by water vapor for separation of $CO_2/CH_4$ and CO2/N2 binary mixtures, Chemical Engineering Journal 270 (2015) 385-392.

[36] P. Rallapalli, K. Prasanth, D. Patil, R. Somani, R. Jasra, H. Bajaj, Sorption studies of $CO_2$, $CH_4$, $N_2$, CO, $O_2$ and Ar on nanoporous aluminium terephthalate [MIL-53(Al)], Journal of Porous Materials 18 (2011) 205-210.

[37] S. Bourrelly, P. Llewellyn, C. Serre, F. Millange, T. Loiseau, G. Férey, Different adsorption behaviours of methane and carbon dioxide in the isotypic nanoporous metal terephthalates MIL-53 and MIL-47, Journal of American Chemical Society 127 (2005) 13519-13521.

[38] L. Vanduyfhuys, G. Maurin, Thermodynamic modeling of the selective adsorption of carbon dioxide over methane in the mechanically constrained breathing MIL-53(Cr), Advanced Theory and Simulations 2 (2019) 1900124.

[39] H. Teo, A. Chakraborty, S. Kayal, Evaluation of $CH_4$ and $CO_2$ adsorption on HKUST-1 and MIL-101(Cr) MOFs employing Monte Carlo simulation and comparison with experimental data, Applied Thermal Engineering 110 (2017) 891-900.

[40] J. Yan, B. Zhang, S. Guo, Z. Wang, Porphyrin-based nanoporous organic polymers for adsorption of carbon dioxide, ethane, and methane, ACS Applied Nano Materials 4 (2021) 10565-10574.

[41] L. Wee, S. Vandenbrande, S. Rogge, J. Wieme, K. Asselman, E. Jardim, J. Silvestre-Albero, J. Navarro, V. Speybroeck, J. Martens, C. Kirschhock, Chlorination of a zeolitic-imidazolate framework tunes packing and Van der Waals interaction of carbon dioxide for optimized adsorptive separation, Journal of the American Chemical Society 143 (2021) 4962-4968.

[42] J. Coelho, A. Lima, A. Rodrigues, D. Azevedo, S. Lucena, Computer simulation of adsorption and sitting of $CO_2$, $N_2$, $CH_4$ and water on a new Al(OH)-fumarate MOF, Adsorption 23 (2017) 423-431.

[43] J. Bae, S. Su, X. Yu, J. Yin, A. Villella, M. Jara, M. Loney, Site trials of ventilation air Methane enrichment with two-stage vacuum, temperature, and vacuum swing adsorption, Industrial and Engineering Chemistry Research 59 (2020) 15732-15741.

[44] P. Küsgens, M. Rose, I. Senkovska, H. Fröde, A. Henschel, S. Siegle, S. Kaskel, Characterization of metal-organic frameworks by water adsorption, Microporous and Mesoporous Materials 120 (2009) 325-330.

[45] J. Álvarez, E. González, E. Pérez, E. Revueltas, A. Martínez, a. Cruz, A. Jácome, E. Zamora, I. Ibarra, Structure stability of HKUST-1 towards water and

ethanol and their effect on its $CO_2$ capture properties, Dalton Transactions 46 (2017) 9192-9200.

[46] T. Hayashi, Water at interfaces: Its behaviour and roles in interfacial phenomena, Chemistry Letters 50 (2021) 1173-1180.

[47] P. Mileo, K. Cho, J. Park, S. Devautour-Vinot, J. Chang, G. Maurin, Unraveling the water adsorption mechanism in the mesoporous MIL-100(Fe) metal-organic framework, Journal of Physical Chemistry C 123 (2019) 23014-23025.

[48] A. Karami, R. Sabouni, M. Ghommem, Experimental investigation of competitive co-adsorption of naproxen and diclofenac from water by an aluminium-based metal-organic framework, Journal of Molecular Liquids 305 (2020) 112808.

[49] A. Rezk, R. Al-Dadah, S. Mahmoud, A. Elsayed, Experimental investigation of metal organic frameworks characteristics for water adsorption chillers, Journal of Mechanical Engineering Science 227 (2013) 992-1005.

[50] J. Liu, X. Tang, X. Liang, L. Wu, F. Zhang, Q. Shi, J. Yang, J. Dong, J. Li, Superhydrophobic zeolitic imidazolate framework with suitable SOD cage for effective $CH_4/N_2$ adsorptive separation in humid environments, Separations: Materials, Devices and Processes 68 (2022) e17589.

[51] H. Shang, F. Zhang, J. Liu, X. Zhang, J. Yang, L. Li, J. Li, Enriching low-concentration coalbed methane using a hydrophobic adsorbent under humid conditions, Industrial and Engineering Chemistry Research 60 (2021) 12689-12697.

[52] Z. Yang, M. Hussain, P. Marín, Q. Jia, N. Wang, S. Ordóñez, Y. Zhu, Y. Xia, Enrichment of low concentration methane: an overview of ventilation air methane, Journal of Materials Chemistry A 10 (2022) 6397-6413.

[53] F. Jeremias, A. Khutia, S. Henninger, C. Janiak, MIL-100(Al, Fe) as water adsorbents for heat transformation purposes – a promising application, Journal of Materials Chemistry 22 (2012) 10148-10151.

[54] M. Schmal, M. Souza, V. Alegre, M. da Silva, D. César, C. Perez, Methane oxidation-effect of support, precursor and pretreatment conditions – in situ reaction XPS and DRIFT, Catalysis Today 118 (2006) 392-401.

[55] M. Mohammadnejad, M. Fakhrefatemi, Synthesis of magnetic HKUST-1 metal-organic framework for efficient removal of mefenamic acid from water, Journal of Molecular Structure 1224 (2021) 129041.

[56] A. Hoffman, L. Vanduyfhuys, I. Nevjestic, J. Wieme, S. Rogge, H. Depauw, P. Van der Voort, H. Vrielinck, V. Speybroeck, Elucidating the vibrational fingerprint of the flexible metal-organic framework MIL-53(Al) using a combined experimental/computational approach, The Journal of Physical Chemistry C 122 (2018) 2734-2746.

[57] F. Gul-E-Noor, B. Jee, A. Pöppl, M. Hartmann, D. Himsl, M. Bertmer, Effects of varying water adsorption on a $Cu_3(BTC)_2$ metal-organic framework (MOF) as studied by 1H and 13C solid-state NMR spectroscopy, Physical Chemistry Chemical Physics 13 (2011) 7783-7788.

[58] D. Ursueguía, E. Díaz, S. Ordóñez, Densification-induced structure changes in Basolite MOFs: Effect on low-pressure CH4 adsorption, Nanomaterials 10 (2020) 1089.

[59] X. Qian, B. Yadian, R. Wu, Y. Long, K. Zhou, B. Zhu, Y. Huang, Structure stability of metal-organic framework MIL-53(Al) in aqueous solutions, International Journal of Hydrogen Energy 38 (2013) 16710-16715.

[60] R. Maia, B. Louis, W. Gao, Q. Wang, $CO_2$ adsorption mechanisms on MOFs: a case study of open metal sites, ultra-microporosity and flexible framework, Reaction Chemistry and Engineering (2021).

[61] M. Du, L. Li, M. Li, R. Si, Adsorption mechanism on metal organic frameworks of Cu-BTC, Fe-BTC and ZIF-8 for CO2 capture investigated by X-ray absorption fine structure, RSC Advances 6 (2016) 62705-62716.

[62] A. Yazaydin, A. Benin, S. Faheem, P. Jakubczak, J. Low, R. Willis, R. Snurr, Enhanced $CO_2$ adsorption in metal-organic frameworks via occupation of open-metal sites by coordinated water molecules, Chemistry of Materials 21 (2009) 1425-1430.

[63] Y. Seo, J. Yoon, J. Lee, U. Lee, Y. Hwang, C. Jun, P. Horcajada, C. Serre, J. Chang, Large scale fluorine-free synthesis of hierarchically porous iron(III) trimesate MIL-100(Fe) with a zeolite MNT topology, Microporous and Mesoporous Materials 157 (2012) 137-145.

[64] X. Wang, F. Zhou, Y. Ling, Y. Xiao, B. Ma, X. Ma, S. Yu, H. Liu, K. Wei, J. Kang, Overview and outlook on utilization technologies of low-concentration coal mine methane, Energy Fuels 35 (2021) 15398-15423.

## 4.3. MODELIZACIÓN Y PASO DE ESCALA DEL PROCESO DE ADSORCIÓN

La variedad de condiciones ensayadas se podrán utilizar para el modelizado matemático de una operación de adsorción en lecho fijo. Un adecuado modelizado del proceso es muy importante en operaciones de adsorción y separación, ya que facilita el diseño y permite la optimización de condiciones experimentales. Además, el modelo será de gran utilidad para la realización de un paso de escala teórico previo a la implantación real.

El modelo matemático propuesto, basado en ecuaciones diferenciales que describen un proceso dinámico de adsorción en lecho fijo, se comprobará a partir de los resultados experimentales obtenidos, correspondientes a una operación de adsorción de una corriente de metano (2%) y nitrógeno (98%) sobre los tres materiales comerciales estudiados: Basolite C300, Basolite F300 y Basolite A100. Teniendo en cuenta las distintas asunciones físicas realizadas para la generación del modelo (unidimensionalidad, carácter isotermo, dispersión radial despreciable, control limitante de la interfase en el transporte de materia, etc.), y asumiendo Langmuir como el modelo de equilibrio, se obtienen buenos resultados en el ajuste de los valores experimentales para los tres materiales, con un $R^2 > 0.94$ en todos los casos. Además, el modelo propuesto muestra un adecuado grado de ajuste a datos experimentales extraídos de la bibliografía para la adsorción de metano en lecho fijo sobre un óxido de silicio en condiciones similares, lo que confirma la validez del modelo matemático. Asimismo, se observa un buen grado de ajuste a la etapa de desorción experimental ($R^2=0.98$) en el caso del MOF con el mejor rendimiento de los estudiados, Basolite C300. Este material es capaz de obtener, tras la desorción, una concentración final de metano de 2.94% en el flujo de salida.

Estos resultados aseguran la posibilidad de simular el proceso completo de adsorción y desorción de metano de baja concentración propuesto, así como varias etapas consecutivas, dando lugar a ciclos. El modelo se valida a partir del software COMSOL Multiphysics, que resuelve la ecuación diferencial propuesta a partir de los datos experimentales suministrados. A partir del modelo validado, es posible la realización de estudios paramétricos de

distintas propiedades físicas: longitud de lecho, flujo de entrada, tamaño de partícula, dispersión axial y difusividad en microporos. Esto permitirá estudiar el efecto de los distintos parámetros sobre la curva de ruptura, siendo de gran utilidad para futuros pasos de escala, así como para la optimización del proceso.

A partir del modelo matemático, se ha estudiado el rendimiento de distintos materiales adsorbentes (carbones activos, zeolitas y MOFs) en procesos TSA y PSA de recuperación y concentración de metano en un lecho fijo adsorbente. Para ello, se utiliza el mismo modelo diferencial, con las mismas asunciones físicas, y se resuelve a partir del software Aspen Adsorption. Los parámetros físicos de cada material estudiado se obtienen a partir de la bibliografía. La concentración inicial de metano simulada (0.57%) se obtiene a partir de registros aportados por explotaciones mineras reales en sus conducciones de ventilación. Los resultados muestran que los materiales carbonosos presentan una capacidad mayor de concentración ($C/C_0$ = 5), con una baja recuperación de metano (30%) y un bajo coste por metano recuperado (1.5 €/kmol). Por otro lado, las zeolitas presentan selectividades muy bajas ($C/C_0$ = 2), con buenas recuperaciones de metano (58%) y un coste elevado (25 €/kmol). Finalmente, los MOFs muestran un factor de concentración intermedio ($C/C_0$ = 2.6), con una práctica totalidad del metano recuperado, pero un coste muy elevado (80 €/kmol). De hecho, se concluye que su elevado coste es la característica más limitante de estos materiales, ya que son materiales con rendimientos muy prometedores pero con un elevado coste de síntesis. En lo relativo a la técnica de adsorción utilizada, TSA muestra mejores resultados para materiales carbonosos y MOFs, mientras que PSA es más adecuado en el trabajo con zeolitas. Por otro lado, en todos los casos la técnica TSA muestra procesos con menores costes asociados.

Por último, conocidos los buenos rendimientos resultantes de la combinación de adsorción con MOFs y la técnica TSA, se realizará una simulación a escala real de un proceso de adsorción y recuperación TSA en lecho fijo, relleno del MOF Basolite C300. Además, este proceso se unirá en serie a una recuperación energética de la corriente resultante mediante una turbina de gas pobre. Por tanto, a partir del modelo de adsorción validado

anteriormente y el diseño de una turbina de gas pobre mediante Aspen Hysys, es posible estimar el rendimiento global y realizar un análisis económico del proceso. La simulación se realiza partiendo de un paso de escala, tomando valores reales registrados en corrientes VAM (4.4 $Nm^3/s$ y 0.57% $CH_4$ en aire). El proceso de adsorción permite obtener una corriente de salida con 1.2% $CH_4$, y un flujo total de 3.8 $Nm^3/s$. Consecuentemente, la turbina genera 490 kW netos, y aporta la energía necesaria en la etapa de desorción de la TSA. Finalmente, un análisis económico del proceso completo indica que el retorno de la inversión inicial depende en gran medida del coste del adsorbente, que debería estar en torno a 0.6 €/kg para comenzar a ser rentable. Los resultados muestran las dificultades de utilización, a día de hoy, de MOFs en procesos reales, con elevados costes asociados a su síntesis, además de los problemas de rendimiento mostrados en la Sección 4.2 en condiciones similares a las reales.

Los resultados obtenidos se presentan y discuten en las siguientes publicaciones científicas:

- David Ursueguía, Eva Díaz, Aurelio Vega, Salvador Ordóñez, Methane separation from diluted mixtures by fixed bed adsorption using MOFs: Model validation and parametric studies, *Separation and Purification Technology* **251** (2020) 117374.
https://doi.org/10.1016/j.seppur.2020.117374
Factor de Impacto (2020): 7.312
Categoría (2020): Chemical Engineering (16/143: Q1)
Número de citas: 5

- David Ursueguía, Eva Díaz, Salvador Ordóñez, Adsorbents selection for the enrichment of low-grade methane coal mine emissions by temperature and pressure swing adsorption technologies, *Journal of Natural Gas Science and Engineering* **105** (2022) 104721.
https://doi.org/10.1016/j.jngse.2022.104721
Factor de Impacto (2021): 5.285
Categoría (2021): Chemical Engineering (35/143: Q1)
Número de citas: 1

- David Ursueguía, Pablo Marín, Eva Díaz, Salvador Ordóñez, A new strategy for upgrading ventilation air methane emissions combining adsorption and combustion in a lean-gas turbine, *Journal of Natural Gas Science and Engineering* **88** (2021) 103808.
https://doi.org/10.1016/j.jngse.2021.103808
Factor de Impacto (2021): 5.285
Categoría (2021): Chemical Engineering (35/143: Q1)
Número de citas: 4

## Methane separation from diluted mixtures by fixed bed adsorption using MOFs: model validation and parametric studies

David Ursueguía, Eva Díaz, Aurelio Vega, Salvador Ordóñez*

Catalysis, Reactors and Control Research Group (CRC), Department of Chemical and Environmental Engineering, University of Oviedo, Julián Clavería s/n, 33006 Oviedo, Spain

*e-mail: sordonez@uniovi.es (S. Ordóñez)

*Separation and Purification Technology* **251** (2020) 117374.

https://doi.org/10.1016/j.seppur.2020.117374

## ABSTRACT

Adsorption of methane from diluted methane/nitrogen mixtures in a fixed bed reactor was experimentally studied and modelled in this work. Three different metal-organic frameworks (MOFs), Basolite C300, F300 and A100 were considered for this purpose, the adsorption bed being operated at 298 K, 0.1 MPa, and an inlet methane concentration of 2%. Methane adsorption capacities decrease in the order: Basolite C300 (0.078 mmol/g) > Basolite F300 (0.040 mmol/g) > Basolite A100 (0.028 mmol/g). In addition, a mechanistic model based on the numerical solution of an heterogeneous one-dimensional model considering axial dispersion has been used for modelling these adsorption results. Proposed model provides a reasonable fitting of the experimental fixed bed results ($R^2$ > 0.9), using internal diffusion and axial dispersion as fitting parameters. Variation of these parameters can be explained in terms of adsorbent morphological features. Proposed model has been successfully extended to other methane adsorption processes reported in the literature, as well as to thermal desorption of methane from MOF-containing fixed bed reactors. The experimentally validated model has been used to predict the effect of main operation parameters on the performance of the MOF-based fixed beds for methane adsorption.

**Keywords**: $CH_4/N_2$ separation; fixed bed; breakthrough curve; COMSOL model; VAM

### 1. Introduction

Coal mines release methane to the atmosphere in the preconditioning stage previous to the coal bed exploitation, as well as during coal mining operations (coal mine methane) and also after the shafts closure [1]. It is estimated that only in the US, coal mines liberate about 112 Tg $CO_2$ eq. annually, of which less than 14% is recovered and used [2]. The remaining methane is vented to the atmosphere, representing a loss of valuable energy source. More than 90% of these coal mine methane emissions are believed to be from underground mines, of which about 70-80% is emitted in very diluted form (typically less than 1% of methane) through the mine ventilation air, which is known as ventilation air methane (VAM) [3]. It must be also considered that these emissions remain even after the coal mine closure. This desorption process may continue for many years after closure but at a rapidly declining rate and, where a mine is flooded, can resume when flooded mine workings are dewatered [4]. As a consequence, this methane constitutes an important hazard, thus exploitation or mitigation of methane from closed underground coal mines will minimize potential hazards, reduce emissions and potentially create revenue [5].

The main features of the VAM emissions are their low methane concentration (0.1-1%) and high flow rates (up to 600 $m^3/s$), a direct upgrading of these streams being strongly hindered [6]. The most feasible and environmentally friendly solution is to pre-concentrate methane in these streams. The main components of the streams are nitrogen, carbon dioxide, oxygen, water and methane [7], being needed to separate methane from the other components [8]. Nitrogen is the main component in the mixture (~ 78%), and it is also the most similar in molecular size to methane (3.64 and 3.80 Å [9], respectively). In addition, both molecules present a null dipole moment. These

features make the separation $CH_4/N_2$ the most complicated to carry out.

Fakhroleslam and Fatemi [10], compare methane purification techniques (pressure swing adsorption, vacuum swing adsorption and temperature swing adsorption) using SAPO-34-core-shell as adsorbent, concluding that temperature swing adsorption (TSA) reaches the best purification efficiency. In fact, TSA is usually recommended in purification processes from lean mixtures (< 2% of the interesting compound) [11]. Concerning the adsorbent, among different materials tested for this separation: inorganic materials [12-15], carbonaceous adsorbents [16], and metal-organic frameworks (MOFs) [17-20], the latter are considered the most promising behavior in the methane separation from a diluted stream. Although several works are focused on the adsorbent selection and the study of the adsorption equilibrium [19, 20], the study of the adsorption dynamics is not so developed, in spite of its larger importance in the design of adsorption-based processes.

If the adsorption of other lean gases is considered, several studies on the modelling of breakthrough curves for $CO_2$ [21], and $H_2S$ [22] gas adsorption have been published. Several previous works deal with the $CO_2$ adsorption from a methane stream [8], and even, Delgado et al. [23] published data on methane adsorption from methane/nitrogen mixtures where methane concentrations vary from 8 to 70%. Although some of these works applied mathematical models to predict the adsorption fixed bed dynamics in terms of partial differential equations [23], with its consequent complexity; it is still required the development of mechanistic and rigorous models for simulating the saturation and operation of the adsorption bed in several conditions. Concerning modelling approach for selective separation from diluted streams [24, 25], most of the works apply Gran Canonical Monte-Carlo (GCMC) method for the simulations, which allows simulating the adsorptive behavior of the materials at certain conditions and with different structural variations in the adsorbents [26, 27], but they are not suitable for providing rigorous simulation of fixed bed adsorption processes at operating conditions.

With this background, the challenge addressed in this work is focused on two underdeveloped fields: the methane/nitrogen separation from streams with low methane concentration, as well as the rigorous modelling of the breakthrough curves of the adsorption process. Fixed-bed adsorption process was numerically modeled using an axially dispersed plug flow model with non-linear isotherms based on the linear driving force (LDF) approximation. A parametric study shows the effect of some operational parameters (particle size, inlet flow and adsorbent bed parameters) on intrinsic parameters (axial dispersion and mass transfer resistance) and then, on the final performance. Simulated data were validated with the experimental results of methane adsorption present in low-concentrated currents from nitrogen in a fixed-bed operated at lab scale, using as adsorbents three of the most used commercial MOFs (Basolite C300, F300 and A100).

## 2. Experimental section

### 2.1. Materials

Basolite F300 [iron 1,3,5 benzenetricarboxylate, $C_9H_3FeO_6$], Basolite C300 [copper 1,3,5 benzenetricarboxylate, $Cu_3(C_9H_3O_6)_2$] and Basolite A100 [Aluminium terephthalate, $C_8H_5AlO_5$], all supplied by Badische Anilin- und Soda-Fabrik (BASF), were used as adsorbents without further purification. All the gases used in this work, methane ($CH_4$), nitrogen ($N_2$) and helium (He), had purity higher than 99.995% mol, and were supplied by Air Liquide. Table 1 provides a morphological description of the three adsorbent materials.

Table 1. Morphological specifications of the materials according to the manufacturer

| Parameter | Basolite C300 | Basolite F300 | Basolite A100 |
|---|---|---|---|
| Density (kg/m³) | 350 | 160-350 | 400 |
| Pore size (Å) | 11/10/4[a] | 18/5.5/8.6[b] | 8.5[c] |
| Specific surface (m²/g) | 1500-2100 | 1300-1600 | 1100-1500 |
| Particle size (μm) | 16 (D50) | 5[d] | 32 (D50) |

[a][28]
[b][29]
[c][30]
[d][31]

### 2.2. Apparatus and experimental procedure

Adsorption experiments were performed by passing gas mixtures through a column packed with the adsorbent. This packed bed consisted of a stainless steel tube of 520 mm length and 6.4 mm of internal diameter. Adsorbents (0.5 g) with particle sizes between 5 and 32 μm were placed in the middle of the tube and in contact with a K-type thermocouple which gave the actual temperature values throughout the experiments. The length of the adsorbent bed is 45 mm for

Basolite C300 and F300, and 39 mm for Basolite A100, respectively. These values confirmed the plug flow regime restrictions [32]: $D/d_p > 10$ and $L/d_p > 50$, being D the adsorbent bed diameter, L the bed length and $d_p$ the particle size. Pressure drop along the fixed bed is about 0.06 MPa for all cases. The remaining void column volume was filled with glass beads (1 mm). The flowrate of each gas was controlled with mass flow controllers (Bronkhorst), being the total flow 50 ml/min at 0.1 MPa and 298 K.

Prior to the adsorption tests, the surface of the adsorbent is cleaned and degasified by a pure helium flow (50 ml/min) at 373 K until no other gases were detected in the analyzer. Then, adsorption experiments were conducted at 298 K, and the gases were mixed before entering to the fixed bed. The effluent gases were analyzed by mass spectrometry in a previously calibrated Pfeiffer Vacuum apparatus. On the other hand, desorption experiments were conducted at 333 K using nitrogen as carrier gas (1 ml/min and 0.1 MPa) through the fixed-bed previously saturated in the problem mixture. As in the adsorption stage, the outlet is analyzed by the mass spectrometer.

In addition, concentrations of both gases (methane and nitrogen) between 0 and 5% in helium were introduced into the fixed bed at the same conditions (298 K, 0.1 MPa) with the aim of obtaining the methane and nitrogen adsorption isotherms. The same experience was performed at 333 K in the desorption stage for different inlet methane concentrations (0 – 5%) for saturation, thus obtaining the desorption constants.

Breakthrough theoretical curves, and subsequent parametric variations, were obtained from a partial differential equations (PDE) solver (COMSOL Multiphysics® Version 5.4.) that solves the theoretical model equations numerically. The accuracy of the predicted models was measured comparing the R-squared method of experimental and theoretical results.

## 3. Mathematical model

### 3.1. Breakthrough curve model

Fixed bed adsorption/desorption experiments were modelled using a dynamic heterogeneous one-dimensional model. Gas and solid phases were independently considered, which allows observing differences in the concentration of both phases. Isothermal conditions, negligible radial dispersion and changes in fluid velocity, as well as spherical and homogeneous in size and density adsorbent particles (bed void fraction constant) are assumed. The isothermal character is assumed considering both the low adsorption enthalpies (~ 20 kJ/mol) [33, 34], and the high adsorbate dilution. This dilution, and the high $D/d_p$ and $L/d_p$ ratios, allow considering the flow through the bed as turbulent.

The differential mass balance for the adsorbate in the gas phase includes accumulation, convection flow, axial dispersion and the interphase transfer or adsorption rate. In the solid phase, accumulation and the interphase transfer terms are included, as summarized in Table 2.

Interphase mass transfer is considered by the dependent variable $q_i$, which corresponds with the *i* component concentration in the solid phase, and correlates this transport with an equilibrium gradient. This last assumption is valid, because of the absence of chemical reaction in both phases as well as the negligibility of physical transport effects on the solid phase.

Equilibrium isotherms were determined in a previous work [35]. A simple Langmuir model was used to adjust it (Equation 1). $Q_{mi}$ and $K_{Li}$ are the parameters of the simple Langmuir model for each gas.

$$W_{ieq} = \frac{Q_{mi} \cdot K_{Li} \cdot C_i}{1 + K_{Li} \cdot C_i} \quad (1)$$

In order to solve the differential equations, Danckwerts boundary conditions (Table 3) were considered as currently proposed for fixed beds [36]. These conditions are taken for the both ends of the fixed bed ($z = 0$ and $z = L_b$).

### 3.2. Physical and transport properties

Gas phase physical properties (density, viscosity, heat capacity and thermal conductivity) are assumed to be the corresponding to the diluent (nitrogen or helium), due to the low methane concentration (max. 5%). Solid physical properties are known or estimated from the specifications of the manufacturer.

One of the most important transport properties is axial dispersion ($D_e$). This property is calculated from Edwards and Richardson's correlation (Equation 2). This correlation is based on the Péclet number (Pe), defined as the relation between convection and diffusion in a mass or heat transport process, in which the particle size is the characteristic length [21]. On the other hand, $D_m$ is the molecular diffusion, calculated by the Fuller-Schettler-Gridding correlation (Equation 3) [37]. The surface velocity ($u_o$) is easily calculated from the inlet flow and the cross-section of the fixed bed. The bed porosity is approximated to 0.4

according to Theuerkauf et al. [38], supposing randomly packed bed of spheres.

$$D_e = 0.73 \cdot D_m + \frac{0.5 \cdot u_0 \cdot d_p}{1 + 9.49 \cdot \frac{D_m}{u_0 \cdot d_p}} \quad (2)$$

$$D_m = \frac{0.001 \cdot T^{1.75} \cdot \left(\frac{1}{M_A} + \frac{1}{M_B}\right)}{P \cdot \left(V_A^{\frac{1}{3}} + V_B^{\frac{1}{3}}\right)^2} \quad (3)$$

In the adsorption process, the interphase mass transport, $dq_i/dt=k_L\cdot(W_{ieq}-W_i)$, controls the mass transfer step in the process and it is described in terms of crystal radius ($r_c$), effective diffusivity ($D_i$) and equilibrium parameters, according to Equation 4 [39].

$$\frac{1}{k_L} = \frac{r_p \cdot W_0}{3k_f \cdot C_0} + \frac{r_p^2 \cdot W_0}{15 \cdot \varepsilon_p \cdot D_p \cdot C_0} + \frac{r_c^2}{15 \cdot D_i} \quad (4)$$

In Equation 4, $k_L$ considers all the mass-transfer resistances for the transport of the adsorbate from the bulk gas phase to the adsorbent surface. The first term is related to the external fluid film resistance, which depends linearly on the adsorbent particle radius ($r_p$), and it is appreciable when the adsorption rate is limited by the flow of the gas to the surface. The $k_f$ parameter is the film mass transfer coefficient and $W_o$ is the solid phase adsorbate concentration in equilibrium with the inlet gas-phase concentration ($C_o$). The second term is related to the diffusion in macropores as the controlling step, which is important when most of the pores in the adsorbent are macropores, or when its size (more than 50 nm) limits the entrance of adsorbate molecules; $D_p$ being the macropore diffusivity. The last term is important when the adsorption is controlled by the diffusion in micropores, as taking place when most of the pores are microporous (up to 2 nm). In this case, $D_i$ is the micropore diffusivity. The great crystallinity of these materials at its original form, makes it possible to assimilate crystal and particle radius.

Due to the high microporous character of MOFs and the small size of their pores, the final equation for the mass transport is (Equation 5):

$$\frac{dq_i}{dt} = 15 \cdot \frac{4D_i}{d_p^2} \cdot \left(W_{ieq} - W_i\right) \quad (5)$$

Where $W_{ieq}$ is the solid-gas equilibrium concentration that can be calculated through the adsorption isotherm of the material. Thus, there is an intraparticle resistance at micropores with a surface diffusion mechanism.

In summary, the final equations for the model are summarized in Table 4.

## 4. Results and discussion

### 4.1. Fixed bed adsorption

#### *4.1.1. Single adsorbate adsorption*

Experimental breakthrough adsorption curves of 5% methane and nitrogen in helium over the three Basolites tested in this work are shown in Figure 1, whereas Table 5 includes the parameters used in COMSOL Multiphysics implementation to perform the theoretical simulations. The microporous diffusivity term ($D_i$) is used as the fit parameter to the experimental data due to its difficult experimental calculation reported by other authors [21, 40]. Basolite C300 presents the highest adsorption capacity for both adsorbates (Table 6) and also, more remarkable for methane, in agreement with the $CH_4/N_2$ adsorption isotherms [35].

The best fitting to the model was obtained for the Basolite A100 ($R^2$ = 0.99 for both methane and nitrogen), followed by Basolite C300 (0.96 and 0.98) and Basolite F300 (0.94 and 0.98). The estimated values of the micropore diffusivity ($D_i$) were $8.1\cdot10^{-10}$, $7.2\cdot10^{-10}$ and $5.1\cdot10^{-11}$ m²/s for C300, F300 and A100, respectively in case of methane, and $8.2\cdot10^{-9}$, $7.3\cdot10^{-9}$ and $4.2\cdot10^{-11}$ m²/s, respectively in case of nitrogen. These values are similar to those presented by Bárcia et al. [41] for MOF-508b, obtained also by fitting the experimental responses, and also to the micropores diffusion obtained experimentally from kinetic studies on Mg-MOF-74 by Bao et al. [42]. Therefore, with a single fit parameter, it is possible to obtain a good fitting to experimental results but with some deviations in the slopes, especially for C300 and F300. Observed deviations are due to consider the same axial dispersion coefficient for all materials, based on the low-sensitive correlation used (Equation 2). Thus, considering $D_e$ another fitting parameter (keeping the previous $D_i$ values), a reduction of axial dispersion coefficients is observed for Basolite F300 and C300: $9.1\cdot10^{-6}$ and $5.2\cdot10^{-6}$ m²/s, respectively for methane, and $2.1\cdot10^{-5}$ and $9.1\cdot10^{-6}$ m²/s, respectively for nitrogen.

Table 2. Terms of the model differential equations.

| | Accumulation | Convection | Dispersion | Interphase | Reaction |
|---|---|---|---|---|---|
| Gas mass balance | $\frac{\partial C_i}{\partial t} =$ | $-\frac{u_0}{\varepsilon_b}\frac{\partial C_i}{\partial z}$ | $+D_e\frac{\partial^2 C_i}{\partial z^2}$ | $-\rho_b\left(\frac{1-\varepsilon_b}{\varepsilon_b}\right)\frac{\partial q_i}{\partial t}$ | |
| Solid mass balance | $\frac{\partial W_i}{\partial t} =$ | | | $+\frac{\partial q_i}{\partial t}$ | |

Table 3. Boundary conditions.

| | z = 0 | z = $L_b$ |
|---|---|---|
| Gass mass balance | $(C)_{0^-} = (C)_{0^+} - \frac{D_e}{v_0}\left(\frac{\partial C}{\partial z}\right)_{0^+}$ | $\left(\frac{\partial C}{\partial z}\right)_{z=L_b} = 0$ |
| Solid mass balance | $\left(\frac{\partial W}{\partial z}\right)_{z=0^+} = 0$ | $\left(\frac{\partial W}{\partial z}\right)_{z=L_b} = 0$ |

Modifications in $D_e$ and $D_i$ parameters do not affect the total adsorption capacity of each material, which remains constant for both simulations. The area behind the breakthrough curve is the same for each material and gas in each case. Simulations led to higher regression coefficients in all cases, Figure 1. Likewise, Basolite A100 keeps the same values. Axial dispersion coefficient is higher for Basolite A100 due to the highest particle diameter, already considered in the correlation (Equation 2). Therefore, the correlation seems to be more applicable for materials with high densities and particle sizes.

Experimental results show that Basolite C300 presents the maximum adsorption capacity of the three studied materials, both for nitrogen and methane (Table 6). This fact corresponds with the order in specific surface of the materials, which is especially important at high pressures, at which there is usually a linear relationship between both parameters [43]. In those cases, the gas is distributed on the surfaces in relation to the available space.

Table 4. Final equations for the proposed model for fixed bed adsorption.

| | Accumulation | Convection | Dispersion | Interphase |
|---|---|---|---|---|
| Gas mass balance | $\frac{\partial C_i}{\partial t} =$ | $-\frac{u_0}{\varepsilon_b}\frac{\partial C_i}{\partial z}$ | $+D_e\frac{\partial^2 C_i}{\partial z^2}$ | $-15\cdot\frac{4\cdot\rho_b\cdot(1-\varepsilon_b)}{\varepsilon_b\cdot d_p^2}\cdot D_i\cdot(W_{ieq}-W_i)$ |
| Solid mass balance | $\frac{\partial W_i}{\partial t} =$ | | | $+15\cdot\frac{4\cdot D_i}{d_p^2}\cdot(W_{ieq}-W_i)$ |

In addition, Basolite C300 also presents a high concentration of open metal sites in its structure (31.5% of copper), compared to 21.2% of iron for Basolite F300 and 12.9% of aluminium in Basolite A100, being remarkable that the trend is the same than in the previous case [44]. This may be one of the reasons why these materials clearly present greater adsorption capabilities than other common adsorbents, such as carbon nanotubes [45] or zeolite 4A [14], at similar temperatures and partial pressures. In any case, the two previous parameters cannot explain certain deviations of the theoretical behavior. For example, Basolite A100 presents higher adsorption capacity for methane than Basolite F300, despite its specific surfaces are very different, as well as its metal content. This fact suggests that mass transfer effects play a key role in the fixed bed dynamics.

At this point, the resulting fitting parameter ($D_i$) is higher for nitrogen. Nitrogen presents smaller molecular size than methane (3.65 and 3.82 Å, respectively), thus it is easier to penetrate in the structure of the adsorbent. However, for Basolite A100, the presence of methane induces the existence of a large-pore configuration that makes $D_i$ higher for methane, promoting the penetration [46], so it could be the reason of the higher adsorption capacity than Basolite F300.

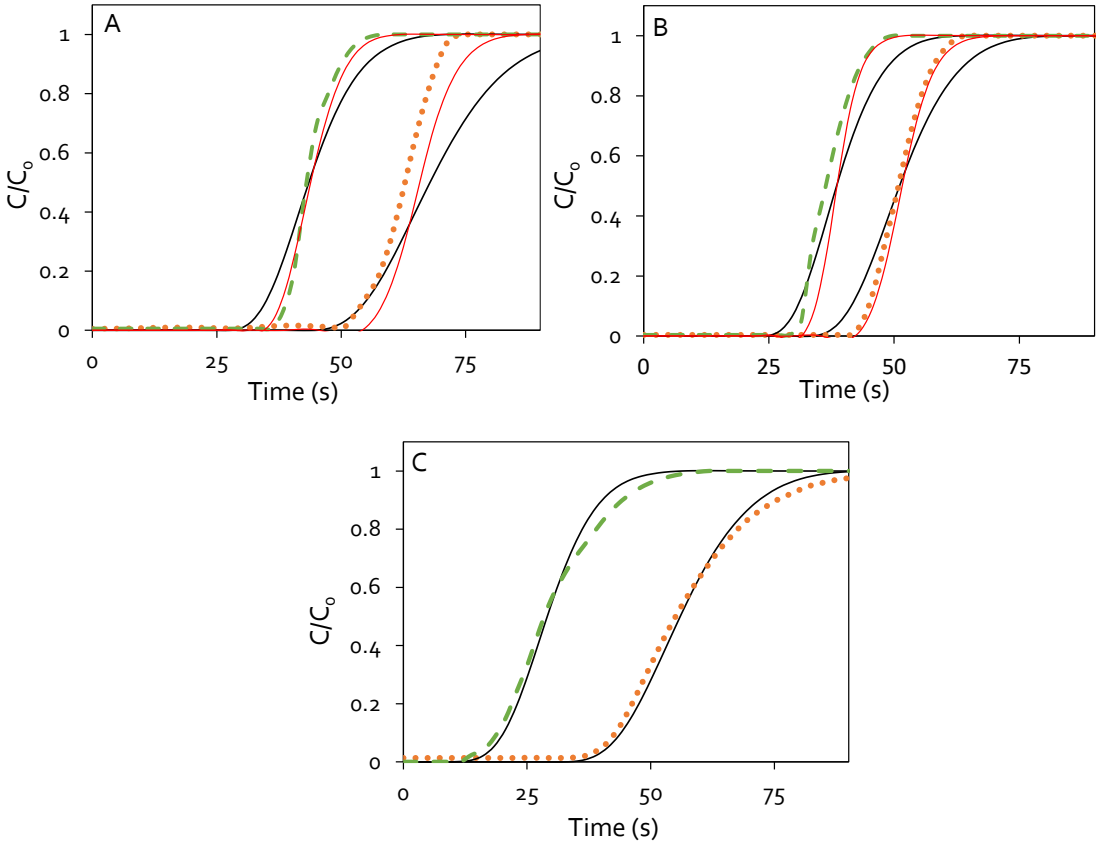


Figure 1. Breakthrough curves of Basolite C300 (A), Basolite F300 (B) and Basolite A100 (C) (5% of methane (orange dotted line) and nitrogen (green discontinuous line) in helium) 298 K, 0.1 MPa. Black solid lines correspond to fitting only considering $C_i$ as fitting parameter whereas coloured solid lines correspond to fit both $D_i$ and $D_e$.

Table 5. Parameters used in COMSOL simulation to solve the differential equations for adsorbate/helium mixtures. A multifrontal massively parallel sparse direct solver (MUMPS) has been implemented as model solver in the program.

| METHANE | | | | | | |
|---|---|---|---|---|---|---|
| Material | $u_0$ (m/s) | $\varepsilon_b$ | $D_e$ (m²/s) | $\rho_b$ (kg/m³) | $d_p$ (m) | $K_{Hi}$ (mol/kg) |
| C300 | 0.026 | 0.4 | $4.6 \cdot 10^{-5}$ | 350 | $16 \cdot 10^{-6}$ | 4.53 |
| F300 | 0.026 | 0.4 | $4.6 \cdot 10^{-5}$ | 350 | $16 \cdot 10^{-6}$ | 3.40 |
| A100 | 0.026 | 0.4 | $4.6 \cdot 10^{-5}$ | 400 | $16 \cdot 10^{-6}$ | 4.08 |
| NITROGEN | | | | | | |
| Material | $u_0$ (m/s) | $\varepsilon_b$ | $D_e$ (m²/s) | $\rho_b$ (kg/m³) | $d_p$ (m) | $K_{Hi}$ (mol/kg) |
| C300 | 0.026 | 0.4 | $5.1 \cdot 10^{-5}$ | 350 | $16 \cdot 10^{-6}$ | 2.88 |
| F300 | 0.026 | 0.4 | $5.1 \cdot 10^{-5}$ | 350 | $5 \cdot 10^{-6}$ | 2.64 |
| A100 | 0.026 | 0.4 | $5.1 \cdot 10^{-5}$ | 400 | $32 \cdot 10^{-6}$ | 2.23 |

Table 6. Adsorption capacity ($W_{ieq}$) of $CH_4$ and $N_2$ (5%) in He at 0.1 MPa of total pressure and 298 K.

| Adsorbent | Methane uptake (mg/g) | Nitrogen uptake (mg/g) |
|---|---|---|
| Basolite C300 | 0.23 | 0.14 |
| Basolite F300 | 0.17 | 0.13 |
| Basolite A100 | 0.20 | 0.11 |

It could also explain the highest adsorption values in case of Basolite C300 despite its smaller pore size, but it has higher micropore volume, 0.56 cm³/g versus 0.30 and 0.35 cm³/g for F300 and A100, respectively, which also eases the accessibility (higher $D_i$) [35]. Finally, physical properties could increase the diffusional effects and also the slope of the breakthrough curve. For

example, in case of Basolite A100, for the same adsorbent weight, due to its higher density, the bed length is reduced. This fact, add to the largest particle size among the three materials, enhances the diffusional effects [32], thus a higher curve inclination is observed. The latter concept highlights the importance of axial dispersion ($D_e$), as it was shown in Figure 1.

The developed model was applied to experimental data obtained from the literature [23], observing the goodness of the fitting, Figure 2. Delgado et al. [23] used silicalite for the designing of a pressure swing adsorption process. The bed length and diameter (0.163 and 0.016 m, respectively) are close to the experimental device used in the present work. Langmuir isotherm was also used by the authors in order to obtain equilibrium data at 0.09 MPa and 298 K for an initial methane concentration of 14% in helium. Applying the COMSOL generated model to the experimental data of the work, the simulated breakthrough time is really similar to the experimental data, but the slope of the curve is higher, indicating a higher simulated dispersion. The value of $D_i$ is $9.1 \cdot 10^{-10}$ $m^2/s$, higher than for methane adsorption on MOFs, which involves the easiness to penetrate into the structure, as it could be expected from the higher pore size and particle macroporosity. The slight deviation of the simulation respect to the slope of the experimental data is corrected in a second simulation, by modifying the value of $D_i$ up to $1.5 \cdot 10^{-9}$ $m^2/s$, which indicates a higher mass transfer rate than the considered initially.

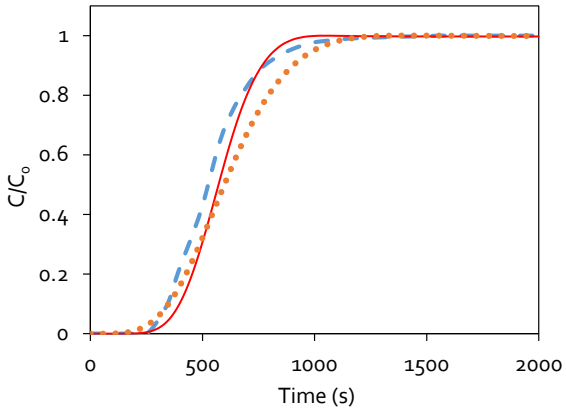


Figure 2. Application of the generated mathematical model to other material and process (silicalite for methane/helium (14/86) at 0.09 MPa and 298 K [23]). This work's model [orange dotted line (first simulation) and red continuous line (second simulation)], other author's data (blue discontinuous line).

Thus, developed model is suitable for a wide range of materials and conditions. In addition, the mass transfer, and, therefore, the morphology and the structure of the materials are the most important parameters for a suitable operation.

4.1.2. $CH_4/N_2$ adsorption

Figure 3 shows the methane breakthrough curve for the 2% of methane/nitrogen feed, at 298 K and 0.1 MPa, showing a situation closer to the VAM stream. Table 7 includes the parameters used in COMSOL Multiphysics implementation to perform the simulations. In this case, adsorption isotherms also consider the presence of nitrogen, which is also an adsorbable gas, since the adsorption of both gases occurs simultaneously [35], (Equation 2). Model fitting correlation ($R^2$) are: 0.99, 0.91 and 0.97 for Basolite C300, F300 and A100, respectively. $D_i$ is used as the only fitting parameter.

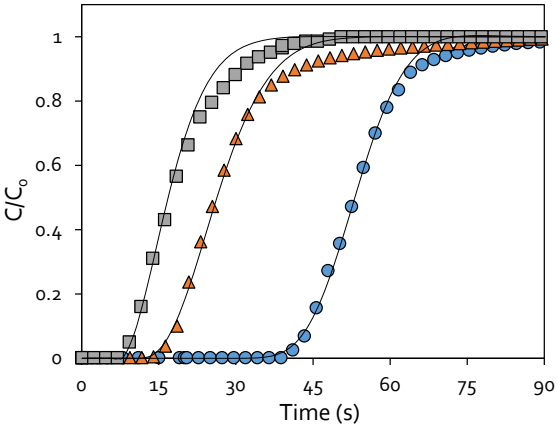


Figure 3. Methane breakthrough curves for low-grade methane adsorption (2% of methane in nitrogen, 50 ml/min) 298 K, 0.1 MPa. Basolite C300 (blue circles), Basolite F300 (orange triangles) and Basolite A100 (grey squares). Black lines symbolize the fit to the breakthrough curve model.

At these conditions, differences in the methane adsorption capacities are more marked than for methane diluted in a noble gas: Basolite C300 (0.078 mmol/g) > Basolite F300 (0.040 mmol/g) > Basolite A100 (0.028 mmol/g). In fact, the adsorption capacity of Basolite C300 is about 48.7% higher than for Basolite F300 in the $CH_4/N_2$ mixture, whereas only a 26.1% higher for experiences in inert diluent, as well as 64.1 versus 13% in Basolite A100 case. Thus, the largest Lewis acid concentration in Basolite C300 due to the metal open sites could favour the selective methane adsorption in presence of nitrogen, due to its higher polarizability [47]

Table 7. Parameters used in COMSOL simulation to solve the differential equations for methane/nitrogen mixtures.

| METHANE | | | | | | | |
|---|---|---|---|---|---|---|---|
| Material | $u_0$ (m/s) | $\varepsilon_b$ | $D_e$ (m2/s) | $\rho_b$ (kg/m3) | $d_p$ (m) | $K_{Li}$ (mol/kg) | $Q_{mi}$ (mol/kg) |
| C300 | 0.026 | 0.4 | $1.6 \cdot 10^{-5}$ | 350 | $16 \cdot 10^{-6}$ | 0.106 | 5.11 |
| F300 | 0.026 | 0.4 | $1.6 \cdot 10^{-5}$ | 350 | $16 \cdot 10^{-6}$ | 0.018 | 7.71 |
| A100 | 0.026 | 0.4 | $1.6 \cdot 10^{-5}$ | 400 | $16 \cdot 10^{-6}$ | 0.118 | 1.59 |

The obtained $D_i$ values are: $1.2 \cdot 10^{-12}$, $2 \cdot 10^{-13}$ and $5 \cdot 10^{-12}$ $m^2/s$, respectively for C300, F300 and A100. Basolite A100 presents the highest diffusivity coefficient in the methane/nitrogen mixture. Although the large-pore configuration of this material also enhances the nitrogen adsorption, its preference for methane adsorption (ratio of 2.12 for pure $CH_4/N_2$ adsorption at 298 K [35]) causes a substantial improvement in methane accessibility. The improved access to open metal sites favors especially methane adsorption, since methane polarizability is higher, thus its adsorption on acid centers [47] would increase the selectivity of the process. Similarly, Couck et al. [48] have observed the favored adsorption of $CO_2$ in the $CO_2/CH_4$ separation.

Concerning Basolite C300, Deniz et al. [49] have demonstrated the existence of two main adsorption sites in the structure. However, at low pressures, only the site near to the metal centers is active. This site allows the $CH_4/N_2$ separation (ratio of 2.04 for pure $CH_4/N_2$ adsorption at 298 K [35]). This adsorption ratio increases until reaching its maximum at 313 K (2.15), which points out a chemical specificity of the open Cu site [35]. Contrary, the same authors [49] have defined for Basolite F300 a single interaction area for all pressure range, with a $CH_4/N_2$ ratio = 2.11.

4.2. Fixed bed desorption

Proposed model will be only useful if it is also able to predict the behavior of the fixed bed during the regeneration. In order to obtain a concentrated methane stream at the outlet of the bed, a desorption curve for Basolite C300 is shown in Figure 4. Modelling of desorption operation after the adsorption one, just considers the operation conditions and the adsorbate transference from the solid to the gas phase. Desorption begins just after the low-grade methane (2%) adsorption stage. Once the bed access valves are closed, the temperature increase begins at 10 K/min until desorption temperature, 333 K, which is maintained for 2 hours. Then, valves are opened and 1 ml/min of nitrogen as drag gas is introduced at 0.1 MPa of total pressure. Nitrogen gas flow was selected as low as possible in order to get a methane concentrated stream. On the other hand, desorption temperature (333 K) was selected as a compromise between the thermal stability of the materials and the operational costs. In addition, the optimum temperature for $CO_2$ desorption from MOFs is about 373 K [50], so, for methane, a lower temperature could be enough due to its slightly weaker interaction. At these operation conditions, the maximum methane concentration obtained is 2.94% in nitrogen, so, a maximum concentration increment of 46.7% was achieved.

Simulation properties were calculated by analogy to adsorption, whereas desorption constant was determined from in situ experiences. Simulation parameters are summarized in Table 8, obtaining a good fit to the experimental data ($R^2$ = 0.98). It is remarkable the increase in the $D_i$ fit value ($9.1 \cdot 10^{-9}$ $m^2/s$), in comparison to adsorption one, which could be related to the temperature increment [51-53]. In addition, axial dispersion ($D_e$) is slightly oversized by the correlation, as expected when working at lower flow rates.

4.3. Parametric study of the effect of design parameters on the adsorption behaviour

Once checked the suitability of the mathematical model to the experimental results, the effect of varying operational parameters was studied in order to identify those parameters influencing adsorption behavior at larger extent. This parametric study was performed for Basolite C300 material. The study is divided into the different modified parameters.

Table 8. Desorption process data to solve differential equations

| METHANE | | | | | | |
|---|---|---|---|---|---|---|
| Material | $u_0$ (m/s) | $\varepsilon_b$ | $D_e$ (m²/s) | $\rho_b$ (kg/m³) | $d_p$ (m) | $K_{Hi}$ (mol/kg) |
| Basolite C300 | 0.00052 | 0.4 | $1.60 \cdot 10^{-6}$ | 350 | $16 \cdot 10^{-6}$ | 0.92 |

Increase in fixed bed length (1 to 8 cm), keeping porosity and density of the adsorbent, enhances the final total methane adsorbed and, hence, the breakthrough time. The equilibrium remains constant without variations in temperature or pressure (Figure 5). However, the pressure drop increases also with the bed length, reaching more than 0.1 MPa from 7 cm according to estimations from mechanical balance. Variations in the shape of the breakthrough curve, which losses its typical 'S' shape [54], were already reported after fixed bed length changes for very complex adsorbate molecules, far from the methane and nitrogen structures.

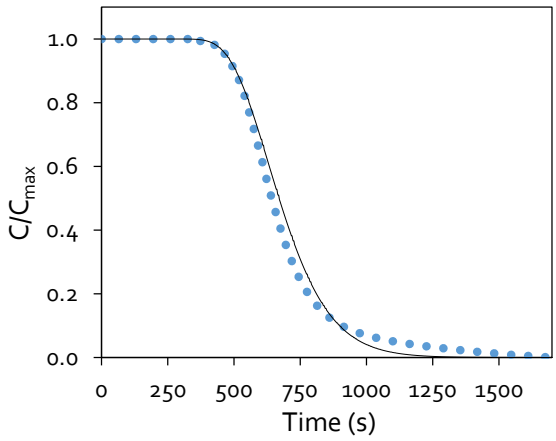


Figure 4. Methane desorption curve after low-grade methane adsorption (333 K, 1 ml/min of nitrogen and 0.1 MPa). Experimental data (blue filled circles). Black line symbolizes the fit to the desorption model generated. $C_{max,CH_4}$ = 2.94%.

Variations in the inlet flow (10 to 80 ml/min) influences directly the surface velocity in the fixed bed, and hence, the axial dispersion (Figure 6). According to Equation 2, the smallest particle size has a great influence on the axial dispersion value, so the variations of inlet flow are irrelevant. Likewise, the pressure drop in the bed increases with the inlet flow, being reduced the breakthrough time [55]. Final methane adsorption capacity does not vary since the equilibrium is unaltered. However, if the surface velocity hinders the appropriate gas-solid contact, a controlling step in the kinetics of the process would generate a premature breakthrough.

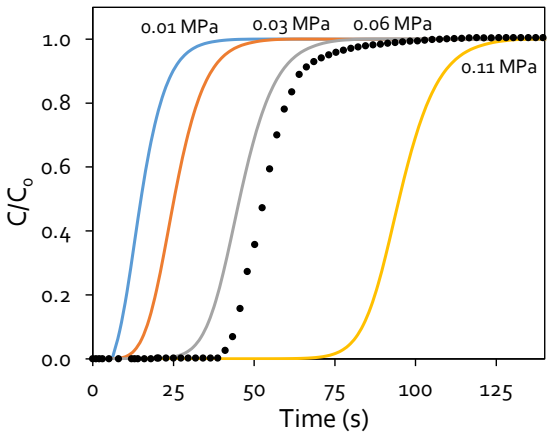


Figure 5. Methane breakthrough curves for low-grade methane adsorption onto Basolite C300 (2% of methane in nitrogen) 298 K and 1 bar for different bed lengths: 1 cm (blue), 2 cm (orange), 4 cm (grey) and 8 cm (yellow). Total pressure drops are provided near to each curve. Black dotted line corresponds to the experimental breakthrough curve.

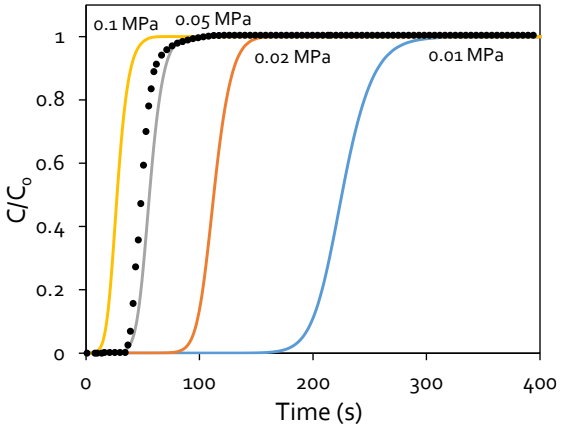


Figure 6. Methane breakthrough curves for low-grade methane adsorption onto Basolite C300 (2% of methane in nitrogen) 298 K and 1 bar for different inlet flows: 10 ml/min (blue), 20 ml/min (orange), 40 ml/min (grey) and 80 ml/min (yellow). Total pressure drops are indicated near to each curve. Black dotted line corresponds to the experimental breakthrough curve.

Adsorbent morphological parameters, specially particle size, undoubtedly affect the pressure drop and the adsorption yield. An increment in the particle size increases the mass transfer resistance, thus influences the adsorption rate due to the reduction of the interphase mass transfer coefficient (Equation 5). In addition, particle size has a direct influence above void fraction, which is an important parameter in the

mechanical balance to the pressure drop calculations. Figure 7 shows several simulations for changes in particle size (10 to 40 µm). Structure and internal parameters of the adsorbents are considered the same as in previous case, but other changes are taken into account, like bed density or bed length.

For the smallest particle sizes, it is observed the highest breakthrough time, since the smallest particles have a shorter diffusion path, thus allowing the adsorbate to penetrate deeper into the adsorbent particle more quickly [56]. On the other hand, high variations in the slopes of the curves are associated with the effect on axial dispersion of particle size increments, in addition to lower breakthrough times. Calculated pressure drops for each case by a mechanical balance are 0.16, 0.06, 0.02 and 0.01 MPa in increasing particle size order, respectively. This makes the pressure drop the limiting step in particle size effect, making necessary to reach a compromise between breakthrough time and pressure drop.

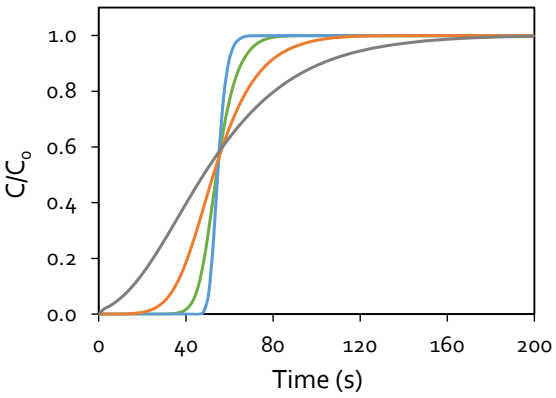


Figure 7. Methane breakthrough curves for low-grade methane adsorption onto Basolite C300 (2% of methane in nitrogen) 298 K and 1 bar for different particle sizes: 10 µm (blue), 16 µm (green), 25 µm (orange) and 40 µm (grey).

Variations in previous parameters involve intrinsic changes in the process, such as axial dispersion and mass transfer coefficient. From Equation 2, axial dispersion depends mainly on the particle diameter, the surface velocity and the molecular diffusion. An increment of any of these parameters results in axial dispersion enhancement. Likewise, the molecular diffusion increases with the temperature and decreases with pressure. Figure 8 shows the variation of the breakthrough curve with variations in axial dispersion ($5{\cdot}10^{-6}$ to $5{\cdot}10^{-4}$ m²/s), with unaltered curves for axial dispersion values lower than $5{\cdot}10^{-6}$ m²/s. Thus, adsorbate transport by axial dispersion is negligible in comparison to the convective transport [57]. Axial dispersion reaches the presented limiting value ($5{\cdot}10^{-4}$ m²/s) at 70 m/s of inlet velocity, 2 cm of particle diameter, 0.25 bar of total pressure or 1300 K of temperature, independently. All that values are unreachable for a device of these characteristics, so axial dispersion is not a limiting parameter.

On the other hand, the mass transfer coefficient depends mainly on the microporous diffusivity and the particle size. Figure 9 shows the influence on the breakthrough curve of the microporous diffusivity ($10^{-12}$ to $10^{-9}$ m²/s). For diffusivities lower than $10^{-12}$ m²/s, it is lost the typical shape due to the low intrapore diffusivity, so the more difficult penetration of the adsorbates in the structure of the adsorbent. In general, the larger the diffusivity, the smaller the diffusion resistance within the micropores, resulting in a steeper breakthrough curve. In addition, a higher particle size and a lower pore size difficult the molecules crossing through the pores, and, therefore, the interaction with open metal sites.

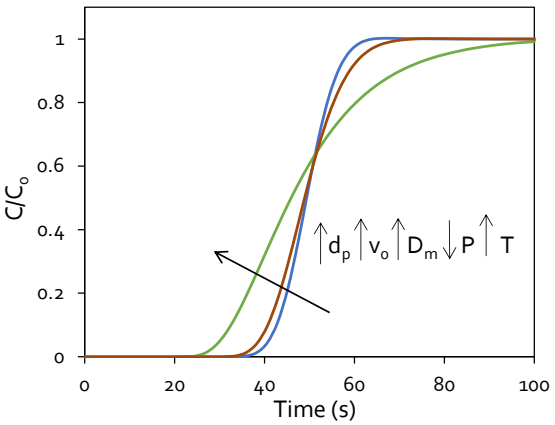


Figure 8. Methane breakthrough curves for low-grade methane adsorption onto Basolite C300 (2% of methane in nitrogen) 298 K and 0.1 MPa for different axial dispersions: $5{\cdot}10^{-4}$ m²/s (green), $5{\cdot}10^{-5}$ m²/s (brown) and $5{\cdot}10^{-6}$ m²/s (blue).

## 5. Conclusions

Materials with well-defined structures such as metal-organic frameworks are potential candidates to be used in gas separation operations. The presence of metal active adsorption sites, its high specific surface areas and the regular pore sizes, in addition to the existence of commercial available types, represent a starting point for industrial-scale production and use. A mathematical model that allows simulating a gas separation at low concentrations has been generated validating it with the laboratory low-methane concentration adsorption experiments on three Basolites (C300, F300 and A100).

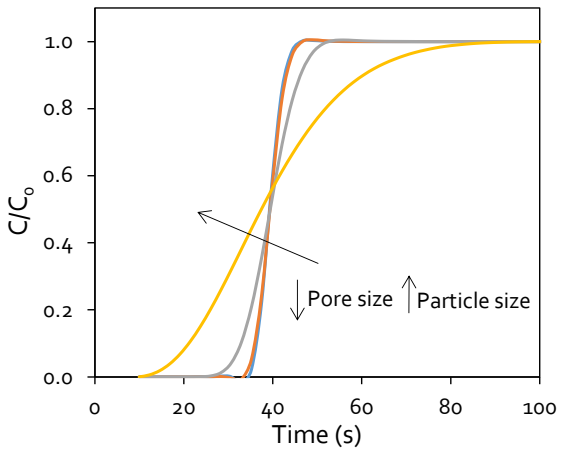


Figure 9. Methane breakthrough curves for low-grade methane adsorption onto Basolite C300 (2% of methane in nitrogen) 298 K and 0.1 MPa for different micropores diffusivities: $10^{-12}$ m²/s (yellow), $10^{-11}$ m²/s (grey), $10^{-10}$ m²/s (orange) and $10^{-9}$ m²/s (blue).

The model has achieved good adjustments both for the three Basolites ($R^2$ = 0.99, 0.91 and 0.97, respectively), and for bibliographic data. Basolite C300 presented the best performance for recovering methane: good selectivity ($CH_4/N_2$ = 1.64) and high uptake capacity (0.078 mmol/g), despite its low concentration (2% $CH_4$), and even higher than some of the most common adsorbents, such as zeolite 4A and carbon nanotubes. These conditions allow obtaining an increment of 46.7% respect to inlet methane concentration after an adequate desorption stage. In addition, the known structure of the materials allowed making parametric studies about several parameters (bed length, inlet flow and particle size) and study its influence on others (axial dispersion and mass transfer coefficient). The model allows variating a vast number of parameters in order to study the effect on the breakthrough curve, which is of high importance for future scale-ups.

**Acknowledgements**

This work was supported by the Research Fund for Coal and Steel of the European Union (contract UE-17-RFCS216-METHENERGY PLUS). David Ursueguía acknowledges the Spanish Ministry of Education for the PhD grant that supports his research.

**References**

[1] D. Zhong, W. Wang, Z. Zou, Y. Lu, J. Yan, K. Ding, Investigation on methane recovery from low-concentration coal mine gas by tetra-n-butyl ammonium chloride semiclathrate hydrate formation, Appl. Energ. 227 (2018) 686-693.

[2] United States Environmental Protection Agency, Inventory of US greenhouse gas emissions and sinks: 1990-2012, EPA 430-R-14-003. Washington, DC: US Environmental Protection Agency; 2014.

[3] UNECE, Best practice guidance for effective methane drainage and use in coal mines, ECE Energy Series No. 47 Cap. 1 Pag. 27, 2016.

[4] UNECE, Best practice guidance for effective methane drainage and use in coal mines, ECE Energy Series No. 47 Cap. 6 Pag. 65, 2016.

[5] A. Duda, A. Krzemien, Forecast of methane emission from closed underground coal mines exploited by longwall mining – A case study of Anna coal mine, J. Sustain. Mining 17 (2018) 184-194.

[6] P. Tremain, A. Maddocks, B. Moghtaderi, Stone dust looping for ventilation air methane abatement: a 1 m3/s pilot-scale study, Energ. Fuels 33 (2019) 12568-12577.

[7] J. Fernández, P. Marín, F. Díez, S. Ordóñez, Combustion of coal mine ventilation air methane in a regenerative combustor with integrated adsorption: Reactor design and optimization, Appl. Therm. Eng. 102 (2016) 167-175.

[8] D. Qu, Y. Yang, Z. Qian, P. Li, J. Yu, A. Ribeiro, A. Rodrigues, Enrichment of low-grade methane gas from nitrogen mixture by VPSA with $CO_2$ displacement process: modeling and experiment, Chem. Eng. J. 380 (2020) 122509.

[9] X. Hou, S. Liu, Y. Zhu, Y. Yang, Experimental and theoretical investigation on sorption kinetics and hysteresis of nitrogen, methane, and carbon dioxide in coals, Fuel 268 (2020) 117349.

[10] M. Fakhroleslam, S. Fatemi, Comparative simulation study of PSA, VSA, and TSA processes for purification of methane from $CO_2$ via SAPO-34 core-shell adsorbent, Sep. Sci. Technol. 51 (2016) 2326-2338.

[11] Yang RT. Adsorbents: fundamentals and applications. 1st ed. John Wiley & Sons; 2003.

[12] P. Li, H. Tezel, Adsorption separation of $N_2$, $O_2$, $CO_2$ and $CH_4$ gases by β-Zeolite, Micropor. Mesopor. Mat. 98 (2007) 94-101.

[13] X. Xu, X. Zhao, L. Sun, X. Liu, Adsorption separation of carbon dioxide, methane and nitrogen on monoethanol amine modified β-zeolite, J. Nat. Gas Chem. 18 (2009) 167-172.

[14] R. Seabra, A. Ribeiro, K. Gleichmann, A. Ferreira, A. Rodrigues, Adsorption equilibrium and kinetics of carbon dioxide, methane and nitrogen on binderless zeolite 4A adsorbents, Micropor. Mesopor. Mat. 277 (2019) 105-114.

[15] L. Zhou, X. Liu, L. Li, N. Wang, Z. Wang, Y. Zhou, Synthesis of ordered mesoporous carbon molecular sieve and its adsorption capacity for $H_2$, $N_2$, $O_2$, $CH_4$ and $CO_2$, Chem. Phys. Lett. 41 (2005) 6-9.

[16] D. Qu, Y. Yang, K. Lu, L. Yang, P. Li, J. Yu, A. Ribeiro, A. Rodrigues, Microstructure effect of carbon materials on the low-concentration methane adsorption separation from its mixture with nitrogen, Adsorption 24 (2018) 357-369.

[17] B. Wang, L-H. Xie, X. Wang, X-M. Liu, J. Li, J-R. Li, Applications of metal-organic frameworks for green energy and environment: New advances in adsorptive gas separation, storage and removal, Green Energy Environ. 3 (2018) 191-228.

[18] L. Li, L. Yang, J. Wang, Z. Zhang, Q. Yang, Y. Yang Y, Highly efficient separation of methane from nitrogen on a squarate-based metal-organic framework, AlChE J. 64 (2018) 3681-3690.

[19] S. Eyer, N. Stadie, A. Borgschulte, L. Emmenegger, J. Mohn, Methane preconcentration by adsorption: a methodology for materials and conditions selection, Adsorption 20 (2014) 5-6.

[20] J. Yang, Y. Wang, L. Li, Z. Zhang, J. Li, Protection of open-metal V(III) sites and their associated $CO_2/CH_4/N_2/O_2/H_2O$ adsorption properties in mesoporous V-MOFs, J. Colloid Interface. Sci. 456 (2015) 197-205.

[21] R. Sabouni, H. Kazemian, S. Rohani, Mathematical modeling and experimental breakthrough curves of carbon dioxide adsorption on metal organic framework CPM-5, Environ. Sci. Technol. 47 (2013) 9372-9380.

[22] P.G. Aguilera, F.J. Gutiérrez Ortiz, Prediction of fixed-bed breakthrough curves for $H_2S$ adsorption from biogas: Importance of axial dispersion for design, Chem. Eng. J. 289 (2016) 93-98.

[23] J. Delgado, M. Uguina, J. Sotelo, B. Ruiz, Modelling of the fixed-bed adsorption of methane/nitrogen mixtures on silicalite pellets, Sep. Purif. Technol. 50 (2006) 192-203.

[24] B. Babu, S. Gupta, Modeling and simulation of fixed bed adsorption column: Effect of velocity variation, Birla Institute of Technology and Science (2005).

[25] S. Nouh, K. Lau, A. Shariff, Modeling and simulation of fixed bed adsorption column using integrated CFD approach, J. Appl. Sci. 10 (2010) 3229-3235.

[26] X. Peng, D. Cao, J. Zhao, Grand canonical Monte Carlo simulation of methane-carbon dioxide mixtures on ordered mesoporous carbon CMK-1, Sep. Pur. Tech. 68 (2009) 50-60.

[27] Q. Yang, C. Zhong, Molecular simulation of carbon dioxide/methane/hydrogen mixture adsorption in metal-organic frameworks, J. Phys. Chem. B 110 (2006) 17776-17783.

[28] Y. Peng, V. Krungleviciute, I. Eryazici, J. Hupp, O. Farha, T. Yildirim, Methane storage in metal-organic frameworks: Current records, surprise findings, and challenges, J. Am. Chem. Soc. 135 (2013) 11887-11894.

[29] M. Sánchez-Sánchez, I. Asua, D. Ruano, K. Díaz, Direct synthesis, structural features, and enhanced catalytic activity of the Basolite F300-like semiamorphous Fe-BTC framework, Cryst. Growth Des. 15 (2015) 4498-4506.

[30] J. Mollmer, M. Lange, A. Moller, C. Patzschke, K. Stein, D. Lassig, J. Lincke, R. Glaser, H. Krautscheid, R. Staudt, Pure and mixed gas adsorption of $CH_4$ and $N_2$ on the metal-organic framework Basolite® A100 and a novel copper-based 1,2,4-triazolyl isophthalate MOF, J. Mater. Chem. 22 (2012) 10274-10286.

[31] A. Dhakshinamoorthy, M. Alvaro, P. Horcajada, E. Gibson, M. Vishnuvarthan, A. Vimont, J. Grenèche, C. Serre, M. Daturi, H. García, Comparison of porous iron trimesates Basolite F300 and MIL-100(Fe) as heterogeneous catalysts for Lewis acid and oxidation reactions: Roles of structural defects and stability, ACS Catal. (2012) 2:2060-2065.

[32] C. Perego, S. Peratello, Experimental methods in catalytic kinetics, Catal. Today 14 (1999) 133-145.

[33] Z. Niu, X. Cui, T. Pham, P. Lan, H. Xing, K. Forrest, L. Wojtas, B. Space, S. Ma, A metal-organic framework based methane nano-trap for the capture of coal-mine methane, Angewandte Chemie 58 (2019) 10138-10141.

[34] D. Wu, X. Guo, H. Sun, A. Navrotsky, Thermodynamics of methane adsorption on copper HKUST-1 at low pressure, J. Phys. Chem. Lett. 6 (2015) 2439-2443.

[35] D. Ursueguía, E. Díaz, S. Ordóñez, Adsorption of methane and nitrogen on Basolite MOFs: equilibrium and kinetic studies, Micropor. Mesopor. Mater. 298 (2020).

[36] G. Standart, The thermodynamic significance of the Danckwerts' boundary conditions, Chem. Eng. Sci. 23 (1968) 645-655.

[37] E. Fuller, P. Schettler, J. Giddings, New method for prediction of binary gas-phase diffusion coefficients, Ind. Eng. Chem. 58 (1966) 18-27.

[38] J. Theuerkauf, P. Witt, D. Schwesig, Analysis of particle porosity distribution in fixed beds using the discrete element method, Powder Technol. 165 (2006) 92-99.

[39] S. Farooq, H. Qinglin, I. Karimi, Identification of transport mechanism in adsorbent micropores from column dynamics, Ind. Eng. Chem. Res. 41 (2002) 1098-1106.

[40] D. Saha, Z. Bao, F. Jia, S. Deng, Adsorption of $CO_2$, $CH_4$, $N_2O$ and $N_2$ on MOF-5, MOF-177, and Zeolite 5A, Environ. Sci. Technol. 44 (2010) 1820-1826.

[41] P. Bárcia, L. Bastin, E. Hurtado, J. Silva, A. Rodrigues, B. Chen, Single and multicomponent sorption of $CO_2$, $CH_4$ and $N_2$ in a Microporous Metal-Organic Framework, Sep. Sci. Tech. 43 (2008) 3494-3521.

[42] Z. Bao, L. Yu, Q. Ren, X. Lu, S. Deng, Adsorption of $CO_2$ and $CH_4$ on a magnesium-based metal organic framework, J. Colloid Interface Sci. 353 (2011) 549-556.

[43] B. Panella, M. Hirscher, S. Roth, Hydrogen adsorption in different carbon nanostructures, Carbon 43 (2005) 2209-2214.

[44] H. Frost, T. Duren, R. Snurr, Effects of surface area, free volume, and heat of adsorption on hydrogen uptake in metal-organic frameworks, J. Phys. Chem. B 110 (2006) 9565-9570.

[45] A. Mukhtar, N. Mellon, S. Saqib, A. Khawar, S. Raqif, S. Ullah, A. Al-Sehemi, M. Babar, M. Bustam, W. Khan, M. Tahir, $CO_2/CH_4$ adsorption over functionalized multi-walled carbon nanotubes; an experimental study, isotherms analysis, mechanism, and thermodynamics, Micropor. Mesopor. Mat. 294 (2020) 109883.

[46] A. Lyubchyk, I. Esteves, F. Cruz, J. Mota, Experimental and theoretical studies of supercritical methane adsorption in the MIL-53(Al) metal organic framework, J. Phys. Chem. C 115 (2011) 20628-20638.

[47] F. Lovas, R. Suenram, J. Coursey, S. Kotochigova, J. Chang, K. Olsen, R. Dragoset, Hydrocarbon spectral database, NIST standard reference database 115 (2004).

[48] S. Couck, J. Denayer, G. Baron, T. Remy, J. Gascon, F. Kapteijn, An amine-functionalized MIL-53 metal-organic framework with large separation power for $CO_2$ and $CH_4$, J. Am. Chem. Soc. 131 (2009) 6326-6327.

[49] E. Deniz, F. Karadas, H. Patel, S. Aparicio, C. Yavuz, M. Atilhan, A combined computational and experimental study of high pressure and supercritical $CO_2$ adsorption on Basolite MOFs, Micropor. Mesopor. Mat. 175 (2013) 34-42.

[50] Z. Li, G. Xiao, Q. Yang, Y. Xiao, C. Zhong, Computational exploration of metal-organic frameworks for $CO_2/CH_4$ separation via temperature swing adsorption, Chem. Eng. Sci. 120 (2014) 59-66.

[51] Z. Zhao, X. Li, Z. Li, Adsorption equilibrium and kinetics of p-xylene on chromium-based metal organic framework MIL-101, Chem. Eng. J. 173 (2011) 150-157.

[52] L. Arnold, G. Averlant, S. Marx, M. Weickert, U. Muller, J. Mertel, C. Horch, M. Peksa, F. Stallmach, Metal Organic Frameworks for natural gas storage in vehicles, Chem. Ing. Tech. 11 (2013) 1726-1733.

[53] R. Hernández-Huesca, L. Díaz, G. Aguilar-Armenta, Adsorption equilibria and kinetics of $CO_2$, $CH_4$ and $N_2$ in natural zeolites, Sep. Pur. Tech. 15 (1999) 163-173.

[54] G. Walker, L. Weatherley, Adsorption of acid dyes on to granular activated carbon in fixed beds, Wat. Res. 31 (1997) 2093-2101.

[55] H. Patel, Fixed-bed column adsorption study: a comprehensive review, Appl. Water Sci. 9 (2019) 45.

[56] E. Malkoc, Y. Nuhoglu, Y. Abali, Cr(VI) adsorption by waste acorn of Quercus Ithaburensis in fixed beds: Prediction of breakthrough curves, Chem. Eng. J. 119 (2006) 61-68.

[57] N. Abdel-Jabbar, S. Al-Asheh, B. Hader, Modeling, parametric estimation, and sensitivity analysis for copper adsorption with moss packed-bed, Sep. Sci. Technol. 36 (2001) 2811-2833.

# Adsorbents selection for the enrichment of low-grade methane coal mine emissions by temperature and pressure swing adsorption technologies

David Ursueguía, Eva Díaz, Salvador Ordóñez*

Catalysis, Reactors and Control Research Group (CRC), Department of Chemical and Environmental Engineering, University of Oviedo, Julián Clavería s/n, 33006 Oviedo, Spain

*e-mail: sordonez@uniovi.es (S. Ordóñez)

*Journal of Natural Gas Science and Engineering* **105** (2022) 104721

https://doi.org/10.1016/j.jngse.2022.104721

## ABSTRACT

This work evaluates the feasibility of common adsorbents (carbonaceous materials, zeolites and metal-organic frameworks) for the adsorption and further methane upgrading of the ventilation air methane (VAM) emissions from underground coal mining (0.57% $CH_4$). Concentration was achieved by adsorption through two different operational procedures based on fixed bed configurations: temperature swing adsorption (TSA) and pressure swing adsorption (PSA). All the combinations have been simulated using a rigorous mathematical model implemented in a commercial simulation package. The main purpose is to evaluate the performance of the different combinations of adsorption technique and adsorbent material, as well as establishing a valid mathematical model able to test a wide range of materials. The comparison has been fulfilled with an economic evaluation of the different combinations. Results show that carbonaceous materials provide the highest concentration factors ($C/C_0$ = 5), with low total methane recoveries (30%) and the lowest cost per kmol of methane recovered (1.5 €/kmol). MOFs can retain substantial amounts of methane, but with lower $CH_4/N_2$ selectivities than carbonaceous materials and lower methane concentration factors ($C/C_0$ = 2.6). For this type of materials, a high recovery of methane is achieved, but at expense of the highest costs (80 €/kmol). Finally, zeolitic materials present the lowest methane concentration factor ($C/C_0$ = 2), with intermediate both methane recoveries (58%) and costs (25 €/kmol). Concerning the adsorption technique, TSA has shown higher final methane concentrations for carbonaceous materials and some MOFs, whereas PSA overperforms for zeolitic materials. In addition, TSA is cheaper in all cases than PSA processes. On the other hand, PSA allows higher total methane recoveries and adsorption capacities for all materials, highlighting the high dependence on adsorption pressure, especially in carbonaceous materials (PSA/TSA = 18.3, in the case of Maxsorb).

**Keywords**: ventilation air methane; fixed-bed adsorption; process simulation; temperature swing adsorption; pressure swing adsorption; coal mine emissions

### 1. Introduction

In the frame of the European Green Deal, the European Commission proposed in September 2020 raising the 2030 greenhouse gas (GHG) emission reduction target, including emissions and removals, to at least 55% compared to 1990 [1]. Among the considered sources, the energy sector accounts for around 75% of the total GHG emissions [2]. Therefore, minimizing the emission of these streams is a requirement for climate neutrality. In this way, methane recovery is a major challenge from two points of view: the reduction of global warming (methane global warming potential is twenty-one times greater than carbon dioxide [3]) and obtaining an efficient and clean fuel source, as well as a basic raw material for synthesizing several chemical products [4]. Most methane emissions have an anthropogenic origin, being classified into biogenic (55%) [5], thermogenic (22%) and pyrogenic (13%), among others [6, 7]. Biogenic methane is generated via microbial methanogenesis, under an anaerobic atmosphere at given ambient conditions, *e.g.*, the methane generated from underground coal or rice crops [8]. Thermogenic methane is related to the methane generated by geological processes and contained in fossil fuels such as coal, oil, and natural gas [9]. Finally, pyrogenic methane is related to biomass or biofuels incomplete combustions [10].

**ABBREVIATIONS**

| | | | |
|---|---|---|---|
| VAM | Ventilation air methane | CHP | Combined heat and power |
| TSA | Temperature swing adsorption | VSA | Vacuum swing adsorption |
| PSA | Pressure swing adsorption | TVSA | Temperature and vacuum swing adsorption |
| MOFs | Metal-organic frameworks | VPSA | Vacuum and pressure swing adsorption |
| GHG | Greenhouse gases | VTVSA | Vacuum and temperature swing adsorption |
| CBM | Coal bed methane | USD1 | Unparametrized supervised discretization |
| AMM | Abandoned mine methane | LDF | Linear driving force |

**SYMBOLS**

| | | | |
|---|---|---|---|
| $u_o$ | Surface velocity (m/s) | $k_f$ | External film mass transport coefficient (m/s) |
| $d_p$ | Particle diameter (m) | $\varepsilon_p$ | Particle porosity |
| $C_b$ | Vessel fixed cost (€) | $D_p$ | Diffusivity in macropores ($m^2/s$) |
| S | Vessel external surface area ($m^2$) | $r_c$ | Crystallite radius (m) |
| t | Time (s) | $D_i$ | Micropores diffusivity term ($m^2/s$) |
| C | Methane concentration in gas phase ($mol/m^3$) | $C_o$ | Initial adsorption concentration ($mol/m^3$) |
| W | Methane concentration in solid phase (mol/kg) | $q_o$ | Initial adsorption capacity ($mol/m^3_{solid}$) |
| Q | Energy required in heat exchanger (W) | dP | Pressure gradient (Pa) |
| $C_p$ | Specific heat (J/mol·K) | $\mu_g$ | Gas viscosity (Pa·s) |
| $\dot{n}$ | Molar flow (mol/s) | $\rho_g$ | Gas density ($kg/m^3$) |
| A | Heat exchanger surface area ($m^2$) | $\rho_b$ | Bed density ($kg/m^3$) |
| $T_2$-$T_1$ | Heat exchanger temperature increment (K) | $D_m$ | Molecular diffusivity ($m^2/s$) |
| U | Overall heat-transfer coefficient ($W/m^2 \cdot K$) | T | Temperature (K) |
| $\Delta T_{ln}$ | Logarithmic mean temperature difference (K) | P | Pressure (Pa) |
| $W_c$ | Compression power (W) | $M_A$ | Molar mass (mol/kg) |
| γ | Adiabatic expansion coefficient | $V_A$ | Molar volume ($mol/m^3$) |
| $V_1$ | Initial volume ($m^3$) | $h_s$ | Heat transfer coefficient ($W/m^2 \cdot K$) |
| $V_2$ | Final volume ($m^3$) | Nu | Nusselt number |
| $P_1$ | Initial pressure (Pa) | $k_g$ | Thermal gas conductivity (W/m·K) |
| $P_2$ | Final pressure (Pa) | Pr | Prandtl number |
| $D_e$ | Axial dispersion coefficient ($m^2/s$) | $a_p$ | Adsorbent surface-to-volume ratio ($m^{-1}$) |
| $\varepsilon_b$ | Bed void fraction | $q_m$ | Langmuir isotherm constant (mol/kg) |
| z | Axial position in the fixed bed (m) | b | Langmuir exponential factor ($m^3/mol$) |
| $\bar{q}$ | Adsorbate concentration equilibrium in gas phase ($mol/m^3$) | L | Fixed bed length (m) |
| $q_e$ | Adsorption equilibrium ($mol/m^3$) | D | Fixed bed diameter (m) |
| $q_e$* | Adsorbate concentration equilibrium in solid phase (mol/kg) | $Y_{CH_4}$ | Methane molar fraction |
| $K_L$ | Overall mass transfer coefficient ($s^{-1}$) | $C/C_o$ | Methane concentration factor |
| $r_p$ | Particle radius (m) | | |

Most of these methane emissions are hardly recoverable, such as those from agriculture, livestock, or transport [11]. The same occurs for fugitive methane emissions from oil and natural gas industries, which consist mainly of gas leaks in conductions, venting, deliberate combustions or even in leaks in the final product storage or transport [12]. Therefore, in these cases, it is recommended to minimize emissions at the source and, if it is not possible, to implement a control operation to meet regulation standards [13].

On the other hand, there are easily recoverable methane emissions using already available equipment in the facility, such as existing ducts, ventilation points and vertical wells: underground coal mining emissions.

There are three types of mining emissions: coal bed methane (CBM), abandoned mine methane (AMM) and ventilation air methane (VAM). CBM comes directly from coal seams in mining, its methane content is high (around 30%), and it supposes about 30% of all the methane emitted in the exploitations [14]. Its extraction process

involves drilling hundreds of wells with extensive infrastructural support facilities. From this source, the United States currently produce 7% of its natural gas [15]. AMM refers to released methane once the mining activity stops, for up to 20 years after the closure [16, 17]. Recovered methane concentrations typically range from 15 to 90%, with negligible oxygen concentrations [18]. Electricity generation or combined heat and power (CHP) production [19] are the main uses of these streams. Finally, VAM is a very diluted methane stream (0.1-1% $CH_4$) [20], which is obtained from ventilation systems designed to keep methane concentration in working galleries below the flammability limit (2% $CH_4$). Although their methane concentrations are very low, their huge flowrates become these emissions into the largest GHG emissions in the coal mining activity [21]. In addition, the efficient use of these streams is not straightforward, due to their low methane content, so they are usually emitted directly into the atmosphere or burned with very low energetic efficiency [22]. In general terms, concentrated streams (CBM and AMM) are used directly for energy production [23], whereas VAM requires a previous concentration step for main uses. In fact, an efficient VAM recovery would mean a great decrease in methane emissions, in addition to generate a resource for energy obtaining or chemical synthesis. For example, it was demonstrated that a previous concentration process would allow obtaining adequate streams for working on gas turbines (> 1% $CH_4$) [24].

Furthermore, add to methane and air, high relative humidity, and carbon dioxide traces (around 0.1% $CO_2$) are also found. Hence, the methane purification process involves the methane gas separation from the air species, water, and carbon dioxide [25]. The most common and easy to scale-up processes for performing gas separations at high scales are swing adsorption methods. Among them, temperature swing adsorption (TSA) and pressure swing adsorption (PSA) are the most used [26, 27], which consist of cyclic variations in temperature or pressure of the fixed bed, respectively, alternating operation conditions between two or more available beds. In recent times, different authors have reported promising results using these techniques. For example, Karimi et al. [28] have doubled the initial methane concentration (10-20%) through a PSA process with Norit R1 activated carbon as adsorbent. On the other hand, Wang et al. [29] have compiled several interesting results obtained through two different techniques: using TSA, the methane concentration was increased from 5 to 20% with more than 99% methane recovery, using silicalite as adsorbent; by VPSA, the methane concentration was improved from 5 to 12.6%, with a methane recovery of 81.9%, using a carbon molecular sieve (CMS) as adsorbent. Finally, Pawlaczyk-Kurek et al. [21] have presented examples of different methane-enriching processes by swing adsorption techniques (PSA, VSA, TVSA, VPSA, VTVSA) with different adsorbents (coconut shell, activated carbon and honeycomb monolithic carbon). These results seem promising for almost all cases, especially in case of VTVSA, even already checked at pilot plant level. Even so, the simplicity of TSA and PSA processes makes them an adequate starting point to know the validity of a material for the desired separation [26, 28, 30-34]. It should be also noted that these techniques can be combined for obtaining optimal results.

Although methane concentration from nitrogen-rich streams is reported in the literature, these studies do not start from concentrations as low as those present in VAM streams (0.1-1%). The scope of these articles is studying in detail a technique and adsorbent lacking the comparison between techniques (PSA and TSA) and adsorbents. Thus, it is difficult to state, with the currently available information, what configuration and what kind adsorbents are better for this purpose. This fact is even more critical if the presence of spectator species (as carbon dioxide) is considered.

This work tries to fill this gap, presenting a systematic comparison of technologies and materials for accomplishing the purpose of significantly increase methane concentration in VAM emissions. For accomplishing this purpose, the $CH_4/N_2/CO_2$ separation performance from VAM streams was systematically evaluated by both PSA and TSA processes with nine different adsorbents, representative of the three main families (carbonaceous materials, zeolites, and MOFs). A rigorous mathematical model (validated at lab-scale in previous works [35]) was proposed for simulating both techniques, solving the corresponding differential equations by Aspen Adsorption software, which was also used for the estimation of the associated costs to each combination. This procedure will allow to determine the best configuration for the separation, in addition to assess the key properties of the material governing its performance for both processes.

## 2. Methodology

### 2.1. TSA and PSA features

The fixed bed design and the distribution of the operation times have been performed based on the same criteria presented in a previous work [24], in which a complete description of the typical layout of these processes has been developed. In this work, two different operation ways were considered: TSA and PSA. In a common fixed bed adsorption process, two or more fixed beds are in series in the same stage, thus maintaining one of them always practically fresh in an alternating mode [36]. Here, only the performance of one of these fixed beds will be considered, focusing more on the comparison of materials and techniques.

In case of TSA (Figure 1), the adsorption and desorption steps are accomplished by varying the temperature of the fixed bed. First, an adsorption stage, in which the temperature is as low as possible, and the components of the inlet mixture are selectively adsorbed depending on their affinity to the adsorbent material. In this case, the adsorption temperature is fixed by the Langmuir isotherm constants of the adsorbents, presented in a later section. Consecutively, at the desorption stage, a hot rinsing stream is introduced in counterflow direction to promote desorption, obtaining a concentrated stream in the most strongly adsorbed components. This rinsing stream is one of the optimizable parameters in the process since it is within the limits that meet the typical surface velocity interval in a fixed bed (0.2 - 0.5 m/s).

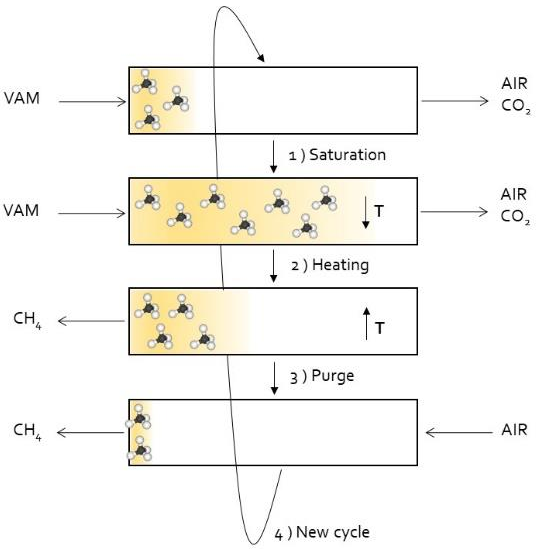


Figure 1. TSA typical stages distribution for a VAM concentration process. The orange gradient indicates the advance of the methane adsorption front in the fixed bed.

In this case, the same flowrate as in the adsorption process is considered to simplify the study. This approach was followed in the literature for comparing technologies and materials [37]. In the same way than adsorption, desorption temperature is fixed by the temperature of the adsorption isotherm constants selected for each case. In fact, the maximum operation temperature depends on the material stability and the process cost. Even so, considering the material and economic viability of the process, and parametric studies, such as Chen et al. [38], it is desirable not to exceed 383 K for desorption. Finally, the cooling stage, which consists of cooling down the bed to return to the initial conditions for starting another new cycle. Generally, the most expensive stage is related to the heating of the streams, so it should be imperatively considered in the economic balance of each operation. The required energy (Q) for the desorption step is calculated assuming a heat exchange (Equation 1) with constant specific heat ($C_p$) value for air (29.17 J/mol·K), which is the cleaning gas, and the calculated molar flow ($\dot{n}$). Once the required energy is known, it is possible to design the tubular heat exchangers for the process, commonly used in processes with gases at low pressure inside the tubes. The cost is directly related to the surface area (A) of the exchanger [39], calculated by Equation 2, whereas the temperature increment ($T_2 - T_1$) is obtained from adsorption isotherm data reported for each material. In addition, the value of the overall heat-transfer coefficient (U) is considered as 20 W/m²·K [40], whereas the logarithmic mean temperature differences ($\Delta T_{ln}$) is obtained assuming a heat exchanger where the hot fluid is steam at 373 K.

$$Q = \dot{n} \cdot C_p \cdot (T_2 - T_1) \quad (1)$$

$$Q = U \cdot A \cdot \Delta T_{ln} \quad (2)$$

In case of PSA (Figure 2), the concentration step is carried out by decreasing the pressure of the fixed bed. The sequence consists of a first high-pressure adsorption stage, in which the pressure is highly variable and depends on the application of the gas to be treated: for example, Canevesi et al. [41] have applied pressures between 3 and 10 bar for upgrading biogas, whereas Luberti et al. [42] have applied pressures up to 65 bar for hydrogen purification.

Afterwards, a pressure reduction step causes the desorption of the previously adsorbed components, obtaining a stream concentrated in the strongest adsorbed components [43]. In addition, some intermediate steps can be added to optimize the systems, such as equalizations, either

product-end or feed-end, to change the fixed bed pressure through connections between different beds working at the same time but in different stages of the process [44]. These steps are very brief, their duration being negligible in comparison to the total cycle time [45]. Finally, the regeneration step, needed when several mixture compounds are strongly retained, even at low pressures. At this last step, a rinsing gas, generally air at low pressure, is introduced for removing these compounds. In PSA, the pressurization is the most expensive stage, so it must be considered in the economic balance. In that way, it is supposed an adiabatic compression. The required power ($W_c$) is calculated through Equation 3, where is known the adiabatic expansion coefficient ($\gamma = 1.4$, for air), the initial volume ($V_1$), and initial and final desired gas pressure ($P_1$ and $P_2$, respectively).

Additionally, the centrifugal-motor compressor cost can be calculated from the total flow treated and the required power [39].

$$W_c = \frac{P_1 V_1 - P_2 V_2}{1 - \gamma} \qquad (3)$$

Regarding to the fixed bed, the design variables have been selected based on a common operating criterion [24]. Thus, the usual surface velocity ($u_0$) of gases in a fixed bed is between 0.2 and 0.5 m/s, the adsorbent particle size ($d_p$) between 0.5 and 10 mm, and the maximum possible dimensions of the fixed bed, 14 and 3.5 m of length and diameter, respectively [39]. Also, the length of the fixed bed must be, at least, three times greater than the bed diameter [46]. The use efficiency of the fixed bed increases with the length of the bed, since the unused part becomes a smaller portion of the total bed [47], but also increases the fixed bed costs and the total pressure drop. In fact, the fixed-bed devices present a fixed bed cost, which depends only on the size of the container: $C_b = 2310 \cdot S^{0.778}$, where $C_b$ (€) is the total cost and S ($m^2$) the area of the external surface of the container [48]. Furthermore, the diameter selection must consider the exothermic nature of the process, avoiding large increases in temperature, so a high surface-to-volume ratio is desirable [49].

### 2.2. Mathematical model

TSA and PSA processes in a fixed bed were simulated using Aspen Adsorption software. All the combinations between adsorbent materials and adsorption techniques were simulated through a dynamic heterogeneous one-dimensional model, also accounting for axial dispersion and axial pressure gradients. For the sake of simplicity, the following assumptions were considered:

- Isothermal conditions in the adsorption step, due to the low methane and nitrogen adsorption heats (around 20 kJ/mol), which are practically constant with the total uptake [50], and the low carbon dioxide concentrations in VAM streams.
- Negligible both radial dispersion and changes in axial flow velocity, due to the limited adsorption capacities and the low methane and carbon dioxide concentrations [51].
- Adsorbent particles are spherical and homogeneous in size and density.
- Uniform bed void ratio for each material.

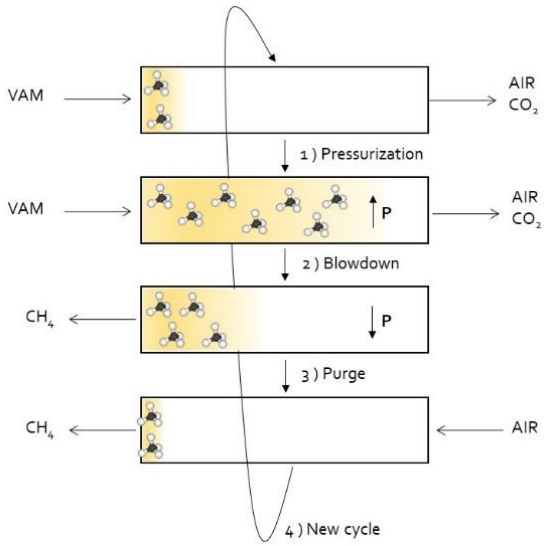


Figure 2. PSA typical stages distribution for a VAM concentration process. The orange gradient indicates the advance of the methane adsorption front in the fixed bed.

Following the previous assumptions, Equation 4 and Equation 5 describe the general model of a fixed-bed adsorption for the gas and solid phases, respectively. This model considers a gas transport over an axial bed, and it includes accumulation, convection, dispersion, and interphase mass transfer terms. The discretization method used to solve the equations is USD1, with 100 nodes along the axial direction. The solution shows the variation of methane concentration with time (t) in the gas (C) and solid (W) phases, respectively. The second term in the gas phase balance considers the axial dispersion ($D_e$) in the process, whereas the third term, convective transport, depends on the surface velocity ($u_0$) and on the bed void fraction ($\varepsilon_b$). The initial and boundary conditions used to solve the differential equations are presented in Table 1.

$$\frac{\partial C}{\partial t} - D_e \frac{\partial^2 C}{\partial z^2} + \frac{u_0}{\varepsilon_b}\frac{\partial C}{\partial z} = -\frac{(1-\varepsilon_b)}{\varepsilon_b}\frac{\partial \bar{q}}{\partial t} \quad (4)$$

$$\frac{\partial W}{\partial t} = -\frac{\partial \bar{q}}{\partial t} \quad (5)$$

Table 1. Initial and boundary conditions used to solve the balance differential equations.

| Condition | Boundary limit |
|---|---|
| $t = 0$ | $C = 0$<br>$W = 0$<br>$\bar{q} = 0$ |
| $z = 0$ | $(C - C_{in}) = \frac{\varepsilon_b \cdot D_e}{u_0}\left(\frac{\partial C}{\partial z}\right)$<br>$\left(\frac{\partial W}{\partial z}\right) = 0$ |
| $z = L$ | $\left(\frac{\partial C}{\partial z}\right) = 0$<br>$\left(\frac{\partial W}{\partial z}\right) = 0$ |

The last term in Equation 4 and Equation 5, interphase mass transfer, has been modelled assuming the existence of a linear driving force (LDF). This assumption relates linearly the mass transport and the adsorption equilibrium ($q_e$), calculated through the adsorption isotherms of each material. This model has been used in many gas-solid adsorption cases with good accuracy to experimental results [52]. Therefore, Equation 6 can model the mass transfer kinetics, where $q_e$* (mol/kg) is the adsorbate concentration at equilibrium, and $K_L$ ($s^{-1}$) is the overall mass transfer coefficient, accounting for transport resistances in the external film, macropores and micropores of each adsorbent. It was obtained from reported experimental data of methane and nitrogen diffusion on each of the considered families of materials [53-55]. It can be also expressed as shown in Equation 7, in which the first term of the equation is related to the transport resistance in the external film of the particle. It depends on the particle radius ($r_p$) and the external film mass transport coefficient ($k_f$). The second term is related to the mass transport in the macropores of the adsorbent, and it depends on the particle radius, the particle porosity ($\varepsilon_p$) and the diffusivity in macropores ($D_p$). Finally, the last term is related to the diffusivity in the micropores, and it depends on the crystallite radius ($r_c$) and the micropores diffusivity term ($D_i$). Depending on the features of each adsorbent, some terms of resistance could be negligible, as in the case of very microporous materials, which present much higher values of the last resistance term [56].

$$\frac{\partial \bar{q}}{\partial t} = K_L\,(q_e^* - \bar{q}) \quad (6)$$

$$\frac{1}{K_L} = \frac{r_p \cdot q_0}{3 \cdot k_f \cdot C_0} + \frac{r_p^2 \cdot q_0}{15 \cdot \varepsilon_p \cdot D_p \cdot C_0} + \frac{r_c^2}{15 \cdot D_i} \quad (7)$$

In addition, momentum balance is calculated through Ergun equation (Equation 8), which relates surface velocity to pressure gradient ($\partial P$), and it depends on the physical properties of the gas ($\mu_g$, $\rho_g$) and of the solid bed ($\rho_b$). Once convective transport is assumed, the value of the axial dispersion coefficient ($D_e$) is estimated from the values of the calculated molecular diffusivities ($D_m$) for each case [57].

$$\frac{\partial P}{\partial z} = \frac{150\mu_g(1-\varepsilon_b)^2}{d_p^2 \cdot \varepsilon_b^3}u_0 + \frac{1.75 \cdot \rho_g \cdot (1-\varepsilon_b)}{d_p \cdot \varepsilon_b^3}u_0^2 \quad (8)$$

The kinetic model assumption is linear lumped resistance with fixed molecular diffusivities ($D_m$), calculated through Fuller-Schettler-Gridding correlation (Equation 9), which depends on temperature (T), pressure (P), molar mass ($M_A$, $M_B$) and molar volume ($V_A$, $V_B$) of each component of the stream. Finally, there are not chemical reactions considered in the process.

$$D_m = \frac{0.001 \cdot T^{1.75} \cdot \left(\frac{1}{M_A} + \frac{1}{M_B}\right)}{P \cdot \left(V_A^{1/3} + V_B^{1/3}\right)^2} \quad (9)$$

In addition, in case of TSA, methane desorption occurs by a drag gas at increased temperature flowing through the fixed bed. Hence, the energy balance to the gas and solid phases (Equation 10 and Equation 11, respectively) should be considered. The velocity at which thermal equilibrium is reached depends on the heat transfer coefficient ($h_s$), calculated using correlation for fixed beds based on Nusselt ($Nu = h_s \cdot d_p/k_g$) and Prandtl ($Pr = C_{p,g} \cdot \mu_g/k_g$) dimensionless numbers [34]. The adsorbent surface-to-volume ratio ($a_p$) is also calculated for each case. The specific heat capacity of the solid ($C_{ps}$) is studied in several works for carbonaceous materials [58], with values between 0.8 and 1.2 J/g·K. Further, guided by the previous assumptions, no variation of the temperature in the solid due to the heat of adsorption is considered since the concentration of the adsorbate is low in the inlet streams. The energy balances are useful for the estimation of the time required for cooling the material after

desorption in TSA processes, as it is not considered instantaneous.

$$\frac{\partial T_g}{\partial t} = -u_0 \frac{\partial T_g}{\partial z} + h_s \frac{a_p}{C_{pg}\rho_g}(T_s - T_g) \quad (10)$$

$$\frac{\partial T_s}{\partial t} = h_s \frac{a_p}{C_{ps}\rho_b}(T_g - T_s) \quad (11)$$

From this model, previously validated with experimental data [35] under similar conditions and for three different adsorbent materials, in combination with adsorbent features and inlet flow properties, both the breakthrough and desorption curves, and the maximum methane concentration obtained at the outlet can be determined.

2.3. Adsorbent selection and adsorption isotherm parameters

Adsorbents typically used in gas adsorption and separation processes can be grouped in three main families: carbonaceous materials, zeolites, and MOFs. The activated carbons are the most representative of the first group [59, 60], with large specific surface areas, high pore volumes and good yields in gas adsorption processes, in addition to being cheap. In case of zeolites, the adsorption and separation process are usually characterized by steric effects, depending on pore and molecular sizes [61, 62], and generally are more expensive than activated carbons. Finally, MOFs have been extensively studied in recent times due to its interesting morphological and surface properties, such as its elevated specific surface area and total pore volume [63]. At this time, most of the MOFs are synthesized exclusively at laboratory or small scales, so it is not possible to obtain a price comparable to the other materials. However, Neves et al. [64] have calculated the costs associated to an ideal MOF large-scale production, setting 8.2 €/kg in the most favourable situation, which is considered in this work. The total associated cost depends on the dimensions of the fixed bed, which are directly related to the total inlet flow and the correspondent surface velocity. The selected adsorbent materials for the process are compiled in Table 2, in addition to some of its most important features.

On the other hand, the adsorption isotherm parameters, supposing Langmuir isotherm (Equation 12), are included in Table 3. This isotherm model has shown to fit the experimental data in practically all the partial pressure range, so it is adequate to use it in adsorption, with low partial pressures, and in desorption, when the methane concentration can reach higher values. In fact, it is one of the most used isotherms in gas adsorption available works [71, 81]. As additional advantages, it allows modelling the adsorption behaviour of the adsorbent in presence of two or more simultaneous potential adsorbates [82], add to be applied in some fixed bed adsorption simulations to obtain the corresponding breakthrough curves [83].

$$q_e = \frac{q_m b C}{1 + bC} \quad (12)$$

2.4. Properties of the considered stream and comparison parameters

Each mining exploitation can present very different flowrates and concentration values in its emissions, the properties of these streams being also variable with time. In addition to methane, nitrogen and carbon dioxide, the considered streams may also contain other compounds, such as water, oxygen, and particulate matter, which could be harmful for the adsorption operation and subsequent processes. Water can be strongly adsorbed over hydrophilic adsorbents and cause structural damages in certain materials, such as MOFs [92], thus it should be removed previously to the adsorption stage [93]. Concerning the oxygen, with a behaviour as adsorbate similar to nitrogen [94], it is in lower concentrations, and it is not usually considered. For example, Bae et al. [95] considered the methane/nitrogen separation to be the most important, both in PSA and TSA processes for methane purification. Finally, the presence of solid particles could significantly reduce the adsorption available surface area of the adsorbent, in addition to be adhered on machinery, reducing thus the life cycle, and modifying the properties of commodities [96]. To avoid its presence, Cheng et al. [97] have compiled a great variety of techniques that could be suitable for that purpose before the adsorption process, so solid particles are not considered in the problem streams. Therefore, the streams are considered purified before the adsorption process (negligible content of solid particles and humidity), so only methane, air (nitrogen) and carbon dioxide are considered at the simulation input. VAM stream features have been selected according to the values presented in the registers of different European mining exploitations, partners of the METHENERGY+ European Research Project. The flowrates of these streams can be large, up to 200 $m^3/s$, with low methane concentrations.

Table 2. Main features of the considered materials (activated carbons, dark grey; zeolites, white; and MOFs, light grey).

| Material | Particle size (mm) | Packing density (g/cm³) | Bed void space (-) | $S_{BET}$ (m²/g) | Pore volume (cm³/g) | Cost (€/kg) | References |
|---|---|---|---|---|---|---|---|
| Norit R1 | 1 | 0.44 | 0.36 | 1450 | 0.47 | 0.25 | [65, 66] |
| BPL | 1.3 | 0.45 | 0.49 | 1150 | 0.43 | 0.62 | [65, 67] |
| Maxsorb | 1.15 | 0.32 | 0.25 | 3250 | 1.79 | 0.6 | [65, 68] |
| β-zeolite | 3 | 0.6 | 0.4 | 664 | 0.3 | 5.1 | [69, 70] |
| Zeolite 13X | 1.6 | 1.13 | 0.54 | 615 | 0.34 | 1.8 | [71, 72] |
| Zeolite 5A | 2.7 | 0.73 | 0.32 | 689 | 0.35 | 1.7 | [73, 74] |
| MIL-101(Cr) | 1.5 | 0.43 | 0.4 | 4100 | 1.9 | 8.2 | [75, 76] |
| MOF-508 | 4.6 | 0.39 | 0.74 | 743 | - | 8.2 | [77, 78] |
| Basolite C300 | 2 | 0.22 | 0.62 | 1467 | 1.24 | 8.2 | [79, 80] |

In this case, a flowrate of 4.4 m³/s, with an inlet composition of 0.57% $CH_4$, 0.1% $CO_2$, 99.3% air is considered as case study [24].

For all this, the main comparison parameters among the results of the different combinations are: 1) adsorption capacity (mol/kg), calculated through the area integration of the breakthrough curve for each scenario, for a given flow rate and feed methane concentration; 2) saturation time (s), considered as the first time at which the $C/C_0$ in the breakthrough curve reaches a value of 1, *i.e.*, when the material is totally saturated in the adsorbate compounds; 3) methane recovery (%), calculated as the ratio of the methane recovered by adsorption, estimated from the adsorption capacity and the quantity of adsorbent material, and the total amount of methane introduced, calculated from the inlet flow and the inlet concentration of methane; and, 4) total cost, estimated from the individual cost of every device and resource used in the process (heaters, compressors, adsorbent material, energy, etc.).

## 3. Results and discussion

Following typical fixed bed design considerations, three identical fixed beds, with dimensions of 10 m of length and 2.5 m of diameter, would be required to treat a total inlet molar rate of 60 mol/s in each one, 180 mol/s total. Two different adsorption techniques are considered: TSA and PSA. The design begins with the selection of the surface velocity, 0.3 m/s, which is an intermediate surface velocity for a fixed bed adsorption process. Desorption flowrate remains as in adsorption stage, in order to keep constant the recommended surface velocity in each fixed bed. The following sections present the design and results obtained for the three most common families of adsorbents and the two adsorption techniques considered, as well as a subsequent performance and economic comparison between all the results obtained.

### 3.1. Carbonaceous materials

Carbonaceous materials are some of the most used materials in gas adsorption processes, especially activated carbons, which present good values of porosity, specific surface area and adsorption capacity of different gases. The performance of three common activated carbons for the methane recovery process has been studied: Norit R1, BPL and Maxsorb.

Table 3. Suitable materials for gas adsorption processes with its Langmuir isotherm constants at different temperatures (activated carbons, dark grey; zeolites, white; and MOFs, light grey).

| | | $CH_4$ | | $CO_2$ | | $N_2$ | | |
|---|---|---|---|---|---|---|---|---|
| Material | T (K) | $q_m$ (mol/kg) | b ($m^3$/mol) | $q_m$ (mol/kg) | b ($m^3$/mol) | $q_m$ (mol/kg) | b ($m^3$/mol) | References |
| Norit R1 Extra | 298 | 0.0381 | 0.0062 | 0.0754 | 0.0067 | 0.0095 | 0.0019 | [65, 84] |
| | 323 | 0.0222 | 0.0040 | 0.0412 | 0.0042 | 0.0057 | 0.0013 | |
| BPL | 298 | 0.0260 | 0.0056 | 0.0809 | 0.0101 | 0.0034 | 0.0468 | [65, 67, 85, 86] |
| | 323 | 0.0159 | 0.0041 | 0.0637 | 0.0071 | 0.0023 | 0.033 | |
| Maxsorb | 298 | 0.0315 | 0.0021 | 0.0595 | 0.0017 | 0.0266 | 0.0042 | [65, 68, 87] |
| | 323 | 0.0186 | 0.0013 | 0.0374 | 0.0014 | 0.0166 | 0.0028 | |
| β-zeolite | 298 | 0.0137 | 0.0164 | 0.1299 | 0.0556 | 0.0059 | 0.0216 | [62, 88] |
| | 323 | 0.0136 | 0.0163 | 0.1298 | 0.0556 | 0.0059 | 0.0216 | |
| Zeolite 13X | 298 | 0.0150 | 0.0001 | 2.8301 | 0.4579 | 0.0095 | 0.0066 | [71] |
| | 323 | 0.0075 | 0.0053 | 0.8584 | 0.2282 | 0.0042 | 0.0005 | |
| Zeolite 5A | 303 | 0.0208 | 0.0214 | 3.9841 | 1.2537 | 0.0076 | 0.0056 | [73, 89] |
| | 323 | 0.0071 | 0.0135 | 1.1250 | 0.3937 | 0.0038 | 0.0065 | |
| MIL-101(Cr) | 288 | 0.0159 | 0.0229 | 0.2711 | 0.1176 | 0.0056 | 0.0011 | [75] |
| | 313 | 0.0055 | 0.0122 | 0.1040 | 0.0467 | 0.0023 | 0.0102 | |
| MOF-508 | 303 | 0.0347 | 0.0202 | 0.0555 | 0.0029 | 0.0468 | 0.0318 | [77] |
| | 323 | 0.0315 | 0.0183 | 0.0349 | 0.0007 | 0.0406 | 0.0301 | |
| Basolite C300 | 298 | 0.0281 | 0.0036 | 0.1662 | 0.0186 | 0.0073 | 0.0009 | [79, 90, 91] |

These three materials present a large contribution of micropores in their porous structure, which influences the adsorption capacity and mechanism, and hence, the predominant resistance of the process [65]. Therefore, the last term of Equation 7, $r_c^2/15 \cdot D_i$, is the prevailing in this case, considering the role of micropores. Table 4 compiles the required parameters for the three considered carbonaceous materials and the simulation conditions in each case.

Mass transport coefficients ($K_L$) are obtained from the adsorption experiments reported by Xu et al. [54] on microporous carbonaceous adsorbents, these values being like those published by Golden et al. [98] for different low-concentrated gases on activated carbon. The simulation is carried out in the Aspen Adsorption simulation software. Figure 3A presents a comparison of the methane breakthrough curves, both by TSA and PSA techniques, as well as the total methane adsorption capacities for each case (Figure 3B).

In case of Norit R1 and BPL, the adsorption capacity follows the same trend as the specific surface area, increasing the difference with pressure. Maxsorb activated carbon can be considered as an exception, since the adsorption capacity in the TSA process is very low in comparison with the other adsorbents despite having larger specific surface area and pore volume. It is demonstrated the high influence of pressure, with a methane adsorption capacity ratio between PSA and TSA of 18.3.

Table 4. Simulation parameters for TSA and PSA for the three carbonaceous materials considered.

| TSA (P = 1 bar) | | | | | |
|---|---|---|---|---|---|
| Material | $\dot{n}$ (mol/s) | L (m) | D (m) | $\varepsilon_b$ | $\rho_b$ (kg/m³) |
| Norit R1 | 60 | 10 | 2.5 | 0.36 | 440 |
| BPL | 60 | 10 | 2.5 | 0.49 | 450 |
| Maxsorb | 60 | 10 | 2.5 | 0.25 | 320 |
| **PSA (T = 298 K)** | | | | | |
| Material | $\dot{n}$ (mol/s) | L (m) | D (m) | $\varepsilon_b$ | $\rho_b$ (kg/m³) |
| Norit R1 | 60 | 10 | 2.5 | 0.36 | 440 |
| BPL | 60 | 10 | 2.5 | 0.49 | 450 |
| Maxsorb | 60 | 10 | 2.5 | 0.25 | 320 |

| TSA (P = 1 bar) | | | | |
|---|---|---|---|---|
| Material | $d_p$ (mm) | $1/K_L$ (s) | $D_m$ (m²/s) (ads/des) | T (K) (ads/des) |
| Norit R1 | 1 | 0.0030 | $2.1\cdot10^{-5}$ / $2.4\cdot10^{-5}$ | 298/323 |
| BPL | 1.3 | 0.0018 | $2.1\cdot10^{-5}$ / $2.4\cdot10^{-5}$ | 298/323 |
| Maxsorb | 1.15 | 0.0023 | $2.1\cdot10^{-5}$ / $2.4\cdot10^{-5}$ | 298/323 |
| **PSA (T = 298 K)** | | | | |
| Material | $d_p$ (mm) | $1/K_L$ (s) | $D_m$ (m²/s) (ads/des) | P (bar) (ads/des) |
| Norit R1 | 1 | 0.0030 | $7\cdot10^{-6}$ / $2.1\cdot10^{-5}$ | 1/3 |
| BPL | 1.3 | 0.0018 | $7\cdot10^{-6}$ / $2.1\cdot10^{-5}$ | 1/3 |
| Maxsorb | 1.15 | 0.0023 | $7\cdot10^{-6}$ / $2.1\cdot10^{-5}$ | 1/3 |

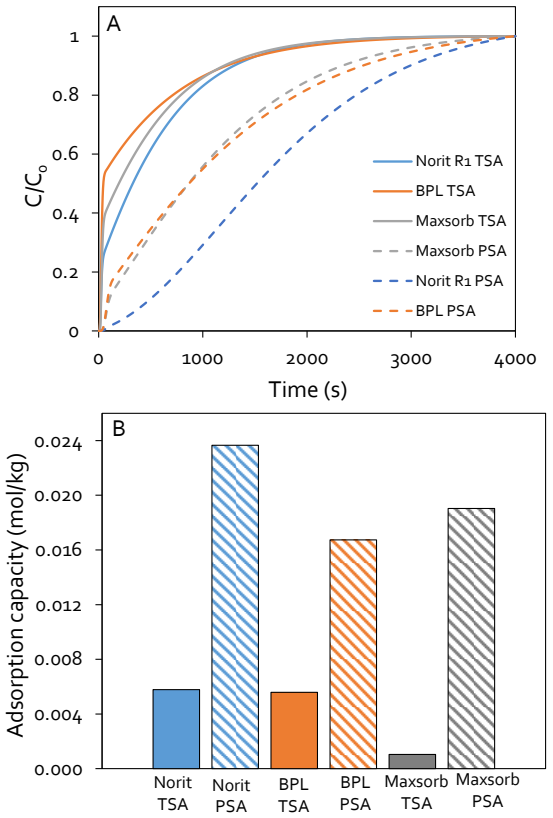


Figure 3. Methane breakthrough curves (A) and methane adsorption capacity (B) for the carbonaceous materials studied. TSA processes performed at 298 K and 1 bar, whereas PSA processes at 298 K and 3 bar.

On the other hand, Figure 4 presents the methane concentration step at the desorption stage by both TSA and PSA. As seen, the low $CH_4/N_2$ selectivity, obtained from the Langmuir isotherm constants, in case of Maxsorb avoids obtaining high methane concentration values, in addition to reduce the methane adsorption capacity in favour to nitrogen at low adsorption pressures. The shape of desorption graphs is similar to the obtained by Xu et al. [99] in case of air separation.

High concentrations were observed for Norit R1 and BPL activated carbon, both over 1%, the necessary minimum concentration for operating a gas turbine [24]. A maximum concentration of 5.1% is obtained for BPL by TSA, which constitutes an enrichment of 88.9% from the inlet stream.

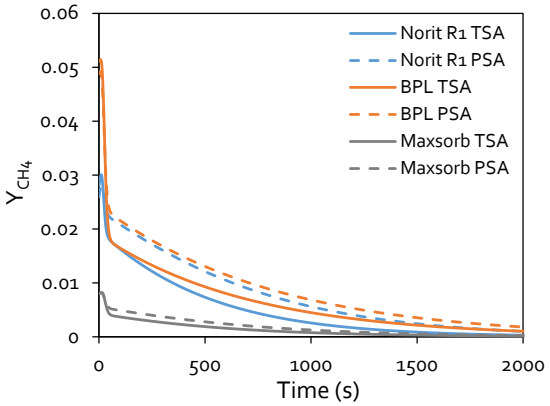


Figure 4. Methane molar fraction in desorption curves for the carbonaceous materials studied. TSA processes simulated at 323 K and 1 bar, whereas PSA processes simulated at 298 K and 1 bar.

On the other hand, Norit R1 carbon achieves a maximum concentration of 3%, which constitutes an enrichment of 81.1%. Norit R1 and BPL present high $CH_4/N_2$ selectivities (5 and 4.1, respectively),

obtained from the Langmuir adsorption isotherms (Equation 12). In addition, in case of BPL, its high affinity for carbon dioxide induces a final maximum molar concentration of 2.6% $CO_2$, whereas it is only 1% for Norit R1, values obtained from the simulation. Thus, it is pointed out the convenience of TSA processes to maximize the methane concentration at the outlet, in agreement with works that recommend TSA in streams with concentrations of the interesting compound lower than 2% [100, 101].

Table 5 summarizes the total recovery of methane for each case, obtained from saturation at 4000 s. The higher adsorption capacities for PSA processes lead to higher total methane recoveries. Therefore, in terms of performance, the lowest methane concentration at the outlet is obtained by PSA, but the total methane recovered is higher than in TSA. Then, a compromise must be reached depending on the final application of the obtained stream. Concerning cycles, it is possible to elucidate the required time to complete each stage of the processes. In case of TSA, a complete cycle takes 4.1 h (adsorption stage, 4000 s; heating, 4500 s; desorption, 2000 s; back to initial conditions, 4000 s), therefore, 1952 cycles/year can be reached, considering 8000 working hours.

These carbonaceous materials have been proposed for VAM concentration, Bae et al. [95, 102] have used carbon fibre composites for the enrichment of 0.54% $CH_4$ VAM streams through a combination of PSA and TSA (6% $CH_4$) and through a two-stage combination of vacuum and temperature (20% $CH_4$). Although their results are better than the reported in our work, they were obtained combining both technologies, with subsequent technical complexity and larger operation costs (not evaluated by the authors). In addition, Ouyang et al. [103] have used coconut shell VPSA to obtain 1.13% $CH_4$ from 0.42% $CH_4$, with a methane recovery of around 88%.

Table 5. Methane recovery values for each process with carbonaceous materials.

| Material | Process | $CH_4$ recovery (%) |
|---|---|---|
| Norit R1 | TSA | 9.2 |
| | PSA | 37.4 |
| BPL | TSA | 9.1 |
| | PSA | 27.1 |
| Maxsorb | TSA | 1.2 |
| | PSA | 21.9 |

The costs associated with methane enrichment are evaluated supposing a flowrate of 4.4 $m^3/s$ for desorption, the same as for adsorption. Desorption cycles are considered finished at outlet methane molar fractions ($Y_{CH_4}$) of $5.7 \cdot 10^{-4}$ and the assumed energy cost is 0.07 €/kW·h [24]. Thereby, the associated costs for each material and adsorption technique are calculated for one year (8000 working hours), average period considered for adsorbent replacement (Table 6). It is observed that the total cost per year is in all cases lower for TSA processes, due to the lower energy requirements associated to the heating process than to pressurization ones. The initial investment corresponds to vessels and exchanger for TSA; and vessels and compressor for PSA. On the other hand, annual costs correspond to adsorbent and heating for TSA, whereas in the case of PSA, they correspond to the pressurisation step. Differences in cost between both techniques are high in all cases, reaching even 71% in case of Norit R1.

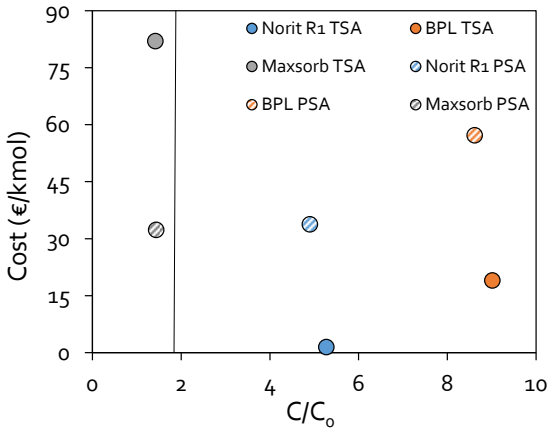


Figure 5. Relation for all the carbonaceous materials between cost per kmol of methane recovered and the concentration times from the initial methane concentration ($C_0$ = 0.57%). Vertical black line points out the minimum concentration factor necessary to use the obtained stream as feed in a gas turbine (1% $CH_4$).

In addition to the costs, potential earnings should also be considered in the final economic profitability estimation. For this, all the methane recovered in each case is supposed to be burned to obtain energy. Simplifying, a complete combustion of each stream is considered, assuming a calorific potential of pure methane of 0.8 MJ/mol [104]. The cost of the energy is supposed the same (0.07 €/kW·h), and the final result is the difference between the costs associated to one cycle and the energetic profit obtained from the methane recovered in the same cycle. The vessels, compressors and heat exchangers costs should be only considered as initial investments and not as annual costs. As shown in Figure 5, the process is not economically profitable in any case. The black line in the graph points out the minimum concentration factor ($C/C_0$) necessary for being able to use the recovered stream as feed in a gas

Table 6. Costs associated to the main stages in TSA and PSA processes [36].

| Material | Adsorbent (k€) | Vessels (k€) | Heating[1] (k€) |
|---|---|---|---|
| Norit R1 | 16.5 | 206.5 | 32.8 |
| BPL | 41.9 | 206.5 | 33.2 |
| Maxsorb | 28.4 | 206.5 | 21.0 |

| Material | Exchanger[1] (k€) | Pressurization[2] (k€) | Compressor[2] (k€) |
|---|---|---|---|
| Norit R1 | 15.2 | 582.5 | 128.8 |
| BPL | 21.5 | 567.9 | 128.8 |
| Maxsorb | 11.4 | 406.3 | 128.8 |

[1]Used in TSA processes
[2]Used in PSA processes

turbine (1% $CH_4$).

Below the 1%, it is Maxsorb activated carbon, the material with the lowest selectivity $CH_4/N_2$ (2.7) and the lowest methane adsorption capacity. Above 1% are both Norit R1 and BPL activated carbons, for which the PSA processes are clearly more expensive than TSA ones. In fact, Norit R1 material with the TSA process (1.47 €/kmol recovered) is near to have a null cost (0 €/kmol), which means that the annual cost of the operation would be zero.

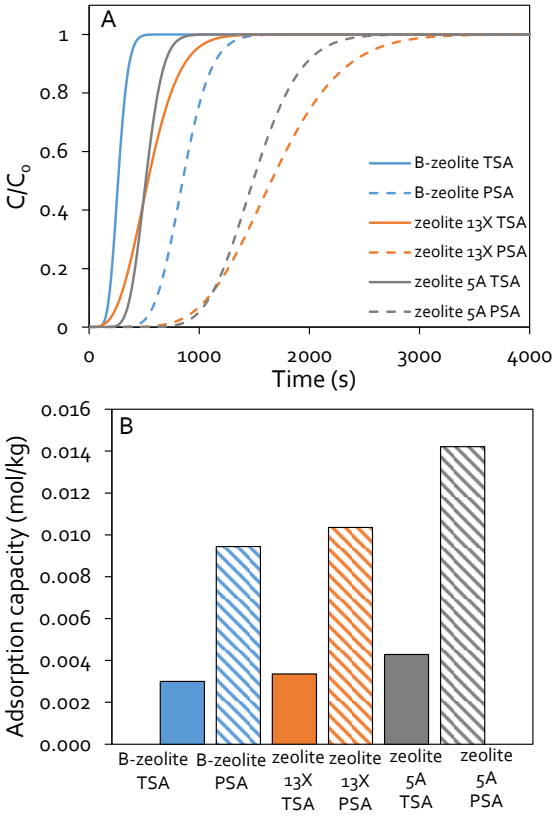


Figure 6. Methane breakthrough curves (A) and methane adsorption capacity (B) for the zeolitic materials considered. TSA processes were performed at 298 K and 1 bar, except 303 K for zeolite 5A, whereas PSA processes were performed at 298 K and 3 bar, except 303 K for zeolite 5A.

### 3.2. Zeolitic materials

Zeolitic materials are very used in gas adsorption processes. Despite not presenting so good values of porosity and specific surface area like carbonaceous materials, the separation based on steric effects make them suitable materials for this purpose. In this case, three zeolitic materials were studied: β-zeolite, zeolite 13X and zeolite 5A. In case of adsorption processes with β-zeolite, the micropores influence is much higher than that of mesopores, with $1/K_L$ values of 0.326 s in case of nitrogen [62]. Zeolite 5A is a similar case, with larger pores [105], and with commercial crystals generally very small and practically with no diffusional limitations, as Silva et al. [106] have demonstrated. On the other hand, adsorption on zeolite 13X is mainly governed by diffusion both in micropores and mesopores.

Therefore, mass transfer coefficient values depend on both last terms of Equation 7, dependent on diffusion in micro and macropores, obtained from Cavenati et al. [107] experiments. Thus, the mathematical model equation used for the modelling is different in case of zeolite 13X, which should maintain microporous and mesoporous resistance terms. Table 7 compiles the simulation parameters of the three zeolitic materials considered in the Aspen Adsorption simulation software and simulation results are presented in Figure 6. Figure 6A presents a comparison of the methane breakthrough curves obtained for the studied materials , both by TSA and PSA as well as the total methane adsorption capacities (Figure 6B).

In this case, the total adsorption capacity is lower than for carbonaceous materials, being zeolite 5A which presents the higher adsorption capacity among these materials, attributed to the high specific surface area and total pore volume (1.79 $cm^3/g$).

Table 7. Simulation parameters for TSA and PSA for the three zeolitic materials considered.

| TSA (P = 1 bar) | | | | | |
|---|---|---|---|---|---|
| Material | $\dot{n}$ (mol/s) | L (m) | D (m) | $\varepsilon_b$ | $\rho_b$ (kg/m³) |
| β-zeolite | 60 | 10 | 2.5 | 0.40 | 600 |
| Zeolite 13X | 60 | 10 | 2.5 | 0.54 | 1130 |
| Zeolite 5A | 60 | 10 | 2.5 | 0.32 | 730 |
| **PSA (T = 298 K)** | | | | | |
| Material | $\dot{n}$ (mol/s) | L (m) | D (m) | $\varepsilon_b$ | $\rho_b$ (kg/m³) |
| β-zeolite | 60 | 10 | 2.5 | 0.40 | 600 |
| Zeolite 13X | 60 | 10 | 2.5 | 0.54 | 1130 |
| Zeolite 5A | 60 | 10 | 2.5 | 0.32 | 730 |

| TSA (P = 1 bar) | | | | |
|---|---|---|---|---|
| Material | $d_p$ (mm) | $1/K_L$ (s) | $D_m$ (m²/s) (ads/des) | T (K) (ads/des) |
| β-zeolite | 3 | 0.0326 | $2.1\cdot10^{-5}/2.4\cdot10^{-5}$ | 298/323 |
| Zeolite 13X | 1.6 | 0.029 | $2.1\cdot10^{-5}/2.4\cdot10^{-5}$ | 298/323 |
| Zeolite 5A | 2.7 | 0.018 | $2.16\cdot10^{-5}/2.4\cdot10^{-5}$ | 303/323 |
| **PSA (T = 298 K)** | | | | |
| Material | $d_p$ (mm) | $1/K_L$ (s) | $D_m$ (m²/s) (ads/des) | P (bar) (ads/des) |
| β-zeolite | 3 | 0.0326 | $7\cdot10^{-6}/2.1\cdot10^{-5}$ | 1/3 |
| Zeolite 13X | 1.6 | 0.029 | $7\cdot10^{-6}/2.1\cdot10^{-5}$ | 1/3 |
| Zeolite 5A | 2.7 | 0.018 | $7.2\cdot10^{-6}/2.16\cdot10^{-5}$ | 1/3 |

The methane adsorption capacity ratio (PSA/TSA) is 3.14, 3.08 and 3.32, respectively, for β-zeolite, zeolite 13X and zeolite 5A, being the differences between materials less significant in this parameter, in contrast to carbonaceous materials. Likewise, the effect of pressure is lower in this case. Figure 7 presents the methane concentration values at the desorption stage by both TSA and PSA.

In this case, all the materials and techniques can provide the desired 1% of methane at the outlet. A maximum concentration of 1.9% is obtained by zeolite 5A by TSA, which constitutes an enrichment of 70% from the inlet stream, whereas β-zeolite achieves a maximum concentration of 1.6% by TSA, which constitutes an enrichment of 64.3% from the inlet stream. Opposite to carbonaceous materials, the maximum concentration obtained in each case is higher in PSA processes, staying also longer times at higher concentrations. In addition, final concentrations obtained are lower than for carbonaceous materials, as well as the $CH_4/N_2$ selectivities: 2.76, 1.94 and 1.87, respectively, for β-zeolite, zeolite 13X and zeolite 5A.

Further, β-zeolite presents high affinity to carbon dioxide, with a final concentration of 2.7% $CO_2$. Table 8 shows the total recovery of methane for each case, although the saturation time depends on both the adsorbent and the technique, Figure 6.

The higher adsorption capacities in case of PSA processes lead to higher total methane recoveries. In addition, the higher material densities than in case of carbonaceous materials provoke the recovery percentages to be higher in case of zeolites.

Table 8. Methane recovery values for each process with zeolites.

| Material | Process | $CH_4$ recovery (%) |
|---|---|---|
| β-zeolite | TSA | 44.39 |
| | PSA | 51.36 |
| Zeolite 13X | TSA | 37.87 |
| | PSA | 53.43 |
| Zeolite 5A | TSA | 50.27 |
| | PSA | 58.07 |

The costs associated with methane enrichment are evaluated supposing a flowrate of 4.4 m³/s for desorption, the same as for adsorption. The calculation procedure and the assumptions are the same than in case of carbonaceous materials, and the results are presented in Table 9.

It is observed that the annual total cost is in all cases lower for TSA processes, as well as in case of carbonaceous materials. Differences in cost between both techniques are lower than in case of carbonaceous materials, reaching 44.4% as maximum in case of zeolite 5A. Profitability calculations, analogous to carbonaceous materials, show that the process is not profitable economically in any case, Figure 8.

Table 9. Costs associated to the main stages in TSA and PSA processes [36].

| Material | Adsorbent (k€) | Vessels (k€) | Heating[1] (k€) |
|---|---|---|---|
| β-zeolite | 450.6 | 206.5 | 16.9 |
| Zeolite 13X | 299.5 | 206.5 | 12.5 |
| Zeolite 5A | 183.7 | 206.5 | 11.9 |

| Material | Exchanger[1] (k€) | Pressurization[2] (k€) | Compressor[2] (k€) |
|---|---|---|---|
| β-zeolite | 15.4 | 163.5 | 128.8 |
| Zeolite 13X | 15.2 | 319.7 | 128.8 |
| Zeolite 5A | 15.4 | 232.2 | 128.8 |

[1]Used in TSA processes
[2]Used in PSA processes

The cost per kmol of methane recovered is much higher than in case of carbonaceous materials. All the materials are above the limit to use the gas in a turbine, with zeolite 13X remarkably close to it. Zeolite 13X corresponds to the material with the lowest BET specific surface area, the lowest total pore volume and low $CH_4/N_2$ selectivity.

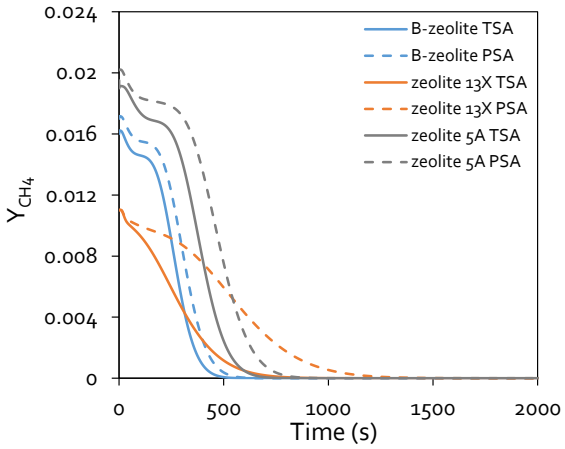


Figure 7. Methane desorption curves for the zeolitic materials considered. TSA processes performed at 323 K, 1 bar, whereas PSA processes performed at 298 K, 1 bar.

### 3.3. MOF materials

As noted in the literature, MOFs are the least used materials among the three considered, mainly due to their novelty, since they present really suitable properties related to adsorption processes. In this work, three different MOFs are studied: MIL-101(Cr), MOF-508 and Basolite C300. MIL-101(Cr) presents an ordered structure based on two sets of mesoporous cages that are accessible through microporous windows of 5.5 and 8.6 Å [87], and Lewis acid sites, which give it remarkable stability towards water [88-90].

The three MOFs have shown resistance to mass transfer in micropores, the coefficients obtained being 0.027 s for MIL-101(Cr) [108], 0.46 s for MOF-508 [109], and 0.012 s for Basolite C300 [35], a commercial MOF homologous to the widely studied HKUST-1.

Table 10 compiles the simulation parameters for the three MOF materials considered in the Aspen Adsorption software. Figure 9A presents a comparison of the methane breakthrough curves obtained for the studied materials, both by TSA and PSA, whereas the total methane adsorption capacities in each case is shown in Figure 9B.

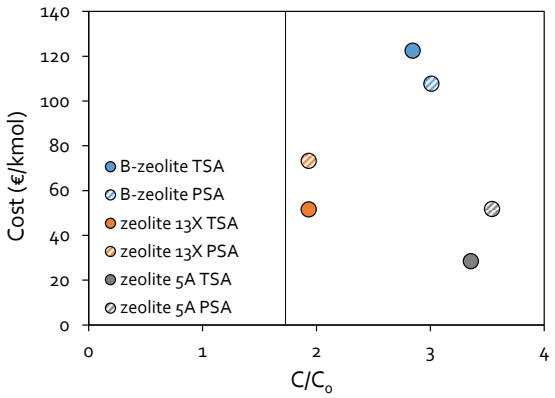


Figure 8. Relation for all the zeolitic materials between cost per kmol of methane recovered and the concentration times from the initial methane concentration ($C_0$ = 0.57%). Vertical black line points out the minimum concentration factor necessary to use the obtained stream as feed in a gas turbine (1% $CH_4$).

The methane adsorption capacity of MOFs is similar to the case of carbonaceous materials. The methane adsorption capacity ratio (PSA/TSA) is 3.4, 3.02 and 3.03, respectively for MIL-101(Cr), MOF-508 and Basolite C300, demonstrating lower pressure influence than in case of carbonaceous materials, and similar to zeolites. As in the case of zeolites, pore size also greatly influences the adsorption process. On the other hand, Figure 10 presents the methane concentration stage at the desorption stream by both techniques. MOF-508 is not able to reach the desired 1% of methane at the outlet, with a maximum concentration of 0.53%, which is, in fact, lower than the incoming methane, due to its large affinity towards nitrogen ($CH_4/N_2$ = 1).

Table 10. Simulation parameters for TSA and PSA for the three MOF materials considered.

| TSA (P = 1 bar) | | | | | |
|---|---|---|---|---|---|
| Material | $\dot{n}$ (mol/s) | L (m) | D (m) | $\varepsilon_b$ | $\rho_b$ (kg/m³) |
| β-zeolite | 60 | 10 | 2.5 | 0.40 | 390 |
| Zeolite 13X | 60 | 10 | 2.5 | 0.74 | 430 |
| Zeolite 5A | 60 | 10 | 2.5 | 0.62 | 220 |
| **PSA (T = 288, 303 and 298 K, respectively for MIL-101, MOF-508 and Basolite C300)** | | | | | |
| Material | $\dot{n}$ (mol/s) | L (m) | D (m) | $\varepsilon_b$ | $\rho_b$ (kg/m³) |
| β-zeolite | 60 | 10 | 2.5 | 0.40 | 390 |
| Zeolite 13X | 60 | 10 | 2.5 | 0.74 | 430 |
| Zeolite 5A | 60 | 10 | 2.5 | 0.62 | 220 |

| TSA (P = 1 bar) | | | | |
|---|---|---|---|---|
| Material | $d_p$ (mm) | $1/K_L$ (s) | $D_m$ (m²/s) (ads/des) | T (K) (ads/des) |
| β-zeolite | 1.5 | 0.027 | $2.1\cdot10^{-5}/2.2\cdot10^{-5}$ | 288/313 |
| Zeolite 13X | 4.6 | 0.46 | $2.16\cdot10^{-5}/2.4\cdot10^{-5}$ | 303/323 |
| Zeolite 5A | 2 | 0.012 | $2.1\cdot10^{-5}/2.4\cdot10^{-5}$ | 298/323 |
| **PSA (T = 288, 303 and 298 K, respectively for MIL-101, MOF-508 and Basolite C300)** | | | | |
| Material | $d_p$ (mm) | $1/K_L$ (s) | $D_m$ (m²/s) (ads/des) | P (bar) (ads/des) |
| β-zeolite | 1.5 | 0.027 | $7\cdot10^{-6}/2.1\cdot10^{-5}$ | 1/3 |
| Zeolite 13X | 4.6 | 0.46 | $7.2\cdot10^{-6}/2.16\cdot10^{-5}$ | 1/3 |
| Zeolite 5A | 2 | 0.012 | $7\cdot10^{-6}/2.1\cdot10^{-5}$ | 1/3 |

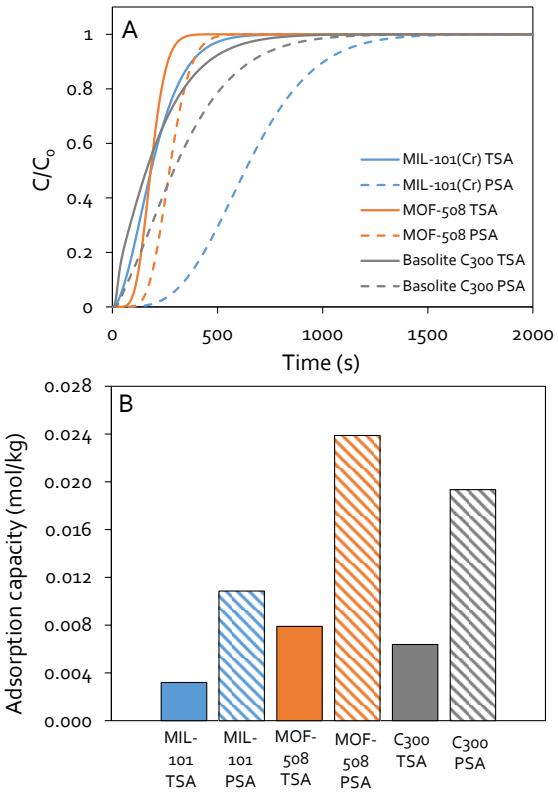


Figure 9. Methane breakthrough curves (A) and methane adsorption capacity (B) for the MOFs considered. TSA processes were performed at 288 K for MIL-101, 303 K for MOF-508 and 298 K for Basolite C300, 1 bar, whereas PSA processes were performed at 288 K for MIL-101, 303 K for MOF-508 and 298 K for Basolite C300, 3 bar.

A maximum concentration of 2.6% is obtained in case of Basolite C300, which constitutes an enrichment of 78%, and 2% in case of MIL-101(Cr), an enrichment of 71.5%

Similarly to zeolitic materials, the maximum concentrations obtained are in case of PSA processes, but the difference between PSA and TSA is lower. The selectivities $CH_4/N_2$ are 2.2, 1 and 1.2, respectively for MIL-101(Cr), MOF-508 and Basolite C300. Basolite C300 demonstrates also large selectivity towards carbon dioxide, with a maximum concentration obtained of 2.7% $CO_2$. Table 11 indicates the total recovery of methane for each case at saturation conditions. The higher adsorption capacities in case of PSA processes lead to higher total methane recoveries. The high recovery of methane in case of MOF-508 is surprising, indicating that it is a material with a high adsorption capacity, but that sacrifices selectivity, without final increase in concentration.

Table 11. Methane recovery values for each process with MOFs.

| Material | Process | $CH_4$ recovery (%) |
|---|---|---|
| MIL-101(Cr) | TSA | 28.2 |
| | PSA | 44.4 |
| MOF-508 | TSA | 99.8 |
| | PSA | 100 |
| Basolite C300 | TSA | 21.6 |
| | PSA | 56.9 |

Table 12. Costs associated to the main stages in TSA and PSA processes [36].

| Material | Adsorbent (k€) | Vessels (k€) | Heating[1] (k€) |
|---|---|---|---|
| MIL-101(Cr) | 530.1 | 206.5 | 22.8 |
| MOF-508 | 470.9 | 206.5 | 8.04 |
| Basolite C300 | 265.6 | 206.5 | 21.3 |

| Material | Exchanger[1] (k€) | Pressurization[2] (k€) | Compressor[2] (k€) |
|---|---|---|---|
| MIL-101(Cr) | 15.4 | 5918.2 | 128.8 |
| MOF-508 | 13.1 | 4800.8 | 128.8 |
| Basolite C300 | 15.2 | 2262.9 | 128.8 |

[1]Used in TSA processes
[2]Used in PSA processes

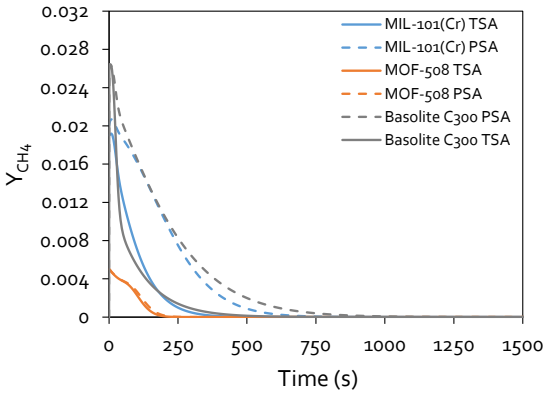


Figure 10. Methane desorption curves for MIL-101(Cr) (blue), MOF-508 (orange) and Basolite C300 (grey). Continuous lines correspond to TSA processes, and discontinuous lines correspond to PSA processes.

It is observed that the total cost per year is in all cases lower for TSA processes, with higher differences than in zeolitic and carbonaceous materials (around 85%). Economic profitability estimation reveals that the process is not profitable economically, as shown in Figure 11. The cost per kmol of methane recovered is much higher than in case of carbonaceous materials and zeolites, mainly related to the high cost of adsorbents. As it can be observed, MOF-508 is below the limit to use the recovered stream as feed in a gas turbine (1% $CH_4$).

3.4. Key properties of adsorbents

Once all the combinations between adsorbent material and adsorption technique have been simulated for the same process, conclusions can be drawn about the key parameters. The adsorption capacity is one of the main parameters to be considered. It can be related to high specific surface areas, high pore volume or even the presence of preferential adsorption sites along the structure. In addition, the adsorption capacity in each technique can be related to the parameters of the Langmuir isotherm ($q_m$ and b) and to the mass transfer resistance ($1/K_L$). Figure 12 plots the relationship between $q_m$ and the adsorption capacity for both techniques, PSA and TSA, demonstrating an almost linear trend, with larger influence in case of PSA. Therefore, it is more convenient to use materials with high $q_m$ values, obtaining better results in case of PSA. Other parameters, such as the resistance parameter, $1/K_L$, and the affinity parameter, b, which can be related to the adsorption enthalpy, show no clear influence on the methane adsorption capacity.

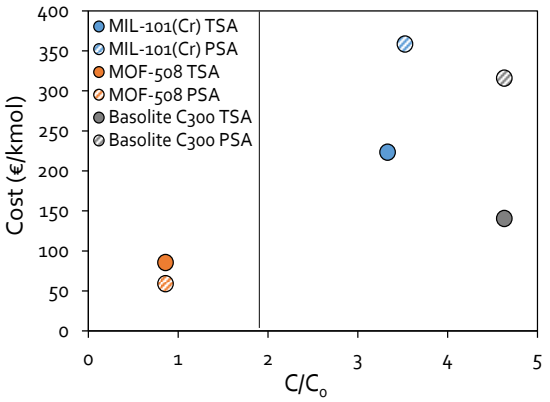


Figure 11. Relation for all the MOF materials between cost per kmol of methane recovered and the concentration times from the initial methane concentration ($C_0$ = 0.57%). Vertical black line points out the minimum concentration factor necessary to use the obtained stream as feed in a gas turbine (1% $CH_4$).

Further, the breakthrough curve shape and time are also important parameters: as it was deduced, the shape depends mainly on the adsorbate mass transfer across the adsorbent structure, whereas the breakthrough time is more related to the adsorption capacity. The highest diffusivities are associated to carbonaceous materials, with resistances based mainly in the micropore transport, which results in a more pronounced shape of the breakthrough curve at low times. Besides, there are also differences between PSA and TSA, the former with higher adsorption capacities, requires longer time to reach saturation. Although the adsorption capacity plays a key role in the methane recovery, it is remarkable that the best recovery values were obtained for zeolites and MOFs, highlighting the

importance of the adsorbent densities, with more methane recovered for the same fixed bed volume. Concerning the concentration factor ($C/C_0$), it depends mainly on the $CH_4/N_2$ and $CH_4/CO_2$ selectivities of each material. An elevated selectivity towards methane increases the final concentration factor, especially in the case of activated carbons. It is also worth mentioning that the selectivity towards $CO_2$ is of interest to be as low as possible, to avoid possible impurity for later applications. This is a key point at which zeolites usually fail. Finally, the total cost associated to the process which depends directly on the material and the technique used. It was demonstrated that PSA processes are more expensive than TSA in all cases, as well as MOFs, with the highest costs per kmol of methane recovered, followed by zeolites, and activated carbons.

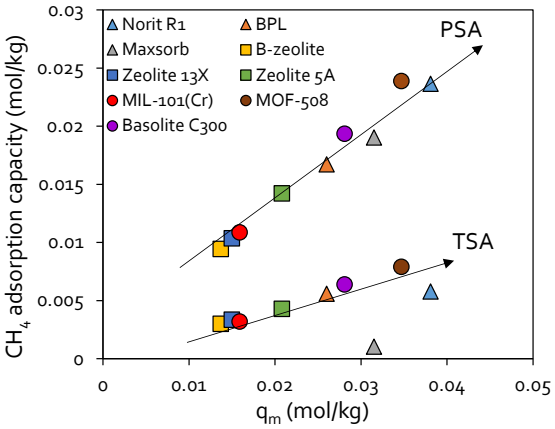


Figure 12. Relationship between methane adsorption capacity and maximum capacity parameter ($q_m$) of Langmuir equation for TSA and PSA based on the different materials studied.

## 4. Conclusions and perspectives

This work studied the diverse ways of harnessing VAM methane emissions generated in the shafts of the underground coal mining exploitations through fixed-bed adsorption. Two variable parameters have been considered: adsorbent material (Norit R1, BPL, Maxsorb, β-zeolite, zeolite 5A, zeolite 13X, Basolite C300, MIL-101(Cr) and MOF-508), and adsorption technique (TSA and PSA). After a design of the operation following the heuristic rules, all possible combinations were simulated, according to a rigorous mathematical model, by Aspen Adsorption software. Carbonaceous materials, especially Norit R1, obtained the highest concentrations in outlet streams, due to their high $CH_4/N_2$ selectivities. These materials also present the lowest methane recoveries (around 30%), mainly related to their low density, and the lowest costs per kmol of methane recovered.

Desorption at maximum concentration spends a brief time in all the cases. In addition, MOFs, especially Basolite C300 and MOF-508, can retain a large amount of methane, due to the presence of open metal sites and high specific surface areas. The $CH_4/N_2$ selectivities are lower than in carbonaceous materials and, therefore, the final methane concentrations obtained are lower. The methane recoveries are really high in these materials, reaching even a 100% in case of MOF-508, but sacrificing certain selectivity towards methane. The costs per kmol of methane recovered are the highest among the materials studied, due mainly to the elevated cost associated to the synthesis of these new materials. Finally, zeolitic materials present the lowest final methane concentration obtained, with intermediate methane recoveries. The costs per kmol of methane recovered are high, due to the low methane adsorption capacity demonstrated and certain affinity to nitrogen and carbon dioxide. Concerning the adsorption technique, TSA has shown higher final methane concentrations in case of carbonaceous materials and some MOFs. On the other hand, PSA allows obtaining higher total methane adsorbed on all the materials, remarking the high dependence of adsorption on the applied pressure, especially on carbonaceous materials. Finally, the economic comparison shows that TSA is, in all cases, more convenient than PSA. Therefore, based on these results, the most competitive combinations include TSA and materials with either high specific surface area or presence of open metal sites, high $CH_4/N_2$ and $CH_4/CO_2$ selectivity, high material density and with the lowest cost per kg as possible. In case of low selectivities or low material density, the application of PSA processes with good working capacities in the pressure working range, can improve the yield of the process.

Finally, concerning the limitations of the work, the most important is the applicability of the mathematical model. The assumptions made allow its application only to low concentration inlet methane streams, as the case of VAM emissions. Therefore, one of the ways of potential future research that opens is to improve and expand the mathematical model to be able to cover a wider range of conditions (CBM and AMM streams), for which a greater record of experimental results at higher concentrations of methane is needed and nowadays not available.

### Credit authorship contribution statement

**David Ursueguía**: Writing-original draft, Software, Data curation, Formal analysis.

**Eva Díaz**: Visualization, Conceptualization, Project administration.

**Salvador Ordóñez**: Visualization, Conceptualization, Supervision, Funding acquisition, Writing-review & editing.

**Acknowledgements**

This work was supported by the Research Fund of Coal and Steel of the European Union (contract RFCS216-754077-METHENERGY PLUS) and the Government of the Principality of Asturias (GRUPIN AYUD/2021/50450).

David Ursueguía acknowledges the Spanish Ministry of Education for the PhD grant that supports his research: FPU2018-01448.

## 5. References

[1] 2030 climate and energy framework. Greenhouse gas emissions – raising the ambition. https://ec.europa.eu/clima/policies/strategies/2030_en (accessed 06/06/2021).

[2] T. Damassa, 2014; Climate Analysis Indicators Tool (CAIT), Encyclopedia of Quality of Life and Well-Being Research (2014).

[3] R. Howarth, 2014; A bridge to nowhere: methane emissions and the greenhouse gas footprint of natural gas, Energy Science and Engineering 2 (2014) 47-60.

[4] S. Kilkis, G. Krajacic, N. Duic, M. Rosen, M. Al-Nimr, 2020; Advances in integration of energy, water, and environment systems towards climate neutrality for sustainable development, Energy Conversion and Management 225 (2020) 113410.

[5] R. Pandey, S. Harpalani, 2019; Evaluation of dynamic flow and production behavior of biogenic methane reservoirs, 53rd U.S. Rock Mechanics/Geomechanics Symposium, New York City, New York, 2019.

[6] M. Schoell, 1988; Multiple origins of methane in the Earth, Chemical Geology 71 (1998) 1-10.

[7] B. Pieprzyk, P. Hilje, 2018; Influence of methane emissions on the GHG emissions of fossil fuels, Biofuels, Bioproducts and Biorefining 13 (2018) 535-551.

[8] S. Park, Y. Liang, 2016; Biogenic methane production from coal: A review on recent research and development on microbially enhanced coalbed methane (MECBM), Fuel 166 (2016) 258-267.

[9] N. Thiagarajan, N. Kitchen, H. Xie, C. Ponton, M. Lawson, M. Formolo, J. Eiler, 2020; Identifying thermogenic and microbial methane in deep water Gulf of Mexico Reservoirs, Geochimica et Cosmochimica Acta 275 (2020) 188-208.

[10] C. Sapart, G. Monteil, M. Prokopiou, R. van de Wal, J. Kaplan, P. Sperlich, K. Krumhardt, C. van der Veen, S. Houweling, M. Krol, T. Blunier, T. Sowers, P. Martinerie, E. Witrant, D. Jensen, T. Röckmann, 2012; Natural and anthropogenic variations in methane sources during the past two millennia, Nature 490 (2012) 85-88.

[11] N. Khokhar, J. Park, 2017; A simplified sampling procedure for the estimation of methane emission in rice fields, Environmental Monitoring and Assessment 189 (2017) 468.

[12] A. Brandt, G. Heath, E. Kort, F. O'Sullivan, G. Pétron, S. Jordaan, P. Tans, J. Wilcox, A. Gopstein, D. Arent, S. Wofsy, N. Brown, R. Bradley, G. Stucky, D. Eardley, R. Harriss, 2014; Methane leaks from North American natural gas systems, Science 343 (2014) 733-735.

[13] L. Klein, M. Ramachandran, T. Kessel, D. Nair, N. Hinds, H. Hamann, N. Sosa, 2018; Wireless sensor networks for fugitive methane emissions monitoring in oil and gas industry, 2018 IEEE International Congress on Internet of Things (ICIOT) (2018) 41-48.

[14] Y. Ju, Y. Sun, Z. Sa, J. Pan, J. Wang, Q. Hou, Q. Li, Z. Yan, J. Liu, 2016; A new approach to estimate fugitive methane emissions from coal mining in China, Science of The Total Environment 543A (2016) 514-523.

[15] S. Kumar, Mineral Exploration: Principles and Applications, 2nd ed. (2018).

[16] N. Kholod, M. Evans, R. Pilcher, V. Roshchanka, F. Ruiz, M. Coté, R. Collings, 2020; Global methane emissions from coal mining to continue growing even with declining coal production, Journal of Cleaner Production 256 (2020) 120489.

[17] A. Duda, A. Krzemien, 2018; Forecast of methane emission from closed underground coal mines exploited by longwall mining – A case study of Anna coal mine, Journal of Sustainable Mining 17 (2018) 184-194.

[18] UNECE, 2019; Best practice guidance for effective methane recovery and use from abandoned coal mines. https://unece.org/fileadmin/DAM/energy/images/CMM/CMM_CE/AMM_BPG_FINAL.pdf (accessed 05/06/2021).

[19] A. Denysenko, M. Evans, N. Kholod, N. Butler, V. Roshchanka, 2018; Legal and regulatory status of abandoned mine methane in selected countries: Considerations for decision makers, Pacific Northwest National Laboratory (2018).

[20] K. Warmuzinski, 2008; Harnessing methane emissions from coal mining, Process Safety and Environmental Protection 86 (2008) 315-320.

[21] Z. Yang, M.Z. Hussain, P. Marín, Q. Jia, N. Wang, S. Ordóñez, Y. Zhu, Y. Xia, 2022; Enrichment of low concentration methane: an overview of ventilation air methane, Journal of Materials Chemistry A 10 (2022) 6397-6413.

[22] X. Yang, Y. Liu, Z. Li, C. Zhang, Y. Xing, 2018; Vacuum exhaust process in pilot-scale vacuum pressure swing adsorption for coal mine ventilation air methane enrichment, Energies 11 (2018) 1030.

[23] C. Karacan, F. Ruiz, M. Cotè, S. Phipps, 2011; Coal mine methane: A review of capture and utilization practices with benefits to mining safety and to greenhouse gas reduction, International Journal of Coal Geology 86 (2011) 121-156.

[24] D. Ursueguía, P. Marín, E. Díaz, S. Ordóñez, 2021; A new strategy for upgrading ventilation air methane emissions combining adsorption and combustion in a

lean-gas turbine, Journal of Natural Gas Science and Engineering 88 (2021) 103808.

[25] D. Ursueguía, E. Díaz, S. Ordóñez, 2021; Metal-organic frameworks (MOFs) as methane adsorbents: From storage to diluted coal mining streams concentration, Science of The Total Environment 790 (2021) 148211.

[26] H. Vogtenhuber, R. Hofmann, F. Helminger, G. Schöny, 2018; Process simulation of an efficient temperature swing adsorption concept for biogas upgrading, Energy 162 (2018) 200-209.

[27] Y. L. Li, Y.S. Liu, X. Yang, 2013; Proportion pressure swing adsorption for low concentration coal mine methane enrichment, 48(8) (2013) 1201-1210.

[28] K. Karimi, S. Fatemi, 2021; Methane capture and nitrogen purification from a nitrogen rich reservoir by pressure swing adsorption; experimental and simulation study, Journal of Environmental Chemical Engineering 9 (2021) 106210.

[29] X. Wang, F. Zhou, Y. Ling, Y. Xiao, B. Ma, X. Ma, S. Yu, H. Liu, K. Wei, J. Kang, 2021; Overview and outlook on utilization technologies of low-concentration coal mine methane, Energy Fuels 35 (2021) 15398-15423.

[30] J. Yang, H. Bai, H. Shang, J. Wang, J. Li, S. Deng, 2020; Experimental and simulation study on efficient $CH_4/N_2$ separation by pressure swing adsorption on silicalite-1 pellets, Chemical Engineering Journal 388 (2020) 124222.

[31] D. Bahamon, L. Vega, 2016; Systematic evaluation of materials for post-combustion $CO_2$ capture in a Temperature Swing Adsorption process, Chemical Engineering Journal 284 (2016) 438-447.

[32] B. Maring, P. Webley, 2013; A new simplified pressure/vacuum swing adsorption model for rapid adsorbent screening for $CO_2$ capture applications, International Journal of Greenhouse Gas Control 15 (2013) 16-31.

[33] T. Dantas, F. Luna, I. Silva, D. Azevedo, C. Grande, A. Rodrigues, R. Moreira, 2011; Carbon dioxide-nitrogen separation through adsorption on activated carbon in a fixed bed, Chemical Engineering Journal 169 (2011) 11-19.

[34] D. Qu, Y. Yang, Z. Qian, P. Li, J. Yu, A. Ribeiro, A. Rodrigues, 2020; Enrichment of low-grade methane gas from nitrogen mixture by VPSA with $CO_2$ displacement process: Modeling and experiment, Chemical Engineering Journal 380 (2020) 122509.

[35] D. Ursueguía, E. Díaz, A. Vega, S. Ordóñez, 2020; Methane separation from diluted mixtures by fixed bed adsorption using MOFs: Model validation and parametric studies, Separation and Purification Technology 251 (2020) 117374.

[36] J. Couper, W. Penney, J. Fair, S. Walas, 2005; Chemical process equipment: Selection and design, third ed. Elsevier, Waltham (MA).

[37] R. Ben-Mansour, N. Qasem, 2018; An efficient temperature swing adsorption (TSA) process for separating $CO_2$ from $CO_2/N_2$ mixture using Mg-MOF-74, Energy Conversion and Management 156 (2018) 10-24.

[38] L. Chen, S. Deng, R. Zhao, Y. Zhu, L. Zhao, S. Li, 2021; Temperature swing adsorption for $CO_2$ capture: Thermal design and management on adsorption bed with single-tube/three-tube internal heat exchanger, Applied Thermal Engineering 199 (2021) 117538.

[39] Equipment costs, 2003. Plant design and economics for chemical engineers. https://www.mhhe.com/engcs/chemical/peters/data/ (accessed 25/05/2021).

[40] R. Perry, D. Green, 1997. Perry's Chemical Engineer's Handbook, 7th edition, McGraw-Hill, 1997. Section 11.

[41] R. Canevesi, C. Borba, E. Silva, C. Grande, 2019; Towards a design of a pressure swing adsorption unit for small scale biogas upgrading at, Energy Procedia 158 (2019) 848-853.

[42] M. Luberti, H. Ahn, 2022; Review of Polybed pressure swing adsorption for hydrogen purification, International Journal of Hydrogen Energy 47 (2022) 10911-10933.

[43] G. Vilardi, C. Bassano, P. Deiana, N. Verdone, 2020; Exergy and energy analysis of biogas upgrading by pressure swing adsorption: Dynamic analysis of the process, Energy Conversion and Management 226 (2020) 113482.

[44] M. Yavary, H. Ebrahim, C. Falamaki, 2015; The effect of number of pressure equalization steps on the performance of pressure swing adsorption process, Chemical Engineering and Processing: Process Intensification 87 (2015) 35-44.

[45] Y. Kim, Y. Nam, Y. Kang, 2015; Study on a numerical model and PSA (pressure swing adsorption) process experiment for $CH_4/CO_2$ separation from biogas, Energy 91 (2015) 732-741.

[46] N. Wilkins, A. Rajendran, S. Farooq, 2020; Dynamic column breakthrough experiments for measurement of adsorption equilibrium and kinetics, Adsorption 27 (2020) 397-422.

[47] A. Gabelman, 2017; Adsorption basics: Part 1. https://www.aiche.org/resources/publications/cep/2301 7/july/adsorption-basics-part-1. (Accessed 15/05/2020).

[48] Costs reports and guidance for air pollution regulations, 2018. https://www.epa.gov/economic-and-cost-analysis-air-pollution-regulations/cost-reports-and-guidance-air-pollution (accessed 20/05/2021).

[49] C. Perego, S. Peratello, 1999; Experimental methods in catalytic kinetics, Catalysis Today 52 (1999) 133-145.

[50] Z. Niu, X. Cui, T. Pham, P. Lan, H. Xing, K. Forrest, L. Wojtas, B. Space, S. Ma, 2019; A metal-organic framework based methane nano-trap for the capture of coal-mine methane, Angewandte Chemie International Edition 58 (2019) 10138-10141.

[51] F. Ortiz, M. Barragán, R. Yang, 2019; Modeling of fixed-bed columns for gas physical adsorption, Chemical Engineering Journal 378 (2019) 121985.

[52] M. Rupa, A. Pal, S. Mitra, B. Saha, 2021; Time adapted linear driving force model for gas adsorption

onto solids, Chemical Engineering Journal 420 (2021) 129785.

[53] U. Chaemwinyoo, P. Marín, C.F. Martín, F.V. Díez, S. Ordóñez, 2022; Assessment of an integrated adsorption-regenerative catalytic oxidation process for the harnessing of lean methane emissions, Journal of Environmental Chemical Engineering 10 (2022) 107013.

[54] H. Xu, D. Tang, J. Zhao, S. Li, S. Tao, 2015; A new laboratory method for accurate measurement of the methane diffusion coefficient and its influencing factors in the coal matrix, Fuel 158 (2015) 239-247.

[55] N. Jensen, T. Rufford, G. Watson, D. Zhang, K. Chan, E. May, 2012; Screening zeolites for gas separation applications involving methane, nitrogen, and carbon dioxide, Journal of Chemical Engineering Data 57 (2012) 106-113.

[56] L. Zhu, D. Shen, K. Luo, 2020; A critical review on VOCs adsorption by different porous materials: Species, mechanisms and modification methods, Journal of Hazardous Materials 389 (2020) 122102.

[57] R. Sabouni, H. Kazemian, S. Rohani, 2013; Mathematical modeling and experimental breakthrough curves of carbon dioxide adsorption on metal organic framework CPM-5, Environmental Science and Technology 47 (2013) 9372-9380.

[58] N. Querejeta, S. García, N. Álvarez-Gutiérrez, F. Rubiera, C. Pevida, 2019; Measuring heat capacity of activated carbons for $CO_2$ capture, Journal of $CO_2$ Utilization 33 (2019) 148-156.

[59] Y. Zheng, Q. Li, C. Yuan, Q. Tao, Y. Xhao, G. Zhang, J. Liu, 2019; Influence of temperature on adsorption selectivity: Coal-based activated carbon for $CH_4$ enrichment from coal mine methane, Powder Technology 347 (2019) 42-49.

[60] D. Peredo-Mancilla, C. Ghimbeu, B. Ho, M. Jeguirim, C. Hort, D. Bessieres, 2019; Comparative study of the $CH_4/CO_2$ adsorption selectivity of activated carbons for biogas upgrading, Journal of Environmental Chemical Engineering 7 (2019) 103368.

[61] F. Gholipour, M. Mofarahi, 2016; Adsorption equilibrium of methane and carbon dioxide on zeolite 13X: Experimental and thermodynamic modeling, The Journal of Supercritical Fluids 111 (2016) 47-54.

[62] P. Li, H. Tezel, 2007; Adsorption separation of $N_2$, $O_2$, $CO_2$ and $CH_4$ gases by β-zeolite, Microporous and Mesoporous Materials 98 (2007) 94-101.

[63] M. Ghazvini, M. Vahedi, S. Nobar, F. Sabouri, 2021; Investigation of the MOF adsorbents and the gas adsorptive separation mechanisms, Journal of Environmental Chemical Engineering 9 (2021) 104790.

[64] M. Neves, E. Gkaniatsou, F. Nouar, M. Pinto, C. Serre, 2021; MOF industrialization: a complete assessment of production costs, Faraday Discussions (2021).

[65] S. Himeno, T. Komatsu, S. Fujita, 2005; High-pressure adsorption equilibria of methane and carbon dioxide on several activated carbons, Journal of Chemical Engineering Data 50 (2005) 369-376.

[66] J. Wu, O. Claesson, I. Fangmark, L. Hammarstrom, 2005; A systematic investigation of the overall rate coefficient in the Wheeler-Jonas equation for adsorption on dry activated carbons, Carbon 43 (2005) 481-490.

[67] J. Delgado, V. Águeda, M. Uguina, J. Sotelo, P. Brea, C. Grande, 2014; Adsorption and diffusion of $H_2$, CO, $CH_4$, and $CO_2$ in BPL activated carbon and 13X zeolite: Evaluation of performance in pressure swing adsorption hydrogen purification by simulation, Industrial and Engineering Chemistry Research 53 (2014) 15414-15426.

[68] M. Sheikh, M. Hassan, K. Loughlin, 1996; Adsorption equilibria and rate parameters for nitrogen and methane on Maxsorb activated carbon, Gas Separation and Purification 10 (1996) 161-168.

[69] M. Han, X. Li, S. Lin, 2002; Diffusion transfer in the course of benzene alkylation with propylene over a β-zeolite catalyst, Theoretical Foundations of Chemical Engineering 36 (2002) 259-263.

[70] J. Du, Q. Wang, Y. Wang, Y. Guo, R. Li, 2019; A hierarchical zeolite Beta with well-connected pores via using graphene oxide, Materials Letters 250 (2019) 139-142.

[71] S. Cavenati, C. Grande, A. Rodrigues, 2004; Adsorption equilibrium of methane, carbon dioxide, and nitrogen on zeolite 13X at high pressures, Journal of Chemical Engineering Data 49 (2004) 1095-1101.

[72] P. Jadhav, R. Chatti, R. Biniwale, N. Labhsetwar, S. Devotta, S. Rayalu, 2007; Monoethanol amine modified zeolite 13X for $CO_2$ adsorption at different temperatures, Energy Fuels 21 (2007) 3555-3559.

[73] Z. Liu, C. Grande, P. Li, J. Yu, A. Rodrigues, 2011; Adsorption and desorption of carbon dioxide and nitrogen on zeolite 5A, Separation Science and Technology 46 (2011) 434-451.

[74] Q. Al-Naddaf, H. Thakkar, F. Rezaei, 2018; Novel zeolite-5A@MOF-74 composite adsorbents with core-shell structure for $H_2$ purification, ACS Applied Materials and Interfaces 10 (2018) 29656-29666.

[75] K. Munusamy, G. Sethia, D. Patil, P. Rallapalli, R. Somani, H. Bajaj, 2012; Sorption of carbon dioxide, methane, nitrogen and carbon monoxide on MIL-101(Cr): Volumetric measurements and dynamic adsorption studies, Chemical Engineering Journal 195-196 (2012) 359-368.

[76] M. Hartmann, M. Fischer, 2012; Amino-functionalized basic catalysts with MIL-101 structure, Microporous and Mesoporous Materials 164 (2012) 38-43.

[77] L. Bastin, P. Bárcia, E. Hurtado, J. Silva, A. Rodrigues, B. Chen, 2008; A microporous metal-organic framework for separation of $CO_2/N_2$ and $CO_2/CH_4$ by fixed-bed adsorption, The Journal of Physical Chemistry C 112 (2008) 1575-1581.

[78] W. Gao, W. Yan, R. Cai, K. Williams, A. Salas, L. Wojtas, X. Shi, S. Ma, 2012; A pillared metal-organic framework incorporated with 1,2,3-triazole moieties exhibiting remarkable enhancement of $CO_2$ uptake, Chemical Communications 48 (2012) 8898-8900.

[79] H. Teo, A. Chakraborty, S. Kayal, 2017; Evaluation of $CH_4$ and $CO_2$ adsorption on HKUST-1 and MIL-101(Cr) MOFs employing Monte Carlo simulation and comparison with experimental data, Applied Thermal Engineering 110 (2017) 891-900.

[80] D. Ursueguía, E. Díaz, S. Ordóñez, 2020; Densification-induced structure changes in Basolite MOFs: Effect on low-pressure $CH_4$ adsorption, Nanomaterials 10 (2020) 1089.

[81] P. Brea, J. Delgado, V. Águeda, M. Uguina, 2017; Modeling of breakthrough curves of $N_2$, $CH_4$, CO, $CO_2$ and a SMR type off-gas mixture on a fixed bed of BPL activated carbon, Separation and Purification Technology 179 (2017) 61-71.

[82] F. Rainone, O. D'Agostino, A. Erto, M. Balsamo, A. Lancia, Biogas upgrading by adsorption onto activated carbon and carbon molecular sieves: Experimental and modelling study in binary $CO_2/CH_4$ mixture, Journal of Environmental Chemical Engineering 9 (2021) 106256.

[83] G. Xiu, P. Li, 2000; Prediction of breakthrough curves for adsorption of lead(II) on activated carbon fibers in a fixed bed, Carbon 38 (2000) 975-981.

[84] F. Dreisbach, R. Staudt, J. Keller, 1999; High pressure adsorption data of methane, nitrogen, carbon dioxide and their binary and ternary mixtures on activated carbon, Adsorption 5 (1999) 215-227.

[85] S. Sircar, T. Golden, M. Rao, 1996; Activated carbon for gas separation and storage, Carbon 34 (1996) 1-12.

[86] J. McEwen, J. Hayman, A. Yazaydin, 2013; A comparative study of $CO_2$, $CH_4$ and $N_2$ adsorption in ZIF-8, zeolite-13X and BPL activated carbon, Chemical Physics 412 (2013) 72-76.

[87] L. Gómez, R. Zacharia, P. Bénard, R. Chahine, 2015; Multicomponent adsorption of biogas compositions containing $CO_2$, $CH_4$ and $N_2$ on Maxsorb and Cu-BTC using extended Langmuir and Doong-Yang models, Adsorption 21 (2015) 433-443.

[88] X. Xu, X. Zhao, L. Sun, X. Liu, 2009; Adsorption separation of carbon dioxide, methane and nitrogen on monoethanol amine modified β-zeolite, Journal of Natural Gas Chemistry 18 (2009) 167-172.

[89] A. Bakhtyari, M. Mofarahi, 2014; Pure and binary adsorption equilibria of methane and nitrogen on zeolite 5A, Journal of Chemical Engineering Data 59 (2014) 626-639.

[90] F. Kloutse, A. Hourri, S. Natarajan, P. Benard, R. Chahine, 2018; Hydrogen separation by adsorption: Experiments and modelling of $H_2$-$N_2$-$CO_2$ and $H_2$-$CH_4$-$CO_2$ mixtures adsorption on CuBTC and MOF-5, Microporous and Mesoporous Materials 271 (2018) 175-185.

[91] S. Nobar, S. Farooq, 2012; Experimental and modeling study of adsorption and diffusion of gases in Cu-BTC, Chemical Engineering Science 84 (2012) 801-813.

[92] P. Schoenecker, C. Carson, H. Jasuja, C. Flemming, K. Walton, 2012; Effect of water adsorption on retention of structure and surface area of metal-organic frameworks, Industrial and Engineering Chemistry Research 51 (2012) 6513-6519.

[93] E. Ryckebosch, M. Drouillon, H. Vervaeren, 2011; Techniques for transformation of biogas to biomethane, Biomass and Bioenergy 35 (2011) 1633-1645.

[94] S. Qadir, D. Li, Y. Gu, Z. Yuan, Y. Zhao, S. Wang, S. Wang, 2021; Experimental and numerical investigations on the separation performance of $[Cu(INA)_2]$ adsorbent for $CH_4$ recovery by VPSA from oxygen-bearing coal mine methane, Chemical Engineering Journal 408 (2021) 127238.

[95] J. Bae, S. Su, X. Yu, 2014; Enrichment of ventilation air Methane (VAM) with carbon fiber composites, Environmental Science and Technology 48 (2014) 6043-6049.

[96] S. Su, J. Agnew, 2006; Catalytic combustion of coal mine ventilation air methane, Fuel 85 (2006) 1201-1210.

[97] W. Cheng, W. Nie, H. Yu, A. Zheng, 2017; Development status of dust-control technologies for the mechanized mining working face in China, NexGen Technologies for Mining and Fuel Industries, Allied Publishers PVT.

[98] T. Golden, R. Kumar, 1993; Adsorption equilibrium and kinetics for multiple trace impurities in various gas streams on activated carbon, Industrial and Engineering Chemistry Research 32 (1993) 159-165.

[99] R. Yang, Adsorbents: fundamentals and applications, 1st ed., John Wiley & Sons (2003).

[100] M. Xu, H. Wu, Y. Lin, S. Deng, 2018; Simulation and optimization of Pressure swing adsorption process for high-temperature air separation by perovskite sorbents, Chemical Engineering Journal 354 (2018) 62-74.

[101] A. Ghoshal, S. Manjare, 2002; Selection of appropriate adsorption technique for recovery of VOCs: an analysis, Journal of Loss Prevention in the Process Industries 15 (2002) 413-421.

[102] J. Bae, S. Su, X. Yu, J. Yin, A. Villella, M. Jara, M. Loney, 2020; Site trials of ventilation air methane enrichment with two-stage vacuum, temperature, and vacuum swing adsorption, Industrial and Engineering Chemistry Research 35 (2020) 15732-15741.

[103] S. Ouyang, S. Xu, N. Song, S. Jiao, 2013; Coconut shell-based carbon adsorbents for ventilation air methane enrichment, Fuel 113 (2013) 420-425.

[104] NIST's Standard Reference Database Number 69. https://doi.org/10.18434/T4D303.

[105] J. Silvestre-Albero, C. Salazar, A. Sepúlveda-Escribano, F. Rodríguez-Reinoso, 2001; Characterization of Microporous solids by immersion calorimetry, Colloids and Surfaces A: Physicochemical and Engineering Aspects 187-188 (2001) 151-165.

[106] J. Silva, A. Ferreira, P. Mendes, A. Cunha, K. Gleichmann, A. Rodrigues, 2015; Adsorption equilibrium and dynamics of fixed bed adsorption of $CH_4/N_2$ in binderless beads of 5A zeolite, Industrial and Engineering Chemistry Research 54 (2015) 6390-6399.

[107] S. Cavenati, C. Grande, A. Rodrigues, 2006; Separation of $CH_4/CO_2/N_2$ mixtures by layered pressure swing adsorption for upgrade of natural gas, Chemical Engineering Science 61 (2006) 3893-3906.

[108] J. Liu, H. Cao, Y. Shi, P. Jiang, 2021; Enhanced methane delivery in MIL-101(Cr) by means of subambient cooling, Energy Fuels 35 (2021) 6898-6908.

[109] P. Bárcia, L. Bastin, E. Hurtado, J. Silva, A. Rodrigues, B. Chen, 2008; Single and multicomponent sorption of $CO_2$, $CH_4$ and $N_2$ in a microporous metal-organic framework, Separation Science and Technology 43 (2008) 3494-3521.

# A new strategy for upgrading ventilation air methane emissions combining adsorption and combustion in a lean-gas turbine

David Ursueguía, Pablo Marín, Eva Díaz, Salvador Ordóñez*

Catalysis, Reactors and Control Research Group (CRC), Department of Chemical and Environmental Engineering, University of Oviedo, Julián Clavería s/n, 33006 Oviedo, Spain

*e-mail: sordonez@uniovi.es (S. Ordóñez)

*Journal of Natural Gas Science and Engineering* **88** (2021) 103808

https://doi.org/10.1016/j.jngse.2021.103808

## ABSTRACT

This work evaluates the feasibility of harnessing a high-flow (4.4 $Nm^3/s$) and low-concentrated (0.57% $CH_4$) methane stream from a coal mine ventilation emission. Two consecutive processes have been coupled: a fixed bed adsorption used for methane concentration by temperature-swing adsorption, and a combustion process in a lean-gas turbine. Both processes have been simulated using rigorous mathematical model implemented in a commercial simulation package. Regarding the adsorption concentration step, optimized results showed the possibility of obtaining an outlet stream with 1.2% $CH_4$ and a total flowrate of 3.8 $Nm^3/s$. The gas turbine generates a net energy output of 490 kW and provides the heating required in the desorption step. The process design has been completed with an economic evaluation of the process. The estimated initial investment of the process is high (4.74 M€), and the return profitability depends a lot on the cost of the adsorbent material. The process would be profitable in a 20-year period with a 4.25% discount rate for an adsorbent cost lower than 0.6 €/kg.

**Keywords**: ventilation air methane; lean-fuel turbine; temperature-swing adsorption; process integration; process simulation

### 1. Introduction

The concern about the role of methane emissions in the anthropogenic global warming effect has been increased in the last years [1-3]. These emissions are not only a source of environmental concern, but also represent a large amount of wasted energy. Among these emissions, coal mine emissions are of key importance, even in the case of abandoned coal mines. The huge increase in these emissions and its climatic consequences have generated a significant global awareness, and strengthened the need of alternative or less harmful procedures to obtain energy and chemicals. Following this trend, the option of capturing and upgrading these emissions has emerged in recent times [4, 5]. In fact, this capture and harnessing would entail two advantages: the greenhouse emissions reduction and the use of a resource that otherwise would be wasted.

There are mainly three different types of mining emissions containing methane: coal bed methane (CBM), abandoned mine methane (AMM) and ventilation air methane (VAM). The first two contain high and medium purity methane (> 30%) and are easily usable with well-known harnessing technologies available. The VAM has a very low concentration (0.1-1%), so it is usually burned with very low energy efficiency [6-8] or even directly released to the atmosphere [9, 10]. Low concentration methane streams are typically generated in areas where workers and facilities need protection from asphyxiations and explosions. The objective is to keep work areas out of the explosive methane/air limit [11]. Extraction systems in coal mines are mainly fans properly situated in order to ensure adequate and safe conditions, even after the shaft is abandoned [9]. The large flows emitted and the poor development in harnessing techniques made VAM emissions to account for up to 90% of all methane emissions from coal mining [12]. Therefore, the challenge is to upgrade these low purity streams and transform them into a more sustainable energy source or raw material.

The research addressed in the present work has been performed in the context of the European Research Project METHENERGY+,

focused on VAM mitigation and upgrading. Different European coal basins were considered: Upper Silesian Basin (Poland and Czech Republic), Asturian Basin (Spain) and Velenje Basin (Slovenia). These mines present VAM average concentrations in the range 0.1 to 0.3% $CH_4$ with very high total flowrates (even as high as 200 $Nm^3/s$). The characteristics of VAM (*i.e.* flowrate and methane concentration) depend on the mining exploitation and varies upon time. In fact, measurements reported by other authors for mining exploitations from other parts of the world show the possibility of higher VAM concentration, up to 0.9% or even higher [13-15]. These differences may be due to the type of coal extracted, the configuration of the shafts, the safety regulations or the efficiency of the ventilation processes; some of these exploitations have low ventilation flow rates (less than 1 $m^3/s$). Therefore, based on average results of several authors, a stream with fair to moderate methane concentration and air flowrate values has been selected for the analysis made in the present work: 0.57% $CH_4$ and 4.4 $Nm^3/s$, respectively.

The recovery of the energy associated to methane from coal mine ventilation air emissions can be done using lean-burn gas turbines (EDL, CSIRO, IR, etc.). These type of turbines are especially suited to work with low methane concentrations and are able to produce work (electricity) directly. Lean-burn turbines are not widely used for the harnessing of VAM, because they require a minimum methane concentration of 1% [16], which is rather high for most VAM emissions. Hence, a previous methane concentration step is needed. Still, there are some cases, such as, the cost-effective lean-burn turbine designed by Su et al. [17], which have obtained 19-21 kWe of electricity output with an inlet stream with 0.8% $CH_4$ in air.

Methane concentration can be achieved by fixed bed adsorption. This is one of the major promising technologies for methane concentration, providing good yields and adequate concentrations for the operation of the gas turbine [18, 19]. Temperature-swing adsorption (TSA) is the most economically feasible, given the lower energy requirements [20], and also the adsorption technique recommended for concentrations lower than 2% [21, 22].

One of the key parameters in TSA processes is the proper selection of the adsorbent material. In this work, we consider two types of adsorbents: metal-organic frameworks (MOFs) and activated carbons. The first have been widely studied and stand out above the others, especially in pure methane gravimetric capacity comparison [23, 24]. MOFs are known for its exceptional storage capacity for gases, such as, hydrogen, methane and carbon dioxide [25]. Active carbons have lower adsorption capacity and selectivity. However, they are major competitors because of their lower cost [26]. Another important parameter is the desorption temperature, related to the energy required to recover the methane concentrated stream from the adsorbent. Studies done by other authors indicate that methane adsorption enthalpy is not very high, which means that the desorption temperature is low [27, 28]. Additionally, the energy required for the desorption step could be obtained from the effluent of the gas turbine [29].

The objective of the present work is the harnessing of a VAM stream using an adsorption-desorption unit, as a first pre-concentration step, and a lean-burn gas turbine to produce electricity. First, the adsorbent material has been selected and the fixed-bed adsorption unit designed. Then, the desorption step has been simulated using Aspen Adsorption software, in order to predict the concentration of methane in the stream sent to the gas turbine. The performance of the lean-burn gas turbine has been simulated using Aspen Hysys and the optimum operating conditions have been determined. The integration of the adsorption-desorption unit with the gas turbine has been evaluated for improving the economy of the overall processes. Finally, the economic evaluation of the process has been presented.

## 2. Methodology

### 2.1. Flowsheet of integrated harnessing process

The harnessing of coal mine ventilation air methane (VAM) emissions has been proposed according to a two-step integrated process: methane concentration in an adsorption-desorption unit, followed by methane combustion in a lean-burn gas turbine. The flowsheet of this process is depicted in Figure 1.

The concentration step is carried out in a fixed bed temperature-swing adsorption (TSA) operation. This unit is inherently discontinuous, with adsorption happening in a first step and, once the adsorbent is saturated, methane in recovered by desorption at a higher temperature. The concentration step must increase methane concentration to a minimum of 1%, in order to use a lean-burn gas turbine for the combustion.

The lean-burn gas turbine is made of three elements: compressor, recuperator and turbine. The turbine is able of generating net work and,

hence, produce electricity. The recuperator is used to pre-heat the feed before the combustion using the part of the energy of the combustion gases. In addition, part of these combustion gases can be used as the drag stream of the desorption process [30], as shown in Figure 1. This level of mass and heat integration is critical, in order to save energy and improve the economy of the process.

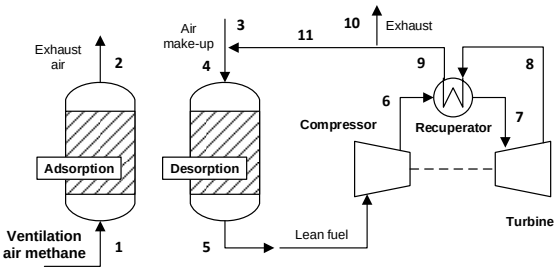


Figure 1. Flowsheet of the TSA-turbine integrated process.

2.2. Selection of the adsorbent material

Both metal organic frameworks (MOF) and active carbons have properties that make them feasible adsorbents for methane. The outstanding properties of MOFs are conferred by large specific surface areas, high pore volume, great porosity and the massive presence of metallic adsorption sites. Regarding active carbons, its low cost, high porosity and large specific surface area stand out as properties. The bottleneck of the process is the separation of methane from nitrogen, as both molecules are very similar in size (3.82 and 3.64 Å, respectively), both have zero dipole and a little higher polarizability in the case of methane ($26{\cdot}10^{-25}$ and $17.6{\cdot}10^{-25}$ $cm^3$, respectively).

Active carbons are commonly used for the separation of volatile organic compounds, where the molecular size of the organic molecules and nitrogen or oxygen is quite different [31]. However, the reported adsorption capacity for methane/nitrogen mixtures is low, *e.g.*, for a commercial activated carbon Norit RB3 methane saturation is 6.75 mmol/g and methane/nitrogen selectivity 1.3 [32]. Its low adsorption capacity questions the possibility of reaching product streams with concentrations high enough to operate the subsequent turbine. On the other hand, separation capacity of MOFs is higher [33]. In many cases, the enhance adsorption capacity is caused by the presence of active metallic sites in the structure, since differences in polarity or polarizability of adsorbate molecules can mean also differences in attraction by these metallic centres through electrostatic interactions [34]. Among the MOFs, Basolite C300 has exceptional yields in gas separation processes [35], in addition to be one of the best performing materials for methane adsorption and storage [36]. Laboratory research on this material has shown the ability to separate methane and nitrogen mixtures at low pressures, obtaining pure methane/nitrogen selectivity up to 2.2 at 0.1 MPa and 298 K [37]. Therefore, Basolite C300 is selected as adsorbent material for the design of the adsorption-desorption unit.

From adsorption isotherms obtained for methane/nitrogen mixtures at 298 K, and also considering the maximum adsorption capacities for both pure gases at different temperatures on Basolite C300 [37], methane/nitrogen adsorption isotherms can be approximated from the initial isotherm at different temperatures (293-353 K). In the approximation, it is supposed that the relative variations in total adsorption gravimetric capacity for each gas ($P_P = 1$) is practically the same in all the points that conform the isotherm ($P_P < 1$). This approximation can be done at low pressures, in which the isotherm shape is similar for all temperatures [38]. Further, similarity in behaviour of nitrogen and oxygen isotherms on Basolite C300 [39], as well as, the large presence of nitrogen in the streams to be treated allow performing the simulation using methane-nitrogen isotherms, with low deviation and even being a conservative design, since nitrogen adsorption capacity is higher than for oxygen. Isotherms obtained are fit to a simple Langmuir model (Equation 1), and the fitting parameters are presented in Table 1.

$$q_e = \frac{q_m K_L P_P}{1 + K_L P_P} \quad ; \; K_L = K_{L0} e^{\frac{-\Delta H}{RT}} \qquad (1)$$

Table 1. Langmuir model parameters for methane-nitrogen adsorption [37].

| Component | Methane | Nitrogen |
|---|---|---|
| $q_m$ (mg $g^{-1}$) | 81.96 | 77.51 |
| $K_{L0}$ (kPa$^{-1}$) | $7.45{\cdot}10^{-8}$ | $4.30{\cdot}10^{-8}$ |
| $\Delta H$ (kJ $mol^{-1}$) | -29.5 | -30.2 |

Values of $q_m$ are independent of temperature, whereas $K_L$ depends strongly on it [40]. Temperature dependence of $K_L$ can be approximated by Van't Hoff equation (Equation 5). This model predicts the equilibrium values of both gases at each partial pressure and temperature. For example, at 298 K and 0.1% $CH_4$ at 100 kPa, methane adsorption capacity is 0.095 mg/g and nitrogen adsorption capacity is 35.68 mg/g.

2.3. Adsorption/desorption simulation

Prior to real scale experimentation, given the investment costs involved, it is proposed the modelling and simulation of a large scale operation that fits as close as possible to the real process. The generation of a realistic model in an appropriate simulation software allows obtaining results for different initial values, making comparisons in key parameters and deciding the best conditions to carry it out, which could be based on economic or yield criteria.

Adsorption in fixed bed can be modelled, and the breakthrough curves predicted, using a dynamic heterogeneous one-dimensional model. The following assumptions have been considered to develop the model equations: isothermal conditions, negligible radial gradients (of fluid velocity, bed void, dispersion coefficient, etc.) and spherical homogeneous adsorbent particle. The gas phase mass balance (Equation 2) includes, respectively, accumulation, convection flow, axial dispersion, and interphase mass transfer terms. The solid phase mass balance (Equation 3) is formed by accumulation and interphase mass transfer terms.

Interphase mass transfer has been modelled using a linear driving force (LDF) expression. This model relates mass transport and the adsorption equilibrium, calculated using the Langmuir adsorption isotherms (Equation 1). This relation depends on the mass-transfer resistances for the transport of the adsorbate from the bulk gas phase to the adsorbent surface. In case of an adsorbent made of micropores, like MOFs, the adsorption mass transfer rate is controlled by diffusion in the micropore network (as indicated in Equation 2 and 3). This model has been validated in the scope of a previous work using break curves obtained in a Basolite C300 fixed-bed and working for different methane/nitrogen concentrations [41].

Desorption of methane is carried out using a drag gas and an increase of temperature, *i.e.*, temperature-swing adsorption (TSA). Hence, the model must be completed with the incorporation of the energy balance to the gas and solid phases (Equation 4 and 5).

In the heating stage, the drag gas enters the fixed bed at elevated temperature, so there is an initial thermal gradient between solid and gas phases [42]. The velocity at which thermal equilibrium is reached depends on the heat transfer coefficient ($h_s$), calculated using correlations for fixed-beds based on Nusselt and Prandtl dimensionless numbers [43]. Additional parameters, such as, the specific heat capacity ($C_{ps}$) are obtained from other works [44]. Variations in temperature through the bed and upon time affect the equilibrium adsorption, predicted using Equation 1. On the other hand, the cooling stage is similar but with air passing at the adsorption temperature.

This set of differential equations, combined with the adsorbent and inlet flow properties, as well as with the adsorption isotherm equation, are able of predicting the behaviour of VAM adsorption. It is possible to obtain the break-through adsorption curve, the concentration of the adsorbates in the solid at saturation conditions, the corresponding desorption curve and the outlet methane concentration obtained at the end of the concentration stage.

The previous model equations have been solved with the help of Aspen Adsorption software. Figure 2 shows the corresponding flowsheet diagram. The discretization method used to solve the equations is UDS1 with 20 nodes. Momentum balance is calculated through Ergun equation.

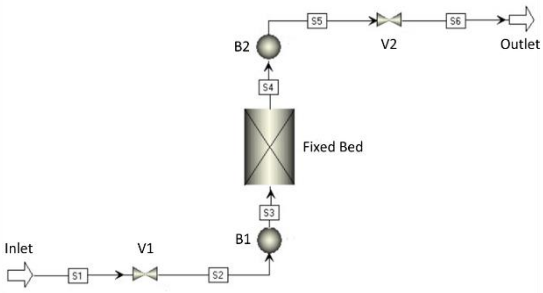


Figure 2. Aspen Adsorption flowsheet diagram for a single-bed adsorption/desorption process.

2.4. Lean-burn turbine simulation

The lean-burn turbine has been simulated using Aspen Hysys. The flowsheet diagram of the process, shown in Figure 3, is formed by three elements [17]: a compressor, a heat exchanger or recuperator, a conversion reactor and an expander.

The compressor is used to increase the pressure of the gas feed (100 kPa); the main design parameter being the pressure ratio (outlet pressure/feed pressure). The compressor is modelled as a single-stage centrifugal compressor with adiabatic efficiency of 75%. In the compressor, temperature also increases, but, in lean-burn turbines, this increase is not enough to trigger the combustion, because methane concentration is below the lower flammability limit (< 5%).

$$\frac{\partial C_i}{\partial t} = -\frac{u_0}{\varepsilon_b}\frac{\partial C_i}{\partial Z} + D_e\frac{\partial^2 C_i}{\partial Z^2} - 15\frac{4\rho_b(1-\varepsilon_b)}{\varepsilon_b {d_p}^2} D_i\left(W_{ieq} - W_i\right) \quad (2)$$

$$\frac{\partial W_i}{\partial t} = 15\frac{4}{{d_p}^2} D_i\left(W_{ieq} - W_i\right) \quad (3)$$

$$\frac{\partial T_g}{\partial t} = -u_0\frac{\partial T_g}{\partial Z} + h_s\frac{a_p}{C_{pg}\rho_g}\left(T_s - T_g\right) \quad (4)$$

$$\frac{\partial T_s}{\partial t} = h_s\frac{a_p}{C_{ps}\rho_b}\left(T_g - T_s\right) \quad (5)$$

Hence, temperature must be increased, at least to 1073 K, using a heat exchanger, called recuperator. The area required by the recuperator is calculated assuming a global heat transfer coefficient of 0.01 kW/m² K (typical of gas-to-gas heat exchangers).

The methane combustion reaction has been modelled using a conversion reactor with 100% methane conversion. The combustion gases are expanded to recover part of their energy as work. An expander with an isentropic efficiency of 75% is used in the model. Finally, the exhaust of the expander, which is at high temperature, is used to supply the energy required in the recuperator.

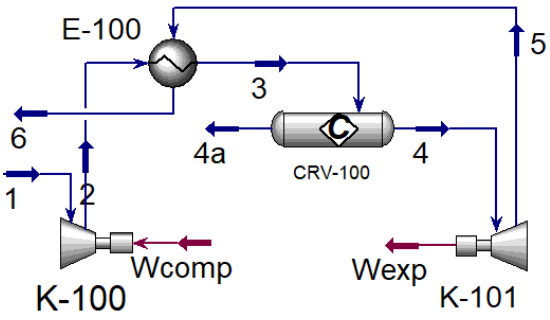


Figure 3. Aspen Adsorption flowsheet diagram for a single-bed adsorption/desorption process.

## 3. **Results and discussion**

### 3.1. Design of fixed bed adsorption-desorption unit

Fixed beds are generally vertical columns with set dimensions and filled with a fixed amount of adsorbent, necessary to reach the performance specifications in both adsorption and desorption processes, which usually are consecutive. The length and diameter depend on the inlet flowrate, as well as on the volume required for locating the required solid adsorbent loading. Likewise, the choice of the adsorbent particle size is also for preventing large pressure drops and ensuring good gas-solid contact. As Gabelman [45] has indicated, surface velocity and particle size selection, and diameter and bed length calculation are the four basic points to estimate in order to make a successful fixed bed design. These parameters, in addition to the operation temperature, could change the final yield of the operation. Table 2 shows the general effects of these parameters on the final adsorption and desorption performance.

The surface velocity provides enough residence time for the required adsorption, and an acceptable pressure drop. Typical surface velocities for gases in a fixed bed are between 0.2 and 0.5 m/s [46].

In case of Basolite C300, 0.24 m/s is selected as surface velocity for adsorption, whereas 0.48 m/s for desorption. Continuing with particle size ($d_p$), in general, the smallest the particle size, the highest the mass-transfer rate, due to the shorter particle diffusion path. Overall, selected particle sizes are generally those that allow the best contact with allowable pressure drops, so a compromise is necessary.

Pressure drop can be estimated by a mechanical balance (Ergun equation, Equation 6). Gas physical properties as viscosity ($\mu_g$ = $1.7{\cdot}10^{-5}$ Pa·s) and density ($\rho_g$ = 1.18 kg/m³) are known at adsorption temperature (298 K), as well as, surface velocity ($u_o$ = 0.24 m/s) and bed porosity ($\varepsilon_b$), which is supposed to be close to 0.4, considering particles almost spherical and randomly packed [47]. Typical particle sizes in an industrial operation are between 0.5 and 10 mm [46]. Based on Figure 4, particles from 2 mm onwards could be used, even in fairly long beds, for both adsorption and desorption processes. Temperature selected in the desorption process is 343 K.

Once the surface velocity, the particle size and the characteristics of the input stream are known, it is possible to calculate the appropriate dimensions of the fixed bed [48]. Couper et al. [46] have indicated that the range of typical operating time for a gas phase in an adsorption process is between 0.5 and 8 hours.

Table 2. Effect of an increase of several operational parameters on the adsorption and desorption performance.

| Parameter | Typical range | Affects to* |
|---|---|---|
| Bed length | 0-14 m | Fixed bed efficiency (+), breakthrough time (+), pressure drop (+), total costs (+) and cycle time (+) |
| Bed diameter | 0-3.5 m | Surface velocity (-), isothermal fixed bed thermal regime (-) and number of total necessary parallel fixed beds (-) |
| Surface velocity | 0.2-0.5 m/s | Residence time (-), breakthrough time (-), pressure drop (+), product dilution (-) and cycle time (-) |
| Particle diameter | 0.5-10 mm | Solid-gas contact (-) and pressure drop (-) |
| Temperature | Upper limit: material decomposition | Adsorption capacity (-), total costs (+) and desorption capacity (+) |

* (+) means an increase and (-) a decrease respect to the increase in the studied parameter.

$$\frac{\partial P}{\partial Z} = \frac{150\mu_g(1-\varepsilon_b)^2}{d_p^2\varepsilon_b^3}u_0 + \frac{1.75\rho_g(1-\varepsilon_b)}{d_p\varepsilon_b^3}u_0^2 \quad (6)$$

Adsorbers 14 m high and 3.5 m in diameter, as maximum sizes, are typically in use. In fact, bed utilization efficiency increases with bed length, because the part of unused bed becomes a smaller portion [45], but also increases the operative fixed costs and the total pressure drop.

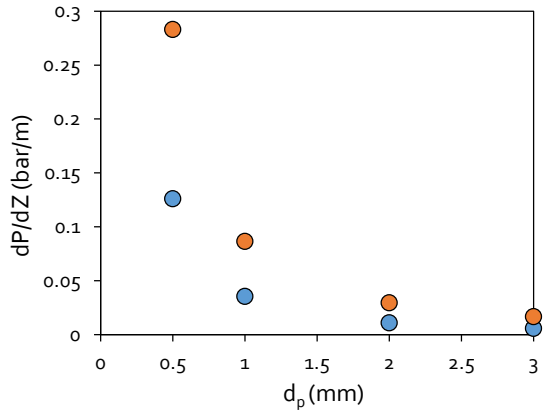


Figure 4. Pressure drop, calculated by Ergun equation (Equation 6), in function of total fixed bed length (bar/m) in the process, for different adsorbent particle sizes. Adsorption (blue circles) and desorption (orange circles).

Diameter selection should also take into account the exothermic nature of adsorption, in order to avoid great temperature increments during the process, thus a relative high surface-to-volume ratio is desirable [48]. In this case, the total inlet flow rate is high (4.4 $Nm^3/s$), so 4 equal fixed beds are assumed to be working in parallel at the adsorption stage, in order to be able to process the entire incoming flow. Each fixed bed is 2.5 m in diameter and 10 m high (Figure 5), which present a surface-to-volume ratio of 1.6, being able to consider it an isothermal operation in the adsorption stage. The total internal volume of each fixed bed is 49 $m^3$, which are completely filled with Basolite C300. The bulk density of the adsorbent is 350 $kg/m^3$, so the total mass of adsorbent in each bed is 17.2 tons, which allow adsorbing 9.3 kg of methane by cycle in equilibrium at 0.57% $CH_4$ in air and 298 K.

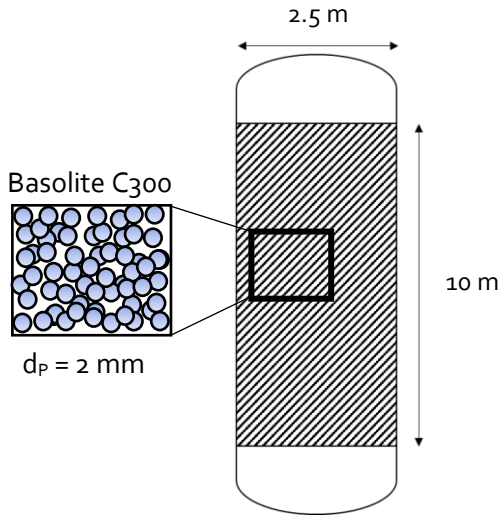


Figure 5. Outline of the fixed-bed dimensions.

### 3.2. Adsorption/Desorption setup

TSA cycles can be divided in four sequential steps: adsorption, heating, desorption and cooling. In case of adsorption, the inlet stream pass through the fixed bed, filled with Basolite C300, at low temperature. The material begins to adsorb methane, following kinetic and thermodynamic rules, describing a typical breakthrough curve, whose final plateau indicates the full saturation of the material. In these cases, a common technique consists of situating two or

more fixed beds in series in the same stage [46]. This disposition allows to be constantly saturating one of the fixed beds, obtaining air practically pure at the outlet, since the second fixed bed is always practically fresh. On the other hand, the inlet stream to the fixed bed at desorption stage is counterflow air at high temperature. It passes through the saturated fixed bed, and the exothermic nature of the adsorption allows to desorb the compounds previously retained, also following kinetic and thermodynamic rules. The desorption fixed bed is situated in parallel to the fixed beds working in adsorption stage. Therefore, the final setup consists of 3 equal fixed beds, 2 in series in adsorption and 1 in parallel in desorption stage, working at the same time. Once the first adsorption bed is saturated, it passes to the desorption stage, and the originally second bed passes to the first position, followed by the third fixed bed that was in desorption. In order to deal with all the inlet flow, 4 identical blocks composed by these three fixed beds are situated in parallel, that is, 12 equal fixed beds working in the process. Figure 6 depicts an scheme of two TSA process blocks with that disposition.

These fixed bed exchanges are made by programmed valve changes at the required times. Figure 7 shows the set of valves and the fixed beds distribution for two fixed bed in series in adsorption stage (1 and 2) and another in parallel in desorption (3). It should be also noted that prior to the start of the adsorption, some time is required to adapt the temperature to each fixed bed (cooling) after the desorption. In case of heating, the drag stream at elevated temperature heats the solid adsorbent at the same time that desorption operation takes place.

### 3.3. TSA process simulation and optimization

From the above-mentioned initial assumptions and the data included in Table 3, it is possible to obtain results for simple single-bed adsorption and desorption processes. In case of adsorption, the breakthrough curve is presented in Figure 8A. As it is observed, necessary time for reaching the bed saturation is about 6000 s. Final methane concentration in the solid after saturation at 298 K is $3.8 \cdot 10^{-5}$ kmol/kg. Once the fixed bed in adsorption is saturated, it passes to desorption stage. Desorption curve is presented in Figure 8B. Starting from the final concentration in the solid resulting of adsorption stage, it is possible to obtain a maximum concentration of methane at the outlet of desorption of 1.3% $CH_4$. The outlet has higher concentration than the inlet of the process during 1459 s, which are usable. The rest, until have cleaned completely the fixed bed (2500 s), can be discharged directly to the atmosphere due to its low methane content (~ 100% air). It is estimated that the atmospheric losses of methane through this purge are 6.9% of the total methane adsorbed. The final selected desorption temperature (343 K) is reached at the half of the stage, approximately, but the average temperature during all the desorption (342 K) is close to it (Figure 8B).

Concerning the process optimization, the final part in a process design is the selection of the optimum value for each parameter that makes the best performance. Table 2 shows how each design parameter affects the adsorption and desorption final performances, and the typical range of each one. Adsorption and desorption are two consecutive stages, so the optimization should be first for the adsorption stage and then for the desorption one. In case of adsorption, there are five parameters that affect greatly the performance: bed length, bed diameter, surface velocity, particle diameter and temperature. In case of temperature, the adsorption is more effective the lower the operation temperature, since it is an exothermic process. Both the lower limit and the selected temperature is the ambient temperature (supposed 298 K), because a cooling stage below that temperature would be economically unaffordable. In case of surface velocity and bed diameter, Figure 9 shows the differences in performance for different values of both parameters.

Surface velocity affects the breakthrough time and the pressure drop along the fixed bed, but it does not affect the final equilibrium values onto the solid. In addition, surface velocity is closely linked to the fixed bed diameter. For a constant surface velocity, the bed diameter defines the number of necessary fixed beds for covering all the inlet flow and vice versa, for a constant bed diameter, it is the surface velocity which defines the necessary parallel fixed beds. It is highly recommendable not to use a large number of fixed beds in parallel, both by total costs and also by available space.

All this data allow to optimize the design of the fixed bed for adsorption stage, which consists of a group of 8 fixed beds of 2.5 m in diameter and 10 m in length, filled with Basolite C300 of 2 mm of particle diameter, with a surface velocity of 0.24 m/s and a consequent pressure drop of 0.1 bar for each one.

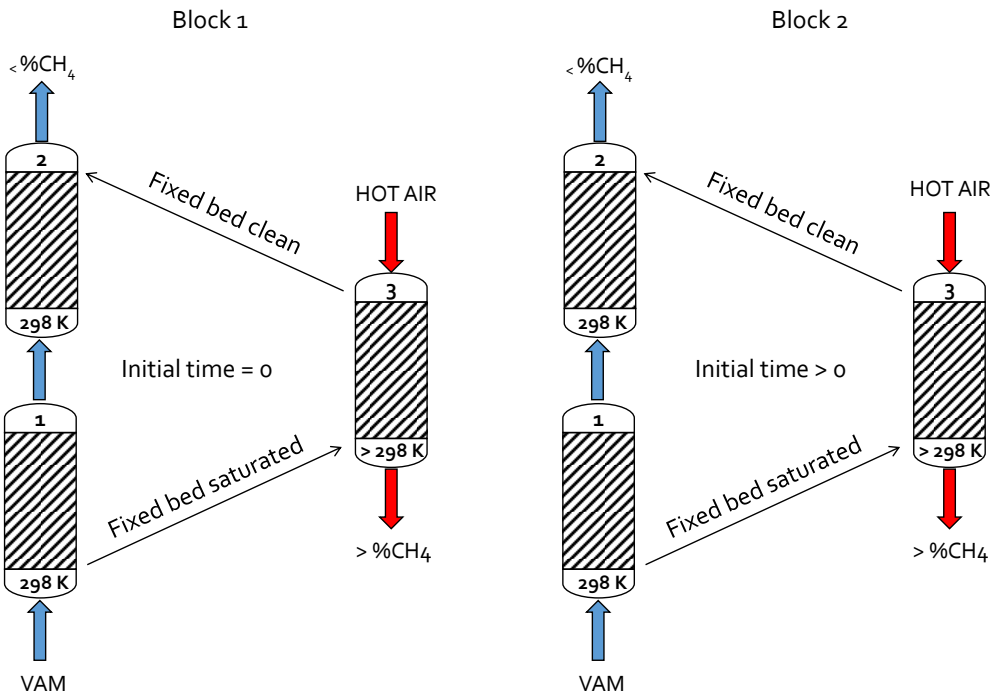


Figure 6. Scheme of two TSA process blocks. Adsorption stage with two fixed beds in series (1, 2) and desorption stage with one fixed bed in parallel (3). Initial time between blocks is different. Black arrows point out changes in fixed bed positions after clean and saturation processes are completed.

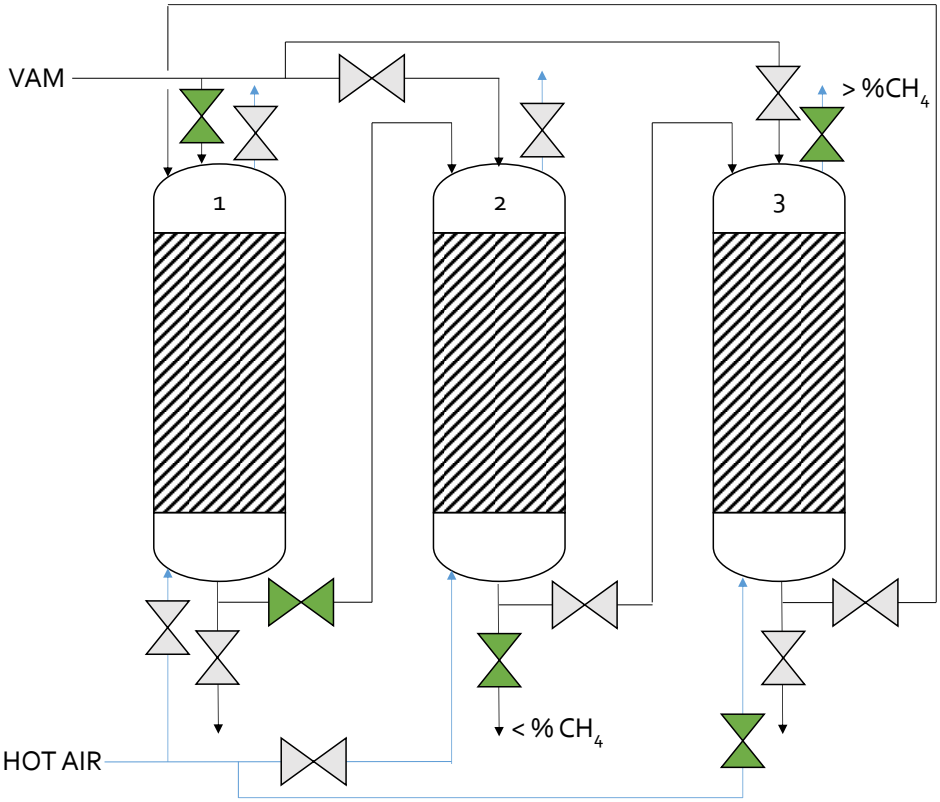


Figure 7. Schematic distribution of a TSA process with two fixed beds in adsorption (1, 2) and one fixed bed in desorption (3) stages. Black line symbolizes adsorption route, whereas blue line the desorption one. Valves in green are open, valves in grey are closed.

Table 3. Parameters introduced in Aspen Adsorption for the simulations.

| Process | Parameter | Values $CH_4$ | Units |
|---|---|---|---|
| Adsorption | Bed length | 10 | m |
| | Bed diameter | 2.5 | m |
| | Bed porosity | 0.4 | - |
| | Bed density | 350 | kg/m³ |
| | Particle diameter | 2 | mm |
| | Mass transfer coefficients | 0.012 | 1/s |
| | Molecular diffusivity | $2.2 \cdot 10^{-5}$ | m²/s |
| | Micropore diffusivity | $2 \cdot 10^{-10}$ | m²/s |
| | $q_m$ | 5.12 | mol/kg |
| | $K_L$ | 1.16 | $bar^{-1}$ |
| | T | 298 | K |
| Desorption | Bed length | 10 | m |
| | Bed diameter | 2.5 | m |
| | Bed porosity | 0.4 | - |
| | Bed density | 350 | kg/m³ |
| | Particle diameter | 2 | mm |
| | Mass transfer coefficients | 0.136 | 1/s |
| | Molecular diffusivity | $2.81 \cdot 10^{-5}$ | m²/s |
| | Micropore diffusivity | $2.26 \cdot 10^{-9}$ | m²/s |
| | $q_m$ | 5.12 | mol/kg |
| | $K_L$* | 0.244 | $bar^{-1}$ |
| | $C_{ps}$ | 0.755 | J/g·K |
| | $h_s$ | 222.1 | W/m²·K |
| | $a_p$ | 6000 | $m^{-1}$ |
| | T | 298-343 | K |

* Function of temperature

The next step consists on performing the parametric study for the desorption step. The fixed bed is the same, so the bed length, bed diameter and the particle size are already defined. This leaves two main parameters to consider, the surface velocity of the drag gas and the desorption temperature. The combination of both parameters affects the total amount of methane that is desorbed, as well as the duration of such desorption, *i.e.* its final concentration (Figure 10). The figure shows lower usable desorption time with higher surface velocity and lower temperature. In addition, simulations show that average methane outlet concentration is higher for large surface velocities, but the total moles of methane desorbed are lower. Final selection consist of four fixed bed parallel to adsorption ones, working at 343 K with a surface velocity of 0.48 m/s and a usable time of 1459 s for each cycle, with a maximum outlet concentration of 1.3% $CH_4$.

Finally, in addition to the simple simulation of the stages (Figure 8), it is necessary to couple all the stages in the same timeline, in order to get a continuous stream with the maximum methane content as possible. The first part is the operation of two fixed beds in series in the adsorption stage. The second fixed bed situated in series starts the adsorption (2500 s) before the complete saturation of the first fixed bed (6000 s), due to not all the methane is adsorbed by the first fixed bed with a complete efficiency. First fixed bed reaches saturation at 6000 s, but the second, instead of reaching it at 12000 s, reaches it at 8500 s (Figure 11). Then, desorption process takes 2500 s itself, but another 1000 s are added for the cooling stage until reaching solid adsorption temperature (298 K) before starting a new cycle. On the other hand, third bed starts adsorption after saturation of the first bed (6000 s) and it is saturated at 12000 s, time when desorption begins. These three fixed beds presented in Figure 11 make up 1 of the 4 independent blocks working in parallel, which are all equal. The time required for each stage will allow successfully coupling one bed with another, thus being able to carry out a continuous process without waiting times. In addition, as seen in Figure 8B, outlet stream from desorption stage possesses a highly variable methane concentration, between 0.57% and 1.3% $CH_4$, not being valid to work with the turbine a concentrations less than 1% $CH_4$. In order to take advantage of the maximum gas flow as possible, a common practice is to desynchronize the starting time between fixed beds in the same stage, in order to obtain a continuous flow of the product, in addition to a

more homogeneous final adsorbate concentration.

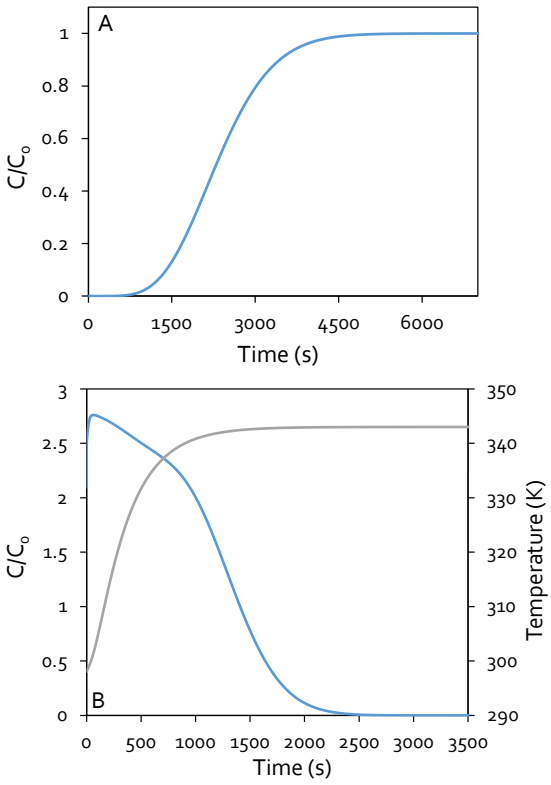


Figure 8. Methane curves of adsorption (A) and desorption (B) for a single-bed adsorption process. Solid temperature is indicated in Figure B (grey line). Co is the methane inlet concentration in the process.

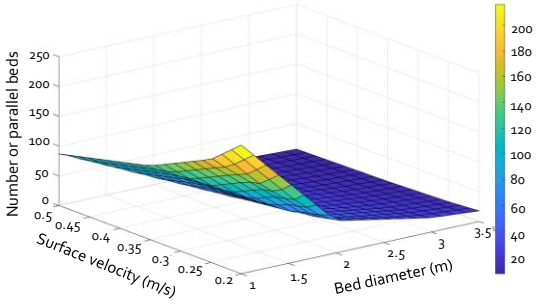


Figure 9. Relation between surface velocity, bed diameter and the number of necessary fixed beds in parallel for treating all the inlet flow (4.4 m$^3$/s and 0.57% $CH_4$) in the adsorption stage.

This causes the turbine to be always fed, without waiting times. The optimum desynchronization time is 625 s between one block and the following. This disposition allow obtaining an average methane concentration at the outlet of 1.2% $CH_4$ and an average continuous product flow of 3.8 Nm$^3$/s at 343 K. In addition, the introduction of an energy balance in the mathematical model allows showing also solid temperature variations during the process in the same simulation (Figure 12).

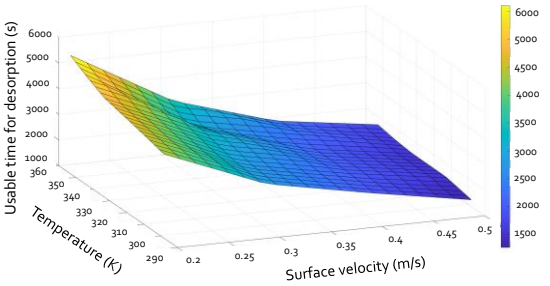


Figure 10. Relation between surface velocity, desorption temperature and the time necessary for making the usable part of desorption in the designed fixed bed (2.5 m in diameter and 10 m length).

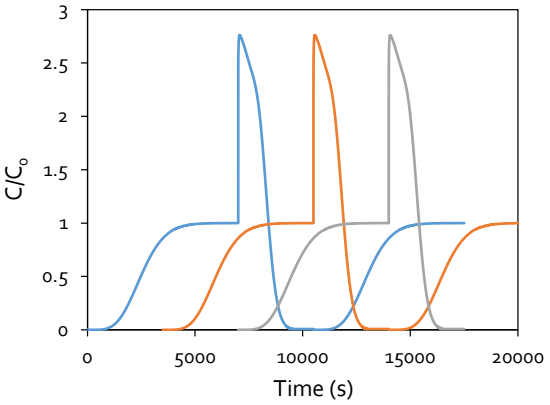


Figure 11. Simulation of a complete cycle for a TSA process with 3 fixed beds of 1 independent block. Fixed bed 1 (blue line) and fixed bed 2 (orange line) are initially in adsorption in series, whereas fixed bed 3 (grey line) is in desorption stage in parallel. $C_o$ is the methane inlet concentration.

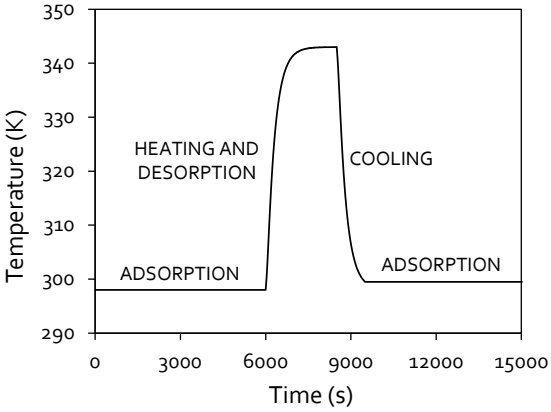


Figure 12. Adsorbent temperature variations during a TSA cycle for one of the fixed beds used.

### 3.4. Lean-burn turbine

As detailed in the previous section, a gas stream of 3.8 Nm$^3$/s containing 1.2% $CH_4$ at 343 K and 100 kPa is generated during the desorption step. This stream is the feed to the gas turbine and set as process specification in the following calculations. Note that methane concentration is low (1.2%), but it is above the minimum limit (1%),

for which special turbines suitable for lean conditions can be used. The design of the lean-burn turbine has been carried out using Aspen Hysys for simulate the turbine behaviour. The used model was detailed in the methodology section.

In this simulation, there is just one degree of freedom for the process design: the pressure ratio of the compressor. Hence, a sensitivity analysis of this variable has been done in the range 1.1 to 3.8. On increasing the pressure ratio, the power consumed in the compressor and generated in the expander increases, but overall a higher net work (i.e., electricity) is produced in the gas turbine. However, the temperature difference between the hot and cold streams in the recuperator decreases on increasing the pressure ratio, as shown in Figure 13. This causes an increase of the heat exchange area required in the recuperator. The minimum thermodynamic limit is a temperature difference of zero, which is achieved for a pressure ratio of 3.8 for this particular case. However, a reasonable minimum temperature difference for gas-to-gas heat transfer is 298 K, which corresponds to a pressure ratio of 3.3. This value is more realistic as the maximum recommended pressure ratio in this simulation.

The trade-offs of the pressure ratio on the annual benefit of the gas turbine can be examined in Figure 13. The annual benefit ($B$) has been calculated by means of a simple economic balance:

$$B = I - E = I - C\left[\frac{i\,(1+i)^n}{(1+i)^n - 1}\right]$$

Where the annual income ($I$) is obtained from the electricity generated by the turbine (0.07 €/kWh) and the annual expenses ($E$) are mainly due to redemption of capital costs ($C$) (a payout time $n$ = 15 years and discount rate $i$ = 4.25% are used to annualize the capital costs, as shown in the equation). The main capital costs of the gas turbine are due to the compressor, expander and recuperator, as summarized in Table 4 [49]. These costs have been calculated using the results of the process simulation carried out in Aspen Hysys.

Figure 13 shows a clear maximum on the annual benefit of the gas turbine for a pressure ratio of 2.4. For this value, the annual benefit of the gas turbine is estimated as 164 500 €/year and the temperature difference in the recuperator is 360 K, which is much higher than the minimum recommended of 298 K for gas-gas heat transfer. Note that the optimum pressure ratio of 2.4 is very close to the range recommend in the literature (2.2 to 2.3) for a similar methane concentration (0.8%) [17].

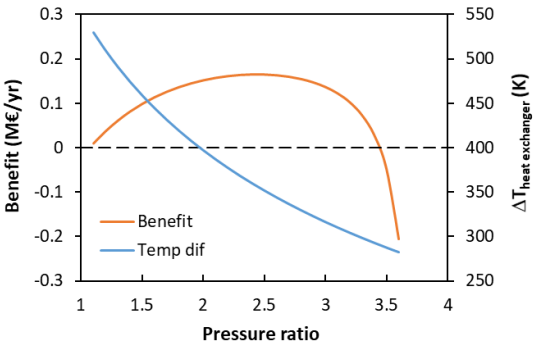


Figure 13. Sensitivity analysis of the compressor pressure ratio on the performance of the gas turbine

According to the results of the sensitivity analysis, the gas turbine has been designed for the optimum pressure ratio of 2.4. The power required by the compressor is 640 kW, while the power generated in the expander is 1130 kW. Consequently, the net work produced by the gas turbine is 490 kW.

## 4. **Economic evaluation**

In addition to yield criteria, projects must prove to be economically viable in order to be implemented or even tested on a larger scale. The entire design done throughout the work includes the material and devices needed to carry out the whole project. The economic evaluation has been done using the guidelines provided by the US Environmental Protection Agency (EPA). This organization has published a document entitled "Air Pollution Control Cost Manual" [50], which provides guidance for the design and costing of the equipment used for pollution control. This manual addresses the case of volatile organic compound abatement using adsorption and provides specific costing correlations for this equipment (they are obtained by average of vendor quotations). Apart from the equipment cost, it is also included a reference to estimate the capital investment and annual operating costs, specifically for environmental protection.

The cost of the Main Equipment are summarized in Table 4. All the costs have been updated to 2019 prices in Euro using CEPCI (Chemical Engineering Plant Cost Index). The cost of the vessel used in the adsorption unit operation is calculated using $C = 2310\ S^{0.778}$, where $C$ is the cost of one unit in Euro and $S$ is the external surface area (in m²) [50].

Table 4. Main equipment cost of the integrated adsorption and gas turbine.

| **EQUIPMENT COST** | | |
|---|---|---|
| Adsorption vessel | $C_{vessel}$ = 2310 N $S^{0.778}$ | 820 586 € |
| Fan | | 6 577 € |
| Gas turbine: compressor | $C_{comp}$ = 1663 $W^{0.9195}$ | 622 588 € |
| Gas turbine: expander | $C_{exp}$ = 4454 $W^{0.5889}$ | 279 740 € |
| Recuperator | $C_{hx}$ = 161 A | 583 541 € |
| Total equipment cost | | 2 313 031 € |

The cost of the fan used in the adsorption step of the process is estimated as 6 577 € for the given gas flow rate of 4.41 $Nm^3/s$ [49]. For the gas turbine, the costs are based on the power (*W* in kW) of the compressor and the expander, and the recuperator area (*A* in $m^2$) [49]. The total Main Equipment Cost is 2.31 M€.

The Main Equipment Costs exclude the piping, instrumentation and auxiliary equipment. These costs are accounted for as direct costs of the Capital Investment, which are estimated as a function of the total Cost of Main Equipment [50]. Final calculated Total Capital Investment (TCI) is 4.74 M€. The Annual Operating Costs have also been estimated (see Table 5) [50]. These costs include labour, materials, maintenance, utilities or administrative charges. A yearly operation of the plant of 8000 h has been considered in the calculations. Additionally, it should be also considered as Annual Operating Cost the necessary replacement of the adsorbent used, since these materials have a lifetime that is lower than of the main equipment, such as, vessels or fans. It has to be replaced periodically, due to degradation and loss of capacity.

For this reason, its cost must be divided and accounted for as annual following the recommendations of the EPA, considering a lifetime of n = 4 years and an interest rate of i = 4.25%, which results in a factor FWF = 0.2346. An additional 8% is added to account for freight and taxes. The cost of the adsorbent is a key parameter in the economic study, so a sensitivity analysis will be performed in order to study the viability of the process depending on it. From now, an arbitrary X value is considered for the cost of one kg of the adsorbent material.

The utilities consist of electricity consumed by the fan, which provides the head required to move the required gas flow rate through the different equipment. Considering an electricity price of 0.07 €/kWh and the power consumption of the fan (147 kW), the annual electricity consumption cost is estimated as 82 320 €/year (Table 5). However, the gas turbine is able to generate 490 kW of net work, directly as electricity. This power should be discounted from that consumed by the process. Considering the same electricity price, the gas turbine generates an earnings of 274 288 €/year, which are included as negative costs in Table 5. As shown, the total annual cost depends heavily on the adsorbent material cost (X).

In addition to the costs reflected in previous tables, it should be taken into account the positive environmental impact of the process. This is accounted for by the carbon emission allowances. Thus, the oxidation of methane to carbon dioxide in the ventilation air reduces the greenhouse gas emissions in 14 479 t $CO_2$-e/year (t $CO_2$-e means equivalent $CO_2$ tons). Considering a price of $CO_2$ of 19.71 €/t $CO_2$-e, the savings in emissions allowances is of 285 380 €/year. The corrected cash flow is calculated as the difference of the savings in emissions allowances (income) and the total annual cost, (52 295·X - 389 232 €/year).

Therefore, from this value of annual cash flow, it is possible to make a sensitivity analysis of the adsorbent cost per kilogram (X). As a first approximation, the value necessary for a cash flow of zero would be 7.45 €/kg. Figure 14 shows the trends of cash flows and Net Present Value (NPV) for different adsorbent costs (X). NPV is estimated for a 20-year period based on a discount rate of 4.25%. From adsorbent costs lower than 0.6 €/kg, the process starts being profitable. In case of activated carbons, there are materials that in large quantities can reach 0.1 €/kg, but it is difficult to reach necessary selectivity and adsorption capacity specifications despite the great variety of raw materials [51].

Table 5. Annual operating costs of the integrated adsorption and gas turbine.

| **ANNUAL OPERATING COSTS** | | |
|---|---|---|
| **Direct Annual Cost** | 8000 h/year | |
| Operating Labour | | |
| Operator | 0.5 h/shift | 12 925 € |
| Supervisor | 15% operator | 1 939 € |
| Operating Materials | - | |
| Maintenance | | |
| Labour | 0.5 h/shift | 13 191 € |
| Materials | 100% labour | 13 191 € |
| Adsorbent replacement | | 52 295·X € |
| Utilities | | |
| Electricity consumed | 0.07€/kWh | 82 320 € |
| Electricity generated | 0.07€/kWh | -274 288 € |
| Total Direct Annual Costs | | 52 295·X – 150 722 € |
| **Indirect Annual Cost** | | |
| Overhead | 60% op. maint. | 24 747 € |
| Administrative charges | 2% TCI | 94 873 € |
| Property taxes | 1% TCI | 47 437 € |
| Insurance | 1% TCI | 47 437 € |
| Capital recovery | | -167 623 € |
| Total Indirect Annual Cost | | 46 870 € |
| Total Annual Cost | | 52 295·X – 103 852 € |

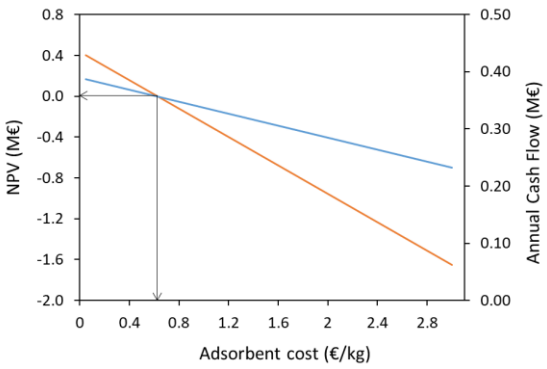


Figure 14. Results of the economic evaluation for different adsorbent costs (X). Annual cash flow (blue line), NPV (orange line). Black arrows point out the necessary adsorbent cost to make the NPV equal to zero.

On the other hand, in case of MOFs, it is difficult to obtain them at such low prices, since they are synthesized almost exclusively in small batches for laboratory work. A future implementation of large-scale synthesis will make this process economically viable, which is an incentive to try to produce these materials with lower costs.

## 5. Conclusions

This work has studied the feasibility of harnessing low-concentrated methane streams by integrating two independent processes: temperature swing adsorption for methane concentration, followed by combustion in a lean-fuel burn turbine for obtaining a surplus of electricity and calorific energy. The design has been made for a VAM inlet stream, which has a flowrate of 4.4 $m^3/s$, with an average methane concentration of 0.57% $CH_4$ in air.

In relation to the adsorption/desorption unit, the simulations of Aspen Adsorption software have shown satisfactory results when working with 4 parallel blocks made up of 3 equal fixed beds each (2 in series in adsorption and 1 in parallel in desorption stage). A proper selection of the adsorbent (Basolite C300), the adequate sizing of the beds (2.5 x 10 m), as well as, the desynchronization of the bed blocks (625 s) make it possible to obtain an increase of 52.5% in methane concentration. The combustion turbine, simulated using Aspen Hysys, has also exhibited

good performance, when fed with the concentrated methane stream obtained in the adsorption/desorption unit. It is selected an optimum pressure ratio of 2.4, which implies a total net-work of 490 kW. Therefore, it is obtained a satisfactory mass and energy integration between both process operations. Despite the good operational results, after in-depth economic analysis of the integration, the process shows a great dependence of the adsorbent cost. This cost should not exceed 0.6 €/kg for the process to be economically feasible (NPV = 0). This leads to the conclusion that the studied process is viable in practice, but it is required to develop adsorbents that are at mid-point of the performance/cost relation. Thus, a larger implementation of MOFs is required on an industrial scale to lower their market price, as they are able to obtain such good results in complex separations and harnessing processes.

**Acknowledgements**

This work has been financed by the Research Fund for Coal and Steel of the European Union (contract RFCS2016/754077-METHENERGY+).

**References**

[1] S. Fletcher, H. Schaefer. Rising methane: A new climate challenge. Science 364 (2019) 932-933.

[2] M. Wahlen. The global methane cycle. Annual Review Of Earth And Planetary Sciences 21 (1993) 407-426.

[3] D. Uprety, V. Reddy, J. Mura. Greenhouse gases: A historical perspective: A historical analysis. Climate Change and Agriculture (2019).

[4] D. Zhong, W. Wang, Z. Zou, Y. Lu, J. Yan, K. Ding. Investigation on methane recovery from low-concentration coal mine gas by tetra-n-butyl ammonium chloride semiclathrate hydrate formation. Applied Energy 227 (2018) 686-693.

[5] S. Seman, I. Idris, A. Abdullah, I. Shamsudin, M. Othman. Optimizing purity and recovery of biogas methane enrichment process in a closed landfill. Renewable Energy 131 (2019) 1117-1127.

[6] J. Kim, A. Maiti, L. Lin, J. Stolaroff, B. Smit, R. Aines. New materials for methane capture from dilute and medium-concentration sources. Nature Communications 4 (2013) 1694.

[7] C. Karacan, F. Ruiz, M. Cotè, S. Phipps. Coal mine methane: A review of capture and utilization practices with benefits to mining safety and to greenhouse gas reduction. International Journal of Coal Geology 86 (2011) 121-156.

[8] D. Cluff, G. Kennedy, J. Bennett, P. Foster. Capturing energy from ventilation air methane a preliminary design for a new approach. Applied Thermal Engineering 90 (2015) 1151-1163.

[9] S. Erdogan, C. Karacan, E. Okandan. Use of reservoir simulation and in-mine Ventilation measurements to estimate coal seam properties. International Journal of Rock Mechanics and Mining Sciences 63 (2014) 148-158.

[10] S. Su, A. Beath, H. Guo, C. Mallett. An assessment of mine methane mitigation and utilisation technologies. Progress in Energy and Combustion Science 31 (2005) 123-170.

[11] K. Spokas, J. Bogner, J. Chanton, M. Morcet, C. Aran, C. Graff, Y. Golvan, I. Hebe. Methane mass balance at three landfill sites: What is the efficiency of capture by gas collection systems?. Waste Management 26 (2006) 516-525.

[12] Y. Cheng, L. Wang, X. Zhang. Environmental impact of coal mine methane emissions and responding strategies in China. International Journal of Greenhouse Gas Control 5 (2011) 157-166.

[13] K. Baris. Assessing ventilation air methane (VAM) mitigation and utilization opportunities: a case study at Kozlu Mine, Turkey. Energy for Sustainable Development 7 (2013) 13-23.

[14] I. Karakurt, G. Aydin, K. Aydiner. Mine ventilation air methane as a sustainable energy source. Renewable and Sustainable Energy Reviews 15 (2011) 1042-1049.

[15] S. Su, J. Han, J. Wu, H. Li, R. Worrall, H. Guo, X. Sun, W. Liu. Fugitive coal mine methane emissions at five mining areas in China. Atmospheric Environment 45 (2011) 2220-2232.

[16] J. Yin, S. Su, X. Yu, Y. Weng. Thermodynamic characteristics of a low concentration methane catalytic combustion gas turbine. Applied Energy 87 (2010) 2102-2108.

[17] S. Su, X. Yu. A 25 kWe low concentration methane catalytic combustion gas turbine prototype unit. Energy 79 (2015) 428-438.

[18] S. Ouyang, S. Xu, N. Song. Activated carbons for ventilation air methane enrichment by vacuum pressure swing adsorption. Advanced Materials Research 773 (2013) 907-911.

[19] J. Chen, J. Buege, F. Cunningham, J. Northam. Scale-up of column adsorption process by computer simulation. Industrial and Engineering Chemistry Process Design and Development 7 (1968) 26-31.

[20] P. Gao. The research progress of the enrichment of ventilation air methane (VAM). International Conference on Environmental Protection, Coal Industry and Metallurgical Mine Safety (2019) Francis Academic Press, UK.

[21] A. Ghosal, S. Manjare. Selection of appropriate adsorption technique for recovery of VOCs: an analysis. Journal of Loss Prevention in the Process Industries 15 (2002) 413-421.

[22] M. Clausse, J. Bonjour, F. Meunier. Adsorption of gas mixtures in TSA adsorbers under various heat removal conditions. Chemical Engineering Science 17 (2004) 3657-3670.

[23] W. Zhou. Methane storage in porous metal-organic frameworks: current records and future perspectives. The Chemical Record 10(3) (2010) 200-204.

[24] H. Wu, J. Simmons, Y. Liu, C. Brown, X. Wang, S. Ma, V. Peterson, P. Southon, C. Kepert, H. Zhou, T. Yildirim, W. Zhou. Metal-organic frameworks with exceptionally high methane uptake: where and how is methane stored?. Chemistry - A European Journal 16 (2010) 5205-5214.

[25] X. Lin, N. Champness, M. Schröder. Hydrogen, methane and carbon dioxide adsorption in metal-organic framework materials. Functional Metal-Organic Frameworks: Gas Storage, Separation and Catalysis. Topics in Current Chemistry 293 (2010) 35-76.

[26] S. Kayal, A. Chakraborty. Activated carbon (type Maxsorb-III) and MIL-101(Cr) metal organic framework based composite adsorbent for higher $CH_4$ storage and $CO_2$ capture. Chemical Engineering Journal 334 (2018) 780-788.

[27] Z. Li, G. Xiao, Q. Yang, Y. Xiao, C. Zhong. Computational exploration of metal-organic frameworks for $CO_2/CH_4$ separation *via* temperature swing adsorption. Chemical Engineering Science 120 (2014) 59-66.

[28] A. García-Blanco, A. Vallone, S. Korili, A. Gil, K. Sapag. A comparative study of several microporous materials to store methane by adsorption. Microporous and Mesoporous Materials 224 (2016) 323-331.

[29] I. Karakurt, G. Aydin, K. Aydiner. Mine ventilation air methane as a sustainable energy source. Renewable and Sustainable Energy Reviews 15 (2011) 1042-1049.

[30] S. Su, A. Beath, H. Guo, C. Mallet. An assessment of mine methane mitigation and utilisation technologies. Progress in Energy and Combustion Science 31 (2005) 123-170.

[31] S. Villar-Rodil, R. Navarrete, R. Denoyel, A. Albiniak, J. Paredes, A. Martínez-Alonso, J. Tascón. Carbon molecular sieve cloths prepared by chemical vapour Deposition of methane for separation of gas mixtures. Microporous and Mesoporous Materials 77 (2005) 109-118.

[32] T. Rufford, G. Watson, T. Saleman, P. Hofman, N. Jensen, E. May. Adsorption equilibria and kinetics of methane + nitrogen mixtures on the activated carbon Norit RB3. Industrial and Engineering Chemistry Research 52 (2013) 14270-14281.

[33] X. Li, L. Zhang, Z. Yang, P. Wang, Y. Yan, J. Ran. Adsorption materials for volatile organic compounds (VOCs) and the key factors for VOCs adsorption process: a review. Separation and Purification Technology 235 (2020) 116213.

[34] S. Bourrelly, P. Llewellyn, C. Serre, F. Millange, T. Loiseau, G. Férey. Different adsorption behaviors of methane and carbon dioxide in the isotypic nanoporous metal terephthalates MIL-53 and MIL-47. Journal of American Chemical Society 127 (2005) 13519-13521.

[35] J. Gutiérrez-Sevillano, J. Vicent-Luna, D. Dubbeldam, S. Calero. Molecular mechanisms for adsorption in Cu-BTC metal organic framework. The Journal of Physical Chemistry C 117 (2013) 11357-11366.

[36] Y. Peng, V. Krungleviciute, I. Eryazici, J. Hupp, O. Farha, T. Yildirim. Methane storage in metal-organic frameworks: current records, surprise findings, and challenges. Journal of the American Chemical Society 135 (2013) 11887-11894.

[37] D. Ursueguía, E. Díaz, S. Ordóñez. Adsorption of methane and nitrogen on Basolite MOFs: Equilibrium and kinetic studies. Microporous and Mesoporous Materials 298 (2020) 110048.

[38] J. Mason, J. Oktawiec, M. Taylor, M. Hudson, J. Rodriguez, J. Bachman, M. Gonzalez, A. Cervellino, A. Guagliardi, C. Brown, P. Llewellyn, N. Masciocchi, J. Long. Methane storage in flexible metal-organic frameworks with intrinsic thermal management. Nature 527 (2015) 357-361.

[39] Q. Wang, D. Shen, M. Bülow, M. Lau, S. Deng, F. Fitch, N. Lemcoff, J. Semanscin. Metallo-organic molecular sieve for gas separation and purification. Microporous and Mesoporous Materials 55 (2002) 217-230.

[40] X. Tang, Z. Li, N. Ripepi, A. Louk, Z. Wang, D. Song. Temperature-dependent diffusion process of methane through dry crushed coal. Journal of Natural Gas Science and Engineering 22 (2015) 609-617.

[41] D. Ursueguía, E. Díaz, A. Vega, S. Ordóñez. Methane separation from diluted mixtures by fixed bed adsorption using MOFs: model validation and parametric studies. Separation and Purification Technologies 251 (2020) 117374.

[42] D. Ko, M. Kim, I. Moon, D. Choi. Analysis of purge gas temperature in cyclic TSA process. Chemical Engineering Science 57 (2002) 179-195.

[43] T. Dantas, F. Luna, I. Silva, D. Azevedo, C. Grande, A. Rodrigues, R. Moreira. Carbon dioxide-nitrogen separation through adsorption on activated carbon in a fixed bed. Chemical Engineering Journal 169 (2011) 11-19.

[44] F. Kloutse, R. Zacharia, D. Cossement, R. Chahine. Specific heat capacities of MOF-5, Cu-BTC, Fe-BTC, MOF-177 and MIL-53 (Al) over wide temperature ranges: Measurements and application of empirical group contribution method. Microporous and Mesoporous Materials 217 (2015) 1-5.

[45] A. Gabelman, 2017. Adsorption basics: Part 1. https://www.aiche.org/resources/publications/cep/2017/july/adsorption-basics-part-1 (accessed 15 May 2020).

[46] J. R. Couper, W. R. Penney, J. R. Fair, S. M. Walas, 2005. Chemical process equipment: selection and design, third ed. Elsevier, Waltham (MA).

[47] J. Theuerkauf, P. Witt, D. Schwesig. Analysis of particle porosity distribution in fixed beds using the discrete element method. Powder Technology 165 (2006) 92-99.

[48] C. Perego, S. Peratello. Experimental methods in catalytic kinetics. Catalysis Today 52 (1999) 133-145.

[49] Equipment Costs: Plant design and economics for chemical engineers, 2003. https://www.mhhe.com/engcs/chemical/peters/data/ (accessed 15 May 2020).

[50] Cost reports and guidance for air pollution regulations, 2018. https://www.epa.gov/economic-and-

cost-analysis-air-pollution-regulations/cost-reports-and-guidance-air-pollution (accessed 15 May 2020).

[51] M. Rafatullah, O. Sulaiman, R. Hashim, A. Ahmad. Adsorption of methylene blue on low-cost adsorbents: A review. Journal of Hazardous Materials 177 (2010) 70-80.

## 4.4. SÍNTESIS DE MATERIALES ADSORBENTES

A lo largo de esta Tesis Doctoral, se han observado los siguientes problemas a la hora de la implantación de los MOFs a escala real: elevado coste de los MOFs, elevada pérdida de carga durante la adsorción en lecho fijo, así como importantes pérdidas de capacidad y destrucción de la estructura en presencia de humedad. En relación con esto, la última parte de la Tesis Doctoral comprende la búsqueda de una solución de compromiso entre la eficacia mostrada en condiciones suaves, y la solución a los problemas inherentes a una operación real.

Con este propósito, se han sintetizado materiales compuestos formados por partículas de alúmina impregnadas con HKUST-1, material homólogo al Basolite C300. Dicho MOF se selecciona por su buen rendimiento en la adsorción y separación de metano, y se sintetiza a partir de una metodología simple y de reducido coste, a diferencia del comercial. Por otro lado, la alúmina se selecciona por su bajo coste, su facilidad de conformar partículas o pellets y su hidrofilicidad, que se espera que proteja al MOF del efecto del agua. Los materiales compuestos se sintetizan a partir de dos métodos sencillos: solvotermal y *dip-coating*, variando las relaciones másicas iniciales entre MOF y alúmina (0.05-1.29), obteniendo así 6 materiales con distintas cargas de HKUST-1. En todos los casos, el tamaño de partícula es similar a las partículas de alúmina (355-710 μm), por lo que se evitan elevadas caídas de presión, procesos de síntesis de gran dificultad y elevados costes. Además, no se observa fragmentación o desgaste de las partículas al conformar el lecho fijo. Por otro lado, una caracterización completa de los materiales (fisisorción de nitrógeno, SEM, TGA y DRX) muestra presencia de MOF en todos ellos, además de un incremento de la cristalinidad y la superficie específica acorde a la cantidad de MOF impregnada, que va desde un 1.1 a un 36.6%.

Por último, estos materiales se han sometido a un envejecimiento en condiciones húmedas, con el objetivo de estudiar la resistencia a la presencia de humedad. Se registra la capacidad de adsorción de metano de los materiales compuestos antes y después de someterse a un tratamiento húmedo (24 h, 100% humedad relativa) en un lecho fijo. Los resultados

muestran que para materiales con un bajo contenido en MOF (< 9%), existe una sinergia entre HKUST-1 y la alúmina que favorece la protección del MOF frente a la humedad e incluso mejora la capacidad de adsorción de metano hasta un 38.8%, mientras que el MOF perdería gran parte de su capacidad actuando individualmente (37%). Además, se observa que una distribución heterogénea del MOF sobre la superficie de la alúmina favorece aún más el proceso. Esto sugiere que los materiales compuestos siguen el mismo principio que la formación de hidratos de metano sobre la superficie de un óxido metálico en presencia de un precursor poroso, como HKUST-1, pero en condiciones mucho más suaves que las típicamente utilizadas. Los resultados obtenidos son prometedores, ya que abren la puerta a utilizar dichos materiales en condiciones reales.

Los resultados obtenidos se recogen y discuten en la siguiente publicación científica:

- David Ursueguía, Eva Díaz, Salvador Ordóñez, Enhanced methane adsorption performance of a polar MOF (HKUST-1) by supporting on a hydrophilic material ($Al_2O_3$). Enviada a revista: *Separation and Purification Technology*.

# Improved stability and adsorption performance of HKUST-1@$Al_2O_3$ composites for methane recovery

David Ursueguía, Eva Díaz, Salvador Ordóñez*

Catalysis, Reactors and Control Research Group (CRC), Department of Chemical and Environmental Engineering, University of Oviedo, Julián Clavería s/n, 33006 Oviedo, Spain

*e-mail: sordonez@uniovi.es (S. Ordóñez)

Submitted to: Separation and Purification Technology

## ABSTRACT

HKUST-1 MOF is considered among the most promising materials for methane adsorption. However, the huge decrease in adsorption capacity under humid conditions, due to water hydrolysis of the structure and blockage of open metal sites, decreases its potential. As possible solutions, composites of HKUST-1 and $Al_2O_3$ particles were synthesized and tested for methane adsorption. MOF impregnation on large particles reduces the pressure drop through the fixed-bed, whereas the known hydrophilicity of the alumina is expected to minimize the water damage to the MOF. Impregnation was carried out in a PTFE autoclave, with different HKUST-1/$Al_2O_3$ initial masic ratios (0.05-1.29) and by two different methods, dip-coating and solvothermal. The loading, dispersion and main morphological features were confirmed by PXRD, SEM, BET and TGA. Water influence was determined by ageing samples in a fixed-bed under air with 100% RH for 24 h and 3 consecutive cycles. Methane adsorption capacity was checked before and after the humid treatment. Adsorption capacity of HKUST-1 decreases about 37%, whereas composites with low MOF loads (< 9%) withstand and even improve the methane adsorption capacity more than 38%. This effect is more noticeable for a more heterogeneous MOF distribution on the alumina surface, following a similar principle to the methane hydrate formation through a surface promoter, but at milder conditions. Surprisingly, it is also registered a relevant improvement in thermal stability for these composites.

**Keywords**: MOFs stability; MOF-inorganic composites; Methane adsorption; Lean methane emission upgrading

### 1. Introduction

HKUST-1, $Cu_3(C_9H_3O_6)_2$, known commercially as Basolite C300, is a promising material for gas adsorption and separation, establishing a benchmark in methane adsorption [1]. Previous works have demonstrated its ability to concentrate methane from low-grade streams on a fixed-bed [2]. Methane molecules, with considerable polarizability, are selectively attracted to the open metal sites (OMS) of the structure above other major components of the stream, such as nitrogen. HKUST-1 has been synthesized and studied in many works, showing very good performance under different scenarios, but in most cases at laboratory scale and mild conditions [3]. However, the scaling-up of processes based on this material for methane recovery from real diluted streams is still challenging.

The first handicap to be overcome is the harmful effect of the moisture in MOF performance [4, 5]. Water hydrolyzes structural organic ligands and is strongly attracted to OMS, blocking them for adsorption. This fact has hindered the application of HKUST-1 to large-scale processes, in which water is usually present in form of humidity [6]. In this way, increasing water stability of this material has received increased interest. The first reported approaches involved modifications of the original synthesis route of the MOF. For example, Goyal et al. [7] have doped the structure with iron ($Fe^{3+}$) ions, whereas Wu et al. [8] have incorporated glycine, and Kanno et al. [9] have synthesized the MOF by plasma in liquid phase. All these changes lead to an improvement, but also imply changes in the morphological and crystalline structure of the MOF, add to be difficult and expensive to carry out, especially at a large scale. Recently, other

authors have proposed the synthesis of composites combining post-synthetic HKUST-1 with another material, which allow the structure of the MOF to be kept and the synthesis process simplified. In this line, Pan et al. [10] have deposited graphene oxide on the HKUST-1 surface, and Majaz et al. [11] have crystallized HKUST-1 inside the mesoporous cavities of silica FDU-12. Despite the promising results, most of the composites are made with expensive either materials, graphene, or techniques, electro-deposition [12, 13]. This again entails very high costs to consider a potential synthesis on an industrial scale.

The other key bottleneck for the industrial use is the large pressure drop associated with fixed-bed adsorption processes, since HKUST-1 is usually synthesized and manufactured as fine powder [3]. As a possible solution, one of the most used and inexpensive techniques is pelletization by mechanical pressure [14]. The material, in the shape of large pills or pellets, would allow to reduce the pressure drop, in addition to increase its particle density, which can favor some gas adsorption and storage applications [15]. Even so, pelletization has been shown to cause structural amorphization and an important reduction of the adsorption capacity of HKUST-1, related to a large reduction in specific surface area and total pore volume, with a total collapse of micropores [16, 17]. HKUST-1 has also shown problems in the conformation of large structures, which could minimize the problems derived of the pressure drop. In fact, it is not stable in the typical dispersion solvents used to make binders [17]. Therefore, a possibility that hinders water harmful effect could be the combination of HKUST-1 with another material in a composite, looking for an improvement of its mechanical properties. Then, a material that can be easily shaped to large particles, as the commercially available extrusions of common catalyst supports as alumina ($Al_2O_3$) or silica ($SiO_2$), is desired. This alternative was tested for the design of membranes able to separate small molecules, increasing the pressure resistance of the original material [18], or also to improve the catalytic yield in certain reactions, enhancing the thermal resistance of the pristine MOF [19]. However, to the best of our knowledge, this approach has been very scarcely studied for fixed-bed adsorption and gas separation processes.

Therefore, this work deals with the preparation of HKUST-1 and alumina composites, with the main purpose of reducing the pressure drop and moisture effect in a methane adsorption process from diluted mixtures. Methane adsorption is considered as reference due to the good results observed under mild conditions and with small fixed-beds, but in absence of scale-up records [2]. Impregnation of HKUST-1 on alumina ($Al_2O_3$) large particles (355-710 µm) was carried out by both solvothermal and dip-coating methods. Alumina is an inexpensive material, easily pelletizable and highly hydrophilic. The large particle size of alumina should reduce notably the pressure drop, whereas its hydrophilicity has already demonstrated modifications in the polar character of porous membranes by adding alumina particles [20]. Therefore, it is expected to avoid large water damage to the MOF structure. Solvothermal and dip-coating methods were chosen since are simple and inexpensive routes for MOF impregnation on mesoporous supports [21]. Once composites are synthesized and tested in adsorption, appropriate results would represent a breakthrough in the use of HKUST-1 under actual applications.

## 2. Materials and methods

### 2.1. Materials

Alumina ($Al_2O_3$) pristine pellets were obtained from BASF, with an original particle size of 2 mm. The rest of the chemicals were used for the HKUST-1 synthesis: cupric nitrate trihydrated, $Cu(NO_3)_2{\cdot}3H_2O$, purchased from CAYMAN Chemical Company, trimesic acid, $C_9H_6O_6$, purchased from PRS PANREAC, ultrapure ethanol (99.99%), $C_2H_5OH$, purchased from VWR Chemicals, and distilled water, $H_2O$. All the gases used (air, methane, nitrogen and helium) were supplied by Air Liquide with purities above 99.995% mol.

### 2.2. Synthesis of HKUST-1@$Al_2O_3$

Firstly, $Al_2O_3$ particles, between 355 and 710 µm, were obtained by crushing in a mortar and a subsequent sieving of the original alumina pellets (2 mm). On the other hand, HKUST-1 was synthesized through the procedure indicated by Gascon et al. [22]: 0.875 g of $Cu(NO_3)_2{\cdot}3H_2O$ were diluted in 12 ml of distilled $H_2O$, whereas 0.42 g of $C_9H_6O_6$ were diluted in 12 ml of $C_2H_5OH$. Both solutions were mixed and stirred for 30 min at ambient conditions. The final mixture was introduced into a PTFE autoclave of 100 ml and heated in an oven at 383 K for 18 h. The product was filtered and washed 3 consecutive times with distilled water. Finally, it was introduced into the oven at 383 K overnight, obtaining a fine dark-blue powder.

Table 1. Different materials synthesized and the corresponding nomenclature used.

| Nomenclature | Procedure | Contact volume (ml)[a] | Precursors (%)[b] |
|---|---|---|---|
| $DC_{100v}$ | dip-coating | 1 | 100 |
| $DC_{240}$ | dip-coating | 2.4 | 100 |
| $DC_{240V}$ | dip-coating | 24 | 10 |
| $S_{240}$ | solvothermal | 2.4 | 100 |
| $S_{2400V}$ | solvothermal | 24 | 100 |
| $S_{240V}$ | solvothermal | 24 | 10 |

[a]Total volume of liquid in the autoclave
[b]Concentration respect to the original precursors of HKUST-1 [22, 23]

For the synthesis of HKUST-1@$Al_2O_3$ composites, two different methodologies were used (Figure S1). Firstly, the solvothermal method [23]: 2.02 g of alumina particles were mixed with the precursors of HKUST-1 in the same proportions as above, and the mixture was taken to the PTFE autoclave (383 K, 18 h). The product was washed with distilled water and filtered. Secondly, the dip-coating method [22]: 2.02 g of alumina particles were impregnated dropwise with the liquid obtained from the filtration of HKUST-1 (mother liquor) and taken to an oven at 393 K, until the complete solvent evaporation. Then, particles were washed with $C_2H_5OH$ and filtered. The product was introduced into the PTFE autoclave with the HKUST-1 precursors (383 K, 18 h) and subsequently washed with distilled water and filtered.

Some modifications have been made to the procedures described above. Alumina quantity was reduced to 1 g in all cases, the total contact volume in the autoclave has been modified to 3 different values (1, 2.4 and 24 ml), and the original concentration of the precursors of HKUST-1 in the contact volume was modified in some cases (100 and 10%). In this way, six different composite materials were synthesized for the process. Nomenclature indicates by numbers (100, 240 and 2400) the amount of MOF in the contact volume, and by letters (v and V), the total contact volume (Table 1).

Once synthesized, the amount of MOF impregnated on alumina for each sample was obtained by thermogravimetry decomposition. Essays were done on a thermobalance TGA 55 (TA Instruments) for 15-30 mg of each sample, under nitrogen atmosphere (40 ml/min) and a temperature ramp of 5 K/min from ambient temperature to 873 K.

2.3. Adsorbents characterization

The textural features of specific surface area and pore volume were obtained by nitrogen physisorption at 77 K in a Micromeritics ASAP 2020 surface area and porosity analyzer. Physisorption data were processed using Brunauer-Emmett-Teller (BET), Barrett-Joyner-Halenda (BJH) and Dubinin-Radushkevich (DR) approaches for determining surface area, total mesopores and micropores volume, respectively. The total volume of pores is the sum of both values (BJH and DR). Scanning electron microscopy (SEM) images and EDX analyses were carried out by using a JEOL 6610LV scanning electron microscope. Samples were coated with gold prior to observation. Finally, the crystallographic structures of the materials were determined by powder X-ray diffraction (PXRD) using a Philips PW 1710 diffractometer, working with the Cu-$K_\alpha$ line ($\lambda$ = 0.154 nm) in the 2$\theta$ range 5-85º at a scanning rate of 2º/min.

2.4. Adsorption experiments

Pure methane adsorption was evaluated by a thermal gravimetric analyzer (TGA 55, TA Instruments). Samples (15-30 mg) were pretreated in situ at 423 K and 0.1 MPa in pure nitrogen flowing at 40 ml/min for 2 h. Afterwards, 40 ml/min of methane were flowed at 298 K for 20 h. All weight changes respect to the adsorption data were corrected using a blank calibration. Purge gas was nitrogen flowing continuously at 60 ml/min.

Water ageing of the materials was performed in a stainless-steel tube, 45 and 0.65 cm in length and diameter, respectively. It is filled with 0.15 g of each material. The temperature of the fixed bed was controlled by an electric tubular furnace (Nabertherm). Water was introduced in liquid

form by a syringe (Hamilton) of 5 ml powered by a Legato 100 syringe pump (KdScientific), being immediately vaporized due to the action of several isolated heaters along the conductions, at 383 K. The gas flow of air (72 ml/min) was introduced by a mass flow controller (MFC) previously calibrated (Bronkhorst) for 24 h. Operation temperature was 298 K, with a total pressure of 0.1 MPa. Water flowrate was selected according to the relative humidity (RH) desired: 0.2 ml/h for 100% RH, corresponding to 59000 ppm. In the cleaning stage, 72 ml/min of dry air were flowed through the fixed-bed and the temperature was increased up to 423 K for 2 h. Three consecutive water-ageing cycles were applied to each sample. Afterwards, pure methane adsorption capacity was checked again on the thermobalance (20 h, 298 K). Subsequently, a thermal decomposition up to 873 K was carried out for all the samples (5 K/min, $N_2$, 40 ml/min, 0.1 MPa), analyzing the effluent gases by a mass spectrometer Pfeiffer Vacuum Omnistar previously calibrated.

## 3. Results and discussion

### 3.1. Adsorbents characterization

The MOF content of composites was calculated by thermal decomposition (Figure S2), by comparison with pristine materials. Table 2 shows the MOF content of each of the studied materials. HKUST-1 shows a slight loss of mass at low temperatures, related to water physisorbed, and a next collapse of the structure by means of the breakage of the organic ligand at 593 K, with a mass loss around 45%. In case of alumina, only a loss related to water linked to the surface (11%) is registered in the whole temperature range. All the composite decomposition curves obtained are intermediate between alumina and HKUST-1, being closer to the alumina. Interestingly, it is observed that the collapse of the organic ligand of the MOF occurs at higher temperature for composite materials, around 650 K, and in a less abrupt way than in the case of pristine HKUST 1. This change in the thermograms is consistent with the results obtained by other authors, in which the synthesis of composites with HKUST-1 achieves more thermally stable materials [24]. The bonds between the MOF and the support strengthen the whole composite structure.

Nitrogen physisorption isotherms are shown in Figure S3. Pristine HKUST-1 exhibits a type-I adsorption isotherm, with a pronounced increase at low partial pressures (~ 500 $cm^3/g$), which is indicative of the large importance of micropores, followed by a flat zone up to $P/P_0$=1. For the composite materials, intermediate curves between the MOF and the alumina are observed. In fact, the specific surface area follows the same order as the MOF amount on the alumina, Table 2, showing the large contribution of the MOF to the available surface of the composite, with less influence on the total pore volume. Consequently, the higher the amount of MOF in the composite, the greater adsorption in the area corresponding to low partial pressures. This effect is especially important in the case of $S_{240oV}$, with a 36.6% HKUST-1. However, all the isotherms present a type-IV isotherm as alumina, that is, a hysteresis cycle that indicates the apparition of capillary condensation in the mesopores. Thus, MOF impregnation does not modify the large mesoporous properties of pristine alumina. Hence, $S_{240V}$, with a very low MOF content, Table 1, exhibits a behavior very close to alumina.

Figure 1 shows the influence of MOF loading, obtained by thermogravimetry, on the BET specific surface area of each composite. All the materials follow a linear trend between alumina and HKUST-1 ($R^2$=0.99), except $S_{2400V}$ and $DC_{100V}$. In fact, these composites differ in the synthesis process, since both start with different HKUST-1/$Al_2O_3$ ratio (1.29 and 0.05, respectively), whereas in the other cases the ratio remains constant, 0.13. A similar behavior was reported by Yang et al. [25] in the synthesis of ZIF-8/CNT composites from values greater than 20% CNT. In fact, limited MOF loadings can be homogeneously distributed on the alumina surface, maximizing the exposed MOF area.

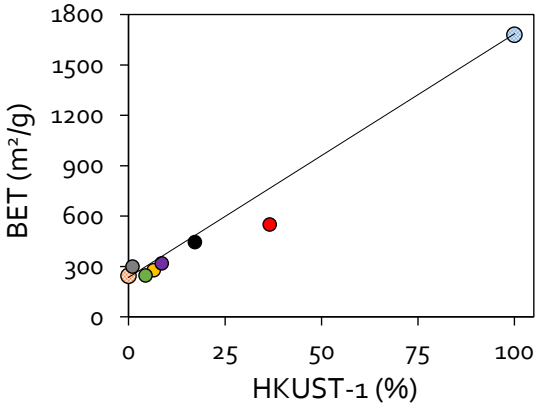


Figure 1. Relation between the BET specific surface area and the quantity of MOF in each material. HKUST-1 (blue stripped), $Al_2O_3$ (orange stripped), $DC_{240}$ (black), $DC_{100V}$ (grey), $DC_{240V}$ (yellow), $S_{240}$ (purple), $S_{240V}$ (green) and $S_{2400V}$ (red). Black line guides the view.

Table 2. Main features of the considered materials.

| Material | % HKUST-1[a] | BET ($m^2/g$) | Total pore volume ($cm^3/g$) |
|---|---|---|---|
| HKUST-1 | 100 | 1680 | 0.833 |
| $Al_2O_3$ | 0 | 246 | 0.505 |
| $DC_{100V}$ | 1.03 | 300 | 0.526 |
| $DC_{240}$ | 17.2 | 445 | 0.639 |
| $DC_{240V}$ | 6.57 | 278 | 0.500 |
| $S_{240}$ | 8.62 | 319 | 0.536 |
| $S_{2400V}$ | 36.6 | 550 | 0.411 |
| $S_{240V}$ | 4.41 | 247 | 0.441 |

[a]Obtained by thermogravimetry

However, high MOF/alumina ratio could promote MOF multilayering instead of a thin-layer distribution, with the subsequent blockage of surface and pores, decreasing the surface availability and reducing the adsorption efficiency.

The same effect was described by Yu et al. [26] in the impregnation of $TiO_2$ with CNTs, with a decrease of available specific surface and morphological properties at high CNTs load. In contrast, other authors refer to the crystal size of HKUST-1 as very decisive in the available BET specific surface area [27]. Therefore, it could be also considered that both the amount of MOF impregnated, as well as the variation of the initial MOF/alumina ratio, influence the crystallization. Finally, differences between both impregnation methodologies are observed in the total pore volume, larger in dip-coating method (Table 2). It may be due to the recrystallization step in the autoclave for dip-coating procedure, which helps to remove unreacted substances initially blocking the pores of the MOF. This effect was previously described by Sule et al. [28], in the synthesis of composites of multi-walled carbon nanotubes and HKUST-1.

Crystalline structures were obtained by PXRD (Figure S4). In case of original HKUST-1, a very crystalline structure is observed, with well resolved peaks along the angle range 2θ = 5-45º. The angle position of the main peaks (2θ = 9.5, 11.6, 13.5º) confirms the typical face-centered cubic (fcc) structure of HKUST-1 [16]. On the other hand, the diffractogram of alumina shows an amorphous material, with three wide characteristic peaks at high diffraction angles (2θ = 37, 46, 67º) [29]. Alumina phase is clearly observed for all the composite materials, as it is the main component. However, in the low-angle corresponding to HKUST-1, greater differences are observed between composite materials.

Materials with the highest MOF content show the best defined peaks in the range 2θ = 5-15º. These materials are $S_{2400V}$, $DC_{240}$, $S_{240}$ and $DC_{240V}$, and the intensity of the main peaks follow the same order than MOF amount impregnated on the alumina. Contrary, $DC_{100V}$ and $S_{240V}$ MOF load is very low, and no crystalline phase presence is distinguished by PXRD. Figure 2 shows a comparative of the main peaks at low angle for composite materials respect to pristine HKUST-1, where the peak 2θ = 9.5º is taken as reference. For $S_{240}$ and $DC_{240V}$, it is observed a little shift to lower values (9º), with absence of new diffractogram peaks, and an important intensity loss. According to Emami et al. [30], these little shifts correspond to a preferred orientation of crystals on the basal space after the composite formation, and not necessarily to a phase change. In addition, other authors indicate that it can also correspond to an expansion of the unit cell [31], accompanied in this case by a decrease in the crystal size, deduced by the growth of the full width at half maximum (FWHM) of the reference peak, following Scherrer equation. These results suggest that the crystal structure of the MOF is not affected by the composite formation, but it greatly influences the total crystallinity of HKUST-1 when combined with an amorphous material at low loads. Similar results were described by Martak et al. [32] in the study of the combination of HKUST-1 and $Al_2O_3$ particles.

On the other hand, different patterns are obtained for materials with highest MOF loadings. Concerning $S_{2400V}$, it maintains the original crystalline phase, with peaks at 2θ = 9, 11.5 and 13.3º, again with a slight shift respect to pristine HKUST-1. However, the presence of several new small peaks: 9.6, 11, 13.5 and 14º is observed, close to the characteristic HKUST-1 peaks indicated above, pointing out a splitting of these initial ones. Ma et al. [33] obtained similar results, which were

attributed to an adequate crystallization of HKUST-1 in combination with high proportion of alumina, which decreases the relative intensity of MOF peaks, leading to this diffraction peaks splitting effect.

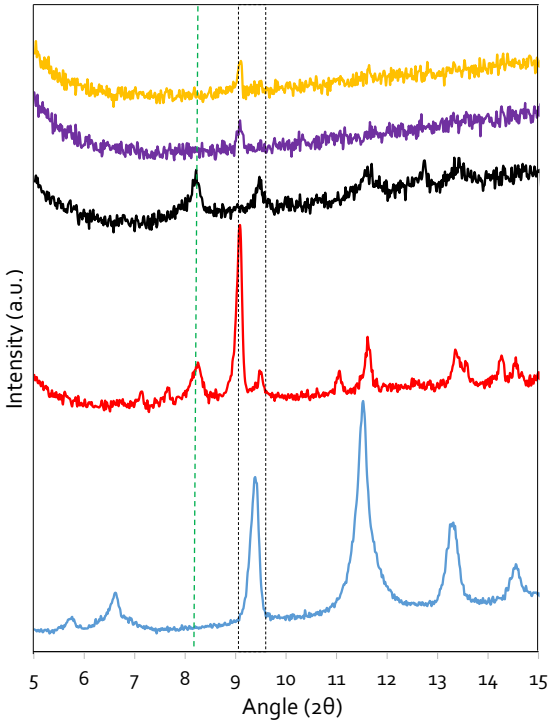


Figure 2. Low-angle diffractograms of HKUST-1 (blue), $S_{240oV}$ (red), $DC_{240}$ (black), $S_{240}$ (purple) and $DC_{240V}$ (yellow). Discontinuous rectangle points out the original position of the characteristic peak of HKUST-1 taken as reference (9.5º).

Surprisingly, in the case of both $S_{240oV}$ and $DC_{240}$, a new peak appears at 8.2º. As far as the authors know, there is no published work about HKUST-1 composites in which these new diffractogram peak has been recorded. According to the results presented by Zheng et al. [34], trimesic acid, which is the organic ligand that conforms the structure of HKUST-1, show a characteristic peak at 2θ values around 8º. Considering other possibilities, it may be also due to changes in the crystallization pattern at high loads of MOF on the alumina. In this way, other authors have also registered affectations in the HKUST-1 crystallization by the combination with another material forming composites [35].

This arrangement is tried to be confirmed by scanning electron microscopy (SEM) combined with EDX. Comparing composite materials with simple materials images, it is possible to identify HKUST-1 particles on the alumina surface, with different sizes and distribution (Figure S5). Defined diamond-shaped particles appear for HKUST-1, octahedral structure characteristic of this crystalline material. In contrast, alumina does not show any regular shape, with large agglomeration in certain zones, probably due to the initial crushing. In case of the composite with the lowest MOF content, $DC_{100V}$, very small particles are observed on the alumina surface, and there is absence of MOF crystals, as it is also obtained by EDX in terms of copper (0.97% Cu). The next composite material, $S_{240V}$, shows the presence of some crystals (2.04% Cu), with a fairly homogeneous distribution and certain alumina agglomerations. Then, SEM images and MOF content of $S_{240}$ and $DC_{240V}$ are very similar, but the distribution of crystals on the surface is more homogeneous in the solvothermal one. It is demonstrated by differences in the copper content on the surface: 1.25 and 5.19%, respectively. For a given HKUST-1 loading, dip-coating composites show more MOF-concentrated areas than solvothermal ones. Therefore, it is noteworthy the more homogeneous distribution of MOF particles on alumina in the case of materials synthesized by the solvothermal method.

Finally, and in the same line than PXRD analyses, striking differences are observed in case of $DC_{240}$ and $S_{240oV}$, the composites with the highest MOF load. Both composites, especially $DC_{240}$, show a new phase mixed with alumina particles and HKUST-1 crystals, not observed in simple materials case, in the form of elongated fibers or nanotubes (Figure 3). These results could be attributable and related to the appearance of the new crystalline phase in these two materials. In fact, some authors have reported that 1,3,5-BTC may be in the shape of fibers in synthesis at high concentration [36]. However, an EDX analysis of an area composed of these fibers in $DC_{240}$ resulted in a copper content of 7.2%, suggesting the presence of HKUST-1 or even copper precursors in a semi-crystalline form. Indeed, the shape of these fibers is very similar to the $Cu(OH)_2$ nanotubes shown by Zhang et al. [37], which were subsequently used by Okada et al. [38] as precursors of HKUST 1. However, the characteristic diffractogram of $Cu(OH)_2$, with characteristic peaks at high diffraction angles, does not coincide with this new phase.

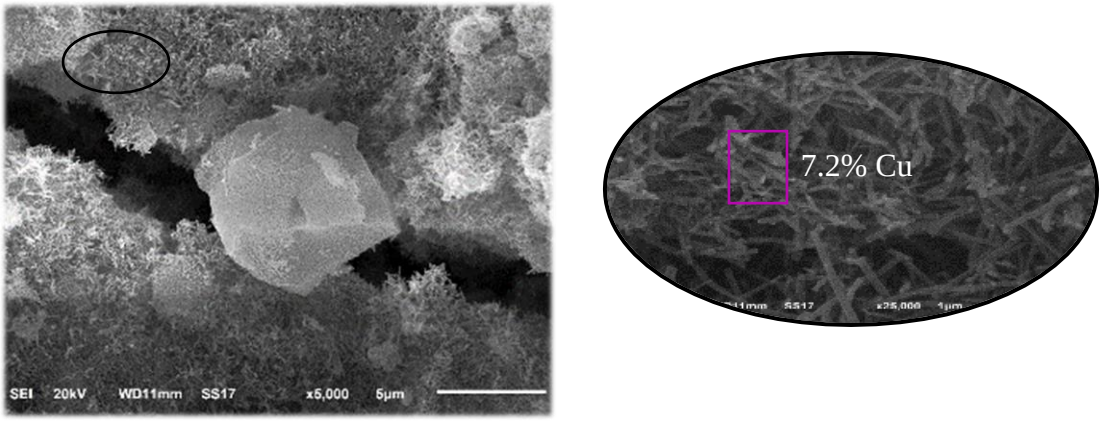


Figure 3. Enlargement of the $DC_{240}$ SEM image in which the elongated fibers can be seen, and the corresponding EDX analysis of the zone (pink rectangle).

3.2. Methane adsorption at mild conditions

Methane adsorption experiences are carried out on a thermobalance at 298 K and 0.1 MPa for 20 h. Results show a pure methane adsorption capacity of 31.8 and 10.6 mg/g for HKUST-1 and $Al_2O_3$, respectively. In case of composites, adsorption capacity decreases as MOF content, crystallinity and specific surface area decrease. However, $DC_{100V}$ (9.84 mg/g) and $DC_{240V}$ (9.12 mg/g) present even worse methane adsorption capacity than simple alumina (Figure 4), although both materials show an initial kinetic trend coincident with $S_{240V}$, above alumina. This initial phase corresponds to the methane adsorption by HKUST-1, more selective towards methane than alumina.

Regarding the kinetic behavior, isotherms have been fit to the Langmuir kinetic model (Equation 1), based on the appropriate results obtained for Basolite C300 in a previous work under similar conditions [39]. Adsorption curves are similar in all cases and fit well to the Langmuir model (Figure S6), which considers the rate of adsorption proportional to the percentage of unoccupied active sites for adsorption, which in case of methane are predominantly the OMS [40]. Thus, the good fitting suggests that methane adsorption occurs mainly in the MOF.

The desorption constant ($k_{des}$) of the model has been found to be negligible, lower than $9 \cdot 10^{-7}$ $s^{-1}$ for all the studied materials, and therefore not further considered. As seen in Table 3, solvothermal composites show higher methane adsorption capacities and lower Langmuir adsorption constants than dip-coating composites, except in $S_{2400V}$ case. Therefore, it suggests that the MOF impregnated by the solvothermal method is more effective for adsorption than the impregnated by dip-coating, in agreement with previous results. As shown by SEM analysis, it can be related with the more homogeneous distribution on the surface for solvothermal composites, which proves to be key in adsorption processes of composite materials [41]. Heterogeneity in dip-coating materials causes faster (higher Langmuir constant) but less effective (lower adsorption capacity) saturation kinetics. In order to corroborate this assumption, Figure 5 relates the methane adsorption capacity registered and the load of MOF for each material. The straight line joining HKUST-1 and alumina indicates a linear behavior between MOF load and adsorption capacity. Materials above the line indicate that the MOF is located on the alumina in an arrangement that favors the adsorption, the opposite in case of materials below the line. As seen, solvothermal materials stay on or above the line, whereas dip-coating materials stay clearly below the line, especially $DC_{240V}$.

$$q_t = q_e \cdot \frac{k_{ads}}{k_{ads}+k_{des}}\left(1 - e^{-(-k_{ads}+k_{des})t}\right) \qquad (1)$$

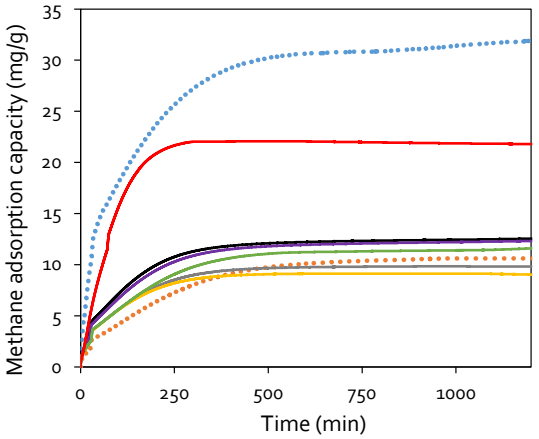


Figure 4. Methane adsorption isotherms at 298 K and 0.1 MPa. HKUST-1 (blue striped), $Al_2O_3$ (orange striped), $DC_{240}$ (black), $DC_{100V}$ (grey), $DC_{240V}$ (yellow), $S_{240}$ (purple), $S_{240V}$ (green) and $S_{2400V}$ (red).

Table 3. Pure methane adsorption capacity (298 K, 0.1 MPa) and value of Langmuir adsorption constant for each material.

| Material | $CH_4$ capacity (mg/g) | $K_{langmuir}$ ($s^{-1}$) | $R^2$ |
|---|---|---|---|
| HKUST-1 | 31.8 | $1.33 \cdot 10^{-4}$ | 0.95 |
| $Al_2O_3$ | 10.6 | $8.11 \cdot 10^{-5}$ | 0.99 |
| $DC_{100V}$ | 9.84 | $1.45 \cdot 10^{-4}$ | 0.98 |
| $DC_{240}$ | 12.5 | $1.52 \cdot 10^{-4}$ | 0.97 |
| $DC_{240V}$ | 9.12 | $1.68 \cdot 10^{-4}$ | 0.98 |
| $S_{240}$ | 12.3 | $1.29 \cdot 10^{-4}$ | 0.98 |
| $S_{2400V}$ | 22.1 | $2.01 \cdot 10^{-4}$ | 0.99 |
| $S_{240V}$ | 11.6 | $1.11 \cdot 10^{-4}$ | 0.98 |

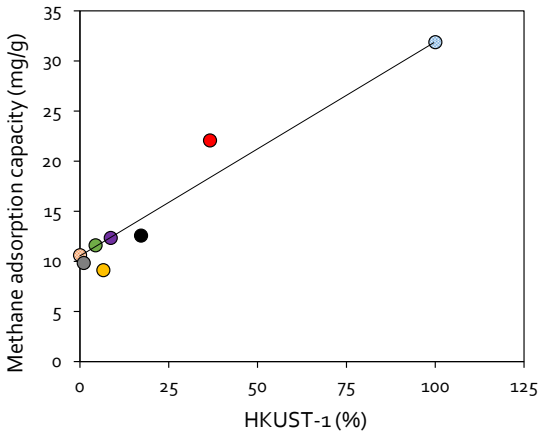


Figure 5. Relation between pure methane adsorption capacity obtained by thermobalance (298 K, 0.1 MPa) and the MOF load on each composite. HKUST-1 (blue striped), $Al_2O_3$ (orange striped), $DC_{240}$ (black), $DC_{100V}$ (grey), $DC_{240V}$ (yellow), $S_{240}$ (purple), $S_{240V}$ (green) and $S_{2400V}$ (red).

### 3.3. Fixed-bed performance and ageing in presence of water

To test the fixed-bed performance and the water resistance of the materials studied, 72 ml/min of air with 100% RH (59000 ppm) are flowed continuously through a fixed-bed of each material (0.15 g) for 24 h, at 298 K and 0.1 MPa. Firstly, pressure drop of a fixed bed packed with pristine HKUST-1 (20 µm) was measured, resulting in $4.7 \cdot 10^5$ Pa/m, due to its large compaction and low void space. In contrast, alumina, with much larger particle size (355-710 µm), exhibits a practically negligible pressure drop, $3.1 \cdot 10^4$ Pa/m. The same trend is followed in case of composites, with a particle size similar to alumina, and a pressure drop around $3.2 \cdot 10^4$ Pa/m in all cases. In addition, composite particles do not show attrition when conforming the fixed-bed. Therefore, composite particles perform much better than HKUST-1 in a fixed-bed in physical terms, in which the pressure drop of the MOF can entail very high associated costs.

Secondly, after the humid treatment for 24 h, materials are treated at 423 K under dry air for 2 h. This procedure simulates an actual adsorption process with an intermediate regeneration cycle at high temperature, similar to a temperature-swing adsorption (TSA) process. Then, methane adsorption capacity is tested in the previous conditions. In case of HKUST-1, the methane adsorption capacity decreases 14.4% respect to the pristine material, whereas alumina shows a loss of 4.8%. As expected, HKUST-1 performance suffers greatly under humid conditions, as water present high attraction towards OMS, reducing the availability of active adsorption sites for methane. On the contrary, alumina withstands the water presence, and shows great hydrophilicity already reported by other authors [42]. HKUST-1 shows a reduction in the Langmuir adsorption constant ($6.4 \cdot 10^{-5}$ $s^{-1}$), suggesting a slight alteration of the active sites for methane adsorption. The same trend is followed by the composites with the highest MOF loadings, $S_{2400V}$ and $DC_{240}$, with 5.9 and 9.4% decrease in methane adsorption capacity, respectively. The presence of alumina diminishes a little the water effect, but the MOF continues to be greatly affected. On the contrary, the trend completely shifts by reducing the MOF load on alumina particles. All the composites with medium and low MOF load present an increase in methane adsorption capacity (Figure 6). Further, the capacity increase is larger for dip-coating composites. This is striking, since dip-coating composites are also the materials with the least efficient MOF distribution for adsorption (Figure 5). This fact suggests that the MOF heterogeneity on the alumina surface increases the MOF stability in presence of water and enhances the methane adsorption capacity, but only at reduced MOF loadings.

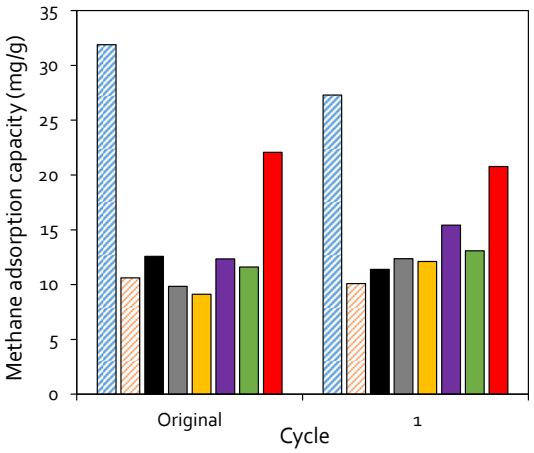


Figure 6. Variation of methane adsorption capacity after the water-ageing cycle applied to each material. HKUST-1 (blue striped), $Al_2O_3$ (orange striped), $DC_{240}$ (black), $DC_{100V}$ (grey), $DC_{240V}$ (yellow), $S_{240}$ (purple), $S_{240V}$ (green) and $S_{2400V}$ (red).

Several authors have proposed HKUST-1 as a powerful precursor to methane-hydrate formation, due to its large pore wettability [31, 43]. Furthermore, it was demonstrated that it is largely favored at low HKUST-1 loadings on a metal-oxide support material, like alumina [44], and even more effective the more the heterogeneous distribution, making up MOF clusters [45]. This could explain the larger improvement registered for dip-coating materials in case of low MOF loadings, with a more heterogeneous distribution of HKUST-1 on the alumina surface. Although high pressure and low temperature are required to methane hydrates formation, and these conditions do not apply in this case, the arrangement of HKUST-1 on the alumina surface, add to the wetting of the high pore volume of the MOF, may favour methane-water-composite contact in a similar wat to the hydrates formation. In fact, several works have demonstrated the improvement in the methane adsorption capacity after wetting the pores of a large porous material [46]. In general terms, water forms a cage structure in MOF pores with certain affinity towards methane. Furthermore, results presented by other authors have demonstrated improvements in the water resistance of HKUST-1 after a combination with other materials in a composite [47, 48].

In order to verify changes in the water-composite interaction, the materials have been subjected to thermal decomposition after humid ageing. Figure S7 plots the effluent gases ($CO_2$ and $H_2O$) profiles obtained by mass spectroscopy. In case of HKUST-1, two main water desorption peaks are observed (343 and 473 K), the first one attributed to water physisorbed. Additionally, it is observed a $CO_2$ large peak at 593 K, related to the structure decomposition, coincident with thermogravimetry results (Figure S2). For alumina, a large water desorption peak at 473 K is observed, related to chemisorbed water. However, the trend clearly shifts in the case of composites. These materials show two well-differentiated water desorption peaks, 373 and 523 K, except for $S_{2400V}$ and $DC_{100V}$, the materials with the highest and lowest MOF loadings, respectively. The presence of a predominant water desorption peak at 523 K, even in composites with high MOF loadings, suggest the formation of stronger bonds between the water molecule and the surface of composites than on alumina or MOF alone. These results suggest that water is preferentially bound by chemisorption to the alumina surface, which is more water-selective than HKUST-1, thus protecting the MOF structure, although there is also water retained in the porous structure of the MOF. This water wetting the MOF pores causes the enhanced methane adsorption, as seen above. Further, it is noteworthy the absence of the $CO_2$ peak from MOF loads of less than 10%, approximately. This is consistent with the results obtained by thermogravimetry, which show greater thermal resistance of composites than HKUST-1. Therefore, the synergy between the MOF and the alumina dramatically increases thermal and moisture stability.

The same humid treatment is applied by three consecutive cycles on all the considered materials in order to confirm the trend (Figure 7). At the last cycle, HKUST-1 losses about 37% of the original methane adsorption capacity, whereas alumina maintains practically the loss registered at the first cycle, around 5%. The kinetic constants of the proposed kinetic Langmuir model are similar than the corresponding to the tests with the parent composites ($6.1 \cdot 10^{-5}$ $s^{-1}$), suggesting that adsorption mechanism is essentially the same, despite the losses in the adsorption capacity. This suggests that water blocks OMS for adsorption, decreasing the Langmuir constant, but it does not destroy the MOF structure. Concerning composites, $S_{2400V}$ and $DC_{240}$ loss again an important part of their adsorption capacity after the third cycle, 27.3 and 15.8%, respectively. Again, at low MOF loadings on the composites, the water effect is the opposite, and the methane adsorption capacity continues above the original capacity. In fact, in some composites, such as $DC_{240V}$, it even increases from the first to the third cycle. Therefore, these results confirm the previously proposed assumption. Table 4 shows the adsorption capacities registered with cycles.

Table 4. Variation in methane adsorption capacity after one and three consecutive cycles in presence of water (100% RH).

| Material | Original (mg/g) | 1st cycle (mg/g) | 3rd cycle (mg/g) |
|---|---|---|---|
| HKUST-1 | 31.8 | 27.3 | 21.2 |
| $Al_2O_3$ | 10.6 | 10.1 | 10.1 |
| $DC_{100V}$ | 9.84 | 12.4 | 12.1 |
| $DC_{240}$ | 12.5 | 11.4 | 10.6 |
| $DC_{240V}$ | 9.12 | 12.1 | 12.6 |
| $S_{240}$ | 12.3 | 15.4 | 14.7 |
| $S_{2400V}$ | 22.1 | 20.7 | 16.1 |
| $S_{240V}$ | 11.6 | 13.1 | 13.7 |

Finally, Figure 8 relates the capacity loss after the third cycle with the MOF content in each composite. As seen, there is a gap between $DC_{240}$ and $S_{240}$, and it goes from a loss of 15.8% to a capacity gain of 18.9% after three humid cycles. Therefore, it can be indicated that in this gap, which include around 9% of MOF load variation, an arrangement of HKUST-1 occurs on the alumina surface that greatly favors the methane-water-composite interaction. Below this value, and regardless of the impregnation method, the presence of water seems favorable in the methane adsorption by HKUST-1@$Al_2O_3$ composites, reaching even an improvement of 38% in the case of $DC_{240V}$. These results suggest that the performance improvement occurs only for low MOF loadings, and with larger intensity in the case of a more heterogeneous distribution (dip-coating), which agrees with the assumptions previously made.

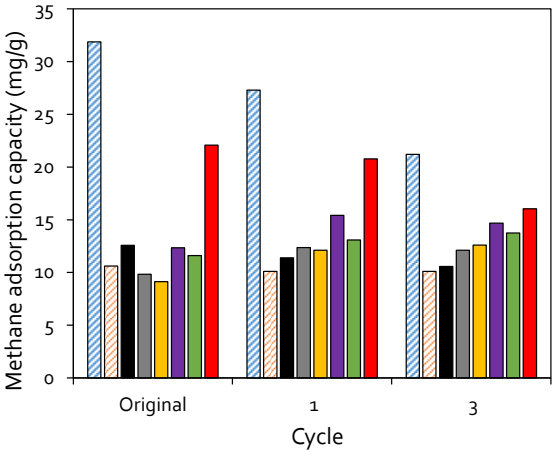


Figure 7. Variation of methane adsorption capacity through the water-ageing cycles applied to each material. HKUST-1 (blue striped), $Al_2O_3$ (orange striped), $DC_{240}$ (black), $DC_{100V}$ (grey), $DC_{240V}$ (yellow), $S_{240}$ (purple), $S_{240V}$ (green) and $S_{2400V}$ (red).

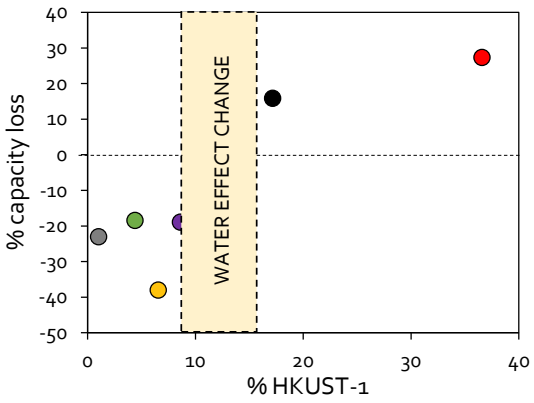


Figure 8. Relation between the methane adsorption capacity loss after three cycles of water ageing (24 h, 100% RH) on a fixed-bed and the HKUST-1 load on each composite. The shaded area indicates the trend change. $DC_{240}$ (black), $DC_{100V}$ (grey), $DC_{240V}$ (yellow), $S_{240}$ (purple), $S_{240V}$ (green) and $S_{2400V}$ (red).

## 4. Conclusions

We have demonstrated in this work that HKUST-1@$Al_2O_3$ present key advantages in comparison to the parent MOF, especially in terms of working with very limited pressure drop in fixed bed adsorption and their enhanced performance stability in presence of water.

Different HKUST-1@$Al_2O_3$ (prepared changing preparation methods and MOF loading) have been tested for methane adsorption. Alumina particles were selected for its large particle size and high hydrophilicity, which can reduce the pressure drop in a fixed-bed and protect the MOF from water, respectively. Composites with high MOF load follow the same trend than pristine HKUST-1, although with lower capacity losses. Surprisingly, in case of composites with HKUST-1 loads lower than 9%, the presence of water increases the methane adsorption capacity, even 38% respect to the original. This effect is more striking in the case of dip-coating composites, with a more hetero-

geneous distribution on the MOF, giving rise to clusters that follow a similar principle to the methane-hydrate formation, but at milder conditions. The alumina selectivity towards water protects the HKUST-1 structure. In addition, thermal decomposition essays show an increase in the thermal stability of the MOF when forming the composites, confirming the synergy between the MOF and the alumina, strengthening the structure. Further, pressure drop is negligible in all composite cases. Results open the possibility of using these composites in actual operations.

**CRediT authorship contribution statement**

**David Ursueguía**: Investigation, writing-original draft, data curation, formal analysis. **Eva Díaz**: Visualization, supervision, project administration, writing-review & editing. **Salvador Ordóñez**: Visualization, conceptualization, supervision, funding acquisition, writing-review & editing.

**Declaration of Competing Interest**

The authors declare that they have no known competing financial interests or personal relationships that could have appeared to influence the work reported in this paper.

**Acknowledgements**

This work was supported by the Asturian Government (contract GRUPIN AYUD/2021/50450) and by the Spanish Agency for Research (PID2020-112587RB-I100).

David Ursueguía acknowledges the Spanish Government for the PhD grant that supports his research (FPU18/01448). Authors would like to acknowledge the technical support provided by *Servicios Científico-Técnicos de la Universidad de Oviedo*.

**References**

[1] K. Nath, A. Ahmed, D. Siegel, A. Matzger, Computational identification and experimental demonstration of high-performance methane sorbents, Angewandte Chemie 134 (2022) e202203575.

[2] D. Ursueguía, E. Díaz, A. Vega, S. Ordóñez, Methane separation from diluted mixtures by fixed bed adsorption using MOFs: Model validation and parametric studies, Separation and Purification Technology 251 (2020) 117374.

[3] E. Tsalaporta, J. MacElroy, A comparative study of the physical and chemical properties of pelletized HKUST-1, ZIF-8, ZIF-67 and UiO-66 powders, Heliyon 6 (2020) E04883.

[4] A. Domán, O. Czakkel, L. Porcar, J. Madarász, E. Geissler, K. László, Role of water molecules in the decomposition of HKUST-1: Evidence from adsorption, thermoanalytical, X-ray and neutron scattering measurements, Applied Surface Science 480 (2019) 138-147.

[5] J. Canivet, A. Fateeva, Y. Guo, B. Coasne, D. Farrusseng, Water adsorption in MOFs: fundamentals and applications, Chemical Society Reviews 43 (2014) 5594-5617.

[6] B. Ray, S. Churipard, S. Peter, An overview of the materials and methodologies for $CO_2$ capture under humid conditions, Journal of Materials Chemistry A 9 (2021) 26498-26527.

[7] P. Goyal, A. Paruthi, D. Menon, R. Behara, A. Jaiswal, K. V, A. Kumar, V. Krishnan, S. Misra, Fe doped bimetallic HKUST-1 MOF with enhanced water stability for trapping Pb(II) with high adsorption capacity, Chemical Engineering Journal 430 (2022) 133088.

[8] Y. Wu, Y. Sun, J. Xiao, X. Wang, Z. Li, Glycine-modified HKUST-1 with simultaneously enhanced moisture stability and improved adsorption for light hydrocarbons separation, ACS Sustainable Chemistry and Engineering 7 (2019) 1557-1563.

[9] M. Kanno, T. Kitao, T. Ito, K. Terashima, Synthesis of a metal-organic framework by plasma in liquid to increase reduced metal ions and enhance water stability, RSC Advances 11 (2021) 22756-22760.

[10] R. Pan, Y. Tang, Y. Guo, J. Shang, L. Zhou, W. Dong, D. He, HKUST-1 and its graphene oxide composites: Finding an efficient adsorbent for $SO_2$ capture, Microporous and Mesoporous Materials 323 (2021) 111197.

[11] M. Majaz, T. Cendak, G. Buscarino, M. Todaro, N. Logar, Confined crystallization of a HKUST-1 metal-organic framework within mesostructured silica with enhanced structural resistance towards water, Journal of Materials Chemistry A 5 (2017) 22305-22315.

[12] P. Jagódka, K. Matus, A. Lamacz, On the HKUST-1/GO and HKUST-1/rGO composites: the impact of synthesis method on physicochemical properties, Molecules 27 (2022) 7082.

[13] S. Xie, W. Monnens, K. Wan, W. Zhang, W. Guo, M. Xu, I. Vankelecom, X. Zhang, J. Fransaer, Cathodic electrodeposition of MOF films using hydrogen peroxide, Angewandte Chemie 133 (2021) 25154-25161.

[14] T. Wang, A. Wright, W. Hoover, K. Stoffel, R. Richardson, S. Rodriguez, R. Flores, J. Siegfried, N. Vermeulen, P. Fuller, M. Weston, O. Farha, W. Morris, Surviving under pressure: the role of solvent, crystal size, and morphology during pelletization of metal-organic frameworks, ACS Applied Materials and Interfaces 13 (2021) 52106-52112.

[15] D. Ursueguía, C. Daniel, C. Collomb, C. Cardenas, D. Farrusseng, E. Díaz, S. Ordóñez, Evaluation of HKUST-1 as volatile organic compound adsorbents for respiratory filters, Langmuir 38 (2022) 14465-14474.

[16] D. Ursueguía, E. Díaz, S. Ordóñez, Densification-induced structure changes in Basolite MOFs: Effect on low-pressure $CH_4$ adsorption, Nanomaterials 10 (2020) 1089.

[17] Z. Wang, L. Liu, Z. Li, N. Goyal, T. Du, J. He, G. Li, Shaping of metal-organic frameworks: A review, Energy and Fuels 36 (2022) 2927-2944.

[18] M. Hamid, Y. Qian, R. Wei, Z. Li, Y. Pan, Z. Lai, H. Jeong, Polycrystalline metal-organic framework (MOF) membranes for molecular separations: Engineering prospects and challenges, Journal of Membrane Science 640 (2021) 119802.

[19] J. Dong, P. Li, H. Guan, C. Ge, Y. Bai, Y. Zhao, X. Zhang, The synthesis of HKUST-1/$SiO_2$ composite material based on 3D printing, Inorganic Chemistry Communications 117 (2020) 107975.

[20] H. Etemadi, S. Afsharkia, S. Zinatloo-Ajabshir, E. Shokri, Effect of alumina nanoparticles on the antifouling properties of polycarbonate-polyurethane blend ultrafiltration membrane for water treatment, Polymer Engineering and Science 61 (2021) 2364-2375.

[21] O. Shekhah, J. Liu, R. Fischer, C. Wöll, MOF thin films: existing and future applications, Chemical Society Reviews 40 (2011) 1081-1106.

[22] J. Gascon, S. Aguado, F. Kapteijn, Manufacture of dense coatings of $Cu_3(BTC)_2$ (HKUST-1) on α-alumina, Microporous and Mesoporous Materials 113 (2008) 132-138.

[23] L. Qin, Y. Zhou, D. Li, L. Zhang, Z. Zhao, Z. Zuhra, C. Mu, Highly dispersed HKUST-1 on millimeter-sized mesoporous γ-$Al_2O_3$ beads for highly effective adsorptive desulfurization, Industrial and Engineering Chemistry Research 55 (2016) 7249-7258.

[24] D. Atinafu, S. Chang, U. Berardi, K. Kim, S. Kim, Potential utility of HKUST-1-graphite nanocomposite to endow alkane with high thermal properties and low electrical resistivity, Journal of Hazardous Materials 402 (2021) 123695.

[25] Y. Yang, L. Ge, V. Rudolph, Z. Zhu, In situ synthesis of zeolitic imidazolate frameworks/carbon nanotube composites with enhanced $CO_2$ adsorption, Dalton Transactions 43 (2014) 70287036.

[26] J. Yu, T. Ma, S. Lu, Enhanced photocatalytic activity of mesoporous $TiO_2$ aggregates by embedding carbon nanotubes as electron-transfer channel, Physical Chemistry Chemical Physics 13 (2011) 3491-3501.

[27] Q. Liu, L. Jin, W. Sun, Facile fabrication and adsorption property of a nano/microporous coordination polymer with controllable size and morphology, Chemical Communications 48 (2012) 8814-8816.

[28] R. Sule, A. Mishra, Synthesis of mesoporous MWCNT/HKUST-1 composite for wastewater treatment, Applied Sciences 9 (2019) 4407.

[29] T. Saleh, Carbon nanotube-incorporated alumina as a support for MoNi catalysts for the efficient hydrodesulfurization of thiophenes, Chemical Engineering Journal 404 (2021) 126987.

[30] N. Emami, M. Farhadian, A. Solaimany, S. Tangestaninejad, Adsorption of cefixime and lamotrigine on HKUST-1/ZIF-8 nanocomposite: isotherms, kinetics models and mechanism, International Journal of Environmental Science and Technology (2022).

[31] S. Denning, A. Majid, J. Lucero, J. Crawford, M. Carreon, C. Koh, Metal-organic framework HKUST-1 promotes methane hydrate formation for improved gas storage capacity, ACS Applied Materials and Interfaces 12 (2020) 53510-53518.

[32] F. Martak, M. Hafiz, D. Sulistiono, A. Rosyidah, Y. Kusumawati, R. Ediati, Direct synthesis of Al-HKUST-1 and its application as adsorbent for removal of congo red in water, Nano-Structures and Nano-Objects 27 (2021) 100773.

[33] X. Ma, S. Peng, W. Li, H. Liu, Y. Chen, Efficient removal of low concentration methyl mercaptan by HKUST-1 membrane constructed on porous alumina granules, CrystEngComm 20 (2018) 407-411.

[34] C. Zheng, H. Ren, Z. Cui, F. Chen, G. Hong, Synthesis and characterization of nano-scale Terbium (III)-trimesic acid (TMA)-1,10-phenanthroline(phen) luminescent complex,

[35] W. Zhao, Y. Long, Y. He, J. Cai, M. Liu, HNTs@HKUST-1 strengthened PAAm hydrogel for strain sensing and antibacterial application, Microporous and Mesoporous Materials 344 (2022) 112207.

[36] K. Liu, Y. Zheng, G. Jia, M. Yang, Y. Song, N. Guo, H. You, Nano/micro-scaled La(1,3,5-BTC)$(H_2O)_6$ coordination polymer: Facile morphology-controlled fabrication and color-tunable photoluminescence properties by co-doping Eu3+, Tb3+, Journal of Solid State Chemistry 183 (2010) 2309-2316.

[37] W. Zhang, X. Wen, S. Yang, Y. Berta, Z. Wang, Single-crystalline scroll-type nanotube arrays of copper hydroxide synthesized at room temperature, Advanced Materials 15 (2003) 822-825.

[38] K. Okada, R. Ricco, Y. Tokudome, M. Styles, A. Hill, M. Takahashi, P. Falcaro, Copper conversion into $Cu(OH)_2$ nanotubes for positioning $Cu_3(BTC)_2$ MOF crystals: Controlling the growth on flat plates, 3D architectures, and as patterns, Advanced Functional Materials 24 (2014) 1969-1977.

[39] D. Ursueguía, E. Díaz, S. Ordóñez, Adsorption of methane and nitrogen on Basolite MOFs: Equilibrium and kinetic studies, Microporous and Mesoporous Materials 298 (2020) 110048.

[40] J. Wang, X. Guo, Adsorption kinetics models: Physical meanings, applications, and solving methods, Journal of Hazardous Materials 390 (2020) 122156.

[41] N. Torasso, A. Vergara, P. Rivas, C. Huck, A. Larrañaga, A. Fernández, S. Cerveny, S. Goyanes, Enhancing arsenic adsorption via excellent dispersion of iron oxide nanoparticles inside poly(vinyl alcohol) nanofibers, Journal of Environmental Chemical Engineering 9 (2021) 104664.

[42] J. Kim, S. Yoo, Y. Kong, S. Cho, E. Lee, Wetting property modification of $Al_2O_3$ by helium ion irradiation: Effects of beam energy and fluence on contact angle, Langmuir 37 (2021) 11301-11308.

[43] S. Denning, A. Majid, J. Crawford, J. Wells, M. Carreon, C. Koh, Methane storage scale-up using hydrates and metal organic framework HKUST-1 in a packed column, Fuel 325 (2022) 124920.

[44] V. Smirnov, A. Manakov, S. Lyrshchikov, T. Rodionova, V. Dyrdin, Z. Ismagilov, Formation and decomposition of methane hydrate in pores of γ-$Al_2O_3$

and θ-$Al_2O_3$: The dependence of water to hydrate transformation degree on pressure and temperature, Journal of Molecular Liquids 328 (2021) 115486.

[45] A. Nesterov, A. Reshetnikov, A. Manakov, T. Rodionova, E. Paukshtis, I. Asanov, S. Bardakhanov, A. Bulavchenko, Promotion and inhibition of gas hydrate formation by oxide powders, Journal of Molecular Liquids 204 (2015) 118-125.

[46] H. Liu, S. Zhan, P. Guo, S. Fan, S. Zhang, Understanding the characteristic of methane hydrate equilibrium in materials and its potential application, Chemical Engineering Journal 349 (2018) 775-781.

[47] J. DeCoste, M. Denny, G. Peterson, J. Mahle, S. Cohen, Enhanced aging properties of HKUST-1 in hydrophobic mixed-matrix membranes for ammonia adsorption, Chemical Science 7 (2016) 2711-2716.

[48] Z. Zhang, W. Huang, X. Li, X. Wang, Y. Zheng, B. Yan, C. Wu, Water-stable composite of HKUST-1 with its pyrolysis products for enhanced $CO_2$ capture capacity, Inorganic Chemistry Communications 146 (2022) 110063.

## 4.5. OTROS USOS DE MOFs

Debido al gran potencial de los MOFs en procesos de adsorción, se ha decidido probar el HKUST-1, homólogo al Basolite C300, en una situación distinta a la adsorción de metano. En este sentido, durante la estancia predoctoral en el centro de investigación IRCELYON, bajo la supervisión del Profesor Farrusseng, se estudió un proceso de adsorción en lecho fijo de ciclohexano poco concentrado (5000 ppm) en aire bajo distintas condiciones operativas. El objetivo principal es la búsqueda de materiales adsorbentes adecuados para la fabricación de máscaras de protección individual, que sean capaces de operar en diferentes escenarios. Se ha tomado el ciclohexano como compuesto orgánico volátil (VOC) de referencia, debido a sus propiedades físico-químicas y su frecuente presencia en multitud de entornos industriales.

La experimentación se lleva a cabo en un lecho fijo relleno del MOF HKUST-1 con distintos tamaños de partícula (20 µm, 300-600 µm y 1-1.18 mm). Las partículas se obtienen mediante compresión mecánica en una prensa hidráulica, a una presión reducida (6000 ton/$m^2$) que evite la destrucción de la estructura y la pérdida de capacidad de adsorción del MOF, visto previamente el gran efecto nocivo de esta técnica sobre estos materiales. Por otro lado, las condiciones experimentales también son variables, ya que se opera bajo diferentes regímenes de humedad relativa (0, 27 y 80%), comparando los resultados con los obtenidos para un carbón activado típico, PICACTIF TA 60, con un tamaño de partícula de 300-600 µm.

Los resultados muestran la fracción 300-600 µm de HKUST-1 como la más adecuada para el proceso, ya que no registra prácticamente pérdidas de capacidad de adsorción tras la compresión, y el incremento de densidad del material (69%) permite incrementar el tiempo de protección personal, hasta valores de 85 min/$cm^3$, incluso bajo condiciones de 80% de humedad relativa. Estos resultados son comparables al carbón activo comercial, y por tanto prometedores para un uso futuro del MOF, tanto en solitario como en una combinación MOF-Carbón. Además, los resultados muestran que la cinética de destrucción de la estructura del MOF por efecto del agua (registrada en trabajos anteriores) es lenta. En el caso de ensayos de

adsorción de un solo paso en presencia de humedad, el material se satura rápidamente en ciclohexano y el agua no afecta gravemente a la estructura.

Los resultados presentados se discuten y recogen en la siguiente publicación científica:

- David Ursueguía, Cecile Daniel, Corentin Collomb, Cristian Cardenas, David Farrusseng, Eva Díaz, Salvador Ordóñez, Evaluation of HKUST-1 as volatile organic compound adsorbents for respiratory filters, Langmuir 38 (2022) 14465-14474. https://doi.org/10.1021/acs.langmuir.2c02332.

Factor de Impacto (2021): 4.331
Categoría (2021): Multidisciplinary Chemistry (72/179: Q2)
Número de citas: 0

## Evaluation of HKUST-1 as volatile organic compounds adsorbent for respiratory filters

David Ursueguía[a,b], Cecile Daniel[a], Corentin Collomb[a], Cristian Cardenas[a], David Farrusseng[a]*, Eva Díaz[b], Salvador Ordóñez[b]

[a]Univ. Lyon, Université Claude Bernard Lyon 1, CNRS, IRCELYON, F-69626, Villeurbanne, France

[b]Catalysis, Reactors and Control Research Group (CRC), Department of Chemical and Environmental Engineering, University of Oviedo, Julián Clavería s/n, 33006 Oviedo, Spain

*e-mail: david.farrusseng@ircelyon.univ-lyon1.fr

*Langmuir* **38** (2022) 14465-14474

https://doi.org/10.1021/acs.langmuir.2c02332

## ABSTRACT

Cyclohexane is a representative of volatile organic compounds. VOCs can cause serious health problems in case of continuous exposure, so it is essential to develop efficient personal protective equipment. Historically, activated carbons are used as VOCs adsorbents. However, the emergence of promising novel adsorbents, such as metal-organic frameworks, has pushed the research to study their behavior under the same conditions. In this work, it is proposed the use of the well-known HKUST-1 MOF of different particle sizes (20 μm, 300-600 μm and 1-1.18 mm) for the adsorption of low-grade (5000 ppm) cyclohexane combined with different water concentrations (dry, 27 and 80% RH) in a fixed bed. Results were compared under the same conditions for a typically used activated carbon, PICACTIF TA 60. HKUST-1 has higher affinity to cyclohexane than PICACTIF for the whole pressure range studied, especially at low partial pressures. It begins to adsorb much earlier (0.0025 kPa) than the activated carbon (0.01 kPa). However, a different adsorption behavior is evidenced for both materials in the presence of water vapor since HKUST-1 is very hydrophilic in the zone near to the copper open metal sites, whereas PICACTIF is hydrophobic. After three consecutive cycles, good stability results were obtained for the MOF, comparable to activated carbon, even in presence of water. As the main finding, whereas the unstability of HKUST-1 is well established at high humid conditions, the kinetic of degradation has not been established so far. Here it is shown that the time usage of HKUST-1 as adsorbent for respiratory mask (single pass) is not affected by the degradation of the structure, which may occur on a longer time scale. Finally, shaping by tableting provides good results since it is possible to increase the MOF density by around 69% with minor loss of adsorption capacity. The best fraction is 300-600 μm, reaching cyclohexane breakthrough times around 85 min/cm$^3$ at 80% RH, comparable with PICACTIF activated carbon and promising for practical applications.

**Keywords**: VOCs; Adsorption; MOF; Activated carbon; Water vapor; Cyclohexane

### 1. Introduction

Volatile organic compounds (VOCs) are organic chemicals with high vapor pressure and low solubility in water. These compounds are the most common pollutants emitted from chemical and petrochemical industries [1], being also present in everyday products, such as paints, wax and cleaning [2]. Long-term exposures have been demonstrated to be a potential risk for the development of certain diseases [3], and these emissions are also precursors of ozone ($O_3$) formation in the atmosphere, which is their main environmental issue [4]. In addition to the negative aspects, these compounds also have high added value, making their recovery a twofold advantage: reducing a harmful emission with a subsequent potential economic benefit [5]. In terms of available technology, adsorption is one of

the most efficient and cheapest methods for controlling these emissions [6], above other techniques, such as absorption, cryogenic separation and membranes [7]. Among the VOCs, cyclohexane ($C_6H_{12}$) has aroused great interest since it is present in some industrial processes, like paint and varnish, it is used for obtaining precursors to nylon, and it also has important effects on the human nervous system in case of long exposures [8-10]. Furthermore, cyclohexane adsorption experiences are relevant since it is the representative organic vapor usually used for benchmarking adsorbents for VOC adsorption, according to the EN 14387 standard [11]. It is an adequate representative because it is non-polar and unreactive, and it is present in the majority of industrial environments. Therefore, its performance analysis is very useful for the design of personal protective equipment, such as respiratory filters, which are canisters filled with a granulated adsorbent material that allow to purify polluted air and make it breathable [12].

According to the available literature, very different values of cyclohexane adsorption capacity have been found for carbonaceous materials, ranging from 15 mg/g for a hydrochar [13] to more than 2100 mg/g for an activated carbon obtained from coconut shell [14]. The cyclohexane adsorption heat is around 55 kJ/mol on a granular activated carbon, an average value between the adsorption of other VOCs and, therefore, another feature to be a good representative of VOCs [15]. The non-polarity of cyclohexane causes weak adsorption, being one of the few VOC molecules with zero dipole moment [16]. In addition, from the registered adsorption experiments, it can be inferred that the diffusion rate controls the adsorption mechanism through the pores of the carbon [17, 18]. Most importantly, humid streams result, for all known adsorbents, in a major reduction of the adsorption capacity and lead to breakthrough time reductions. For activated carbons, the negative impact of humid streams is generally observed for RH > 50%, which corresponds to air purification applications in almost all relevant conditions of use. In the case of higher RH (> 80%), up to 85% of the adsorption capacity usually drops [19]. In this way, Do et al. [20] proposed a model for water adsorption on different activated carbons, showing that micropores contribute greatly to the water adsorption in these materials, thus hindering the transport of cyclohexane. This harmful effect of humidity on the adsorption capacity of activated carbon motivates the development of alternative adsorbents for which humid streams have less impact on performances.

An alternative is the application of metal-organic frameworks (MOFs), which present microporous structures for adsorption processes. They have gained importance in recent times due to their very large microporous volume and surface area [21]. For specific MOFs, the presence of open metal sites (OMS) in the structure generates polar sites that can favor the separation and adsorption of different gas molecules [22]. Among all the available MOFs with OMS, HKUST-1 is the most studied for cyclohexane adsorption since it is one of the few large-scale synthesizable MOFs [23]. Available literature shows a cyclohexane adsorption capacity for HKUST-1 between 120 and 500 mg/g [24-26], with an adsorption enthalpy around 47 kJ/mol [27]. Results show that most of the cyclohexane adsorption capacity is accomplished at low partial pressures, corresponding to the micropores filling mechanism. In addition, it is pointed out the importance of the presence of OMS in the adsorption of some polar molecules, such as water. Further, HKUST-1 presents very interesting adsorption results compared to activated carbon for other types of adsorbates, such as $H_2S$ [28] and $NH_3$ [29], so its use could cover a greater spectrum of adsorption concerning safety and protection issues.

Finally, due to the large pressure drop associated with small grain sizes, it is mandatory to shape adsorbents in millimeter-sized bodies, typically covering 4 x 8 - 8 x 12 mesh. Also, the performance shall be measured in terms of breakthrough time concerning bed volume and not bed mass, as the space in personal protective devices shall be minimized. Indeed, the certification norm (EN 14387) provides acceptance criteria of a minimum breakthrough time to be reached for a given bed volume. Hence, adsorbents with low density are strongly penalized. Grain and packing densities have to be considered when developing new adsorbents. In the case of activated carbons, fully implemented at the industrial level, it is really common to operate in granular or monolithic shapes, which depends on the carbon synthesis methods (rotary kilns, fluidized-bed, etc.) [30]. On the other hand, MOFs are usually tested in powder form at a lab scale for primary testing without considering higher VOC pressures and possible intergranular water condensation due to large pressure drops [31]. As far as the authors know, there are no studies concerning the effect of different body sizes on the adsorptive properties of MOFs,

despite densification processes by tableting, which allow the shaping of grains and bodies with different sizes [32, 33].

This work seeks to study the cyclohexane adsorption performance using the well-known HKUST-1 MOF as an adsorbent. Unlike previous works, experimental dynamic adsorption is carried out in a fixed-bed column filled with HKUST-1 at different particle sizes and under different water relative humidity levels. The breakthrough adsorption profiles are discussed in terms of adsorption properties and column configuration, and compared with a reference activated carbon material. All this experimentation under different scenarios allows to know if the material considered is suitable for the adsorption process.

## 2. Materials and methods

### 2.1. Materials

HKUST-1 synthesized by spray-drying process at demonstration scale was provided by MOFapps (Norway). PICACTIF TA 60 is a commercially available activated carbon, provided by SP-Defense, Honeywell. PICACTIF TA 60 was used with a particle size between 300-600 µm, whereas pristine HKUST-1 (20 µm) was initially pressed by a hydraulic press at 6000 ton/m², obtaining circular tablets of 13 mm. These tablets were crushed in a mortar and subsequently sieved to two different particle sizes: 300-600 µm and 1-1.18 mm, without the use of any binder. Both materials were used without any chemical modification and kept in air tight vessels. Cyclohexane (99.5% purity) was purchased from Sigma Aldrich. From now, in order to facilitate the reading of the text, the following notation shall be used: M1, M2, M3 and C1, respectively for pristine HKUST-1, 300-600 µm HKUST-1, 1-1.18 mm HKUST-1 and 300-600 µm PICACTIF TA 60.

### 2.2. Materials characterization

The specific surface area and pore volume of the materials were estimated by manometric (volumetric) adsorption isotherms, using nitrogen at 77 K in a BELSORP MAX II surface area and porosity analyzer (MICROTRAC BEL). Activated carbon was desorbed at 573 K, while HKUST 1 was degassed at 393 K in a vacuum ramp (BELPREP, MICROTRAC BEL). The specific surface area was estimated using the Brunauer-Emmett-Teller (BET) model. Cyclohexane ($C_6H_{12}$) and water ($H_2O$) adsorption isotherms were carried out with the same instrument in vapor configuration at 293K.

Furthermore, the porosity of HKUST-1 particles was measured by mercury (Hg) intrusion in an Autopore IV 9500 equipment (Micromeritics), whereas the morphology and the shape of the particles were studied by scanning electron microscopy (SEM) imaging in a Hitachi S4800 electronic microscope.

### 2.3. Adsorption equipment and procedure

Fixed-bed adsorption measurements were carried out in an apparatus described in Figure S1. The adsorbent was loaded in a glass-tube of 0.4 cm of internal diameter (ID) and gently tapped to get a 1 cm bed length. Adsorption took place at 293 K thanks to a thermostated bath (JULABO). The VOC feed (5000 ± 250 ppm cyclohexane in nitrogen) was generated with a commercial diluter LiqMix (ALYTECH). Nitrogen flow crossing a glass bubbler, controlled in temperature, was used to prepare the wet feed. Concentrations of $C_6H_{12}$ and $H_2O$ were quantified by FT-IR online analysis (spectrometer IS10 and gas cell ThermoFisher). The water concentration was as well measured by an on-line hygrometer (MICHELL). Before the adsorption experiment, $C_6H_{12}$ and $H_2O$ flows were systematically checked by FT-IR bypassing the column, while the adsorbent bed is flushed under a dry $N_2$ flow. After an adsorption experiment, the material was regenerated under a $N_2$ flow (50 ml/min) at 393 K, controlled by an electric furnace, for 2 h.

## 3. Results and discussion

### 3.1. Materials' characterization

According to the methodology section, sizes of 20 µm (M1), 300-600 µm (M2) and 1-1.18 mm (M3) were used for HKUST-1, and 300-600 µm (C1) for PICACTIF TA 60. Table 1 summarizes the morphological characterization results. The largest BET specific surface area corresponds to M1, the same as the total pore volume, showing a decrease of around 22% after mechanical pressurization (6000 ton/m²) and sieving. Nitrogen adsorption isotherms are presented in the supplementary information (Figure S2). The mechanical pressurization increases density both for M2 and M3 shaped particles by a factor of 3.2. On the other hand, a loss of surface area and total pore volume are observed due to tableting pressure, which is in line with previous results [34]. In fact, M2 and M3 are in the same surface area range, with a variation of 7%, considering that, in case of large specific surface areas, the particle size is not very influential.

Table 1. Porous properties of HKUST-1 of different particle sizes and PICACTIF activated carbon.

| Materials | Surface Area ($m^2/g$) | Tapped density[a] ($g/cm^3$) | Pore volume[b] ($cm^3/g$) | $C_6H_{12}$ capacity[c] (mmol/g) |
|---|---|---|---|---|
| M1 | 1546 | 0.17 | 0.68 | 4.44 |
| M2 | 1217 | 0.55 | 0.53 | 3.69 |
| M3 | 1313 | 0.55 | 0.56 | 4.31 |
| C1 | 1128 | 0.49 | 0.47 | 2.95 |

[a]Column density of a filled 4mm ID tube
[b]Measured by nitrogen adsorption at $P/P_0$ = 0.98 (77 K)
[c]Measured by cyclohexane adsorption isotherms at 293 K and 5000 ppm (0.51 kPa)

This decrease of porosity after pressurization has a minor impact on the cyclohexane capacity (5-15%) at low cyclohexane partial pressures (5000 ppm). Surprisingly, whereas the specific surface area of C1 is almost in the same range as M2 and M3, it is observed that the adsorption capacity of cyclohexane at low partial pressures is significantly lower than for shaped HKUST-1 samples (-30%).

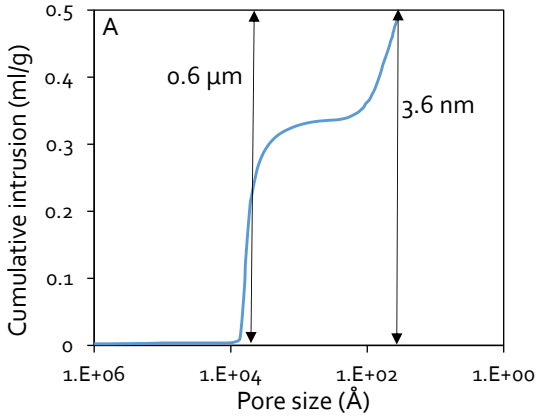


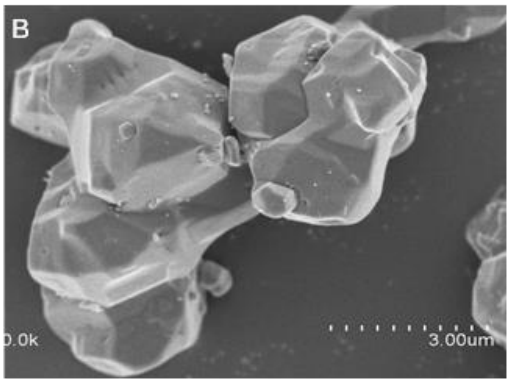


Figure 1. HKUST-1 inter-granular porosity profile calculation obtained by mercury porosimetry (A). SEM image of M1 particles (B).

The porosity of HKUST-1 after mechanical compression, crushing and sieving was analysed by mercury intrusion. The pore size analysis indicates a very distinct intrusion at 0.6 µm, which corresponds around 32% of all the mercury introduced, corresponding to the macropores fraction (Figure 1A). This macroporosity result is consistent with the packing of HKUST-1, which consists of crystalline aggregates of a few micrometers large, as observed in SEM imaging (Figure 1B). The packing of MOF particles generates inter-particle macropores of around 0.6 µm. The measured mesoporous volume may possibly arise from interfaces of particle aggregates.

Figure 2 shows the packing of the adsorbents in a column of 4 mm inner diameter for different particles sizes. The figure highlights differences in bed packing and consequently in bed porosity of the different materials, especially between (M1: A) and the other size fractions (M2: B, M3: C and C1: D). On the other hand, (B) and (D) show certain similarity since both materials, M2 and C1, are sieved at 300-600 µm.

Concerning the cyclohexane adsorption capacity, the values presented in Table 1 were obtained from cyclohexane adsorption isotherms at 293 K and 5000 ppm, 0.51 kPa (Figure 3). In order to simplify the graphical comparison, the cyclohexane adsorption isotherms for M1 and M3 are presented in the supplementary information (Figure S3). The M2 cyclohexane adsorption capacity is higher than the corresponding to the C1. More surprisingly, we can observe step-type adsorption profiles at low pressure for M2 and C1 (Figure 3B). The pressure at which the adsorption step is observed is significantly lower for M2 (0.0025 kPa) than for C1 (0.01 kPa). The same trend is followed in case of M1 and M3.

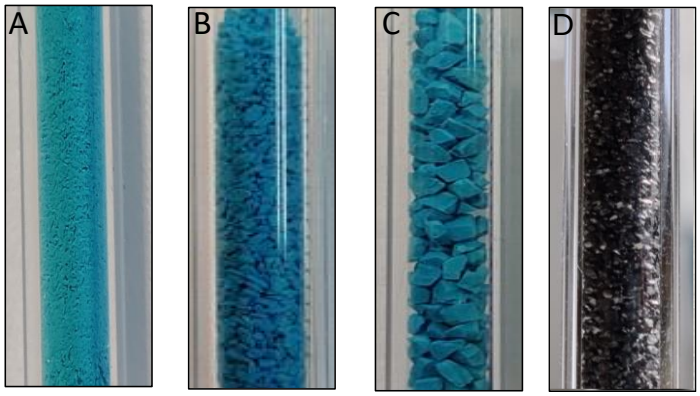


Figure 2. Packing of fixed beds in 4 mm ID reactors according to particle sizes. M1 (A), M2 (B), M3 (C) and C1 (D).

Figure 4 shows water adsorption isotherms for the considered materials M2 and C1. Isotherms of M1 and M3 are presented in the supplementary information (Figure S4). M2 exhibits a IV-type isotherm (IUPAC classification) while C1 presents a V-type isotherm. A wide hysteresis cycle is observed for the two materials, with a flatter segment in the middle zone of the isotherm in the case of M2.

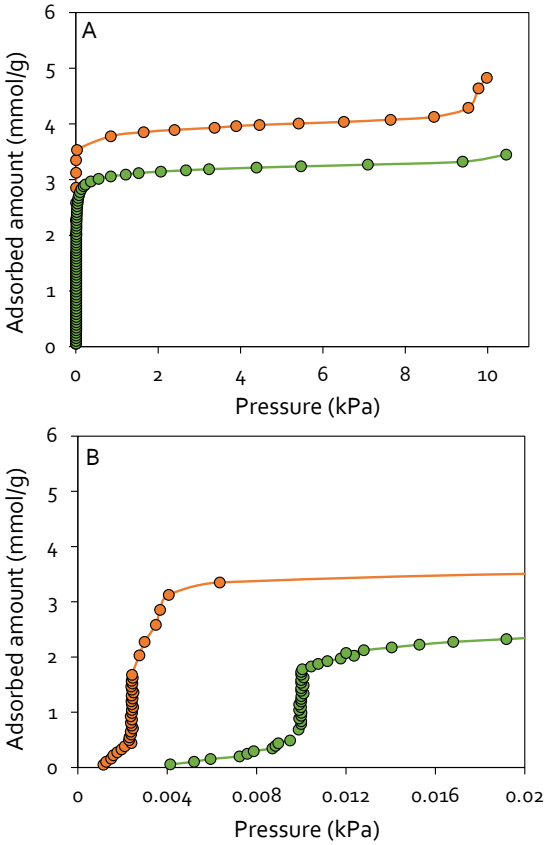


Figure 3. Cyclohexane adsorption isotherms (293 K) for M2 (orange) and C1 (green). Figure B is an enlargement of Figure A at low pressures.

Adsorption capacity at saturation pressure is vastly higher for water (35 and 18 mmol/g) in both cases than for cyclohexane (5 and 3.2 mmol/g), respectively for M2 and C1. As in the previous case, the same trend is followed by M1 and M3.

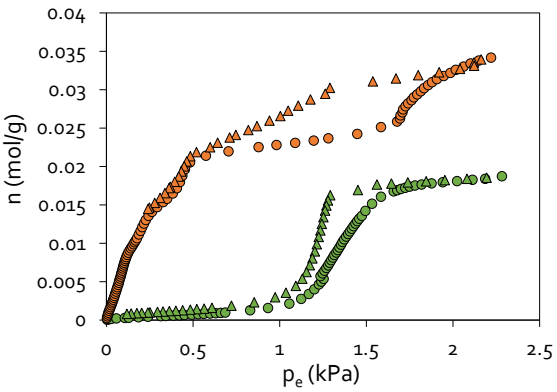


Figure 4. Water adsorption isotherms (293 K) for M2 (orange) and C1 (green). Circles and triangles point out adsorption and desorption stages, respectively.

### 3.2. Breakthrough experiments

Breakthrough measurements were carried out under three different scenarios, keeping constant the total nitrogen flow (50 ml/min), the cyclohexane concentration (5000 ppm) and the adsorption temperature (293 K). The relative humidity (RH) was varied between 0, 27 and 80%. The experiments were carried out with the same fixed-bed volume (0.125 $cm^3$). Obviously, the columns are filled with different weight loadings for the same bed volume because of the different obtained tapped density (Table 1). Therefore, for sake of easier visualization, breakthrough curves are presented normalized by unit of mass (min/g), while tabulated capacities at breakthrough time are also reported per unit of bed volume. It is established as a criterion to consider the breakthrough point at the time $C/C_0$ = 0.1 is reached, named as $T_{10}$ in the following. Such $T_{10}$ values are typical for comparing adsorbent performances in protective filtrations.

3.2.1. Dry condition

Figure 5 shows the breakthrough curves under a flow of 5000 ppm of cyclohexane in dry nitrogen. All the materials, except M3, show similar mass-normalized breakthrough times at $T_{10}$, around 200 min/g. In addition, it is observed that C1 shows the steepest breakthrough curve, reaching a complete saturation of the material in less time. The adsorption capacities obtained from the integration of the adsorption breakthrough curves are presented in Table S1 and compared with the capacities obtained by the cyclohexane isotherms. The pressure drops registered were 0.052, 0.009 and 0.009 bar for M1, M2 and M3, respectively, and 0.01 bar for C1. As expected, higher pressure drop is observed for the powder fraction.

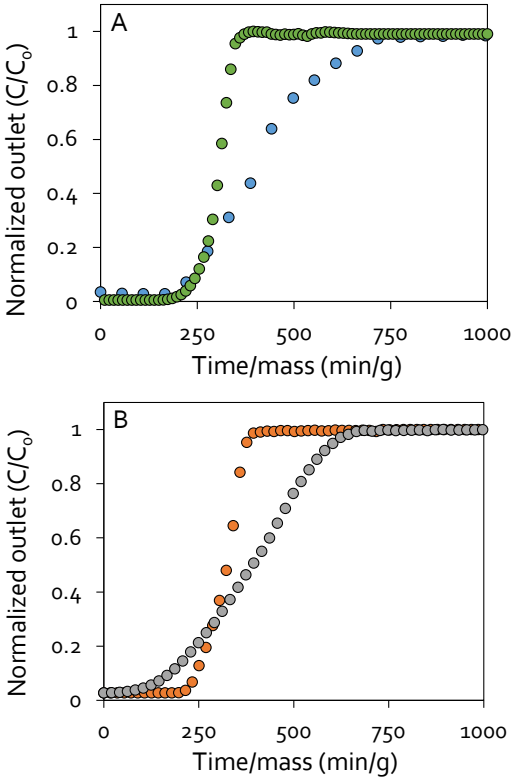


Figure 5. Cyclohexane (5000 ppm) breakthrough curves for (A) M1 (blue) and C1(green) and (B) M2 (orange) and M3 (grey) at 293 K.

3.2.2. 27% RH conditions

Figure 6 shows the results obtained for the breakthrough experiments of 5000 ppm of cyclohexane in nitrogen with a 27% of RH, which corresponds to 6300 ppm of water. Both cyclohexane (circles) and water (triangles) breakthrough curves are presented. The cyclohexane breakthrough times on a mass basis are practically maintained for all the materials, and $C/C_0 = 1$ is reached in less than 500 min/g for all of them. Although similar breakthrough curves for cyclohexane adsorption are observed, water breakthrough profiles look very different between the MOF and the activated carbon. For HKUST-1, it is observed a roll-up ($C/C_0 > 1$) for cyclohexane breakthrough curves, while water is completely adsorbed on the material ($C/C_0 \sim 0$). On the contrary, the water breaks almost immediately for the activated carbon, and water roll-up occurs when $C_6H_{12}$ breaks.

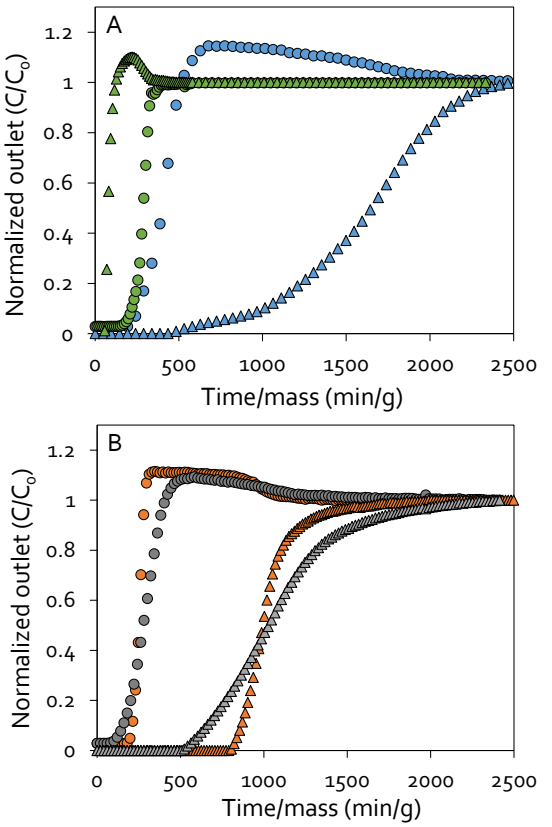


Figure 6. Cyclohexane (circles) and water (triangles) breakthrough curves for (A) M1 (blue) and C1 (green) and (B) M2 (orange) and M3 (grey) at 293 K and 0.1 MPa in presence of 27% of relative humidity and 5000 ppm of cyclohexane.

3.2.3. 80% RH conditions

Figure 7 shows the results obtained for the breakthrough experiments of 5000 ppm of cyclohexane in nitrogen with an 80% of RH, corresponding to 18700 ppm of water. Similar observations than for a 27% RH can be made with enlarged phenomena magnitude. A minor decrease in breakthrough time ($T_{10}$) is observed concerning cyclohexane breakthrough time for the MOF and the activated carbon. Nevertheless, this decrease is much more striking in case of water, with a major reduction in breakthrough time for all the materials, especially M2 and M3 fractions. In addition, the roll-up keeps the same shape, corresponding to water in the case of activated carbon and to cyclohexane in the case of

MOF, but reaching higher values of $C/C_0$ than in case of 27% RH for the cyclohexane, and maintained practically the same for water. Furthermore, the inclination of the curves is similar in all cases, unlike previous cases in which the activated carbon was steeper.

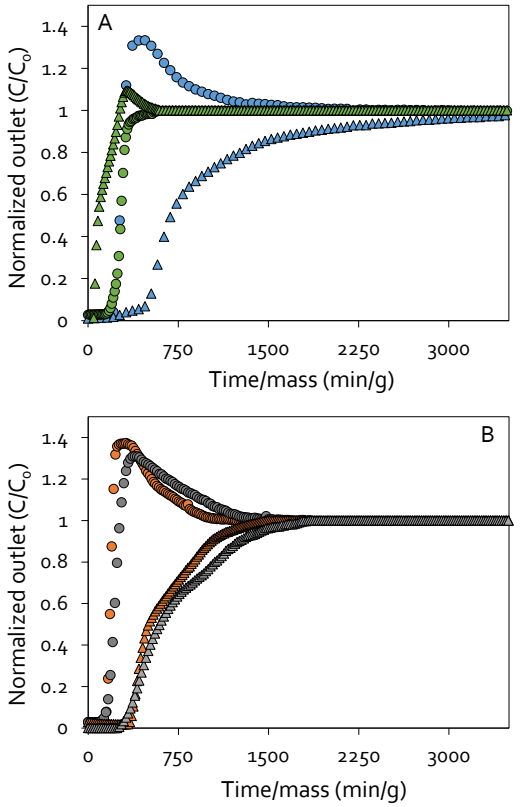


Figure 7. Cyclohexane (circles) and water (triangles) breakthrough curves for (A) M1 (blue) and C1 (green) and (B) M2 (orange) and M3 (grey) at 293 K and 0.1 MPa in presence of 80% of relative humidity and 5000 ppm of cyclohexane.

### 3.2.4. HKUST-1 breakthrough time vs. activated carbon benchmark

In addition to the direct comparison of the breakthrough graphs, it is possible to obtain useful data about the performance of the materials in different scenarios. The breakthrough curves can reveal the effective operating time on two basis, mass (min/g) and volume ($min/cm^3$). The breakthrough time taken is the correspondent to T10, which corresponds with a limit of 500 ppm of cyclohexane at the outlet of the column. A comparison of the different materials is attached in Figure 8. The breakthrough time on a mass basis is favorable for M1, M2 and C1, whereas M2 also stands out in the case of volume basis together with C1.

Another important parameter in the adsorption performance is the stability or recyclability of the adsorbent materials. In order to estimate it, the same experiments have been carried out three consecutive times on the same MOF material, with an intermediate desorption period of 2 h at 393 K with only nitrogen flow (50 ml/min).

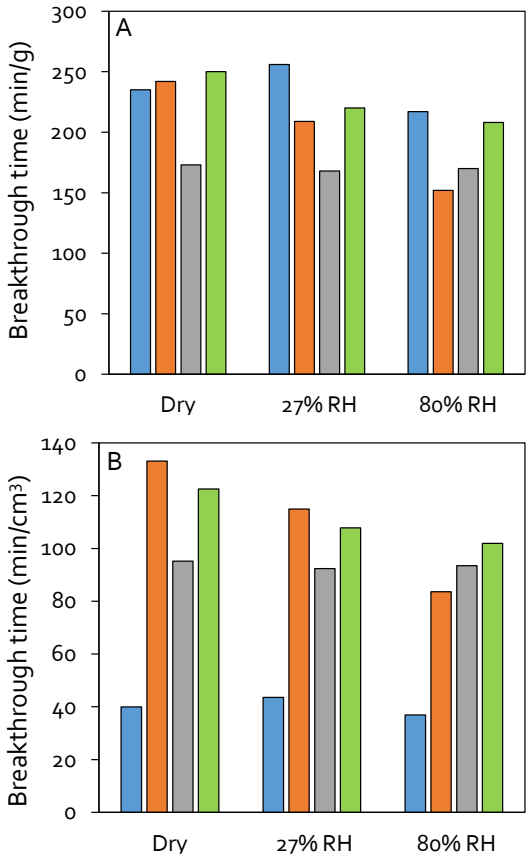


Figure 8. Cyclohexane breakthrough time at T10 for all the materials studied on mass (A) and volume (B) basis. Blue, M1; orange, M2; grey, M3 and green, C1.

The results of three consecutive cycles are shown in Figure 9. From the results, the normalized breakthrough time (min/g) for an identical bed volume can be compared. Figure 9 shows that all the different fractions of HKUST-1 resist during three consecutive cycles, regardless of the water content.

### 3.3. Discussion of the results

According to the literature, a large reduction in specific surface area and total pore volume is observed when pressurizing HKUST-1 at high pressures [35]. Therefore, relatively low pressures (6000 ton/$m^2$) were applied in this work, enough to compact the material without micropore structure collapsing, as it was checked by characterization (Table 1). Figure S2 shows that porous structure of HKUST-1 is preserved, with very similar nitrogen physisorption curves, regardless of the pressurization strength applied and the subsequent sieving. It should be noted that very large losses of

morphological properties were registered at higher pressures applied [32]. The same work [32] demonstrates that, at low mechanical pressures applied (~ 55 MPa), the crystallinity losses are small, around 20%, and with a slight effect on adsorption capacity.

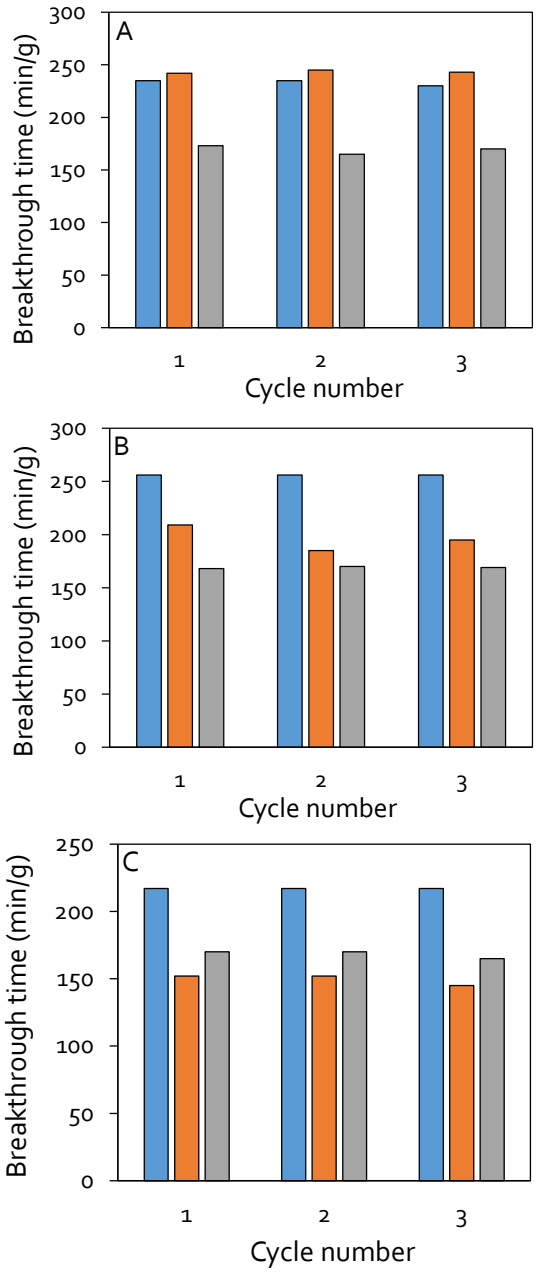


Figure 9. Normalized breakthrough time (min/g) at T10 after 3 consecutive cycles for HKUST-1 of different particle sizes (blue, M1; orange, M2 and grey, M3) in the fixed bed. A is for dry experiments, B is for 27% RH and C for 80% RH with 5000 ppm of cyclohexane.

However, there are also large differences in literature results depending on the origin or synthesis route of the pressed HKUST-1 [36]. In addition to these properties, Table 1 shows that the pressurization does not greatly affect the cyclohexane adsorption capacity at low partial pressures (5000 ppm, 0.51 kPa) and 293 K. The adsorption capacity of the MOF stays larger than PICACTIF for all the fractions. This fact is striking since other works show large drops in the adsorption capacity after a mechanical pressurization of HKUST-1 [37, 38]. In addition, the HKUST-1 studied could compete with other materials specifically selected for cyclohexane adsorption, such as the COFs presented by Moroni et al. [39], with registered capacities around 6.5 mmol/g for pure cyclohexane. At low partial pressures (0.51 kPa), HKUST-1 also outperforms many of the several MOFs presented by Jansen et al. [40].

Cyclohexane adsorption isotherms feature two steps for HKUST-1 (Figure 2). The first step takes place at low partial pressures, filling the microporous volume, which in this case remains conserved after pressurization, even for the rest of the particle sizes (Figure S2). Van Assche et al. [26] observed the same phenomenon for other linear and cyclic alkanes. According to the same authors, this pressure step profile can be assigned to the small pore window of 5-7 Å, connected with larger cavities of 11-12 Å in diameter. The kinetic diameter of cyclohexane, 6 Å, is of similar size to the pore window. This type of adsorption profile has already been observed in zeolites, whose porous structures also possess large cavities that are accessible through a window of diameter close to or even smaller than the kinetic diameter of the adsorbate. Very surprisingly, a similar step adsorption profile is observed for the PICACTIF TA 60, whose majority of micropores are ranging between 5-12 Å, according to Zou et al. [41]. To the best of our knowledge, it is the first time that such step adsorption phenomena has been observed, very likely because previous studies did not pay attention to adsorption capacity at 10-100 ppm concentration levels. The phenomena at the origin of this surprising adsorption profile is beyond the scope of this paper. Nevertheless, and interestingly enough, the adsorption step occurs at lower pressure in HKUST-1 than in the activated carbon PICACTIF TA 60. The MOF is much more effective in cyclohexane adsorption at very low partial pressures, which can be very useful at low concentrations of the pollutant. HKUST-1 also shows greater effectiveness at low partial pressures of cyclohexane than the zeolites presented by Slawek et al. [42], which have studied adsorption at low pressures by simulation.

HKUST-1 adsorbs water from lower partial pressures than PICACTIF. The water molecule is small (2.6 Å) [43], and strong forces related to the copper open metal sites (OMS), available on the

MOF structure, play an important role. Multiple works describe the water vapor adsorption on this MOF, sometimes even considering it as a harmful adsorbate to the structure due to the possibility of breaking structural bonds by hydrolysis [44]. In this way, notable differences in the water vapor adsorption enthalpy between both materials are observed, being 76 and 39 kJ/mol, respectively for HKUST-1 [45] and PICACTIF [46]. The adsorption on the OMS corresponds to the first part of the water vapor adsorption isotherm (Figure 3), followed by a flat zone, corresponding to the formation of water clusters filling the HKUST-1 cages, and the last zone, the adsorption on pores and the outer space of the crystals [47]. It corresponds to a type IV isotherm. Despite the presence of OMS, with high affinity to water, the diffusion of cyclohexane is mainly controlled by intracrystalline diffusion [48, 49]. On the other hand, in the case of PICACTIF, it shows a type V isotherm. It presents scarce adsorption capacity at reduced partial pressures, characteristic of a hydrophobic surface, followed by a steep uptake, corresponding to a microporous structure [50], also with enough particle size to the apparition of hysteresis. Therefore, it is observed the opposite water vapor adsorption mechanism between both materials, which affects the corresponding breakthrough curves.

Under dry conditions (Figure 5), both PICACTIF and HKUST-1 present different profile of breakthrough curve, with a steeper one in the case of the activated carbon, related either to the lower adsorption capacity, the easier accessibility through the pores or the size of the particles considered. The breakthrough time at $T_{10}$ in mass basis (min/g) is similar for all the materials, being lower in the case of M3, with higher diffusional effects, related to the channeling effect due to the much larger visible bed porosity and the relative short bed with respect to M3 grain size. Other phenomena are observed when incorporating water vapor at the inlet stream at two different partial pressures, 27 and 80% RH. The cyclohexane breakthrough curves in the case of HKUST-1 were modified in shape, towards a steeper one, similar to the PICACTIF case. In addition, part of the cyclohexane adsorbed is displaced out of the adsorbent due to the water vapor adsorbing more strongly, causing the roll-up. The steeper cyclohexane breakthrough curve may be provoked by the occupation of the OMS by water molecules, while cyclohexane remains adsorbed in zones with easier accessibility, due to its null polarity. The opposite is observed in case of PICACTIF, since the water adsorbed is displaced by cyclohexane, which is more akin to the material at low partial pressures. Cyclohexane is adsorbed on the activated carbon at much lower pressures than water. In contrast, in the case of the MOF, the initial adsorption pressure is similar for both adsorbates, but with a much larger affinity and adsorption capabilities for water, especially near the OMS. Therefore, the cyclohexane roll-up in case of the MOF is higher. Despite the water presence, cyclohexane breakthrough times for all the materials remain large, with differences for dry condition. Several studies show that the water presence, always considered very harmful to HKUST-1 [51, 52], does not affect very much the adsorption capacity of non-polar compounds [53, 54]. As noted, both molecules preferentially occupy different areas of the adsorbent, with practically no interference between them.

The presence of water vapor opens the critical aspect of stability of the material, especially in the case of the MOF. According to the literature, and based on the features commented above, HKUST-1 is sensitive to the presence of water under certain conditions [55]. Following the results, it is stable for a quite good breakthrough time under the conditions presented in this work. This breakthrough time can be even compared with the activated carbon, which does not record problems about water presence in the literature [56]. In addition, the application of several consecutive cycles under the same conditions and with intermediate cleaning stages does not practically affect the performance of the material (Figure 9). These results are promising, especially considering the reusability results obtained by Zhang et al. [9] for cyclohexane adsorption in case of activated hydrochars.

On the other hand, the shaping effect is interesting when considering breakthrough time with respect to volume basis (min/cm$^3$). Fine powder cannot be used in actual applications because of the high pressure drop associated with small particle sizes and the low volume-based breakthrough time due to its original low density (Figure 8). The pressure drops associated with M1 under dry conditions (0.052 bar) are 5.6 times higher than the pressure drops associated with the M2 particles, and the volume-based breakthrough time at $T_{10}$ (39 min/cm$^3$) is 3.5 times lower than in case of the M2 particles. The shaping procedure (mechanical pressing and sieving) allows obtaining a taped density of 0.55 g/cm$^3$, similar to the activated carbon. These shaped materials demonstrate significant breakthrough time on a volume basis, especially the M2 fraction (Table S2). For example, an efficient exposition time of

60 min requires a volume of 1.53, 0.44, and 0.49 $cm^3$ of M1, M2, and C1, respectively. In addition, in the case of the M2 fraction, the breakthrough time on a mass basis is also comparable to the one obtained for M1 and C1, together with the adsorption capacity for $T_{10}$ of the cyclohexane breakthrough curve (Table S3). These results are adequate even in presence of water vapor, with relative humidity as high as 80%.

Finally, HKUST-1 also has the advantage that it is an adsorbent with proved performances in the adsorption of other contaminants, such as $H_2S$ and $NH_3$ [28, 29]. In contrast, activated carbons do not show good adsorption capacities for these contaminants, unless they are impregnated with metal salt solutions ($Zn^{2+}$, $Cu^{2+}$) [56, 57]. Thus, it allows the use of adsorbents with a wide spectral range of potentially harmful substances.

## 4. Conclusions

The renowned HKUST-1 is a performing adsorbent in the adsorption of VOCs and may complement of current filtration systems based on impregnated activated carbons. The conclusion has been reached from an analysis of fixed bed adsorption of cyclohexane, taken as reference VOC, with HKUST-1 and PICACTIF TA 60 as adsorbents. The analysis of adsorption isotherms shows that the MOF could be more efficient in cyclohexane adsorption at lower partial pressures than the activated carbon and other studied materials in literature. The densification of the HKUST-1, achieved after mechanical tableting, increases the adsorption performance per unit volume of adsorbent and limits the pressure drop, which is essential in the case of face mask filters. The tableted MOF exhibits a good resistance to several consecutive cycles of adsorption and desorption, even in the presence of water vapor, which is a really exciting milestone. It corresponds to the main finding, whereas the unstability of HKUST-1 is well established at high humid conditions, the kinetic of degradation has not been established so far. It is shown that the time usage of HKUST-1 as adsorbent for respiratory mask (single pass) is not affected by the degradation of the structure, which may occur on a longer time scale.

The authors believe that HKUST-1 is a valuable VOC adsorbent from air and could complement advantageously activated carbon based filtration systems. Nevertheless, the mechanical resistance is also one of the points to improve in the case of MOFs, since the appearance of attrition is common when assembling the beds or during the operation.

## Supporting information

Breakthrough set up diagram

Nitrogen, cyclohexane and water adsorption isotherms

Cyclohexane breakthrough time and adsorption capacity on two basis (mass and volume)

## Corresponding author

David Farrusseng

## Funding Sources

This study was carried out in the frame of the program MODYTICS (ANR-20-ASCT-0033-01).

## Acknowledgements

The authors thank the DGA and ANR.

David Ursueguía acknowledges the Spanish Ministry of Education for the PhD grant that supports his research (FPU2018-01448) and the funding for the stay in a foreign research centre.

David Ursueguía appreciates the hospitality of the members of the IRCELYON.

## Abbreviations

**VOCs**, volatile organic compounds; **MOFs**, metal-organic frameworks; **OMS**, open metal sites; **RH**, relative humidity; **ID**, internal diameter; **SEM**, scanning electron microscopy; **FT-IR**, Fourier transformed infrared; **$T_{10}$**, breakthrough time for $C/C_0$ = 0.1; **M1**, pristine HKUST-1; **M2**, 300-600 µm HKUST-1; **M3**, 1-1.18 mm HKUST-1; **C1**, 300-600 µm PICACTIF TA 60.

## References

[1] Khan, F.; Ghoshal, A. Removal of volatile organic compounds from polluted air. Journal of Loss Prevention in the Process Industries 2000, 13, 527-545.

[2] Anand, S.; Mehendale, H. Volatile organic compounds (VOC). Encyclopedia of Toxicology (Second Edition) 2005, 450-455.

[3] Yu, S.; Koh, E.; Kim, S.; Lee, S.; Lee, J.; Son, S.; Hwang, S. Integrated analysis of multi-omics data on epigenetic changes caused by combined exposure to environmental hazards. Environmental Toxicology 2021, 36, 1001-1010.

[4] He, Z.; Wang, X.; Ling, Z.; Zhao, J.; Guo, H.; Shao, M.; Wang, Z. Contributions of different anthropogenic volatile organic compound sources to ozone formation at a receptor site in the Pearl River Delta region and its policy implications. Atmospheric Chemistry and Physics 2019, 19, 8801-8816.

[5] Wang, H.; Guo, H.; Zhao, Y.; Dong, X.; Gong, M. Thermodynamic analysis of a petroleum volatile organic compounds (VOCs) condensation recovery system combined with mixed-refrigerant refrigeration. International Journal of Refrigeration 2020, 116, 23-35.

[6] Yang, Y.; Sun, C.; Lin, B.; Huang, Q. Surface modified and activated waste bone char for rapid and efficient VOCs adsorption. Chemosphere 2020, 256, 127054.

[7] Song, C.; Zhang, Z.; Li, R.; Lian, S.; Guo, H.; Jia, C.; Liu, Q. Optimization of membrane-cryogenic hybrid propane recovery process: From molecular to process simulation. Journal of Cleaner Production 2021, 321, 129049.

[8] Emparan, M.; Gonzalez, J.; Gonzalez, G.; Ceballos, S.; Canales, J.; Aguayo, I.; Muñiz, R. Dynamic adsorption separation of benzene/cyclohexane mixtures on micro-mesoporous silica SBA-2. Microporous and Mesoporous Materials 2020, 294, 109942.

[9] Zhang, X.; Xiang, W.; Wang, B.; Fang, J.; Zou, W.; He, F.; Li, Y.; Tsang, D.; Ok, Y.; Gao, B. Adsorption of acetone and cyclohexane onto $CO_2$ activated hydrochars. Chemosphere 2020, 245, 125664.

[10] Alshaheri, A.; Tahir, M.; Rahman, M.; Ravoof, T.; Saleh, T. Catalytic oxidation of cyclohexane using transition metal complexes of dithiocarbazate Schiff base. Chemical Engineering Journal 2017, 327, 423-430.

[11] Okrasa, M.; Hitz, J.; Nowak, A.; Brochocka, A.; Thelen, C.; Walczak, Z. Adsorption performance of activated-carbon-loaded nonwoven filters used in filtering facepiece respirators. Environmental Research and Public Health 2019, 16, 1973.

[12] Wood, G. Estimating service lives of organic vapor cartridges II: A single vapor at all humidities. Journal of Occupational and Environmental Hygiene 2010, 7, 472-492.

[13] Zhang, X.; Gao, B.; Fang, J.; Zou, W.; Dong, L.; Cao, C.; Zhang, J.; Li, Y.; Wang, H. Chemically activated hydrochars as an effective adsorbent for volatile organic compounds (VOCs). Chemosphere 2019, 218, 680-686.

[14] Valencia, A.; Muñiz, R.; Ceballos, S.; Rojas, C.; Bonilla, A.; Gonzalez, J.; Aguayo, I. Cyclohexane and benzene separation by Fixed-bed adsorption on activated carbons prepared from coconut shell. Environmental Technology and Innovation 2022, 25, 102076.

[15] Pré, P.; Delage, F.; Brasquet, C.; Cloirec, P. Quantitative structure-activity relationships for the prediction of VOCs adsorption and desorption energies onto activated carbon. Fuel Processing Technology 2002, 77-78, 345-351.

[16] Wang, S.; Huang, L.; Zhang, Y.; Li, L.; Lu, X. A mini-review on the modeling of volatile organic compound adsorption in activated carbons: Equilibrium, dynamics, and heat effects. Chinese Journal of Chemical Engineering 2021, 31, 153-163.

[17] Zhang, X.; Gao, B.; Creamer, A.; Cao, C.; Li, Y. Adsorption of VOCs onto engineered carbon materials: A review. Journal of Hazardous Materials 2017, 338, 102-123.

[18] Huang, S.; Chung, T.; Wu, H. Effects of molecular properties on adsorption of six-carbon VOCs by activated carbon in a fixed adsorber. ACS Omega 2021, 6, 5825-5835.

[19] Chen, T.; Fu, C.; Liu, Y.; Pan, F.; Wu, F.; You, Z.; Li, J. Adsorption of volatile organic compounds by mesoporous graphitized carbon: Enhanced organophilicity, humidity resistance, and mass transfer. Separation and Purification Technology 2021, 264, 118464.

[20] Do, D.; Do, H. A model for water adsorption in activated carbon. Carbon 2000, 38, 767-773.

[21] Severino, M.; Gkaniatsou, E.; Nouar, F.; Pinto, M.; Serre, C. MOFs industrialization: a complete assessment of production costs. Faraday Discussions 2021, 231, 326-341.

[22] Mukherjee, S.; Sensharma, D.; Qazvini, O.; Dutta, S.; Macreadie, L.; Ghosh, S.; Babarao, R. Advances in adsorptive separation of benzene and cyclohexane by metal-organic framework adsorbents. Coordination Chemistry Reviews 2021, 437, 213852.

[23] McKinstry, C.; Cussen, E.; Fletcher, A.; Patwardhan, S.; Sefcik, J. Scalable continuous production of high quality HKUST-1 via conventional and microwave heating. Chemical Engineering Journal 2017, 326, 570-577.

[24] Ma, F.; Liu, S.; Liang, D.; Ren, G.; Wei, F.; Chen, Y.; Su, Z. Adsorption of volatile organic compounds in porous metal-organic frameworks functionalized by polyoxometalates. Journal of Solid State Chemistry 2011, 184, 3034-3039.

[25] Saini, V.; Pires, J. Development of metal organic framework-199 immobilized zeolite foam for adsorption of common indoor VOCs. Journal of Environmental Sciences 2017, 55, 321-330.

[26] Van Assche, T.; Duerinck, T.; Gutiérrez, J.; Calero, S.; Baron, G.; Denayer, J. High adsorption capacities and two-step adsorption of polar adsorbates on copper-benzene-1,3,5-tricarboxylate metal-organic framework. The Journal of Physical Chemistry C 2013, 117, 18100-18111.

[27] Münch, A.; Mertens, F. The Lewis acidic and basic character of the internal HKUST-1 surface determined by inverse gas chromatography. CrystEngComm 2015, 17, 438-447.

[28] Shi, R.; Zhang, Z.; Fan, H.; Zhen, T.; Shangguan, J.; Mi, J. Cu-based metal-organic framework/activated carbon composites for sulfur compounds removal. Applied Surface Science 2017, 394, 394-402.

[29] Supronowicz, B.; Mavrandonakis, A.; Heine, T. Interaction of small gases with the unsaturated metal centers of the HKUST-1 metal organic framework. The Journal of Physical Chemistry C 2013, 117, 14570-14578.

[30] Henning, K.; Kienle, H. Activated carbon. Industrial Carbon and Graphite Materials, Volume I: Raw materials, production and applications 2021, 1.

[31] Anand, B.; Younis, S.; Szulejko, J.; Kim, K.; Zhang, W. The potential utility of HKUST-1 for adsorptive removal of benzene vapour from gaseous streams using a denuder versus a packed-bed adsorption system. Journal of Cleaner Production 2020, 275, 122359.

[32] Ursueguía, D.; Díaz, E.; Ordóñez, S. Densification-induced structure changes in Basolite MOFs: Effect on low-pressure $CH_4$ adsorption. Nanomaterials 2020, 10, 1089.

[33] Beurroies, I.; Boulhout, M.; Llewellyn, P.; Kuchta, B.; Férey, G.; Serre, C.; Denoyel, R. Using pressure to

provoke the structural transition of metal-organic frameworks. Angewandte Chamoe International Edition 2010, 49, 7526-7529.

[34] Dhainaut, J.; Avci-Camur, C.; Troyano, J.; Legrand, A.; Canivet, J.; Imaz, I.; Maspoch, D.; Reisch, H.; Farrusseng, D. Systematic study of the impact of MOF densification into tablets on textural and mechanical properties. CrystEngComm 2017, 19, 4211-4218.

[35] Fonseca, J.; Gong, T. Fabrication of metal-organic framework architectures with macroscopic size: A review. Coordination Chemistry Reviews 2022, 462, 214520.

[36] Terracina, A.; Todaro, M.; Mazaj, M.; Agnello, S.; Gelardi, F.; Buscarino, G. Unveiled the source of the structural instability of HKUST-1 powders upon mechanical compaction: Definition of a fully preserving tableting method. The Journal of Physical Chemistry C 2018, 123, 1730-1741.

[37] Domán, A.; Madarász, J.; Sáfrán, G.; Wang, Y.; Lászlo, K. Copper benzene-1,3,5-tricarboxylate (HKUST-1) – Graphene oxide pellets for methane adsorption. Microporous and Mesoporous Materials 2021, 316, 110948.

[38] Peng, Y.; Krungleviciute, V.; Eryazici, I.; Hupp, J.; Farha, O.; Yildirim, T. Methane storage in metal-organic frameworks: Current records, surprise findings, and challenges. Journal of American Chemical Society 2013, 135, 11887-11894.

[39] Moroni, M.; Roldán, E.; Vismara, R.; Galli, S.; Navarro, J. Impact of pore flexibility in imine-linked covalent organic frameworks on benzene and cyclohexane adsorption. ACS Applied Materials and Interfaces 2022, 14, 40890-40901.

[40] Jansen, C.; Assahub, N.; Spieb, A.; Liang, J.; Schmitz, A.; Xing, S.; Gökpinar, S.; Janiak, C. The complexity of comparative adsorption of C6 hydrocarbons (benzene, cyclohexane, n-hexane) at metal-organic frameworks. Nanomaterials 2022, 12, 3614.

[41] Zou, L.; Liu, H.; Gong, L. Cryogenic adsorption of nitrogen on activated carbon: Experiment and modeling. Cryogenics 2018, 90, 20-29.

[42] Slawek, A.; Grybowska, K.; Vicent-Luna, J.; Makowski, W.; Calero, S. Adsorption of cyclohexane in pure silica zeolites: High-throughput computational screening validated by experimental data. ChemPhysChem 2018, 19, 3364-3371.

[43] Borjigin, T.; Sun, F.; Zhang, J.; Cai, K.; Ren, H.; Zhu, G. A microporous metal-organic framework with high stability for GC separation of alcohols from water. Chemical Communications 2012, 48, 7613-7615.

[44] Canivet, J.; Fateeva, A.; Guo, Y.; Coasne, B.; Farrusseng, D. Water adsorption in MOFs: fundamentals and applications. Chemical Society Reviews 2014, 43, 5594-5617.

[45] Xue, W.; Zhang, Z.; Huang, H.; Zhong, C.; Mei, D. Theoretical insights into the initial hydrolytic breakdown of HKUST-1. The Journal of Physical Chemistry C 2020, 124, 1991-2001.

[46] Baudu, M.; Cloirec, P.; Martin, G. First approach of desorption energies of water and organic molecules onto activated carbon by differential scanning calorimetry studies. Water Research 1993, 27, 69-76.

[47] Al-Janabi, N.; Hill, P.; Torrente, L.; Garforth, A.; Gorgojo, P.; Siperstein, F.; Fan, X. Mapping the Cu-BTC metal-organic framework (HKUST-1) stability envelope in the presence of water vapour for CO2 adsorption from flue gases. Chemical Engineering Journal 2015, 281, 669-677.

[48] Heinke, L.; Gu, Z.; Wöll, C. The surface barrier phenomenon at the loading of metal-organic frameworks. Nature Communications 2014, 5, 4562.

[49] Mukherjee, S.; Manna, B.; Desai, A.; Yin, Y.; Krishna, R.; Babarao, R.; Ghosh, S. Harnessing Lewis acidic open metal sites of metal-organic frameworks: the foremost route to achieve highly selective benzene sorption over cyclohexane. Chemical Communications 2016, 52, 8215-8218.

[50] Liu, L.; Tan, S.; Horikawa, T.; Do, D.; Nicholson, D.; Liu, J. Water adsorption on carbon – A review. Advances in Colloid and Interface Science 2017, 250, 64-78.

[51] Zhao, Z.; Wang, S.; Yang, Y.; Li, X.; Li, J.; Li, Z. Competitive adsorption and selectivity of benzene and water vapor on the microporous metal organic frameworks (HKUST-1). Chemical Engineering Journal 2015, 259, 79-89.

[52] Sudan, S.; Gladysiak, A.; Valizadeh, B.; Lee, J.; Stylianou, K. Sustainable capture of aromatic volatile organic compounds by a pyrene-based metal-organic framework under humid conditions. Inorganic Chemistry 2020, 59, 9029-9036.

[53] Chevalier, V.; Martin, J.; Peralta, D.; Roussey, A.; Tardif, F. Performance of HKUST- 1 metal-organic framework for a VOCs mixture adsorption at realistic concentrations ranging from 0.5 to 2.5 ppmv under different humidity conditions. Journal of Environmental Chemical Engineering 2019, 7, 103131.

[54] Jia, L.; Shi, J.; Long, C.; Lian, F.; Xing, B. VOCs adsorption on activated carbon with initial water vapour contents: adsorption mechanism and modified characteristic curves. Science of The Total Environment 2020, 731, 139184.

[55] Li, Z.; Wang, L.; Qin, L.; Lai, C.; Wang, Z.; Zhou, M.; Xiao, L.; Liu, S.; Zhang, M. Recent advances in the application of water-stable metal-organic frameworks: Adsorption and photocatalytic reduction of heavy metal in water. Chemosphere 2021, 285, 131432.

[56] Boutillara, Y.; Tombeur, J.; Weireld, G.; Lodewyckx, P. In-situ copper impregnation by chemical activation with CuCl2 and its application to $SO_2$ and $H_2S$ capture by activated carbons. Chemical Engineering Journal 2019, 372, 631-637.

[57] Subrenat, A.; Leuch, L.; Cloirec, P. Electrodeposition of copper and iron oxides on to activated carbon fibre cloths: Application to H2S and $NH_3$ removal from air. Environmental Technology 2008, 29, 993-1000.

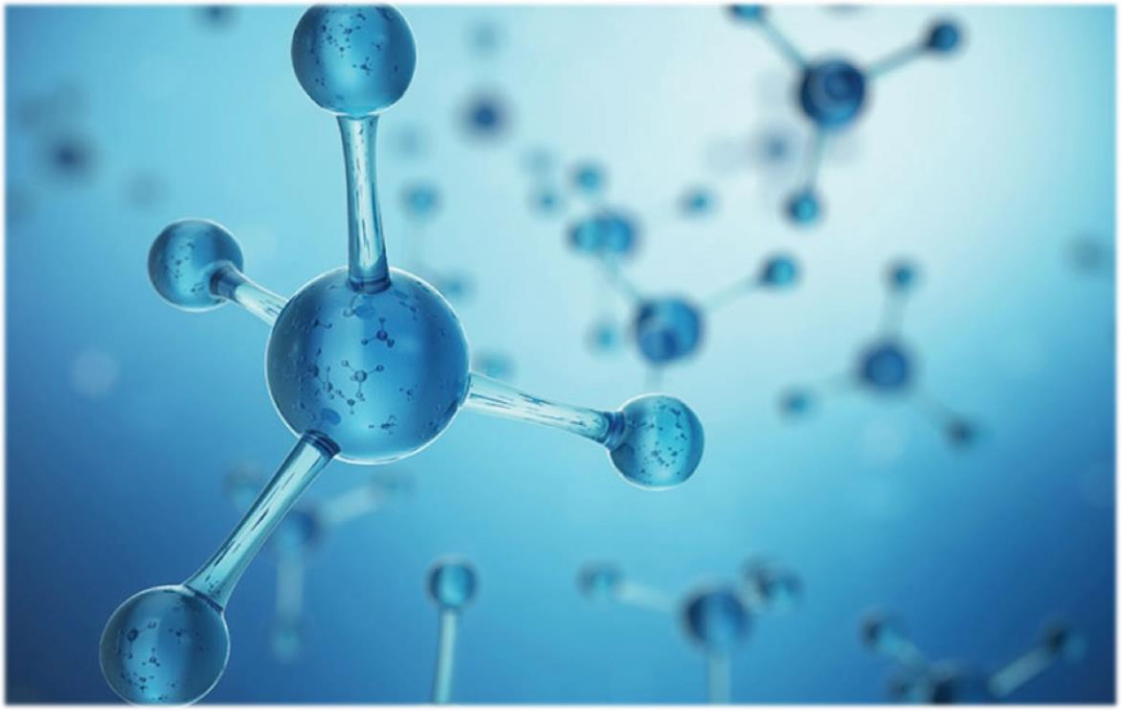

# 5. CONCLUSIONES

El objetivo principal de esta Tesis Doctoral consistía en la recuperación y concentración del metano procedente de las emisiones de ventilación de la minería subterránea de carbón. De esta forma, se evita la emisión atmosférica de un potente gas de efecto invernadero, así como se posibilita un posterior aprovechamiento energético de la corriente. Las principales conclusiones de cada capítulo desarrollado en la sección *Discusión de Resultados* se detallan a continuación:

**Materiales adsorbentes: MOFs** *(Capítulo 4.1)*

Uno de los parámetros fundamentales en los procesos de adsorción es la selección del material adsorbente, del que dependerá gran parte del diseño posterior de la operación. Se buscarán materiales con adecuados valores de selectividad $CH_4/N_2$, cuya separación es la más complicada de llevar a cabo, debido a la similitud de ambas moléculas, tanto en tamaño molecular como en polaridad. Los carbones activos y zeolitas, típicamente utilizados, muestran bajos rendimientos en dicha separación, además de limitadas capacidades de adsorción de metano. Estos resultados abren la puerta a la utilización de *metal-organic frameworks* (MOFs), que registran buenos resultados en la separación y almacenamiento de gases. Estos materiales poseen propiedades morfológicas muy interesantes para la adsorción, como elevada superficie específica y volumen de poro, así como la posible presencia de open metal sites (OMS), muy afines a moléculas polares, como $H_2O$, o con

elevada polarizabilidad, como $CO_2$ o $CH_4$. Una revisión bibliográfica del comportamiento de estos materiales en procesos de almacenamiento y separación de metano muestra que, en condiciones de elevada presión, la superficie específica y el volumen de poro dominan el proceso. Por otro lado, en condiciones moderadas, se demuestra que la presencia de OMS y la densidad de átomos metálicos estructurales son los parámetros más determinantes. En consecuencia, ciertos MOFs diseñados específicamente para el proceso, con una combinación de fuerzas de Van der Waals (tamaño de poro) y Coulomb (centros metálicos activos), y un equilibrio entre la densidad de OMS y su fortaleza, muestran resultados muy prometedores para la separación de metano.

**Estudio de la adsorción de VAM sobre MOFs** *(Capítulo 4.2)*

Se seleccionan tres MOFs comerciales (Basolite C300, Basolite F300 y Basolite A100), lo que asegura reproducibilidad y disponibilidad a escala industrial. Basolite C300 y A100 muestran elevada cristalinidad y volumen de microporos, mientras que F300 es mesoporoso y amorfo. La densidad de OMS sigue el orden: C300 > F300 > A100. Las buenas propiedades morfológicas del Basolite C300, 1514 $m^2/g$ de superficie específica y 1.25 $cm^3/g$ de volumen de poros, aseguran una buena capacidad de adsorción de metano (52 mg/g). Además, la elevada entalpía de adsorción registrada sugiere una fuerte interacción $CH_4$-OMS, lo que se corresponde con una mayor selectividad $CH_4/N_2$ para el Basolite C300 (2.2), el material con la mayor densidad de OMS disponibles. El estudio de las isotermas de adsorción, con un buen ajuste a los modelos de Freundlich y Sips, confirma la importancia de la heterogeneidad superficial.

Sin embargo, los materiales comerciales muestran severas deficiencias al trabajar en condiciones similares a las reales: elevadas caídas de presión en lecho fijo y sensibilidad estructural a la presencia de humedad. En lo relativo a la caída de presión, se plantea un incremento del tamaño de partícula mediante un pelletizado por presurización mecánica. El mejor MOF en la adsorción, Basolite C300, también muestra ser el más afectado por la presurización, con la pérdida de gran parte de su cristalinidad, propiedades porosas y capacidad de adsorción, especialmente a partir de 111.8 MPa. Por

otro lado, los Basolite A100 y F300 registran menores pérdidas, debido principalmente a su flexibilidad estructural y a su naturaleza amorfa y mesoporosa, respectivamente. Sin embargo, el Basolite C300 continúa registrando los mejores resultados de adsorción tras la compresión, debido a la gran influencia de los OMS.

En lo relativo a la presencia de humedad, el agua, con un gran momento dipolar, influye negativamente en el proceso de adsorción, ya que se ve muy atraída por los OMS, bloqueándolos para la adsorción de metano. En consecuencia, el Basolite C300 es el material más afectado a elevadas humedades relativas (75-100% HR), impidiendo la adsorción de metano y modificando la morfología del material, pudiendo llegar a hidrolizar y destruir la estructura. Por otro lado, el Basolite F300, con menor influencia de los OMS, no se ve tan afectado por la presencia de agua. En el caso del $CO_2$, también presente a nivel de trazas (0.1%) en el VAM, éste muestra un efecto despreciable sobre los materiales estudiados.

**Modelización y paso de escala del proceso de adsorción** *(Capítulo 4.3)*

La multiplicidad de condiciones ensayadas permite la elaboración de un modelo matemático diferencial que describa el proceso de adsorción. La solución del modelo matemático, heterogéneo y unidimensional, se ajusta ($R^2$>0.9) a los resultados experimentales obtenidos en lecho fijo bajo distintas condiciones, así como a datos experimentales obtenidos de la bibliografía y a la etapa de desorción del proceso. El Basolite C300 se muestra como el material más adecuado para el proceso, ya que permite concentrar el metano en un 46.7% respecto de la alimentación. A partir del modelo validado, se han simulado procesos de adsorción mediante técnicas TSA y PSA para distintos materiales adsorbentes (carbonosos, zeolitas y MOFs). Los MOFs muestran los mejores resultados, ya que poseen un factor de concentración levemente inferior a los materiales carbonosos, pero retienen elevadas cantidades de metano y muestran un gran rendimiento de recuperación, especialmente en el caso de poseer OMS. En cuanto a la técnica, TSA muestra mejores resultados en el caso de MOFs y materiales carbonosos, además de menor coste que PSA en todos los casos. Por tanto, la mejor combinación estudiada consiste en MOFs y TSA. Sin embargo, un

balance económico muestra que el coste de los MOFs es demasiado elevado, lo que constituye un factor determinante a la hora de su implantación a escala real.

Resultados similares se han obtenido en el caso de la simulación de una operación de adsorción TSA a escala real (4.4 $Nm^3/s$, 0.57% $CH_4$), con Basolite C300 como adsorbente, combinada en serie con una turbina de gas pobre. Tras la optimización, con lechos fijos de 2.5 x 10 m, dos en serie en adsorción y uno en paralelo en desorción, se obtiene un incremento de 52.5% en la concentración, y un caudal de salida de 3.8 $Nm^3/s$. La corriente de salida se introduce en la turbina, con una ratio de presión óptimo de 2.4, y permite la generación neta de 490 kW, además de alimentar en su totalidad la etapa de desorción del proceso TSA. Sin embargo, y en concordancia con resultados anteriores, el elevado coste de los MOFs imposibilita el paso de escala real del proceso, anulando completamente la rentabilidad.

**Síntesis de materiales adsorbentes** *(Capítulo 4.4)*

Se busca una síntesis de materiales adsorbentes para solventar los problemas principales observados en una operación a escala real: elevado coste del material adsorbente, elevada caída de presión en lecho fijo, y descenso de la capacidad en condiciones de humedad. Se han sintetizado materiales compuestos entre un MOF (HKUST-1, homólogo al Basolite C300) y un material mesoporoso inorgánico ($Al_2O_3$). Los procedimientos de síntesis son sencillos y de bajo coste (solvotermal y *dip-coating*), así como los materiales utilizados. Los materiales compuestos poseen elevado tamaño de partícula (355-710 μm), evitando grandes caídas de presión. En el caso de elevadas cargas de MOF (> 18%), los materiales siguen la misma tendencia que el MOF original, elevadas pérdidas de rendimiento en presencia de humedad. Sin embargo, bajas cargas de MOF (< 9%) registran incluso un incremento (38%) de la capacidad de adsorción de metano en presencia de humedad, más importante cuanto más heterogénea sea la distribución superficial, obtenida por *dip-coating*. Además, la formación de materiales compuestos mejora la estabilidad térmica del MOF, evitando la descomposición del ligando orgánico a elevadas temperaturas. Los resultados

plantean la posibilidad de utilizar los MOFs a escala industrial en forma de materiales compuestos.

**Otros usos de MOFs** *(Capítulo 4.5)*

Se ha estudiado el rendimiento del MOF HKUST-1 en un proceso de adsorción de ciclohexano en lecho fijo bajo distintas condiciones de humedad y varios tamaños de partícula. HKUST-1 es más efectivo en la adsorción de ciclohexano a bajas presiones parciales que el ampliamente utilizado PICACTIF TA 60. Además, la densificación de las partículas (300-600 μm) mejora en gran medida la capacidad de adsorción por volumen de adsorbente, y muestra también cierta resistencia a ciclos consecutivos, incluso en presencia de agua. La cinética de degradación en entornos húmedos es lenta, por lo que ciclos rápidos de adsorción y desorción se muestran muy favorables. Los resultados son prometedores, indicando que el MOF podrá sustituir y complementar a los carbones activos comúnmente utilizados en estos procesos.

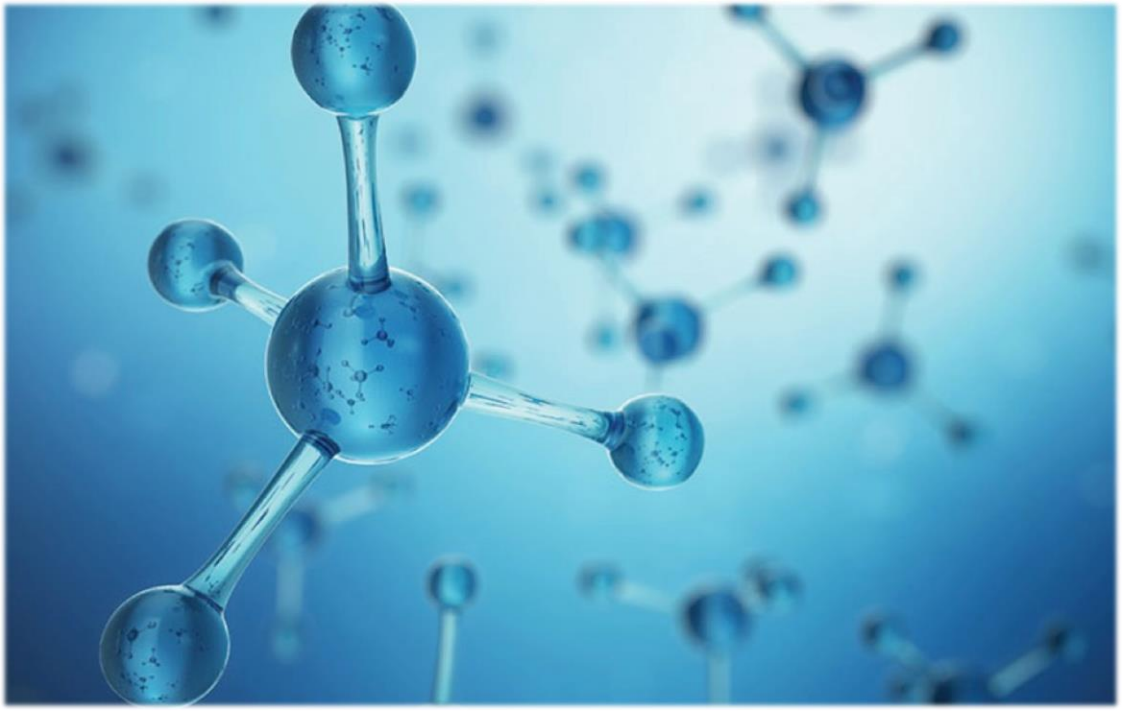

# 6. CONCLUSIONS

The main objective of this PhD Thesis was the lean-methane recovery and concentration from ventilation emissions from underground coal mining. In this way, the emission of a powerful greenhouse gas is avoided, and it enables a subsequent energetic profit. The main conclusions of each chapter of the *Discussion of Results* section are detailed below:

**Adsorbent materials: MOFs** *(Chapter 4.1)*

One of the key parameters in adsorption processes is the selection of the adsorbent material, which influences all the subsequent operation design. Materials with adequate values of $CH_4/N_2$ selectivity are desired, since it is the most challenging separation, due to the similarity of molecules, both in molecular size and polarity. Activated carbons and zeolites, both adsorbent materials widely used, show low yields in the separation, in addition to limited methane adsorption capacities. These results open the possibility of using metal-organic frameworks (MOFs), which show good results in gas separation and storage. MOFs present interesting morphological properties for adsorption, such as elevated specific surface area and pore volume, add to the possible presence of open metal sites (OMS), which are preferential zones for both polar molecules, such $H_2O$, or with high polarizability, such as $CO_2$ and $CH_4$. A literature review shows that specific surface area and pore volume dominate the adsorption process at high pressure conditions. On the other hand, OMS presence and structural metallic ions density are the most

determining parameters under mild conditions. Therefore, certain MOFs specifically designed for the process, with a specific combination of Van der Waals (pore size) and Coulomb (open metal sites) forces, add to an equilibrium between OMS density and force, show very promising results for methane separation.

**Study of VAM adsorption on MOFs** *(Chapter 4.2)*

Three commercial MOFs were selected (Basolite C300, Basolite F300 and Basolite A100), which ensures reproducibility, as well as availability at industrial scale. Basolite C300 and A100 show high crystallinity and micropore volume, whereas F300 is mesoporous and amorphous. The OMS density follow the order: C300 > F300 > A100. The good morphological properties of Basolite C300, 1514 $m^2/g$ of specific surface area and 1.25 $cm^3/g$ of total pore volume, achieves good methane adsorption capacity (52 mg/g). Further, the large adsorption enthalpy registered suggests a strong $CH_4$-OMS interaction, which corresponds with higher $CH_4/N_2$ selectivity for Basolite C300 (2.2), material with the highest OMS density. The study of adsorption isotherms, with good adjustment to Freundlich and Sips models, confirms the importance of the surface heterogeneity.

However, commercial MOFs show large deficiencies when working under actual conditions: high pressure drop in fixed-bed and structural sensitivity to humidity. Concerning pressure drop, it is raised an increment of particle size through pelletization by mechanical pressure. The best MOF in adsorption, Basolite C300, is also the most affected by pressurization, registering the loss of most of its crystallinity, porous properties and adsorption capacity, especially from 111.8 MPa. On the other hand, Basolite A100 and F300 show lower losses, due to structural flexibility and the amorphous and mesoporous structure, respectively. However, Basolite C300 continues to show the best adsorption results after compression, due to the large influence of OMS.

Regarding humid conditions, the large dipole moment of water influences negatively the adsorption process, since it is very attracted by OMS, blocking them for methane adsorption. Therefore, Basolite C300 is the most affected material at elevated relative humidity (75-100% RH), hindering

the methane adsorption and modifying the morphological properties of the material, even hydrolysing the structure. On the other hand, Basolite F300, with lower OMS influence, it is not so affected by water presence. In the case of $CO_2$, also present at trace level (0.1%) in VAM, it shows a negligible effect on the studied materials.

**Modellization and scale-up of the adsorption process** *(Chapter 4.3)*

Multiplicity of adsorption conditions tested allow to elaborate a differential mathematical model that describes the adsorption process. The solution of the model, heterogeneous and unidimensional, is well-adjusted ($R^2$>0.9) to the experimental results obtained in fixed-bed under different conditions, as well as to experimental data from bibliography and to the desorption stage of the process. Basolite C300 is shown as the most adequate material for the process, since it concentrates methane 46.7% respect to the feed. From the validated model, adsorption processes by TSA and PSA techniques for different adsorbents (carbonaceous, zeolites and MOFs) were simulated. MOFs show the best results, since they present a concentration factor slightly lower than carbonaceous materials, but high methane retentions and a large recuperation yield, especially in case of having OMS. Concerning the technique, TSA shows better results in case of MOFs and carbonaceous materials, further to a lower cost than PSA in all cases. Therefore, the best combination is MOFs and TSA. However, an economic balance shows that MOFs cost is too high, which constitutes a determining factor in large-scale implementation.

Similar results were obtained in the simulation of a TSA adsorption process at actual scale (4.4 $Nm^3/s$ and 0.57% $CH_4$), with Basolite C300 as adsorbent, combined in series with a lean-gas turbine. After optimization, with fixed-beds of 2.5 x 10 m, two in series in adsorption and one in parallel in desorption, it is obtained an increase of 52.5% in concentration, with a flowrate of 3.8 $Nm^3/s$. The output stream is introduced in the turbine, with an optimum pressure ratio of 2.4, which generates 490 kW, add to feed completely the desorption stage of TSA. However, according to previous results, the high cost of MOFs hinders a scale-up, nullifying profitability.

**Adsorbent materials synthesis** *(Chapter 4.4)*

Adsorbent materials synthesis is intended to solve the main problems raised in a large-scale operation: high cost of adsorbent material, high pressure drop in fixed-bed and capacity decrease under humid conditions. Composite materials between a MOF (HKUST-1, homologous to Basolite C300) and a mesoporous inorganic material ($Al_2O_3$) were synthesized. Synthesis procedures are simple and low-cost (solvothermal and dip-coating), as are materials used. Composites show large particle size (355-710 μm), avoiding large pressure drop. In case of elevated MOF loads (> 18%), composites follow the same trend than HKUST-1: large yield losses under water presence. However, low MOF loads (< 9%) register even an adsorption capacity increase (38%) under humid conditions, more important the greater heterogeneous surface distribution, corresponding to dip-coating. Further, the composite formation improves the thermal stability of the MOF, thus avoiding organic ligand decomposition at high temperatures. Results raise the possibility of using MOFs at large scale in the shape of composites.

**Other uses of MOFs** *(Chapter 4.5)*

The yield of HKUST-1 in a cyclohexane adsorption process was studied under different humidity conditions and particle sizes. HKUST-1 is more effective in the cyclohexane adsorption at low partial pressures than the widely used PICACTIF TA 60. Further, the particles densification (300-600 μm) largely improves the adsorption capacity per adsorbent volume, showing also resistance to consecutive cycles, even in presence of water. Degradation kinetics in humid environments is slow, thus fast adsorption and desorption cycles are really favourable. Results are promising, pointing out that MOFs can substitute and complement activated carbons, usually used in these processes.

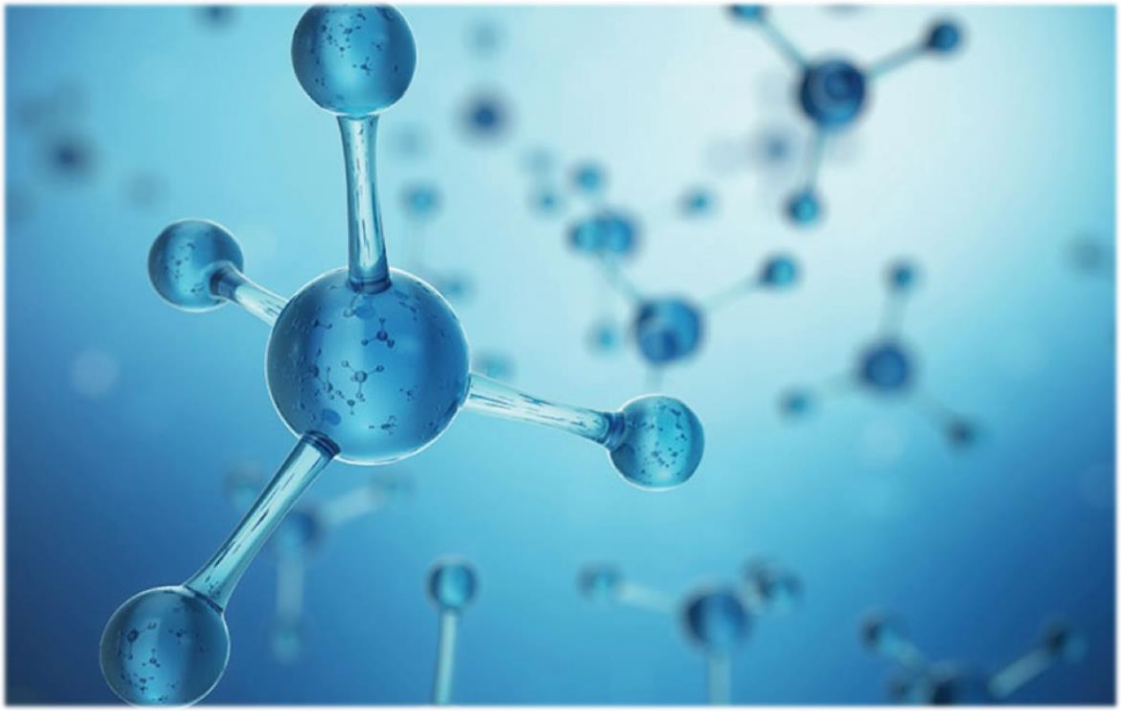

# 6. ANEXOS

# LISTA DE ABREVIATURAS

| | |
|---|---|
| ADC | Anthracene-9,10-dicarboxylate |
| AMM | Abandoned mine methane |
| BET | Brunanuer-Emmett-Teller |
| bdc | Benzene-1,4-dicarboxylate |
| BJH | Barret-Joyner-Halenda |
| BSE | Backscattered electron |
| BTC | Benzene-1,3,5-tricarboxylate |
| CBM | Coal bed methane |
| CEPCI | Chemical Engineering Plant Cost Index |
| CFC | Clorofluorocarbonos |
| CHP | Combined heat and power |
| CMM | Coal mine methane |
| CNT | Carbon nanotube |
| COF | Covalent Organic Framework |
| COP | Conferencia de las Partes |
| CUS | Coordinatively unsaturated sites |
| DE | Di-ethylene |
| DOE | Department of Energy |
| DRIFT | Diffuse reflectance infrared Fourier transform spectroscopy |
| DRX | Difracción de rayos X |
| DSC | Differential Scanning Calorimetry |
| DUT | Dresden University of Technology |
| EDL | The Energy Development Limited |
| EDX | Energía dispersiva de rayos X |
| EGA | Effluent gas analysis |
| EM | Electronic microscopy |
| EPA | Environmental Protection Agency |
| fcc | Face-centered cubic |

| | |
|---|---|
| FT-IR | Fourier transform infrared |
| FWF | Future worth factor |
| GCMC | Gran Canonical Monte Carlo |
| GHG | Greenhouse gas |
| GWP | Global warming potential |
| HR | Humedad relativa |
| HR-TEM | High-resolution transmission electron microscopy |
| ID | Internal diameter |
| IPCC | Intergovernmental Panel on Climate Change |
| IRMOF | Isoreticular metal-organic framework |
| IUPAC | International Union of Pure and Applied Chemistry |
| LDAR | Leak detection and repair |
| LDF | Linear driving force |
| lp | Large-pore phase |
| MAF | Metal-azolate framework |
| MCT/A | Mercury cadmium telluride analyzer |
| MFC | Mass flow controller |
| MIL | Materials Institute Lavoisier |
| MOF | Metal-organic framework |
| MS | Mass spectrometry |
| MTN | Mobil thirty-nine |
| MUMPS | Multifrontal massively parallel sparse direct solver |
| MWCNT | Microwave carbon nanotubes |
| NJU-Bai | Nanjing University Bai's Group |
| np | Narrow-pore phase |
| NPV | Net present value |
| NU | Northwestern University |
| OCDE | Organización para la Cooperación y el Desarrollo Económicos |
| OMS | Open metal sites |
| PCN | Porous coordination polymer |

| | |
|---|---|
| PDE | Partial differential equation |
| PNOPs | Porphyrin-based nanoporous organic polymers |
| PPN | Porous polymer network |
| PSA | Pressure-swing adsorption |
| PTFE | Politetrafluoroetileno |
| PXRD | Powder X-ray diffraction |
| RCO | Regenerative catalytic oxidation |
| SE | Secondary electrons |
| SEM | Scanning electron microscopy |
| SOC | Square-octahedral |
| STP | Standard temperature and pressure |
| TCD | Thermal conductivity detector |
| TE | Tri-ethylene |
| TGA | Thermal gravimetric analyzer |
| TPD | Temperature programmed desorption |
| TPO | Temperature programmed oxidation |
| TPR | Temperature programmed reduction |
| TSA | Temperature-swing adsorption |
| TVSA | Temperature and vacuum swing adsorption |
| UE | Unión Europea |
| UiO | Universitetet i Oslo |
| USD1 | Unparametrized supervised discretization |
| UTSA | University of Texas San Antonio |
| VAM | Ventilation air methane |
| VdW | Van der Waals |
| VOC | Volatile organic compound |
| VPSA | Vacuum and pressure swing adsorption |
| VSA | Vacuum swing adsorption |
| VTVSA | Vacuum and temperature swing adsorption |
| ZIF | Zeolitic imidazolate framework |

| | |
|---|---|
| ZJU | Zhejiang University |

## LISTA DE SÍMBOLOS

| | |
|---|---|
| $\alpha$ | Ángulo de celda (º, *visto en DRX*) |
| $\beta$ | Anchura pico característico (º, *visto en DRX*) |
| $\beta$ | Ángulo de celda (º, *visto en DRX*) |
| $\gamma$ | Ángulo de celda (º, *visto en DRX*) |
| $\gamma$ | Coeficiente de expansion adiabática |
| $\varepsilon_b$ | Porosidad del lecho |
| $\varepsilon_p$ | Porosidad de la partícula |
| $\rho_b$ | Densidad del lecho (kg/m$^3$) |
| $\rho_g$ | Densidad del gas (kg/m$^3$) |
| $\mu_g$ | Viscosidad del gas (Pa·s) |
| $\lambda$ | Longitud de onda (m) |
| $\theta$ | Fracción ocupada (*visto en modelo Hill-Deboer*) |
| $2\theta$ | Ángulo de Bragg (*visto en DRX*) |
| $\omega$ | Parámetro de interacción (*visto en modelo Fowler-Guggenheim*) |
| $\Delta Tln$ | Diferencia de temperatura media logarítmica (K) |
| $\Delta P$ | Caída de presión (Pa) |
| $\Delta H/RT$ | Término de Van't Hoff |
| | |
| A | Superficie de un cambiador de calor (m$^2$) |
| a | Constante de afinidad (*visto en modelo Sips*) |
| a | Parámetro de celda (*visto en DRX*) |
| $a_p$ | Ratio superficie-volumen (m$^{-2}$) |
| b | Constante del modelo de Temkin |
| b | Parámetro de celda (*visto en DRX*) |
| B | Beneficios anuales (€) |
| C | Costes capitales (€) |
| $C/C_0$ | Concentración del efluente |

| | |
|---|---|
| $C_i$ | Concentración componente i (mol/m$^3$) |
| C | Espesor de la capa límite (m) |
| c | Parámetro de celda (*visto en DRX*) |
| $C_b$ | Coste fijo de un tanque (€) |
| $C_p$ | Calor específico (J/mol·K) |
| $C_{ps}$ | Calor específico del sólido (J/mol·K) |
| $d_p$ | Diámetro de partícula (m) |
| $D_p$ | Diámetro de poro (m) |
| D | Diámetro de lecho (m) |
| $D_e$ | Dispersión axial (m$^2$/s) |
| $D_k$ | Coeficiente de difusión de Knudsen (m$^2$/s) |
| $D_m$ | Difusión molecular (m$^2$/s) |
| $D_i$ | Difusividad efectiva en microporos (m$^2$/s) |
| $D_p$ | Difusividad en macroporos (m$^2$/s) |
| E | Costes anuales (€) |
| $h_s$ | Coeficiente de transferencia de calor (W/m$^2$·K) |
| I | Ingresos anuales (€) |
| i | Tipo de descuento |
| K | Factor adimensional (*visto en ecuación de Scherrer*) |
| $k_f$ | Constante del modelo de pseudoprimer orden (s$^{-1}$) |
| $k_s$ | Constante del modelo de pseudosegundo orden (g/mg·s) |
| $K_{ads}$ | Constante de adsorción Langmuir (s$^{-1}$) |
| $k_{des}$ | Constante de desorción Langmuir (s$^{-1}$) |
| $K_H$ | Constante isoterma de Henry (l/g) |
| $K_1$ | Primera constante isoterma de Hill-Deboer (l/g) |
| $K_2$ | Segunda constante isoterma de Hill-Deboer (kJ/mol) |
| $K_{FG}$ | Constante isoterma de Fowler-Guggenheim (l/g) |
| $K_F$ | Constante isoterma de Freundlich (l/g) |
| $K_T$ | Constante isoterma de Temkin (l/g) |
| $K_{Li}$ | Constante isoterma de Langmuir (mg/g) |

| | |
|---|---|
| $k_f$ | Coeficiente de transferencia de masa en película (mol/s·m$^2$) |
| $K_L$ | Coeficiente global de transferencia de materia (mol/s·m$^2$) |
| $k_g$ | Conductividad térmica del gas (W/m·K) |
| $K_{L0}$ | Factor prexponencial de la ecuación de Arrhenius (mg/g) |
| L | Longitud de lecho (m) |
| m | Resistencia a la difusión del modelo de orden fraccional |
| $M_i$ | Peso molecular (g/mol) |
| n | Fuerza impulsora del modelo de orden fraccional |
| n | Intensidad de la adsorción del modelo de Freundlich |
| n | Constante de heterogeneidad del modelo de Sips |
| $\dot{n}$ | Flujo molar (mol/s) |
| Nu | Número adimensional de Nusselt |
| n | Tiempo de pago (year) |
| P | Presión real de $N_2$ en ensayos de fisisorción (Pa) |
| $P_0$ | Presión de saturación de $N_2$ en ensayos de fisisorción (Pa) |
| Pe | Número adimensional de Péclet |
| $P_1$ | Presión inicial (Pa) |
| $P_2$ | Presión final (Pa) |
| Pr | Número adimensional de Prandtl |
| $Q_{mi}$ | Máxima capacidad de la isoterma de Langmuir (mg/g) |
| $q_{ads}$ | Cantidad de $N_2$ adsorbida en la fisisorción de $N_2$ (cm$^3$/g) |
| $q_i$ | Metano adsorbido (mg/g) |
| $q_e$* | Concentración de equilibrio en la fase sólida (mol/kg) |
| $q_e$ | Concentración de adsorbato en equilibrio (mol/m$^3$) |
| Q | Energía requerida en un intercambiador de calor (W) |
| $r_c$ | Radio de cristalita (m) |
| R | Constante gases ideales (atm·L/K·mol) |
| $R^2$ | Coeficiente de correlación |
| $r_p$ | Radio de partícula (m) |
| S | Superficie externa de un tanque (m$^2$) |

| | |
|---|---|
| $t$ | Tiempo (s) |
| $T$ | Temperatura (K) |
| $T_2$-$T_1$ | Incremento de temperatura de intercambiador de calor (K) |
| $T_g$ | Temperatura del gas (K) |
| $T_s$ | Temperatura del sólido (K) |
| $TCI$ | Inversión de capital total (€) |
| $T_{10}$ | Tiempo de ruptura para $C/C_0 = 0.1$ |
| $u_0$ | Velocidad superficial (m/s) |
| $U$ | Coeficiente de transmisión de energía global ($W/m^2 \cdot K$) |
| $V_i$ | Volumen molecular ($m^3/mol$) |
| $V_1$ | Volumen inicial ($m^3$) |
| $V_2$ | Volumen final ($m^3$) |
| $W_c$ | Potencia de compresión (W) |
| $W_{ieq}$ | Equilibrio sólido-gas ($mol/m^3$) |
| $W$ | Potencia de turbina (W) |
| $X$ | Coste del material adsorbente (€/kg) |
| $Y_{CH4}$ | Fracción molar de metano |
| $z$ | Posición axial del lecho (m) |

## SUPPLEMENTARY INFORMATION

### EFFECT OF WATER AND CARBON DIOXIDE ON THE PERFORMANCE OF BASOLITE MOFs FOR METHANE ADSORPTION

(Supplementary Information)

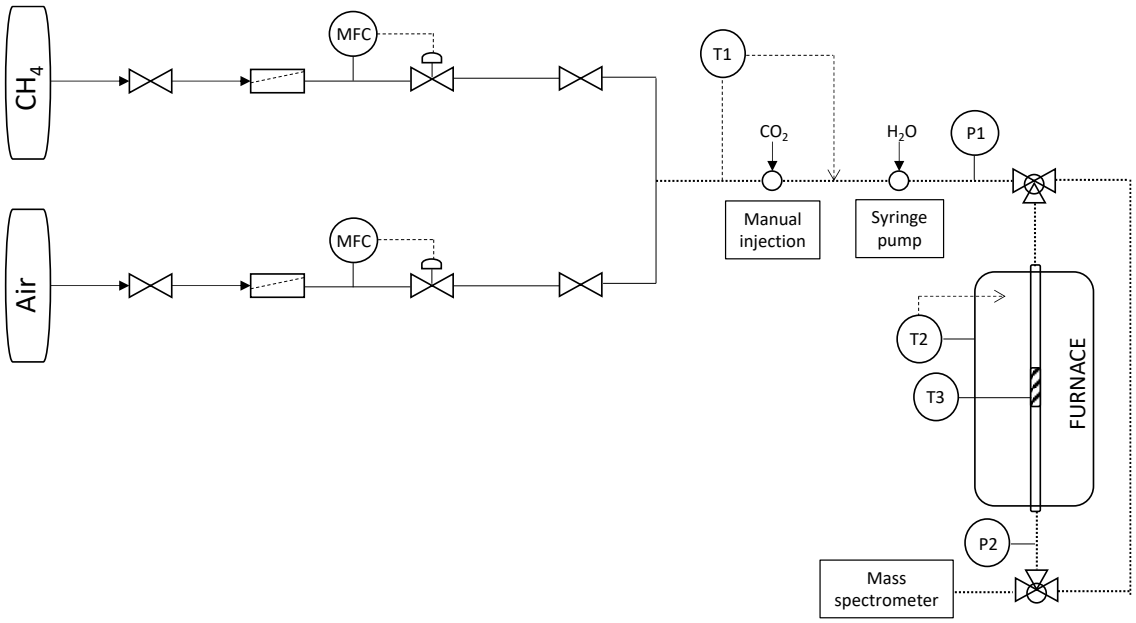


Figure S1. Fixed-bed device scheme. Dotted line points out the heated and isolated line. Discontinuous line indicates the electrical signals.

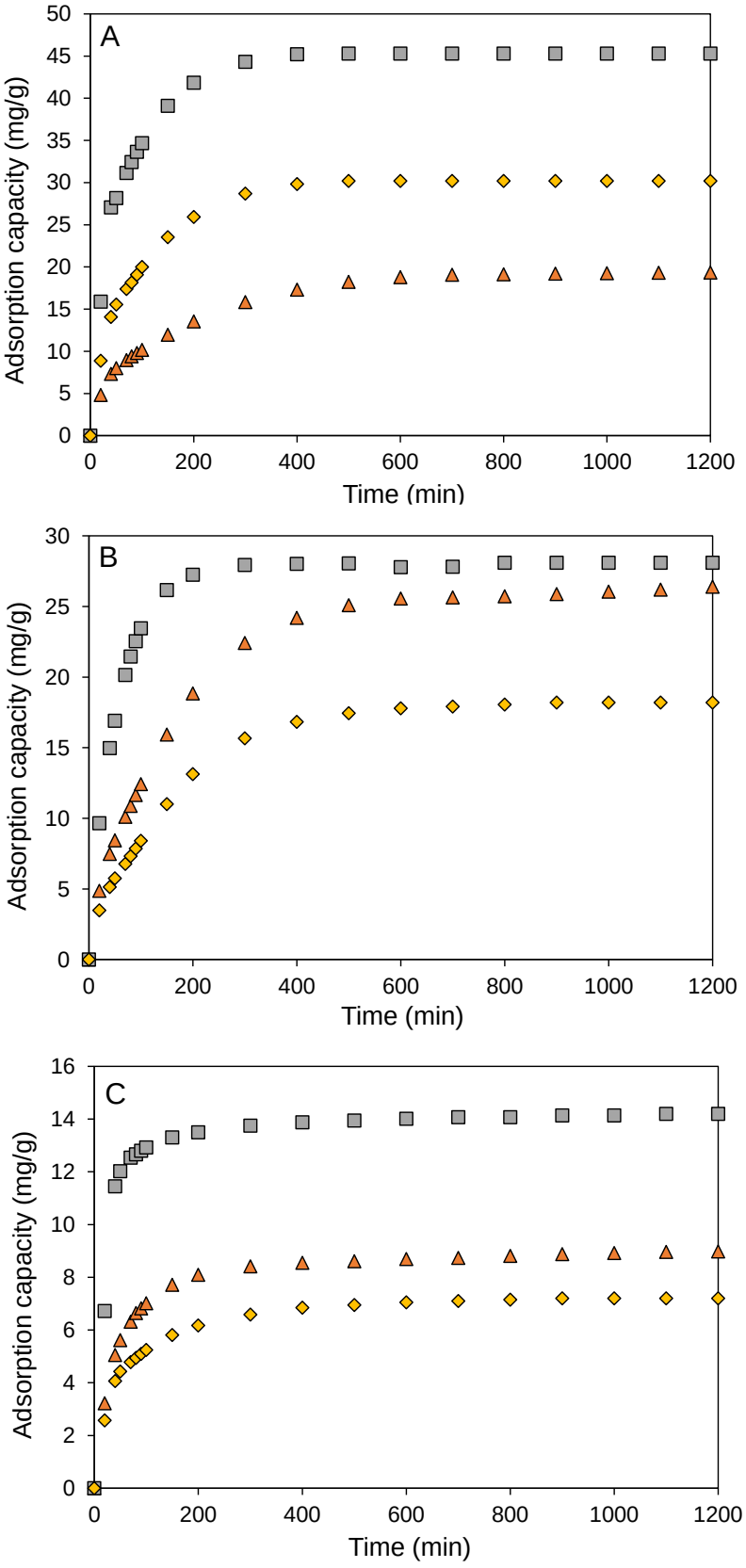


Figure S2. Adsorption of methane (grey squares), nitrogen (yellow rhombus) and oxygen (orange triangles) at 298 K on the three pristine materials, determined by thermobalance. Basolite C300 (A), Basolite F300 (B) and Basolite A100 (C).

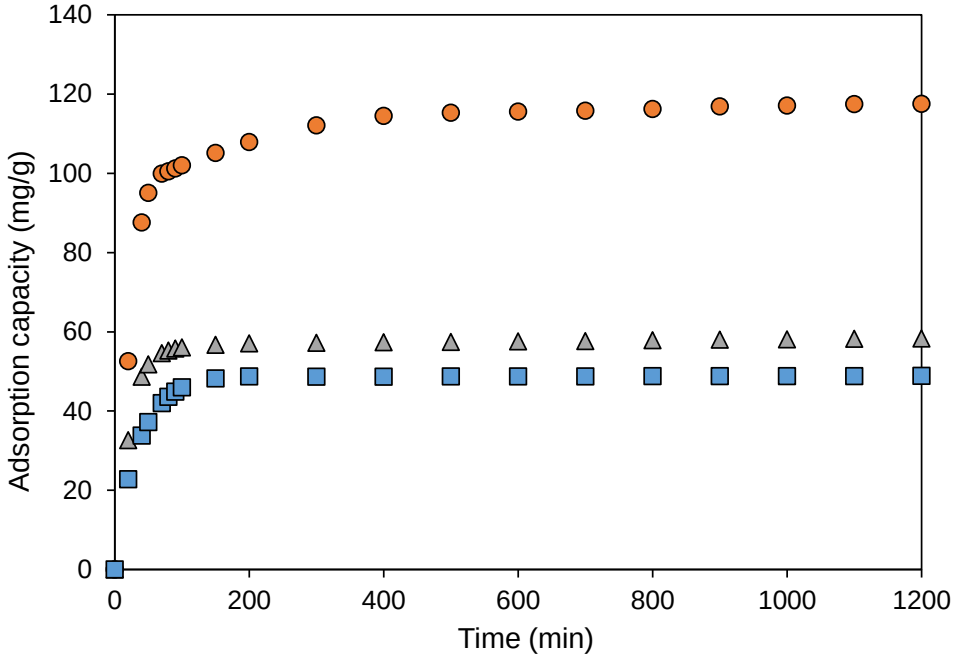


**Figure S3**. Adsorption of carbon dioxide at 298 K on the three pristine materials (orange circles: Basolite C300; grey triangles: Basolite A100; blue squares: Basolite F300), determined by thermobalance.

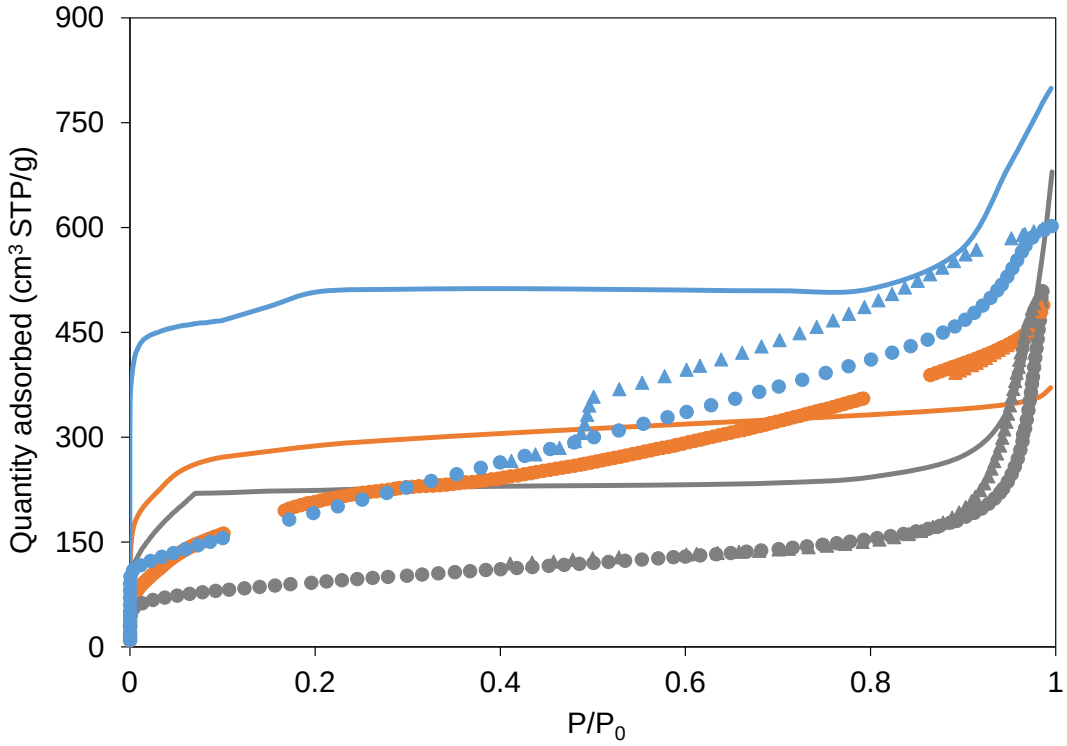


**Figure S4**. Nitrogen physisorption measurements at 77 K and comparison between pristine materials (solid line) and moist-treated materials (circles line for adsorption and triangles line for desorption). Basolite C300, blue; Basolite F300, orange and Basolite A100, grey.

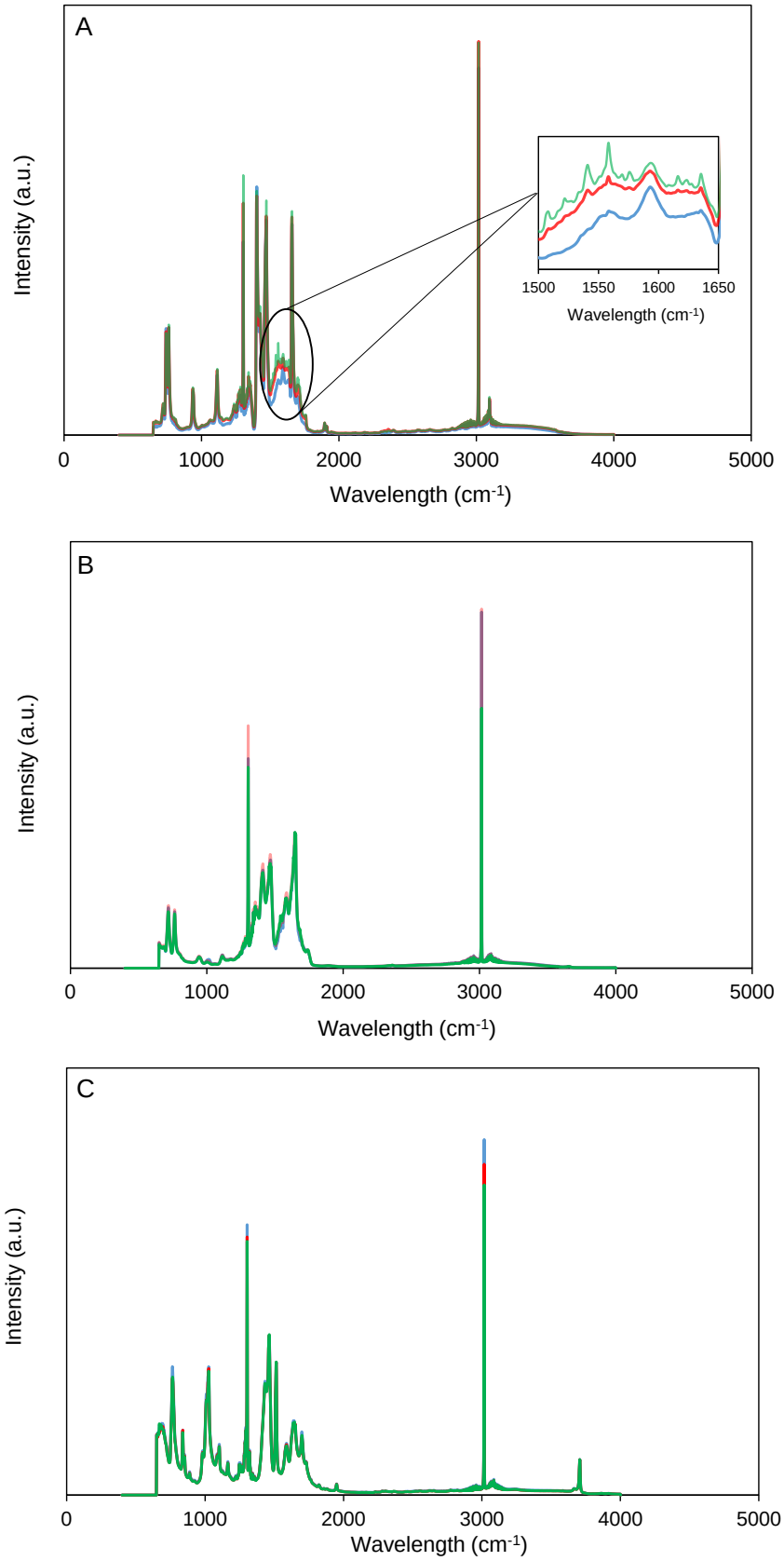


Figure S5. DRIFT patterns of the MOFs aged in presence of different gaseous mixtures adsorption (5% $CH_4$, 95% air, 298 K and 40 ml/min) (A: C300, B: F300, C: A100). 5% $CH_4$, 95% air, blue; 5% $CH_4$, 95% air, 75% RH, red; 5% $CH_4$, 95% air, 100% RH, green.

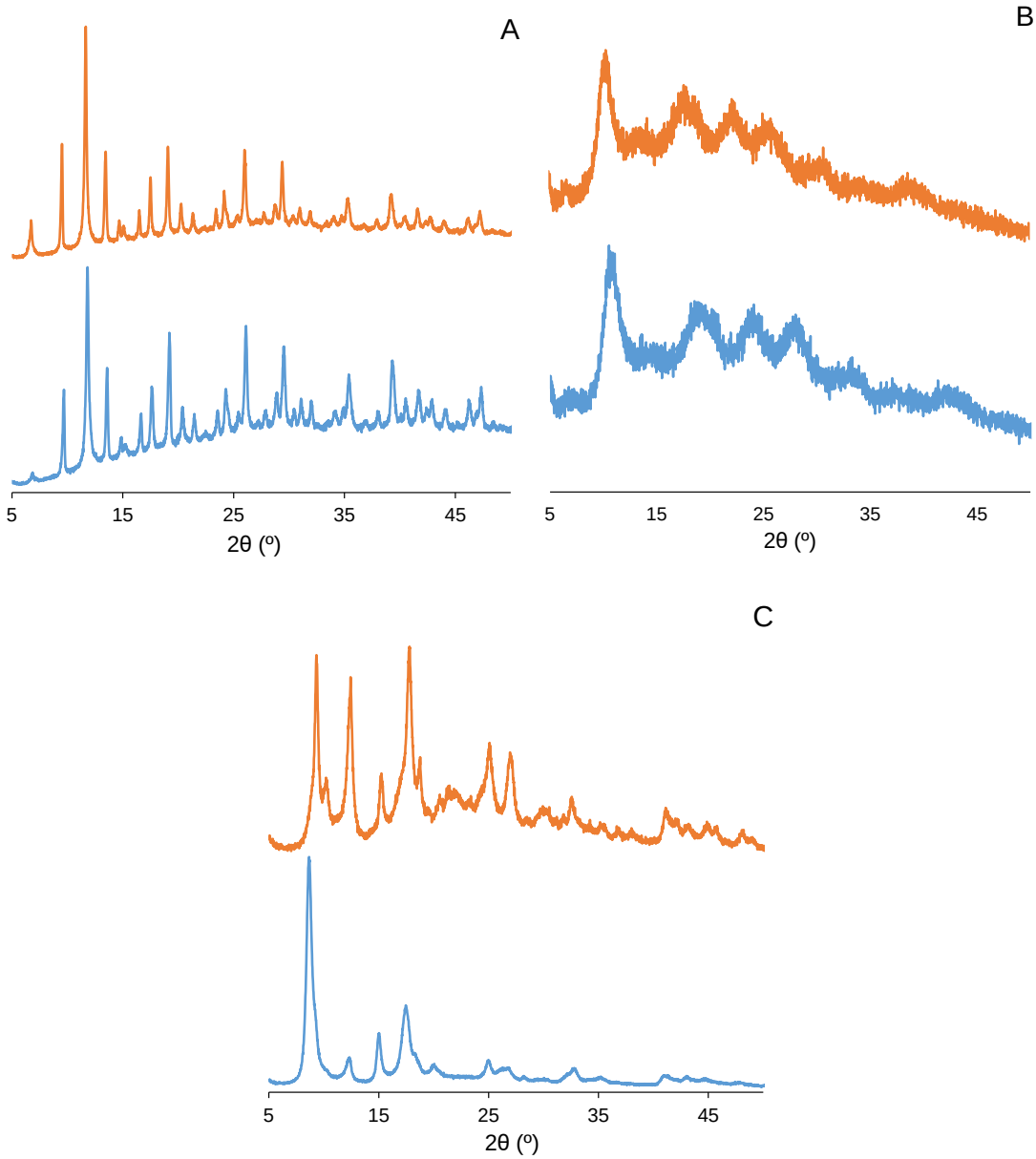


Figure S6. PXRD profiles of the three materials before (blue) and after (orange) water treatment (100% RH). Basolite C300 (A), Basolite F300 (B), Basolite A100 (C).

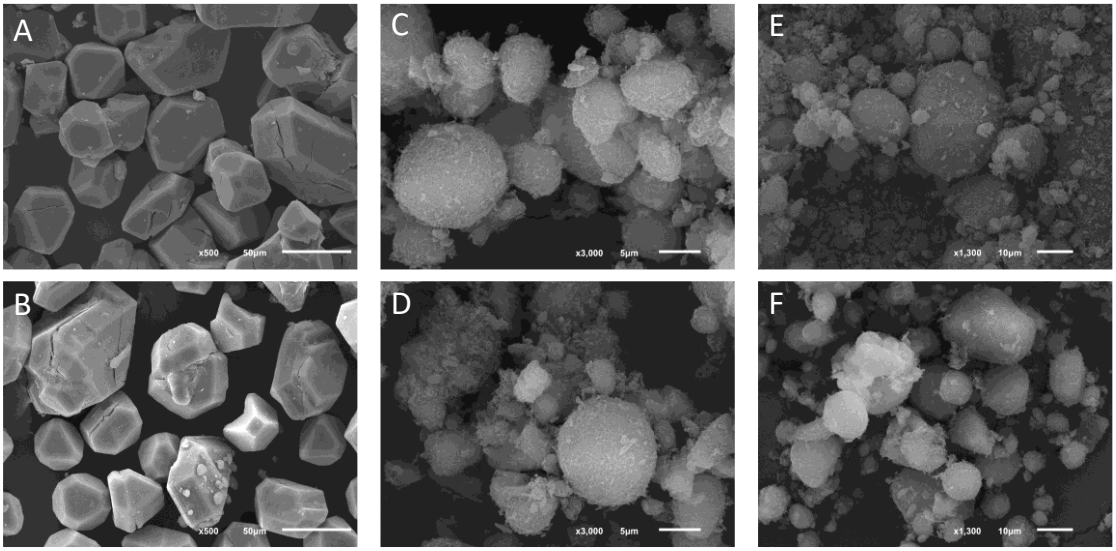


Figure S7. SEM images of the three materials before and after water treatment (100% RH, 24 h). Basolite C300 (A: Before, B: After), Basolite F300 (C: Before, D: After), Basolite A100 (E: Before, F: After). Scale and total magnification are reflected at the bottom of each photograph.

## ENHANCED WATER AND THERMAL STABILITY OF A POLAR MOF (HKUST-1) BY SUPPORTING ON A HYDROPHILIC MATERIAL ($Al_2O_3$)

(Supplementary Information)

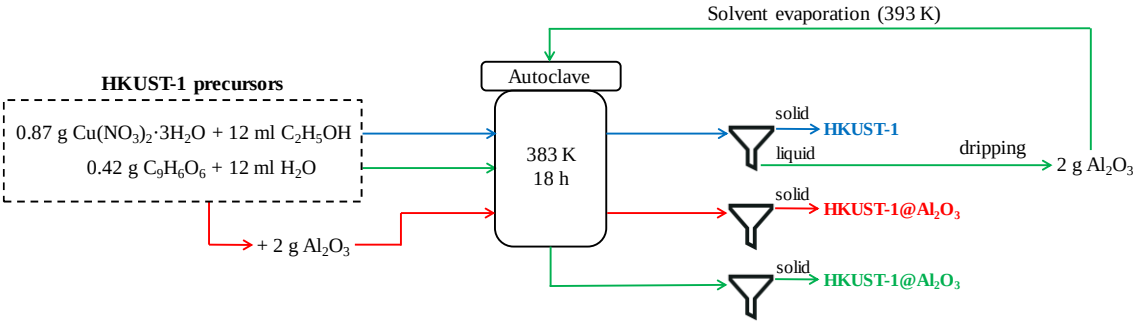


Figure S1. Scheme of the different synthesis routes for HKUST-1 (blue line), HKUST-1@$Al_2O_3$ solvothermal (red line) and HKUST-1@$Al_2O_3$ dip-coating (green line).

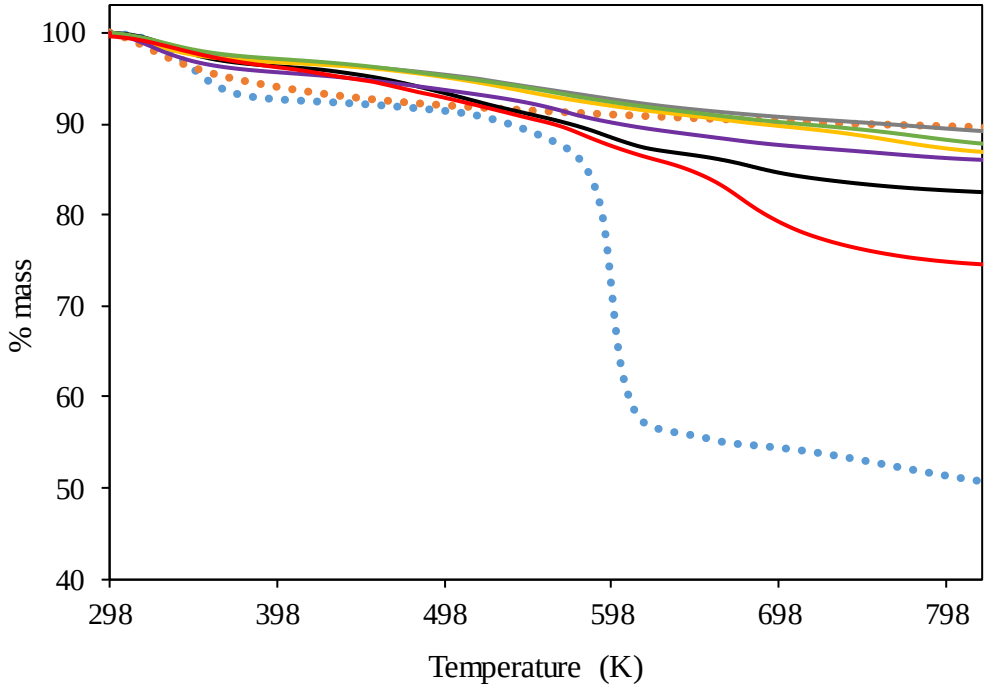


Figure S2. Thermal decomposition of all the materials studied: HKUST-1 (blue broken line), $Al_2O_3$ (orange broken line), $DC_{240}$ (black line), $DC_{100V}$ (grey line), $DC_{240V}$ (yellow line), $S_{240}$ (purple line), $S_{240V}$ (green line), $S_{2400V}$ (red line). Experiments were done under nitrogen flow (40 ml/min, 0.1 MPa) on a thermobalance.

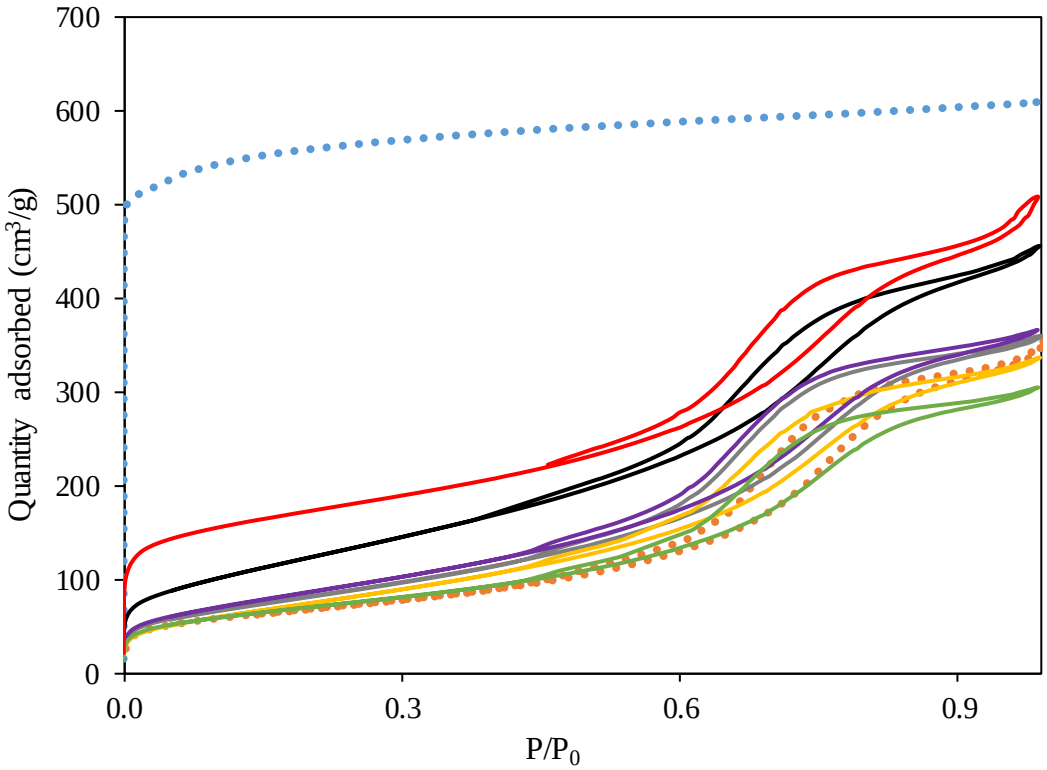


Figure S3. Nitrogen physisorption (77 K) isotherms for all the materials studied: HKUST-1 (blue broken line), $Al_2O_3$ (orange broken line), $DC_{240}$ (black line), $DC_{100V}$ (grey line), $DC_{240V}$ (yellow line), $S_{240}$ (purple line), $S_{240V}$ (green line), $S_{2400V}$ (red line).

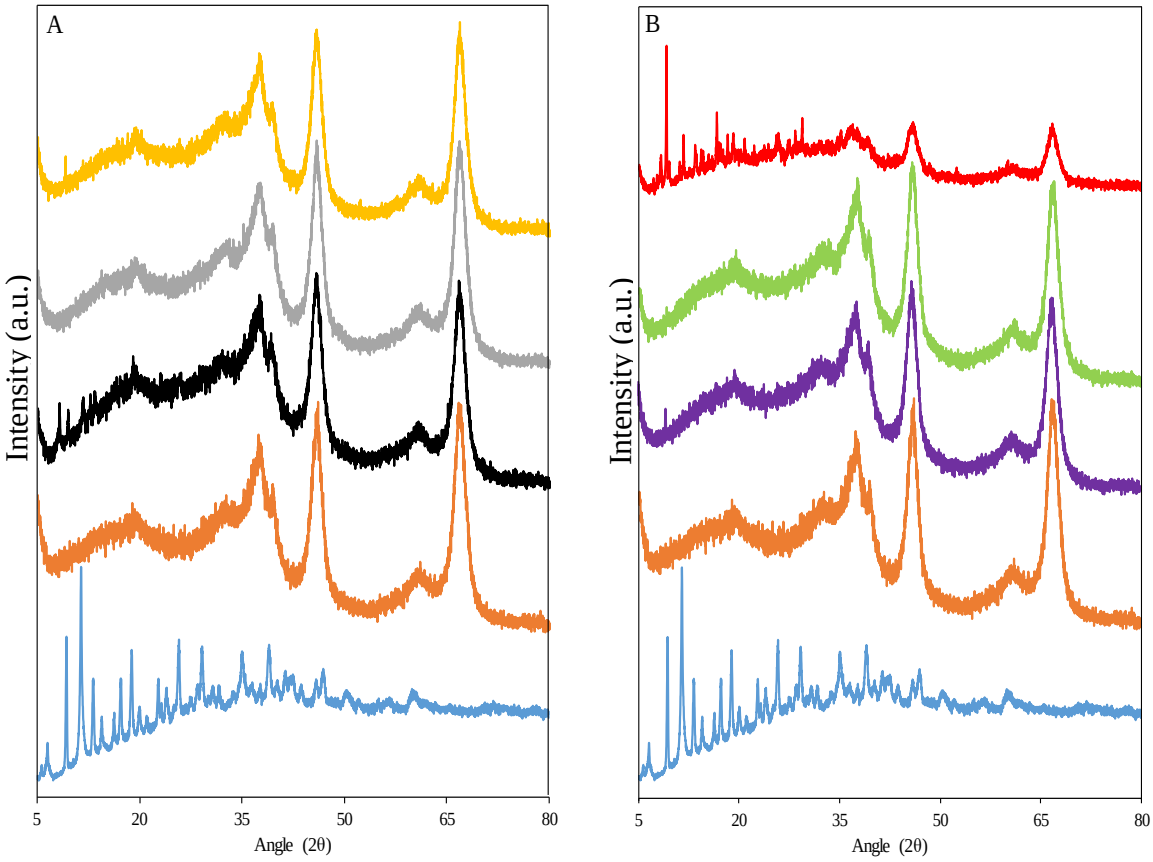


Figure S4. X-ray diffraction patterns for all the composite materials in comparison with HKUST-1 (blue) and $Al_2O_3$ (orange) diffractograms. $DC_{240}$ (black), $DC_{100V}$ (grey), $DC_{240V}$ (yellow), $S_{240}$ (purple), $S_{240V}$ (green), $S_{2400V}$ (red). A: dip-coating composites; B: solvothermal composites.

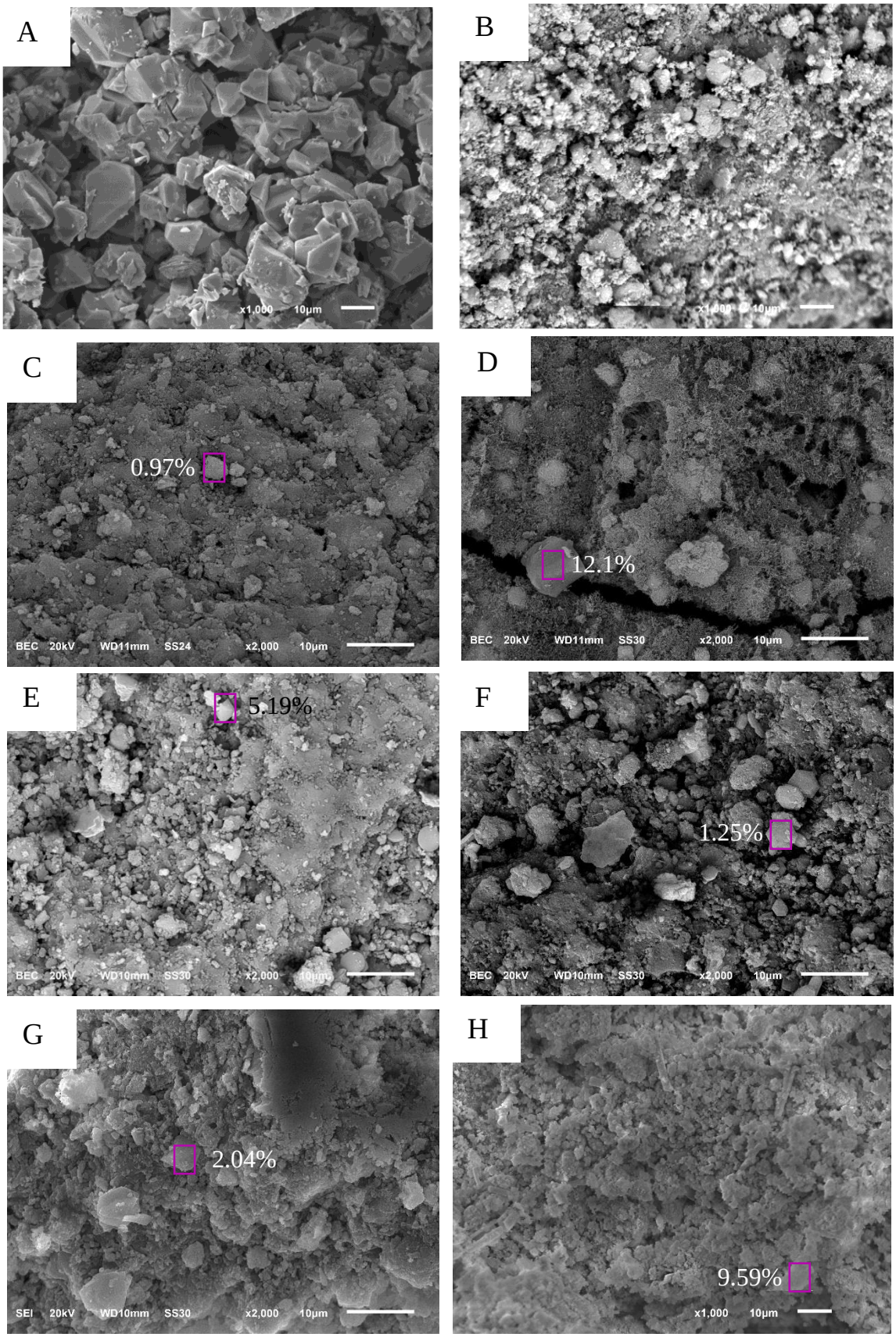


Figure S5. SEM images of all the composites synthesized for comparison with HKUST-1 (A) and $Al_2O_3$ (B). $DC_{100V}$ (C), $DC_{240}$ (D), $DC_{240V}$ (E), $S_{240}$ (F), $S_{240V}$ (G), $S_{2400V}$ (H). Pink rectangles indicate the EDX analysis zone. Next to each rectangle, it is attached the quantity (%) of copper registered.

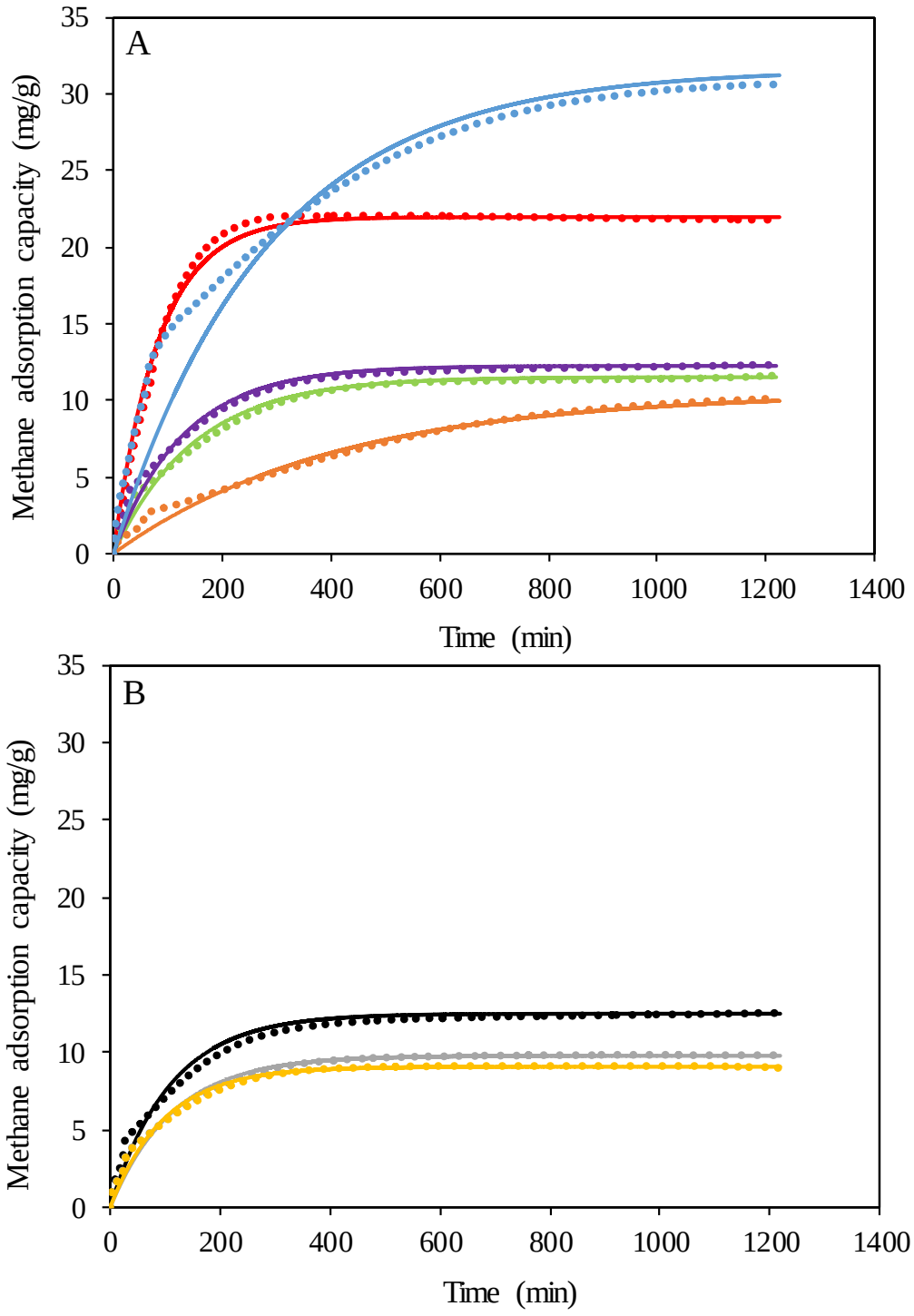


Figure S6. Comparative between experimental methane adsorption isotherms (broken lines) and the Langmuir model (continuous line). A: HKUST-1 (blue), $Al_2O_3$ (orange), $S_{240}$ (purple), $S_{240V}$ (green) and $S_{2400V}$ (red). B: $DC_{100V}$ (grey), $DC_{240}$ (black) and $DC_{240V}$ (yellow).

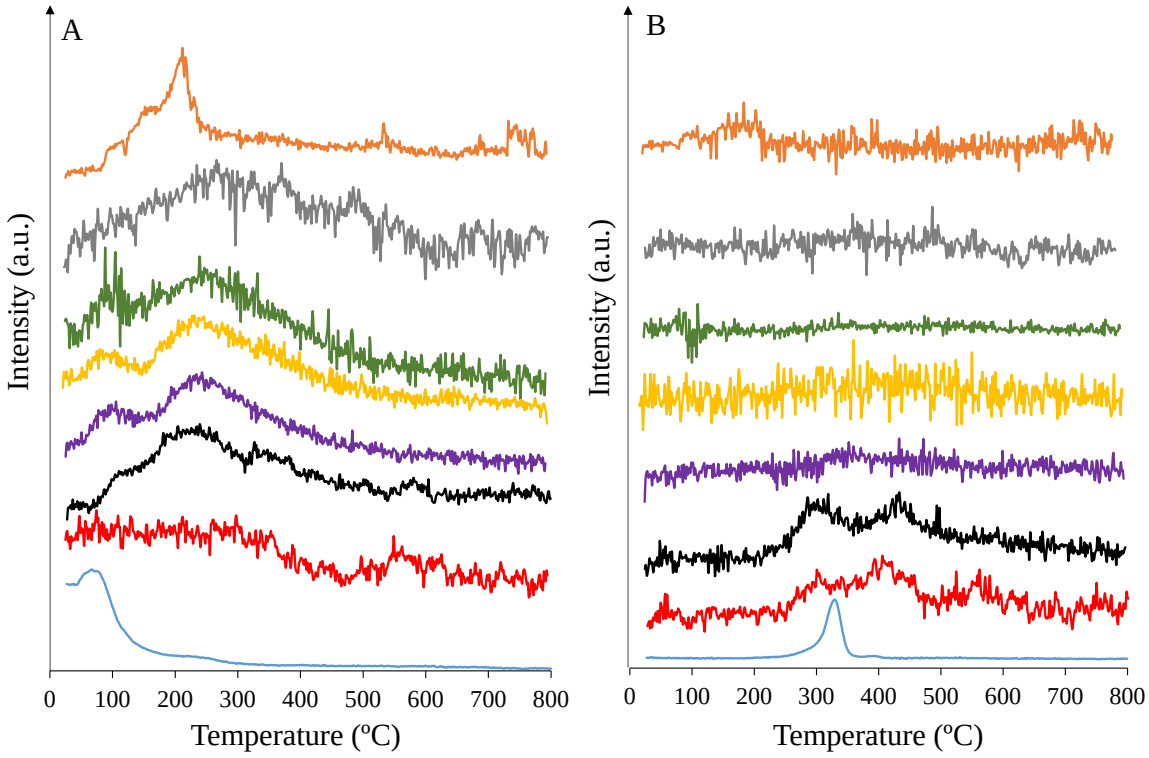


Figure S7. Water (A) and carbon dioxide (B) signal intensities obtained by mass spectroscopy during a thermal treatment ($N_2$, 40 ml/min, 0.1 MPa). HKUST-1 (blue), $Al_2O_3$ (orange), $DC_{240}$ (black), $DC_{100V}$ (grey), $DC_{240V}$ (yellow), $S_{240}$ (purple), $S_{240V}$ (green), $S_{240ooV}$ (red).

**EVALUATION OF HKUST-1 AS VOLATILE ORGANIC COMPOUNDS ADSORBENT FOR RESPIRATORY FILTERS**

(Supplementary Information)

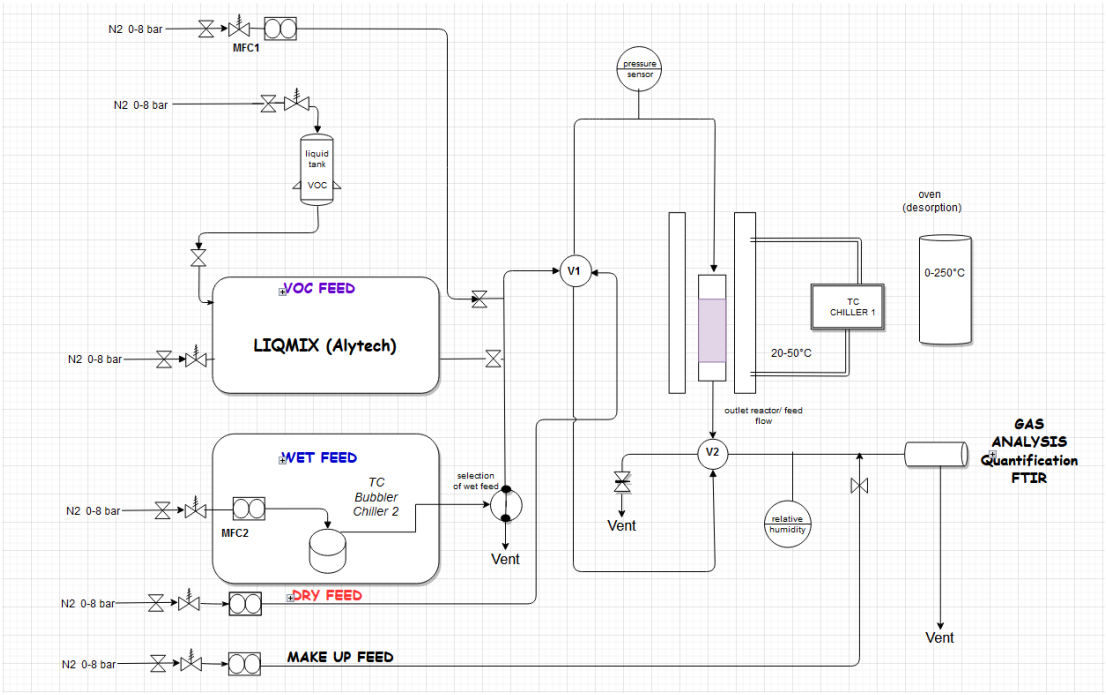


Figure S1. Breakthrough set up diagram flow.

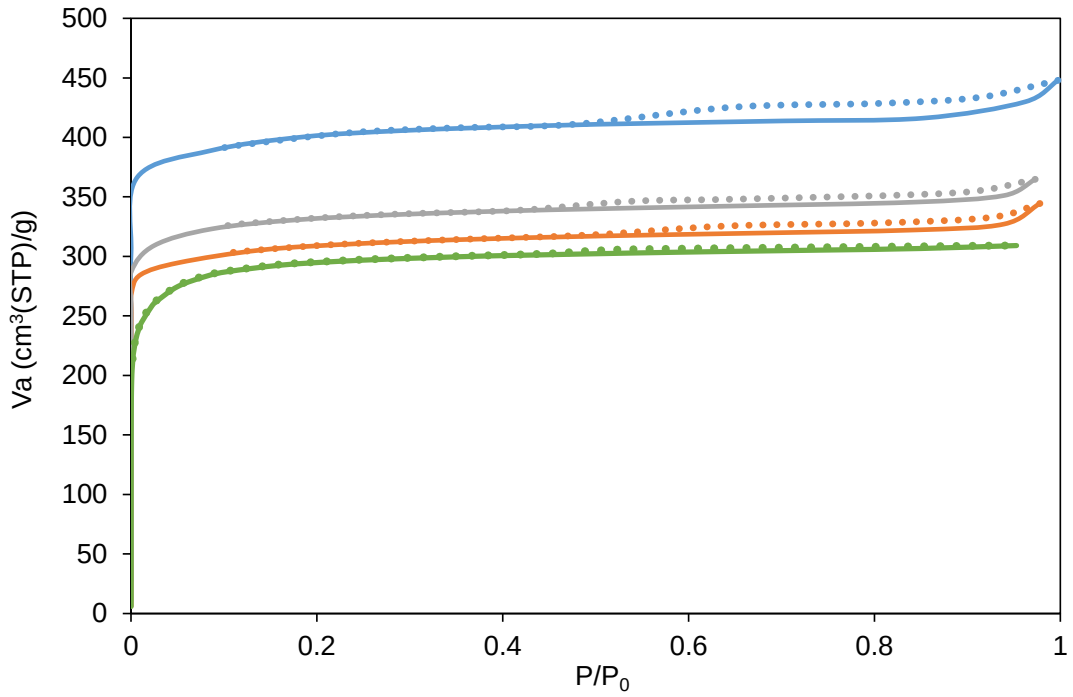


Figure S2. Nitrogen (77 K) adsorption isotherms for all the materials studied (Blue, M1; Orange, M2; grey, M3 and green, C1). Continuous line points out adsorption stage and pointed line, desorption stage.

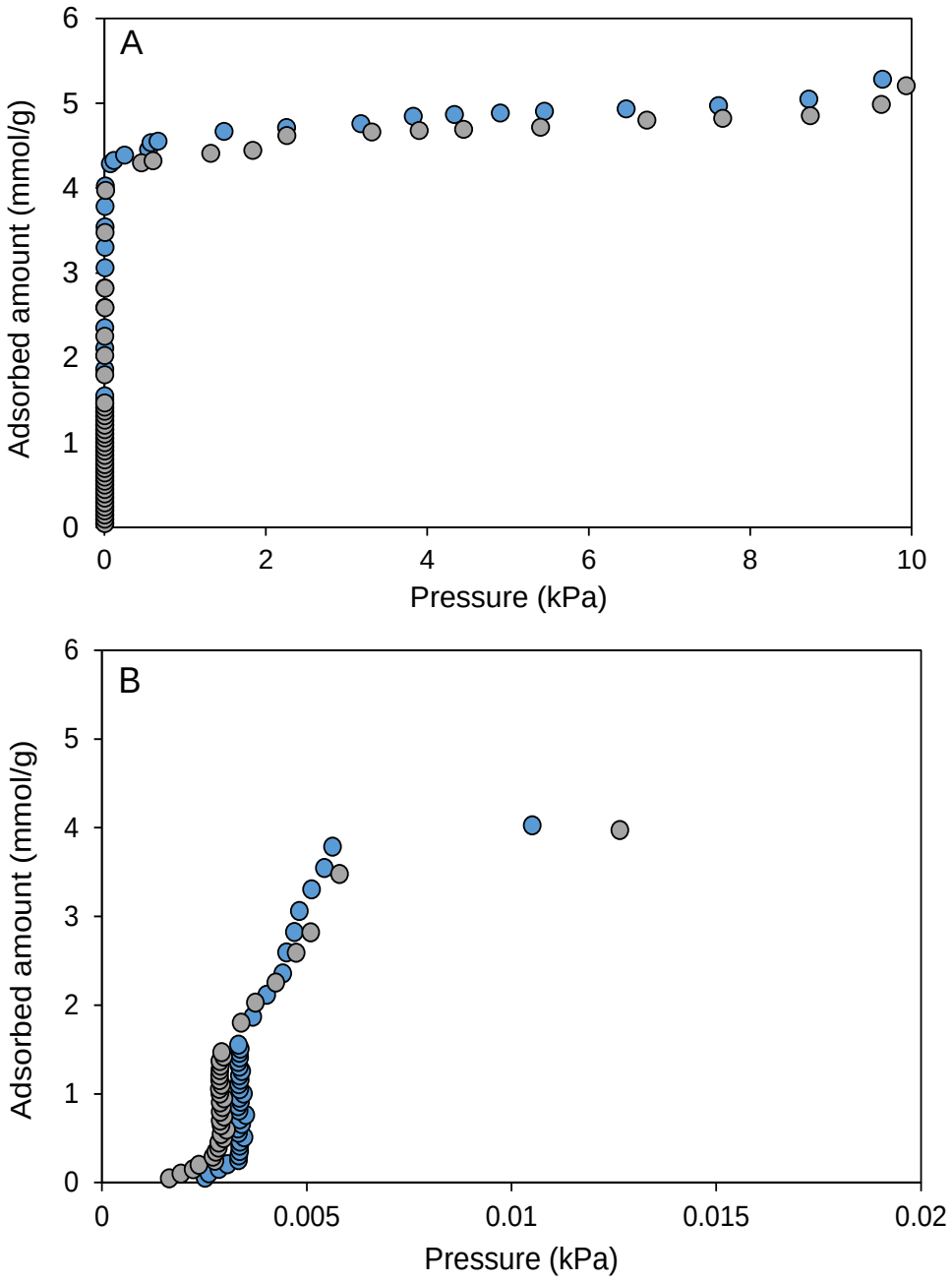


Figure S3. Cyclohexane adsorption isotherms (293 K) for M1 (blue) and M3 (grey). Figure B is an enlargement of Figure A at low pressures.

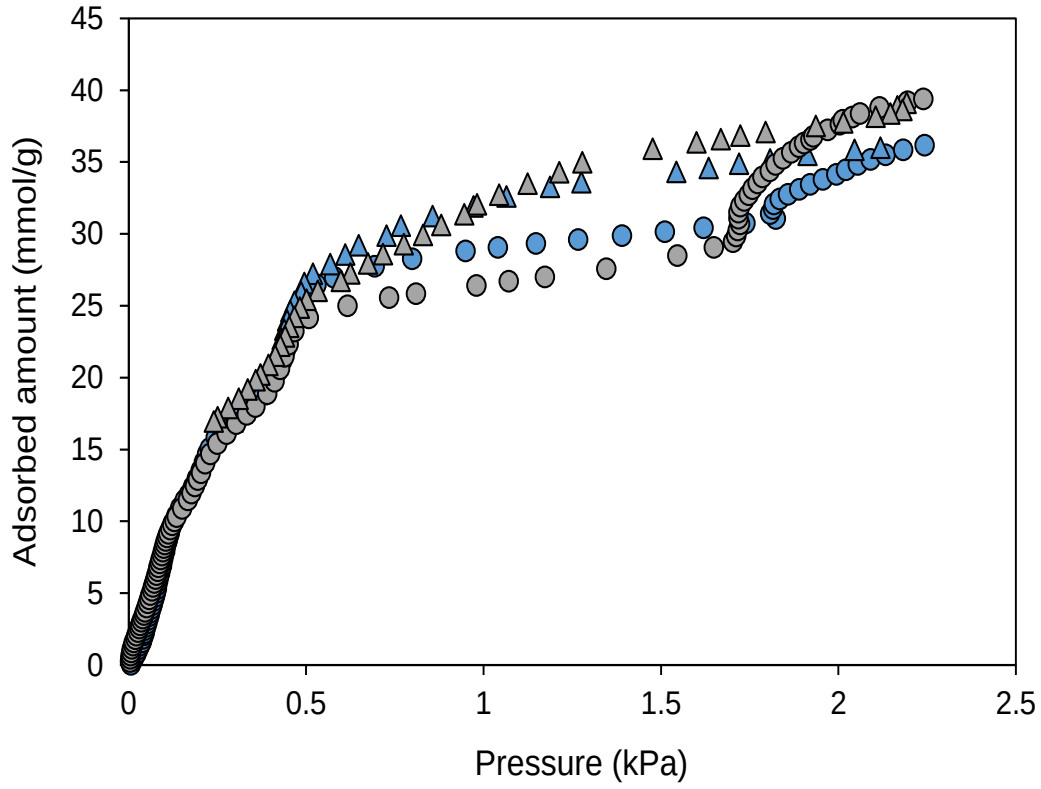


Figure S4. Water adsorption isotherms (293 K) for M1 (blue) and M3 (grey). Circles and triangles point out adsorption and desorption stages, respectively.

Table S1. $C_6H_{12}$ adsorption capacity given by breakthrough versus isotherms at dry conditions.

| | Adsorption capacity (mmol/g) | |
|---|---|---|
| Material | Isotherm (0.5 kPa, 293 K) | Breakthrough $T_{100}$ (0.5 kPa, 293 K) |
| M1 | 4.45 | 5.45 |
| M2 | 3.73 | 3.40 |
| M3 | 4.22 | 4.15 |
| C1 | 2.95 | 3.11 |

Table S2. Cyclohexane breakthrough time at $T_{10}$ for all the materials studied on two different basis, mass and volume.

| Mass basis (min/g) | | | |
|---|---|---|---|
| Material | Dry | 27% RH | 80% RH |
| M1 | 235 | 256 | 217 |
| M2 | 242 | 209 | 152 |
| M3 | 173 | 168 | 170 |
| C1 | 250 | 220 | 208 |
| Volume basis (min/cm$^3$) | | | |
| Material | Dry | 27% RH | 80% RH |
| M1 | 39 | 42 | 36 |
| M2 | 134 | 116 | 84 |
| M3 | 96 | 93 | 94 |
| C1 | 121 | 107 | 101 |

Table S3. Cyclohexane breakthrough adsorption capacity at $T_{10}$ for all the materials studied on two different basis, mass and volume.

| Mass basis (mol/g) | | | |
|---|---|---|---|
| Material | Dry | 27% RH | 80% RH |
| M1 | 0.178 | 0.195 | 0.165 |
| M2 | 0.181 | 0.151 | 0.119 |
| M3 | 0.111 | 0.104 | 0.113 |
| C1 | 0.184 | 0.162 | 0.153 |
| Volume basis (mol/cm$^3$) | | | |
| Material | Dry | 27% RH | 80% RH |
| M1 | 0.030 | 0.033 | 0.028 |
| M2 | 0.099 | 0.083 | 0.065 |
| M3 | 0.061 | 0.057 | 0.062 |
| C1 | 0.090 | 0.078 | 0.074 |